Title
Electrochemistry, Spectroscopy, and Reactivity of Uranium Complexes Supported by Ferrocene Diamide Ligands

Author
Duhovic, Selma

Publication Date
2012

Peer reviewed|Thesis/dissertation

UNIVERSITY OF CALIFORNIA

Los Angeles

Electrochemistry, Spectroscopy, and Reactivity of Uranium Complexes Supported by Ferrocene Diamide Ligands

A dissertation submitted in partial satisfaction of the

requirements for the degree Doctor of Philosophy

in Chemistry

by

Selma Duhovic

2012

ABSTRACT OF THE DISSERTATION

Electrochemistry, Spectroscopy, and Reactivity of Uranium

Complexes Supported by Ferrocene Diamide Ligands

by

Selma Duhovic

Doctor of Philosophy in Chemistry

University of California, Los Angeles, 2012

Professor Paula L. Diaconescu, Chair

This work culminates a systematic study of various uranium complexes supported by ferrocene diamide ligands. **Chapter 1** reports the synthesis of 1,1'-ferrocene diamines and describes their electronic and steric properties in both neutral and oxidized forms. **Chapter 2** describes an efficient synthesis of uranium dialkyl complexes supported by a single 1,1'-ferrocene diamide ligand, while **Chapter 3** explores their reactivity with several aromatic heterocycles. **Chapter 4** focuses on the electrochemical behavior of ferrocene-based uranium halide, alkyl, aryloxide, and amide ligands. Finally, **Chapter 5** explains electrochemical, spectroscopic, and magnetic properties of uranium bis(1,1'-diamidoferrocene) complexes in an attempt to establish how well uranium mediates electronic communication between two iron centers.

The Dissertation of Selma Duhović is approved.

Ohyun Kwon

Yi Tang

Paula L. Diaconescu, Committee Chair

University of California, Los Angeles

2012

To my mother, father, and brother

TABLE OF CONTENTS

LIST OF FIGURES AND CHARTS

CHAPTER 1

CHAPTER 2

CHAPTER 3

CHAPTER 4

CHAPTER 5

LIST OF TABLES

CHAPTER 1

CHAPTER 4

CHAPTER 5

LIST OF SCHEMES

CHAPTER 2

CHAPTER 3

CHAPTER 4

LIST OF ACRONYMS

fc = ferrocene
DCM = dichloromethane
THF = tetrahydrofuran
Et_2O = diethyl ether
TFT = trifluorotoluene
NN^{py} = pyridine-based ligand
NN^{fc} = ferrocene diamide ligand
TMS = trimethylsilyl, $-SiMe_3$
TBS = dimethyl-tert-butyl silyl, $-SiMe_2{}^tBu$
DMP = dimethylphenyl silyl, $-SiMe_2Ph$
MES = mesityl, 2,4,6-$Me_3C_6H_2$
NP = neopentyl, $-CMe_3$
XYL = xylyl, 3,5-$Me_2C_6H_3$
im = methylimidazole
mbi = methylbenzimidazole
pic = picoline
py = pyridine
boz = benzoxazole
btz = benzothiazole
qn = quinoline

ACKNOWLEDGEMENTS

As a graduate student, the most valuable lesson I learned was summed up 18 years ago:

> *Life can be much broader once you discover one simple fact. And that is: everything around you that you call life was made up by people that were no smarter than you. And you can change it, you can influence it, you can build your own things that other people can use. And the minute you understand that you can poke life and actually something will – if you push in – something will pop out the other side, then, you can change it, you can mold it. That's maybe the most important thing, is to shake off this erroneous notion that life is there and you're just going to live in it versus embrace it, change it, improve it, make your mark upon it. I think that's very important. And however you learn that, once you learn it, you'll want to change life and make it better, because it's kind of messed up in a lot of ways. Once you learn that, you'll never be the same again.*
>
> – Steve Jobs

I express my gratitude to my mentors, family, friends, and colleagues.

All the great things that the future has in store for me will have been attributed to my advisor, **Prof. Paula Diaconescu**. Singlehandedly, she has transformed insecure into confident, weak into strong, and institutional into enterprising. Looking back, I realize that my lack of focus, obedience, and discipline required an enormous amount of patience on her part and although I always managed to do something wrong, I have never forgotten all the work she has put into me. No authority in the "real" world will put up with – let alone accommodate – my eccentric and often spoiled disposition as much as she has. Before my advancement to candidacy, she has patiently taught me how to think and work like a scientist. Subsequently, she delegated to me a method that was less than familiar to the group – electrochemistry. Several months after I immersed myself in the task and applied what she has taught me earlier, she came to trust my "expertise" and asked

me to help a senior student with electrochemical analysis. That request alone established a great sense of confidence in my ability to solve a problem. It also strengthened my idealistic mentality and taught me the most valuable lesson that was so nicely expressed by Steve Jobs in 1994.

As my undergraduate academic advisor and my general chemistry professor, **Prof. Kim Lance** was the first person to fuel my interest in the field of inorganic chemistry. He did so mainly by placing emphasis on studying for the sake of learning and not for the sake of getting good grades. My entire life as a student was wasted on caring about the latter and when he put that to shame, Dr. Lance opened up a whole new world for me. He was also among the first people who actively voiced his faith in me. He nudged me to pursue higher education because he believed that I had potential to succeed. I was very hesitant to waste time, money, and effort in the application process because I was convinced I didn't stand a chance of getting accepted to grad school. I remember being especially worried about the GRE but he quickly dispelled my concern by saying "Ohio State has yet to look at my GRE score." To this day, I am fascinated by and grateful for the fact that the direction of my life was forever changed because he believed in me.

Dr. Carolyn Knobler saw me struggle and rooted for me from the very beginning. She always found the time and made the effort to chat with me and I am especially thankful for a single conversation we had in April 2008. She does not know it but that day, I was on my way to Murphy Hall to officially drop out of school. Words cannot express how grateful I am for that conversation.

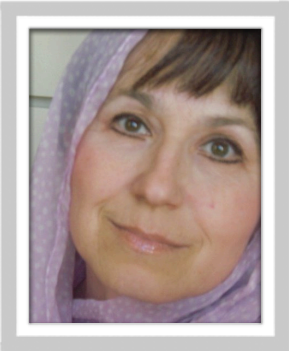
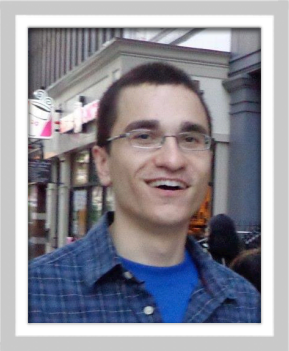

In *The Brook Kerith* by George A. Moore, Jesus states that a man travels the world over in search of what he needs, and returns home to find it. Half way into my decade-long journey, I had the same realization. During those 10 years, my mother, **Emina Duhović**, and brother, **Emir Duhović**, have stood by me every single day. Their courage and optimism never seem to fade and if I possessed an ounce of their strength, I would rule the world. I am especially grateful to my mom for daring to leave behind everything she knew and had, so that my brother and I could take advantage of the opportunities that this nation offers.

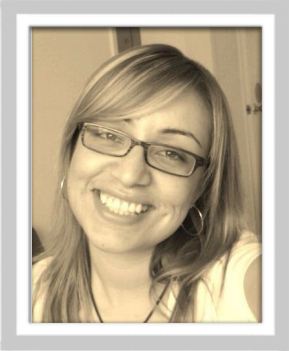


I became convinced that I could not complete this degree unless I focused. That meant I had to make sacrifices. The greatest of those was my social life. **Iris Rauda** and **Lisa Dudek** have been my anchors to the real world. Even when I was deep in the trenches, they remembered me. They remembered to invite me to social gatherings (including my own birthday celebrations) even though they knew very well that my reply would be "I have to go to lab in the morning..." Unsurprisingly and justifiably so, most people gave up on me after they heard that excuse two or three times, so I am thankful to both for not taking my negligence personally. Despite my decision to sacrifice the one thing that makes life worth living, I was able to make two friends for life.



It is of utmost importance that I acknowledge **Kevin Miller**, **Chain Lee** and **James LeVangie**, who have unknowingly dispelled many of my irrational and high-strung thoughts. The carefree view with which they perceive the world and the easy-going demeanor with which they lead their lives have, on numerous occasions, been a saving grace.

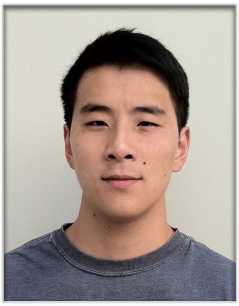

I need to express my gratitude to **Jason Lee**, whose unlikely friendship got me through the last year of my journey. Never has anyone become my confidant so quickly. Except for the time he abandoned me, every hangout was raw, authentic, and fulfilling. I am so happy our paths crossed because it is the closest to Sid I will ever get.

I conclude this section by offering many thanks to the past and current members of the Diaconescu group, my doctoral committee members, and the department staff: Colin Carver, Marisa Monreal, Erin Broderick, Wenliang Huang, Aaron Green, Brianna Upton, Michael Lopez, Jon Brosmer, Jeremy Oria, Stephanie Quan, Kirk Wang, Prof. Ohyun Kwon, Prof. Xiangfeng Duan, Prof. Yi Tang, Dr. Saeed Khan, Dr. Ignacio Martini, Dr. Robert Taylor, Ricky Ruiz, and Joe Rangel.

VITA

EDUCATION

Ohio Wesleyan University, Delaware, OH, USA ..... May 2006
Bachelor of Arts, Chemistry and Psychology
Prof. Kim Lance

RESEARCH EXPERIENCE

University of California, Los Angeles ..... May 2008 – September 2012
Prof. Paula L. Diaconescu
University of California, Los Angeles ..... July 2006 – April 2008
Prof. Omar M. Yaghi
University of Houston ..... June – August 2005
Prof. Allan J. Jacobson

TEACHING EXPERIENCE

University of California, Los Angeles
General and Organic Chemistry 14CL ..... Spring 2012
Prof. Maher Henary
Inorganic and Metalorganic Lab C174 ..... Winter 2012
Prof. Alfred Bacher
Advanced Inorganic Chemistry 172 ..... Fall 2011
Prof. Paula L. Diaconescu
General and Organic Chemistry 14CL ..... Summer 2011
Prof. Maher Henary
Advanced Inorganic Chemistry 172 ..... Spring 2011
Prof. Paula L. Diaconescu
Organometallic Chemistry 207 ..... Winter 2011
Prof. Paula L. Diaconescu
General and Organic Chemistry 14CL ..... Summer, Fall 2010
Prof. Maher Henary
Biochemical Methods I 153L ..... 2009 – 2010
Prof. Steven Kim
General and Organic Chemistry 14BL ..... Summer 2009
Prof. Maher Henary
General Chemistry 30AL ..... Spring 2009
Prof. Maher Henary
Chemical Structure 20A ..... Winter 2009
Prof. Delroy Baugh
General Chemistry 30AL ..... Fall 2008
Prof. Maher Henary
Thermodynamics, Electrochemistry, and Kinetics 14B ..... Summer 2008
Prof. Delroy Baugh
Chemical Structure 20A ..... Summer 2008
Prof. Delroy Baugh
General Chemistry 30AL ..... Spring 2008
Prof. Maher Henary
Intermediate Inorganic Chemistry 171 ..... Winter 2008
Prof. Omar M. Yaghi
General Chemistry 30AL ..... Spring 2007
Prof. Maher Henary
Intermediate Inorganic Chemistry 171 ..... Winter 2007
Prof. Omar M. Yaghi
General Chemistry 30AL ..... Fall 2006
Prof. Maher Henary

HONORS

Ohio Wesleyan University Dean's List 2003, 2005
Ohio Wesleyan University Ralph E. Hall Fellowship 2005
Ohio Wesleyan University Chemistry Faculty Prize 2005
Ohio Wesleyan University Charles H. Schafer Chemistry Scholarship 2004

INTRODUCTION

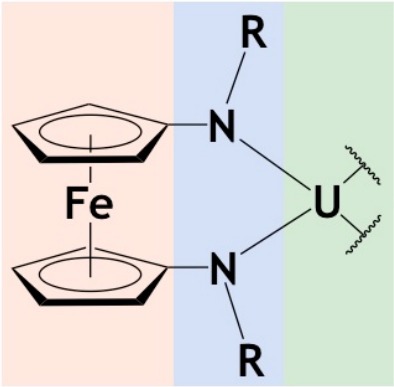

Thomas J. Kealy and Peter L. Pauson in Duquesne University reported[1] the first synthesis of ferrocene in 1951. It is said, however, that using a different procedure, Samuel A. Miller, John A. Tebboth, and John F. Tremaine from the British Oxygen Company synthesized it in 1948 but failed to publish it until 1952.[2] Notwithstanding the true pioneer, many are quick to credit the discovery of this sandwich compound with reviving the organometallic field of chemistry.[3] Since then, countless derivatives of ferrocene have been prepared and extensively characterized.[4] One of those derivatives is the ferrocene diamine, in which various amine substituents are appended to both cyclopentadienyl rings. The traits and properties of ferrocene relevant to this work include the redox activity of the iron center and the specific properties of the organometallic framework. For example, while the ferrocene backbone is a rigid linker when compared to saturated alkyl units, because the Fe-C bonds are weaker than C-C bonds, there is more geometrical flexibility associated with it than is possible with organic aromatic linkers. Additionally, the ferrocene fragment can accommodate changes in the electron density of a metal of interest better than most organic ligands because its frontier orbitals are more likely to match those of other metals.

The use of ferrocene diamides as ancillary ligands as opposed to other donors for uranium is important. Incorporation of nitrogen subtituents provides for a richer electronic

structure than that of ferrocene. Previous studies have established that nitrogen based ligands contribute energetically low-lying orbitals that can enhance covalent metal-ligand interactions involving 5f orbitals.[5] Depending on the substituents on the nitrogen atoms, both electron density and steric bulk of the overall ligand can be tuned without necessarily changing the coordination sphere of the metal center. These electronic and geometric changes can then impart enhanced activity to the uranium center.

As an early actinide element, uranium is considered a hard Lewis acid. Its coordination chemistry is analogous to that of transition metals, but what distinguishes uranium from them is that its valence electrons reside in f orbitals.[6] Unlike the 4f and 5d orbitals of lanthanides, both 5f and 6d orbitals of uranium are actually less contracted and can have better overlap with ligand-based orbitals.[7] Another distinction is that the greater number of valence orbitals (seven f orbitals vs. five d orbitals for transition metals) allows uranium to support more types of coordination modes. Additionally, uranium can access a wide range of oxidation states that are typically less accessible to transition metals. For example, uranium complexes are known for each oxidation state from +3 to +6.

All the characteristics described above lead to a unique behavior for uranium compounds, and its potential to catalyze a remarkable range of transformations has clearly been exposed in the last couple of decades.[8] Organouranium compounds have been shown to participate in a variety of processes, including activation of small molecules, such as H_2,[9, 10] N_2,[11-13] CO,[14-16] and CO_2,[17-20] activation of elemental sulfur, selenium, and tellerium[21] as well as white phosphorus,[22] activation of azides,[23-25] hydrazines,[26] amines,[27, 28] alkanes,[29] alkynes,[30] and aromatic heterocycles,[31-34] as well as hydroamination and hydrosilylation.[35, 36] It is not surprising then that chemists in both basic and applied disciplines have become increasingly interested in and focused on the reactivity and application of uranium complexes.

Research described in this dissertation was prefaced and influenced by the initial work of Marisa Monreal, who described her findings between 2007 and 2010. These reports not only provided structural and theoretical evidence for the existence and nature of a weak interaction between uranium and iron,[37, 38] but also revealed that, with the support of a ferrocene diamide ligand, uranium was capable of mediating double C-H activation, as well as coupling, ring-opening, and migratory insertion.[33, 34]

What follows is a description of 1,1'-ferrocene diamines (Chapter 1), synthesis (Chapter 2) and reactivity (Chapter 3) of uranium alkyl complexes supported by them, electrochemical properties of iodide, aryloxide, and diphenylamide analogues (Chapter 4), and electronic communication between Fe^{2+} and Fe^{3+} centers in bis(1,1'-ferrocenediamide) uranium complexes (Chapter 5).

REFERENCES

1. Kealy, T. J.; Pauson, P. L., A New Type of Organo-Iron Compound. *Nature* **1951,** 168, (4285), 1039-1040.

2. Miller, S. A.; Tebboth, J. A.; Tremaine, J. F., Dicyclopentadienyliron. *J. Chem. Soc.* **1952**, 632-635.

3. Astruc, D., History of Organometallic Chemistry
Organometallic Chemistry and Catalysis. In Springer Berlin Heidelberg: 2007; pp 5-20.

4. Togni, A.; Hayashi, T., *Ferrocenes: Homogeneous Catalysis, Organic Synthesis, Materials Science*. John Wiley & Sons: 2008.

5. Morris, D. E.; Da Re, R. E.; Jantunen, K. C.; Castro-Rodriguez, I.; Kiplinger, J. L., Trends in Electronic Structure and Redox Energetics for Early-Actinide Pentamethylcyclopentadienyl Complexes. *Organometallics* **2004,** 23, (22), 5142-5153.

6. Kaltsoyannis, N.; Scott, P., *The f elements*. Oxford University Press: 1999.

7. Kaltsoyannis, N.; Hay, P. J.; Li, J.; Blaudeau, J.-P.; Bursten, B. E., Theoretical Studies of the Electronic Structure of Compounds of the Actinide Elements. In *The Chemistry of the Actinide and Transactinide Elements*, Morss, L. R.; Edelstein, N. M.; Fuger, J., Eds. Springer Netherlands: 2011; pp 1893-2012.

8. Fox, A. R.; Bart, S. C.; Meyer, K.; Cummins, C. C., Towards uranium catalysts. *Nature* **2008,** 455, (7211), 341-349.

9. Evans, W. J.; Miller, K. A.; Kozimor, S. A.; Ziller, J. W.; DiPasquale, A. G.; Rheingold, A. L., Actinide Hydride Complexes as Multielectron Reductants: Analogous Reduction Chemistry from $[(C_5Me_5)_2UH]_2$, $[(C_5Me_5)_2UH_2]_2$, and $[(C_5Me_5)_2ThH_2]_2$. *Organometallics* **2007,** 26, (14), 3568-3576.

10. Fagan, P. J.; Manriquez, J. M.; Maatta, E. A.; Seyam, A. M.; Marks, T. J., Synthesis and properties of bis(pentamethylcyclopentadienyl) actinide hydrocarbyls and hydrides. A new class of highly reactive f-element organometallic compounds. *J. Am. Chem. Soc.* **1981,** 103, (22), 6650-6667.

11. Korobkov, I.; Gambarotta, S.; Yap, G. P. A., A Highly Reactive Uranium Complex Supported by the Calix[4]tetrapyrrole Tetraanion Affording Dinitrogen Cleavage, Solvent Deoxygenation, and Polysilanol Depolymerization. *Angew. Chem. Int. Ed.* **2002,** 41, (18), 3433-3436.

12. Cloke, F. G. N.; Hitchcock, P. B., Reversible Binding and Reduction of Dinitrogen by a Uranium(III) Pentalene Complex. *J. Am. Chem. Soc.* **2002,** 124, (32), 9352-9353.

13. Roussel, P.; Scott, P., Complex of Dinitrogen with Trivalent Uranium. *J. Am. Chem. Soc.* **1998,** 120, (5), 1070-1071.

14. Parry, J.; Carmona, E.; Coles, S.; Hursthouse, M., Synthesis and Single Crystal X-ray Diffraction Study on the First Isolable Carbonyl Complex of an Actinide, $(C_5Me_4H)_3U(CO)$. *J. Am. Chem. Soc.* **1995,** 117, (9), 2649-2650.

15. Summerscales, O. T.; Cloke, F. G. N.; Hitchcock, P. B.; Green, J. C.; Hazari, N., Reductive Cyclotetramerization of CO to Squarate by a U(III) Complex: The X-ray Crystal Structure of $[(U(\eta\text{-}C_8H_6\{Si^iPr3\text{-}1,4\}_2)(\eta\text{-}C_5Me_4H)]_2(\mu\text{-}\eta^2\text{:}\ \eta^2\text{-}C_4O_4)$. *J. Am. Chem. Soc.* **2006,** 128, (30), 9602-9603.

16. Brennan, J. G.; Andersen, R. A.; Robbins, J. L., Preparation of the first molecular carbon monoxide complex of uranium, $(Me_3SiC_5H_4)_3UCO$. *J. Am. Chem. Soc.* **1986,** 108, (2), 335-336.

17. Mansell, S. M.; Kaltsoyannis, N.; Arnold, P. L., Small Molecule Activation by Uranium Tris(aryloxides): Experimental and Computational Studies of Binding of N_2, Coupling of CO, and Deoxygenation Insertion of CO_2 under Ambient Conditions. *J. Am. Chem. Soc.* **2011,** 133, (23), 9036-9051.

18. Castro-Rodriguez, I.; Nakai, H.; Zakharov, L. N.; Rheingold, A. L.; Meyer, K., A Linear, O-Coordinated η^1-CO_2 Bound to Uranium. *Science* **2004,** 305, (5691), 1757-1759.

19. Lam, O. P.; Anthon, C.; Meyer, K., Influence of Steric Pressure on the Activation of Carbon Dioxide and Related Small Molecules by Uranium Coordination Complexes. *Dalton Transactions* **2009**, (44), 9677-9691.

20. Berthet, J.-C.; Le Maréchal, J.-F.; Nierlich, M.; Lance, M.; Vigner, J.; Ephritikhine, M., Synthesis and crystal structure of the oxo-bridged bimetallic organouranium complex $[(Me_3SiC_5H_4)_3U]_2[\mu\text{-}O]$. *J. Organomet. Chem.* **1991,** 408, (3), 335-341.

21. Lam, O. P.; Heinemann, F. W.; Meyer, K., Activation of elemental S, Se and Te with uranium(III): bridging U-E-U (E = S, Se) and diamond-core complexes U-$(E)_2$-U (E = O, S, Se, Te). *Chemical Science* **2011,** 2, (8), 1538-1547.

22. Frey, A. S. P.; Cloke, F. G. N.; Hitchcock, P. B.; Green, J. C., Activation of P_4 by $U(\eta^5\text{-}C_5Me_5)(\eta^8\text{-}C_8H_6(Sii Pr_3)_2\text{-}1,4)(THF)$; the X-ray structure of $[U(\eta^5\text{-}C_5Me_5)(\eta^8\text{-}C_8H_6(Sii Pr_3)_2\text{-}1,4)]_2(\mu\text{-}\eta^2\text{:}\eta^2\text{-}P_4)$. *New J. Chem.* **2011,** 35, (10), 2022-2026.

23. Evans, W. J.; Kozimor, S. A.; Ziller, J. W., Molecular Octa-Uranium Rings with Alternating Nitride and Azide Bridges. *Science* **2005,** 309, (5742), 1835-1838.

24. Brennan, J. G.; Andersen, R. A., Electron-transfer reactions of trivalent uranium. Preparation and structure of the uranium metallocene compounds $(MeC_5H_4)_3U$–NPh and $[(MeC_5H_4)_3U]_2[\mu\text{-}\eta^1,\eta^2\text{-}PhNCO]$. *J. Am. Chem. Soc.* **1985,** 107, (2), 514-516.

25. Warner, B. P.; Scott, B. L.; Burns, C. J., A Simple Preparative Route to Bis(imido)uranium(VI) Complexes by the Direct Reductions of Diazenes and Azides. *Angew. Chem. Int. Ed.* **1998,** 37, (7), 959-960.

26. Peters, R. G.; Warner, B. P.; Burns, C. J., The Catalytic Reduction of Azides and Hydrazines Using High-Valent Organouranium Complexes. *J. Am. Chem. Soc.* **1999,** 121, (23), 5585-5586.

27. Hayton, T. W.; Boncella, J. M.; Scott, B. L.; Batista, E. R., Exchange of an Imido Ligand in Bis(imido) Complexes of Uranium. *J. Am. Chem. Soc.* **2006,** 128, (39), 12622-12623.

28. Hayton, T. W.; Boncella, J. M.; Scott, B. L.; Batista, E. R.; Hay, P. J., Synthesis and Reactivity of the Imido Analogues of the Uranyl Ion. *J. Am. Chem. Soc.* **2006,** 128, (32), 10549-10559.

29. Kiplinger, J. L.; Scott, B. L.; Schelter, E. J.; Pool Davis Tournear, J. A., sp^3 versus sp^2 C-H Bond Activation Ahemistry of 2-picoline by Th(IV) and U(IV) Metallocene Complexes. *J. Alloys Compd.* **2007,** 444-445, 477-482.

30. Smith, G. M.; Carpenter, J. D.; Marks, T. J., Intramolecular vs. intermolecular alkyl carbon-hydrogen bond activation. Complete thermodynamic and kinetic parameters for a reversible cyclometalation. *J. Am. Chem. Soc.* **1986,** 108, (21), 6805-6807.

31. Duhović, S.; Monreal, M. J.; Diaconescu, P. L., Reactions of Aromatic Heterocycles with Uranium Alkyl Complexes. *Inorg. Chem.* **2010,** 49, (15), 7165-7169.

32. Duhović, S.; Monreal, M. J.; Diaconescu, P. L., Ring opening of aromatic heterocycles by uranium complexes. *J. Organomet. Chem.* **2010,** 695, (25-26), 2822-2826.

33. Monreal, M. J.; Diaconescu, P. L., Reversible C–C Coupling in a Uranium Biheterocyclic Complex. *J. Am. Chem. Soc.* **2010,** 132, (22), 7676-7683.

34. Monreal, M. J.; Khan, S.; Diaconescu, P. L., Beyond C-H Activation with Uranium: A Cascade of Reactions Mediated by a Uranium Dialkyl Complex. *Angew. Chem. Int. Ed.* **2009,** 48, (44), 8352-8355.

35. Haskel, A.; Straub, T.; Eisen, M. S., Organoactinide-Catalyzed Intermolecular Hydroamination of Terminal Alkynes. *Organometallics* **1996,** 15, (18), 3773-3775.

36. Broderick, E. M.; Gutzwiller, N. P.; Diaconescu, P. L., Inter- and Intramolecular Hydroamination with a Uranium Dialkyl Precursor. *Organometallics* **2010,** 29, (15), 3242-3251.

37. Monreal, M. J.; Carver, C. T.; Diaconescu, P. L., Redox Processes in a Uranium Bis(1,1'-diamidoferrocene) Complex. *Inorg. Chem.* **2007,** 46, (18), 7226-7228.

38. Monreal, M. J.; Diaconescu, P. L., A Weak Interaction between Iron and Uranium in Uranium Alkyl Complexes Supported by Ferrocene Diamide Ligands. *Organometallics* **2008,** 27, (8), 1702-1706.

CHAPTER 1

An Experimental and Computational Study of 1,1'-Ferrocene Diamines

TABLE OF CONTENTS

1.1 INTRODUCTION

Its unintentional discovery in 1951[1, 2] has led to the rebirth of organometallic chemistry and perhaps no other compound is more synonymous with that field than ferrocene. Because of its versatility, ferrocene has intrigued chemists for over 60 years. Its derivatives have found applications in fields ranging from petrochemistry[3-5] to medicine.[6-9] The use of ferrocene derivatives in our group stems from our interest in ligands with electronic and steric properties capable of influencing bonding and enhancing reactivity of transition metals, lanthanides, and actinides.[10-20] More specifically, our group works with chelating 1,1'-

diamidoferrocene ligands, which, as a result of their redox activity, are capable of accommodating both electronic and steric changes of metals in various oxidation states.[21, 22] In order to examine the interaction between iron and those metal centers, we first set out to study systematically how the modification of nitrogen substituents changes both structural and functional aspects of 1,1'-ferrocene diamines (**Chart 1.1**). This chapter details our experimental and theoretical findings.

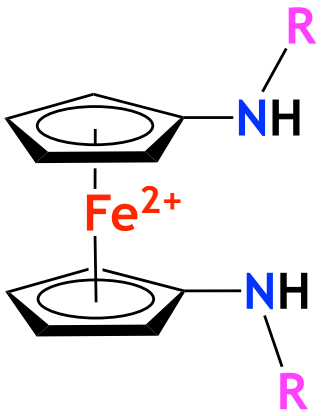

R =	
H	H_2NN^H
$SiMe_3$	H_2NN^{TMS}
$SiMe_2{}^tBu$	H_2NN^{TBS}
$SiMe_2Ph$	H_2NN^{DMP}
$CH_2{}^tBu$	H_2NN^{NPL}
3,5-$Me_2C_6H_3$	H_2NN^{XYL}
2,4,6-$Me_3C_6H_2$	H_2NN^{MES}

Chart 1.1. 1,1'-ferrocene diamines.

1.2 DISCUSSION OF EXPERIMENTAL RESULTS

1.2.1 Cyclic voltammetry

Because the oxidation state of iron affects the reactivity of metal complexes supported by disubstituted ferrocene ligands, understanding the basic electrochemical properties of 1,1'-ferrocene diamines will ultimately enable us to enhance that reactivity through rational design. The most fundamental behavior of ferrocene-based ligands is their reversible oxidation. Cyclic voltammetry experiments were conducted in THF solutions of tetrabutylammonium hexafluorophosphate ($TBAPF_6$) using a platinum disk as the working electrode.

All 1,1'-ferrocene diamines exhibit one quasi-reversible redox event and are more easily oxidized than the parent ferrocene (**Figure 1.1**). This decrease in oxidation potential is

expected because the electron-donating ability of the amino substituents can stabilize the positive charge on iron upon oxidation. Taking only electronic factors into account, the oxidation potential of H_2NN^{TBS} should have the greatest negative shift because *tert*-butyl is a better electron donor than either a methyl or phenyl substituent. Similarly, the oxidation potential of H_2NN^{MES} should have the smallest shift because mesityl is less electron donating than all three silyl substituents. Although the observed order deviates from the expected trend based solely on electronic factors, the difference between the redox potentials is insignificant.

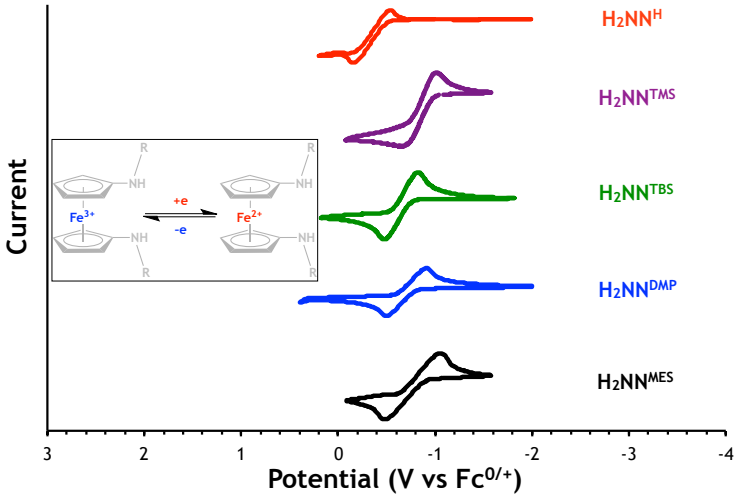

Figure 1.1. Cyclic voltammetry of 1,1'-ferrocene diamines in THF solutions of $TBAPF_6$ at 50 mV/s.

The calculated value of the oxidation potential of ferrocene (0.89 V vs SCE) is in good agreement with the experimental data (0.80 V[23]). While the same method correctly predicts lower oxidation potentials for 1,1'-ferrocene diamines relative to the parent compound, the magnitude of the difference as well as the relative order within the series are not consistent with experimental data (**Table 1.1**). For example, cyclic voltammetry measurements reveal that the oxidation potential follows the order fc > H_2NN^{TBS} > H_2NN^{DMP} > H_2NN^{MES} > H_2NN^{TMS}, while the calculations show fc > H_2NN^{DMP} > H_2NN^{MES} > H_2NN^{TMS} > H_2NN^{TBS}. The trend predicted by calculations follows that based on electronic effects. Since both the calculated and

experimental differences between all amines are small, it is possible that the changes are a consequence of solvent and/or steric effects.

Table 1.1. Experimental and calculated (in THF, PCM method) oxidation potentials of 1,1'-ferrocene diamines.

Oxidation Potential			
	Experimental		Calculated
	(V vs $Fc^{0/+}$)	*(V vs SCE)*	*(V vs SCE)*
H_2NN^{H}	-0.62	-	-
H_2NN^{TBS}	-0.69	-1.57	-1.47
H_2NN^{DMP}	-0.70	-1.58	-1.43
H_2NN^{MES}	-0.72	-1.60	-1.43
H_2NN^{TMS}	-0.73	-1.61	-1.46

1.2.2 Electronic Absorption Spectroscopy

The absorption spectrum of ferrocene contains two bands in the UV-Vis region, both corresponding to spin-allowed d-d transitions.[24-27] As shown in **Figure 1.2**, the absorption spectra of all 1,1'-ferrocene diamines exhibit one band centered between 447 and 452 nm. That this red shift is very small is expected because the electronic transition that occurs at this energy involves the orbitals of relatively pure metal character and thus should be essentially insensitive to the substitution of the cyclopentadienyl rings.[24, 28] The intensity of these forbidden transitions, however, is greater than that observed for the parent ferrocene. Furthermore, an intense shoulder is observed below 280 nm (ε = 5000 $M^{-1}cm^{-1}$) and is likely due to ligand-to-metal charge transfer.[25]

Ferrocenium exhibits several bands in the UV and visible regions. For example, a band centered at 617 nm (ε = 450 $M^{-1}cm^{-1}$) is sensitive to ligand substitution and has therefore been attributed to ligand-to-metal charge transfer. More specifically, it corresponds to a symmetry-allowed excitation from a ligand-based e_{1u} to the iron-based e_{2g} (HOMO) orbital.[26, 29] Similarly, bands centered at 283 nm (ε = 9700 $M^{-1}cm^{-1}$), 250 nm (ε = 15900 $M^{-1}cm^{-1}$) and 198

nm (ε = 14200 $M^{-1}cm^{-1}$) have been assigned to a single excitation from the ligand-based $1e_{2u}$ orbital to the iron-based $2e_{1g}$ orbital.[26] Finally, four weak bands between 565 nm and 380 nm (ε = 150-350 $M^{-1}cm^{-1}$) have been attributed to spin-allowed d-d transitions.[26]

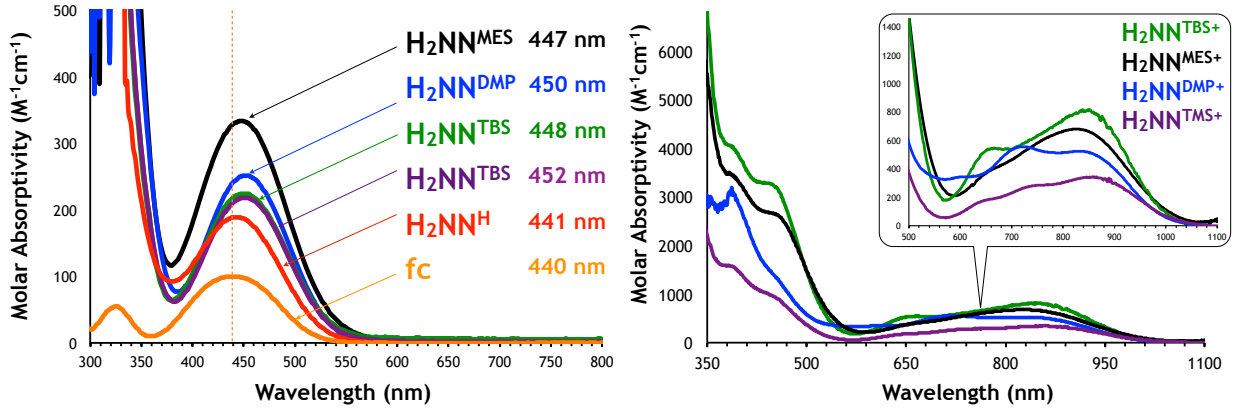

Figure 1.2. UV-Vis spectra of neutral (left) and oxidized (right) 1,1'-ferrocene diamines.

Absorption spectra of amine-substituted ferrocenium derivatives exhibit one broad band in the visible-near IR. On closer inspection, it becomes obvious that the former is actually a convolution of more than one band. For example, **H_2NN^{TMS+}** appears to contain three bands at 642 nm (ε = 165 $M^{-1}cm^{-1}$), 733 nm (ε = 275 $M^{-1}cm^{-1}$), and 856 nm (ε = 343 $M^{-1}cm^{-1}$), while **H_2NN^{TBS+}** features two bands centered at 659 nm (ε = 544 $M^{-1}cm^{-1}$) and 847 (ε = 809 $M^{-1}cm^{-1}$). Similarly, the visible-near IR region in the spectrum of **H_2NN^{DMP+}** exhibits three bands at 595 (ε = 340 $M^{-1}cm^{-1}$), 716 nm (ε = 554 $M^{-1}cm^{-1}$), and 838 (ε = 523 $M^{-1}cm^{-1}$), while **H_2NN^{MES+}** shows two at 643 (ε = 351 $M^{-1}cm^{-1}$) and 825 (ε = 679 $M^{-1}cm^{-1}$). Based on the assignment of the parent ferrocenium, it is likely that the bands in the visible-near IR region correspond to charge transfer from various Cp ligands to Fe^{3+} and spin-allowed d-d transitions. The latter are expected to have different energies as those in the unsubstituted cation due to different symmetries.[30] Similarly, relative to the parent compound, appearance of ligand-to-metal charge transfer bands at lower energies is consistent with electrochemical measurements described previously. Without further investigation, we hesitate to issue more specific

assignments of these bands. That is, distinguishing between spin-allowed d-d transitions and charge transfer bands is difficult because, according to the electrochemical measurements described previously, the latter are not expected to differ drastically across the substituent series.

Finally, two strong bands in the UV-visible region are also apparent in the spectra of 1,1'-ferrocenium diamines (**Figure 1.2**). More specifically, these bands are centered at 451 nm (ε = 945 $M^{-1}cm^{-1}$) and 379 nm (ε = 1584 $M^{-1}cm^{-1}$) in $\mathbf{H_2NN^{TMS+}}$, 445 nm (ε = 3270 $M^{-1}cm^{-1}$) and 383 nm (ε = 4070 $M^{-1}cm^{-1}$) in $\mathbf{H_2NN^{TBS+}}$, 446 nm (ε = 2673 $M^{-1}cm^{-1}$) and 379 nm (ε = 3471 $M^{-1}cm^{-1}$) in $\mathbf{H_2NN^{MES+}}$, and 447 nm (ε = 1444 $M^{-1}cm^{-1}$) and 387 nm (ε = 3195 $M^{-1}cm^{-1}$) in $\mathbf{H_2NN^{DMP+}}$. The origin of these bands is uncertain. No change in absorption energy is apparent when the substituent changes, suggesting that the transition occurs within the iron core. However, the argument against d-d transitions is obvious when the intensity of each absorption band is taken into consideration. Together with electrochemical results described in the previous section (i.e. difference between substituents' electron-donating abilities is negligible), these absorption intensities suggest that ligand-to-metal charge transfer gives rise to both high-energy bands.

1.2.3 Vibrational Spectroscopy

In order to gain further insight into the electronic structures, we studied the infrared spectra of each 1,1'-ferrocene diamine in both neutral and oxidized states, then used computational methods to facilitate the interpretation of the major vibrational modes. It is important to mention that the calculations were performed for structures in the gas phase, and in case of oxidized species, the counter anions were excluded. Consequently, the calculated bands are systematically shifted from those observed experimentally. Additionally,

both the extent of shifting and the band intensities were dependent on the basis set. For example, as shown in **Figure 1.3** for ferrocene, inclusion of polarization functions on all atoms in the computational method (6-31G*) yielded better agreement with the experimental spectrum.

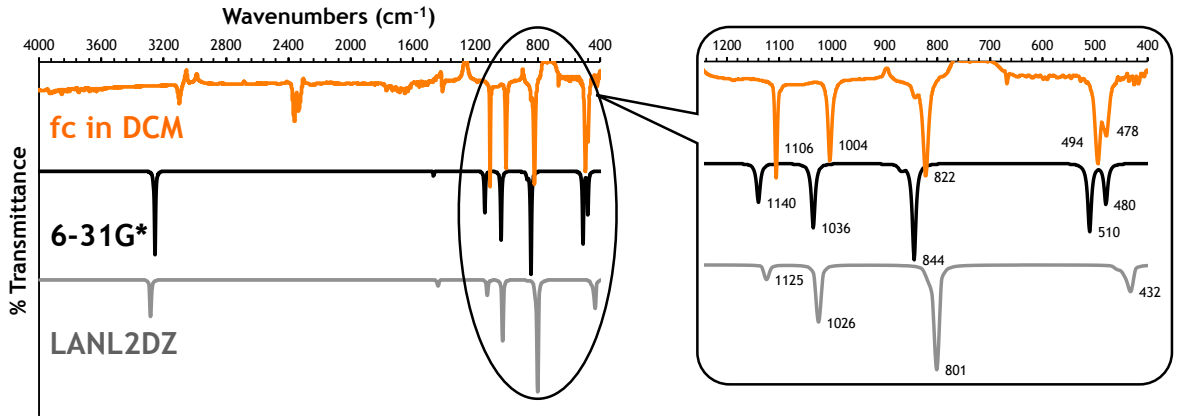

Figure 1.3. Comparison of experimental and theoretical IR spectrum of ferrocene.

The assignment of the fundamental vibrational modes for ferrocene is well established.[31-33] Based on our calculations, ferrocene shows four strong bands at low energy. The band at 1106 cm^{-1} corresponds to both symmetric and asymmetric C–C stretching, while the band at 1004 cm^{-1} corresponds to C–H rocking. The lowest energy band at 478 cm^{-1} is due to ring-metal stretching, while the band centered at 494 cm^{-1} corresponds to symmetric and asymmetric ring-metal-ring tilting.[32] It has been shown that the perpendicular bending of C–H bonds is affected by the electron density on iron, and is thus the most diagnostic of its oxidation state.[34] The frequency of this vibration is centered at 815 cm^{-1} in ferrocene (**Figure 1.3**; in our hands, the corresponding vibration was observed at 822 cm^{-1}) and upon oxidation shifts to 851 cm^{-1}. Similar effects have also been observed for polyferrocene species.[34-38] Appending the primary amine functionality to both rings shifts this band to lower frequencies in $\mathbf{H_2NN^H}$ (**Figure 1.4**), resulting in a much broader band centered at 801 cm^{-1}. This width is due to separate vibrations of the individual C–H components on the cyclopentadienyl rings. For example, the perpendicular C–H bending of the two fragments closest to the nitrogen is

located at 847 cm^{-1}, while the same mode involving those farthest from nitrogen is located at 800 cm^{-1}.

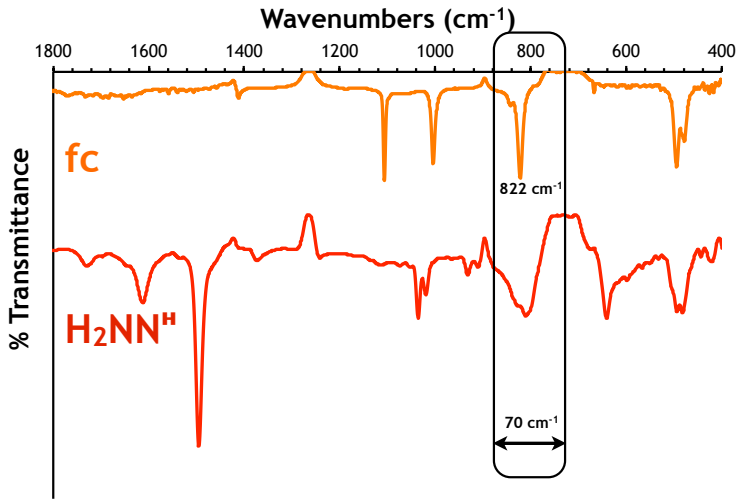

Figure 1.4. Experimental IR spectra of ferrocene and H_2NN^H in dichloromethane.

The spectral features are similar for all 1,1'-ferrocene diamines (**Figure 1.5**, **1.6**). Based on our calculations, N-H and C-H stretches are apparent between 3000 cm^{-1} and 3500 cm^{-1}. The strongest band, observed at approximately 1500 cm^{-1}, corresponds to Cp C-N stretching, while the weaker bands at 1200-1300 cm^{-1} are due to wagging of Cp rings relative to the iron center. At approximately 1100 cm^{-1}, a single band is present only in H_2NN^{DMP} and H_2NN^{MES} and involves stretching of the phenyl rings. The set of bands in its vicinity (1000-1100 cm^{-1}) represent asymmetric twisting of the Cp rings. All 1,1'-ferrocene diamines have three strong bands between 830 cm^{-1} and 940 cm^{-1}, which are due to various stretching and bending modes involving the carbon and hydrogen atoms of the amine substituents. The bands of those bearing silylamino substituents, however, appear to be sharper and better defined than those of H_2NN^{MES}. Reflecting the greater electron density on iron due to donating amine substituents, the perpendicular C-H bending was calculated to occur at lower energy for all 1,1'-ferrocene diamines (750-800 cm^{-1}). Moreover, the corresponding bands are predicted to be inherently weak, and consequently, are not observed experimentally (**Figure 1.6**). Finally,

the ring-metal-ring tilting seems to be insensitive to substitution, and appears between 400 cm^{-1} and 500 cm^{-1}.

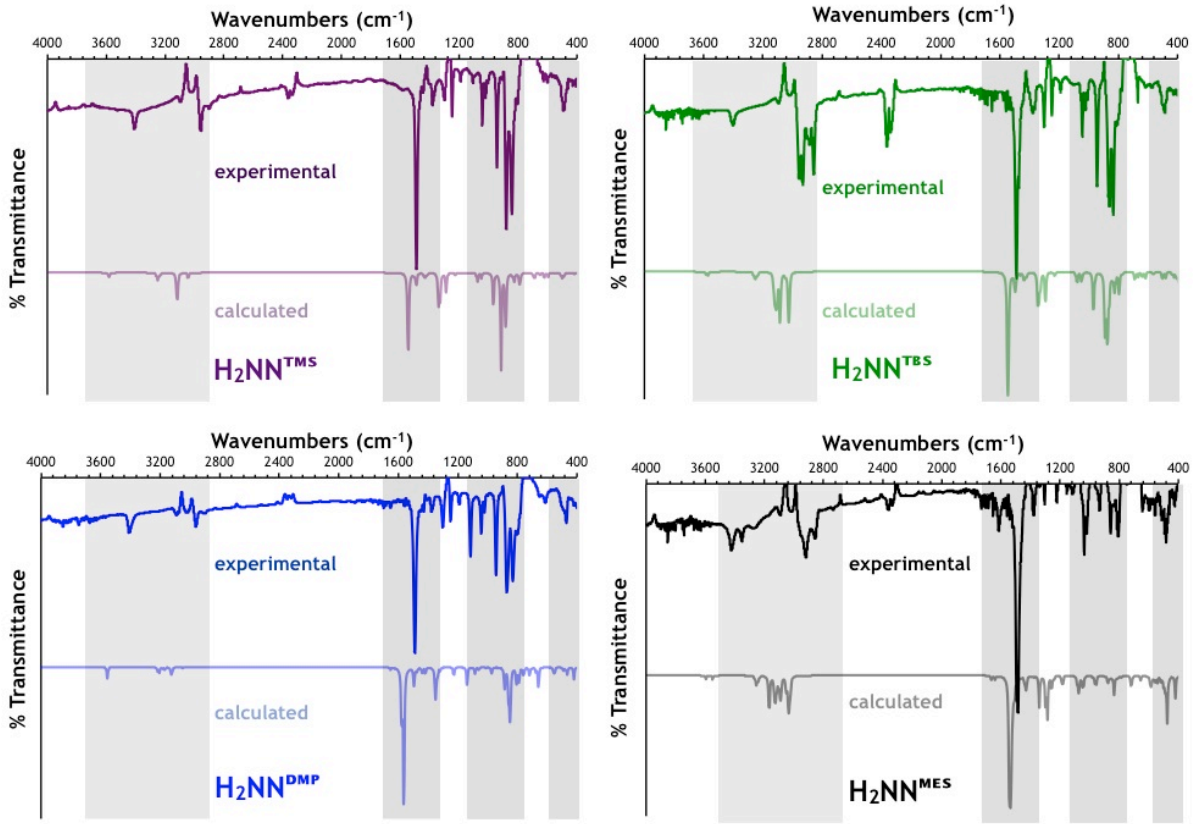

Figure 1.5. Full IR spectra of neutral 1,1'-ferrocene diamines in dichloromethane.

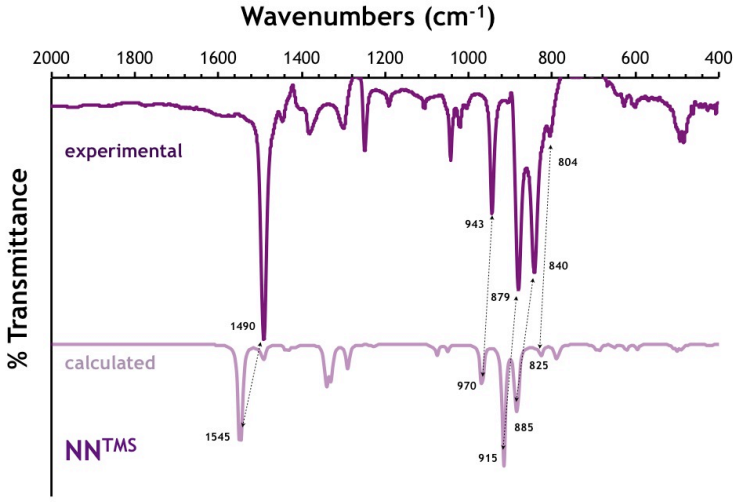

Figure 1.6. IR spectrum of H_2NN^{TMS} in the region 2000-400 cm^{-1} obtained experimentally and computationally.

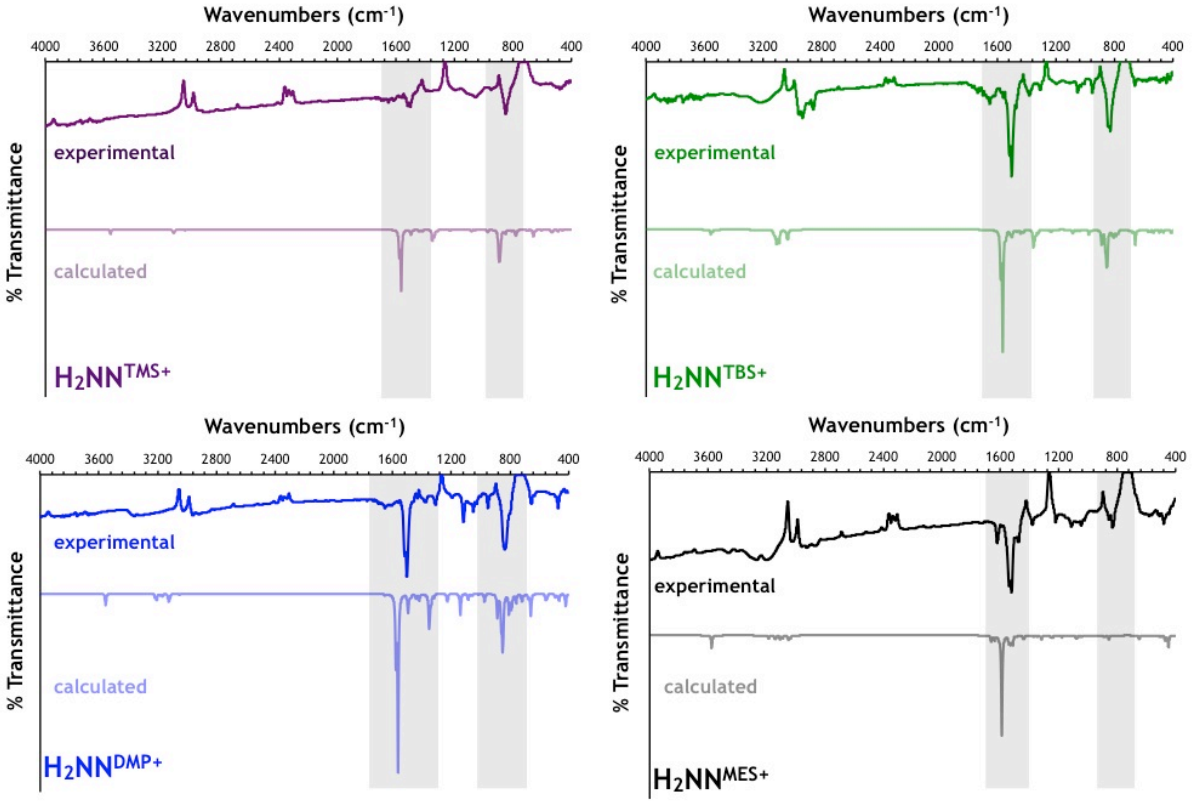

Figure 1.7. IR spectra of oxidized 1,1'-ferrocene diamines in dichloromethane.

Unsurprisingly, our calculations reveal that the band arising from perpendicular C–H bending shifts to higher energy upon oxidation of the iron center. For example, symmetric bending is centered at 851 in $\mathbf{H_2NN^{TMS+}}$ (825 cm^{-1} in $\mathbf{H_2NN^{TMS}}$) and 847 cm^{-1} in $\mathbf{H_2NN^{TBS+}}$ (824 cm^{-1} in $\mathbf{H_2NN^{TBS}}$), respectively. This band is weak relative to those arising from Cp C–N stretching at ~1500 cm^{-1} and methyl C–H wagging at 930 cm^{-1}. According to our calculations, the intense bands around 800 cm^{-1} (or 900 cm^{-1} from 6-31G*) found in the spectra of the silyl amines correspond to various vibrational modes involving methyl groups on the silyl substituents. As shown in **Figure 1.7**, only silyl derivatives exhibit a strong band in this region, thus supporting this interpretation.

1.2.4 Magnetic Susceptibility

In the presence of an external magnetic field, ferrocenium diamines exhibit similar behavior. All four species produce a field that is aligned with the external field (**Figure 1.8**). At room temperature and zero applied magnetic field, ferrocenium diamines bearing silyl substituents exhibit spontaneous magnetization, which is indicative of magnetic ordering.[39] Such an effect is not observed for the arylamine-based derivative, H_2NN^{MES+}, suggesting that it is simply paramagnetic.[40]

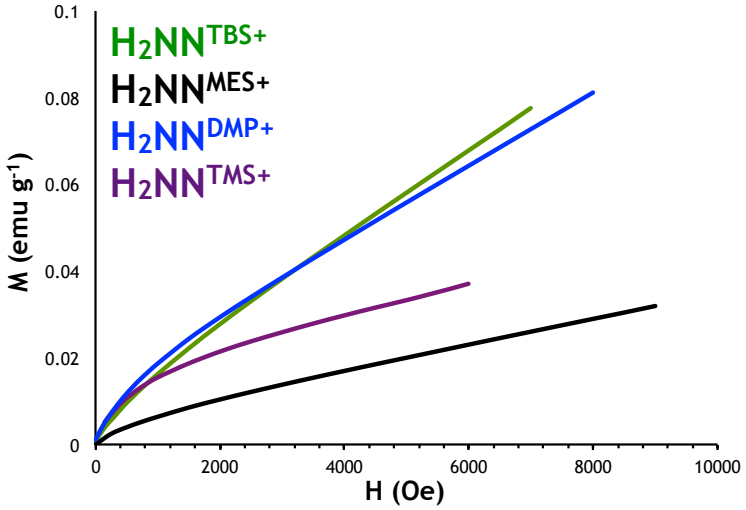

Figure 1.8. Magnetization field dependence of 1,1'-ferrocenium diamines at 298 K.

Temperature dependence of molar magnetic susceptibility of 1,1'-ferrocenium diamines was measured at 1500 G. Molar susceptibility increases rapidly with decreasing temperature below 50 K but is essentially constant above 100 K. **Figure 1.9** shows the product of molar magnetic susceptibility and temperature, X_mT, as a function of temperature. For an ideal paramagnetic material, the magnetic moment is temperature independent. Thus, the plot of X_mT versus T would exhibit a straight line, whose y-intercept corresponds to the Curie constant. It is evident from **Figure 1.9** that, for H_2NN^{TMS+} and H_2NN^{TBS+}, as temperature decreases, X_mT and thus, the magnetic moment tend to zero. Such behavior is characteristic

of antiferromagnetic interactions.[41, 42] H_2NN^{DMP+} and H_2NN^{MES+}, on the other hand, show temperature independent behavior above 50 K and 200 K, respectively.

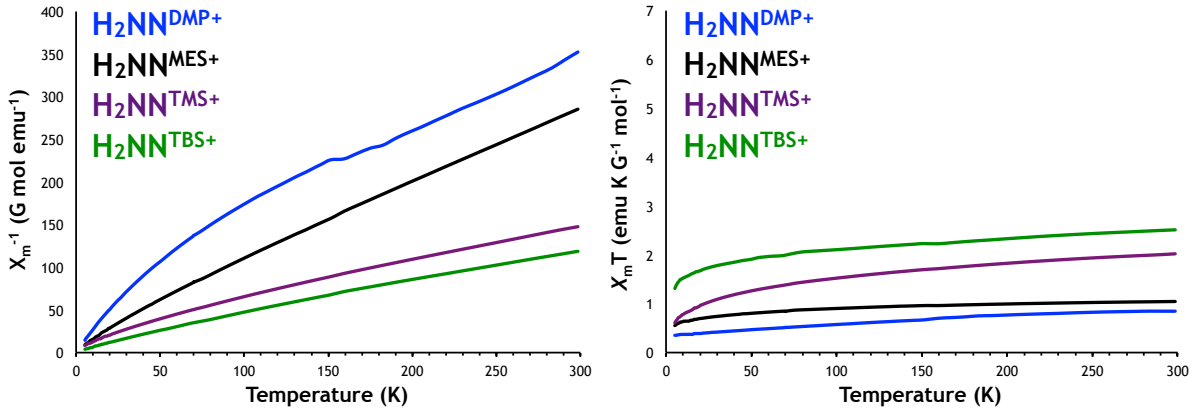

Figure 1.9. Molar magnetic susceptibility temperature product and inverse molar magnetic susceptibility of 1,1'-ferrocenium diamines at 1500 G.

Divergence from ideal paramagnetic behavior is further displayed in the plot of inverse molar magnetic susceptibility as a function of temperature (**Figure 1.9**). As described by the Curie-Weiss law,[43] magnetic susceptibility of a truly paramagnetic material is inversely proportional to temperature. Therefore, the plot of inverse molar magnetic susceptibility as a function of temperature would exhibit a positive-slope line that passes through the origin. As shown in **Figure 1.9**, all four ferrocenium diamines obey the Curie law[43] above 150 K. The positive deviation from ideal paramagnetic behavior confirms the presence of antiferromagnetic interactions.[44] Using the high temperature data, the reciprocal susceptibility was fitted to the Curie-Weiss equation, from which the Weiss constant was extrapolated. As shown in **Table 1.2**, all four species have negative Weiss constants, consistent with antiferromagnetic coupling between magnetic moments. At low temperature, their magnetic behavior no longer follows the magnetic field proportionally. The slight curvature observed below 150 K is characteristic of *ferrimagnetic* interactions, whereby incomplete cancellation of spins occurs.

Finally, as shown in **Figure 1.10** and **Table 1.2**, the effective magnetic moment of each ferrocenium diamine deviates significantly from the spin-only value for a single unpaired electron (S=1/2, μ = 1.73).[43] Because no crystal structures are available, it is difficult to interpret the observed values of the effective magnetic moments, which is influenced by numerous factors ranging from the magnitude of the distortion from D_5 symmetry[45, 46] and crystal packing to the tilt angle between the Cp rings and the extent and nature of their substitution.[47] Moreover, such high values may be due to a contribution from orbital moment.[46, 48-51] If indeed that was the case, it would suggest that the low-symmetry Jahn-Teller distortion of the iron d-orbitals is not very large.[52]

Table 1.2. Weiss constants (θ) and magnetic moments (μ_{eff}) of 1,1'-ferrocenium diamines at 1500 G and 298 K.

	θ	μ_{eff}
	(K)	*(u_B)*
H_2NN^{TMS+}	-74.65	4.02
H_2NN^{TBS+}	-52.86	4.48
H_2NN^{DMP+}	-93.99	2.60
H_2NN^{MES+}	-32.79	2.89

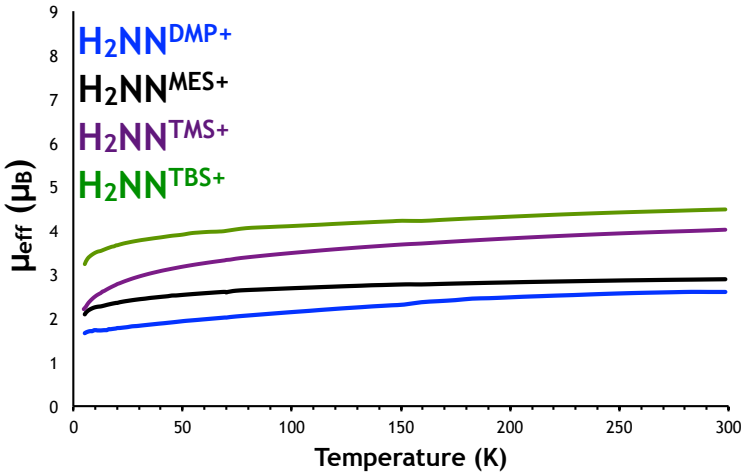

Figure 1.10. Effective magnetic moment of 1,1'-ferrocenium diamines at 1500 G.

1.3 DISCUSSION OF COMPUTATIONAL RESULTS

1.3.1 Methods

The computational study of the title compounds was therefore conducted with Gaussian09,[53] using the unrestricted hybrid functional B3LYP.[68, 69] Moreover, atoms were modeled with an all-electron 6-31G*[54-60] basis set and, unless noted otherwise, all species discussed in this report correspond to minima with no imaginary frequencies. For the sake of comparison, we also employed an all-electron LANL2DZ[61] basis set. In order to ascertain the accuracy of the computational methods used, we performed the same calculations on ferrocene/ferrocenium using different methods and basis sets, and compared our results to both experimental[62-64] and theoretical[65-68] data reported previously. As shown in **Table 1.3**, results obtained using the unrestricted B3LYP functional[69, 70] and 6-31G* basis set were in best agreement with the experimental data. Because no structural parameters exist, we built upon the crystallographic coordinates of **NN^{H}** and optimized the geometry of each 1,1'-ferrocene diamine using a fragment-based algorithm.[71] No thermal parameters were specified, so all calculated temperature-dependent values assume 298 K.

Table 1.3. Comparison of the distance between Fe and the center of Cp rings obtained experimentally and with different computational methods; [a] From references [63, 72].

Theory	Basis	Fe-Cp (Å)
uB3LYP	LANL2DZ	1.728
	cc-pVTZ	1.692
	6-31G*	1.654
uBP86	6-31G*	1.620
uBLYP	6-31G*	1.653
Experimental		**1.66**[a]

What follows is a discussion of structural features and frontier molecular orbitals. Each section begins with a discussion of the neutral species, followed by a comparison with the

oxidized derivatives. Furthermore, to put our results into context, we preface each discussion with an overview of the parent compounds (i.e. ferrocene and/or $\mathbf{H_2NN^H}$).

1.3.2 Structural Features

The structural parameters of the optimized geometry of ferrocene are dependent on the basis set. For example, using LANL2DZ, the distance between iron and the center of each Cp ring is 1.73 Å and 1.76 Å in ferrocene and ferrocenium, respectively. The values decrease to 1.65 Å and 1.68 Å when the 6-31G* basis set is used. As mentioned above, the latter is in better agreement with the experimental data.[62, 65, 73, 74] As shown in **Figure 1.11**, the *change* in Fe-Cp distance upon oxidation of the iron center is nonetheless insignificant (0.029 Å in LANL2DZ and 0.023 Å in 6-31G*).

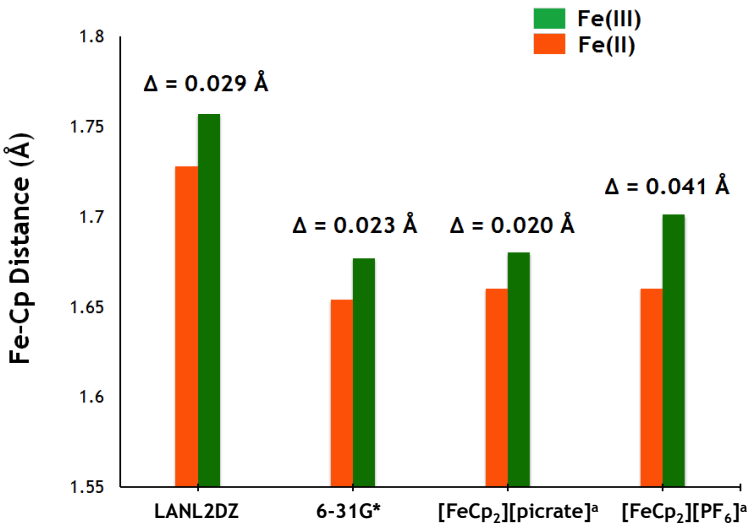

Figure 1.11. Comparison of calculated and experimental distances between iron and Cp rings in ferrocene and ferrocenium derivatives. [a]From reference [75].

A more significant difference lies in the conformation of the Cp rings relative to each other. Previously published studies have established that the Cp rings are staggered in the solid state[76-79] but eclipsed in gas phase.[62, 72, 80] Similarly, others have calculated the rotational barrier to be 0.9-1.1 kcal/mol and from crystallographic data, concluded that up to 60 % of ferrocene molecules in a single crystal feature Cp rings in an eclipsed conformation.[63]

Theoretical studies have also predicted the greater stability of the eclipsed isomer.[65] Consistent with these studies, our calculations show that in gas phase, ferrocene has D_{5h} symmetry. The staggered isomer is predicted to be essentially isoenergetic (+0.11 kcal/mol). Such a low barrier to rotation is therefore consistent with previous studies.

While both basis sets predict ferrocene to be eclipsed, 6-31G* shows that the rings are staggered when iron is in the higher oxidation state. More specifically, convergence to an eclipsed isomer of ferrocenium using 6-31G* is accompanied by one imaginary frequency centered at approximately -5 cm^{-1}, suggesting that the structure corresponds to a transitional state for the rotation of the Cp rings.[81] The barrier to rotation is less than 1 kcal/mol. These results are consistent with previous theoretical and experimental reports of various ferrocenium salts [75, 82-84].

Having established the validity of both methods, we performed geometry optimization and frequency analysis for six 1,1'-ferrocene diamines bearing silyl, alkyl, and aryl substituents, as well as the parent 1,1'-ferrocene diamine. For the sake of clarity, the following discussion will use structural motifs and nomenclature (**Figure 1.12**) in line with the established categorization of 1,1'-disubstituted ferrocene systems.[73, 74]

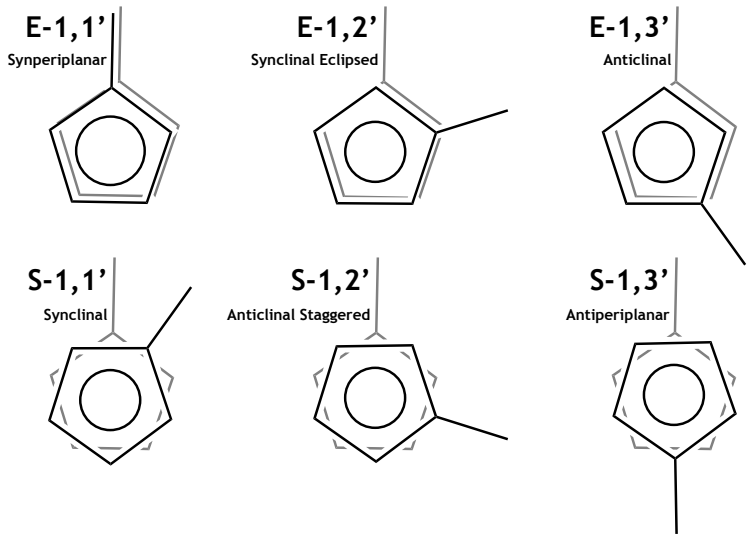

Figure 1.12. Possible conformations of symmetrically disubstituted ferrocene systems.

Structural features of H_2NN^H, calculated using both basis sets, are in good agreement with those measured experimentally. It has previously been shown that two different conformations of H_2NN^H (**Figure 1.13**) exist in the same crystallographic unit cell.[85] For E-1,1'-H_2NN^H, the distance between iron and the center of the Cp ring was overestimated by less than 4% using LANL2DZ (Fe-Cp distance = 1.74 Å versus 1.66 Å). When polarization functions were added to all atoms, the structure was modeled more accurately (Fe-Cp distance = 1.658 Å). Vibrational analysis of E-1,1'-H_2NN^H using LANL2DZ and 6-31G*, however, yielded one imaginary frequency centered at -23 cm^{-1} and -33 cm^{-1}, respectively. This implies that both methods model the eclipsed geometry as a first-order saddle point, which corresponds to a transitional structure for the rotation of the Cp rings.

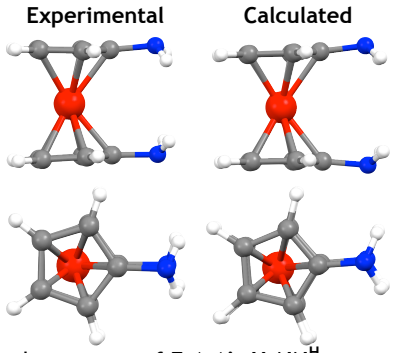

Figure 1.13. Experimental and calculated structure of E-1,1'- H_2NN^H.

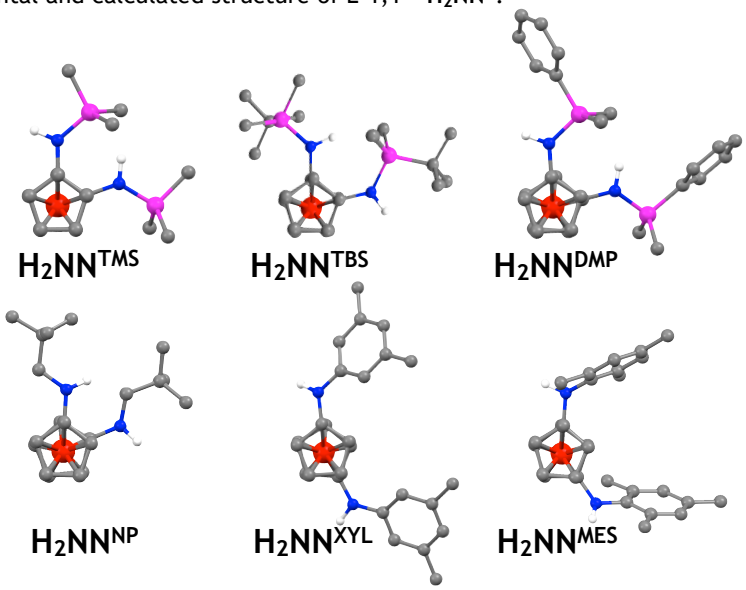

Figure 1.14. Conformation of neutral 1,1'-ferrocene diamines at minimum potential energy.

Unsurprisingly, the optimized geometry of each 1,1'-ferrocene diamine derivative was dependent on the conformation of the initial structure. The most stable structures (**Figure 1.14**), which all further discussion will be based upon, did not depend on the basis set, however. It is evident that the orientation of the amino substituents changes to either a 1,2' (**H_2NN^{TMS}**, **H_2NN^{TBS}**, **H_2NN^{DMP}**, **H_2NN^{NP}**) or 1,3' (**H_2NN^{XYL}** and **H_2NN^{MES}**) eclipsed conformation, as a consequence of steric and electronic interactions. Moreover, in the latter class, both amine hydrogen atoms point outward, while in the silyl and alkyl derivatives, one H atom points inward. The most stable conformation of **H_2NN^{TMS}**, **H_2NN^{NP}**, and **H_2NN^{TBS}** is likely caused by lack of steric demand. However, any steric influence seems to be suppressed in **H_2NN^{DMP}**, which, unlike the aryl analogues, does not converge to a 1,3' configuration despite being the largest 1,1'-ferrocene diamine overall (as deemed by the calculated value for electronic spatial extent). This can be explained by considering the different type of bonding that the nitrogen atom participates in. In **H_2NN^{DMP}**, the lone pair of electrons on nitrogen can overlap with the empty d orbitals on the silicon.[86-89] In contrast these electrons are more labile in **H_2NN^{MES}** because carbon does not have d orbitals available for interaction with the lone pair on nitrogen. Thus, the probability of finding these electrons localized on the nitrogen atom itself increases. As a result, they are more likely to repel each other, thereby lowering the stability of the 1,2'-**H_2NN^{MES}** rotamer. The increase in the silicon-nitrogen bond angles in the **H_2NN^{DMP}** ligand compared to those in **H_2NN^{MES}** supports this explanation (**Figure 1.15**). The same effect has been observed in simple silylamines and explains why, for example, $N(SiH_3)_3$ is trigonal planar, while $N(CH_3)_3$ is pyramidal.[88] Again, we emphasize that the overall trend and the *relative* values of the structural parameters in general do not vary with the choice of basis set.

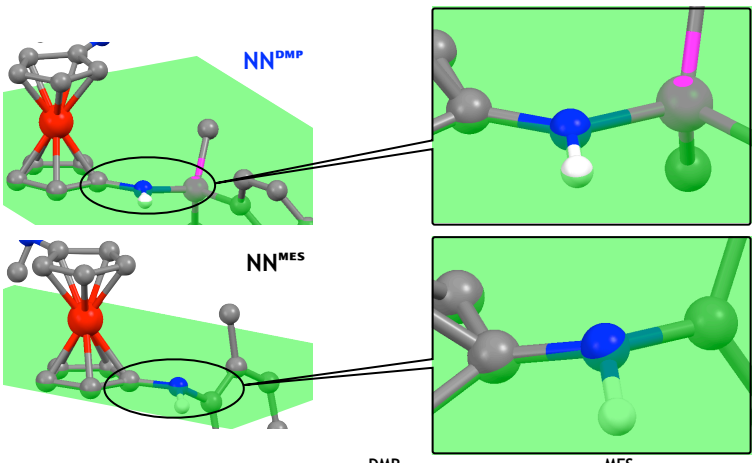

Figure 1.15. Relative geometry around nitrogen in H_2NN^{DMP} (planar) and H_2NN^{MES} (pyramidal).

Geometry optimizations of the respective oxidized 1,1'-ferrocene diamines were conducted by using the optimized Cartesian coordinates of the neutral counterparts at two different conformations but changing the charge and multiplicity values in the input file. The most stable conformations are shown in **Figure 1.16**.

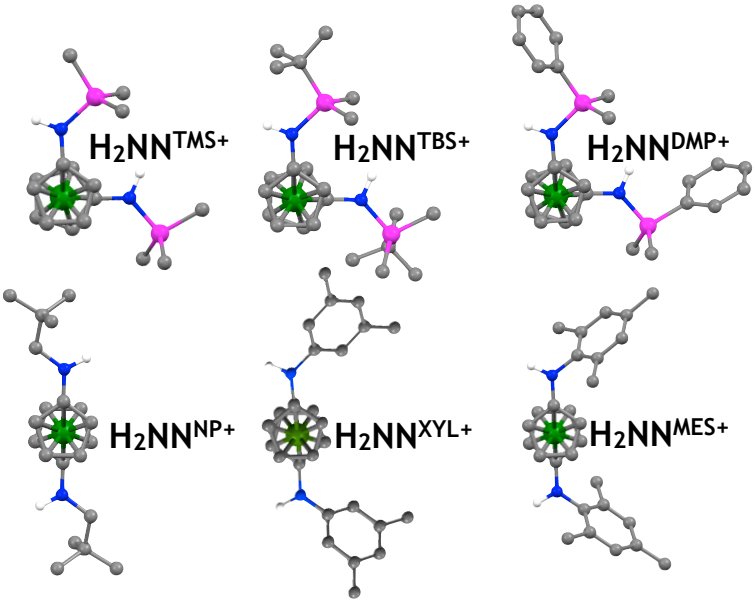

Figure 1.16. The most stable conformations of oxidized ferrocene diamines.

As shown in **Table 1.4**, the distance between the Cp carbon and nitrogen atoms decreases for all 1,1'-ferrocene diamines, while the distance between iron and the ring's center increases upon removal of an electron. For example, the distance between iron and

each Cp ring changes by approximately 0.07 Å. This is significantly greater than the increase in the parent compound (**Δ** = 0.02 Å) and is a reflection of weaker metal-ligand bonding brought about upon oxidation.[90] It has been suggested that this decrease in metal-ligand distance is due to removal of an electron from the bonding e_2 orbital or the simultaneous electronic rearrangement.[62] While increasing the oxidation state decreases the metal-ligand distance for main group metal ions (due to the decrease in ionic size as well as the increase in electron affinity of the metal center), the same effect is not always true for transition metals.[91] In other words, a metal-ligand distance will change upon oxidation depending on whether it remains in the same spin state. For example, the ionic radii of low-spin Fe^{2+} and Fe^{3+} with a coordination number of 6 are 0.61 Å and 0.55 Å, respectively.[92] Similarly, the ionic radii of high-spin Fe^{2+} and Fe^{3+} with a coordination number of 6 are 0.78 Å and 0.64 Å, respectively. Therefore, the metal-ligand distance is naturally expected to decrease if both Fe^{2+} and Fe^{3+} are of low (or high) spin. If, however, the spin state of the iron center changes from low to high upon removal of an electron (i.e. low-spin Fe^{2+} → high-spin Fe^{3+}), then the metal-ligand distance would remain roughly the same. In the present case, all calculations were performed for singlet metallocenes, so for a given ligand, the distance is expected to decrease upon oxidation.

Table 1.4. Distance between iron and Cp rings and C_{Cp}-N bond length changes upon oxidation.

6-31G*	Fe-Cp (Å)			C_{Cp}-N (Å)		
	Fe^{2+}	Fe^{3+}	Δ	Fe^{2+}	Fe^{3+}	Δ
H_2NN^{MES}	1.661	1.734	0.073	1.413	1.353	-0.060
H_2NN^{TMS}	1.661	1.731	0.070	1.399	1.357	-0.041
H_2NN^{TBS}	1.661	1.730	0.069	1.400	1.358	-0.042
H_2NN^{XYL}	1.661	1.730	0.069	1.400	1.355	-0.045
H_2NN^{DMP}	1.662	1.730	0.068	1.400	1.357	-0.043
H_2NN^{NP}	1.665	1.733	0.068	1.400	1.345	-0.055
fc	1.654	1.677	0.023	-	-	-

A more interesting structural change brought on by oxidation is the distortion of the cyclopentadienyl rings. That is, the planar conformation of both rings becomes disrupted (**Figure 1.17**). This deviation is more pronounced in alkyl- and aryl- than in silyl-substituted 1,1'-ferrocene diamines. Loss of ring aromaticity and disruption of conjugation is expected to weaken the overlap between Fe^{3+} and ring orbitals.[93] Because the iron-ring interaction provides the greatest stabilization within the ferrocene backbone,[26] such a structural perturbation may be important not only for the oxidized 1,1'-ferrocene diamines, but also for the metal centers that they support.

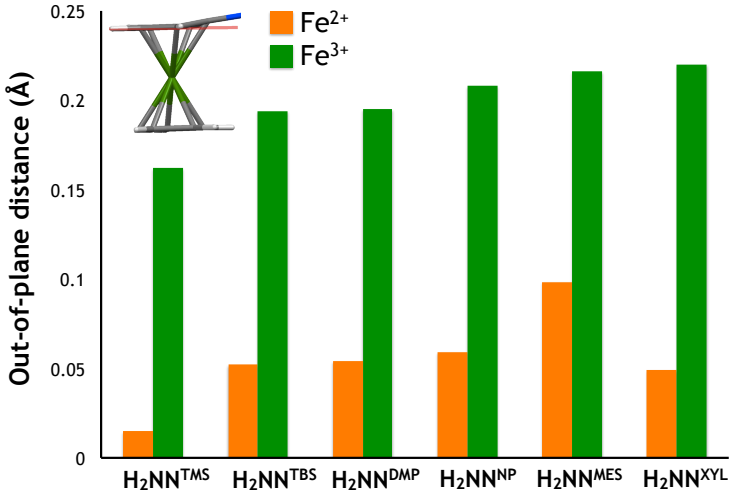

Figure 1.17. Distortion of the Cp ring as defined by the out-of-place displacement of the amino carbon.

1.3.3 Electronic Structure

Both LANL2DZ and 6-31G* basis sets paint a qualitatively similar picture of the electronic structure of ferrocene. The ground state configuration of eclipsed ferrocene (D_{5h}) was calculated to possess highest occupied orbitals of a'_1 and e'_2 symmetry. The energy difference between these two orbitals is small and their relative ordering in the staggered conformation has been debated.[24-27, 68, 94, 95] Studies favoring $a_1 > e_2$ were based on a staggered conformation. Indeed, one report describing the substitution effects on the electronic structure of ferrocene has shown that the energy order of a_1 and e_2 orbitals is dependent on

the relative conformation of the Cp rings.[96] Our calculations of the eclipsed isomer show that $e'_2 > a'_1$ (**Figure 1.18**).

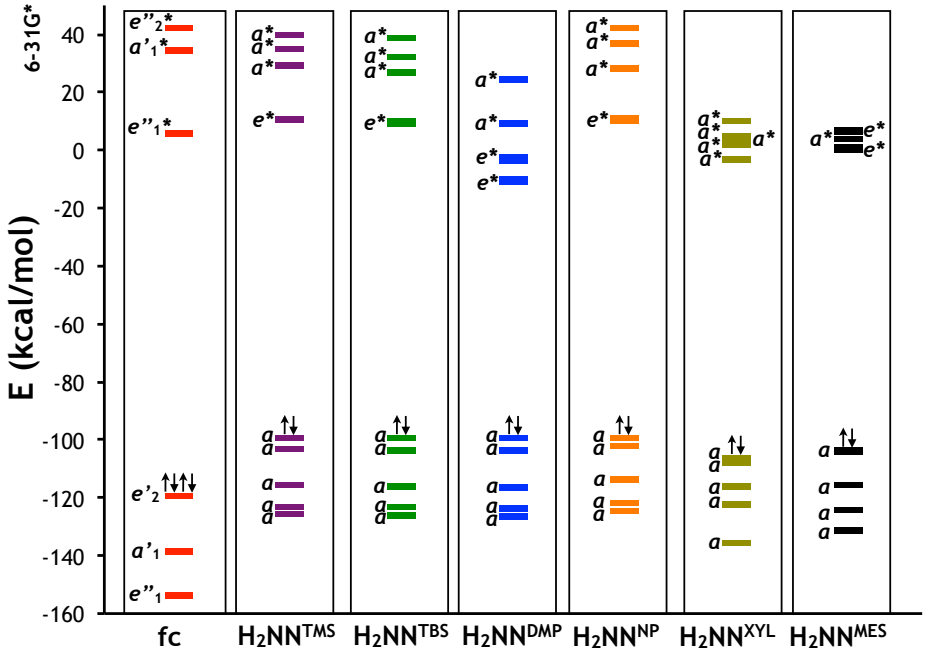

Figure 1.18. Molecular orbital diagrams of ferrocene and its derivatives (energy levels showing electron pairs represent the highest occupied MO).

Figures 1.18 and **1.19** show molecular orbital diagrams of neutral 1,1'-ferrocene diamines relative to ferrocene. As shown in **Figure 1.20**, the HOMO remains purely iron-based in all except H_2NN^{XYL} and H_2NN^{MES} species, whose highest occupied molecular orbitals show a mixing of iron and nitrogen atomic orbitals. Furthermore, the energy of the HOMO in all derivatives increases relative to ferrocene (**Figure 1.21**). The increase in energy of the highest occupied molecular orbital is greatest in derivatives bearing silyl substituents. This is expected because silyl groups are stronger electron donors than aryl substituents. Similarly, our calculations reveal that the iron-based e_{1g} orbitals (LUMO in ferrocene) remain degenerate in 1,1'-ferrocene diamines bearing no phenyl substituents (H_2NN^{TMS}, H_2NN^{TBS}, H_2NN^{NP}). In contrast, the corresponding orbitals lose their degeneracy in H_2NN^{DMP}, H_2NN^{XYL}, and H_2NN^{MES} derivatives (**Figure 1.19**).

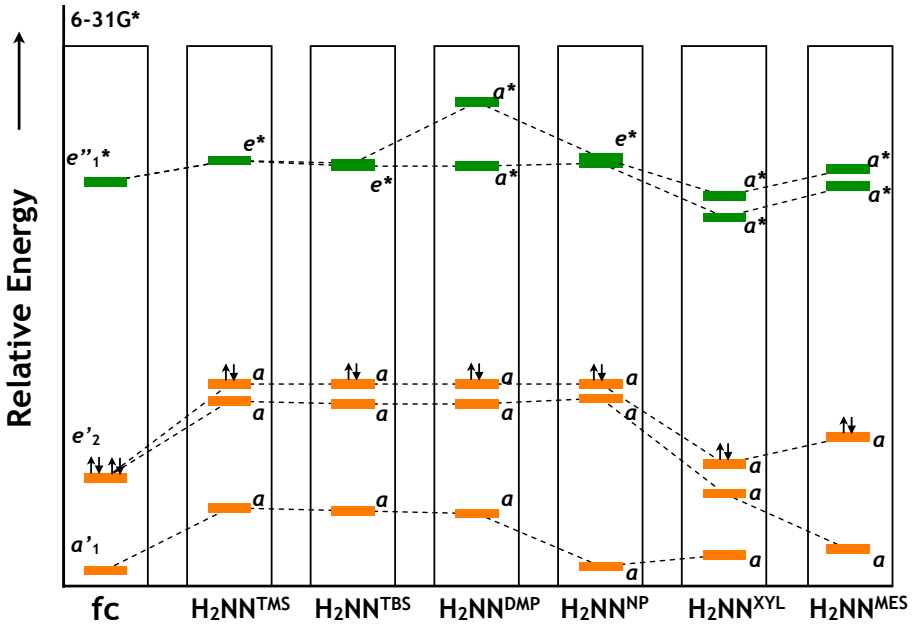

Figure 1.19. Ligand-field splitting of iron d-orbitals in 1,1'-ferrocene diamines.

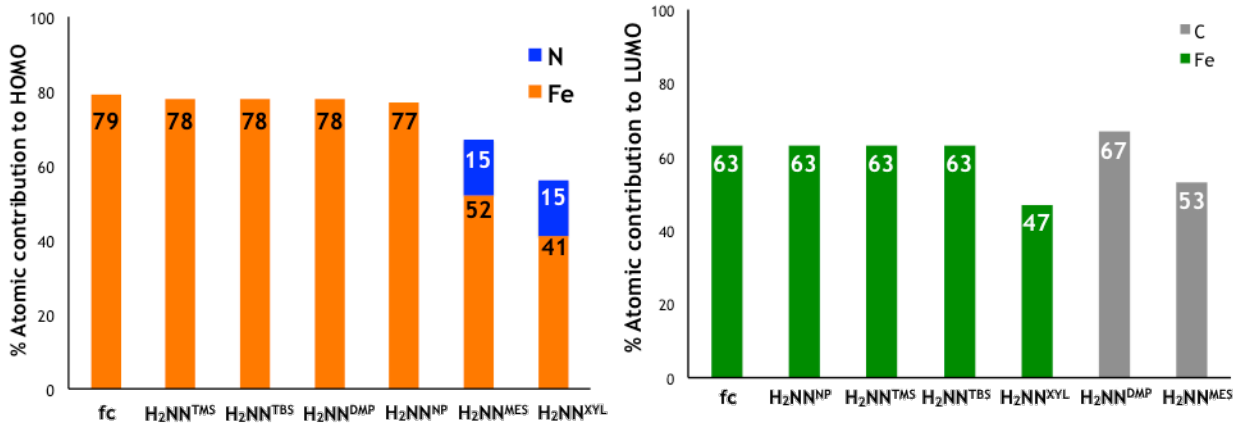

Figure 1.20. Atomic contributions to highest occupied and lowest unoccupied molecular orbitals.

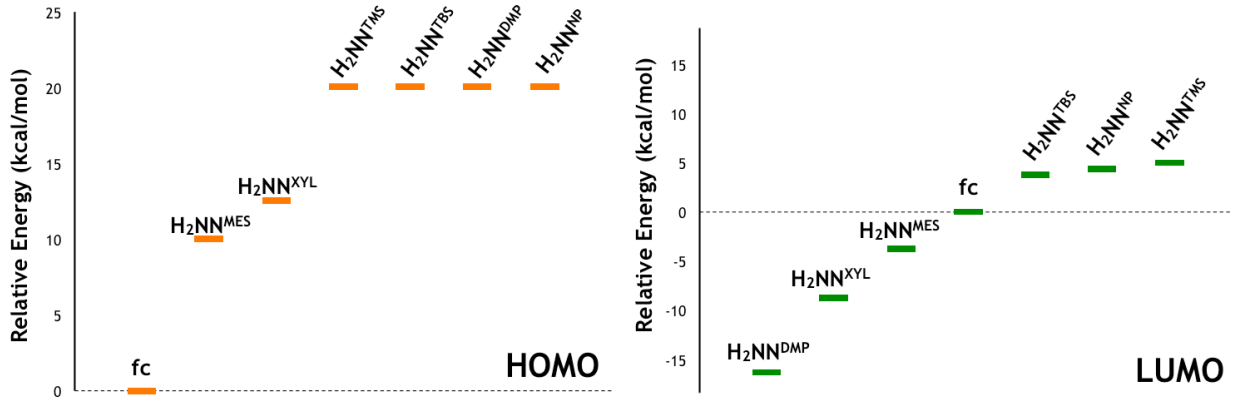

Figure 1.21. Energy of highest occupied and lowest unoccupied molecular orbitals relative to those of ferrocene, which are defined as 0 kcal/mol).

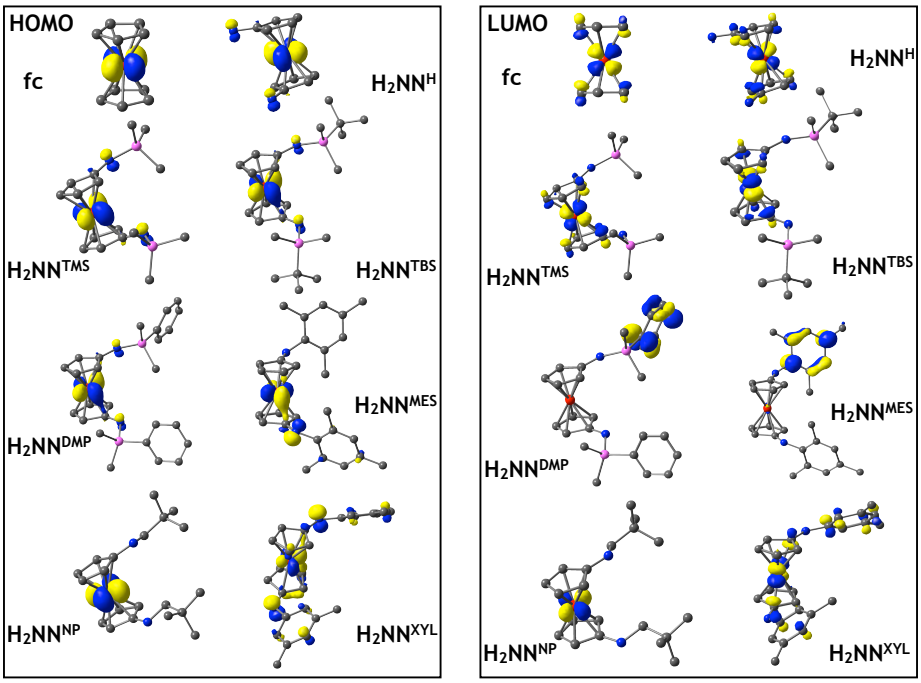

Figure 1.22. HOMO (left) and LUMO (right) of 1,1'-ferrocene diamines.

With the exception of H_2NN^{DMP}, H_2NN^{XYL}, and H_2NN^{MES}, the energy of the lowest unoccupied molecular orbital also increases relative to ferrocene (**Figure 1.21**). These exceptions, however, are consistent with the nature of the LUMO on 1,1'-ferrocene diamines bearing aromatic groups, which is localized largely on the phenyl rings, with predominant contribution originating from the phenyl π orbitals. The trend in the resulting HOMO-LUMO gap, which can be attributed to conjugation effects, further reflects and supports this anomaly. As a result of smaller HOMO-LUMO gap, H_2NN^{DMP} is expected to be kinetically less stable and more reactive than other 1,1'-ferrocene diamines.[97, 98]

Finally, the ground state configuration of the parent ferrocenium is iron-based and of e_{2g} symmetry, which is consistent with previous studies.[44, 82, 99] Although substitution on the Cp rings does not affect their character, the highest occupied molecular orbitals split to various degrees in all 1,1'-ferrocenium diamines, making their ground state configuration non-degenerate. Distortion due to the low-symmetry of the ligand field is small, however. This is consistent with the observed magnetic moments.[52]

1.4 CONCLUSIONS

We have presented a systematic experimental and computational treatment of several 1,1'-ferrocene and ferrocenium diamines bearing alkyl, aryl, and silyl substituents. Electrochemical measurements reveal the amine groups on Cp rings donate electron density to the iron center, allowing it to undergo oxidation more easily. The extent of this change in oxidation potential, however, diminishes as various substituents are appended on the amine group. Similarly, electronic spectra of 1,1'-ferrocenium diamines reveal that the energy of charge transfer from Cp ligands to Fe^{3+} does not depend on the substituents on the nitrogen. Since ligand to metal charge transfer is, in essence, a reduction of the metal, this implies that the electron density on Fe^{3+} is similar throughout the series and that the electron donating ability of the amine groups is unaffected by substitution. Our calculations support this conclusion. More specifically, the distance between iron and the Cp rings, which is one factor that determines the energy required to promote an electron from a ligand-based orbital to the metal center, was calculated to be nearly identical within the series. Finally, computational treatment of 1,1'-ferrocene diamines shows that aromatic substituents on the nitrogen atoms impose the greatest influence on the electronic structure of the neutral species by not only lowering the energy difference between frontier orbitals but also by changing the nature of the lowest occupied molecular orbital from metal to ligand character.

1.5 APPENDIX A

1.5.1 Synthesis

General Considerations. All experiments were performed under a dry nitrogen atmosphere using standard Schlenk techniques or an MBraun inert-gas glovebox. Solvents were purified using a two-column solid-state purification system by the method of Grubbs[100] and transferred

to the glovebox without exposure to air. NMR solvents were obtained from Cambridge Isotope Laboratories, degassed, and stored over activated molecular sieves prior to use. ^{1}H and ^{13}C NMR spectra were recorded on a Bruker300 spectrometer at room temperature in C_6D_6. ^{1}H and ^{13}C chemical shifts are reported with respect to C_6D_6 residual peak, 7.16 ppm and 128.5 ppm, respectively. Cyclic voltammetry measurements were conducted on a CH Instruments CHI630D potentiostat using a 2 mm platinum disk as the working electrode, 3 mm glassy carbon disk as the counter electrode, and 0.25 mm silver wire as the pseudo-reference electrode. UV-Vis spectra were recorded on a Varian Carey 5000 spectrophotometer from 230 to 1600 nm using matched 1 cm quartz cells; all spectra were obtained using a solvent reference blank in a cuvette with an air-free Teflon adapter. IR spectra were recorded on a JASCO FT-IR-420 spectrophotometer from 4000 to 400 cm^{-1} using a sealed liquid cell from International Crystals Laboratory with a 1 mm path length and KBr windows. CHN analysis was performed on an Exeter Analytical, Inc. CE-440 Elemental Analyzer. Magnetic properties of 1,1'-ferrocenium diamines were investigated using a Quantum Design Model MPMS® sample magnetometer under a zero-field cooled, reciprocating sample option. Magnetization was measured as a function of magnetic field at 298 K or as a function of temperature at 1500 G.

All amines were synthesized following previously published procedures and their purity was determined by comparison of ^{1}H NMR shifts. Shafir, et al. reported the synthesis of fc[NH_2]$_2$ (fc = 1,1′-ferrocenylene, **H_2NN^{H}**),[85] fc[$NHSiMe_3$]$_2$ (**H_2NN^{TMS}**),[101] and fc[NHMes]$_2$ (**H_2NN^{MES}**),[102] while Siemling, et al. reported the synthesis of fc[$NHCH_2$(t-Bu)]$_2$ (**H_2NN^{NP}**).[103] Amines fc[NHSi(t-Bu)Me_2]$_2$ (**H_2NN^{TBS}**)[10] and fc[NHXyl]$_2$ (**H_2NN^{XYL}**)[19] were previously prepared in our group. Dimethylphenylsilyl chloride and iodine were purchased from Alfa Aesar and used as received. Tetrabutylammonium hexafluorophosphate ($TBAPF_6$) was purchased from Sigma Aldrich and recrystallized from THF before use.

Synthesis of H_2NN^{DMP}. In a 20-mL scintillation vial charged with a stir bar, H_2NN^{H} (496 mg, 2.29 mmol) was dissolved in dichloromethane and cooled to -190 °C for 30 min. At room temperature, triethylamine (533 mg, 5.28 mmol) and dimethylphenylsilyl chloride (809 mg, 4.7 mmol) were slowly added to the above solution. The mixture was stirred for 24 h. Dichloromethane was removed under reduced pressure to yield an orange oil, which was then dissolved in *n*-pentane and filtered through alumina. The solution was concentrated and stored at -35 °C. Large, dark-red clusters of crystalline needles formed after 12 h. Yield: 337 mg, 30%. H_2NN^{DMP} is soluble in hexanes, pentane, diethyl ether, toluene, benzene, tetrahydrofuran, dichloromethane, and chloroform. *Note: Use of more than 2.1 equivalents of dimethylphenylsilyl chloride makes subsequent isolation and purification of* NN^{DMP} *difficult.*

Synthesis of $[H_2NN^{TMS}][I]$. In a 20 mL scintillation vial, a hexanes solution of I_2 (58 mg, 0.23 mmol) was added to a cold pentane solution of H_2NN^{TMS} (195 mg, 0.54 mmol). The reaction mixture was stirred at room temperature. A fluffy olive green solid precipitated immediately but adhered to the vial wall after 15 min, leaving a clear solution that was then decanted. The product was washed with 10 mL of diethyl ether and dried under reduced pressure. Yield: 102 mg, 77 %. $[H_2NN^{TMS}][I]$ is soluble in tetrahydrofuran, dichloromethane, and chloroform but insoluble in hexanes, pentane, diethyl ether, toluene, and benzene.

Synthesis of $[H_2NN^{DMP}][I]$. In a 20 mL scintillation vial, a hexanes solution of I_2 (12 mg, 0.05 mmol) was added to a cold pentane solution of H_2NN^{DMP} (60 mg, 0.12 mmol). The reaction mixture was stirred at room temperature. A bright green solid precipitated immediately but adhered to the vial wall after 15 min, leaving a clear solution that was then decanted. The solid was washed with diethyl ether and dried under reduced pressure. The crude powder was then dissolved in approximately 5 mL of THF and crashed out of solution with addition of an

equal volume of hexanes. The precipitate was collected on a fine-porosity frit and washed with a mixture of hexanes and diethyl ether. Yield: 35 mg, 95 %. **[H_2NN^{DMP}][I]** is soluble in tetrahydrofuran, dichloromethane, and chloroform but insoluble in hexanes, pentane, diethyl ether, toluene, and benzene.

Synthesis of [H_2NN^{MES}][I_3]. In a 20 mL scintillation vial, a hexanes solution of I_2 (81 mg, 0.32 mmol) was added to a cold pentane solution of **H_2NN^{MES}** (123 mg, 0.27 mmol). A yellow-green solid precipitated immediately and the reaction mixture was stirred at room temperature for 10 min. The precipitate was allowed to settle and after the supernatant was decanted, it was washed with 10 mL of toluene and dried under reduced pressure. Yield: 157 mg, 70 %. **[H_2NN^{MES}][I_3]** is soluble in tetrahydrofuran, dichloromethane, and chloroform but insoluble in hexanes, pentane, toluene, and benzene. *Note: the fine powder becomes a thick sludge upon exposure to diethyl ether and is hard to handle*.

1.5.2 Elemental analysis

H_2NN^{DMP}
$C_{26}H_{42}N_2Si_2Fe$ (485 g/mol)
Calculated: 64.45 %C, 6.66 %H, 5.78 %N
Found: 64.41 %C, 6.65 %H, 5.55 %N

[H_2NN^{DMP}][I]
$C_{26}H_{42}N_2Si_2FeI$ (621 g/mol)
Calculated: 50.43 %C, 5.29 %H, 4.42 %N
Found: 51.07 %C, 5.27 %H, 4.58 %N

[H_2NN^{TMS}][I]
$C_{16}H_{38}N_2Si_2FeI$ (487 g/mol)
Calculated: 39.43 %C, 5.79 %H, 5.75 %N
Found: 39.16 %C, 5.23 %H, 5.64 %N

[H_2NN^{MES}][I_3](C_7H_8)
$C_{35}H_{40}FeI_3N_2$ (925 g/mol)
Calculated: 45.43 %C, 4.36 %H, 3.03 %N
Found: 45.10 %C, 4.27 %H, 3.18 %N

1.5.3 ^{1}H and ^{13}C NMR spectroscopy

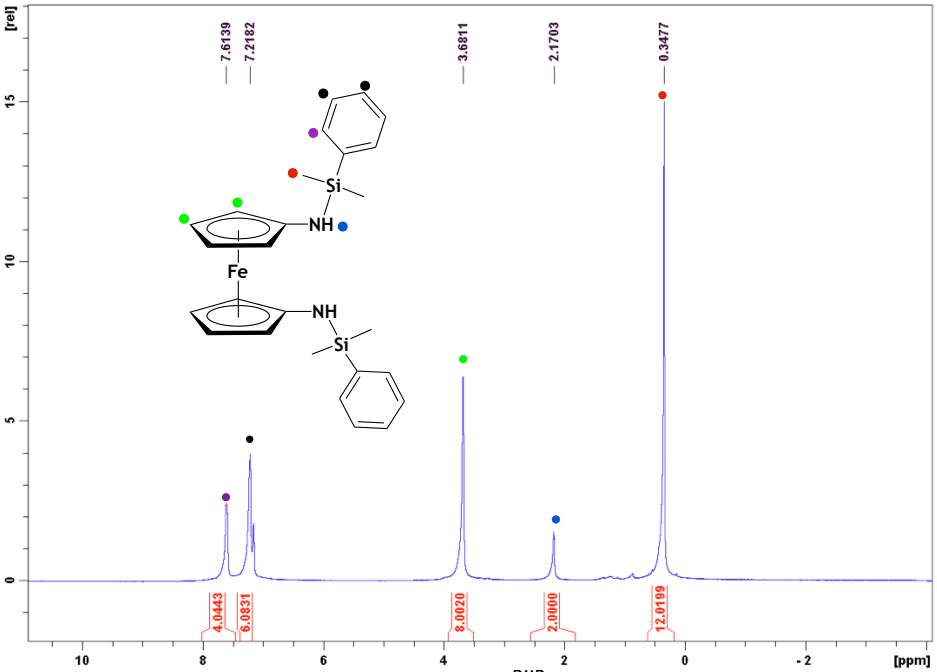

Figure A1. ^{1}H NMR spectrum (300 MHz, 25 ºC, C_6D_6) of $\mathbf{H_2NN^{DMP}}$; δ(ppm): 7.60 (m, 4H, C_6H_5), 7.22 (m, 6H, C_6H_5), 3.71 (s, 8H, Cp-C*H*), 2.16 (s, 2H, N*H*), 0.35 (s, 12H, Si(CH_3)$_2$).

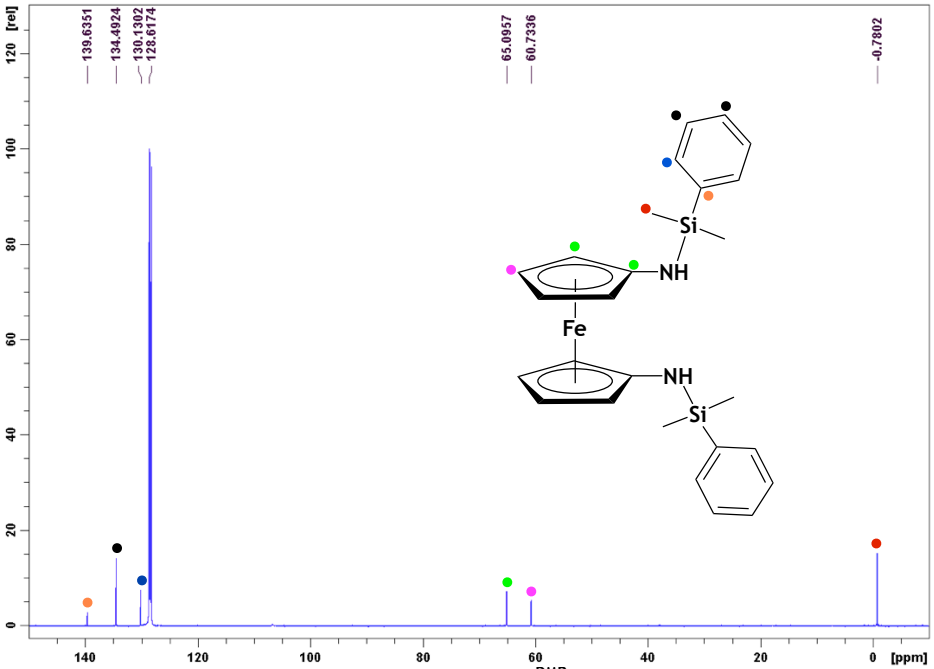

Figure A2. ^{13}C NMR spectrum (500 MHz, 25 ºC, C_6D_6) of $\mathbf{H_2NN^{DMP}}$; δ (ppm): 139.6 (s, 2C, Si-C_6H_5), 134.5 (s, 6C, meta/para-C_6H_6), 130.1 (s, 4C, ortho-C_6H_6), 65.1 (s, 6C, HN-C_5H_4), 60.7 (s, 4C, HN-C_5H_4), -0.78 (s, 4C, Si-CH_3).

1.5.4 Cyclic voltammetry

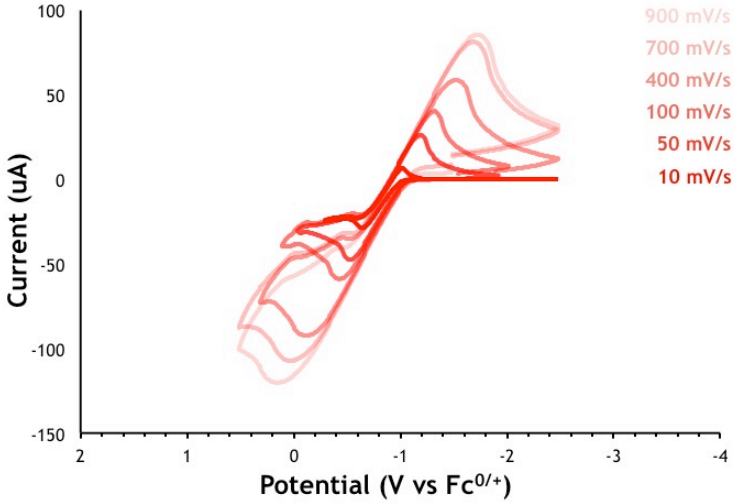

Figure A3. Cyclic voltammogram of H_2NN^H (12.7 mM) in THF with $TBAPF_6$ as the supporting electrolyte.

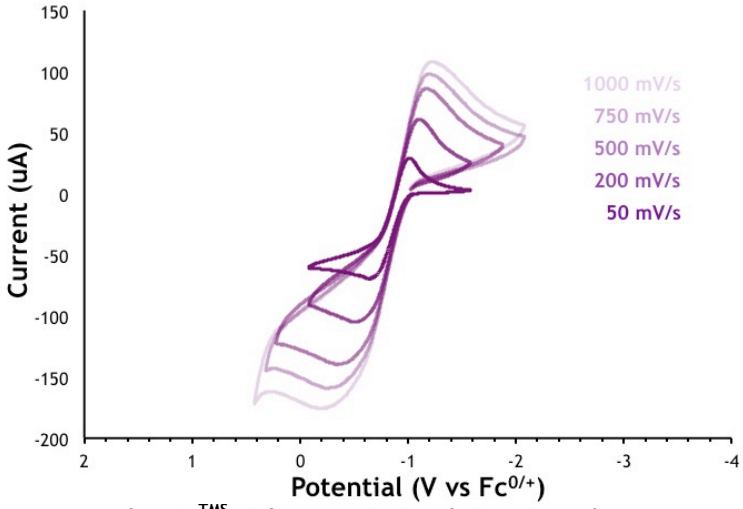

Figure A4. Cyclic voltammogram of H_2NN^{TMS} (5.9 mM) in THF with $TBAPF_6$ as the supporting electrolyte.

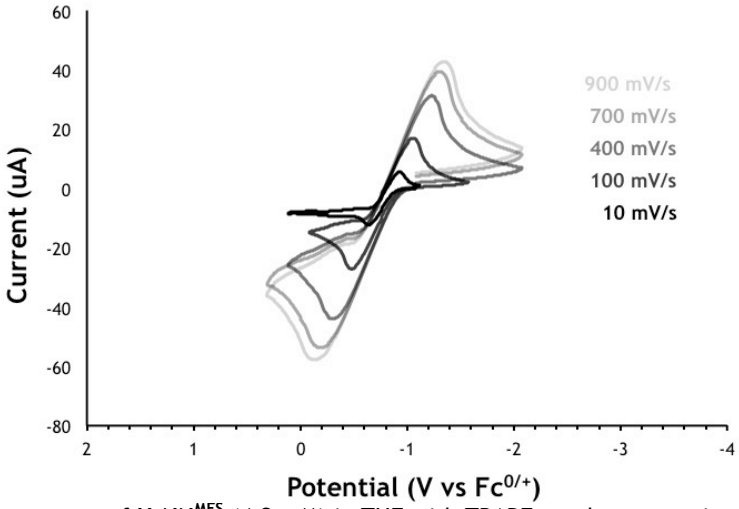

Figure A5. Cyclic voltammogram of H_2NN^{MES} (4.2 mM) in THF with $TBAPF_6$ as the supporting electrolyte.

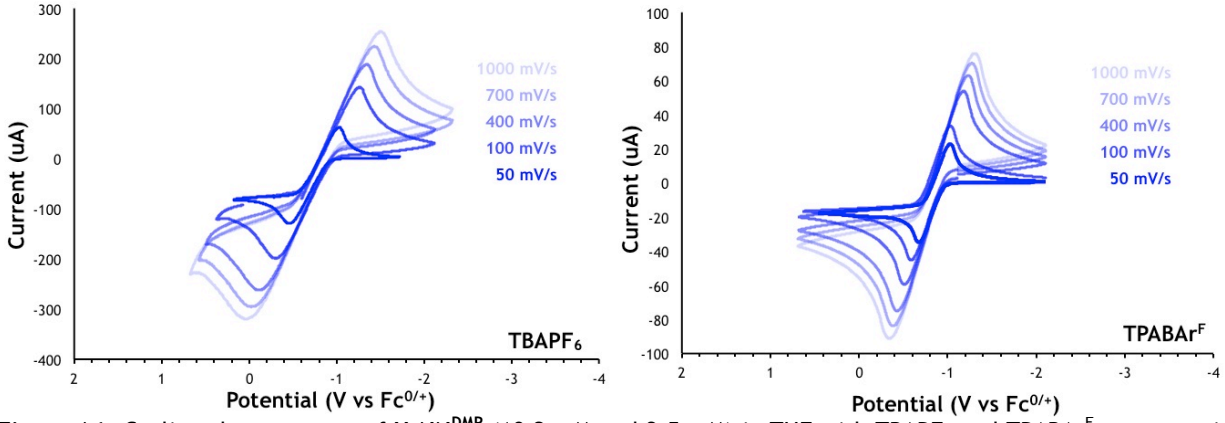

Figure A6. Cyclic voltammogram of H_2NN^{DMP} (10.2 mM and 3.5 mM) in THF with $TBAPF_6$ and $TPABAr^F$ as supporting electrolytes.

1.5.5 UV-Vis spectroscopy

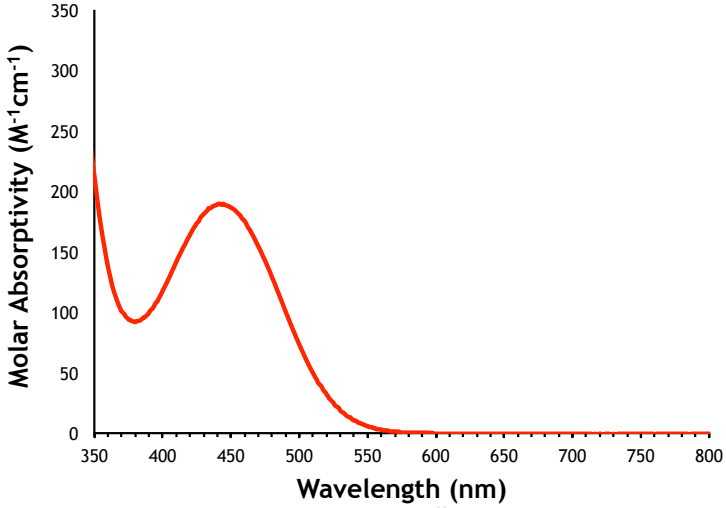

Figure A7. UV-Vis spectrum of a 5.9 mM CH_2Cl_2 solution of H_2NN^H.

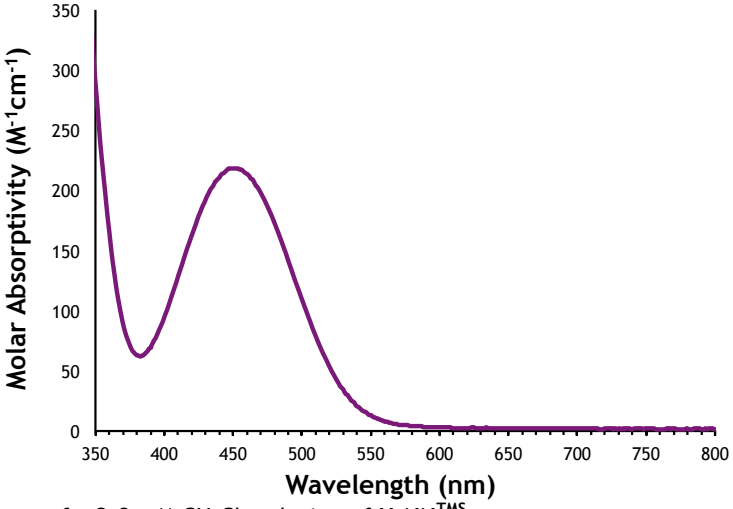

Figure A8. UV-Vis spectrum of a 2.8 mM CH_2Cl_2 solution of H_2NN^{TMS}.

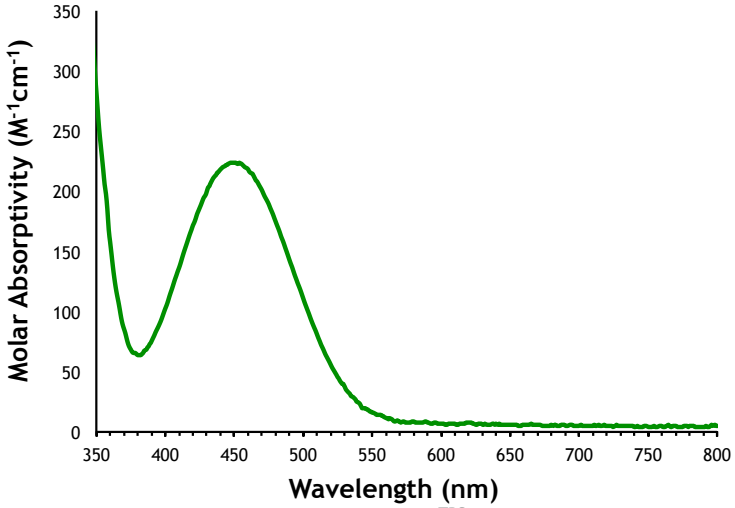

Figure A9. UV-Vis spectrum of a 2.3 mM CH_2Cl_2 solution of H_2NN^{TBS}.

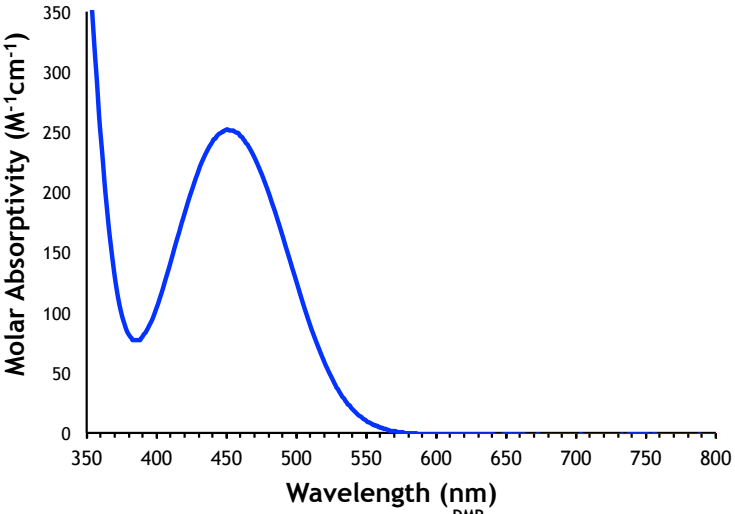

Figure A10. UV-Vis spectrum of a 3.4 mM CH_2Cl_2 solution of H_2NN^{DMP}.

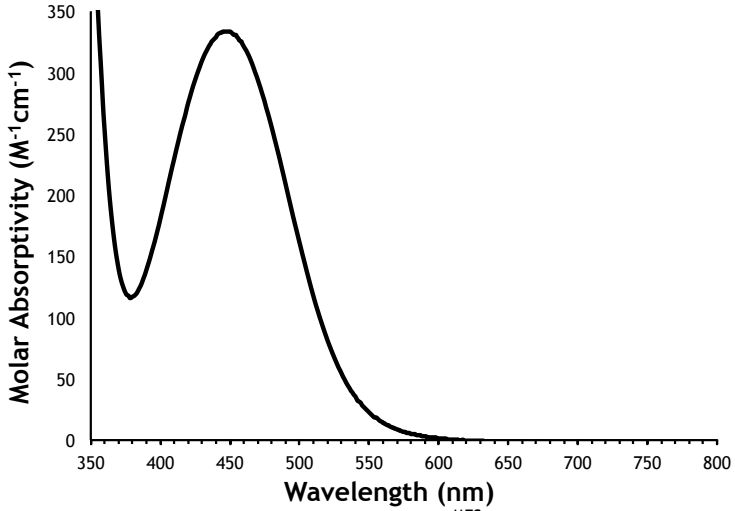

Figure A11. UV-Vis spectrum of a 3.8 mM CH_2Cl_2 solution of H_2NN^{MES}.

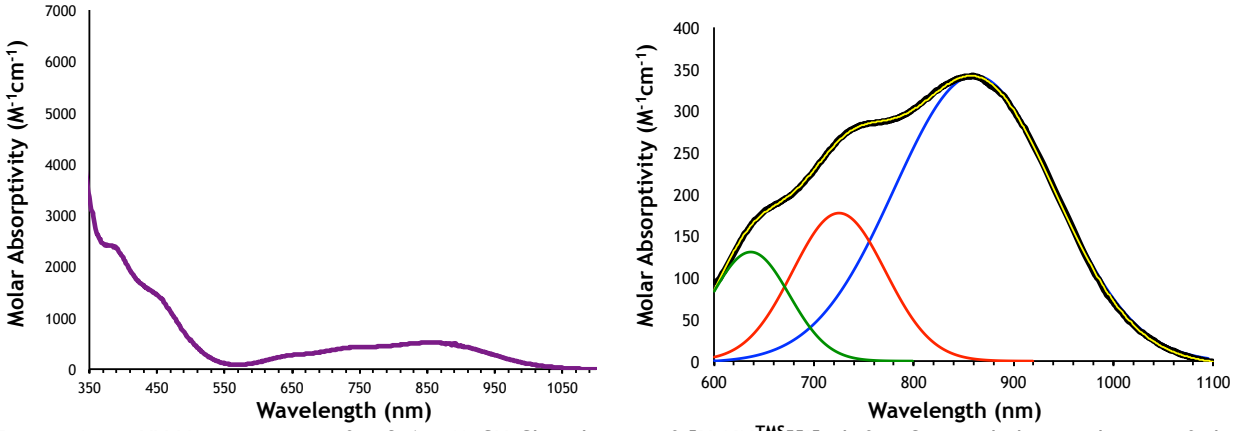

Figure A12. UV-Vis spectrum of a 2.6 mM CH_2Cl_2 solution of **[H_2NN^{TMS}][I]** (left). Spectral deconvolution of the charge transfer band in the visible/near IR region (right).

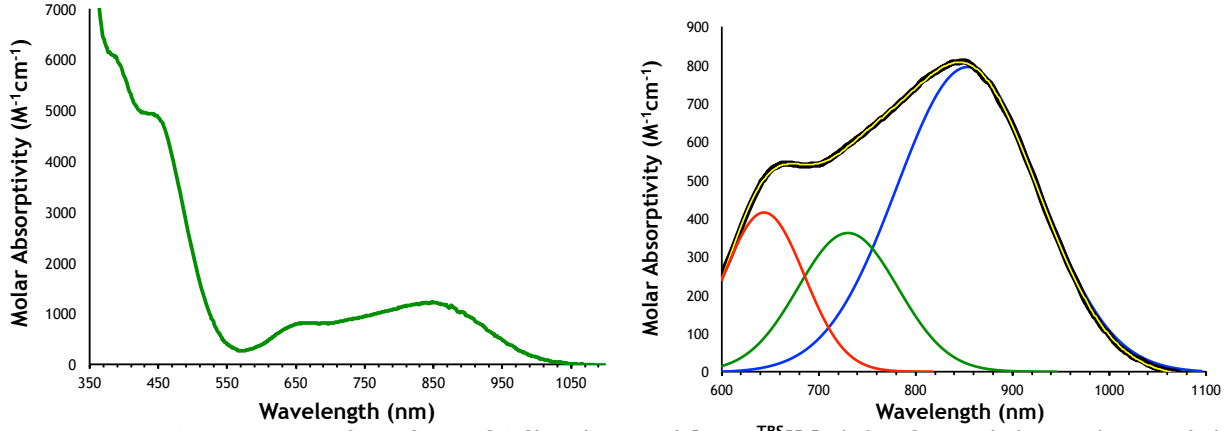

Figure A13. UV-Vis spectrum of a 1.3 mM CH_2Cl_2 solution of **[H_2NN^{TBS}][I]** (left). Spectral deconvolution of the charge transfer band in the visible/near IR region (right).

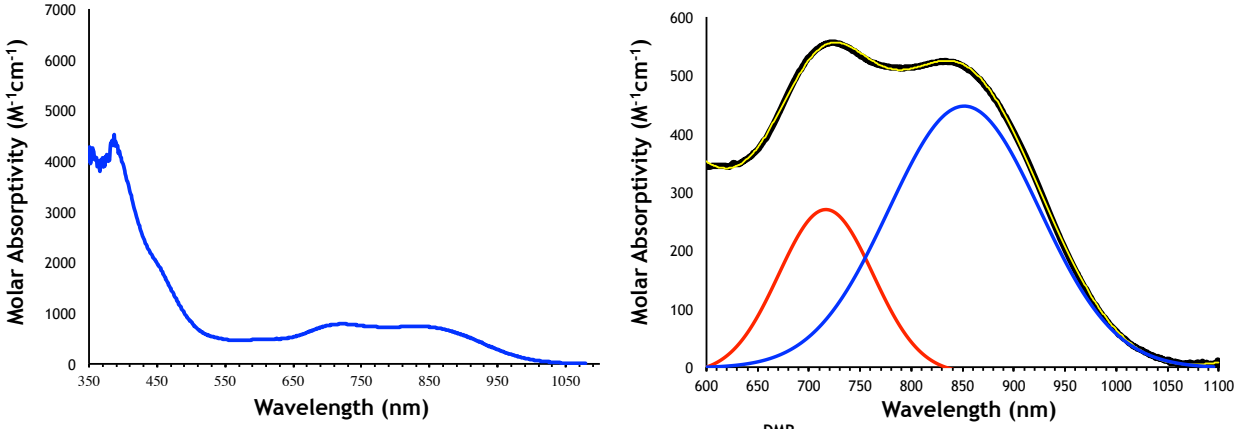

Figure A14. UV-Vis spectrum of a 0.42 mM CH_2Cl_2 solution of **[H_2NN^{DMP}][I]** (left). Spectral deconvolution of the charge transfer band in the visible/near IR region (right).

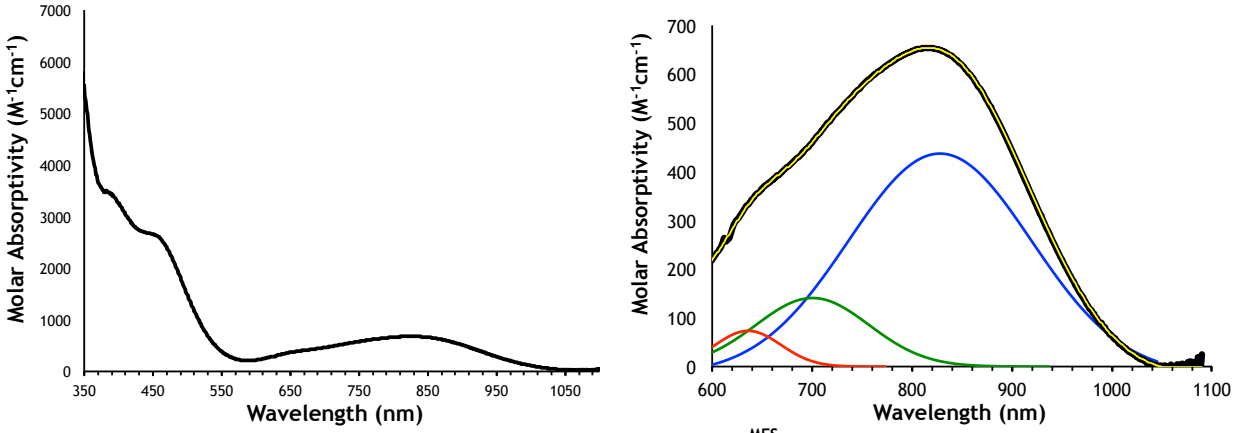

Figure A15. UV-Vis spectrum of a 0.2 mM CH_2Cl_2 solution of **[H_2NN^{MES}][I_3]** (left). Spectral deconvolution of the charge transfer band in the visible/near IR region (right).

1.5.6 IR spectroscopy

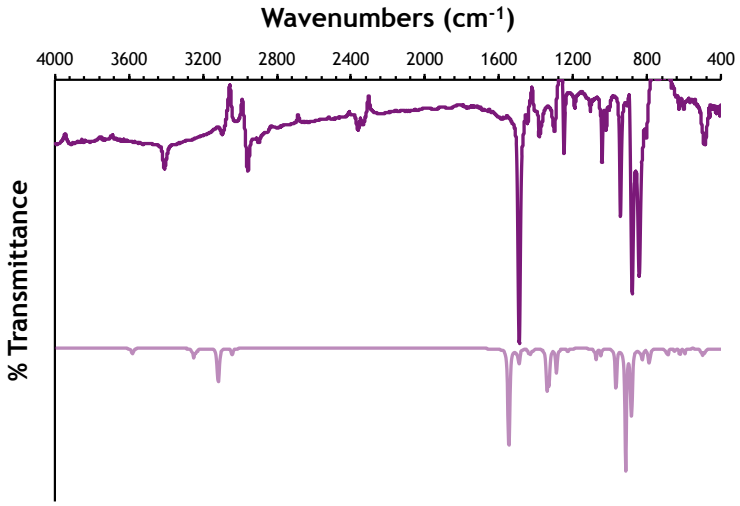

Figure A16. Experimental (top, in dichloromethane) and calculated (bottom) IR spectrum of **H_2NN^{TMS}**.

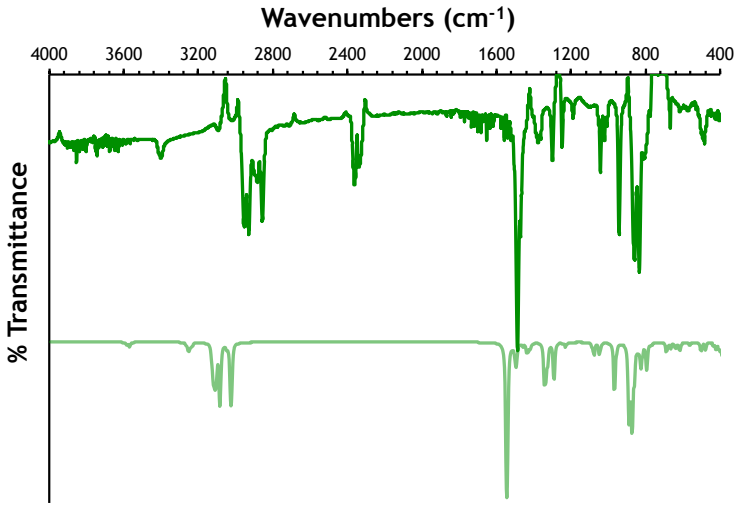

Figure A17. Experimental (top, in dichloromethane) and calculated (bottom) IR spectrum of **H_2NN^{TBS}**.

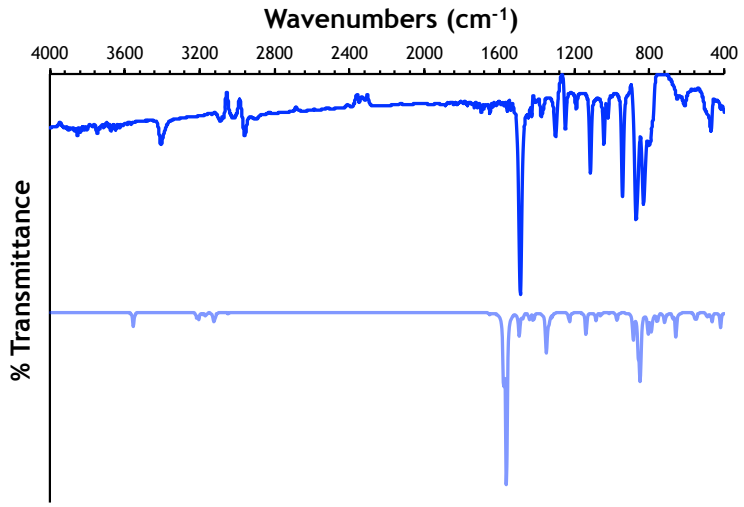

Figure A18. Experimental (top, in dichloromethane) and calculated (bottom) IR spectrum of H_2NN^{DMP}.

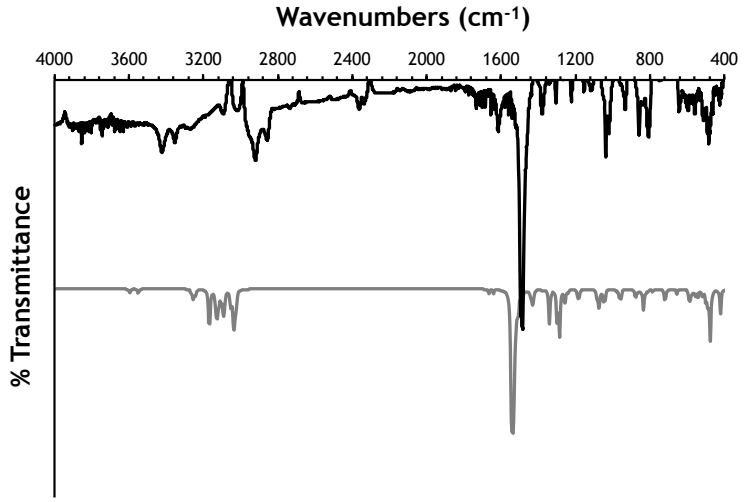

Figure A19. Experimental (top, in dichloromethane) and calculated (bottom) IR spectrum of H_2NN^{MES}.

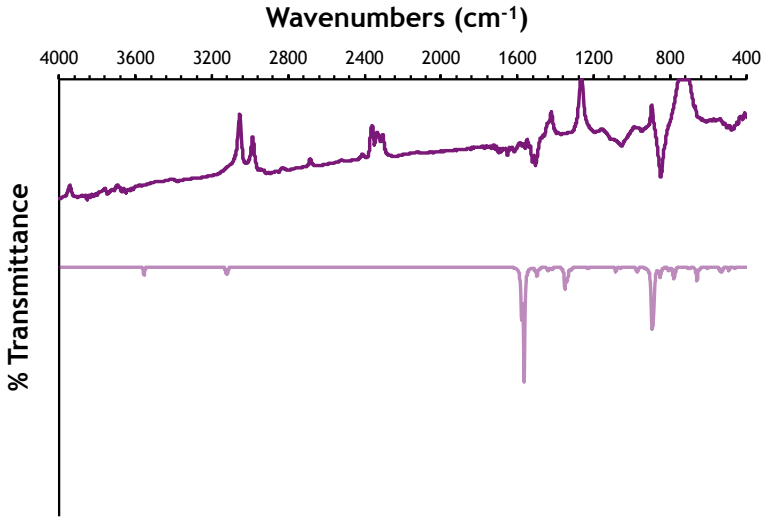

Figure A20. Experimental (top, in dichloromethane) and calculated (bottom) IR spectrum of $[H_2NN^{TMS}][I]$.

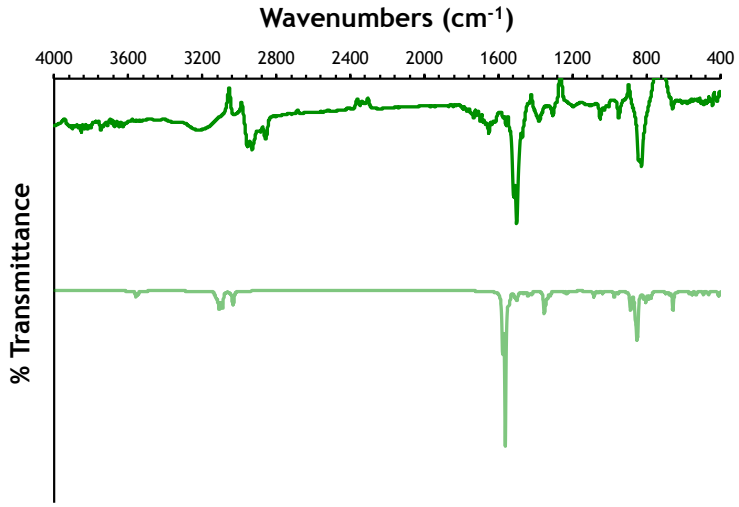

Figure A21. Experimental (top, in dichloromethane) and calculated (bottom) IR spectrum of **[H_2NN^{TBS}][I]**.

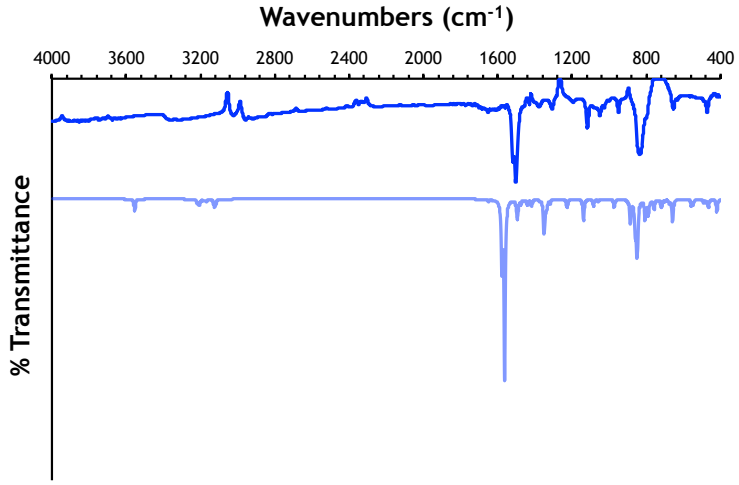

Figure A22. Experimental (top, in dichloromethane) and calculated (bottom) IR spectrum of **[H_2NN^{DMP}][I]**.

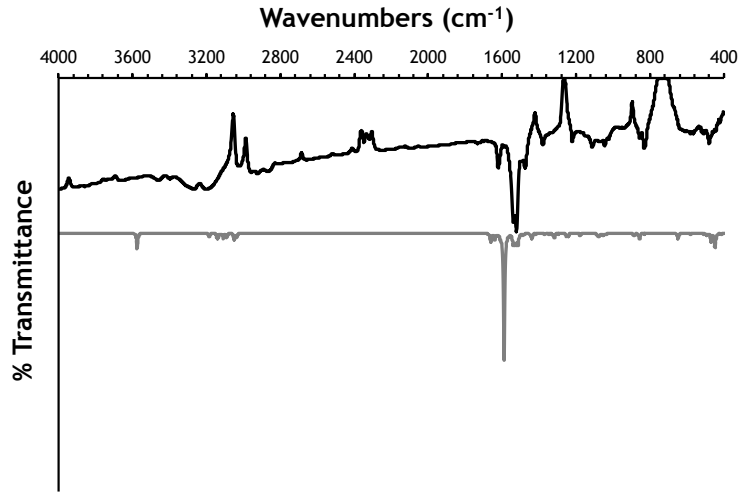

Figure A23. Experimental (top, in dichloromethane) and calculated (bottom) IR spectrum of **[H_2NN^{MES}][I_3]**.

1.5.7 Magnetometry

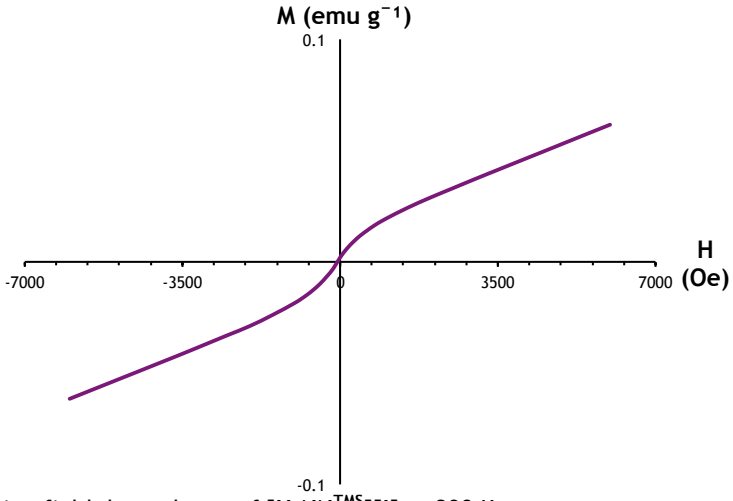

Figure A24. Magnetization field dependence of **[H_2NN^{TMS}][I]** at 298 K.

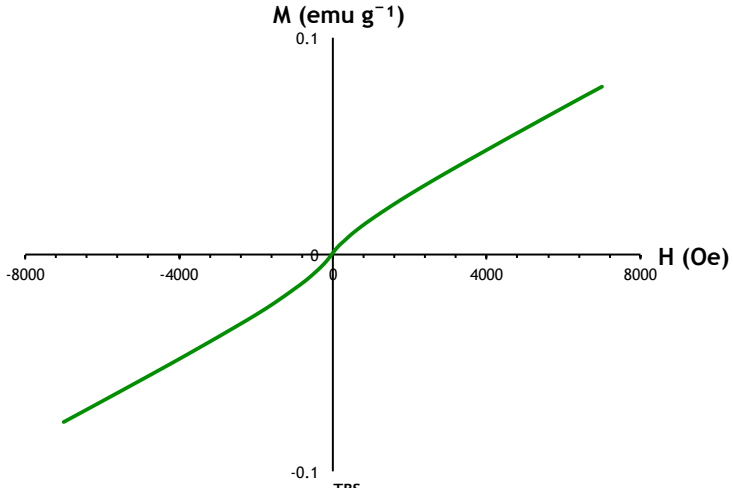

Figure A25. Magnetization field dependence of **[H_2NN^{TBS}][I]** at 298 K.

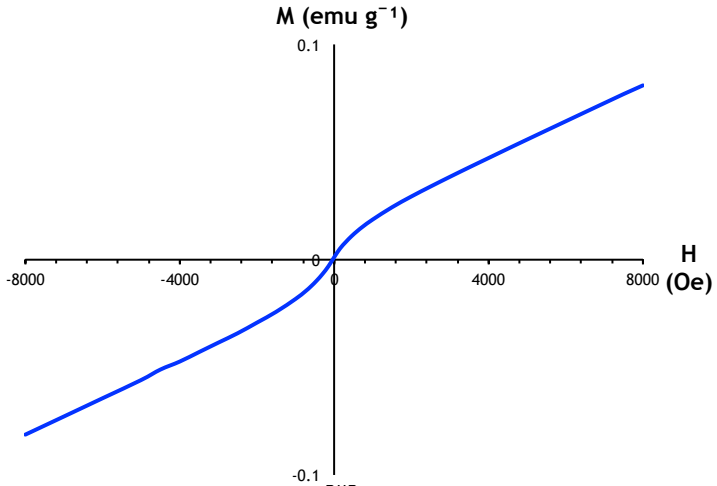

Figure A26. Magnetization field dependence of **[H_2NN^{DMP}][I]** at 298 K.

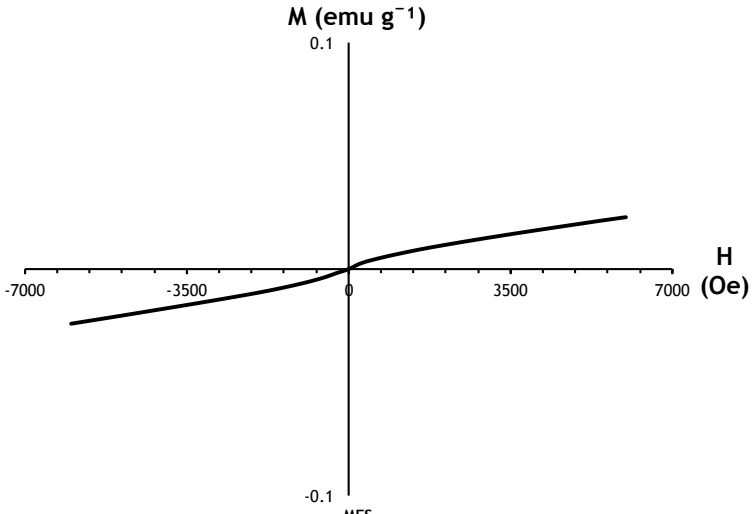

Figure A27. Magnetization field dependence of **[H_2NN^{MES}][I_3]** at 298 K.

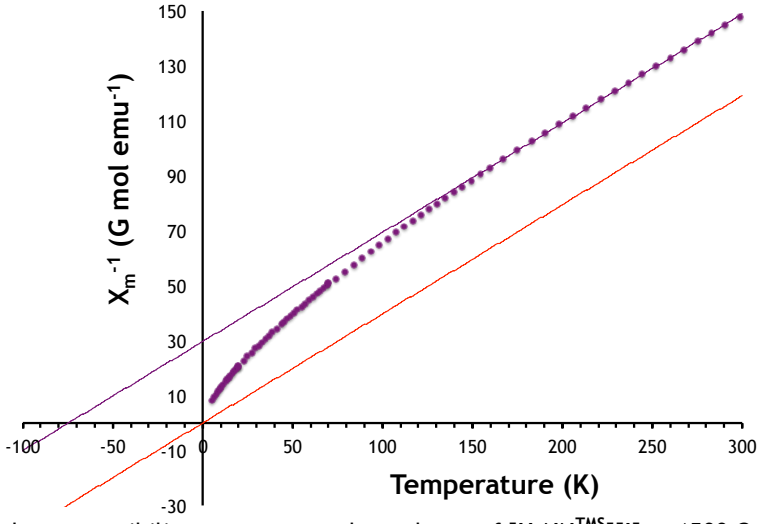

Figure A28. Inverse molar susceptibility temperature dependence of **[H_2NN^{TMS}][I]** at 1500 G.

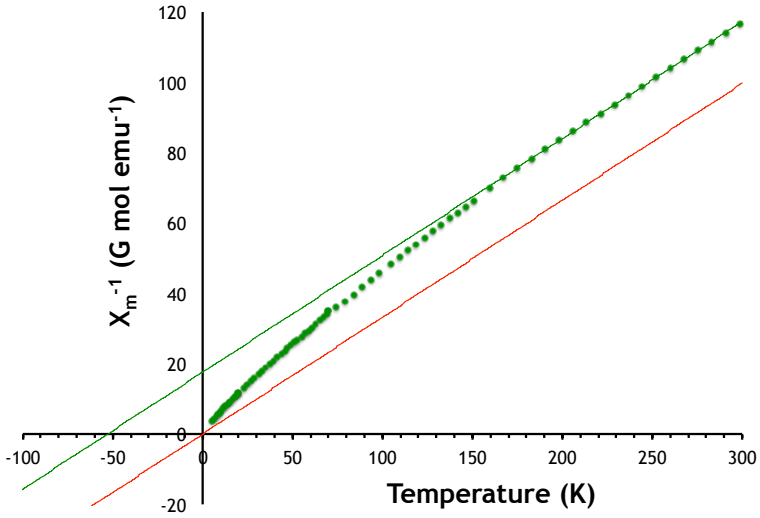

Figure A29. Inverse molar susceptibility temperature dependence of **[H_2NN^{TBS}][I]** at 1500 G.

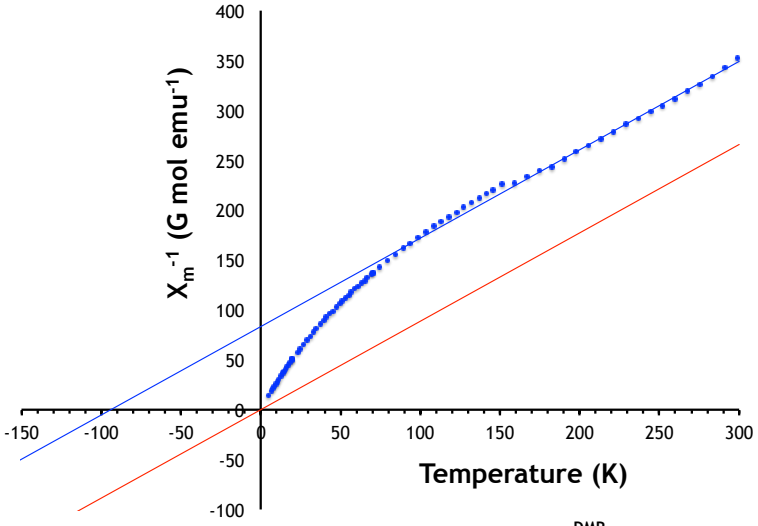

Figure A30. Inverse molar susceptibility temperature dependence of **[H_2NN^{DMP}][I]** at 1500 G.

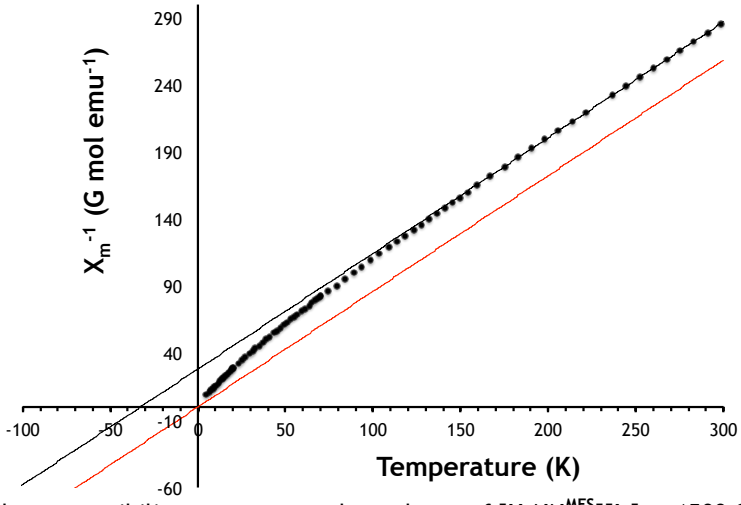

Figure A31. Inverse molar susceptibility temperature dependence of **[H_2NN^{MES}][I_3]** at 1500 G.

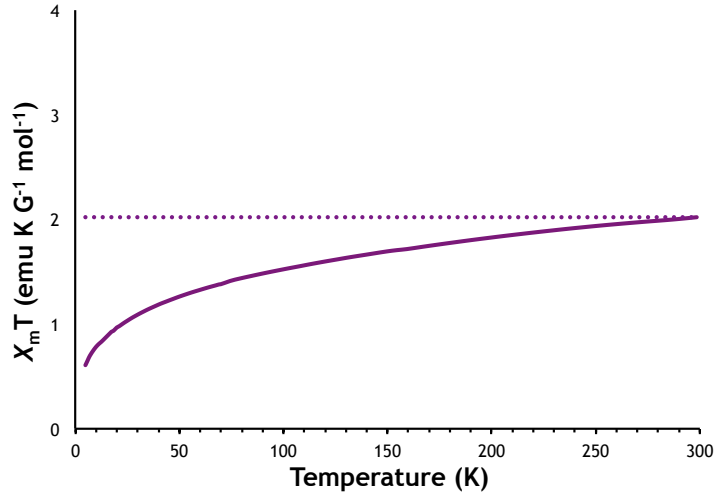

Figure A32. Molar susceptibility temperature product of **[H_2NN^{TMS}][I]** at 1500 G.

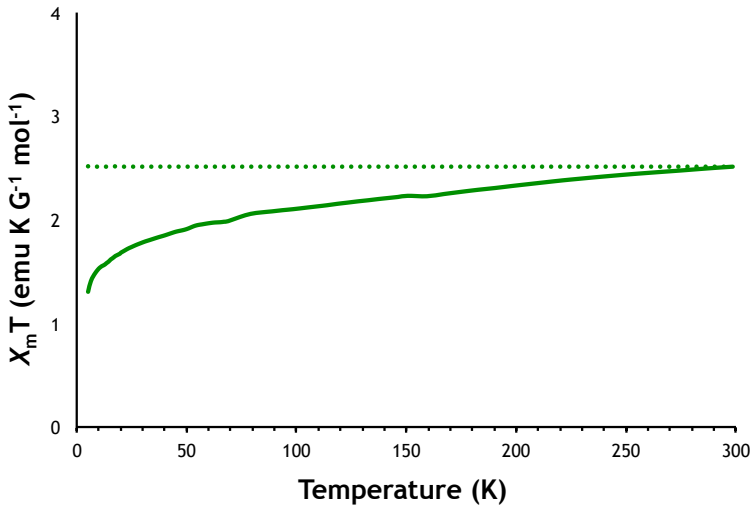

Figure A33. Molar susceptibility temperature product of **[H_2NN^{TBS}][I]** at 1500 G.

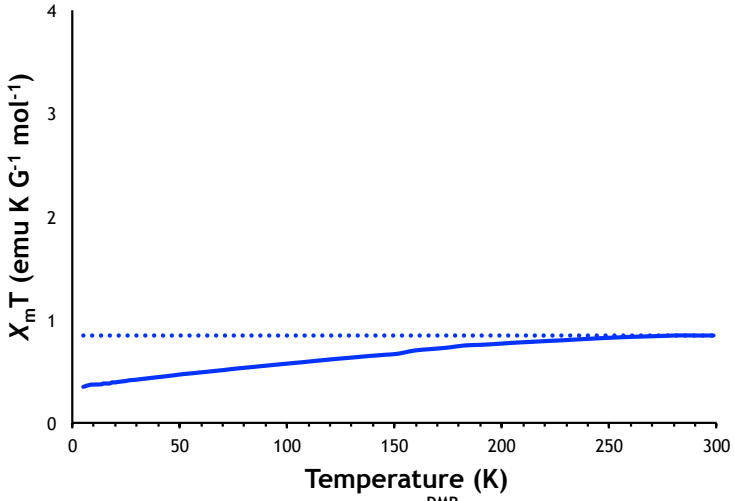

Figure A34. Molar susceptibility temperature product of **[H_2NN^{DMP}][I]** at 1500 G.

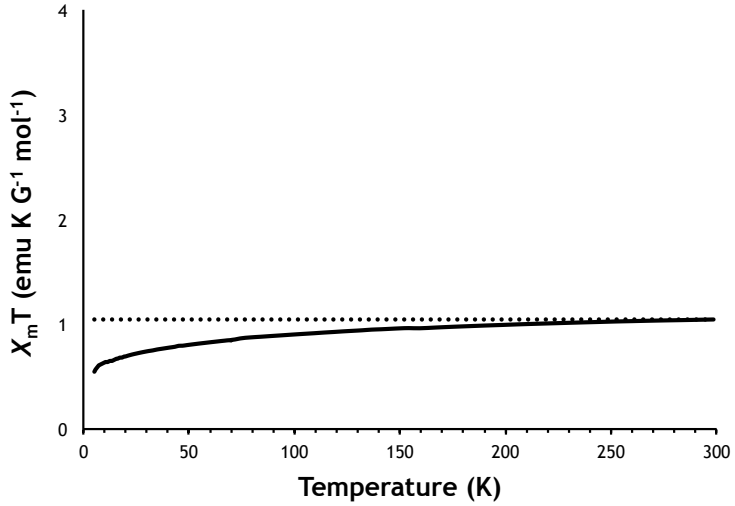

Figure A34. Molar susceptibility temperature product of **[H_2NN^{MES}][I_3]** at 1500 G.

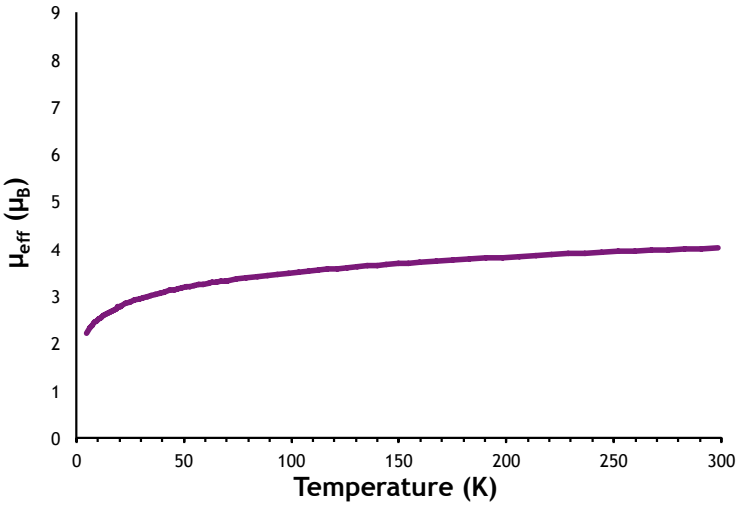

Figure A35. Magnetic moment of **[H_2NN^{TMS}][I]** at 1500 G.

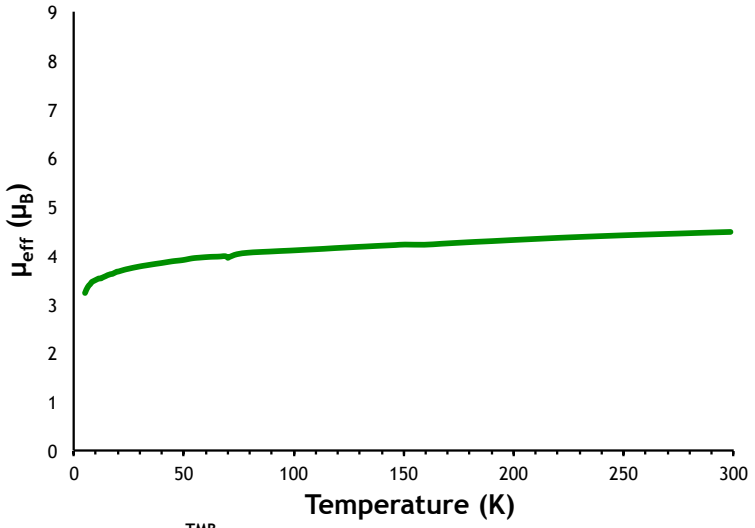

Figure A36. Magnetic moment of **[H_2NN^{TMB}][I]** at 1500 G.

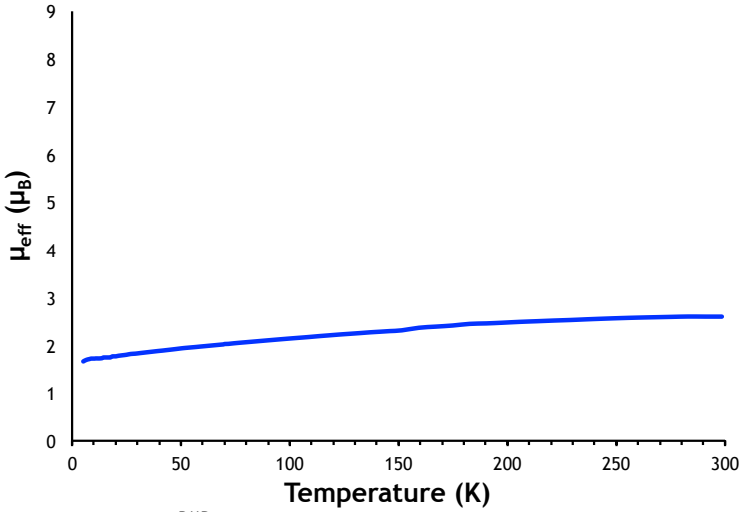

Figure A37. Magnetic moment of **[H_2NN^{DMP}][I]** at 1500 G.

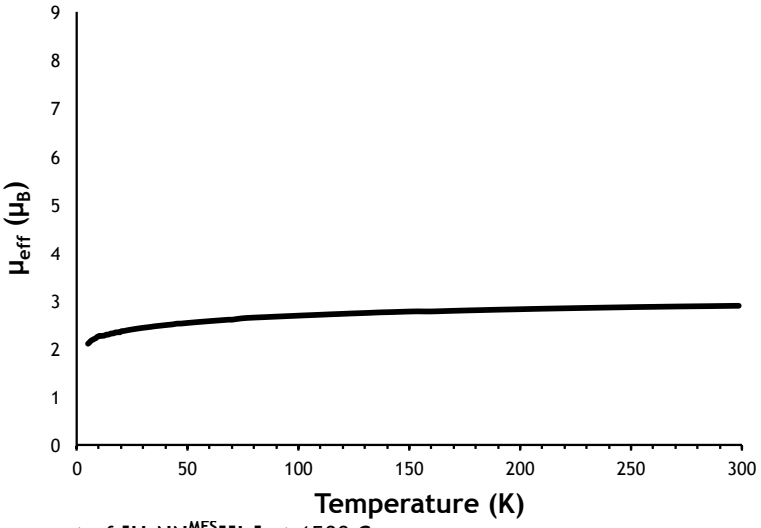

Figure A38. Magnetic moment of **[H_2NN^{MES}][I_3]** at 1500 G.

1.5.8 DFT

Geometry optimization (uB3LYP/6-31G*)

Table A1. ferrocene (D_{5h})

Item	Value	Threshold	Converged?
Maximum Force	0.000052	0.00045	YES
RMS Force	0.000012	0.0003	YES
Maximum Displacement	0.001432	0.0018	YES
RMS Displacement	0.000188	0.0012	YES

Center Number	Atomic Number	Coordinates (Angstroms) X	Y	Z
1	26	0	-0.000303	-0.000519
2	6	1.653649	-0.626116	1.040931
3	6	-1.653648	-0.625888	1.041068
4	6	1.653514	0.796439	0.917328
5	6	1.654795	-1.183288	-0.273792
6	6	-1.654795	-1.183347	-0.273534
7	6	-1.653514	0.796639	0.917155
8	6	1.653892	1.118503	-0.473689
9	6	1.654823	-0.104988	-1.209805
10	6	-1.654823	-0.105252	-1.209782
11	6	-1.653892	1.118399	-0.473933
12	1	1.644591	-1.184085	1.968455
13	1	-1.644589	-1.183656	1.968713
14	1	1.6441	1.505993	1.734632
15	1	1.646649	-2.237737	-0.517997
16	1	-1.64665	-2.237849	-0.51751
17	1	-1.644099	1.506374	1.734302
18	1	1.64483	2.115042	-0.896041
19	1	1.646838	-0.198577	-2.288134
20	1	-1.646838	-0.199078	-2.28809
21	1	-1.644831	2.114846	-0.896503

Table A2. Ferrocenium (D_{5h})

Item	Value	Threshold	Converged?
Maximum Force	0.000029	0.00045	YES
RMS Force	0.00001	0.0003	YES
Maximum Displacement	0.001727	0.0018	YES
RMS Displacement	0.000254	0.0012	YES

Center Number	Atomic Number	Coordinates (Angstroms) X	Y	Z
1	26	0	-0.00152	-0.000071
2	6	-1.675774	0.633582	-1.038288
3	6	1.675774	0.633729	-1.038199
4	6	-1.675203	1.183784	0.281243
5	6	-1.677764	-0.791338	-0.922755
6	6	1.677764	-0.791208	-0.922865
7	6	1.675203	1.183744	0.281409
8	6	-1.676303	0.098701	1.212
9	6	-1.67798	-1.121841	0.467935
10	6	1.677981	-1.121907	0.467779
11	6	1.676301	0.09853	1.212016
12	1	-1.656583	1.196765	-1.96243
13	1	1.656583	1.197043	-1.962261
14	1	-1.655533	2.23655	0.531546
15	1	-1.660404	-1.496141	-1.743921
16	1	1.660407	-1.495896	-1.744129
17	1	1.655535	2.236474	0.531862
18	1	-1.657395	0.18594	2.290668
19	1	-1.660181	-2.120687	0.884243
20	1	1.660179	-2.120815	0.883936
21	1	1.657393	0.185621	2.290695

******* 1 imaginary frequencies (negative signs) *******
Frequencies: -17.4488

Table A3. ferrocene (D_{5d})

Item	Value	Threshold	Converged?
Maximum Force	0.000098	0.00045	YES
RMS Force	0.000024	0.0003	YES
Maximum Displacement	0.001765	0.0018	YES
RMS Displacement	0.00028	0.0012	YES

Center Number	Atomic Number	Coordinates (Angstroms) X	Y	Z
1	26	-0.000001	-0.000186	-0.001006
2	6	-1.655965	1.212694	0.060484
3	6	1.654579	0.945958	0.761939
4	6	-1.654973	0.317473	1.17223
5	6	-1.657408	0.431805	-1.134429
6	6	1.656468	1.01674	-0.663626
7	6	1.655084	-0.43177	1.135163
8	6	-1.655445	-1.016563	0.66446
9	6	-1.656661	-0.945888	-0.761072
10	6	1.657669	-0.317214	-1.171481
11	6	1.656656	-1.212552	-0.059855
12	1	-1.64018	2.293614	0.113852
13	1	1.637503	1.788786	1.440831
14	1	-1.638234	0.60061	2.216775
15	1	-1.643822	0.816985	-2.145883
16	1	1.64179	1.922716	-1.255708
17	1	1.639007	-0.817039	2.146557
18	1	-1.639648	-1.922557	1.256457
19	1	-1.64193	-1.788739	-1.439972
20	1	1.643904	-0.600193	-2.216143
21	1	1.641614	-2.293439	-0.113486

****** 1 imaginary frequencies (negative signs) ******
Frequencies: -19.0528

Table A4. Ferrocenium (D_{5d})

Item	Value	Threshold	Converged?
Maximum Force	0.000077	0.00045	YES
RMS Force	0.000017	0.0003	YES
Maximum Displacement	0.001605	0.0018	YES
RMS Displacement	0.000238	0.0012	YES

Center Number	Atomic Number	Coordinates (Angstroms) X	Y	Z
1	26	0.00000	-0.00079	-0.00142
2	6	-1.67662	1.17359	-0.31763
3	6	1.67527	1.13670	0.43302
4	6	-1.67524	0.66535	1.01819
5	6	-1.67813	0.06025	-1.21378
6	6	1.67735	0.76282	-0.94637
7	6	1.67515	-0.05976	1.21486
8	6	-1.67601	-0.76219	0.94755
9	6	-1.67786	-1.13605	-0.43187
10	6	1.67874	-0.66460	-1.01708
11	6	1.67737	-1.17308	0.31854
12	1	-1.65375	2.21813	-0.60085
13	1	1.65140	2.14814	0.81792
14	1	-1.65131	1.25747	1.92396
15	1	-1.65641	0.11372	-2.29467
16	1	1.65497	1.44127	-1.78953
17	1	1.65111	-0.11345	2.29571
18	1	-1.65252	-1.44100	1.79021
19	1	-1.65625	-2.14755	-0.81660
20	1	1.65763	-1.25661	-1.92310
21	1	1.65514	-2.21768	0.60121

Table A5. H_2NN^{TMS}

Item		Value	Threshold	Converged?
Maximum Force		0.000003	0.00045	YES
RMS Force		0.000001	0.0003	YES
Maximum Displacement		0.000844	0.0018	YES
RMS Displacement		0.000135	0.0012	YES
Center	Atomic	Coordinates (Angstroms)		
Number	Number	X	Y	Z
1	26	-0.014382	-1.667066	-0.007711
2	6	1.459765	-0.461063	-0.907294
3	6	-0.965097	-0.508234	1.39388
4	6	0.494863	-0.924551	-1.856562
5	6	2.025338	-1.614573	-0.277394
6	6	-0.368136	-1.664929	1.994249
7	6	-1.942212	-0.948974	0.445423
8	6	0.504657	-2.35683	-1.849925
9	6	1.454822	-2.78392	-0.877628
10	6	-0.944292	-2.820955	1.39185
11	6	-1.902745	-2.377918	0.42505
12	7	1.800355	0.8748	-0.671833
13	1	-0.7193	0.519983	1.625186
14	1	-0.12125	-0.290314	-2.482614
15	1	2.767466	-1.607475	0.509823
16	1	0.391421	-1.654915	2.765074
17	7	-2.807463	-0.14757	-0.30781
18	1	-0.102433	-2.997887	-2.476197
19	1	1.702463	-3.807663	-0.628958
20	1	-0.706276	-3.851245	1.622414
21	1	-2.518394	-3.011549	-0.202029
22	1	1.170105	1.530398	-1.117735
23	1	2.13888	3.829786	0.239164
24	1	-1.895512	3.704931	-0.49561
25	1	-3.303316	-0.664153	-1.024241
26	14	3.187526	1.547424	0.176534
27	1	3.980605	1.629992	2.551204
28	1	5.667231	1.229517	0.028538
29	14	-3.17108	1.565914	-0.167095
30	1	-4.296186	1.598501	-2.412403
31	1	-3.918408	3.065514	1.692453
32	6	3.110074	1.204586	2.035659
33	1	2.209904	1.646298	2.479317
34	1	3.090364	0.130796	2.255015
35	6	-1.685177	2.638559	-0.646022
36	1	-0.800739	2.386697	-0.049099
37	1	-1.427745	2.494968	-1.702852
38	6	-3.706153	1.993667	1.592465
39	1	-4.61303	1.443102	1.867918
40	1	-2.933329	1.739025	2.326243
41	6	4.797692	0.848704	-0.52172
42	1	4.82297	-0.245344	-0.465222
43	1	4.917785	1.125403	-1.57556
44	6	-4.583248	1.860351	-1.386637
45	1	-5.472657	1.275077	-1.124951
46	1	-4.875217	2.91738	-1.390979
47	6	3.080543	3.408245	-0.133019
48	1	3.896665	3.932301	0.378677
49	1	3.157211	3.644246	-1.201

Table A6. H_2NN^{TMS+}

Item		Value	Threshold	Converged?
Maximum Force		0.000005	0.00045	YES
RMS Force		0.000001	0.0003	YES
Maximum Displacement		0.001349	0.0018	YES
RMS Displacement		0.000262	0.0012	YES
Center	Atomic	Coordinates (Angstroms)		
Number	Number	X	Y	Z
1	26	-0.006443	-1.401703	-0.009687
2	6	1.696993	-0.296293	-1.003165
3	6	-1.089946	-0.199415	1.335321
4	6	0.547681	-0.524838	-1.838268
5	6	2.052017	-1.575773	-0.453646
6	6	-0.27069	-1.1626	2.0036
7	6	-2.121933	-0.894217	0.613107
8	6	0.335027	-1.933378	-1.954672
9	6	1.265457	-2.584332	-1.093282
10	6	-0.702305	-2.459174	1.598963
11	6	-1.790431	-2.291019	0.687777
12	7	2.254317	0.907686	-0.715797
13	1	-1.006273	0.874035	1.436513
14	1	0.005189	0.247422	-2.369621
15	1	2.843752	-1.756326	0.260273
16	1	0.530242	-0.938052	2.695396
17	7	-3.146206	-0.348155	-0.091217
18	1	-0.396052	-2.413609	-2.591617
19	1	1.371296	-3.651451	-0.949134
20	1	-0.293564	-3.405955	1.926594
21	1	-2.345576	-3.086898	0.206795
22	1	1.80778	1.682431	-1.196569
23	1	3.066491	3.728786	0.312282
24	1	-2.80348	3.453302	-1.124053
25	1	-3.728537	-1.038108	-0.5558
26	14	3.762531	1.323418	0.195424
27	1	4.402437	1.214752	2.592254
28	1	6.133894	0.628243	-0.016751
29	14	-3.742668	1.357827	-0.16836
30	1	-5.128132	0.827757	-2.188221
31	1	-4.445634	3.002424	1.552637
32	6	3.516781	0.915924	2.018248
33	1	2.658548	1.454244	2.436969
34	1	3.367196	-0.155187	2.197953
35	6	-2.449974	2.418487	-1.039742
36	1	-1.494996	2.447422	-0.501724
37	1	-2.25849	2.053713	-2.055719
38	6	-4.068483	1.972805	1.578032
39	1	-4.822862	1.356399	2.079557
40	1	-3.169677	1.972503	2.204611
41	6	5.203998	0.362674	-0.534304
42	1	5.083084	-0.722626	-0.444019
43	1	5.33857	0.595175	-1.596561
44	6	-5.316847	1.220318	-1.182047
45	1	-6.060486	0.576559	-0.697968
46	1	-5.775719	2.208644	-1.302064
47	6	3.92618	3.173939	-0.081891
48	1	4.817466	3.554796	0.430276
49	1	4.035049	3.42109	-1.144414

Table A7. H_2NN^{TBS}

Item		Value	Threshold	Converged?
Maximum Force		0.000009	0.00045	YES
RMS Force		0.000002	0.0003	YES
Maximum Displacement		0.001773	0.0018	YES
RMS Displacement		0.000234	0.0012	YES
Center	Atomic	Coordinates (Angstroms)		
Number	Number	X	Y	Z
1	26	-0.028592	1.970778	-0.077296
2	6	-1.45363	0.597556	-0.796414
3	6	0.88683	1.099835	1.540235
4	6	-0.417489	0.845475	-1.752769
5	6	-2.043862	1.859987	-0.473843
6	6	0.184558	2.289109	1.921216
7	6	1.901113	1.460061	0.595801
8	6	-0.407624	2.244058	-2.058956
9	6	-1.416372	2.871181	-1.271848
10	6	0.732701	3.379728	1.1856
11	6	1.780297	2.864492	0.357318
12	7	-1.812082	-0.662458	-0.301386
13	1	0.682056	0.103585	1.909454
14	1	0.233982	0.092235	-2.178946
15	1	-2.840437	2.023434	0.238201
16	1	-0.627009	2.341433	2.635344
17	7	2.8661	0.620696	0.027187
18	1	0.250667	2.733829	-2.765021
19	1	-1.667036	3.923982	-1.269064
20	1	0.419016	4.413956	1.241596
21	1	2.400967	3.43844	-0.32027
22	1	-1.175667	-1.38884	-0.609179
23	1	-1.868353	-2.955848	1.799876
24	1	2.038539	-3.24955	0.232731
25	1	3.369501	1.063295	-0.731919
26	14	-3.219041	-1.229798	0.597478
27	1	-4.226386	-0.669745	2.814725
28	14	3.266599	-1.052985	0.390391
29	1	3.79864	-2.291945	2.508601
30	6	-3.496408	-0.187051	2.153392
31	1	-2.557362	-0.08687	2.709758
32	1	-3.865426	0.8225	1.943667
33	6	1.845336	-2.217449	-0.083881
34	1	0.912957	-1.894666	0.394502
35	1	1.674934	-2.223919	-1.167079
36	6	3.601833	-1.246716	2.241609
37	1	4.463438	-0.64727	2.555555
38	1	2.742952	-0.912669	2.834161
39	6	-2.725134	-2.982596	1.116219
40	1	-3.544752	-3.490092	1.637514
41	1	-2.447552	-3.608254	0.259479
42	6	4.836955	-1.444113	-0.651235
43	6	4.558902	-1.255835	-2.158814
44	6	6.004941	-0.522856	-0.237165
45	6	5.250368	-2.912318	-0.406227
46	1	3.748612	-1.904602	-2.51195
47	1	4.286378	-0.222704	-2.409072
48	1	5.454797	-1.502291	-2.74693
49	1	6.274741	-0.654478	0.817122
50	1	6.900411	-0.747065	-0.834948
51	1	5.769031	0.53782	-0.385287
52	1	6.154152	-3.156193	-0.983133
53	1	5.477675	-3.103826	0.649407
54	1	4.468571	-3.617028	-0.714252
55	6	-4.8123	-1.274825	-0.484256
56	6	-5.212797	0.145807	-0.936329
57	6	-4.560998	-2.140287	-1.737145
58	6	-5.977297	-1.88513	0.325776
59	1	-5.432232	0.800702	-0.084106
60	1	-4.427765	0.623935	-1.53234
61	1	-6.121093	0.105581	-1.555705
62	1	-4.317419	-3.178512	-1.479
63	1	-5.458458	-2.166125	-2.37252
64	1	-3.73911	-1.742458	-2.343802
65	1	-6.891396	-1.91687	-0.285041
66	1	-5.766014	-2.91339	0.644402
67	1	-6.208639	-1.297144	1.222675

Table A8. H_2NN^{TBS+}

Item		Value	Threshold	Converged?
Maximum Force		0.000005	0.00045	YES
RMS Force		0.000001	0.0003	YES
Maximum Displacement		0.001206	0.0018	YES
RMS Displacement		0.00026	0.0012	YES
Center	Atomic	Coordinates (Angstroms)		
Number	Number	X	Y	Z
1	26	-0.017419	1.623496	-0.055435
2	6	-1.711286	0.351229	-0.849745
3	6	1.038978	0.713041	1.517768
4	6	-0.53033	0.389188	-1.67388
5	6	-2.061763	1.720509	-0.593999
6	6	0.190705	1.77177	1.972393
7	6	2.0851	1.277803	0.706666
8	6	-0.292217	1.739499	-2.077322
9	6	-1.238802	2.56447	-1.402966
10	6	0.620348	2.976594	1.344143
11	6	1.736513	2.658676	0.511507
12	7	-2.285972	-0.767187	-0.337127
13	1	0.966313	-0.32325	1.818079
14	1	0.016461	-0.482207	-2.012297
15	1	-2.873321	2.052999	0.036634
16	1	-0.628976	1.669946	2.671103
17	7	3.135586	0.633019	0.139463
18	1	0.466581	2.068567	-2.774946
19	1	-1.33146	3.639178	-1.488156
20	1	0.19031	3.960699	1.475685
21	1	2.296566	3.359665	-0.095182
22	1	-1.821217	-1.617809	-0.640973
23	1	-2.648447	-2.819687	1.975149
24	1	2.81783	-3.290416	-0.213525
25	1	3.714642	1.242895	-0.429111
26	14	-3.798923	-1.060922	0.623827
27	1	-4.632429	-0.155257	2.771042
28	14	3.765078	-1.050511	0.352885
29	1	4.437818	-2.364413	2.356877
30	6	-3.875482	0.173939	2.049217
31	1	-2.919604	0.218687	2.583714
32	1	-4.147921	1.190582	1.747702
33	6	2.49005	-2.253524	-0.351548
34	1	1.520047	-2.154816	0.150379
35	1	2.33253	-2.096063	-1.42448
36	6	4.011238	-1.367629	2.193565
37	1	4.693145	-0.636404	2.640477
38	1	3.070324	-1.326164	2.753989
39	6	-3.504129	-2.798247	1.290241
40	1	-4.37706	-3.151242	1.850719
41	1	-3.317634	-3.52855	0.494222
42	6	5.40344	-1.056274	-0.630422
43	6	5.157782	-0.719728	-2.118885
44	6	6.399967	-0.035619	-0.035117
45	6	6.025133	-2.470538	-0.537333
46	1	4.478971	-1.434075	-2.599034
47	1	4.739558	0.285468	-2.263185
48	1	6.105836	-0.750975	-2.67178
49	1	6.637508	-0.25402	1.012103
50	1	7.343734	-0.06094	-0.595728
51	1	6.028108	0.996234	-0.082352
52	1	6.971309	-2.500515	-1.093571
53	1	6.250184	-2.756588	0.496868
54	1	5.373053	-3.23987	-0.967664
55	6	-5.328515	-0.964659	-0.519572
56	6	-5.464882	0.439702	-1.147407
57	6	-5.205556	-2.010328	-1.649523
58	6	-6.593544	-1.265798	0.318341
59	1	-5.579174	1.224102	-0.389082
60	1	-4.605143	0.695837	-1.778374
61	1	-6.357143	0.480214	-1.786526
62	1	-5.157576	-3.034834	-1.262204
63	1	-6.080251	-1.956294	-2.311389
64	1	-4.317892	-1.839874	-2.271062
65	1	-7.484853	-1.226774	-0.322065
66	1	-6.565572	-2.264888	0.769569
67	1	-6.742226	-0.535271	1.122648

Table A9. H_2NN^{DMP}

Item	Value	Threshold	Converged?
Maximum Force	0.000004	0.00045	YES
RMS Force	0.000001	0.0003	YES
Maximum Displacement	0.001689	0.0018	YES
RMS Displacement	0.000333	0.0012	YES

Center	Atomic	Coordinates (Angstroms)		
Number	Number	X	Y	Z
1	26	0.015257	-2.504856	-0.023971
2	14	3.810162	0.047541	-0.154255
3	14	-2.770138	0.927754	0.836118
4	6	1.48559	-1.373498	-1.010274
5	6	-0.502259	-1.480618	1.679868
6	6	0.274726	-1.452292	-1.769367
7	6	1.92235	-2.713847	-0.765689
8	6	0.101094	-2.741037	1.995495
9	6	-1.694952	-1.729499	0.928287
10	6	-0.005201	-2.830824	-2.033469
11	6	1.015509	-3.611622	-1.417152
12	6	-0.693835	-3.769491	1.411182
13	6	-1.791153	-3.143119	0.73834
14	6	-4.301212	1.454271	-0.133345
15	6	-5.382094	2.113238	0.478659
16	6	-6.502571	2.509251	-0.25499
17	6	-6.567559	2.250614	-1.624672
18	6	-5.507661	1.596618	-2.256369
19	6	-4.389929	1.207524	-1.517376
20	6	4.98644	-0.65162	-1.454769
21	6	3.977753	1.922351	-0.017111
22	6	4.893335	2.646086	-0.801622
23	6	-1.258185	1.887525	0.224336
24	6	4.183916	-0.755612	1.515766
25	6	-2.989793	1.234083	2.685631
26	6	5.01296	4.032859	-0.687949
27	6	4.212411	4.730862	0.216938
28	6	3.295081	4.035812	1.007831
29	6	3.18445	2.649761	0.891447
30	7	2.129235	-0.194037	-0.615788
31	7	-2.623505	-0.785558	0.475617
32	1	-0.120077	-0.510683	1.969868
33	1	-0.317443	-0.605123	-2.093451
34	1	2.793129	-3.003007	-0.19255
35	1	1.00602	-2.88023	2.572656
36	1	-0.846169	-3.209255	-2.600288
37	1	1.094473	-4.690871	-1.43034
38	1	-0.507179	-4.834104	1.46472
39	1	-2.580075	-3.647675	0.19361
40	1	1.596692	0.640919	-0.828922
41	1	4.858631	-0.154242	-2.42282
42	1	-3.573177	0.701206	-2.029231
43	1	-3.378643	-1.195339	-0.060776
44	1	4.791515	-1.718941	-1.610756
45	1	5.233917	-0.60118	1.793538
46	1	-3.901555	0.758807	3.064485
47	1	-1.338341	2.949478	0.486685
48	1	4.302911	5.810397	0.306732
49	1	6.035682	-0.54843	-1.152312
50	1	2.669203	4.573115	1.716061
51	1	-0.326153	1.506173	0.657483
52	1	-1.171605	1.821837	-0.866739
53	1	3.561693	-0.325853	2.309165
54	1	3.999938	-1.836145	1.501745
55	1	-2.147159	0.812541	3.245956
56	1	-3.038555	2.304586	2.919839
57	1	2.466353	2.127448	1.521281
58	1	5.524708	2.123218	-1.516274
59	1	5.729344	4.56757	-1.306695
60	1	-5.354943	2.320189	1.545953
61	1	-7.324964	3.016862	0.242931
62	1	-7.439021	2.557035	-2.197646
63	1	-5.551546	1.392353	-3.323302

Table A10. H_2NN^{DMP+}

Item	Value	Threshold	Converged?
Maximum Force	0.000009	0.00045	YES
RMS Force	0.000001	0.0003	YES
Maximum Displacement	0.001653	0.0018	YES
RMS Displacement	0.000271	0.0012	YES

Center	Atomic	Coordinates (Angstroms)		
Number	Number	X	Y	Z
1	26	-0.046375	-2.159735	-0.134818
2	14	4.189939	-0.265132	0.059373
3	14	-3.197293	1.154666	0.689548
4	6	1.733191	-1.197519	-1.146332
5	6	-0.72973	-1.089694	1.541812
6	6	0.475247	-1.028941	-1.826057
7	6	1.870774	-2.607614	-0.906419
8	6	-0.037919	-2.287877	1.905346
9	6	-1.948169	-1.448343	0.865477
10	6	-0.037207	-2.317365	-2.173166
11	6	0.825803	-3.295435	-1.598782
12	6	-0.747695	-3.389097	1.344271
13	6	-1.878412	-2.866969	0.643847
14	6	-4.894988	1.422699	-0.049124
15	6	-6.033942	0.854276	0.556595
16	6	-7.306244	1.035956	0.015251
17	6	-7.467766	1.797679	-1.144223
18	6	-6.355388	2.374934	-1.758229
19	6	-5.083258	2.187781	-1.215394
20	6	5.321763	-1.339988	-0.989116
21	6	4.705548	1.533775	0.059891
22	6	4.929645	2.20964	-1.156758
23	6	-1.860389	2.128608	-0.212753
24	6	4.007466	-0.962536	1.798776
25	6	-3.145228	1.496488	2.537973
26	6	5.316214	3.549327	-1.178194
27	6	5.493815	4.242175	0.021559
28	6	5.282667	3.592193	1.23838
29	6	4.891719	2.252335	1.25544
30	7	2.558389	-0.20601	-0.726561
31	7	-2.922088	-0.615024	0.421432
32	1	-0.437351	-0.086141	1.818969
33	1	0.051362	-0.075426	-2.115788
34	1	2.680305	-3.077966	-0.365606
35	1	0.860872	-2.340732	2.505358
36	1	-0.918843	-2.5092	-2.770429
37	1	0.720973	-4.369747	-1.674303
38	1	-0.488877	-4.435784	1.434859
39	1	-2.622186	-3.448793	0.113558
40	1	2.234729	0.726444	-0.96491
41	1	5.445223	-0.926731	-1.996182
42	1	-4.231543	2.649195	-1.709481
43	1	-3.66801	-1.087489	-0.080396
44	1	4.957923	-2.368205	-1.0945
45	1	4.97321	-0.966408	2.317862
46	1	-3.918605	0.934128	3.072422
47	1	-2.019231	3.20628	-0.088531
48	1	5.800709	5.284234	0.007254
49	1	6.315908	-1.389847	-0.529169
50	1	5.425171	4.126936	2.173309
51	1	-0.862412	1.903416	0.181934
52	1	-1.854615	1.914363	-1.287474
53	1	3.306556	-0.375191	2.402573
54	1	3.650594	-1.999163	1.782277
55	1	-2.17963	1.244031	2.990599
56	1	-3.325097	2.562221	2.722857
57	1	4.735973	1.764899	2.214873
58	1	4.810761	1.68513	-2.103429
59	1	5.486688	4.050168	-2.127158
60	1	-5.933344	0.266866	1.467552
61	1	-8.170832	0.590639	0.499514
62	1	-8.45862	1.943868	-1.565021
63	1	-6.478245	2.971928	-2.657572

Table A11. H_2NN^{NP}

Item		Value	Threshold	Converged?
Maximum Force		0.000008	0.00045	YES
RMS Force		0.000002	0.0003	YES
Maximum Displacement		0.000878	0.0018	YES
RMS Displacement		0.000147	0.0012	YES
Center	Atomic	Coordinates (Angstroms)		
Number	Number	X	Y	Z
1	26	-0.436928	-2.229002	0.088667
2	6	1.348235	-1.602774	-0.841217
3	6	-1.132983	-0.68329	1.263442
4	6	0.342657	-1.956718	-1.796581
5	6	1.561796	-2.736229	0.00066
6	6	-0.894622	-1.867456	2.037477
7	6	-2.1316	-0.984952	0.28542
8	6	-0.021226	-3.324288	-1.577293
9	6	0.730824	-3.805644	-0.467279
10	6	-1.720769	-2.906395	1.521472
11	6	-2.465351	-2.368759	0.423409
12	7	2.043778	-0.387395	-0.817198
13	1	-0.666184	0.278987	1.419017
14	1	-0.036108	-1.309832	-2.578589
15	1	2.242362	-2.784843	0.839312
16	1	-0.206234	-1.949436	2.868525
17	7	-2.737486	-0.104085	-0.613788
18	1	-0.742548	-3.888534	-2.154485
19	1	0.684716	-4.801305	-0.045498
20	1	-1.774284	-3.924114	1.885608
21	1	-3.186304	-2.902578	-0.183743
22	1	1.493906	0.358956	-1.229434
23	1	-3.12475	-0.598791	-1.408343
24	6	2.577517	2.984508	-0.527814
25	6	2.711083	0.027727	0.41739
26	1	2.010261	0.110617	1.269906
27	1	3.428964	-0.75572	0.695144
28	14	3.709785	1.6407	0.188544
29	6	4.340215	2.180006	1.891191
30	6	5.157522	1.321333	-0.98474
31	1	1.70744	3.162996	0.11645
32	1	2.20826	2.724009	-1.527539
33	1	3.113908	3.936351	-0.62384
34	1	4.801575	0.908957	-1.935485
35	1	5.862905	0.599238	-0.555998
36	1	5.714626	2.240832	-1.201311
37	1	3.513404	2.375329	2.584598
38	1	4.935476	3.098441	1.820551
39	1	4.97746	1.410741	2.344172
40	6	-2.042934	1.138779	-1.003106
41	6	-1.765726	4.197257	-0.743755
42	1	-0.954768	1.038336	-0.862554
43	14	-2.753245	2.694596	-0.135718
44	6	-4.566866	2.86301	-0.650873
45	6	-2.634023	2.562889	1.747754
46	1	-2.184415	1.281037	-2.083444
47	1	-1.594943	2.578732	2.097875
48	1	-3.092397	1.63618	2.110007
49	1	-3.1529	3.403063	2.226024
50	1	-4.666507	3.006988	-1.733959
51	1	-5.045624	3.718253	-0.158983
52	1	-5.129531	1.9623	-0.380267
53	1	-1.842854	4.31674	-1.831614
54	1	-0.700237	4.110024	-0.496993
55	1	-2.132647	5.12427	-0.286449

Table A12. H_2NN^{NP+}

Item		Threshold	Converged?	
Maximum Force		0.000005	0.00045	YES
RMS Force		0.000001	0.0003	YES
Maximum Displacement		0.00029	0.0018	YES
RMS Displacement		0.000043	0.0012	YES
Center	Atomic	Coordinates (Angstroms)		
Number	Number	X	Y	Z
1	26	-0.000058	0.000184	-0.000384
2	6	2.063716	-0.966578	-0.167228
3	6	-1.433768	1.054508	-1.12262
4	6	1.080807	-1.409826	-1.119623
5	6	1.433413	-1.054271	1.122075
6	6	-0.205811	1.784197	-0.980625
7	6	-2.063768	0.966992	0.166847
8	6	-0.010424	-2.006669	-0.406506
9	6	0.205502	-1.783953	0.979702
10	6	0.01043	2.007099	0.405505
11	6	-1.080641	1.410369	1.11895
12	7	3.279872	-0.467736	-0.45371
13	1	-1.86925	0.737728	-2.060111
14	1	1.214803	-1.420608	-2.19416
15	1	1.86865	-0.737584	2.059711
16	1	0.429433	2.105378	-1.795532
17	7	-3.279853	0.468171	0.453664
18	1	-0.843143	-2.529839	-0.857474
19	1	-0.429936	-2.105238	1.794417
20	1	0.84327	2.530305	0.856209
21	1	-1.214374	1.421267	2.193518
22	1	3.516655	-0.357744	-1.430655
23	6	5.785999	1.020677	-1.245784
24	1	-3.516429	0.358312	1.430675
25	6	4.190022	0.133482	0.52129
26	6	-4.190131	-0.133291	-0.521067
27	6	-6.482331	-0.834016	-1.158589
28	1	3.856976	1.15507	0.763701
29	1	-4.133785	0.459226	-1.44113
30	6	-5.658499	-0.173691	-0.03575
31	6	-5.784974	-1.021442	1.246519
32	6	-6.179936	1.253825	0.216084
33	1	4.133054	-0.458897	1.441399
34	1	-3.856759	-1.15471	-0.76374
35	6	5.658618	0.173198	0.036574
36	6	6.482245	0.833381	1.159646
37	6	6.179577	-1.254574	-0.214785
38	1	-6.122404	1.862709	-0.693775
39	1	-5.611285	1.768215	0.99899
40	1	-7.22802	1.226192	0.532669
41	1	-5.383809	-2.032028	1.102467
42	1	-6.837483	-1.119946	1.531662
43	1	-5.273954	-0.571066	2.108621
44	1	-6.14051	-1.855851	-1.362789
45	1	-6.417894	-0.260849	-2.091076
46	1	-7.538579	-0.887876	-0.875276
47	1	5.38514	2.031438	-1.102105
48	1	5.275229	0.570329	-2.108046
49	1	6.838679	1.118745	-1.530452
50	1	5.611048	-1.768862	-0.997845
51	1	6.12139	-1.863267	0.695161
52	1	7.227812	-1.227434	-0.530917
53	1	6.140779	1.855404	1.363495
54	1	7.538644	0.886726	0.876793
55	1	6.417146	0.260424	2.092215

Table A13. H_2NN^{XYL}

Item		Value	Threshold	Converged?
Maximum Force		0.000003	0.00045	YES
RMS Force		0.000001	0.0003	YES
Maximum Displacement		0.001429	0.0018	YES
RMS Displacement		0.000209	0.0012	YES
Center	Atomic	Coordinates (Angstroms)		
Number	Number	X	Y	Z
1	26	0.17484	-1.700704	0.294693
2	6	-1.638517	-1.178622	1.202008
3	6	0.883061	-1.047788	-1.534025
4	6	-0.689914	-0.108339	1.253396
5	6	-1.046098	-2.311801	1.842
6	6	-0.184909	-1.986097	-1.695918
7	6	1.943526	-1.69958	-0.828119
8	6	0.461229	-0.566325	1.972321
9	6	0.245205	-1.930829	2.321199
10	6	0.203938	-3.212515	-1.083462
11	6	1.506353	-3.029764	-0.525438
12	7	-2.924651	-1.175917	0.642401
13	1	0.894883	-0.034591	-1.907399
14	1	-0.831274	0.878278	0.835996
15	1	-1.512834	-3.282119	1.955897
16	1	-1.122759	-1.787254	-2.199019
17	7	3.23142	-1.243129	-0.540271
18	1	1.344622	0.018666	2.190455
19	1	0.934555	-2.570572	2.856651
20	1	-0.381669	-4.121409	-1.034343
21	1	2.083323	-3.770112	0.015066
22	1	-3.172266	-2.028933	0.159428
23	1	3.926761	-1.968143	-0.44281
24	6	-3.668091	-0.055767	0.25555
25	6	-3.60495	1.162445	0.950879
26	6	-4.397343	2.246546	0.561801
27	6	-5.277391	2.102892	-0.516444
28	6	-5.374465	0.890521	-1.210349
29	6	-4.560124	-0.174861	-0.824217
30	6	-4.289561	3.564811	1.295114
31	6	-6.35872	0.730596	-2.346655
32	6	3.70328	0.061794	-0.415436
33	6	5.097492	0.266794	-0.419678
34	6	5.64002	1.541178	-0.284881
35	6	4.774361	2.637726	-0.147492
36	6	3.390159	2.460124	-0.137271
37	6	2.857864	1.169907	-0.264053
38	6	7.137439	1.748166	-0.305419
39	6	2.460302	3.645094	-0.00215
40	1	5.188732	3.638486	-0.045022
41	1	5.759458	-0.590201	-0.535603
42	1	-5.898862	2.943807	-0.817202
43	1	-2.953856	1.255571	1.813968
44	1	1.785925	1.023136	-0.21096
45	1	-4.616045	-1.118232	-1.365793
46	1	-6.457505	1.656675	-2.923526
47	1	-7.359017	0.474514	-1.972263
48	1	-6.05455	-0.06553	-3.034489
49	1	-4.044443	3.417267	2.352494
50	1	-5.225209	4.131156	1.239585
51	1	-3.500844	4.196349	0.864155
52	1	7.676499	0.796297	-0.262279
53	1	7.467268	2.360668	0.542195
54	1	7.45494	2.267737	-1.21881
55	1	2.99196	4.53145	0.358455
56	1	1.640555	3.436327	0.695214
57	1	2.003548	3.904495	-0.966517

Table A14. H_2NN^{XYL+}

Item		Value	Threshold	Converged?
Maximum Force		0.000002	0.00045	YES
RMS Force		0	0.0003	YES
Maximum Displacement		0.001063	0.0018	YES
RMS Displacement		0.000116	0.0012	YES
Center	Atomic	Coordinates (Angstroms)		
Number	Number	X	Y	Z
1	26	-0.00287	-1.152731	0.440605
2	6	-1.989705	-0.816052	1.484229
3	6	-1.186697	0.359579	1.298664
4	6	-1.131172	-1.796454	2.090761
5	6	0.05301	0.177419	1.996773
6	6	0.087522	-1.155903	2.487018
7	7	-3.253736	-1.0447	1.054596
8	1	-1.511343	1.265853	0.808556
9	1	-1.413871	-2.81642	2.320372
10	1	0.818856	0.931219	2.123655
11	1	0.883391	-1.61601	3.057553
12	1	-3.587767	-1.997936	1.123751
13	6	-4.107807	-0.131601	0.367199
14	6	-4.271791	1.180395	0.821476
15	6	-5.129272	2.053999	0.143187
16	6	-5.830116	1.577542	-0.971527
17	6	-5.698767	0.258316	-1.421922
18	6	-4.819009	-0.59265	-0.744261
19	6	-5.300646	3.481475	0.607218
20	6	-6.501027	-0.237081	-2.60185
21	1	-6.507543	2.248639	-1.495174
22	1	-3.76355	1.511296	1.722391
23	1	-4.689497	-1.619127	-1.080891
24	1	-6.514482	0.499056	-3.412559
25	1	-7.544253	-0.421303	-2.315935
26	1	-6.098901	-1.173525	-3.00039
27	1	-4.937286	3.619562	1.630137
28	1	-6.352016	3.785724	0.578165
29	1	-4.746563	4.17505	-0.038311
30	6	1.099187	-0.508362	-1.241345
31	6	-0.122826	-1.166081	-1.605136
32	6	1.972258	-1.475826	-0.641247
33	6	-0.072831	-2.49507	-1.10775
34	6	1.176949	-2.655564	-0.427242
35	1	1.365543	0.505294	-1.500746
36	1	-0.933289	-0.711745	-2.159695
37	7	3.25991	-1.345863	-0.238751
38	1	-0.8329	-3.257665	-1.214546
39	1	1.524865	-3.560984	0.054821
40	1	3.714079	-2.205105	0.044361
41	6	4.106451	-0.204456	-0.282039
42	6	5.469265	-0.418708	-0.518598
43	6	6.362669	0.654011	-0.538873
44	6	5.862315	1.946099	-0.326345
45	6	4.505614	2.179241	-0.083974
46	6	3.627508	1.087965	-0.051088
47	6	7.835335	0.432688	-0.790173
48	6	3.993364	3.584141	0.132898
49	1	6.549856	2.788846	-0.343855
50	1	5.832467	-1.428199	-0.698553
51	1	2.582276	1.252745	0.187737
52	1	8.062629	-0.624264	-0.956277
53	1	8.436322	0.776198	0.060093
54	1	8.173978	0.991611	-1.67027
55	1	4.685985	4.171519	0.744268
56	1	3.017992	3.587576	0.630435
57	1	3.877735	4.112675	-0.822032

Table A15. H_2NN^{MES}

Item		Value	Threshold	Converged?
Maximum Force		0.000006	0.00045	YES
RMS Force		0.000001	0.0003	YES
Maximum Displacement		0.001581	0.0018	YES
RMS Displacement		0.000201	0.0012	YES
Center	Atomic	Coordinates (Angstroms)		
Number	Number	X	Y	Z
1	26	0.003598	-1.887995	0.013432
2	6	2.048496	-1.567981	-0.309826
3	6	-1.182531	-0.595163	1.106795
4	6	1.247121	-0.792593	-1.204704
5	6	1.703121	-2.942016	-0.498369
6	6	-0.433626	-1.470178	1.96029
7	6	-2.035478	-1.394938	0.288241
8	6	0.437649	-1.687539	-1.972101
9	6	0.713084	-3.015289	-1.525945
10	6	-0.79296	-2.812471	1.639908
11	6	-1.765344	-2.76616	0.591169
12	7	3.053374	-1.091458	0.562334
13	1	-1.148272	0.485572	1.111329
14	1	1.281784	0.284988	-1.292798
15	1	2.137642	-3.776002	0.037879
16	1	0.267943	-1.159816	2.723717
17	7	-2.985358	-0.947007	-0.654688
18	1	-0.274672	-1.404281	-2.735449
19	1	0.252942	-3.921765	-1.898067
20	1	-0.402203	-3.710474	2.100561
21	1	-2.23885	-3.619099	0.119945
22	1	2.916344	-1.367816	1.524987
23	1	3.365803	-0.037358	3.304706
24	1	-1.582709	2.400243	-2.245743
25	1	-3.637603	-1.689985	-0.879645
26	6	3.654825	0.181724	0.406438
27	6	4.368005	0.485209	-0.775844
28	6	4.979122	1.737267	-0.886848
29	6	4.943031	2.685923	0.13895
30	6	4.272102	2.341315	1.314674
31	6	3.621461	1.113831	1.466754
32	1	5.368317	-0.260093	-2.529888
33	1	5.528235	1.964426	-1.799236
34	1	5.893338	4.459192	0.9448
35	1	4.243217	3.051786	2.139061
36	6	-3.649615	0.312246	-0.453892
37	6	-4.843528	0.374625	0.290901
38	6	-5.480544	1.609761	0.442968
39	6	-4.958794	2.781935	-0.112389
40	6	-3.771612	2.689949	-0.844189
41	6	-3.11188	1.471901	-1.039876
42	1	-5.797945	-1.577703	0.158929
43	1	-6.401459	1.658024	1.021417
44	1	-6.214286	4.155575	0.999011
45	1	-3.351403	3.589159	-1.290777
46	6	-5.673605	4.103938	0.047691
47	1	-4.97317	4.945114	0.010717
48	1	-6.410114	4.259475	-0.752323
49	6	-5.430321	-0.870173	0.916172
50	1	-4.691519	-1.405444	1.523419
51	1	-6.279558	-0.619091	1.558589
52	6	5.599248	4.037579	-0.022584
53	1	6.496246	3.975578	-0.649019
54	1	4.922815	4.760492	-0.499186
55	6	4.526366	-0.52809	-1.883489
56	1	4.706153	-1.527876	-1.473371
57	1	3.631864	-0.603532	-2.51351
58	6	-1.868441	1.404435	-1.892672
59	1	-1.022133	0.974711	-1.348894
60	1	-2.033378	0.763403	-2.767001
61	6	2.902496	0.797655	2.758407
62	1	2.916019	1.66078	3.43058
63	1	1.853847	0.528723	2.582731

Table A16. H_2NN^{MES+}

Item		Value	Threshold	Converged?
Maximum Force		0.000003	0.00045	YES
RMS Force		0.000001	0.0003	YES
Maximum Displacement		0.001315	0.0018	YES
RMS Displacement		0.000198	0.0012	YES
Center	Atomic	Coordinates (Angstroms)		
Number	Number	X	Y	Z
1	26	0.000207	-1.234137	0.003238
2	6	2.037665	-1.225516	-1.029255
3	6	-1.207296	-0.071833	1.27358
4	6	1.207921	-0.079329	-1.273848
5	6	1.215641	-2.376272	-1.281974
6	6	-0.000002	-0.507848	1.913886
7	6	-2.037008	-1.219747	1.036935
8	6	0.001108	-0.519668	-1.912035
9	6	0.005324	-1.941307	-1.91643
10	6	-0.003836	-1.929418	1.927169
11	6	-1.214411	-2.368666	1.296147
12	7	3.300558	-1.237225	-0.545876
13	1	-1.503366	0.953707	1.102565
14	1	1.503667	0.947336	-1.109108
15	1	1.521982	-3.405734	-1.143281
16	1	0.770296	0.142166	2.307
17	7	-3.30056	-1.234929	0.555299
18	1	-0.769037	0.127701	-2.309745
19	1	-0.756696	-2.591671	-2.325302
20	1	0.75864	-2.576994	2.339601
21	1	-1.520528	-3.399071	1.164119
22	1	3.676511	-2.139169	-0.278443
23	1	4.656178	-1.795004	2.083841
24	1	-4.351937	-0.457096	-3.167356
25	1	-3.676338	-2.138694	0.293865
26	6	4.089247	-0.076215	-0.240877
27	6	4.502022	0.786756	-1.273807
28	6	5.271691	1.902005	-0.923294
29	6	5.657501	2.16079	0.394734
30	6	5.265908	1.253396	1.386159
31	6	4.485735	0.133268	1.094375
32	1	4.882947	1.049578	-3.374357
33	1	5.599012	2.574737	-1.712653
34	1	7.150201	3.190466	1.577808
35	1	5.578263	1.4209	2.414384
36	6	-4.09006	-0.076317	0.243198
37	6	-4.498834	0.795604	1.269253
38	6	-5.262851	1.912778	0.910045
39	6	-5.65091	2.161157	-0.408563
40	6	-5.257759	1.24785	-1.394794
41	6	-4.483637	0.126496	-1.094624
42	1	-4.218816	-0.519768	2.969572
43	1	-5.581386	2.596416	1.693497
44	1	-6.463155	4.122193	0.020343
45	1	-5.562186	1.413859	-2.425772
46	6	-6.503097	3.356911	-0.760337
47	1	-6.181576	3.81369	-1.702435
48	1	-7.554374	3.067009	-0.884059
49	6	-4.170731	0.545738	2.72278
50	1	-3.164963	0.893962	2.990574
51	1	-4.877077	1.074916	3.368124
52	6	6.470318	3.384664	0.742185
53	1	7.066305	3.725248	-0.110009
54	1	5.819214	4.217194	1.039348
55	6	4.17719	0.523652	-2.725734
56	1	4.228668	-0.543743	-2.963643
57	1	3.170794	0.866637	-2.997886
58	6	-4.107568	-0.856367	-2.17941
59	1	-3.037958	-1.096138	-2.166475
60	1	-4.651038	-1.806075	-2.07547
61	6	4.113572	-0.844501	2.185142
62	1	4.361558	-0.440621	3.170302
63	1	3.043768	-1.083662	2.177262

Table A17. Ferrocene (D_{5h})			(Hartree/Particle)
Zero-point correction			0.17041
Thermal correction to Energy			0.178964
Thermal correction to Enthalpy			0.179908
Thermal correction to Gibbs Free Energy			0.135836
Sum of electronic and zero-point Energies			-1650.532812
Sum of electronic and thermal Energies			-1650.524258
Sum of electronic and thermal Enthalpies			-1650.523314
Sum of electronic and thermal Free Energies			-1650.567385
	E (Thermal)	CV	S
	KCal/Mol	Cal/Mol-Kelvin	Cal/Mol-Kelvin
Total	112.302	36.069	92.757
Electronic	0	0	0
Translational	0.889	2.981	41.568
Rotational	0.889	2.981	29.231
Vibrational	110.524	30.107	21.958

Table A18. Ferrocene (D_{5d})			(Hartree/Particle)
Zero-point correction			0.170408
Thermal correction to Energy			0.178068
Thermal correction to Enthalpy			0.179013
Thermal correction to Gibbs Free Energy			0.138112
Sum of electronic and zero-point Energies			-1650.532637
Sum of electronic and thermal Energies			-1650.524977
Sum of electronic and thermal Enthalpies			-1650.524033
Sum of electronic and thermal Free Energies			-1650.564933
	E (Thermal)	CV	S
	KCal/Mol	Cal/Mol-Kelvin	Cal/Mol-Kelvin
Total	111.74	34.096	86.083
Electronic	0	0	0
Translational	0.889	2.981	41.568
Rotational	0.889	2.981	29.233
Vibrational	109.962	28.134	15.282

Table A19. Ferrocenium (D_{5h})			(Hartree/Particle)
Zero-point correction			0.170944
Thermal correction to Energy			0.17882
Thermal correction to Enthalpy			0.179765
Thermal correction to Gibbs Free Energy			0.137519
Sum of electronic and zero-point Energies			-1650.278479
Sum of electronic and thermal Energies			-1650.270603
Sum of electronic and thermal Enthalpies			-1650.269658
Sum of electronic and thermal Free Energies			-1650.311904
	E (Thermal)	CV	S
	KCal/Mol	Cal/Mol-Kelvin	Cal/Mol-Kelvin
Total	112.212	34.092	88.914
Electronic	0	0	1.377
Translational	0.889	2.981	41.568
Rotational	0.889	2.981	29.273
Vibrational	110.434	28.13	16.695

Table A20. Ferrocenium (D_{5d})			(Hartree/Particle)
Zero-point correction			0.170993
Thermal correction to Energy			0.179793
Thermal correction to Enthalpy			0.180737
Thermal correction to Gibbs Free Energy			0.134888
Sum of electronic and zero-point Energies			-1650.278557
Sum of electronic and thermal Energies			-1650.269758
Sum of electronic and thermal Enthalpies			-1650.268813
Sum of electronic and thermal Free Energies			-1650.314662
	E (Thermal)	CV	S
	KCal/Mol	Cal/Mol-Kelvin	Cal/Mol-Kelvin
Total	112.822	36.073	96.496
Electronic	0	0	1.377
Translational	0.889	2.981	41.568
Rotational	0.889	2.981	29.273
Vibrational	111.044	30.111	24.278

Table A21. H_2NN^{TMS}			(Hartree/Particle)
Zero-point correction			0.406451
Thermal correction to Energy			0.433839
Thermal correction to Enthalpy			0.434783
Thermal correction to Gibbs Free Energy			0.348179
Sum of electronic and zero-point Energies			-2578.388703
Sum of electronic and thermal Energies			-2578.361316
Sum of electronic and thermal Enthalpies			-2578.360371
Sum of electronic and thermal Free Energies			-2578.446976
	E (Thermal)	CV	S
	KCal/Mol	Cal/Mol-Kelvin	Cal/Mol-Kelvin
Total	272.238	103.103	182.274
Electronic	0	0	0
Translational	0.889	2.981	43.537
Rotational	0.889	2.981	34.825
Vibrational	270.461	97.141	103.911

Table A22. H_2NN^{TMS+}			(Hartree/Particle)
Zero-point correction			0.408579
Thermal correction to Energy			0.435776
Thermal correction to Enthalpy			0.43672
Thermal correction to Gibbs Free Energy			0.349349
Sum of electronic and zero-point Energies			-2578.20505
Sum of electronic and thermal Energies			-2578.177853
Sum of electronic and thermal Enthalpies			-2578.176909
Sum of electronic and thermal Free Energies			-2578.26428
	E (Thermal)	CV	S
	KCal/Mol	Cal/Mol-Kelvin	Cal/Mol-Kelvin
Total	273.453	102.012	183.888
Electronic	0	0	1.377
Translational	0.889	2.981	43.537
Rotational	0.889	2.981	35.013
Vibrational	271.676	96.051	103.96

Table A23. H_2NN^{TBS}			(Hartree/Particle)
Zero-point correction			0.578025
Thermal correction to Energy			0.613154
Thermal correction to Enthalpy			0.614098
Thermal correction to Gibbs Free Energy			0.511583
Sum of electronic and zero-point Energies			-2814.078926
Sum of electronic and thermal Energies			-2814.043797
Sum of electronic and thermal Enthalpies			-2814.042852
Sum of electronic and thermal Free Energies			-2814.145368
	E (Thermal)	CV	S
	KCal/Mol	Cal/Mol-Kelvin	Cal/Mol-Kelvin
Total	384.76	134.469	215.762
Electronic	0	0	0
Translational	0.889	2.981	44.163
Rotational	0.889	2.981	36.374
Vibrational	382.983	128.507	135.226

Table A24. H_2NN^{TBS+}			(Hartree/Particle)
Zero-point correction			0.579987
Thermal correction to Energy			0.615039
Thermal correction to Enthalpy			0.615983
Thermal correction to Gibbs Free Energy			0.512213
Sum of electronic and zero-point Energies			-2813.896824
Sum of electronic and thermal Energies			-2813.861773
Sum of electronic and thermal Enthalpies			-2813.860829
Sum of electronic and thermal Free Energies			-2813.964599
	E (Thermal)	CV	S
	KCal/Mol	Cal/Mol-Kelvin	Cal/Mol-Kelvin
Total	385.943	133.612	218.403
Electronic	0	0	1.377
Translational	0.889	2.981	44.163
Rotational	0.889	2.981	36.523
Vibrational	384.165	127.651	136.339

Table A25. H_2NN^{DMP}			(Hartree/Particle)
Zero-point correction			0.515093
Thermal correction to Energy			0.54839
Thermal correction to Enthalpy			0.549334
Thermal correction to Gibbs Free Energy			0.445632
Sum of electronic and zero-point Energies			-2961.746394
Sum of electronic and thermal Energies			-2961.713096
Sum of electronic and thermal Enthalpies			-2961.712152
Sum of electronic and thermal Free Energies			-2961.815854
	E (Thermal)	CV	S
	KCal/Mol	Cal/Mol-Kelvin	Cal/Mol-Kelvin
Total	344.12	128.419	218.261
Electronic	0	0	0
Translational	0.889	2.981	44.419
Rotational	0.889	2.981	37.281
Vibrational	342.343	122.458	136.56

Table A26. H_2NN^{DMP+}			(Hartree/Particle)
Zero-point correction			0.515093
Thermal correction to Energy			0.54839
Thermal correction to Enthalpy			0.549334
Thermal correction to Gibbs Free Energy			0.445632
Sum of electronic and zero-point Energies			-2961.746394
Sum of electronic and thermal Energies			-2961.713096
Sum of electronic and thermal Enthalpies			-2961.712152
Sum of electronic and thermal Free Energies			-2961.815854
	E (Thermal)	CV	S
	KCal/Mol	Cal/Mol-Kelvin	Cal/Mol-Kelvin
Total	344.12	128.419	218.261
Electronic	0	0	0
Translational	0.889	2.981	44.419
Rotational	0.889	2.981	37.281
Vibrational	342.343	122.458	136.56

Table A27. H_2NN^{NP}			(Hartree/Particle)
Zero-point correction			0.486685
Thermal correction to Energy			0.511825
Thermal correction to Enthalpy			0.512769
Thermal correction to Gibbs Free Energy			0.430017
Sum of electronic and zero-point Energies			-2154.042272
Sum of electronic and thermal Energies			-2154.017133
Sum of electronic and thermal Enthalpies			-2154.016188
Sum of electronic and thermal Free Energies			-2154.09894
	E (Thermal)	CV	S
	KCal/Mol	Cal/Mol-Kelvin	Cal/Mol-Kelvin
Total	321.175	99.245	174.166
Electronic	0	0	0
Translational	0.889	2.981	43.505
Rotational	0.889	2.981	35.083
Vibrational	319.397	93.283	95.579

Table A28. H_2NN^{NP+}			(Hartree/Particle)
Zero-point correction			0.487428
Thermal correction to Energy			0.51302
Thermal correction to Enthalpy			0.513964
Thermal correction to Gibbs Free Energy			0.428092
Sum of electronic and zero-point Energies			-2153.858911
Sum of electronic and thermal Energies			-2153.833319
Sum of electronic and thermal Enthalpies			-2153.832374
Sum of electronic and thermal Free Energies			-2153.918246
	E (Thermal)	CV	S
	KCal/Mol	Cal/Mol-Kelvin	Cal/Mol-Kelvin
Total	321.925	99.926	180.732
Electronic	0	0	1.377
Translational	0.889	2.981	43.505
Rotational	0.889	2.981	35.19
Vibrational	320.147	93.964	100.661

Table A29. H_2NN^{XYL}			(Hartree/Particle)
Zero-point correction			0.475629
Thermal correction to Energy			0.5039
Thermal correction to Enthalpy			0.504844
Thermal correction to Gibbs Free Energy			0.41238
Sum of electronic and zero-point Energies			-2380.296941
Sum of electronic and thermal Energies			-2380.26867
Sum of electronic and thermal Enthalpies			-2380.267726
Sum of electronic and thermal Free Energies			-2380.36019
	E (Thermal)	CV	S
	KCal/Mol	Cal/Mol-Kelvin	Cal/Mol-Kelvin
Total	316.202	109.338	194.606
Electronic	0	0	0
Translational	0.889	2.981	44.025
Rotational	0.889	2.981	36.523
Vibrational	314.424	103.376	114.058

Table A30. H_2NN^{XYL+}			(Hartree/Particle)
Zero-point correction			0.476956
Thermal correction to Energy			0.505251
Thermal correction to Enthalpy			0.506195
Thermal correction to Gibbs Free Energy			0.411869
Sum of electronic and zero-point Energies			-2380.107829
Sum of electronic and thermal Energies			-2380.079533
Sum of electronic and thermal Enthalpies			-2380.078589
Sum of electronic and thermal Free Energies			-2380.172916
	E (Thermal)	CV	S
	KCal/Mol	Cal/Mol-Kelvin	Cal/Mol-Kelvin
Total	317.05	108.708	198.526
Electronic	0	0	1.377
Translational	0.889	2.981	44.025
Rotational	0.889	2.981	36.643
Vibrational	315.272	102.746	116.481

Table A31. H_2NN^{MES}			(Hartree/Particle)
Zero-point correction			0.531907
Thermal correction to Energy			0.562891
Thermal correction to Enthalpy			0.563836
Thermal correction to Gibbs Free Energy			0.46638
Sum of electronic and zero-point Energies			-2458.862857
Sum of electronic and thermal Energies			-2458.831873
Sum of electronic and thermal Enthalpies			-2458.830928
Sum of electronic and thermal Free Energies			-2458.928383
	E (Thermal)	CV	S
	KCal/Mol	Cal/Mol-Kelvin	Cal/Mol-Kelvin
Total	353.22	120.116	205.112
Electronic	0	0	0
Translational	0.889	2.981	44.216
Rotational	0.889	2.981	36.791
Vibrational	351.442	114.154	124.104

Table A32. H_2NN^{MES+}			(Hartree/Particle)
Zero-point correction			0.533041
Thermal correction to Energy			0.564147
Thermal correction to Enthalpy			0.565091
Thermal correction to Gibbs Free Energy			0.468084
Sum of electronic and zero-point Energies			-2458.682108
Sum of electronic and thermal Energies			-2458.651002
Sum of electronic and thermal Enthalpies			-2458.650058
Sum of electronic and thermal Free Energies			-2458.747065
	E (Thermal)	CV	S
	KCal/Mol	Cal/Mol-Kelvin	Cal/Mol-Kelvin
Total	354.008	120.282	204.169
Electronic	0	0	1.377
Translational	0.889	2.981	44.216
Rotational	0.889	2.981	36.853
Vibrational	352.23	114.32	121.723

Calculation of oxidation potentials

As shown below, oxidation potential of ferrocene was determined using previously established computational methods.[104-109]

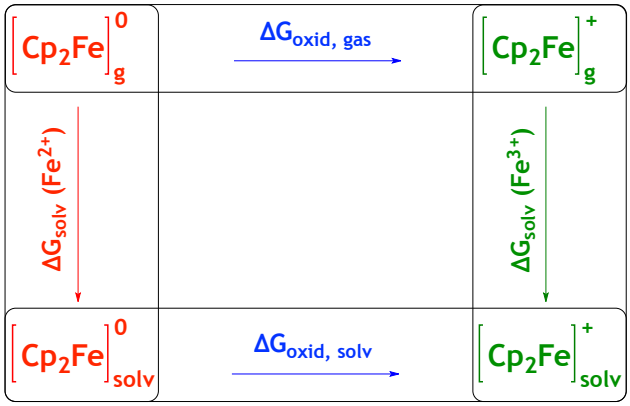

$[Cp_2Fe]^0_g$ and $[Cp_2Fe]^0_{solv}$

(1) E_g^{SCF} = -1650.70322176 Hartree

(2) $G_g^{Fe^{2+}}$ (Sum of Electronic and Thermal Free Energies) = -1650.567385 Hartree

(3) E_{solv}^{SCF} = -1650.70617147 Hartree

(4) $E^{SCF} = E_{solv}^{SCF} - E_g^{SCF}$ = -0.00294971000017 Hartree

(5) $\Delta G[Cp_2Fe]^0_{solv} = G_g^{Fe^{2+}} + E^{SCF}$ = -1650.57033471 Hartree

$[Cp_2Fe]^+_g$ and $[Cp_2Fe]^+_{solv}$

(1) E_g^{SCF} = -1650.44955020 Hartree

(2) $G_g^{Fe^{3+}}$ (Sum of Electronic and Thermal Free Energies) = -1650.3170672 Hartree

(3) E_{solv}^{SCF} = -1650.51192588 Hartree

(4) $E^{SCF} = E_{solv}^{SCF} - E_g^{SCF}$ = -0.062375680 Hartree

(5) $\Delta G[Cp_2Fe]^{0+}_{solv} = G_g^{Fe^{3+}} + E^{SCF}$ = -1650.37944 Hartree

$\mathbf{\Delta\Delta G = \Delta G[Cp_2Fe]^{0}_{solv} - \Delta G[Cp_2Fe]^{0+}_{solv}}$

ΔΔG = (-1650.57033471) – (-1650.37944288) = -0.190891 Hartree = -119.78693 kcal/mol

$\mathbf{\Delta G^{ox}_{solv} = -FE^{\circ}_{calc}}$ (F is Faraday's constant, -23.06 kcal/mol)

$\mathbf{E^{\circ}_{calc}} = \frac{\mathbf{\Delta G^{ox}_{solv}}}{\mathbf{-F}} = E^{\circ}_{calc} = \frac{-119.78693432\ \text{kcal mol}^{-1}}{-23.06\ \text{kcal mol}^{-1}\ \text{V}^{-1}} = 5.19\ \text{V}$ (absolute oxidation potential)

$E_{SHE} = E^{\circ}_{calc} - 4.3\ \text{V} = 0.89\ \text{V}$ (vs SHE)

Experimental oxidation potential of ferrocene in THF with $TBAPF_6$ as the supporting electrolyte was previously reported to be 0.56 V (vs SCE)[23] or 0.80 V (vs SHE). Therefore, our calculation of the oxidation potential of ferrocene (0.89 V vs SHE) is in good agreement with the experimental value.

Table A33. Ionization potential of 1,1'-ferrocene diamines in the gas phase.

gaseous	**HF (au)**		**Ionization Potential**			Normalized
	Neutral	Oxidized	$E(Fe^{3+}) - E(Fe^{2+})$			
	(Fe^{2+})	(Fe^{3+})	*au*	*kcal/mol*	*eV*	*eV*
fc	-1650.703	-1650.450	0.253	158.760	6.884	0.000
H_2NN^{TMS}	-2578.795	-2578.614	0.181	113.579	4.925	-1.959
H_2NN^{TBS}	-2814.657	-2814.477	0.180	112.952	4.898	-1.986
H_2NN^{DMP}	-2962.261	-2962.082	0.179	112.324	4.871	-2.013
H_2NN^{MES}	-2459.395	-2459.215	0.180	112.952	4.898	-1.986

Table A34. Ionization potential of 1,1'-ferrocene diamines in THF.

solvated	**HF (au)**		**Ionization Potential**			Normalized
	Neutral	Oxidized	$E(Fe^{3+}) - E(Fe^{2+})$			
	(Fe^{2+})	(Fe^{3+})	*au*	*kcal/mol*	*eV*	
fc	-1650.706	-1650.512	0.194	121.891	5.285	0.000
H_2NN^{TMS}	-2578.801	-2578.665	0.136	85.438	3.705	-1.580
H_2NN^{TBS}	-2814.663	-2814.526	0.136	85.594	3.712	-1.573
H_2NN^{DMP}	-2962.270	-2962.132	0.138	86.287	3.742	-1.543
H_2NN^{MES}	-2459.402	-2459.266	0.137	85.667	3.715	-1.570

Table A35. Gibbs free energy of 1,1'-ferrocene diamines.

Neutral					
	E(SCF)		ΔE (au)	$\Delta G_{neutral}$ (au)	ΔG + ΔE
	gaseous	*solvated*			au
fc	-1650.703	-1650.706	-0.003	-1650.567	-1650.570
H_2NN^{TMS}	-2578.795	-2578.801	-0.006	-2578.447	-2578.453
H_2NN^{TBS}	-2814.657	-2814.663	-0.006	-2814.145	-2814.151
H_2NN^{DMP}	-2962.261	-2962.270	-0.008	-2961.816	-2961.824
H_2NN^{MES}	-2459.395	-2459.402	-0.007	-2458.928	-2458.936

Table A36. Gibbs free energy of 1,1'-ferrocenium diamines.

Oxidized					
	E(SCF)		ΔE (au)	ΔG_{ox} (au)	ΔG + ΔE
	gaseous	solvated			au
fc	-1650.44955	-1650.511926	-0.06237568	-1650.317067	-1650.379443
H_2NN^{TMS}	-2578.613628	-2578.664944	-0.05131598	-2578.26428	-2578.315596
H_2NN^{TBS}	-2814.476812	-2814.526256	-0.04944439	-2813.964599	-2814.014043
H_2NN^{DMP}	-2962.082223	-2962.132362	-0.05013872	-2961.635812	-2961.685951
H_2NN^{MES}	-2459.21515	-2459.265687	-0.0505379	-2458.747065	-2458.797603

Table A37. Redox potential of 1,1'-ferrocene diamines.

	ΔΔG		**Redox Potential**	
	$\Delta G_{neutral}$ - ΔG_{oxid}		E° = (-ΔG/F)	
	au	kcal/mol	Absolute	vs SHE
			V	V
fc	-0.19089259	-119.7870092	5.194579755	0.894579755
H_2NN^{TMS}	-0.13732454	-86.1725221	3.736883005	-0.563116995
H_2NN^{TBS}	-0.13703267	-85.98937075	3.728940622	-0.571059378
H_2NN^{DMP}	-0.13828508	-86.77527055	3.763021273	-0.536978727
H_2NN^{MES}	-0.13822288	-86.73623943	3.761328683	-0.538671317

1.6 REFERENCES

1. Kealy, T. J.; Pauson, P. L., A New Type of Organo-Iron Compound. *Nature* 1951, 168, (4285), 1039-1040.

2. Miller, S. A.; Tebboth, J. A.; Tremaine, J. F., Dicyclopentadienyliron. *J. Chem. Soc.* 1952, 632-635.

3. Braun, A.; Huggins, F. E.; Kelly, K. E.; Mun, B. S.; Ehrlich, S. N.; Huffman, G. P., Impact of Ferrocene on the Structure of Diesel Exhaust Soot as Probed with Wide-Angle X-Ray Scattering and C(1s) NEXAFS Spectroscopy. *Carbon* 2006, 44, (14), 2904-2911.

4. Ritrievi, K. E.; Longwell, J. P.; Sarofim, A. F., The Effects of Ferrocene Addition on Soot Particle Inception and Growth in Premixed Ethylene Flames. *Combust. Flame* 1987, 70, (1), 17-31.

5. Hirasawa, T.; Sung, C.-J.; Yang, Z.; Joshi, A.; Wang, H., Effect of Ferrocene Addition on Sooting Limits in Laminar Premixed Ethylene-Oxygen-Argon Flames. *Combust. Flame* 2004, 139, (4), 288-299.

6. Top, S.; Dauer, B.; Vaissermann, J.; Jaouen, G., Facile Route to Ferrocifen, 1-[4-(2-dimethylaminoethoxy)]-1-(phenyl-2-ferrocenyl-but-1-ene), First Organometallic Analogue of Tamoxifen, by the McMurry Reaction. *J. Organomet. Chem.* 1997, 541, (1-2), 355-361.

7. Top, S.; Vessieres, A.; Cabestaing, C.; Laios, I.; Leclercq, G.; Provot, C.; Jaouen, G., Studies on Organometallic Selective Estrogen Receptor Modulators (SERMs): Dual Activity in the Hydroxy-Ferrocifen Series. *J. Organomet. Chem.* 2001, 637-639, (0), 500-506.

8. Delhaes, L.; Abessolo, H.; Biot, C.; Berry, L.; Delcourt, P.; Maciejewski, L.; Brocard, J.; Camus, D.; Dive, D., *In vitro* and *In vivo* Antimalarial Activity of Ferrochloroquine, a Ferrocenyl Analogue of Chloroquine Against Chloroquine-Resistant Malaria Parasites. *Parasitol. Res.* 2001, 87, (3), 239-244.

9. Top, S.; Vessieres, A.; Leclercq, G.; Quivy, J.; Tang, J.; Vaissermann, J.; Huché, M.; Jaouen, G., Synthesis, Biochemical Properties and Molecular Modelling Studies of Organometallic Specific Estrogen Receptor Modulators (SERMs), the Ferrocifens and Hydroxyferrocifens: Evidence for an Antiproliferative Effect of Hydroxyferrocifens on both Hormone-Dependent and Hormone-Independent Breast Cancer Cell Lines. *Chem. Eur. J.* 2003, 9, (21), 5223-5236.

10. Monreal, M. J.; Carver, C. T.; Diaconescu, P. L., Redox Processes in a Uranium Bis(1,1'-diamidoferrocene) Complex. *Inorg. Chem.* 2007, 46, (18), 7226-7228.

11. Carver, C. T.; Monreal, M. J.; Diaconescu, P. L., Scandium Alkyl Complexes Supported by a Ferrocene Diamide Ligand. *Organometallics* 2008, 27, (3), 363-370.

12. Broderick, E. M.; Diaconescu, P. L., Cerium(IV) Catalysts for the Ring-Opening Polymerization of Lactide. *Inorg. Chem.* 2009, 48, (11), 4701-4706.

13. Carver, C. T.; Benitez, D.; Miller, K. L.; Williams, B. N.; Tkatchouk, E.; Goddard, W. A.; Diaconescu, P. L., Reactions of Group III Biheterocyclic Complexes. *J. Am. Chem. Soc.* 2009, 131, (29), 10269-10278.

14. Diaconescu, P. L., d^0f^n-Metal Complexes Supported by Ferrocene-Based Chelating Ligands. *Comments Inorg. Chem.* 2010, 31, (5-6), 196-241.

15. Duhović, S.; Monreal, M. J.; Diaconescu, P. L., Reactions of Aromatic Heterocycles with Uranium Alkyl Complexes. *Inorg. Chem.* 2010, 49, (15), 7165-7169.

16. Huang, W.; Khan, S. I.; Diaconescu, P. L., Scandium Arene Inverted-Sandwich Complexes Supported by a Ferrocene Diamide Ligand. *J. Am. Chem. Soc.* 2011, 133, (27), 10410-10413.

17. Monreal, M. J.; Diaconescu, P. L., A Weak Interaction between Iron and Uranium in Uranium Alkyl Complexes Supported by Ferrocene Diamide Ligands. *Organometallics* 2008, 27, (8), 1702-1706.

18. Broderick, E. M.; Guo, N.; Vogel, C. S.; Xu, C.; Sutter, J.; Miller, J. T.; Meyer, K.; Mehrkhodavandi, P.; Diaconescu, P. L., Redox Control of a Ring-Opening Polymerization Catalyst. *J. Am. Chem. Soc.* 2011, 133, (24), 9278-9281.

19. Lee, J. A.; Williams, B. N.; Ogilby, K. R.; Miller, K. L.; Diaconescu, P. L., Synthesis of Symmetrically and Unsymmetrically 3,5-Dimethylbenzyl-Substituted 1,1'-Ferrocene Diamines. *J. Organomet. Chem.* 2011, 696, (25), 4090-4094.

20. Williams, B. N.; Huang, W.; Miller, K. L.; Diaconescu, P. L., Group 3 Metal Complexes of Radical-Anionic 2,2'-Bipyridyl Ligands. *Inorg. Chem.* 2010, 49, (24), 11493-11498.

21. Shafir, A.; Arnold, J., Stabilization of a Cationic Ti Center by a Ferrocene Moiety: Remarkably Short Ti-Fe Interaction in the Diamide $\{[(\eta^5\text{-}C_5H_4NSiMe_3)_2Fe]TiCl\}_2^{2+}$. *J. Am. Chem. Soc.* 2001, 123, (37), 9212-9213.

22. Astruc, D., Organoiron Electron-Reservoir Complexes. *Acc. Chem. Res.* 1986, 19, (12), 377-383.

23. Connelly, N. G.; Geiger, W. E., Chemical Redox Agents for Organometallic Chemistry. *Chem. Rev.* 1996, 96, (2), 877-910.

24. Scott, D. R.; Becker, R. S., Ligand Field Absorption Bands and d-orbital Splitting in Ferrocene. *J. Organomet. Chem.* 1965, 4, (5), 409-411.

25. Armstrong, A. T.; Smith, F.; Elder, E.; McGlynn, S. P., Electronic Absorption Spectrum of Ferrocene. *J. Chem. Phys.* 1967, 46, (11), 4321-4328.

26. Gray, H. B.; Sohn, Y. S.; Hendrickson, N., Electronic Structure of Metallocenes. *J. Am. Chem. Soc.* 1971, 93, (15), 3603-3612.

27. Rohmer, M.-M.; Veillard, A.; Wood, M. H., Excited States and Electronic Spectrum of Ferrocene. *Chem. Phys. Lett.* 1974, 29, (3), 466-468.

28. Weinmayr, V., The Condensation of Dicyclopentadienyliron with Aromatic Diazonium Salts. *J. Am. Chem. Soc.* 1955, 77, (11), 3012-3014.

29. Prins, R., Visible Absorption Spectra of Substituted Ferricenium Cations. *J. Chem. Soc. D: Chem. Commun.* 1970, (5), 280-281.

30. Dowben, P. A.; Driscoll, D. C.; Tate, R. S.; Boag, N. M., Comparison of the Electronic Structures of Disubstituted Ferrocenes. *Organometallics* 1988, 7, (2), 305-308.

31. Lippincott, E. R.; Nelson, R. D., The Vibrational Spectra and Structure of Ferrocene and Ruthenocene. *Spectrochim. Acta* 1958, 10, (3), 307-329.

32. Lippincott, E. R.; Nelson, R. D., The Vibrational Spectra and Structure of Ferrocene and Ruthenocene. *J. Chem. Phys.* 1953, 21, (7), 1307-1308.

33. Lippincott, E. R.; Nelson, R. D., The Thermodynamic Functions of Bis-cyclopentadienyl Iron, Bis-cyclopentadienylnickel and Bis-cyclopentadienylruthenium. *J. Am. Chem. Soc.* 1955, 77, (19), 4990-4993.

34. Kramer, J. A.; Hendrickson, D. N., Electron Transfer in Mixed-Valent Diferrocenylacetylene and [2.2]ferrocenophane-1,13-diyne. *Inorg. Chem.* 1980, 19, (11), 3330-3337.

35. Dong, T. Y.; Hendrickson, D. N.; Pierpont, C. G.; Moore, M. F., Mixed-Valence 1',6' -Dihalobiferrocenium Salts: The Effects of the Solid-State Environment on Electron-Transfer Rates. *J. Am. Chem. Soc.* 1986, 108, (5), 963-971.

36. Jiao, J.; Long, G. J.; Rebbouh, L.; Grandjean, F.; Beatty, A. M.; Fehlner, T. P., Properties of a Mixed-Valence $(Fe^{2+})_2(Fe^{3+})_2$ Square Cell for Utilization in the Quantum Cellular Automata Paradigm for Molecular Electronics. *J. Am. Chem. Soc.* 2005, 127, (50), 17819-17831.

37. Pal, S. K.; Alagesan, K.; Samuelson, A. G.; Pebler, J., Synthesis and Characterization of Novel Charge Transfer Complexes Formed by N,N'-Bis(Ferrocenylmethylidene)-P-Phenylenediamine and N-(Ferrocenylmethylidene)aniline. *J. Organomet. Chem.* 1999, 575, (1), 108-118.

38. Dong, T. Y.; Hsu, T. L., Electron Transfer in Mixed-Valence 1,1'-Bis(triphenylmethyl)biferrocenium Triiodide. *J. Organomet. Chem.* 1989, 367, (3), 313-319.

39. Buschow, K. H. J.; de Boer, F. R., *Physics of Magnetism and Magnetic Materials*. Kluwer Academic/Plenum Publishers: New York, 2003; p vii, 182 p.

40. Selwood, P. W., *Magnetochemistry*. Lightning Source Incorporated: 2007.

41. Gama, V.; Almeida, M., Metallocenium Salts of Transition Metal Bisdichalcogenate Anions; Structure and Magnetic Properties. In *Conducting and Magnetic Organometallic Molecular Materials*, Fourmigué, M.; Ouahab, L., Eds. Springer Berlin / Heidelberg: 2009; Vol. 27, pp 97-140.

42. Miller, J. S.; Epstein, A. J.; Reiff, W. M., Ferromagnetic Molecular Charge-Transfer Complexes. *Chem. Rev.* 1988, 88, (1), 201-220.

43. Weber, W., Introduction to Magnetism. In *Magnetism and Synchrotron Radiation*, Beaurepaire, E.; Bulou, H.; Scheurer, F.; Jean-Paul, K., Eds. Springer Berlin Heidelberg: 2010; Vol. 133, pp 1-41.

44. Sohn, Y. S.; Hendrickson, D. N.; Gray, H. B., Electronic Structure of Ferricenium Ion. *J. Am. Chem. Soc.* 1970, 92, (10), 3233-3234.

45. Chi, K. M.; Calabrese, J. C.; Reiff, W. M.; Miller, J. S., Ferromagnetic Behavior of Linear-Chain Electron-Transfer Complexes. Synthesis and Characterization Of Decaethylferrocene, $Fe(C_5Et_5)_2$, and its Electron-Transfer Salts: Structure and Magnetic Properties of $[Fe(C_5Et_5)_2]^+[A]^-$ [A = TCNE and TCNQ]. *Organometallics* 1991, 10, (3), 688-693.

46. Kollmar, C.; Couty, M.; Kahn, O., A Mechanism for the Ferromagnetic Coupling in Decamethylferrocenium Tetracyanoethenide. *J. Am. Chem. Soc.* 1991, 113, (21), 7994-8005.

47. Miller, J. S.; Glatzhofer, D. T.; O'Hare, D. M.; Reiff, W. M.; Chakraborty, A.; Epstein, A. J., Ferromagnetic Behavior in Linear Charge-Transfer Complexes. Structural and Magnetic Characterization of Octamethylferrocene: $[Fe(C_5Me_4H)_2]^+[A]^-$ (A = TCNE, TCNQ). *Inorg. Chem.* 1989, 28, (15), 2930-2939.

48. Kollmar, C.; Kahn, O., Spin Polarization and Ferromagnetic Coupling in Metallocenium Charge Transfer Complexes. *J. Chem. Phys.* 1992, 96, (4), 2988-2997.

49. Miller, J. S.; Glatzhofer, D. T.; Vazquez, C.; McLean, R. S.; Calabrese, J. C.; Marshall, W. J.; Raebiger, J. W., Electron-Transfer Salts of 1,2,3,4,5-Pentamethylferrocene, $Fe(C_5Me_5)(C_5H_5)$. Structure and Magnetic Properties of Two 1:1 and Two 2:3 $Fe(C_5Me_5)(C_5H_5)$ Electron-Transfer Salts of Tetracyanoethylene. *Inorg. Chem.* 2001, 40, (9), 2058-2064.

50. Akishin, P. A.; Ramlidi, N. G.; Bredikhina, T. N., Electron-Diffraction Study of The Ferrocene Molecule. *J. Struct. Chem.* 1961, 2, (4), 443-443.

51. Seibold, E. A.; Sutton, L. E., Structure of Ferrocene. *J. Chem. Phys.* 1955, 23, (10), 1967-1967.

52. Gray, H. B.; Hendrickson, D. N.; Sohn, Y. S., Magnetic Susceptibility Study of Various Ferricenium and Iron(III) Dicarbollide Compounds. *Inorg. Chem.* 1971, 10, (8), 1559-1563.

53. M. J. Frisch; G. W. Trucks; H. B. Schlegel; G. E. Scuseria; M. A. Robb; J. R. Cheeseman; G. Scalmani; V. Barone; B. Mennucci; G. A. Petersson; H. Nakatsuji; M. Caricato; X. Li; H. P. Hratchian; A. F. Izmaylov; J. Bloino; G. Zheng; J. L. Sonnenberg; M. Hada; M. Ehara; K. Toyota; R. Fukuda; J. Hasegawa; M. Ishida; T. Nakajima; Y. Honda; O. Kitao; H. Nakai; T. Vreven; J. A. Montgomery, J.; J. E. Peralta; F. Ogliaro; M. Bearpark; J. J. Heyd; E. Brothers; K. N. Kudin; V. N. Staroverov; T. Keith; R. Kobayashi; J. Normand; K. Raghavachari; A. Rendell; J. C. Burant; S. S. Iyengar; J. Tomasi; M. Cossi; N. Rega; J. M. Millam; M. Klene; J. E. Knox; J. B. Cross; V. Bakken; C. Adamo; J. Jaramillo; R. Gomperts; R. E. Stratmann; O. Yazyev; A. J. Austin; R. Cammi; C. Pomelli; J. W. Ochterski; R. L. Martin; K. Morokuma; V. G. Zakrzewski; G. A. Voth; P. Salvador; J. J. Dannenberg; S. Dapprich; A. D. Daniels; Ö. Farkas; J. B. Foresman; J. V. Ortiz; J. Cioslowski; D. J. Fox, *Gaussian 09, Revision B.01*. Gaussian, Inc.: Wallingford, CT, 2009.

54. Ditchfield, R.; Hehre, W. J.; Pople, J. A., Self-Consistent Molecular-Orbital Methods. IX. An Extended Gaussian-Type Basis for Molecular-Orbital Studies of Organic Molecules. *J. Chem. Phys.* 1971, 54, (2), 724-728.

55. Francl, M. M.; Pietro, W. J.; Hehre, W. J.; Binkley, J. S.; Gordon, M. S.; DeFrees, D. J.; Pople, J. A., Self-Consistent Molecular Orbital Methods. XXIII. A Polarization-type Basis Set for Second-row Elements. *J. Chem. Phys.* 1982, 77, (7), 3654-3665.

56. Hariharan, P. C.; Pople, J. A., Accuracy of AH_n Equilibrium Geometries by Single Determinant Molecular Orbital Theory. *Mol. Phys.* 1974, 27, (1), 209-214.

57. Hariharan, P. C.; Pople, J. A., The Influence of Polarization Functions on Molecular Orbital Hydrogenation Energies. *Theo. Chim. Acta* 1973, 28, (3), 213-222.

58. Hehre, W. J.; Ditchfield, R.; Pople, J. A., Self-Consistent Molecular Orbital Methods. XII. Further Extensions of Gaussian-Type Basis Sets for Use in Molecular Orbital Studies of Organic Molecules. *J. Chem. Phys.* 1972, 56, (5), 2257-2261.

59. Rassolov, V. A.; Pople, J. A.; Ratner, M. A.; Windus, T. L., 6-31G* Basis Set for Atoms K through Zn. *J. Chem. Phys.* 1998, 109, (4), 1223-1229.

60. Rassolov, V. A.; Ratner, M. A.; Pople, J. A.; Redfern, P. C.; Curtiss, L. A., 6-31G* Basis Set for Third-row Atoms. *J. Comput. Chem.* 2001, 22, (9), 976-984.

61. Hay, P. J.; Wadt, W. R., Ab Initio Effective Core Potentials for Molecular Calculations. Potentials for K To Au Including the Outermost Core Orbitals. *J. Chem. Phys.* 1985, 82, (1), 299-310.

62. Haaland, A., Molecular Structure and Bonding in the 3d Metallocenes. *Acc. Chem. Res.* 1979, 12, (11), 415-422.

63. Haaland, A.; Nilsson, J. E., Determination of Barriers to Internal Rotation by Means of Electron Diffraction. Ferrocene and Ruthenocene. *Acta Chem. Scand.* 1968, 22, (8), 2653-2670.

64. Hay, P. J.; Dunning, T. H., *Modern Theoretical Chemistry*. Plenum: New York, 1976; Vol. 3.

65. Mayor-Lopez, M. J.; Weber, J., DFT Calculations of the Binding Energy of Metallocenes. *Chem. Phys. Lett.* 1997, 281, (1-3), 226-232.

66. Klopper, W.; Lüthi, H. P., Towards the Accurate Computation of Properties of Transition Metal Compounds: The Binding Energy of Ferrocene. *Chem. Phys. Lett.* 1996, 262, (5), 546-552.

67. Koch, H.; Jorgensen, P.; Helgaker, T., The Molecular Structure of Ferrocene. *J. Chem. Phys.* 1996, 104, (23), 9528-9530.

68. Pierloot, K.; Persson, B. J.; Roos, B. O., Theoretical Study of the Chemical Bonding in [Ni(C_2H_4)] and Ferrocene. *J. Chem. Phys.* 1995, 99, (11), 3465-3472.

69. Lee, C.; Yang, W.; Parr, R. G., Development of the Colle-Salvetti Correlation-Energy Formula into a Functional of the Electron Density. *Phys. Rev. B* 1988, 37, (2), 785-789.

70. Becke, A. D., Density-Functional Thermochemistry. III. The Role of Exact Exchange. *J. Chem. Phys.* 1993, 98, (7), 5648-5652.

71. Young, D. C., *Computational Chemistry: A Practical Guide for Applying Techniques to Real World Problems*. Wiley: 2001.

72. Haaland, A., Organometallic Compounds Studied by Gas-Phase Electron Diffraction. *Top. Curr. Chem.* 1975, (53), 1-23.

73. Kirin, S. I.; Kraatz, H.-B.; Metzler-Nolte, N., Systematizing Structural Motifs and Nomenclature in 1,n'-Disubstituted Ferrocene Peptides. *Chem. Soc. Rev.* 2006, 35, (4), 348-354.

74. Gan, K.-S.; Hor, T. S. A., 1,1'-Bis(diphenylphosphino)ferrocene: Coordination Chemistry, Organic Synthesis, and Catalysis. In *Ferrocenes: Homogeneous Catalysis, Organic Synthesis, Materials Science*, Togni, A.; Hayashi, T., Eds. VCH Publishers: New York, 1995; pp 3-96.

75. Martinez, R.; Tiripicchio, A., Structure of Ferrocenium Hexafluorophosphate. *Acta Crystallogr. Sec. C* 1990, 46, (2), 202-205.

76. Pfab, W.; Fischer, E. O., Zur Kristallstruktur der Di-cyclopentadienyl-verbindungen des zweiwertigen Eisens, Kobalts und Nickels. *Z. Anorg. Allg. Chem.* 1953, 274, (6), 316-322.

77. Eiland, P. F.; Pepinsky, R., X-Ray Examination of Iron Biscyclopentadienyl. *J. Am. Chem. Soc.* 1952, 74, (19), 4971-4971.

78. Dunitz, J. D.; Orgel, L. E., Bis-cyclopentadienyl Iron: a Molecular Sandwich. *Nature* 1953, 171, (4342), 121-122.

79. Dunitz, J. D.; Orgel, L. E.; Rich, A., The Crystal Structure of Ferrocene. *Acta Crystallogr*. 1956, 9, (4), 373-375.

80. Bohn, R. K.; Haaland, A., On the Molecular Structure of Ferrocene, $Fe(C_5H_5)_2$. *J. Organomet. Chem*. 1966, 5, (5), 470-476.

81. Wight, C. A.; Boldyrev, A. I., Potential Energy Surface and Vibrational Frequencies of Carbonic Acid. *J. Chem. Phys*. 1995, 99, (32), 12125-12130.

82. Kirchner, R. F.; Loew, G. H.; Mueller-Westerhoff, U. T., A Theoretical Study of the Electromagnetic Properties of Ferrocene and the Ferrocenium Ion. *Theor. Chim. Acta* 1976, 41, (1), 1-6.

83. Chàvez, I.; Alvarez-Carena, A.; Molins, E.; Roig, A.; Maniukiewicz, W.; Arancibia, A.; Arancibia, V.; Brand, H.; Manuel Manriquez, J., Selective Oxidants for Organometallic Compounds Containing a Stabilising Anion of Highly Reactive Cations: $(3,5(CF_3)_2C_6H_3)_4B^-)Cp_2Fe^+$ and $(3,5(CF_3)_2C_6H_3)_4B^-)Cp^*_2Fe^+$. *J. Organomet. Chem*. 2000, 601, (1), 126-132.

84. Bagus, P. S.; Walgren, U. I.; Almlof, J., A Theoretical Study of the Electronic Structure of Ferrocene and Ferricinium: Application to Mössbauer Isomer Shifts, Ionization Potentials, and Conformation. *J. Chem. Phys*. 1976, 64, (6), 2324-2334.

85. Shafir, A.; Power, M. P.; Whitener, G. D.; Arnold, J., Synthesis, Structure, and Properties of 1,1'-Diamino- and 1,1'-Diazidoferrocene. *Organometallics* 2000, 19, (19), 3978-3982.

86. MacDiarmid, A. G., Silyl Compounds. *Quarterly Reviews, Chemical Society* 1956, 10, (2), 208-229.

87. Ebsworth, E. A. V.; Emeleus, H. J., The Preparation and Donor Properties of Some Silylamines. *J. Chem. Soc. (Resumed)* 1958, 2150-2156.

88. Hedberg, K., The Molecular Structure of Trisilylamine, $(SiH_3)_3N$. *J. Am. Chem. Soc*. 1955, 77, (24), 6491-6492.

89. Jarvie, A. W.; Lewis, D., A Comparative Study of the Basicity of Some Silylamines. *J. Chem. Soc. (Resumed)* 1963, 1073-1076.

90. Carty, P.; Clare, K. C.; Creighton, J. R.; Metcalfe, E.; Raper, E. S.; Dawes, H. M., The Preparation, Crystal Structure and Thermal Analysis of Bis(ferrocenium) [μ_2-oxo bis(trichloroferrate(III))]. *Inorg. Chim. Acta* 1986, 112, (2), 113-117.

91. Swart, M., Metal-Ligand Bonding in Metallocenes: Differentiation between Spin State, Electrostatic and Covalent Bonding. *Inorg. Chim. Acta* 2007, 360, (1), 179-189.

92. Shannon, R., Revised Effective Ionic Radii and Systematic Studies of Interatomic Distances in Halides and Chalcogenides. *Acta Crystallogr. Sec. A* 1976, 32, (5), 751-767.

93. Nagy, A. G.; Dezsi, I.; Hillman, M., Mossbauer Study of Bridged Ferrocene Derivatives. *J. Organomet. Chem.* 1976, 117, (1), 55-59.

94. Driscoll, D. C.; Dowben, P. A.; Boag, N. M.; Grade, M.; Barfuss, S., The Electronic Structure of the Chloroferrocenes. *J. Chem. Phys.* 1986, 85, (9), 4802-4807.

95. Ballhausen, C. J.; Dahl, J. P.; Buchardt, O.; Olsen, G. E.; Pedersen, C.; Toft, J., Molecular Orbitals for the Protonated Sandwich Compounds. *Acta Chem. Scand.* 1961, 15, 1333-1336.

96. Zhang, G.; Zhang, H.; Sun, M.; Liu, Y.; Pang, X.; Yu, X.; Liu, B.; Li, Z., Substitution Effect on the Geometry and Electronic Structure on the Ferrocene. *J. Comput. Chem.* 2007, 28, (14), 2260-2274.

97. Aihara, J. I., Reduced HOMO-LUMO Gap as an Index of Kinetic Stability for Polycyclic Aromatic Hydrocarbons. *J. Chem. Phys. A* 1999, 103, (37), 7487-7495.

98. Knickelbein, M. B., Reactions of Transition Metal Clusters with Small Molecules. *Annu. Rev. Phys. Chem.* 1999, 50, (1), 79-115.

99. Kirchner, R. F.; Loew, G. H.; Mueller-Westerhoff, U. T., Theoretical Study of the Electromagnetic Properties of Bis(fulvalene)diiron in its Three Oxidation States. *Inorg. Chem.* 1976, 15, (11), 2665-2670.

100. Pangborn, A. B.; Giardello, M. A.; Grubbs, R. H.; Rosen, R. K.; Timmers, F. J., Safe and Convenient Procedure for Solvent Purification. *Organometallics* 1996, 15, (5), 1518-1520.

101. Shafir, A.; Power, M. P.; Whitener, G. D.; Arnold, J., Silylated 1,1'-Diaminoferrocene: Ti and Zr Complexes of a New Chelating Diamide Ligand. *Organometallics* 2001, 20, (7), 1365-1369.

102. Shafir, A.; Arnold, J., Zirconium Complexes Incorporating Diaryldiamidoferrocene Ligands: Generation of Cationic Derivatives and Polymerization Activity Towards Ethylene and 1-Hexene. *Inorg. Chim. Acta* 2003, 345, (0), 216-220.

103. Siemeling, U.; Farber, C.; Leibold, M.; Bruhn, C.; Mucke, P.; Winter, R. F.; Sarkar, B.; von Hopffgarten, M.; Frenking, G., Six-Membered N-Heterocyclic Carbenes with a 1,1'-Ferrocenediyl Backbone: Bulky Ligands with Strong Electron-Donor Capacity and Unusual Non-Innocent Character. *Eur. J. Inorg. Chem.* 2009, 2009, (31), 4607-4612.

104. Roy, L. E.; Jakubikova, E.; Guthrie, M. G.; Batista, E. R., Calculation of One-Electron Redox Potentials Revisited. Is It Possible to Calculate Accurate Potentials with Density Functional Methods? *J. Chem. Phys. A* 2009, 113, (24), 6745-6750.

105. Dong, S. S.; Nielsen, R. J.; Palmer, J. H.; Gray, H. B.; Gross, Z.; Dasgupta, S.; Goddard, W. A., Electronic Structures of Group 9 Metallocorroles with Axial Ammines. *Inorg. Chem.* 2011, 50, (3), 764-770.

106. Baik, M.-H.; Friesner, R. A., Computing Redox Potentials in Solution: Density Functional Theory as a Tool for Rational Design of Redox Agents. *J. Chem. Phys. A* 2002, 106, (32), 7407-7412.

107. Davis, A. P.; Fry, A. J., Experimental and Computed Absolute Redox Potentials of Polycyclic Aromatic Hydrocarbons are Highly Linearly Correlated Over a Wide Range of Structures and Potentials. *J. Chem. Phys. A* 2010, 114, (46), 12299-12304.

108. D'andrade, B. W.; Datta, S.; Forrest, S. R.; Djurovich, P.; Polikarpov, E.; Thompson, M. E., Relationship between the Ionization and Oxidation Potentials of Molecular Organic Semiconductors. *Org. Electron.* 2005, 6, (1), 11-20.

109. Namazian, M.; Lin, C. Y.; Coote, M. L., Benchmark Calculations of Absolute Reduction Potential of Ferricinium/Ferrocene Couple in Nonaqueous Solutions. *J Chem Theory Comput* 2010, 6, (9), 2721-2725.

CHAPTER 2

In Situ Generation of Uranium Alkyl Complexes

TABLE OF CONTENTS

2.1 INTRODUCTION

Tuning the electronic and steric properties of ancillary-ligand framework has previously been shown to influence the reactivity of uranium complexes.[1-9] As described in Chapter 1, ferrocene–based ligands are redox active. Therefore, electronic changes at the iron center can impart enhanced activity to the uranium center. Furthermore, even slight adjustments of their structural motif can have profound effects on the reactivity. Previous examples of such influence include novel C–H activation reactions by a uranium dibenzyl complex supported by a ferrocene diamide, **(NN^{TBS})U(CH$_2$Ph)$_2$**, in which both benzyl ligands engage an sp^2 C–H bond of 1-methylimidazole.[10, 11] In order to determine whether these effects are unique to uranium complexes supported by ferrocene diamide ligands, synthesis of analogous complexes supported by a tridentate, dianionic pyridine-based ligand was carried out. Pyridine–based ligands have an extremely rigid core, which is believed to be responsible for the exceptional thermal stability of their complexes. The electron density donation from

the pyridyl nitrogen reduces the Lewis acidity of the metal center, resulting in greater stability of the high oxidation state.[12] Complexes of Ti(IV),[13-15] Zr(IV),[16-19] Ta(V),[20, 21] lanthanides[22-24] and Th(IV)[12, 25] supported by pyridine-diamide ligands are known. A method typically employed for the synthesis of actinide dialkyl complexes calls for two separate steps. For example, thorium dialkyl complexes were synthesized from KCH_2Ph or $LiCH_2SiMe_3$ and the respective thorium dichloride, $(NN^{py})ThCl_2(DME)$ was produced in the salt-metathesis reaction between $ThCl_4(DME)_2$ and $Li_2[NN^{py}]$.[12, 25] The complex **$(NN^{TBS})U(CH_2Ph)_2$** was also synthesized by the salt-metathesis reaction of KCH_2Ph and **$(NN^{TBS})UI_2(THF)$**, obtained directly from $UI_3(THF)_4$[26-28] and $[K(OEt_2)_2]_2[NN^{fc}]$.[29] Since $UI_3(THF)_4$[26-28] is a readily available starting material and U-I bonds are weaker and, therefore, easier to involve in salt-metathesis reactions than U-Cl bonds, we decided to follow the same reaction protocol for the synthesis of a $(NN^{py})UI_2$ starting material, even though the formation of the uranium(IV) complex would require the disproportionation of the uranium(III) complex $UI_3(THF)_4$.[1, 2, 29, 30] This chapter describes an *in situ* synthesis of a series of uranium dialkyl complexes supported by either one dianionic bidentate 1,1'-ferrocene diamide (H_2NN^{TMS} or H_2NN^{TBS}, where TMS = $SiMe_3$ and TBS = $SiMe_2{}^tBu$) or tridentate bis(2,6-diisopropylanilidomethyl)pyridine (H_2NN^{py}) ligand (**Chart 2.1**).

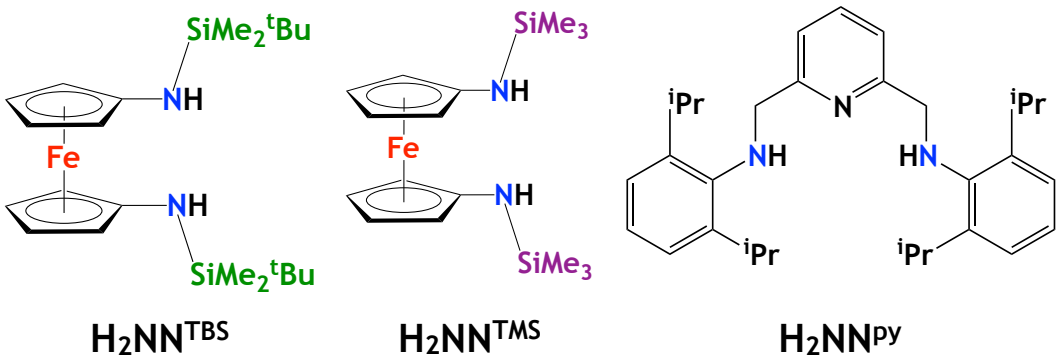

Chart 2.1. 1,1'-ferrocene and pyridine diamines.

2.2 DISCUSSION OF RESULTS

2.2.1 Uranium(IV) supported by a pyridine-based ligand

The reaction between $UI_3(THF)_4$ and $[K(OEt_2)_2]_2[NN^{py}]$ gave a mixture of products that proved intractable. However, the reaction between $UI_3(THF)_4$ and two equivalents of $[Li(OEt_2)_2]_2[NN^{py}]$ (**Figure 2.1**) led to the isolation of **$(NN^{py})_2U$**.

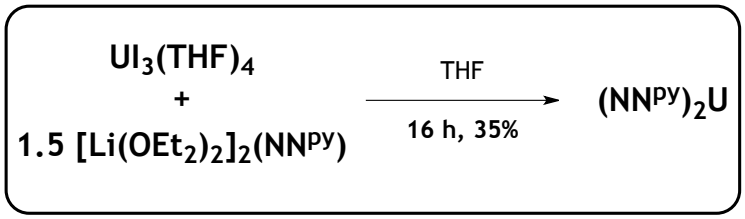

Figure 2.1. Synthesis of **$(NN^{py})_2U$**.

Although **$(NN^{py})_2U$** was too insoluble in hydrocarbons or diethyl ether to allow its purification, a single-crystal X-ray diffraction study confirmed the solid state structure of **$(NN^{py})_2U$** (**Figure 2.2**). The average distance between uranium and the aniline nitrogen is 2.34 Å, while that between uranium and the pyridine nitrogen atoms is 2.52 Å. Moreover, the angle defined by N_{amide}-U-N_{amide} is 128.6°, while the angle between all three nitrogen atoms (i.e. N_{amide}-N_{py}-N_{amide}) is 105.4°. Finally, the ligands are rotated approximately 58° from one other (dihedral angle defined as two planes formed by two aniline nitrogen atoms on each ligand).

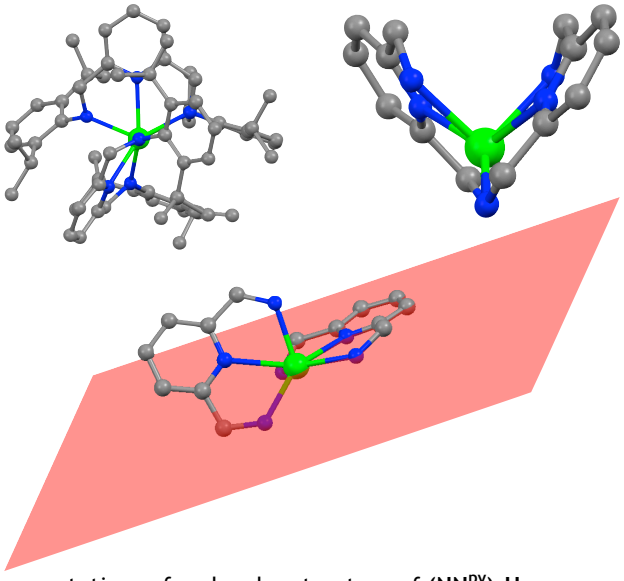

Figure 2.2. Ball-and-stick representations of molecular structure of **$(NN^{py})_2U$**.

Using only one equivalent of $[Li(OEt_2)_2]_2[NN^{py}]$ did not result in a **$(NN^{py})UI_2$** complex. Inspired by a report from the Hayton group on the synthesis of homoleptic uranium alkyl complexes[31] and encouraged by the fact that $(NN^{py})Th(CH_2SiMe_3)_2$ was accessible from an *in situ* reaction between "$Cl_2Th(CH_2SiMe_3)_2$" and H_2NN^{py}, the synthesis of uranium alkyl complexes supported by NN^{py} was achieved by generating but not isolating their alkyl precursors. Thus, the reaction of $UI_3(THF)_4$ and three equivalents of KCH_2Ph, followed by the addition of 0.75 equivalents of H_2NN^{py} at low temperatures, led to the formation of the uranium(IV) dibenzyl complex, **$(NN^{py})U(CH_2Ph)_2$** (**Figure 2.3**).

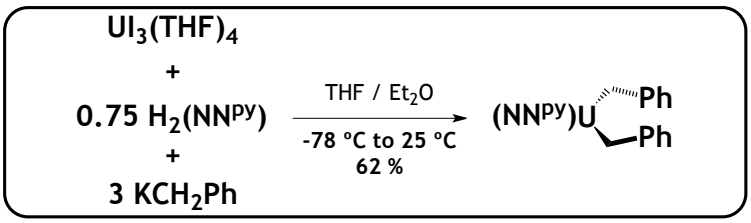

Figure 2.3. Formation of **$(NN^{py})U(CH_2Ph)_2$**.

The reaction was reproducible and allowed the isolation of **$(NN^{py})U(CH_2Ph)_2$** in 54–62% yield consistently. Complex **$(NN^{py})U(CH_2Ph)_2$** was characterized by elemental analysis, ^1H NMR spectroscopy, and X-ray crystallography (**Figure 2.4**). The distance between uranium and the aniline nitrogen atoms is 2.24 Å, while that between uranium and the pyridine nitrogen is 2.48 Å. Moreover, the angle defined by N_{amide}-U-N_{amide} is slightly greater than that in **$(NN^{py})_2U$** (130.6° versus 128.6°), while the angle between all three nitrogen atoms is slightly smaller than that in **$(NN^{py})_2U$** (103.88° versus 105.4°). As shown in **Figure 2.4**, one phenyl ring lies above the pyridine ring of the ligand backbone. It is, however, displaced by approximately 1.0 Å, precluding any π-π interaction. The distance between the centers of each ring is 3.79 Å.

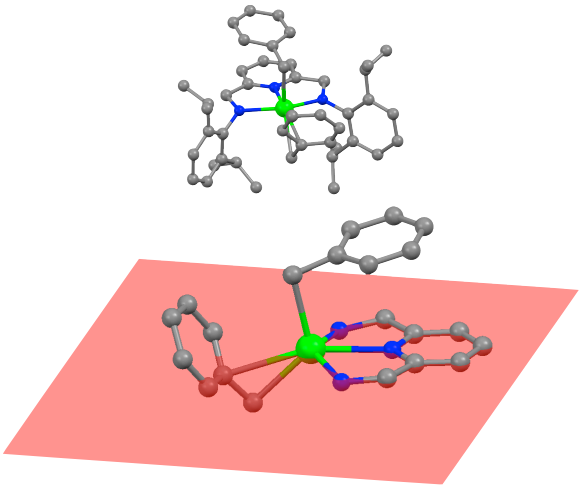

Figure 2.4. Ball-and-stick representation of molecular structure of **$(NN^{py})U(CH_2Ph)_2$**.

By changing the stoichiometry and employing two equivalents of KCH_2Ph in a reaction with $UI_3(THF)_4$ and 0.75 equivalents of H_2NN^{py}, a new product, **$(NN^{py})UI(CH_2Ph)$**, was obtained (**Figure 2.5**), along with trans-1,2-diphenylethylene (*trans*-stilbene). The reaction was also reproducible and occurred consistently in 68–76% yield. As shown in **Figure 2.6**, NN^{py}, iodide, and benzyl ligands form a distorted square pyramid around the uranium center. Both diisopropylaniline substituents point downwards, leaving I^- greatly exposed to attack. The angle defined by iodide, uranium, and pyridine nitrogen atoms is 96.7°. The distance between uranium and iodide is slightly shorter than that in uranium diiodide complexes supported by ferrocene diamide ligands (3.03 Å[29] versus 3.04 Å). The distance between uranium and aniline nitrogen atoms is 2.22 Å, while that between uranium and the pyridine nitrogen is 2.48 Å. Finally, the N_{amide}-U-N_{amide} angle is 128.9°, while N_{amide}-N_{py}-N_{amide} is 102.4°.

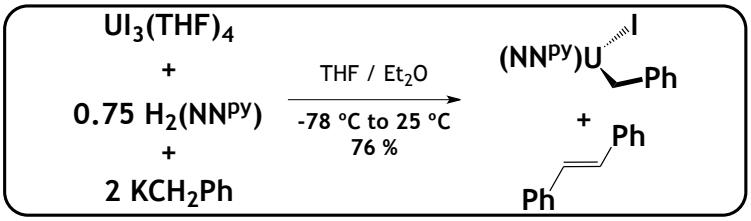

Figure 2.5. Formation of **$(NN^{py})UI(CH_2Ph)$**.

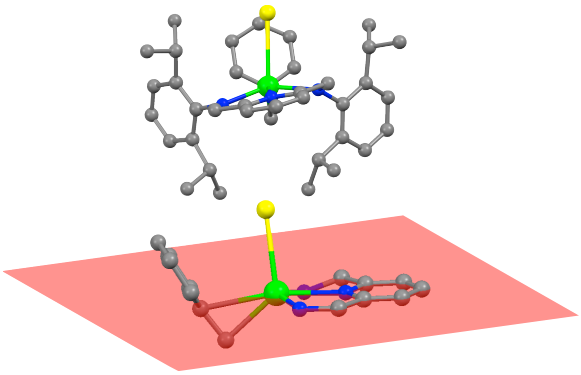

Figure 2.6. Ball-and-stick representations of molecular structure of **(NN^{py})UI(CH_2Ph)**.

Cyclic voltammetry of **(NN^{py})UI(CH_2Ph)** reveals two oxidation events at -0.23 V and 0.38 V, in addition to two irreversible reduction processes at -2.24 V and -2.54 V (**Figure 2.7**), all which were assigned to uranium-based processes.

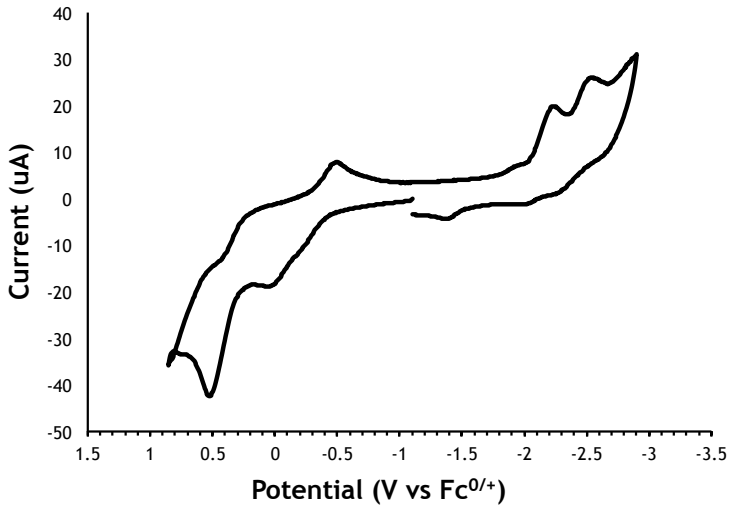

Figure 2.7. Cyclic voltammogram of **(NN^{py})UI(CH_2Ph)** in THF and $TBAPF_6$ at 200 mV/s, with Pt wire, glassy carbon disk, and silver wire as working, counter, and reference electrodes, respectively.

We propose that $U(CH_2Ph)_3(THF)_x$ or $UI(CH_2Ph)_2(THF)_y$, generated *in situ* in the reactions shown in **Figures 2.3** and **2.5**, respectively, reacts with H_2NN^{py} when the disproportionation to the uranium(IV) product occurs; the disproportionation of either species to uranium(IV) complexes and uranium(0) before the reaction with H_2NN^{py} is also possible. The formation of **(NN^{py})UI(CH_2Ph)** is especially noteworthy since our attempts to generate the analogous **(NN^{TBS})UI(CH_2Ph)** from **(NN^{TBS})UI_2(THF)** and one equivalent of KCH_2Ph or by

comproportionation from **(NN^{TBS})UI$_2$(THF)** and **(NN^{TBS})U(CH$_2$Ph)$_2$** does not lead to the analogous mixed ligand system.

2.2.2 Uranium(IV) supported by a ferrocene-based ligand

Encouraged by the formation of **(NN^{py})U(CH$_2$Ph)$_2$** and **(NN^{py})UI(CH$_2$Ph),** we decided to explore the reaction scope of the *in situ* generation of uranium alkyl complexes. To that end, similar reaction conditions as those presented in **Figure 2.4** were used in order to generate **(NN^{TMS})U(CH$_2$Ph)$_2$**, where NN^{TMS} = fc(NSiMe$_3$)$_2$ (**Chart 2.1**). Although we had observed the formation of **(NN^{TMS})UI$_2$(THF)** from UI$_3$(THF)$_4$ and [K(OEt$_2$)$_2$]$_2$[NN^{TMS}] previously, the reaction was not reproducible thus prompting us to employ the tert-butyldimethyl variant, NN^{TBS} = fc(NSi^{t}BuMe$_2$)$_2$.

The reaction between UI$_3$(THF)$_4$ and three equivalents of KCH$_2$Ph, followed by the addition of 0.75 equivalents of H$_2$NN^{TMS} at low temperatures, led to the formation of **(NN^{TMS})U(CH$_2$Ph)$_2$** (**Scheme 2.1**), in 51–77% yield, obtained again consistently and reproducibly. Furthermore, the same reaction conditions could be applied to the synthesis of **(NN^{TMS})U(CH$_2$SiMe$_3$)$_2$** in 60–80% yield (**Scheme 2.1**), circumventing the need to isolate a halide starting material. The complexes **(NN^{TBS})U(CH$_2$Ph)$_2$** and **(NN^{TBS})U(CH$_2$^{t}Bu)$_2$**, previously reported,[29] and **(NN^{TMS})U(CH$_2$SiMe$_3$)$_2$** were also synthesized by the present method (**Scheme 2.1**) in better yields than those recorded for their syntheses from **(NN^{TBS})UI$_2$(THF)** (84% vs. 52% for **(NN^{TBS})U(CH$_2$Ph)$_2$**, 54% vs. 27% for **(NN^{TBS})U(CH$_2$^{t}Bu)$_2$**, and 87% for **(NN^{TBS})U(CH$_2$SiMe$_3$)$_2$**. Attempts to isolate the mixed alkyl-iodide uranium complexes supported by ferrocene diamide ligands were unsuccessful using the present method.

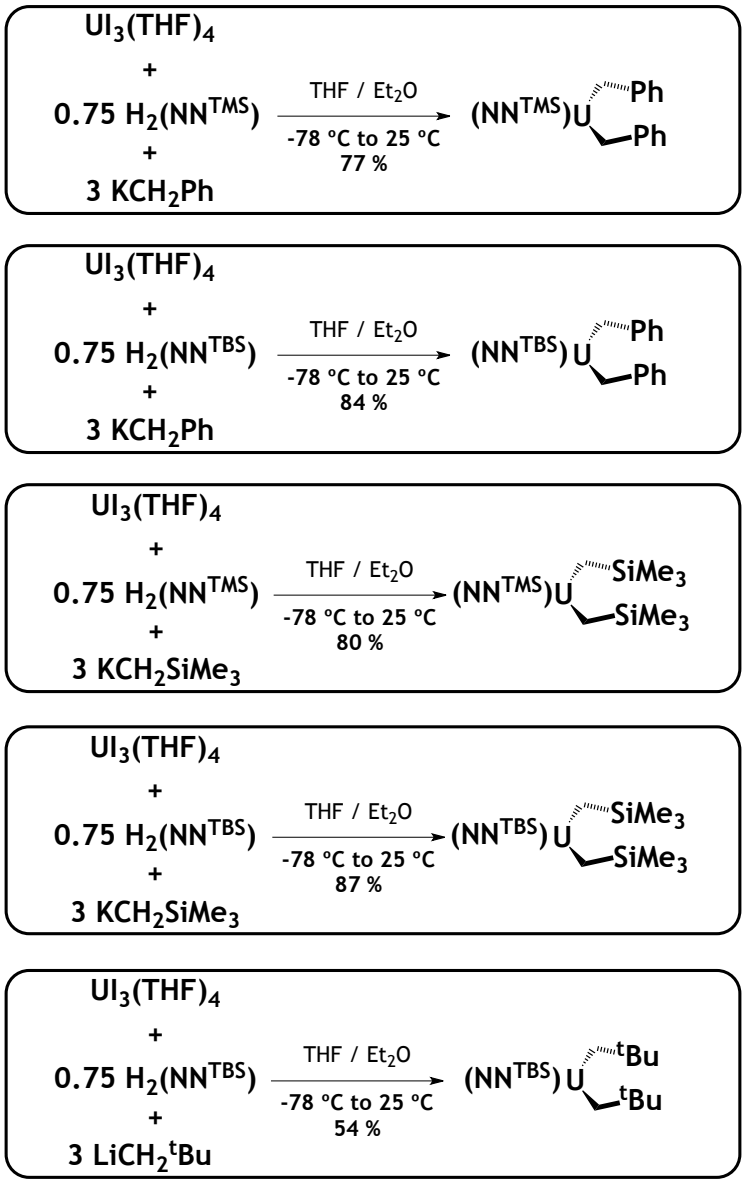

Scheme 2.1. Formation of uranium dialkyl complexes supported by ferrocene diamide ligands.

2.3 CONCLUSION

In conclusion, a general method for the synthesis of uranium(IV) alkyl complexes has been presented. This one-pot procedure starts from a readily available uranium precursor, $UI_3(THF)_4$, and bypasses the need to isolate halide or homoleptic-alkyl uranium starting materials. The products of all reactions were uranium(IV) complexes, presumably formed by the disproportionation of uranium(III) intermediates. Both potassium benzyl and lithium alkyl reagents were employed and the ancillary ligands targeted included pyridine and ferrocene-

based diamides. We are currently in the process of extending the present procedure to the formation of other uranium alkyl complexes.

2.4 APPENDIX B

2.4.1 Synthesis

General Considerations. All experiments were performed under a dry nitrogen atmosphere using standard Schlenk techniques or an MBraun inert-gas glove box. Solvents were purified using a two-column solid- state purification system by the method of Grubbs[32] and transferred to the glove box without exposure to air. NMR solvents were obtained from Cambridge Isotope Laboratories, degassed, and stored over activated molecular sieves prior to use. Uranium turnings were purchased from Argonne National Laboratories. $LiCH_2SiMe_3$ was purchased from Acros as an n-pentane solution (1 M), which was filtered through Celite; the volatiles were removed to leave a white solid, which was used without further purification. Compounds $UI_3(THF)_4$,[26-28] $LiCH_2CMe_3$,[33] H_2NN^{TBS},[34] H_2NN^{TMS},[35] KCH_2Ph,[36] 2,6-bis(chloromethyl)pyridine,[37] **$(NN^{TBS})U(CH_2Ph)_2$** and **$(NN^{TBS})U(CH_2{}^tBu)_2$**[29] were prepared following published procedures. Syntheses of H_2NN^{py}[17] and $[Li(OEt_2)_2]_2[NN^{py}]$[12] were slightly modified from reported procedures. nBuLi was purchased from Alfa Aesar as a hexanes solution (2.88 M); all other chemicals were purchased and used as received. ^1H NMR spectra were recorded on Bruker300 or Bruker500 spectrometers at room temperature in C_6D_6 unless otherwise specified. Chemical shifts are reported with respect to solvent residual peak, 7.16 ppm (C_6D_6). CHN analyses were performed by UC Berkeley Micro-Mass facility, 8 Lewis Hall, College of Chemistry, University of California, Berkeley, CA 94720.

Synthesis of H_2NN^{py}. A cold THF solution of 2,6-diisopropylaniline (1.4615 g, 7.986 mmol) was added to a stirring THF solution of 2,6-bis(chloromethyl)pyridine (0.6605 g, 3.803 mmol) at -78 °C. The mixture was warmed to room temperature and stirred for 19 h. The reaction was

quenched with a saturated solution of Na_2CO_3 and extracted into diethyl ether three times. The fractions were combined and dried with $MgSO_4$. Volatiles were removed under reduced pressure and a small amount of hexanes was added to the resulting dark yellow oil to yield a sticky white precipitate, which was collected on a medium-porosity frit and dried. The off-white solid was dissolved in diethyl ether, filtered through alumina, and crystallized at room temperature by slow evaporation. Yellow needle crystals formed in a 91% yield (1.58 g, 3.461 mmol).

Synthesis of $[Li(OEt_2)_2]_2[NN^{py}]$. In a 20-mL scintillation vial charged with a stir bar, H_2NN^{py} (0.2140 g, 0.467 mmol) was dissolved in toluene, and then cooled for 30 min. To this white suspension, a cold hexanes solution of nBuLi (35 mL, 0.2360 g, 0.981 mmol) was added slowly and the resulting dark-orange mixture was stirred at room temperature for 10 min. The volatiles were removed under reduced pressure and the orange gel was washed with cold hexanes. The yellow solid was collected on a medium-porosity frit, washed with a small amount of cold hexanes, and dried. Yield: 90% (0.1930 g, 0.4203 mmol).

Synthesis of $(NN^{py})_2U$. A 5-mL THF solution of **$[Li(OEt_2)_2]_2[NN^{py}]$** (0.1420 g, 0.3 mmol) was added to a THF solution of $UI_3(THF)_4$ (0.3670 g, 0.4 mmol). The mixture was stirred for 16 h, filtered through Celite, and dried. The crude product was extracted into toluene, the solution was filtered through Celite and dried; the extraction was repeated one more time. After washing with hexanes, the brown-yellow product was dissolved in Et_2O, the solution was filtered through Celite, and set to crystallize at -35 ºC. Large, black icosahedra formed after 48 h. The mother liquor was decanted and the crystals were dried. Further recrystallization attempts were unsuccessful due to the compound's insolubility in organic solvents. Yield (based on **$[Li(OEt_2)_2]_2[NN^{py}]$**): 49% (169 mg, 0.147 mmol). *Note: The yields of the following compounds were calculated with respect to their proligands.*

Synthesis of (NN^{py})U(CH_2Ph)$_2$. In a 20-mL scintillation vial, $UI_3(THF)_4$ (0.6262 g, 0.691 mmol) was dissolved in 6 mL of THF and cooled to -78 °C for 1 h. KCH_2Ph (0.2700 g, 2.074 mmol) was added to the cold dark-purple solution and stirred until it warmed to room temperature. A cold diethyl ether solution of H_2NN^{py} (0.2360 g, 0.518 mmol) was added the reaction mixture, which was then allowed to stir at room temperature for 3 h. The final mixture was filtered through Celite, washed with toluene, and dried. The product was extracted into toluene, the solution was filtered through Celite and dried; the extraction was repeated one more time. After washing with hexanes, the product was extracted into diethyl ether, filtered through Celite, and set to crystallize at -35 °C. Large, red needles formed overnight that were recrystallized one more time. Yield: 62% (282 mg, 0.322 mmol).

Synthesis of (NN^{py})UI(CH_2Ph). In a 20-mL scintillation vial, $UI_3(THF)_4$ (0.403 g, 0.444 mmol) was dissolved in approximately 4 mL of THF and cooled to -78 °C for 1 h. KCH_2Ph (0.1290 g, 0.933 mmol) was added to the dark-purple solution and stirred until it warmed to room temperature. A cold diethyl ether solution of H_2NN^{py} (0.1526 g, 0.3330 mmol) was added the final reaction mixture, which was allowed to stir at room temperature for 3 h. The final mixture was filtered through Celite, washed with toluene, and dried. The product was extracted into toluene, the solution was filtered through Celite and dried; the extraction was repeated one more time. After washing with hexanes, the product was extracted into diethyl ether, filtered through Celite, and set to crystallize at -35 °C. Small, pale-orange crystals formed overnight and were recrystallized one more time. Yield: 76% (231 mg, 0.253 mmol).

Synthesis of (NN^{TMS})U(CH_2Ph)$_2$. A THF solution of $UI_3(THF)_4$ (0.5183 g, 0.5720 mmol) was cooled to -78 °C for 1 h and KCH_2Ph (0.2401 g, 1.830 mmol) was added to this slurry. The mixture was allowed to stir at -78 °C for 1 h, at which point a cold diethyl ether solution of H_2NN^{TMS} (0.1547 g, 0.4291 mmol) was added drop wise. After an additional hour of stirring at -

40 °C, the volatiles were removed under reduced pressure and the resulting solid was dissolved in toluene, filtered through Celite, and dried. The dark red solid was extracted into hexanes, filtered through Celite, and set to crystallize at -35 °C. Dark-red needle crystals formed after 1 d. Yield: 77% (257 mg, 0.330 mmol).

Synthesis of $(NN^{TMS})U(CH_2SiMe_3)_2$. A THF solution of $UI_3(THF)_4$ (0.5136 g, 0.5670 mmol) was cooled to -78 °C for 1.5 h and $LiCH_2SiMe_3$ (0.1698 g, 1.814 mmol) was added to this slurry. The mixture was allowed to stir at -78 °C for 1 h, at which point a cold diethyl ether solution of H_2NN^{TMS} (0.1523 g, 0.4250 mmol) was added drop wise. After an additional hour of stirring at -40 °C, the volatiles were removed under reduced pressure and the resulting solid was dissolved in toluene, filtered through Celite, and dried. The yellow-brown solid was washed with hexanes, extracted into diethyl ether, filtered through Celite, and set to crystallize at -35 °C. Large, brown, hexagonal crystals formed after 2 d. Yield: 80% (262 mg, 0.340 mmol).

Synthesis of $(NN^{TBS})U(CH_2SiMe_3)_2$. A THF solution of $UI_3(THF)_4$ (0.2110 g, 0.2328 mmol) was cooled to -78 °C for 1.5 h and $LiCH_2SiMe_3$ (0.0695 g, 0.7450 mmol) was added to this slurry. The mixture was allowed to stir at -78 °C for 1 h, at which point a cold diethyl ether solution of H_2NN^{TBS} (0.0776 g, 0.1746 mmol) was added dropwise. After an additional hour of stirring at -40 °C, the volatiles were removed under reduced pressure and the resulting solid was dissolved in toluene, filtered through Celite, and dried. The yellow-brown solid was washed with hexanes, extracted into diethyl ether, filtered through Celite, and set to crystallize at -35 °C. Large, brown, hexagonal crystals formed after 2 d. Yield: 87% (130 mg, 0.152 mmol).

2.4.2 Elemental analysis

$(NN^{py})_2U$
Because of its limited solubility, **$(NN^{py})_2U$** could not be obtained analytically pure.

$(NN^{py})U(CH_2Ph)_2$
$C_{45}H_{55}N_3U$, 876 g/mol
Calculated: 61.70 %C, 6.33 %H, 4.80 %N
Found: 61.89 %C, 6.15 %H, 4.79 %N

$(NN^{py})UI(CH_2Ph)$
$C_{38}H_{48}IN_3U$, 911 g/mol
Calculated: 50.06 %C, 5.31 %H, 4.61 %N
Found: 50.96 %C, 5.42 %H, 4.27 %N

$(NN^{TMS})U(CH_2Ph)_2$
$C_{30}H_{40}FeN_2Si_2U$, 779 g/mol
Calculated: 46.27 %C, 5.18 %H, 3.60 %N
Found: 45.92 %C, 5.19 %H, 3.50 %N

$(NN^{TMS}U)$ $(CH_2SiMe_3)_2$
$C_{24}H_{48}FeN_2Si_4U$, 771 g/mol
Calculated: 37.39 %C, 6.28 %H, 3.63 %H
Found: 37.28 %C, 6.10 %H, 3.16 %N

$(NN^{TBS})U(CH_2SiMe_3)_2$
$C_{30}H_{60}FeN_2Si_4U$, 855 g/mol
Calculated: 42.14 %C, 7.07 %H, 3.28 %N
Found: 42.22 %C, 6.92 %H, 3.16 %N

2.4.3 ^{1}H NMR spectroscopy

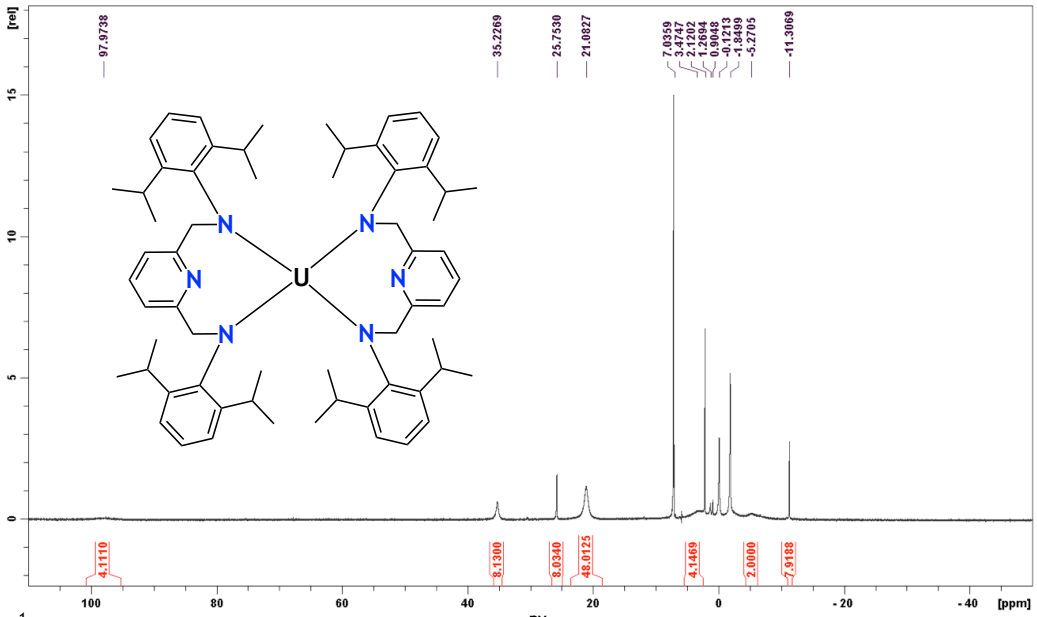

Figure B1. ^{1}H NMR spectrum (300 MHz, 25 °C, C_6D_6) of **$(NN^{py})_2U$**; δ (ppm): 97.97 (s, 2H, aromatic-C*H*), 35.22 (s, 4H, aromatic-C*H*, NCH_2, or C*H*$(CH_3)_2$), 25.57 (s, 4H, aromatic-C*H*, NCH_2, or C*H*$(CH_3)_2$), 21.53 (s, 24H, CH$(CH_3)_2$), 3.47 (s, 2H, aromatic-C*H*), -5.27 (s, 1H, C_5H_3N), -11.30 (s, 4H, aromatic-C*H*, NCH_2, or C*H*$(CH_3)_2$).

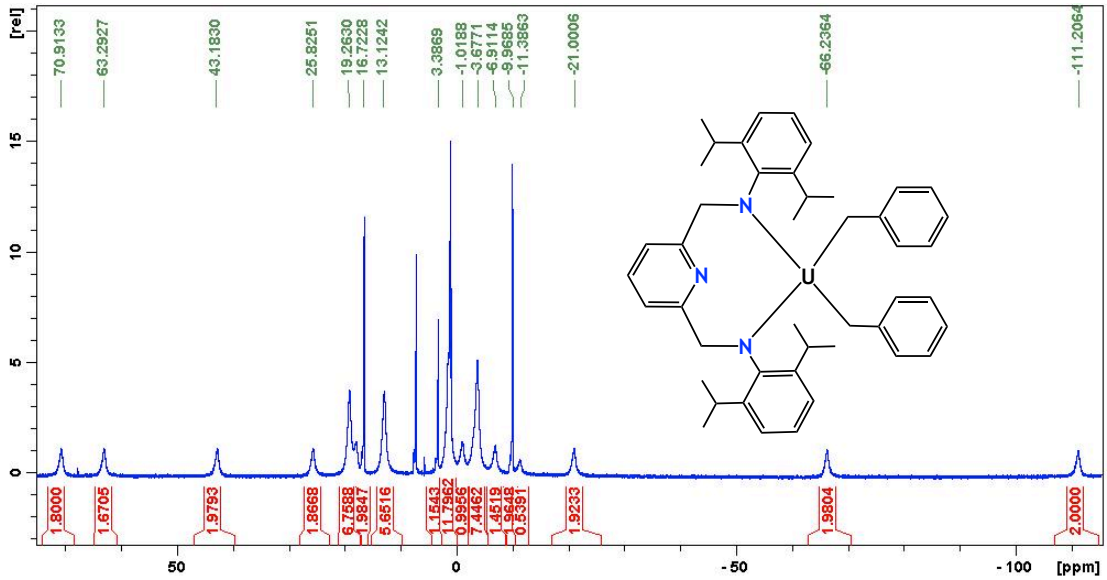

Figure B2. ^{1}H NMR (500 MHz, C_6D_6) of **$(NN^{py})U(CH_2Ph)_2$**; δ (ppm): 70.91 (s, 2H, aromatic-C*H* or CH_2), 63.29 (s, 2H, aromatic-C*H* or CH_2), 43.18 (s, 2H, aromatic-C*H* or CH_2), 25.82 (s, 2H, aromatic-C*H* or CH_2), 19.26 (s, 6H, CH$(CH_3)_2$), 16.72 (s, 2H, aromatic-C*H* or CH_2), 13.12 (s, 6H, CH$(CH_3)_2$), 3.38 (s, 6H, CH$(CH_3)_2$), 1.34 (s, 2H, aromatic-C*H* or CH_2), -3.67 (s, 6H, CH$(CH_3)_2$), -6.91 (s, 2H, aromatic-C*H* or CH_2), -9.97 (s, 2H, aromatic-C*H* or CH_2), -11.38 (s, 1H, *p*-NC_5H_3 or *p*-C_6H_5), -21.00 (s, 2H, aromatic-C*H* or CH_2), -66.24 (s, 2H, aromatic-C*H* or CH_2), -111.21 (s, 2H, aromatic-C*H* or CH_2). *Note: U–CH_2 protons are likely not observed.*

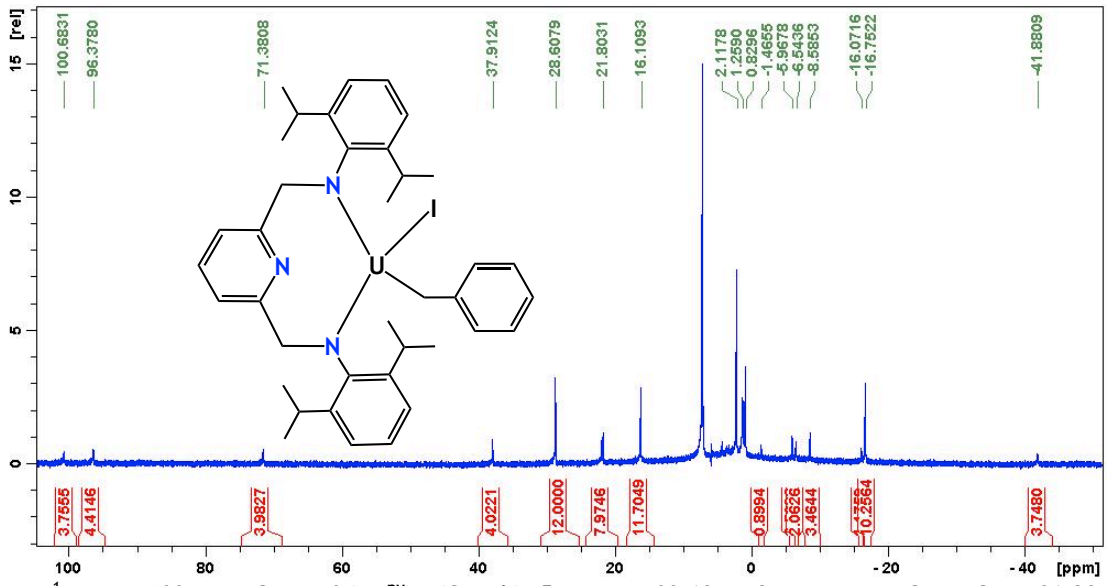

Figure B3. ^{1}H NMR (500 MHz, C_6D_6) of **(NN^{py})UI(CH_2Ph)**; δ (ppm): 100.68 (s, 2H, aromatic-C*H* or CH_2), 96.38 (s, 2H, aromatic-C*H* or CH_2), 71.58 (s, 2H, aromatic-C*H* or CH_2), 37.91 (s, 2H, aromatic-C*H* or CH_2), 28.61 (s, 6H, CH(CH_3)$_2$), 21.92 (s, 1H, *p*-NC$_5$*H*$_3$, *p*-C$_6$*H*$_3$, or *p*-C$_6$*H*$_5$), 21.68 (s, 1H, *p*-NC$_5$*H*$_3$, *p*-C$_6$*H*$_3$, or *p*-C$_6$*H*$_5$), 16.17 (s, 6H, CH(CH_3)$_2$), 1.38 (s, 2H, aromatic-C*H* or CH_2), 0.79 (s, 6H, CH(CH_3)$_2$), -1.54 (s, 1H, *p*-NC$_5$*H*$_3$, *p*-C$_6$*H*$_3$, or *p*-C$_6$*H*$_5$), -5.98 (s, 2H, aromatic-C*H* or CH_2), -6.54 (s, 2H, aromatic-C*H* or CH_2), -8.58 (s, 2H, aromatic-C*H* or CH_2), -16.13 (s, 1H, *p*-NC$_5$*H*$_3$, *p*-C$_6$*H*$_3$, or *p*-C$_6$*H*$_5$), -16.76 (s, 6H, CH(CH_3)$_2$), -41.88 (s, 2H, aromatic-C*H* or CH_2).

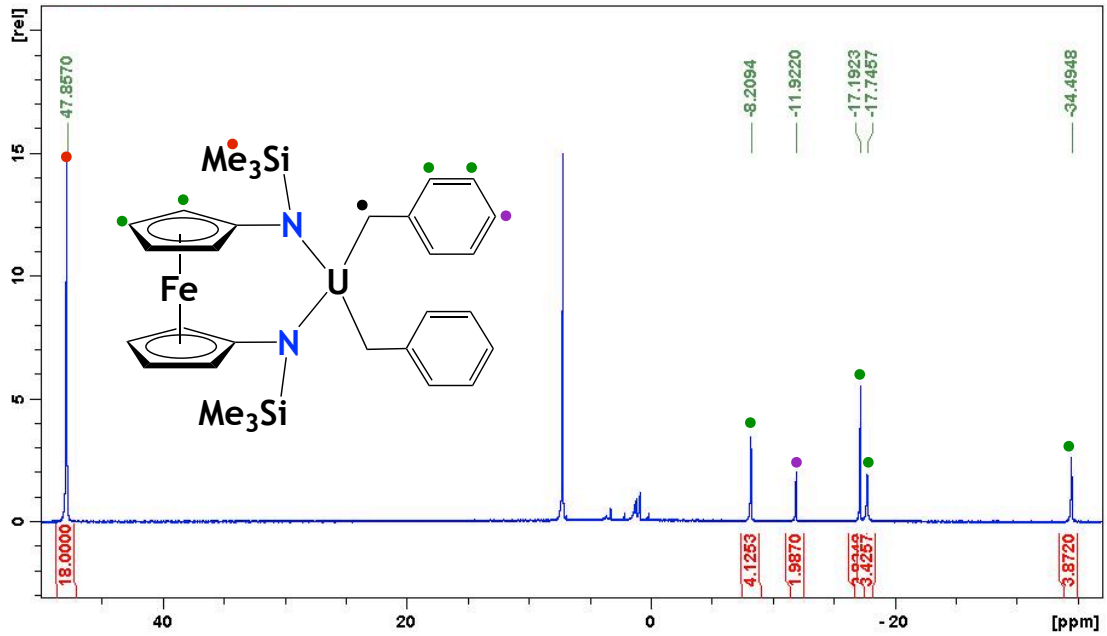

Figure B4. ^{1}H NMR (300 MHz, C_6D_6) of **(NN^{TMS})U(CH_2Ph)$_2$**; δ (ppm): 47.86 (s, 18H, Si(CH_3)$_3$), -8.21 (s, 4H, C$_5$*H*$_4$ or C$_6$*H*$_5$), -11.92 (s, 2H, *p*-C$_6$*H*$_5$), -17.19 (s, 4H, C$_5$*H*$_4$ or C$_6$*H*$_5$), -17.75 (s, 4H, C$_5$*H*$_4$ or C$_6$*H*$_5$), -34.49 (s, 4H, C$_5$*H*$_4$ or C$_6$*H*$_5$). *Note: U–CH_2 protons (black dot) are likely not observed.*

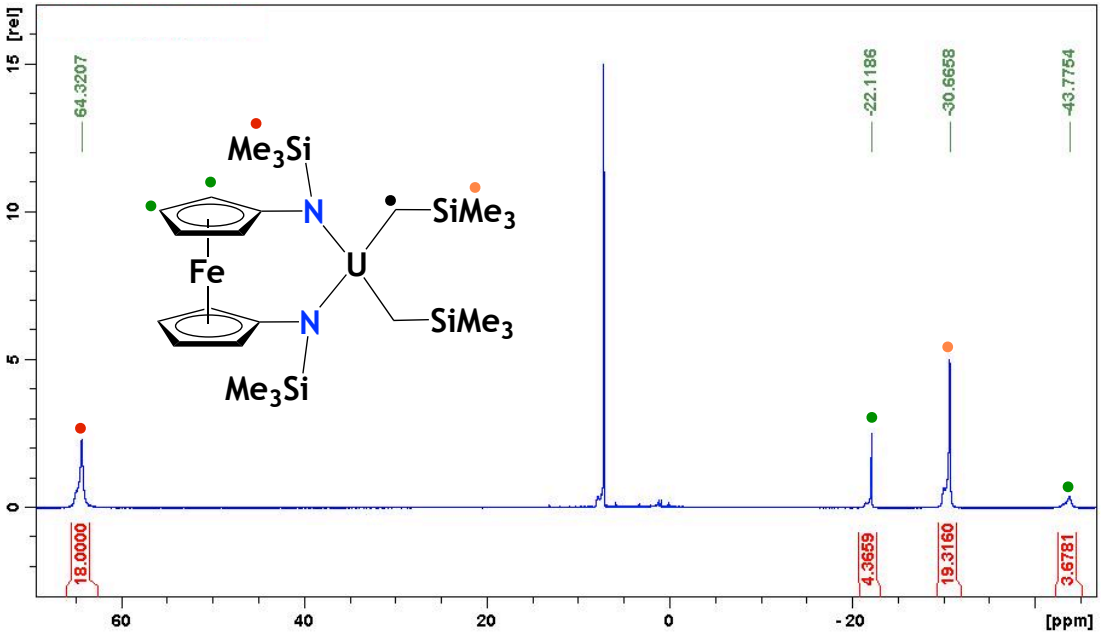

Figure B5. ^{1}H NMR (300 MHz, C_6D_6) of **(NN^{TMS})U(CH$_2$SiMe$_3$)$_2$**; δ (ppm): 64.04 (s, 18H, SiC(CH_3)$_3$), -21.84 (s, 4H, C_5H_4), -30.40 (s, 18H, Si(CH_3)$_3$), -43.38 (s, 4H, C_5H_4). *Note: U–CH_2 protons (black dot) are likely not observed.*

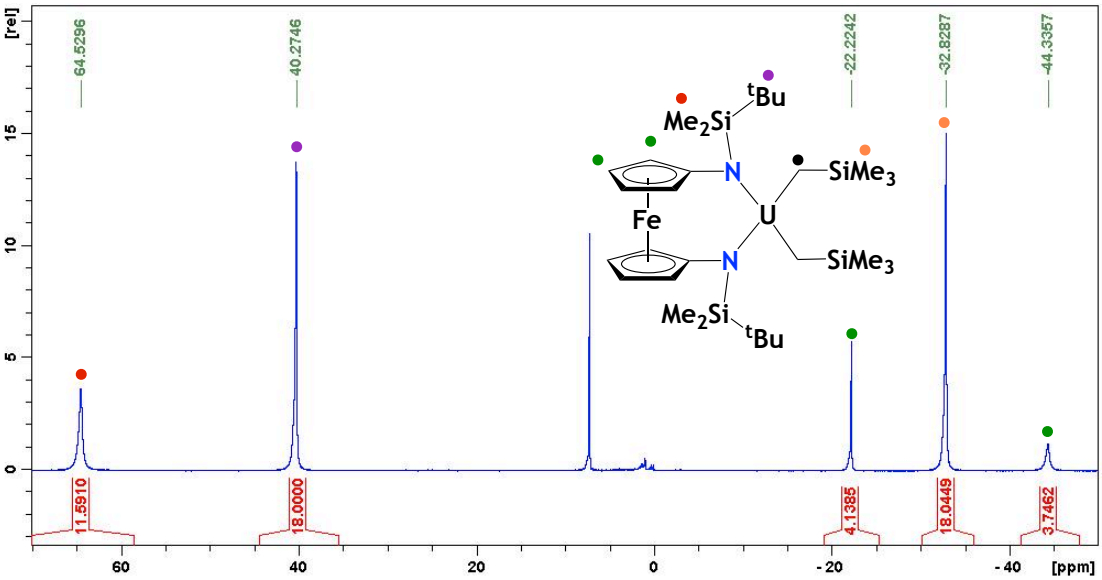

Figure B6. ^{1}H NMR (300 MHz, C_6D_6) of **(NN^{TBS})U(CH$_2$SiMe$_3$)$_2$**; δ (ppm): 64.53 (s, 12H, Si(CH_3)$_2$), 40.27 (s, 18H, SiC(CH_3)$_3$), -22.22 (s, 4H, C_5H_4), -32.83 (s, 18H, Si(CH_3)$_3$), -44.34 (s, 4H, C_5H_4). *Note: U–CH_2 protons (black dot) are likely not observed.*

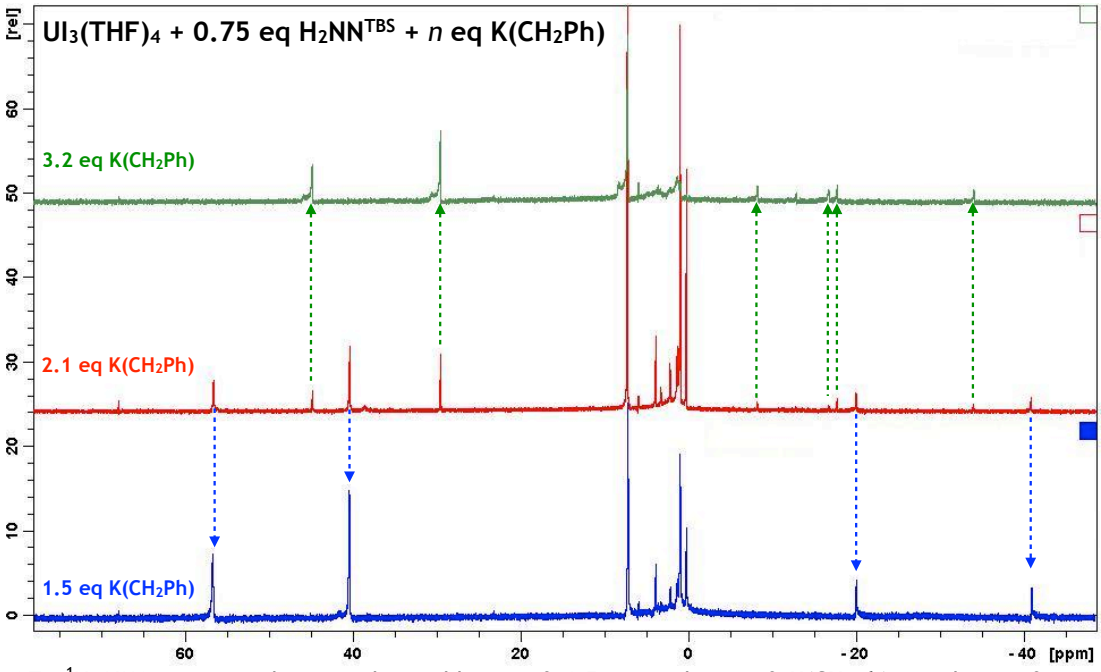

Figure B7. ^{1}H NMR spectra showing that addition of 1.5 equivalents of **K(CH$_2$Ph)** results in formation of **(NN^{TBS})UI$_2$(THF)** and 3.2 equivalents of it results in **(NN^{TBS})U(CH$_2$Ph)$_2$**. More importantly, no formation of **(NN^{TBS})UI(CH$_2$Ph)** is observed upon addition of 2.1 equivalents of **K(CH$_2$Ph)**; instead, a mixture of **(NN^{TBS})UI$_2$(THF)** and **(NN^{TBS})U(CH$_2$Ph)$_2$** is apparent.

2.4.4. Crystal structures

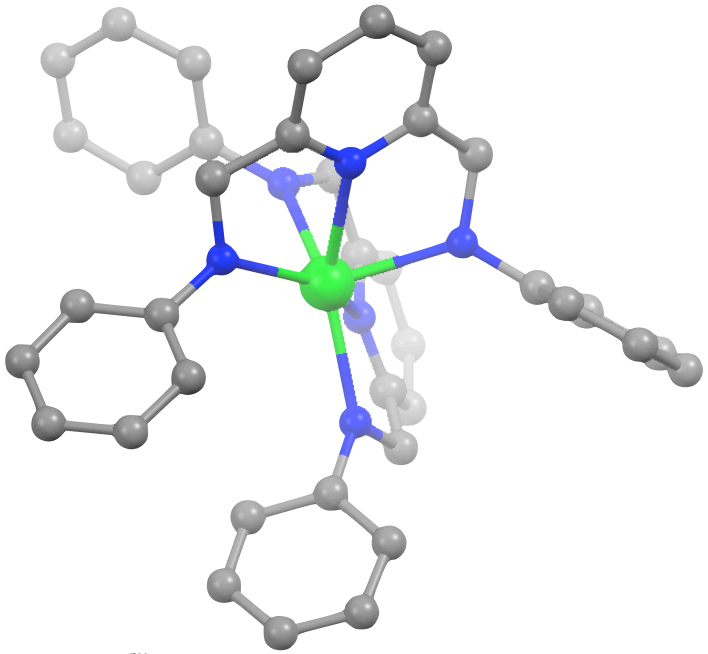

Figure B8. Crystal data for **(NN^{py})$_2$U** (hydrogen and solvent atoms were omitted for clarity), formula $C_{62}H_{82}N_6U{\cdot}0.8(C_6H_{14})$, monoclinic, space group *C*2/c, *a* = 19.828(2) Å, *b* = 22.158(2) Å, *c* = 14.7466(16) Å, β = 108.964(1)°, V = 6127.3(11) Å^3, Z = 4, μ = 2.693 mm^{-1}, F(000) = 2496, *T* = 100(2) K, 30847 measured reflections, 9054 unique (R_{int} = 0.0281), R_1 = 0.0255, wR_2 = 0.0651 for $I > 2s(I)$.

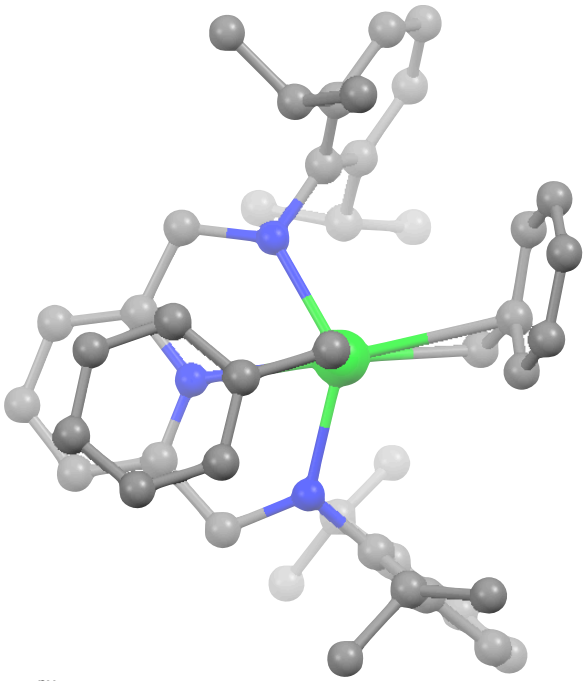

Figure B9. Crystal data for **(NN^{py})U(CH$_2$Ph)$_2$** (hydrogen and solvent atoms were omitted for clarity), formula $C_{45}H_{55}N_3U{\cdot}OC_4H_{10}$, triclinic, space group $P\bar{1}$, a = 10.5281(10) Å, b = 12.7043(12) Å, c = 17.9213(16) Å, β = 105.205(1)°, V = 2213.0(4) Å^3, Z = 2, μ = 3.705 mm^{-1}, F(000) = 960, T = 100(2) K, 22255 measured reflections, 12383 unique (R_{int} = 0.0196), R_1 = 0.0313, wR_2 = 0.0806 for $I > 2s(I)$.

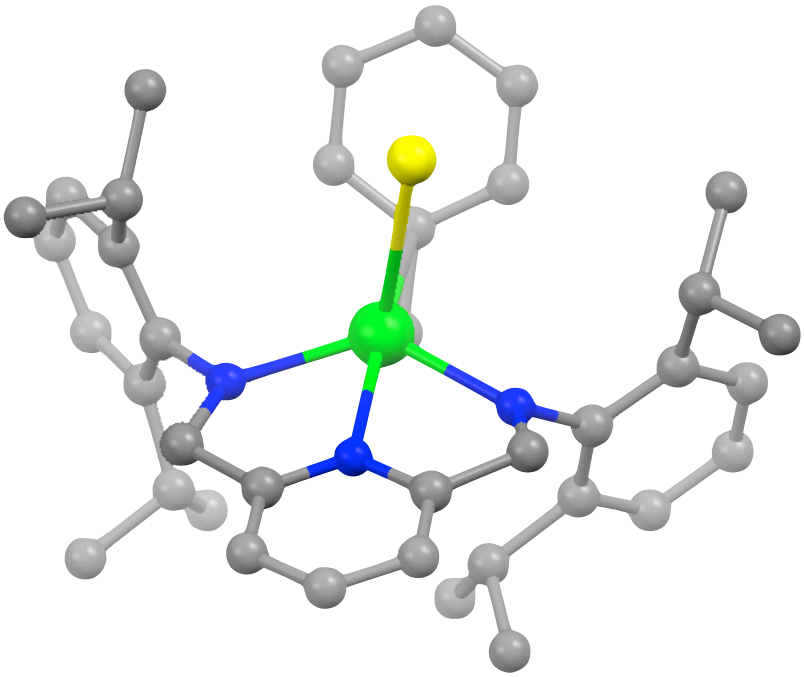

Figure B10. Crystal data for **(NN^{py})UI(CH$_2$Ph)** (hydrogen and solvent atoms were omitted for clarity), formula $C_{38}H_{48}N_3IU{\cdot}C_7H_5$, monoclinic, space group $P2_1/c$, a = 11.3927(15), b = 13.9847(19), c = 25.077(3), β = 95.235(2)°, V = 3978.7(9) Å^3, Z = 4, μ = 4.890 mm^{-1}, F(000) = 1956, T = 100(2) K, 26600 measured reflections, 6513 unique (R_{int} = 0.0829), R_1 = 0.0397, wR_2 = 0.0769 for $I > 2s(I)$.

2.5 REFERENCES

1. Diaconescu, P. L.; Arnold, P. L.; Baker, T. A.; Mindiola, D. J.; Cummins, C. C., Arene-Bridged Diuranium Complexes: Inverted Sandwiches Supported by δ-Backbonding. *J. Am. Chem. Soc.* **2000,** 122, (25), 6108-6109.

2. Diaconescu, P. L.; Cummins, C. C., Diuranium Inverted Sandwiches Involving Naphthalene and Cyclooctatetraene. *J. Am. Chem. Soc.* **2002,** 124, (26), 7660-7661.

3. Castro-Rodriguez, I.; Nakai, H.; Gantzel, P.; Zakharov, L. N.; Rheingold, A. L.; Meyer, K., Evidence for Alkane Coordination to an Electron-Rich Uranium Center. *J. Am. Chem. Soc.* **2003,** 125, (51), 15734-15735.

4. Lam, O. P.; Anthon, C.; Meyer, K., Influence of Steric Pressure on the Activation of Carbon Dioxide and Related Small Molecules by Uranium Coordination Complexes. *Dalton Transactions* **2009**, (44), 9677-9691.

5. Cantat, T.; Scott, B. L.; Morris, D. E.; Kiplinger, J. L., What a Difference a 5f Element Makes: Trivalent and Tetravalent Uranium Halide Complexes Supported by One and Two Bis[2-(diisopropylphosphino)-4-methylphenyl]amido (PNP) Ligands. *Inorg. Chem.* **2009,** 48, (5), 2114-2127.

6. Cantat, T.; Graves, C. R.; Scott, B. L.; Kiplinger, J. L., Challenging the Metallocene Dominance in Actinide Chemistry with a Soft PNP Pincer Ligand: New Uranium Structures and Reactivity Patterns. *Angew. Chem. Int. Ed.* **2009,** 48, (20), 3681-3684.

7. Summerscales, O. T.; Cloke, F. G. N.; Hitchcock, P. B.; Green, J. C.; Hazari, N., Reductive Cyclotetramerization of CO to Squarate by a U(III) Complex: The X-ray Crystal Structure of $[(U(\eta\text{-}C_8H_6\{Si^iPr3\text{-}1,4\}_2)(\eta\text{-}C_5Me_4H)]_2(\mu\text{-}\eta^2\text{:}\ \eta^2\text{-}C_4O_4)$. *J. Am. Chem. Soc.* **2006,** 128, (30), 9602-9603.

8. Arnold, P. L.; Patel, D.; Wilson, C.; Love, J. B., Reduction and Selective Oxo Group Silylation of the Uranyl Dication. *Nature* **2008,** 451, (7176), 315-317.

9. Evans, W. J.; Kozimor, S. A.; Ziller, J. W., Molecular Octa-Uranium Rings with Alternating Nitride and Azide Bridges. *Science* **2005,** 309, (5742), 1835-1838.

10. Monreal, M. J.; Khan, S.; Diaconescu, P. L., Beyond C-H Activation with Uranium: A Cascade of Reactions Mediated by a Uranium Dialkyl Complex. *Angew. Chem. Int. Ed.* **2009,** 48, (44), 8352-8355.

11. Carver, C. T.; Williams, B. N.; Ogilby, K. R.; Diaconescu, P. L., Coupling of Aromatic N-Heterocycles Mediated by Group 3 Complexes. *Organometallics* **2010,** 29, (4), 835–846.

12. Cruz, C. A.; Emslie, D. J. H.; Harrington, L. E.; Britten, J. F.; Robertson, C. M., Extremely Stable Thorium(IV) Dialkyl Complexes Supported by Rigid Tridentate 4,5-Bis(anilido)xanthene and 2,6-Bis(anilidomethyl)pyridine Ligands. *Organometallics* **2007,** 26, (3), 692-701.

13. Guérin, F.; McConville, D. H.; Payne, N. C., Conformationally Rigid Diamide Complexes: Synthesis and Structure of Titanium(IV) Alkyl Derivatives. *Organometallics* **1996,** 15, (24), 5085-5089.

14. Guérin, F.; McConville, D. H.; Vittal, J. J., Synthesis, Structure, and Reactivity of Titanacyclopentadiene Complexes Bearing Ancillary Pyridine Diamide Ligands. *Organometallics* **1997,** 16, (7), 1491-1496.

15. Kang, K. K.; Hong, S.-P.; Jeong, Y.-T.; Shiono, T.; Ikeda, T., The Synthesis and Polymerization Behavior of Bimetallic Pyridine Diamide Complexes Containing Transition Metal (Ti, Zr). *J. Polym. Sci., Part A: Polym. Chem.* **1999,** 37, (20), 3756-3762.

16. Guérin, F.; Del Vecchio, O.; McConville, D. H., Ortho-Substituted Aryl Diamido Complexes of Zirconium: Observation of Rotameric Isomers. *Polyhedron* **1998,** 17, (5-6), 917-923.

17. Guérin, F.; McConville, D. H.; Vittal, J. J., Conformationally Rigid Diamide Complexes of Zirconium: Electron Deficient Analogues of Cp_2Zr. *Organometallics* **1996,** 15, (26), 5586-5590.

18. Guérin, F.; McConville, D. H.; Vittal, J. J.; Yap, G. A. P., Synthesis, Structure, and Reactivity of Zirconium Alkyl Complexes Bearing Ancillary Pyridine Diamide Ligands. *Organometallics* **1998,** 17, (23), 5172-5177.

19. Ziniuk, Z.; Goldberg, I.; Kol, M., Zirconium Complexes of Chelating Dianionic Bis(Pentafluorophenylamido) Ligands: Synthesis, Structure and Ethylene Polymerisation Activity. *Inorg. Chem. Commun.* **1999,** 2, (11), 549-551.

20. Guerin, F.; McConville, D. H.; Vittal, J. J., Conformationally Rigid Diamide Complexes: Synthesis and Structure of Tantalum(III) Alkyne Derivatives. *Organometallics* **1995,** 14, (7), 3154-3156.

21. Guérin, F.; McConville, D. H.; Vittal, J. J.; Yap, G. A. P., Successive Insertion of Alkynes into a Tantalum-Alkynyl Bond: Implications for the Coordination Polymerization of Alkynes. *Organometallics* **1998,** 17, (7), 1290-1296.

22. Zimmermann, M.; Estler, F.; Herdtweck, E.; Törnroos, K. W.; Anwander, R., Distinct C-H Bond Activation Pathways in Diamido-Pyridine-Supported Rare-Earth Metal Hydrocarbyl Complexes. *Organometallics* **2007,** 26, (24), 6029-6041.

23. Zimmermann, M.; Törnroos, K. W.; Waymouth, R. M.; Anwander, R., Structure-Reactivity Relationships of Amido-Pyridine-Supported Rare-Earth-Metal Alkyl Complexes. *Organometallics* **2008,** 27, (17), 4310-4317.

24. Estler, F.; Eickerling, G.; Herdtweck, E.; Anwander, R., Organo-Rare-Earth Complexes Supported by Chelating Diamide Ligands. *Organometallics* **2003,** 22, (6), 1212-1222.

25. Cruz, C. A.; Emslie, D. J. H.; Robertson, C. M.; Harrington, L. E.; Jenkins, H. A.; Britten, J. F., Cationic Thorium Alkyl Complexes of Rigid NON- and NNN-Donor Ligands: π-Arene Coordination as a Persistent Structural Motif. *Organometallics* **2009,** 28, (6), 1891-1899.

26. Avens, L. R.; Bott, S. G.; Clark, D. L.; Sattelberger, A. P.; Watkin, J. G.; Zwick, B. D., A Convenient Entry into Trivalent Actinide Chemistry: Synthesis and Characterization of $AnI_3(THF)_4$ and $An[N(SiMe_3)_2]_3$ (An = U, Np, Pu). *Inorg. Chem.* **1994,** 33, (10), 2248-2256.

27. Clark, D. L.; Sattelberger, A. P.; Andersen, R. A., Lewis Base Adducts of Uranium Triiodide and Tris[Bis(Trimethylsilyl)Amido]Uranium. In *Inorg. Synth.*, John Wiley & Sons, Inc.: 2007; pp 307-315.

28. Clark, D. L.; Sattelberger, A. P.; Bott, S. G.; Vrtis, R. N., Lewis Base Adducts of Uranium Triiodide: A New Class of Synthetically Useful Precursors for Trivalent Uranium Chemistry. *Inorg. Chem.* **1989,** 28, (10), 1771-1773.

29. Monreal, M. J.; Diaconescu, P. L., A Weak Interaction between Iron and Uranium in Uranium Alkyl Complexes Supported by Ferrocene Diamide Ligands. *Organometallics* **2008,** 27, (8), 1702-1706.

30. Carver, C. T.; Monreal, M. J.; Diaconescu, P. L., Scandium Alkyl Complexes Supported by a Ferrocene Diamide Ligand. *Organometallics* **2008,** 27, (3), 363-370.

31. Fortier, S.; Melot, B. C.; Wu, G.; Hayton, T. W., Homoleptic Uranium(IV) Alkyl Complexes: Synthesis and Characterization. *J. Am. Chem. Soc.* **2009,** 131, (42), 15512-15521.

32. Pangborn, A. B.; Giardello, M. A.; Grubbs, R. H.; Rosen, R. K.; Timmers, F. J., Safe and Convenient Procedure for Solvent Purification. *Organometallics* **1996,** 15, (5), 1518-1520.

33. Schrock, R. R.; Fellmann, J. D., Multiple Metal-Carbon Bonds. 8. Preparation, Characterization, and Mechanism of Formation of the Tantalum and Niobium Neopentylidene Complexes, $M(CH_2CMe_3)_3(CHCMe_3)$. *J. Am. Chem. Soc.* **1978,** 100, (11), 3359-3370.

34. Monreal, M. J.; Carver, C. T.; Diaconescu, P. L., Redox Processes in a Uranium Bis(1,1'-diamidoferrocene) Complex. *Inorg. Chem.* **2007,** 46, (18), 7226-7228.

35. Shafir, A.; Power, M. P.; Whitener, G. D.; Arnold, J., Silylated 1,1'-Diaminoferrocene: Ti and Zr Complexes of a New Chelating Diamide Ligand. *Organometallics* **2001,** 20, (7), 1365-1369.

36. Bailey, P. J.; Coxall, R. A.; Dick, C. M.; Fabre, S.; Henderson, L. C.; Herber, C.; Liddle, S. T.; Lorono-Gonzalez, D.; Parkin, A.; Parsons, S., The First Structural Characterisation of a Group 2 Metal Alkylperoxide Complex: Comments on the Cleavage of Dioxygen by Magnesium Alkyl Complexes. *Chem. Eur. J.* **2003,** 9, (19), 4820-4828.

37. Baker, R. T.; Calabrese, J. C.; Glassman, T. E., Unsaturated, PCy_2-Bridged Re-M Heterobimetallics (M = rhodium, iridium, palladium; Cy = cyclohexyl): Metal-Metal Bond Isomerism, Reversible Phosphorus-Hydrogen Bond Activation and Cooperative Reactivity. *Organometallics* **1988,** 7, (8), 1889-1891.

CHAPTER 3

Reactions of Aromatic Heterocycles with Uranium Alkyl Complexes

TABLE OF CONTENTS

3.1 INTRODUCTION

Since the 1950s, activation of strong, localized bonds, particularly C–H, C–N, and C–O, by transition metals has been studied intensively.[1, 2] In the last two decades, the reactivity of f-block elements has been increasingly studied because of the unique chemical behavior of their complexes and potential to catalyze a wide range of transformations.[3-6] Our group has been interested in the reactivity of metal–carbon bonds toward aromatic heterocycles because these substrates are relevant to hydrodenitrogenation processes and are important components of natural products and pharmaceuticals.[2, 7-10] Complexes with d^0f^n metal–carbon bonds show diverse reactivity toward aromatic heterocycles, from functionalization to ring opening.[2, 7, 11] Early transition metal, lanthanide, and actinide alkyl or hydride complexes often react with these substrates to produce ortho-metalated complexes that show subsequent reactivity.[2, 12-24] Although less commonly, alkyl ligands of d^0f^n metal complexes will undergo a 1,3-alkyl migration when they are transferred to the coordinated aromatic N-heterocycle.[25-27]

Scheme 3.1. Reactions of 1-methylimidazole mediated by **1-$(CH_2Ph)_2$**.

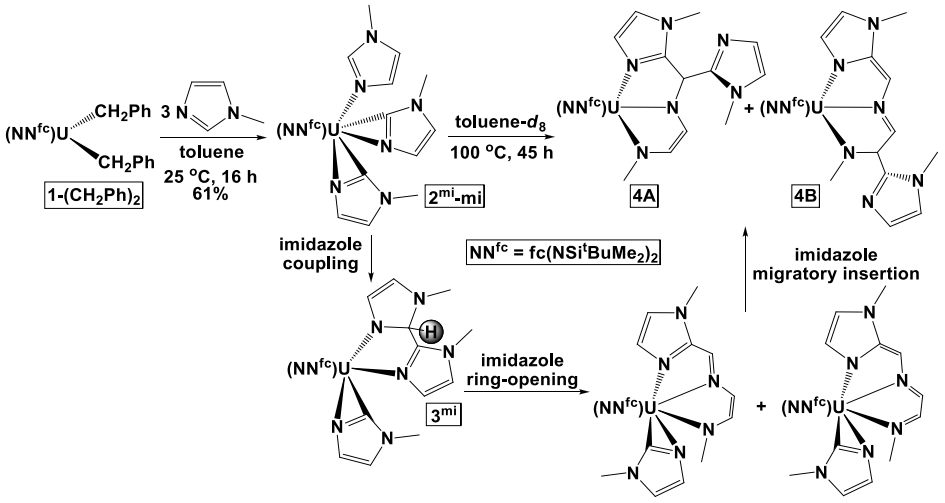

We have been investigating the reactivity of group 3[27-30] and uranium dialkyl[31] complexes supported by a 1,1'-ferrocenylene-diamide ligand[32-34] toward aromatic N-heterocycles.[29, 35-38] In particular, the uranium dibenzyl reactivity has held our attention since **$(NN^{fc})U(CH_2Ph)_2$**, **1-$(CH_2Ph)_2$** (**NN^{fc}** = $fc(NSi^tBuMe_2)_2$, fc = 1,1'-ferrocenylene),[31] has two alkyl groups that can both engage in reactions with the same substrate. For example, we recently reported a novel C−H activation by **1-$(CH_2Ph)_2$** showing that both benzyl ligands react with an sp^2-C–H bond of 1-methylimidazole (mi) to give **2^{mi}-mi (Scheme 3.1)**.[35, 39] In addition to this double C−H activation, an interesting cascade of functionalization reactions could be thermally induced. Specifically, upon heating, **2^{mi}-mi** underwent C–C coupling to give **3^{mi}** and ring opening followed by the migratory insertion of imidazolyl ligands, ultimately leading to an isomeric mixture of **4A** and **4B (Scheme 3.1)**.[35] This cascade of reactions represents the first example of aromatic N-heterocycle cleavage by actinide complexes where no oxygen atoms[40] or redox processes[41] are involved. We decided to investigate the generality of this reactivity behavior; herein, we report the reactions of **1-$(CH_2Ph)_2$** with other aromatic heterocycles. Substrates analogous to imidazole, such as benzoxazole and benzothiazole, as well as pyridine substrates were studied.

3.2 DISCUSSION OF RESULTS

Reactions between **1-$(CH_2Ph)_2$** and one equivalent of pyridine or picoline (Scheme 2) led to the corresponding ortho-metalated products ($(NN^{fc})U(CH_2Ph)(\eta^2$-N,C-pyridyl), **$5^{py}$**, or $(NN^{fc})U(CH_2Ph)$(6-Me-η^2-N,C-pyridyl), **5^{pic}**), with one benzyl group engaging in C−H activation. These reactions are analogous to the formation of the imidazolyl complexes $(NN^{fc})U(CH_2Ph)(\eta^2$-N,C-1-methylimidazolyl), **5^{mi}**, and $(NN^{fc})U(CH_2Ph)(\eta^2$-N,C-1-methylbenzimidazolyl), **5^{mbi}**, from **1-$(CH_2Ph)_2$** and one equivalent of 1-methylimidazole (**mi**) or 1-methylbenzimidazole (**mbi**), respectively.[39] Similar observations were made by the Kiplinger group when starting from $Cp^*_2AnR_2$ (An = Th, U; R = Ph, CH_2Ph)[18, 20, 21] and by Dormond et al.[15] and the Scott group[13] using cyclometalated-amide thorium and/or uranium complexes and pyridine substrates. The reaction of **1-$(CH_2Ph)_2$** with pyridine was three times faster than the analogous reaction of $Cp^*_2UMe_2$.[21]

Scheme 3.2. Reactions of **1-$(CH_2Ph)_2$** with pyridine and 2-picoline.

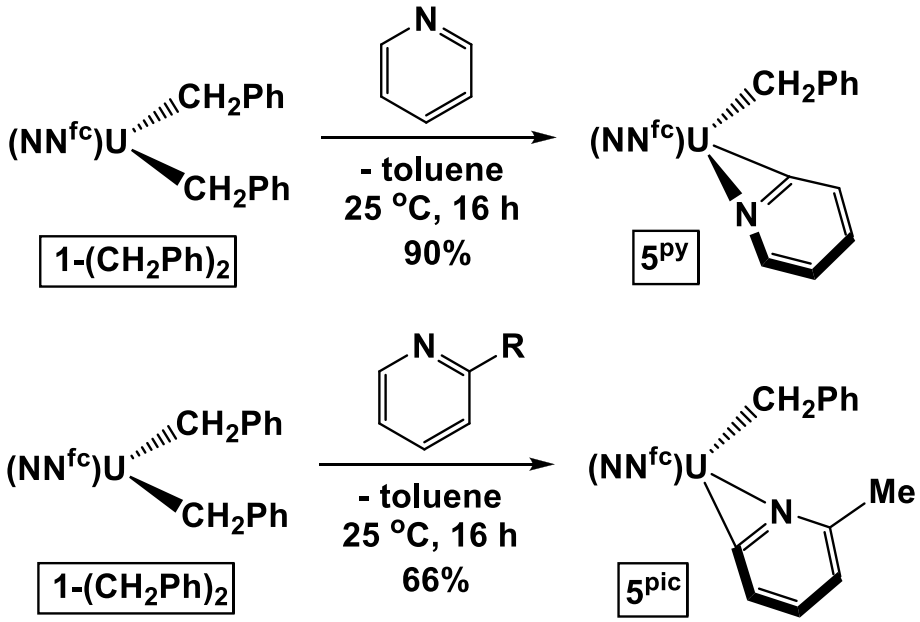

Although two isomers are possible for the pyridyl complexes **5^{py}** and **5^{pic}**, only one was observed. For **5^{pic}**, the isomer featuring the methyl group and the nitrogen donor of the

picolyl ligand pointing toward the benzyl ligand is analogous to the isomer reported by the Kiplinger group for the metallocene complex.[20] However, the other isomer was isolated for **5**^{py} (**Figure 3.1**).

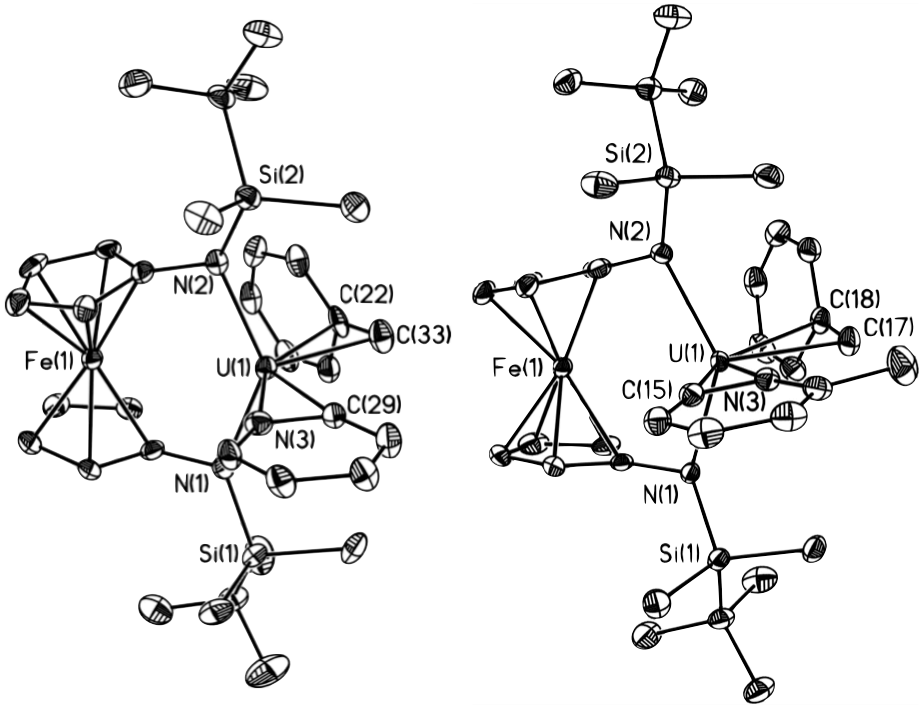

Figure 3.1. Thermal-ellipsoid (50% probability) representation of **5**^{py} (left) and **5**^{pic} (right). Hydrogen atoms were removed for clarity.

The solid-state structures of the newly synthesized η^2-N,C-pyridyl complexes are not unusual and compare well to those of analogous uranium complexes. For example, the U–N_{py} distances of 2.3700(40) Å in **5**^{py} and 2.3932(25) Å in **5**^{pic}, although relatively short, are in the range exhibited by other pyridyl complexes. A similar situation is encountered for the U–C_{py} distances of 2.4059(46) Å in **5**^{py} and 2.3967(30) Å in **5**^{pic}.[13, 20, 21, 39] The X-ray crystal structures also reveal an η^2-coordination of the benzyl ligands with U–C distances of 2.5076(52) Å (U–C33) and 2.8433(48) Å (U–C22) in **5**^{py} and 2.5215(30) Å (U–C17) and 2.8558(30) Å (U–C18) in **5**^{pic} and UCC angles of 87.60(30)° in **5**^{py} and 87.52(18)° in **5**^{pic}.

The reaction between **5**^{het} (**het** = pyridyl, 6-picolyl, 1-methylimidazolyl, and 1-methylbenzimidazolyl) and excess pyridine produced mixtures that proved intractable. We

also observed the formation of complex mixtures when the reactions of group 3 alkyl complexes and pyridine were conducted. Based on the comparison of the ^{1}H NMR spectra of these reaction mixtures with those of reactions with other aromatic N-heterocycles that led to one major product, we proposed that multiple and competitive pathways occur with pyridine.[27, 29, 36-38] Although such an assertion is difficult to transfer to the case of uranium because of the paramagnetism of the species involved, the reactions described below attest to the possibility that a similar situation is likely for this element as well.

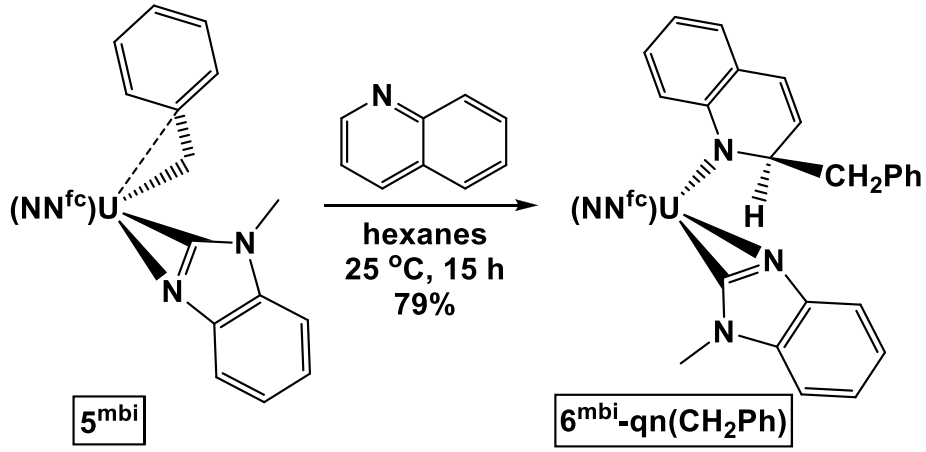

Figure 3.2. Reaction between **5**^{mbi} and quinoline.

The reaction of one of the uranium benzyl complexes, **5**^{mbi}, with quinoline was investigated in order to determine whether this substrate undergoes C–H activation, as observed with a scandium benzyl supported by the same ferrocene-diamide ligand,[29] or alkyl transfer, as observed with isoquinoline and group 3 benzyl complexes.[27] Consequently, when **5**^{mbi} was mixed with quinoline in hexanes at room temperature for 15 hours, no toluene formation was observed (**Figure 3.2**).

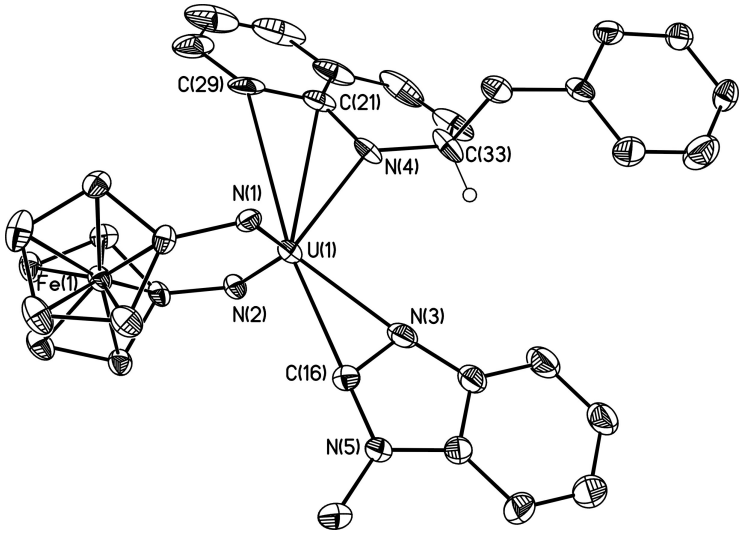

Figure 3.3. Thermal-ellipsoid (35% probability) representation of **6^{mbi}-qn(CH_2Ph)**. Irrelevant hydrogen atoms and silyl groups were removed for clarity.

The isolation and characterization of the major product, **6^{mbi}-qn(CH_2Ph)**, by X-ray crystallography indicated that an alkyl transfer occurred from uranium to the 2-position of quinoline (**Figure 3.3**). Metrical parameters are consistent with the dearomatization of the pyridine ring. For example, the C–C distances are 1.412(14), 1.447(18), 1.333(17), and 1.487(14) Å, with the longest distance to the sp^3-carbon atom. Also, the U–N distance to the dearomatized pyridine ring, 2.3034(64) Å, is only 0.08 Å longer than the U–N distances (2.2196(66) and 2.2342(69) Å) to the ferrocene-diamide ligand. The NCC angles of 113.01(92) and 111.05(73)° and the CCC angle of 110.77(76)° around the sp^3-carbon atom are in agreement with the above structural assignment. The dearomatized quinoline ligand coordinates in an approximate κ^3-NCC fashion, as evidenced by the U–C21 and U–C29 distances 2.9594(88) and 3.0432(91) Å, respectively, which are similar to the distances between uranium and the *ipso*-carbon atoms of the ferrocene-diamide ligand (2.8810(78) and 2.8896(80) Å). The solid-state structure also confirms the presence of the imidazolyl ligand, which retained its η^2-coordination: the U-N_{mbi} distance of 2.4135(82) Å and the U-C_{mbi} distance

of 2.4295(86) Å are similar to the analogous distances of 2.3708(24) and 2.4811(27) Å, respectively, in $\mathbf{5}^{\mathbf{mbi}}$.[39]

Scheme 3.3. Reactions of uranium η^2-N,C-pyridyl complexes with benzoxazole and benzothiazole with proposed mechanism.

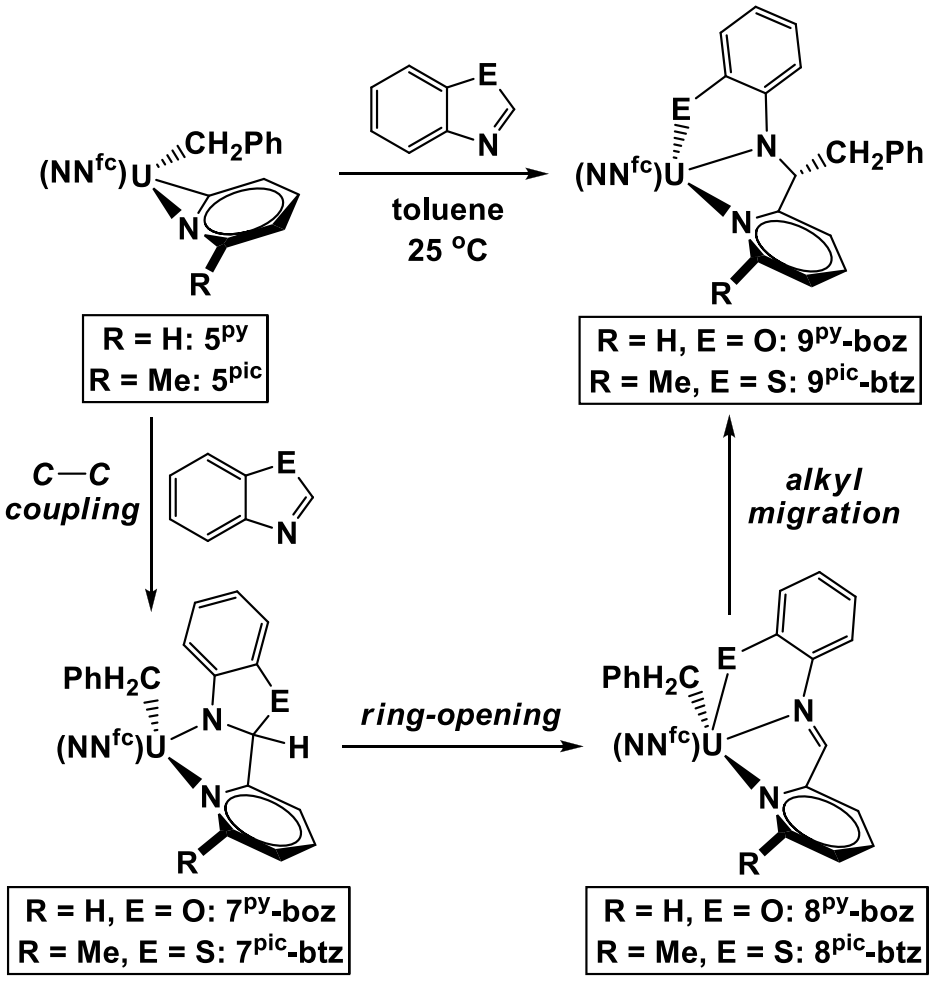

The alkyl transfer observed with quinoline is reminiscent of the last step proposed to occur during the transformation of $\mathbf{2}^{\mathbf{mi}}$**-mi** to **4A** and **4B**, with the difference that in the former case the migratory insertion takes place with an sp^2-C–U and not an sp^3-C–U bound ligand (**Scheme 3.1**). We decided to determine whether the C–C coupling and heterocycle ring-opening reactions would be observed for other aromatic heterocycles as well. The reaction between $\mathbf{5}^{\mathbf{py}}$ and benzoxazole or between $\mathbf{5}^{\mathbf{pic}}$ and benzothiazole, substrates analogous to imidazoles, led to products reminiscent of **4A** and **4B**. We propose that reactions

involving similar steps as those described in **Scheme 3.1** take place in the present cases as well (**Scheme 3.3**): the coordination of benzoxazole or benzothiazole is followed by coupling to the pyridyl ligand and the dearomatization of the diheteroatom ring (**7^{py}-boz** or **7^{pic}-btz**). This intermediate undergoes ring opening to form **8^{py}-boz** or **8^{pic}-btz**. The imine functionality is still reactive and engages the benzyl ligand in a migratory insertion to form the final product, **9^{py}-boz** or **9^{pic}-btz**.

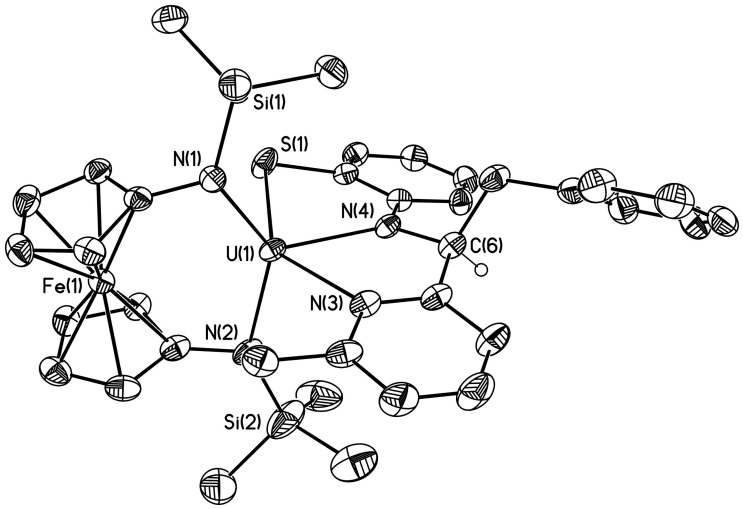

Figure 3.4. Thermal-ellipsoid (50% probability) representation of **9^{pic}-btz**. Irrelevant hydrogen atoms and *t*-butyl-methyl groups were removed for clarity.

The products **9^{py}-boz** and **9^{pic}-btz** were both characterized by X-ray crystallography (**Figure 3.4**); however, the structure of **9^{py}-boz** showed a high degree of thermal disorder and is only included in the Appendix to display the atom connectivity. The complex **9^{pic}-btz** features metrical parameters consistent with the structure proposed in **Scheme 3.3**. For example, the U–N_{amide} distance of 2.3534(36) Å is longer by ca. 0.1 Å than the U–N_{fc} distances of 2.2406(36) and 2.2421(38) Å. The U–S distance of 2.6914(12) Å is in the range reported for other uranium-thiolate distances.[42-45] The other distances also support the above structural assignment. For example, the N_{amide}–C distances are 1.4665(55) and 1.5074(63) Å, and the NCC and CCC angles around C6 are 110.85(38), 112.05(36), and 110.54(38)°.

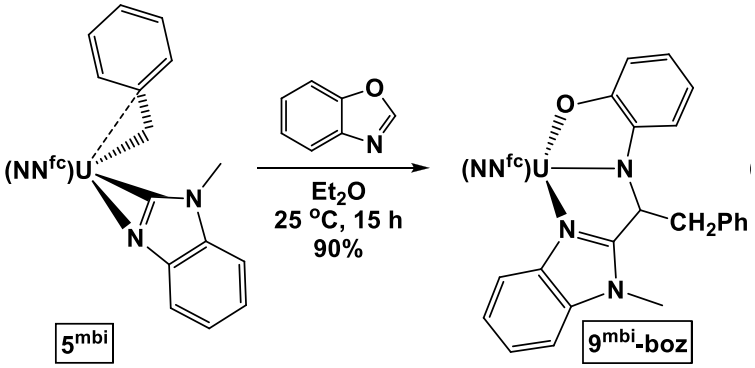

Figure 3.5. Reaction between $\mathbf{5}^{mbi}$ and benzoxazole.

The reaction observed between $\mathbf{5}^{py}$ and benzoxazole or between $\mathbf{5}^{pic}$ and benzothiazole was extended to $\mathbf{5}^{mbi}$ and benzoxazole. The isolation of $\mathbf{9}^{mbi}$**-boz** in 90% attests to the generality of the reaction sequences proposed to occur for these transformations. The complex $\mathbf{9}^{mbi}$**-boz** was characterized by ^{1}H NMR spectroscopy and elemental analysis; a comparison of its ^{1}H NMR spectrum with those of $\mathbf{9}^{py}$**-boz** and $\mathbf{9}^{pic}$**-btz** showed analogous features.

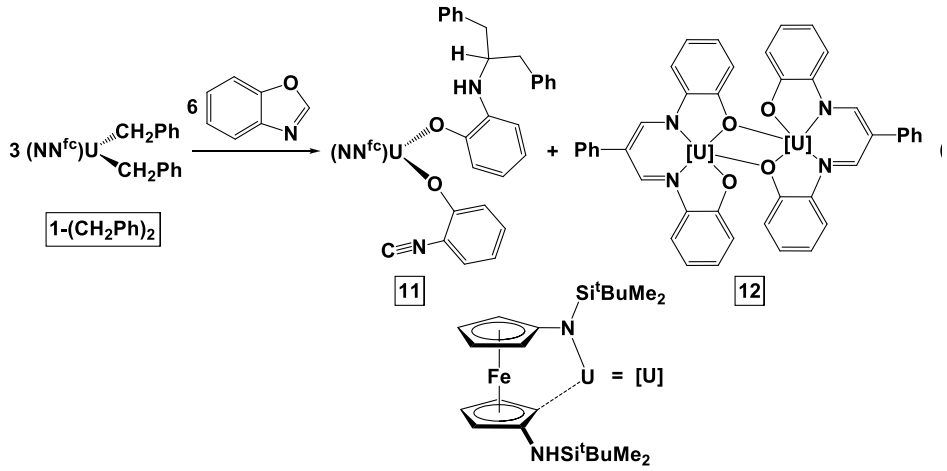

Figure 3.6. Reaction between **1-$(CH_2Ph)_2$** and two equivalents of benzoxazole.

The reaction between **1-$(CH_2Ph)_2$** and two equivalents of benzoxazole was also carried out. Although the conditions were modified numerous times in an attempt to favor the formation of a single product, all reactions consistently led to mixtures that proved difficult to separate and reproduce. However, the structures of two products **11** and **12** (**Figure 3.6**),

containing ring-opened oxazoles, were determined by single-crystal X-ray diffraction (**Figures 3.7 and 3.8**). Unfortunately, these products were difficult to purify for full characterization.

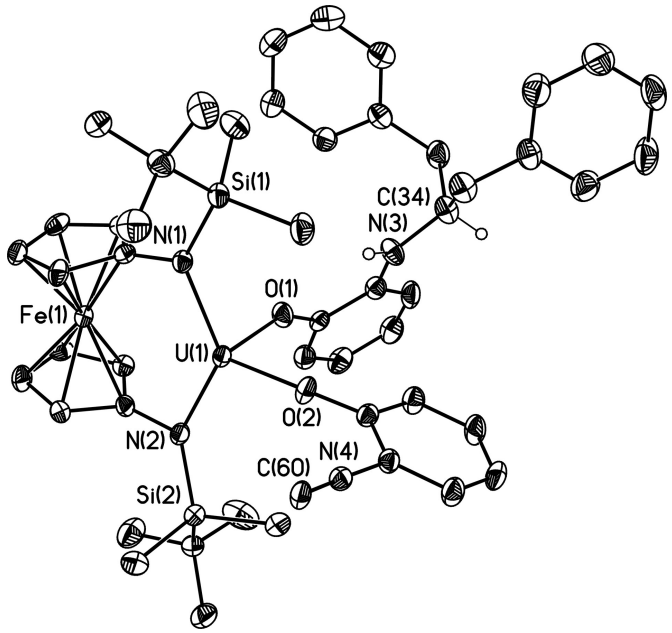

Figure 3.7. Thermal-ellipsoid (50% probability) representation of **11**. Hydrogen atoms and silyl groups were removed for clarity.

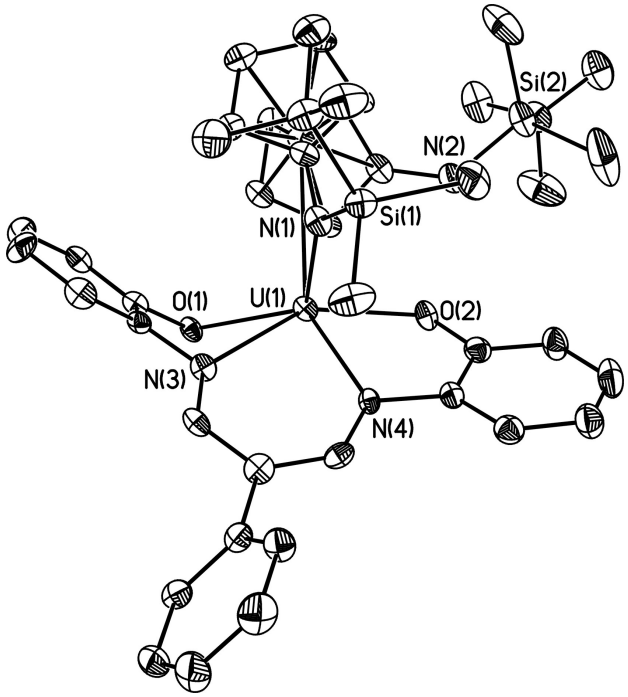

Figure 3.8. Thermal-ellipsoid (50% probability) representation of **12**. Only the monomeric unit is represented; hydrogen and solvent atoms were removed for clarity.

Scheme 3.4. Reaction of **1-$(CH_2Ph)_2$** with benzoxazole and proposed mechanism.

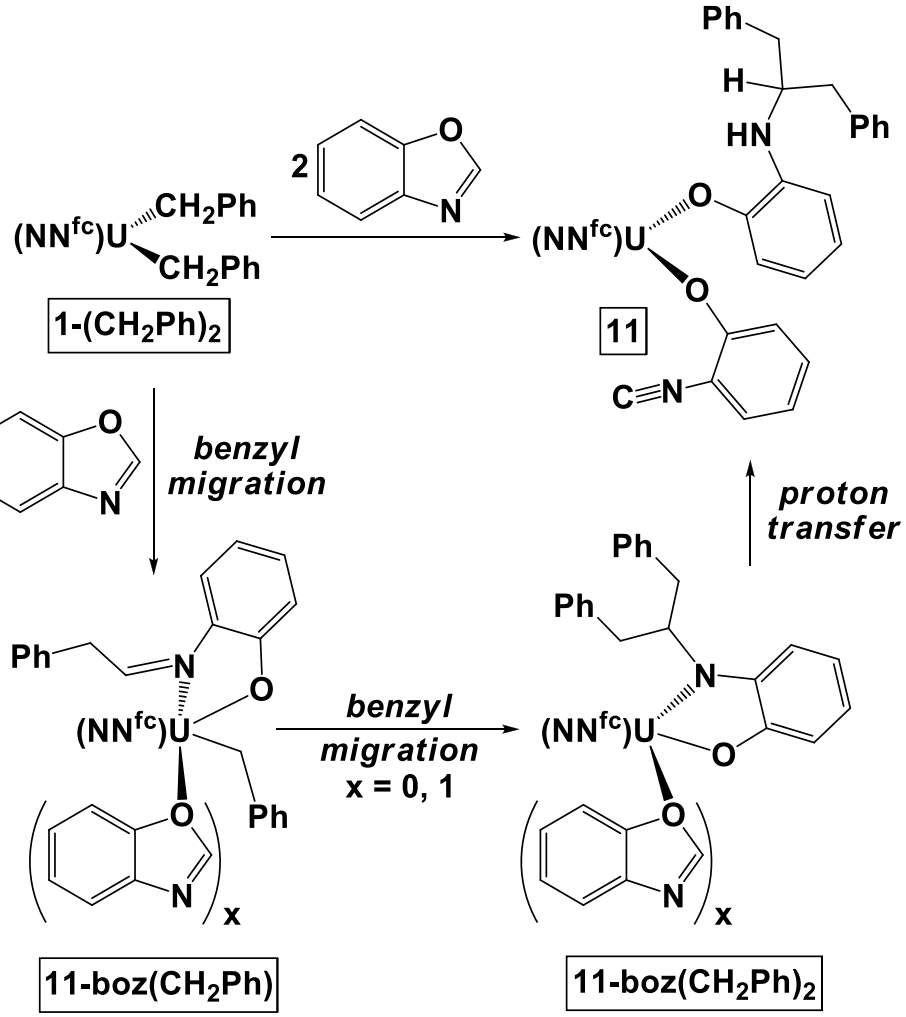

In order to explain the formation of **11**, we propose that an initial benzyl transfer to a coordinated benzoxazole determines its ring opening and the formation of an imine group (**11-boz(CH_2Ph)**), which is susceptible to another benzyl migration upon formation of **11-boz($CH_2Ph)_2$**, an intermediate, containing an amide functionality that may coordinate to the uranium center. The polarization of the newly formed U–N bond may lead to the deprotonation of another benzoxazole molecule, which is likely coordinated to the uranium center. Deprotonation of oxazoles is known to induce ring opening and formation of isonitriles[46, 47] thus validating the formation of **11**. The route to **12** is likely more complicated and but must involve a C–H activation step since one of the benzyl groups is not part of the product. Furthermore, even though the ferrocene ligand is still chelating through a weak

interaction between uranium and one of the cyclopentadienyl carbon atoms, one of the ferrocene amides is protonated and dissociated.

3.3 CONCLUSIONS

We have shown that uranium alkyl complexes mediate various reactions with aromatic N-heterocycles. The reactions between the uranium dibenzyl complex **1-$(CH_2Ph)_2$** and one equivalent of pyridine or 2-picoline led to the formation of alkyl-η^2-N,C-pyridyl complexes through C−H activation. These benzyl-pyridyl complexes transfer the benzyl ligand to quinoline and engage in complex reactions with benzoxazole or benzothiazole. The reaction sequences proposed to explain the formation of the final products are reminiscent of the transformation of the uranium bis(η^2-N,C-imidazolyl) complex **2^{mi}** into **4A** and **4B**. The intimate reaction steps are based on C−C coupling, heterocycle ring opening, and alkyl transfer. The reactions reported herein add to the list of reactions observed for uranium alkyl complexes with aromatic N-heterocycles, a statement of the rich reactivity behavior of these complexes when they are supported by ferrocene-diamide ligands.

3.4 APPENDIX C

3.4.1 Synthesis

General Considerations. All experiments were performed under a dry nitrogen atmosphere using standard Schlenk techniques or an MBraun inert-gas glovebox. Solvents were purified using a two-column solid-state purification system by the method of Grubbs[48] and transferred to the glovebox without exposure to air. NMR solvents were obtained from Cambridge Isotope Laboratories, degassed, and stored over activated molecular sieves prior to use. Uranium turnings were purchased from Argonne National Laboratories. Compounds 1-$(CH_2Ph)_2$[31] and 5^{mbi}[35] were prepared following published procedures. The aromatic heterocycles were distilled

or recrystallized before use; all other materials were used as received. ^{1}H NMR spectra were recorded on Bruker300 or Bruker500 spectrometers (supported by the NSF grant CHE-9974928) at room temperature in C_6D_6 unless otherwise specified. Chemical shifts are reported with respect to solvent residual peak, 7.16 ppm (C_6D_6). CHN analyses were performed by UC Berkeley Micro-Mass facility, 8 Lewis Hall, College of Chemistry, University of California, Berkeley, CA 94720.

Synthesis of 5^{py}. Pyridine (0.0264 g in ~3 mL toluene, 2 equiv) was added dropwise to a stirring toluene solution (5 mL) of **1-(CH$_2$Ph)$_2$** (0.1441 g, 0.167 mmol) in a 20-mL scintillation vial and allowed to stir vigorously at room temperature for 16 h. The solvent was removed under reduced pressure and the dried product was extracted with hexanes and filtered through Celite. The filtrate was dried under reduced pressure and the above extraction/filtration procedure was repeated. The filtrate was concentrated and placed into a -35 °C freezer. Crystals formed overnight. The mother liquor was decanted and placed back into the freezer. Two additional crops of crystals were obtained in this manner. Yield: 0.1257 g, 89%.

Synthesis of 5^{pic}. 2-picoline (2 mL of 0.116 M solution in hexanes, 0.232 mmol, 2 equiv) was added dropwise to a stirring solution of **1-(CH$_2$Ph)$_2$** (100 mg in 5 mL hexanes, 0.116 mmol) in a 12-mL Schlenk tube. The reaction mixture was stirred at room temperature for 30 h. The solvent was removed under reduced pressure and the dried product was extracted in hexanes, filtered through Celite, concentrated, and placed into a -35 ºC freezer. Yield: 66%.

Synthesis of 6^{mbi}-qn(CH$_2$Ph). Quinoline (13.5 mg, 0.1 mmol) was dissolved in 2 mL of hexanes and slowly added to a stirring hexanes solution of **5^{mbi}** (89.9 mg, 0.1 mmol). The reaction mixture was stirred at room temperature for 15 h, filtered through Celite, and dried. Yield (crude): 79%. The brown-yellow oil was redissolved in fresh hexanes, passed through Celite,

and stored at -35 ºC as a highly concentrated solution. Brown block crystals suitable for X-ray structure analysis formed after 3 d.

Synthesis of 9^{py}-boz. A 2-mL benzene solution of benzoxazole (13 mg, 0.11 mmol) was slowly added to a 2-mL benzene solution of $\mathbf{5}^{py}$ (43 mg, 0.051 mmol). The reaction mixture was stirred at room temperature for 12 h. The volatiles were removed under reduced pressure and the resulting dark-red powder was dissolved in diethyl ether, filtered through Celite, concentrated, and stored at -35 ºC. X-ray quality crystals formed overnight. Yield: 61%.

Synthesis of 9^{pic}-btz. A 2-mL pentane solution of benzothiazole (72.7 mg, 0.522 mmol) was slowly added to a 2-mL *n*-pentane solution of $\mathbf{5}^{pic}$ (347 mg, 0.401 mmol). The reaction mixture was left at room temperature without stirring. The pink precipitate that formed after 10 h was separated, dried, dissolved in diethyl ether, filtered through Celite, and stored at -35 ºC. Yield: 54%. X-ray quality crystals formed overnight.

Synthesis of 9^{mbi}-boz. Benzoxazole (7.9 mg, 0.066 mmol) was dissolved in 2 mL of diethyl ether and added to a 2-mL diethyl ether solution of $\mathbf{5}^{mbi}$ (58.6 mg, 0.065 mmol). The reaction mixture was stirred at room temperature for 15 h. The volatiles were removed under reduced pressure and the dried product was extracted with hexanes, filtered through Celite, and dried again. Yield (crude): 90%. The pale-orange powder was dissolved in fresh hexanes, passed through Celite, and stored at -35 ºC. Clumps of dark-red needles embedded in salmon-pink powder formed after 48 h. The product is stable in solution at room temperature indefinitely.

Synthesis of 11 and 12. A hexanes solution (10 mL) of $\mathbf{1\text{-}(CH_2Ph)_2}$ (94.7 mg, 0.11 mmol) was cooled to -78 ºC for 30 min. Solid benzoxazole (14 mg, 0.11 mmol) that was kept at -35 ºC was added and the reaction mixture was allowed to stir at room temperature overnight. Volatiles were removed under reduced pressure and a pentane solution of the resulting red solid was

filtered through Celite. Yellow clusters of **11** and red blocks of **12** co-crystallized from a dilute diethyl ether solution. All attempts to separate and fully characterize the two products were not successful.

3.4.2 Elemental analysis

5^{py}
$C_{34}H_{49}FeN_3Si_2U$, g/mol
Calculated: 48.05 %C, 5.81 %H, 4.94 %N
Found: 47.68 %C, 5.81 %H, 4.93 %N

5^{pic}
$C_{35}H_{51}FeN_3Si_2U$, g/mol
Calculated: 48.66 %C, 5.95 %H, 4.86 %N
Found: 48.46 %C, 6.04 %H, 4.77 %N

6^{mbi}-qn(CH_2Ph)
$C_{46}H_{59}FeN_5Si_2U$, 1032 g/mol
Calculated: 53.51 %C, 5.78 %H, 6.79 %N
Found: 53.18 %C, 5.43 %H, 6.39 %N

9^{py}-boz
$C_{41}H_{55}FeN_4OSi_2U$, 970 g/mol
Calculated: 50.77 %C, 5.72 %H, 5.78 %N
Found: 50.53 %C, 5.73 %H, 5.53 %N

9^{pic}-btz
$C_{42}H_{57}FeN_4SSi_2U[(C_7H_8)_{1/3}]$, 1030 g/mol
Calculated: 51.64 %C, 5.83 %H, 5.44 %N
Found: 51.66 %C, 5.78 %H, 5.63 %N

9^{mbi}-boz
$C_{44}H_{57}FeN_5OSi_2U$, 1021 g/mol
Calculated: 51.71 %C, 5.62 %H, 6.85 %N
Found: 52.01 %C, 5.70 %H, 6.57 %N

3.4.3 ^{1}H NMR spectroscopy

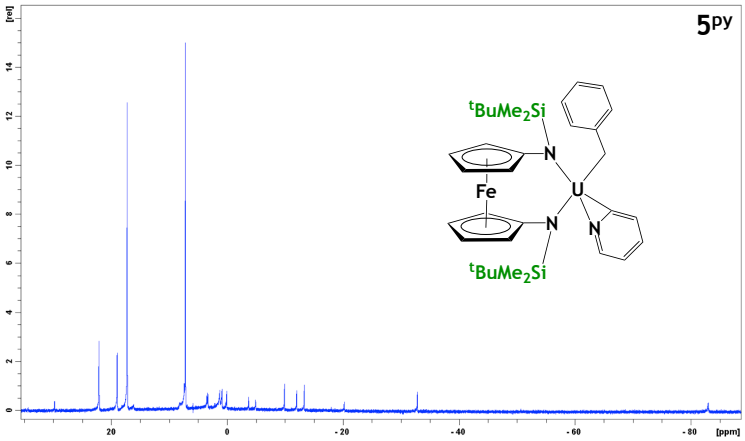

Figure C1. ^{1}H NMR (C_6D_6, 500 MHz, 25°C) of **5^{py}**; δ (ppm): 21.97 and 18.87 (s, 12H, $SiCH_3$), 17.13 (s, 18H, $SiC(CH_3)_3$), 3.33, 0.09, -9.83, -11.94, -13.23, and -32.69 (s, 2H each, $CH_2C_6H_5$ or C_5H_4), 7.40, 3.53, -3.67, -4.82, and -20.06 (s, 1H each, C_5H_4 or NC_5H_4), -82.52 (s, 2H, $CH_2C_6H_5$).

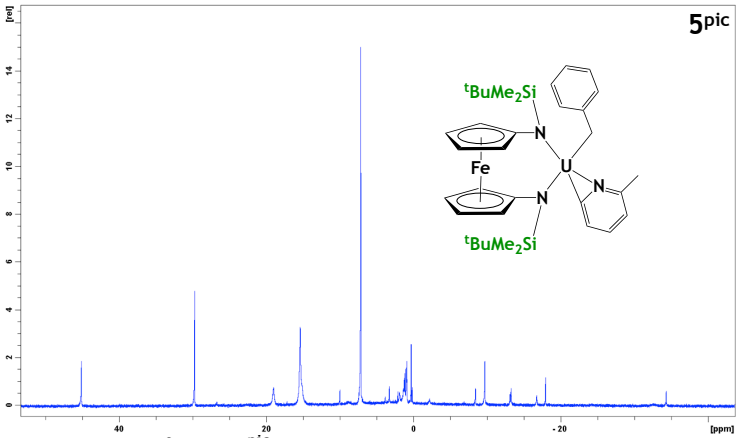

Figure C2. ^{1}H NMR (C_6D_6, 500 MHz, 25°C) of **5^{pic}**; δ (ppm): -71.13 (s, 2H, $CH_2C_6H_5$), 18.80 and 14.96 (s, 12H, $SiCH_3$), 15.23 (s, 18H, $SiC(CH_3)_3$), 1.91, -13.09, -24.35, and -32.42 (s, 2H each, $CH_2C_6H_5$ or C_5H_4), 9.98, 8.70, -2.12, and -9.53 (s, 1H each, C_5H_4 or NC_5H_4), -9.53 (s, 3H, $NCCH_3$).

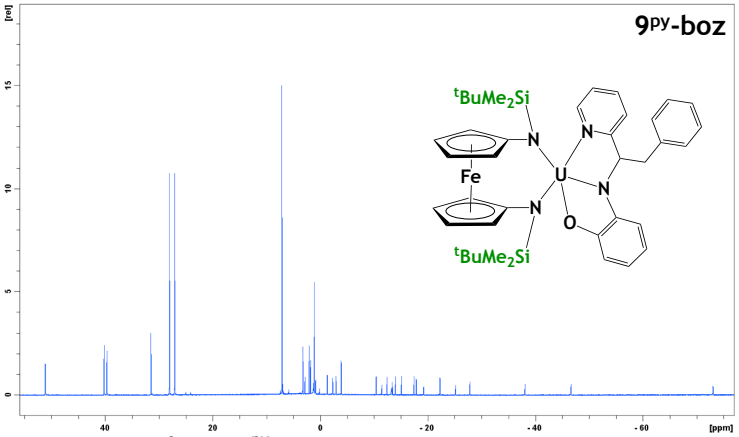

Figure C3. ^{1}H NMR (C_6D_6, 500 MHz, 25°C) of **9^{py}-boz**; δ (ppm): 51.22, 40.27, 39.62, and 31.57 (s, 3H each, $SiCH_3$), 28.01 and 27.15 (s, 9H each, $SiC(CH_3)_3$), 1.85 (t, 2H, CH_2Ph), 2.89, -1.25, -2.28, -2.90, -10.38, and -12.38 (t, 1H each, C_5H_4, aromatic-C*H*, or NC_5H_3), -3.81, -15.08, -17.41, -17.79, -19.19, -22.19, and -25.13 (d, 1H each, C_5H_4, aromatic-C*H*, or NC_5H_3), -3.88, -11.42, -13.17, -13.39, -13.95, -27.80, -38.07, -46.63, and -73.03 (s, 1H each, C_5H_4, aromatic-C*H*, or NC_5H_3).

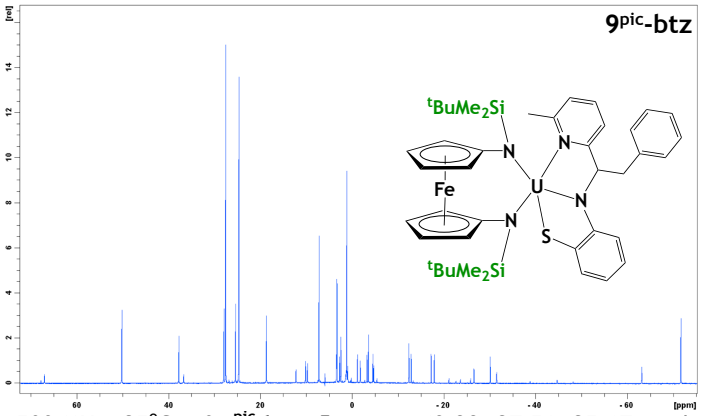

Figure C4. ^{1}H NMR (C_6D_6, 500 MHz, 25°C) of **9^{pic}-btz**; δ (ppm): 49.38, 27.51, 25.17, and 18.45 (s, 3H each, SiCH_3), 27.06 and 24.32 (s, 9H each, SiC(CH_3)$_3$), -12.14 (s, 2H, CH_2Ph), 10.08, 9.58, 3.47, 2.77, 2.49, -1.08, and -30.98 (t, 1H each, C_5H_4, aromatic-C*H*, or NC_5H_3), -3.44, -16.94, and -26.17 (d, 1H each, C_5H_4, aromatic-C*H*, or NC_5H_3), 12.17, -1.76, -3.15, -4.44, -4.77, -12.70, -17.61, -29.59, and -62.44 (s, 1H each, C_5H_4, aromatic-C*H*, or NC_5H_3), -70.70 (s, 3H, NCCH_3).

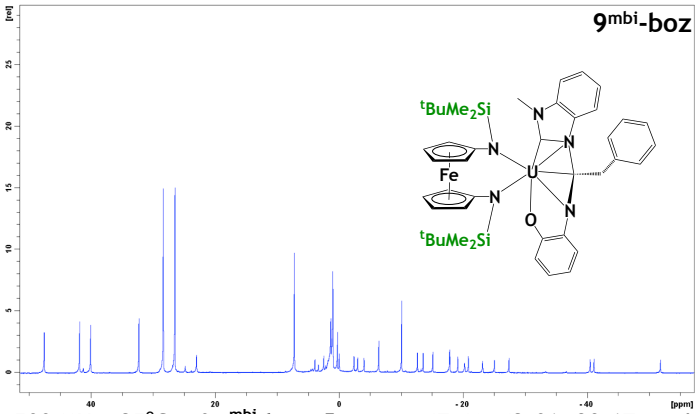

Figure C5. ^{1}H NMR (C_6D_6, 500 MHz, 25°C) of **9^{mbi}-boz**; δ (ppm): 47.41, 42.06, 39.67, and 32.26 (s, 3H each, SiCH_3), 28.31 and 26.45 (s, 9H each, SiC(CH_3)$_3$), 2.43, -0.06, -2.27, -2.92, -4.08, -20.44, -23.24, and -25.15 (t, 1H each, C_5H_4, aromatic-C*H*, or NC_5H_3), -6.44 (d, 2H, CH_2Ph), -10.22 (s, 3H, NCCH_3), -19.09, -20.78, and -41.10 (d, 1H each, C_5H_4, aromatic-C*H*, or NC_5H_3), -12.63, -13.59, -15.12, -17.82, -18.02, -27.40, -40.29, and -51.89 (s, 1H each, C_5H_4, aromatic-C*H*, or NC_5H_3).

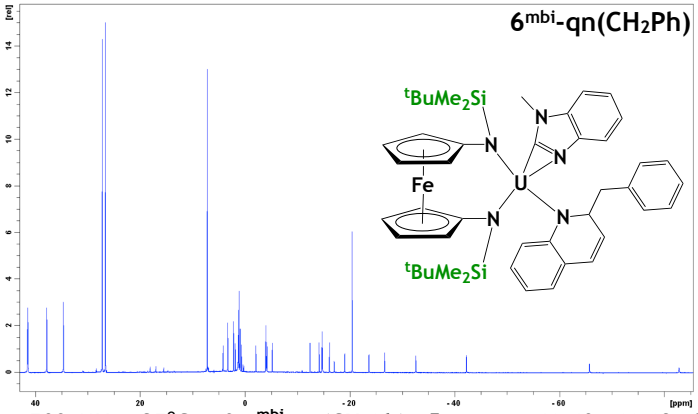

Figure C6. ^{1}H NMR (C_6D_6, 500 MHz, 25°C) of **6^{mbi}-qn(CH$_2$Ph)**; δ (ppm): 41.40, 41.13, 37.68, 34.37 (s, 3H each, SiCH_3), 27.12, 26.50 (s, 9H each, SiC(CH_3)$_3$), 2.20 (t, 2H, CH_2Ph), 1.86, -2.06, -16.99, -65.57 (t, 1H each, C_5H_4, aromatic-C*H*, or NC_5H_3), 4.17, 0.69, -4.08, -4.20, -5.19, -14.80, -23.62 (d, 1H each, C_5H_4, aromatic-C*H*, or NC_5H_3), -3.94, -3.98, -12.42, -14.16, -14.63, -14.70, -16.12, -19.03, -26.57, -32.52, -42.23, -82.59 (s, 1H each, C_5H_4, aromatic-C*H*, or NC_5H_3), -20.39 (s, 3H, NCCH_3).

3.4.4 X-ray crystallography

X-ray quality crystals were obtained from various concentrated solutions stored at –35 ºC in the glove box. Inside the glove box, the crystals were coated with oil (STP Oil Treatment) on a microscope slide, which was brought outside the glove box. The X-ray data collections were carried out on a Bruker AXS single crystal X-ray diffractometer using MoKα radiation and a SMART APEX CCD detector. The data was reduced by SAINTPLUS and an empirical absorption correction was applied using the package SADABS. The structures were solved and refined using SHELXTL (Bruker 1998, SMART, SAINT, XPREP AND SHELXTL, Bruker AXS Inc., Madison, Wisconsin, USA). All atoms were refined anisotropically and hydrogen atoms were placed in calculated positions unless specified otherwise. Tables with atomic coordinates and equivalent isotropic displacement parameters, with all the bond lengths and angles, and with anisotropic displacement parameters are listed in the CIFs.

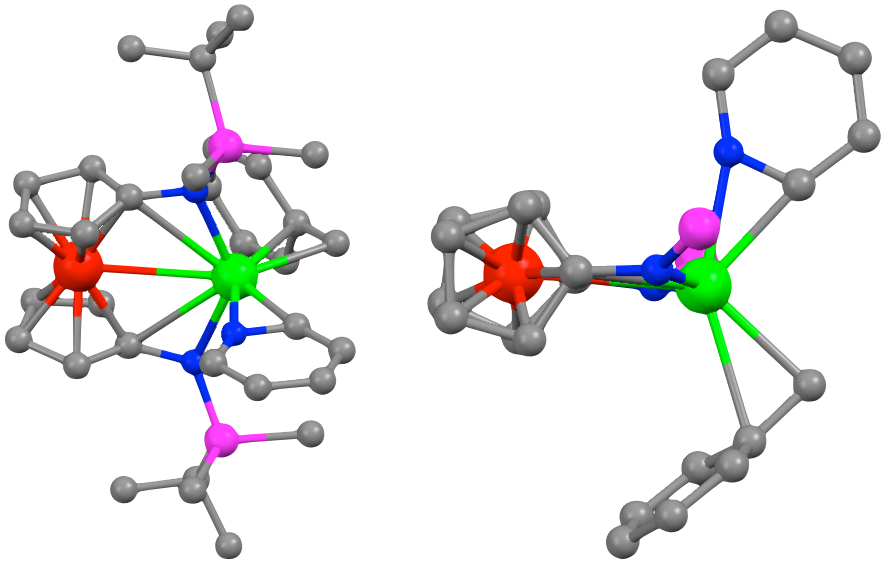

Figure C7. Crystal data for **5**^{py}. X-ray quality crystals were obtained from a concentrated Et_2O solution. A total of 8332 reflections ($-13 \le h \le 13$, $-15 \le k \le 15$, $-23 \le l \le 23$) was collected at T = 100(2) K with $2q_{max}$ = 56.24º, of which 6737 were unique (R_{int} = 0.0406). The residual peak and hole electron density were 1.47 and -2.35 eA^{-3}. The least-squares refinement converged normally with residuals of R_1 = 0.0593 and GOF = 1.043. Crystal and refinement data for 5^{py}: formula $C_{34}H_{49}N_3Si_2FeU$, space group $P\bar{1}$, a = 9.8710(16), b = 11.7017(19), c = 17.624(3), α = 76.825(2), ß = 74.133(2), γ = 65.740(2)º, V = 1769.7(5) Å^3, Z = 2, μ = 5.07 mm^{-1}, F(000) = 840, R_1 = 0.0412 and wR_2 = 0.0759 (based on all 8332 data, $I > 2s(I)$).

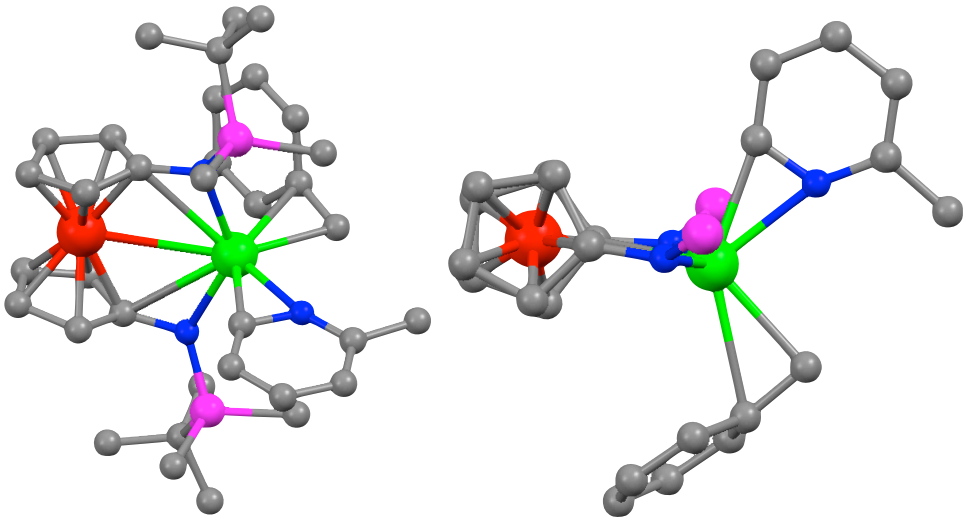

Figure C8. Crystal data for **5**^{pic}. X-ray quality crystals were obtained from a concentrated hexanes solution. A total of 9077 reflections ($-13 \le h \le 13$, $-15 \le k \le 15$, $-24 \le l \le 24$) was collected at T = 100(2) K with $2q_{max}$ = 57.43°, of which 8169 were unique (R_{int} = 0.0221). The residual peak and hole electron density were 1.44 and -0.81 eA^{-3}. The least-squares refinement converged normally with residuals of R_1 = 0.0253 and GOF = 1.021. Crystal and refinement data for 5^{pic}: formula $C_{35}H_{51}N_3Si_2FeU$, space group $P\bar{1}$, a = 9.805(4), b = 11.590(5), c = 18.359(8), α = 73.400(4), ß = 87.716(4), γ = 66.498(4)°, V = 1826.9(13) Å^3, Z = 2, μ = 4.92 mm^{-1}, F(000) = 856, R_1 = 0.0299 and wR_2 = 0.0555 (based on all 9077 data, $I > 2s(I)$).

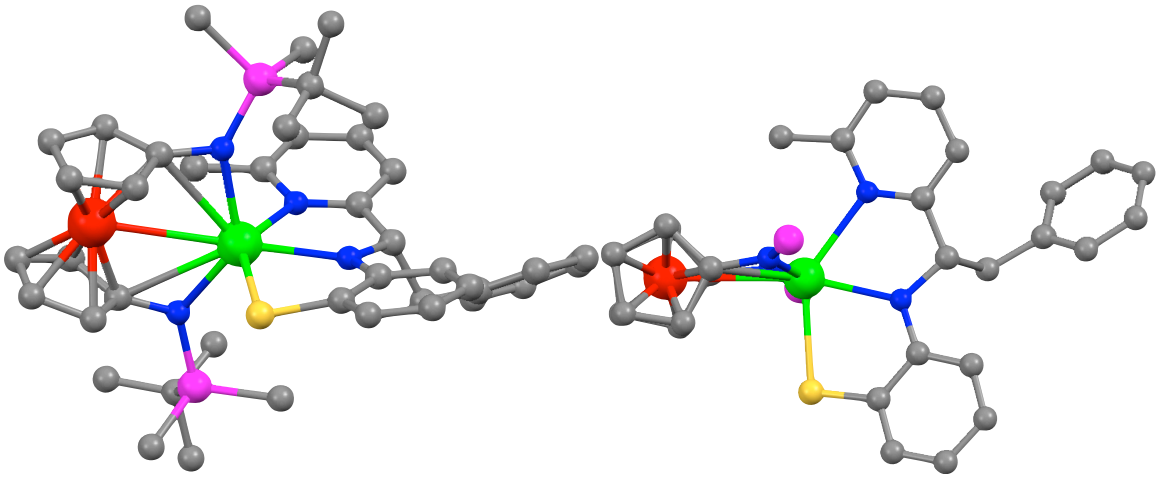

Figure C9. Crystal data for **9**^{pic}**-btz.** X-ray quality crystals were obtained from a concentrated *n*-pentane solution. A total of 41865 reflections ($-32 \le h \le 33$, $-24 \le k \le 24$, $-31 \le l \le 32$) was collected at T = 100(2) K with q_{max} = 30.77°, of which 12252 were unique (R_{int} = 0.0361). The residual peak and hole electron density were 3.00 and -2.61 eA^{-3}. The least-squares refinement converged normally with residuals of R_1 = 0.0408 and GOF = 1.034. Crystal and refinement data for 9^{pic}-btz: formula $C_{42}H_{56}N_4Si_2FeSU$, space group $C2/c$, a = 23.049(2), b = 17.1069(16), c = 22.439(2), ß = 109.840(1)°, V = 8322.7(14) Å^3, Z = 8, μ = 4.377 mm^{-1}, F(000) = 3984, R_1 = 0.0599 and wR_2 = 0.1052 (based on all 12252 data, $I > 2s(I)$).

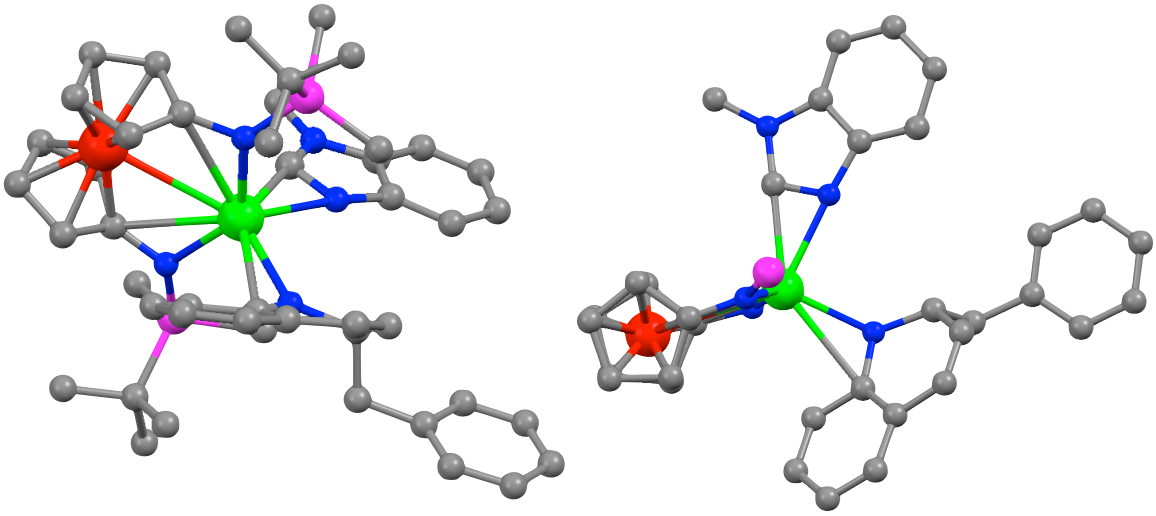

Figure C10. Crystal data for **6^{mbi}-qn(CH$_2$Ph).** X-ray quality crystals were obtained from a concentrated hexanes solution. A total of 81489 reflections (-25 ≤ *h* ≤ 25, -26 ≤ *k* ≤ 25, -31 ≤ *l* ≤ 31) was collected at *T* = 100(2) K with q_{max} = 28.33°, of which 11284 were unique (R_{int} = 0.1686). The residual peak and hole electron density were 2.31 and -2.16 eA^{-3}. The least-squares refinement converged normally with residuals of R_1 = 0.0628 and GOF = 1.028. Crystal and refinement data for 6^{mbi}-qn(CH$_2$Ph): formula $C_{46}H_{59}N_5Si_2FeU$, space group *P*bca, *a* = 19.096(5), *b* = 19.896(6), *c* = 23.964(7), ß = 90°, V = 9105(4) Å^3, Z = 8, μ = 3.961 mm^{-1}, F(000) = 4128, R_1 = 0.1363 and wR_2 = 0.1492 (based on all 11284 data, $I > 2s(I)$).

3.5 REFERENCES

1. Labinger, J. A.; Bercaw, J. E., Understanding and Exploiting C-H bond Activation. *Nature* **2002,** 417, (6888), 507-514.

2. Diaconescu, P. L., Reactions of Early Transition Metal-Carbon Bonds with N-Heterocycles. *Curr. Org. Chem.* **2008,** 12, 1388-1405.

3. Fox, A. R.; Bart, S. C.; Meyer, K.; Cummins, C. C., Towards uranium catalysts. *Nature* **2008,** 455, (7211), 341-349.

4. Hong, S.; Marks, T. J., Organolanthanide-Catalyzed Hydroamination. *Acc. Chem. Res.* **2004,** 37, (9), 673-686.

5. Hou, Z.; Wakatsuki, Y., Recent Developments in Organolanthanide Polymerization Catalysts. *Coord. Chem. Rev.* **2002,** 231, (1-2), 1-22.

6. Konkol, M.; Okuda, J., Non-Metallocene Hydride Complexes of the Rare-Earth Metals. *Coord. Chem. Rev.* **2008,** 252, (15-17), 1577-1591.

7. Weller, K. J.; Fox, P. A.; Gray, S. D.; Wigley, D. E., Homogeneous Models for Hydrodenitrogenation Catalysis. *Polyhedron* **1997,** 16, (18), 3139-3163 and references therein.

8. D'Souza, D. M.; Muller, T. J. J., Multi-Component Syntheses of Heterocycles by Transition-Metal Catalysis. *Chem. Soc. Rev.* **2007,** 36, (7), 1095-1108.

9. Nakamura, I.; Yamamoto, Y., Transition-Metal-Catalyzed Reactions in Heterocyclic Synthesis. *Chem. Rev.* **2004,** 104, (5), 2127-2198.

10. Furimsky, E.; Massoth, F. E., Hydrodenitrogenation of Petroleum. *Catal. Rev.-Sci. Eng.* **2005,** 47, (3), 297 - 489 and references therein.

11. Jordan, R. F., Chemistry of Cationic Dicyclopentadienyl Group-4 Metal Alkyl Complexes. *Adv. Organomet. Chem.* **1991,** 32, 325-387.

12. Boaretto, R.; Roussel, P.; Kingsley, A. J.; Munslow, I. J.; Sanders, C. J.; Alcock, N. W.; Scott, P., Structure and Reactions of a Metallacyclic Complex Containing a Remarkably Long Uranium–Carbon Bond. *Chem. Commun.* **1999**, 1701-1702.

13. Boaretto, R.; Roussel, P.; Alcock, N. W.; Kingsley, A. J.; Munslow, I. J.; Sanders, C. J.; Scott, P., Synthesis of a Highly Strained Uranacycle: Molecular Structures of Organometallic Products Arising from Reduction, Oxidation and Protonolysis. *J. Organomet. Chem.* **1999,** 591, (1-2), 174-184.

14. den Haan, K. H.; Wielstra, Y.; Teuben, J. H., Reactions of Yttrium-Carbon Bonds with Active Hydrogen-Containing Molecules. A Useful Synthetic Method for Permethylyttrocene Derivatives. *Organometallics* **1987,** 6, (10), 2053-2060.

15. Dormond, A.; El Bouadili, A. A.; Moïse, C., Reactivity of the Actinoid–Carbon σ Bond: Reaction of $[(Me_3Si)_2N]_2MCH_2Si(Me)_2NSiMe_3$ with Acidic Hydrogen, Ready C–H activation. *J. Chem. Soc., Chem. Commun.* **1985**, 914-916.

16. Duchateau, R.; Brussee, E. A. C.; Meetsma, A.; Teuben, J. H., Synthesis and Reactivity of Bis(alkoxysilylamido)yttrium η^2-Pyridyl and η^2-α-Picolyl Compounds. *Organometallics* **1997,** 16, (25), 5506-5516.

17. Duchateau, R.; van Wee, C. T.; Teuben, J. H., Insertion and C-H Bond Activation of Unsaturated Substrates by Bis(benzamidinato)yttrium Alkyl, $[PhC(NSiMe_3)_2]_2YR$ (R = $CH_2Ph.THF$, $CH(SiMe_3)_2$), and Hydrido, $\{[PhC(NSiMe_3)_2]_2Y(\mu\text{-}H)\}_2$, Compounds. *Organometallics* **1996,** 15, (9), 2291-2302.

18. Jantunen, K. C.; Scott, B. L.; Kiplinger, J. L., A Comparative Study of the Reactivity of Zr(IV), Hf(IV) and Th(IV) Metallocene Complexes: Thorium is not a Group IV Metal after all. *J. Alloys Compd.* **2007,** 444-445, 363-368.

19. Jordan, R. F.; Guram, A. S., Scope and Regiochemistry of Ligand Carbon-Hydrogen Activation Reactions of $Cp_2Zr(CH_3)(THF)^+$. *Organometallics* **1990,** 9, (7), 2116-2123.

20. Kiplinger, J. L.; Scott, B. L.; Schelter, E. J.; Pool Davis Tournear, J. A., sp^3 versus sp^2 C-H Bond Activation Ahemistry of 2-picoline by Th(IV) and U(IV) Metallocene Complexes. *J. Alloys Compd.* **2007,** 444-445, 477-482.

21. Pool, J. A.; Scott, B. L.; Kiplinger, J. L., Synthesis of Actinide η^2-pyridyl and η^2-α-picolyl Complexes by Carbon-Hydrogen Bond Activation. *J. Alloys Compd.* **2006,** 418, (1-2), 178-183.

22. Thompson, M. E.; Baxter, S. M.; Bulls, A. R.; Burger, B. J.; Nolan, M. C.; Santarsiero, B. D.; Schaefer, W. P.; Bercaw, J. E., "σ−Bond Metathesis" for Carbon−Hydrogen Bonds of Hydrocarbons and Sc−R (R = H, alkyl, aryl) Bonds of Permethylscandocene Derivatives. Evidence for Noninvolvement of the π System in Electrophilic Activation of Aromatic and Vinylic C−H Bonds. *J. Am. Chem. Soc.* **1987,** 109, (1), 203-219.

23. Watson, P. L., Facile Carbon-Hydrogen Activation by Lutetium-Methyl and Lutetium-Hydride Complexes. *J. Chem. Soc., Chem. Commun.* **1983**, (6), 276-277.

24. Jantunen, K. C.; Scott, B. L.; Gordon, J. C.; Kiplinger, J. L., Reactivity of $(C_5Me_5)Lu(CH_2SiMe_3)_2(THF)$ with Pyridine Ring Systems: Synthesis and Structural Characterization of an η^2-(N,C)-Pyridyl (Mono)pentamethylcyclopentadienyl Lutetium(III) Complex. *Organometallics* **2007,** 26, (10), 2777-2781.

25. Jantunen, K. C.; Scott, B. L.; Hay, P. J.; Gordon, J. C.; Kiplinger, J. L., Dearomatization and Functionalization of Terpyridine by Lutetium(III) Alkyl Complexes. *J. Am. Chem. Soc.* **2006,** 128, 6322-6323.

26. Cameron, T. M.; Gordon, J. C.; Scott, B. L.; Tumas, W., C-H Activation of a 2,2'-Bipyridine Ligand within (Mono)pentamethylcyclopentadienyl Lutetium Complexes. *Chem. Commun.* **2004**, (12), 1398-1399.

27. Miller, K. L.; Williams, B. N.; Benitez, D.; Carver, C. T.; Ogilby, K. R.; Tkatchouk, E.; Goddard, W. A.; Diaconescu, P. L., Dearomatization Reactions of N-Heterocycles Mediated by Group 3 Complexes. *J. Am. Chem. Soc.* **2010,** 132, 342-355.

28. Carver, C. T.; Monreal, M. J.; Diaconescu, P. L., Scandium Alkyl Complexes Supported by a Ferrocene Diamide Ligand. *Organometallics* **2008,** 27, (3), 363-370.

29. Carver, C. T.; Benitez, D.; Miller, K. L.; Williams, B. N.; Tkatchouk, E.; Goddard, W. A.; Diaconescu, P. L., Reactions of Group III Biheterocyclic Complexes. *J. Am. Chem. Soc.* **2009,** 131, (29), 10269-10278.

30. Jie, S.; Diaconescu, P. L., Reactions of Aromatic N-Heterocycles with Yttrium and Lutetium Benzyl Complexes Supported by a Pyridine-Diamide Ligand. *Organometallics* **2010,** 29, (5), 1222-1230.

31. Monreal, M. J.; Diaconescu, P. L., A Weak Interaction between Iron and Uranium in Uranium Alkyl Complexes Supported by Ferrocene Diamide Ligands. *Organometallics* **2008,** 27, (8), 1702-1706.

32. Shafir, A.; Power, M. P.; Whitener, G. D.; Arnold, J., Synthesis, Structure, and Properties of 1,1'-Diamino- and 1,1'-Diazidoferrocene. *Organometallics* **2000,** 19, (19), 3978-3982.

33. Shafir, A.; Arnold, J., Stabilization of a Cationic Ti Center by a Ferrocene Moiety: Remarkably Short Ti-Fe Interaction in the Diamide $\{[(\eta^5\text{-}C_5H_4NSiMe_3)_2Fe]TiCl\}_2^{2+}$. *J. Am. Chem. Soc.* **2001,** 123, (37), 9212-9213.

34. Monreal, M. J.; Carver, C. T.; Diaconescu, P. L., Redox Processes in a Uranium Bis(1,1'-diamidoferrocene) Complex. *Inorg. Chem.* **2007,** 46, (18), 7226-7228.

35. Monreal, M. J.; Khan, S.; Diaconescu, P. L., Beyond C-H Activation with Uranium: A Cascade of Reactions Mediated by a Uranium Dialkyl Complex. *Angew. Chem. Int. Ed.* **2009,** 48, (44), 8352-8355.

36. Carver, C. T.; Diaconescu, P. L., Insertion Reactions of Scandium Pyridyl Complexes Supported by a Ferrocene Diamide Ligand. *J. Alloys Compd.* **2009,** 488, 518-523.

37. Carver, C. T.; Diaconescu, P. L., Ring-Opening Reactions of Aromatic N-Heterocycles by Scandium and Yttrium Alkyl Complexes. *J. Am. Chem. Soc.* **2008,** 130, 7558-7559.

38. Carver, C. T.; Williams, B. N.; Ogilby, K. R.; Diaconescu, P. L., Coupling of Aromatic N-Heterocycles Mediated by Group 3 Complexes. *Organometallics* **2010,** 29, (4), 835–846.

39. Monreal, M. J.; Diaconescu, P. L., Reversible C–C Coupling in a Uranium Biheterocyclic Complex. *J. Am. Chem. Soc.* **2010,** 132, (22), 7676-7683.

40. Pool, J. A.; Scott, B. L.; Kiplinger, J. L., Carbon-Nitrogen Bond Cleavage in Pyridine Ring Systems Mediated by Organometallic Thorium(IV) Complexes. *Chem. Commun.* **2005**, (20), 2591-2593.

41. Arunachalampillai, A.; Crewdson, P.; Korobkov, I.; Gambarotta, S., Ring Opening and C-O and C-N Bond Cleavage by Transient Reduced Thorium Species. *Organometallics* **2006,** 25, 3856-3866.

42. Roger, M.; Barros, N.; Arliguie, T.; Thuéry, P.; Maron, L.; Ephritikhine, M., $U(SMes^*)_n$, (n = 3, 4) and $Ln(SMes^*)_3$ (Ln = La, Ce, Pr, Nd): Lanthanide(III)/Actinide(III) Differentiation in Agostic Interactions and an Unprecedented η^3 Ligation Mode of the Arylthiolate Ligand, from X-ray Diffraction and DFT Analysis. *J. Am. Chem. Soc.* **2006,** 128, 8790-8802.

43. Diaconescu, P. L.; Arnold, P. L.; Baker, T. A.; Mindiola, D. J.; Cummins, C. C., Arene-Bridged Diuranium Complexes: Inverted Sandwiches Supported by δ-Backbonding. *J. Am. Chem. Soc.* **2000,** 122, (25), 6108-6109.

44. Lescop, C.; Arliguie, T.; Lance, M.; Nierlich, M.; Ephritikhine, M., Bispentamethylcyclopentadienyl Uranium(IV) Thiolate Compounds. Synthesis and Reactions with CO_2 and CS_2. *J. Organomet. Chem.* **1999,** 580, (1), 137-144.

45. Clark, D. L.; Miller, M. M.; Watkin, J. G., Synthesis, Characterization, and X-ray Structure of the Uranium Thiolate Complex $U(S\text{-}2,6\text{-}Me_2C_6H_3)[N(SiMe_3)_2]_3$. *Inorg. Chem.* **1993,** 32, (5), 772-774.

46. Whitney, S. E.; Rickborn, B., Substituted Oxazoles: Syntheses *via* Lithio Intermediates. *J. Org. Chem.* **1991,** 56, 3058-3063.

47. Pirrung, M. C.; Ghorai, S.; Ibarra-Rivera, T. R., Multicomponent Reactions of Convertible Isonitriles. *J. Org. Chem.* **2009,** 74, 4110-4117.

48. Pangborn, A. B.; Giardello, M. A.; Grubbs, R. H.; Rosen, R. K.; Timmers, F. J., Safe and Convenient Procedure for Solvent Purification. *Organometallics* **1996,** 15, (5), 1518-1520.

CHAPTER 4

Redox Processes of 1,1'-Diamidoferrocene Uranium(IV) Complexes

TABLE OF CONTENTS

4.1 INTRODUCTION

To appreciate, understand, and ultimately regulate the reactivity of a given organometallic system, it is necessary to study the basic principles behind electron transfer. In this respect, electrochemical methods are tools of utmost importance. This chapter details an investigation conducted using cyclic voltammetry and discusses oxidation and reduction processes in uranium diiodide, bis(aryloxide), dibenzyl, bis(amide) and mixed aryloxide-iodide complexes supported by one 1,1'-diamidoferrocene ligand (**Chart** 4.**1**).

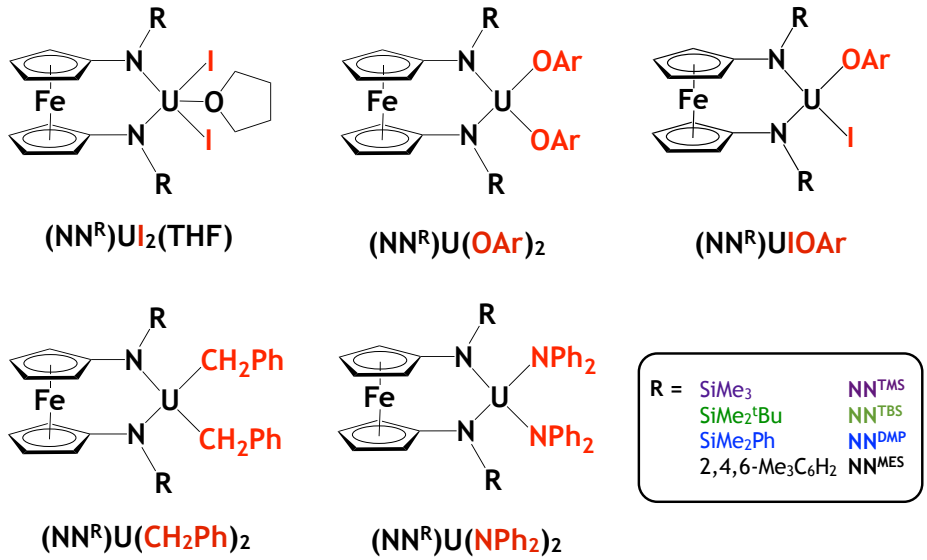

Chart 4.1. Four classes of 1,1'-diamidoferrocene uranium complexes analyzed by cyclic voltammetry.

4.2 DISCUSSION OF RESULTS

Most voltammetric measurements were conducted in tetrahydrofuran (THF) with tetraisopropylammonium tetrakis[3,5-bis(trifluoromethyl)phenyl]borate ($TPABAr^F$) as the supporting electrolyte. In some experiments, dichloromethane (DCM), trifluorotoluene (TFT), and diethyl ether (Et_2O) were used as solvents, while sodium tetrakis[3,5-bis(trifluoromethyl)phenyl]borate ($NaBAr^F$), tetrabutylammonium iodide (TBAI), and tetrabutylammonium hexafluorophosphate ($TBAPF_6$) served as electrolytes. ^1H NMR spectra of all complexes were taken before and after each experiment in order to verify that no decomposition occurred in due course. When possible, electrochemical behavior of each compound was studied in various media to aid interpretation of data. A 2-mm platinum disk, 3-mm glassy carbon disk, and 0.25-mm silver wire were used as working, counter, and reference electrodes, respectively. Moreover, all redox potential values are mentioned with respect to that of ferrocene. The following discussion is divided according to the class of compounds and describes anodic and cathodic events separately except in cases when the two processes appear to be interdependent. When comparing two or more types of systems

reported herein, we refer to the data obtained under same conditions (i.e. electrolyte, solvent, and scan rates are equivalent).

4.2.1 Uranium Diiodide Complexes, $(NN^R)UI_2(THF)$

Full electrochemical profiles of **$(NN^R)UI_2(THF)$** complexes are shown in **Figure 4.1**. The voltammograms of uranium diiodide complexes supported by silylamido ferrocene derivatives are intricate, displaying reduction of uranium and oxidation of iron centers. The overall profile of **$(NN^{MES})UI_2(THF)$** is unremarkable, exhibiting reversible reduction and oxidation events at –2.06 V and 0 V, respectively. Therefore, further discussion of its electrochemical behavior is unwarranted.

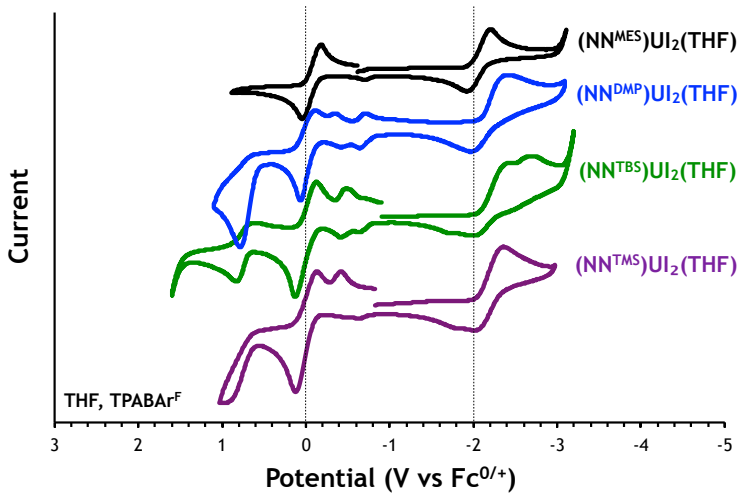

Figure 4.1. Cyclic voltammograms of **$(NN^R)UI_2(THF)$** complexes.

As expected, the reduction potential of uranium in all four derivatives decreases (i.e. becomes less negative) with more electron withdrawing groups on the ferrocene Cp rings. In other words, uranium is easiest to reduce when it is supported by a ferrocene ligand bearing mesitylamido groups and hardest to reduce when supported by a ligand bearing silylamido substituents. Values for the latter complexes range between –2.2 V and –2.4 V. Similar electronic effects have been reported for a series of methyl-substituted titanocene and zirconocene dichloride complexes.[1-4] To further put these potential values into perspective,

the reduction of uranium occurs at –1 V when it is supported by four iodide ligands (**Figure 4.2**). Similarly, this potential increases when two iodides are replaced with two pentamethylcyclopentadienyl ligands or one bis[2-(diisopropylphosphino)-4-methylphenyl]amido ligand (PNP), in which case the reduction of uranium occurs at –1.95 V[5] and –2.19 V,[6] respectively. When two iodides are instead replaced with one dianionic 1,1'-ferrocene diamide ligand, the reduction potential increases even more. This suggests that 1,1'-ferrocene diamines donate more electron density than the cyclopentadienyl ligand, and are thus more suitable for stabilizing high-valent than low-valent uranium centers.[5, 7] Therefore, the overall trend in the difficulty of uranium(IV) reduction follows the order $UI_4(Et_2O)_2$ < $(C_5Me_5)_2UCl_2$ < $(PNP)UCl_2$ < **$(NN^R)UI_2(THF)$**. Because they exhibit the most complex cathodic profiles, the following discussion will focus on the underlying mechanisms of the reductive events in **$(NN^{TMS})UI_2(THF)$** and **$(NN^{TBS})UI_2(THF)$**.

As shown in **Figure 4.2**, uranium diiodide supported by the NN^{TMS} ligand exhibits a single reduction event (wave A) and is considerably more difficult to reduce than the parent complex, **$UI_4(Et_2O)_2$**. The difference in the chemical properties of the coordinated THF and Et_2O solvent molecules[8] is not expected to have a significant effect on the electron density on uranium, and in turn, its reduction potential. Accordingly, the only structural distinction between **$UI_4(Et_2O)_2$** and **$(NN^{TMS})UI_2(THF)$** lies in the replacement of two iodide ligands with one dianionic ferrocene diamide. This modification of the local environment around the uranium center results in an increased reduction potential (-0.97 V before versus -2.4 V after), thus suggesting that coordination of diamidoferrocene increases the electron density on uranium.

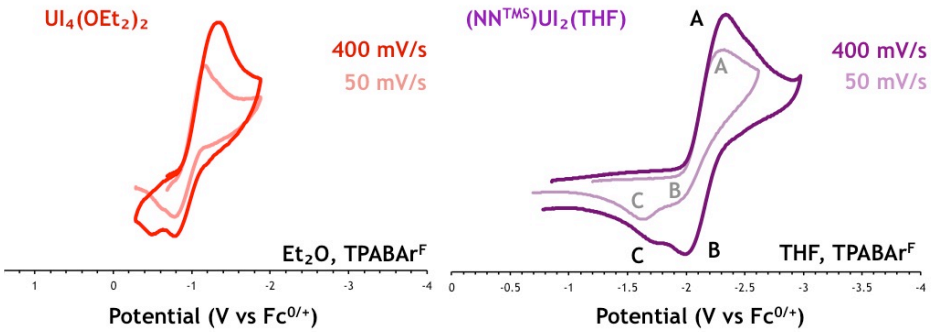

Figure 4.2. Reduction of $UI_4(Et_2O)_2$ (left) and $(NN^{TMS})UI_2(THF)$ (right). For clarity, the height of 50 mV/s scans was scaled by a factor of 0.5 and 3 in $UI_4(Et_2O)_2$ and $(NN^{TMS})UI_2(THF)$, respectively.

Furthermore, two poorly resolved waves (B and C in **Figure 4.2**), whose relative intensities depend on the scan rate, are revealed on the reverse scan. At slow scan rates, the first re-oxidation (wave B) generates less current than the subsequent event (wave C). When the scan rate is increased, however, the first re-oxidation wave becomes larger. These observations are consistent with a mechanism involving a chemically coupled redox process. More specifically, reduction of $(NN^{TMS})UI_2(THF)$, represented by A in **Figure 4.2**, is proposed to first generate $[(NN^{TMS})UI_2(THF)]^-$. This anion can be observed if the rate of measurement is high and it is oxidized back to the neutral complex. This re-oxidation is represented by the wave labeled B in **Figure 4.2**. However, if the potential is applied slowly, the anion has enough time to transform into a species that itself undergoes oxidation at a more positive potential. That event is represented by the wave labeled C in **Figure 4.2** and is also barely observed when the potential is scanned 400 mV/s, suggesting that even higher scan rates are necessary to avoid the anion's transformation. Similar mechanisms have previously been proposed for the reduction of bis(cyclopentadienyl) dichloride complexes of uranium and group IV transition metals.[7, 9-17]

Scheme 4.1 shows the proposed mechanism of reduction of $(NN^{TMS})UI_2(THF)$ at high and low scan rates. The former simply involves an exchange of one electron between the working electrode and $(NN^{TMS})UI_2(THF)$. The latter case, however, is proposed to involve a chemical transformation of the reduction product, $[(NN^{TMS})UI_2(THF)]^-$, whereby one iodide

ligand dissociates to generate the neutral trivalent uranium iodide, **(NN^{TMS})UI(THF)**. When the potential is reversed, this species is oxidized to the tetravalent uranium iodide cation, **[(NN^{TMS})UI(THF)]$^{+}$**, which then coordinates the iodide ligand that initially dissociated as a result of reduction. We emphasize that it is unclear whether dissociation/association of iodide occurs concertedly or step-wise. Finally, because the voltammetric measurements were conducted in THF, coordination of THF is expected to be involved in the redox equilibrium at all times. Finally, we note that dissociation of 1,1'-ferrocene diamine (instead of iodide ligand) is also likely because our attempts to reduce **(NN^{TMS})UI$_2$(THF)** with KC_8 in toluene have resulted in formation of **(NN^{TMS})$_2$U**.

Scheme 4.1. Proposed mechanism of **(NN^{TMS})UI$_2$(THF)** reduction; At very high scan rates, wave B is dominant, but at low scan rates, a chemical transformation takes place and wave C dominates.

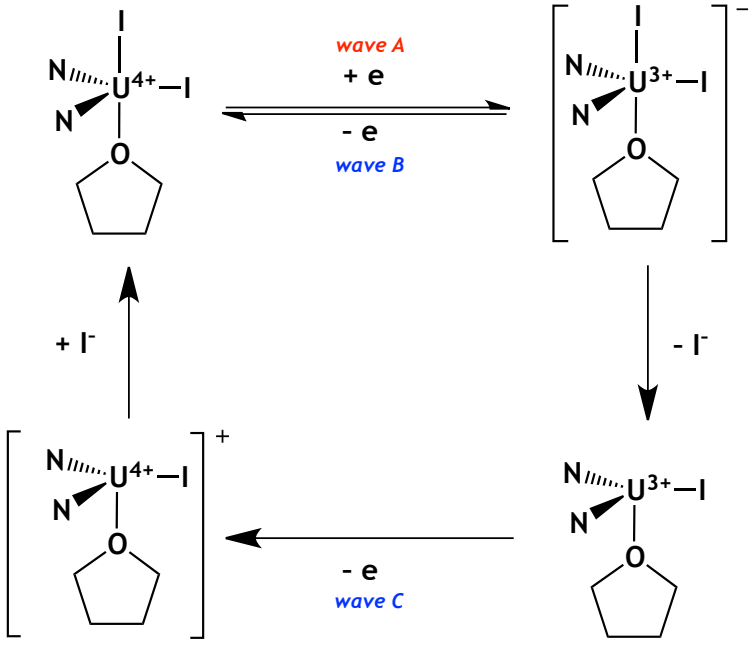

Compared to **(NN^{TMS})UI$_2$(THF)**, the reduction process for **(NN^{TBS})UI$_2$(THF)** adds another layer of complexity. In order to elucidate the underlying mechanism, we conducted cyclic voltammetry experiments in various media because the appearance of the reduction process depends on both the solvent and the supporting electrolyte used.

When the measurement is conducted in a THF solution of $TPABAr^F$, two poorly resolved reduction events (A and B in **Figure 4.3**) are revealed at -2.40 and -2.70 V regardless of the magnitude of scan rate employed. The separation between the two events is 300 mV. In a THF solution of $NaBAr^F$, however, only one reduction event (A in **Figure 4.3**) occurs at -2.4 V. This observation is expected. Changing the supporting electrolyte from $TPABAr^F$ to $NaBAr^F$ increases ion pairing between the anionic reduction products and the electrolyte cation, thus lowering the separation between two peak potentials (A and B) in a multi-electron process. A similar voltammetric response has been described for a tetraferrocenyl(nickel dithiolene) complex.[18] In both cases, reversing the potential sweep reveals two oxidative events between -1.5 V and -2.0 V (**Figure 4.3**, waves C and D for $TPABAr^F$ and waves B and C for $NaBAr^F$).

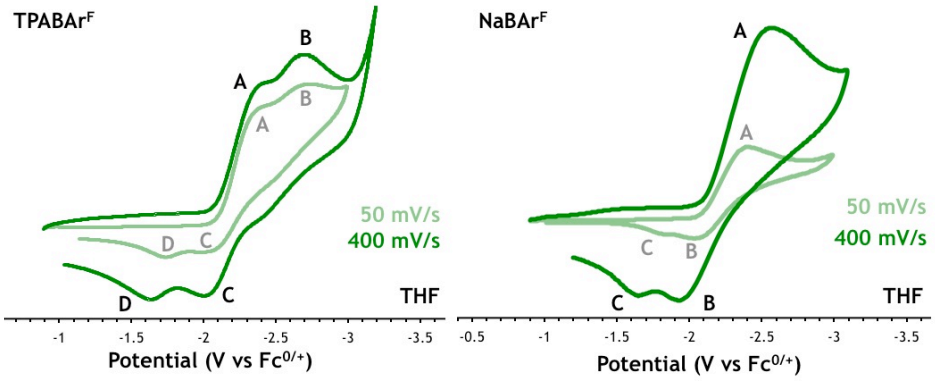

Figure 4.3. Reduction of **$(NN^{TBS})UI_2(THF)$** in THF with $TPABAr^F$ (left) and $NaBAr^F$ (right). For clarity, the plot on the left corresponding to 50 mV/s was scaled by a factor of 2.

As shown in **Figure 4.4**, conducting the measurement in a THF solution of $TBAPF_6$ reveals two reduction processes (A and B) at -2.52 V and -2.97 V. However, on scan reversal, the resolution of these waves decreases (C and D). This can be attributed to the greater ion pairing between the Lewis acidic uranium center and the smaller, more strongly coordinating hexafluorophosphate anion. Lastly, conducting cyclic voltammetry measurements in a THF solution of TBAI unveils one reduction event (wave A in **Figure 4.4**) at approximately -1.95 V regardless of the magnitude of scan rate employed. On scan reversal, only one re-oxidation

(wave B) is observed. The separation between the peak potentials is considerably large, however. While such behavior may be due to inherently slow electron transfer at the working electrode,[19] it is more likely a consequence of the highly resistive medium employed (i.e. TBAI is not completely soluble in THF).

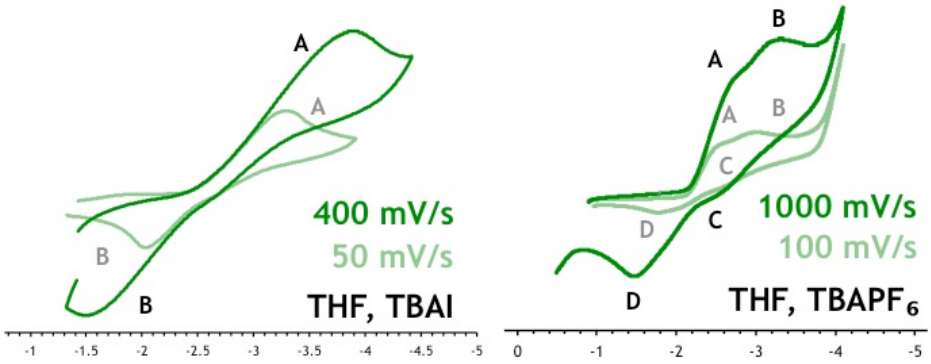

Figure 4.4. Reduction of **$(NN^{TBS})UI_2(THF)$** in THF solutions of tetrabutylammonium iodide (left) and tetrabutylammonium hexafluorophosphate (right).

With four different measurement conditions in hand, a mechanism involving cleavage of uranium-iodide bonds is proposed for the reduction of **$(NN^{TBS})UI_2(THF)$**. Such a proposal finds support in the observed chemical reversibility of the reduction when excess iodide (in the form of TBAI) is used. When a less coordinating non-halide anion is used in the supporting electrolyte, dissociation of one or both iodide ligands is therefore inevitable. This is further supported by the appearance of small waves corresponding to oxidation of iodide at –0.5 V and –0.7 V. Moreover, depending on the scan direction, a crucial change is observed in this potential region. For example, as shown in **Figure 4.5**, when the potential is scanned oxidatively (i.e. positive direction), the current generated at –0.5 V and –0.7 V during the initial cycle is lower than that generated during subsequent cycles (i.e. after uranium is reduced). On the other hand, if the potential is first scanned reductively (i.e. negative direction), the generated current remains the same during all cycles because the reduction of uranium occurs *before* the scan reaches the potential required for iodide oxidation.

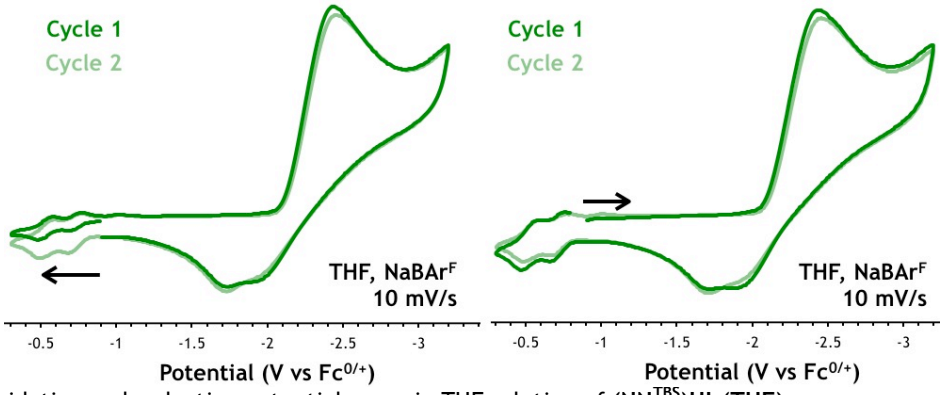

Figure 4.5. Oxidative and reductive potential scans in THF solution of **(NN^{TBS})UI$_2$(THF)**.

Because a single THF molecule is coordinated to the uranium center in solid state,[20] its role in the reduction process is warranted. In order to determine the extent of its involvement, we measured the current response to the applied negative potential in a non-coordinating solvent with low donating strength. As shown in **Figure 4.6**, two waves (A and B) are observed at -1.8 and -2.2 V in a dichloromethane solution of TPABAr^F. The former disappears when approximately 0.1 mL of THF is added, proving that, in the absence of THF, the first electron transfer from the working electrode to **(NN^{TBS})UI$_2$(THF)** is accompanied by an irreversible dissociation of THF from the uranium center. Similar behavior is observed in **(NN^{DMP})UI$_2$(THF)** when the experiment is conducted in diethyl ether (see Appendix D).

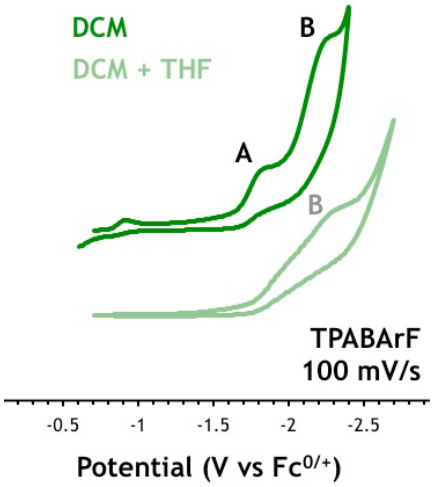

Figure 4.6. Reduction of **(NN^{TBS})UI$_2$(THF)** in DCM before and after addition of THF.

Taken together, these experiments bring to light a redox mechanism that is slightly different from that taking place with **(NN^{TMS})UI$_2$(THF)**. **Scheme 4.2** unveils the proposed mechanism for the reduction of **(NN^{TBS})UI$_2$(THF)**. The first step is analogous to that proposed for **(NN^{TMS})UI$_2$(THF)**. First, an electron is transferred from the working electrode to the uranium center, generating **[(NN^{TBS})UI$_2$(THF)]$^-$**. This is represented by the wave labeled A in **Figure 4.3**. The THF molecule dissociates, leaving a coordinately unsaturated trivalent uranium center in the form **[(NN^{TBS})UI$_2$]$^-$**, which undergoes dimerization to form a dinuclear complex whereby two tetravalent uranium centers, coordinated to one iodide and 1,1'-ferrocene diamide, are bridged by two iodide ligands. The wave labeled B in **Figure 4.3** represents the reduction of this dimer, yielding a mixed-valent anionic species **[(NN^{TBS})IUI)$_2$]$^-$**, from which one terminal iodide on each uranium dissociates, leaving two coordinately unsaturated U^{3+} centers each supported by H_2NN^{TBS} and bridged by two iodide ligands. Subsequent oxidation of one U^{3+} center in this neutral dinuclear complex, **[(NN^{TBS})UI]$_2$**, is represented by the wave labeled C in **Figure 4.3**. In the resulting mixed-valent species undergoes uranium-iodide bond formation when an iodide ligand in the vicinity coordinates to U^{4+}. Either simultaneously or subsequently, a THF molecule coordinates to the trivalent uranium center. The resulting asymmetric dinuclear species decomposes into **(NN^{TBS})UI(THF)** and **(NN^{TBS})UI$_2$**, both of which form the original 1,1'-diamidoferrocene uranium diiodide complex via different pathways. Specifically, oxidation (wave D in **Figure 4.3**) of **(NN^{TBS})UI(THF)** generates a cationic tetravalent uranium complex, which coordinates an iodide ligand to form the original 1,1'-diamidoferrocene uranium diiodide complex. The other component, namely **(NN^{TBS})UI$_2$**, merely coordinates a THF molecule to produce the same result. We emphasize that more thorough investigations are required in order to distinguish between concerted and step-wise pathways of electrochemical (i.e. electron transfer) and chemical (i.e. ligand dissociation, dimerization, bond formation) reactions.

Scheme 4.2. Proposed mechanism of reduction of uranium in **(NN^{TBS})UI$_2$(THF)**.

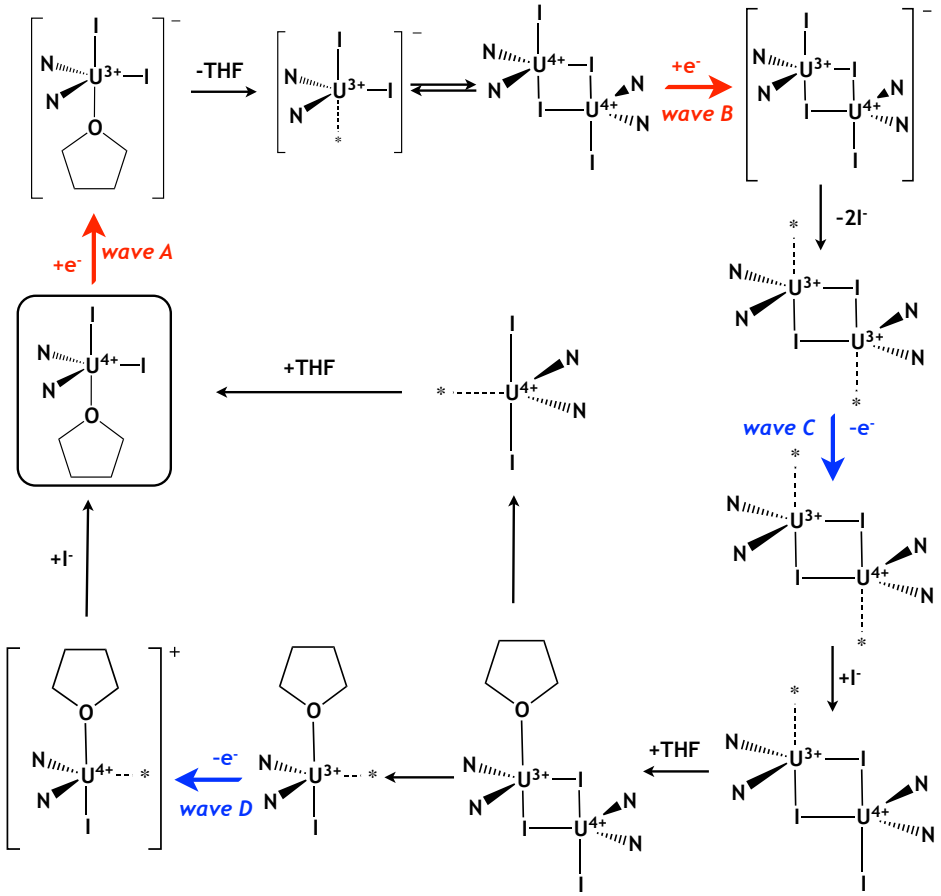

The unremarkable anodic profile of **(NN^{MES})UI$_2$(THF)** reveals one reversible oxidation at approximately 0 V (**Figure 4.1**). Complexes bearing silylamido substituents on the ferrocene ligand exhibit a similar, albeit a quasi-reversible, oxidative event approximately 0 V. In contrast to **(NN^{MES})UI$_2$(THF)**, their anodic profiles feature an additional oxidation event between 0.70 V and 0.90 V. Moreover, two relatively small waves are observed at approximately -0.40 V (**Figure 4.1**) and are likely due to oxidation of the dissociated iodide ligand[21, 22] as discussed previously.

We attribute the first principal anodic event at 0 V to oxidation of iron on the basis that trivalent iron is more stable than pentavalent uranium, whose existence is seldom reported in literature as a result of its susceptibility to disproportionation[23-25] and overall notorious lack of stability.[26] This assignment is also made by comparison to uranium dihalide

complexes supported by pentamethylcyclopentadienyl ligands, which do not undergo uranium-based oxidation processes within the electrochemical window limited by oxidation of the supporting medium. Finally, this assignment is consistent with the greater difficulty of iron oxidation relative to that in ferrocene diamines. In the latter, the oxidation potential is shifted to more negative values due to the electron-donating nitrogen substituents. Naturally, the extent of electron donation to iron decreases in uranium complexes because charge density is divided between two metals. Consequently, the iron center becomes more difficult to oxidize.

We ascribe the anodic event observed between 0.5 V and 1.0 V to oxidation of uranium. Our reasoning is based on the observation that electron-donation ability of ferrocene-based ligands is strong enough to destabilize the trivalent state (i.e. more negative reduction potential values) and at the same time, stabilize the pentavalent state of uranium (i.e. less positive oxidation potential values). The wave representing this oxidation exhibits a non-Nernstian shape (**Figure 4.7**). Regardless of the scan rate, no current is generated on reversal of the potential sweep, indicating that the lifetime of this doubly oxidized species (i.e. Fe^{3+} U^{5+}) is expectedly small on the voltammetric time scale. Finally, assignment of this oxidative event has precedent. Morris, et al. reported that tetravalent pentamethylcyclopentadienyl uranium complexes bearing strongly electron-donating nitrogen ligands, such as imides, hydrazonates, and ketimides, display distinct uranium-based oxidation events at similar values.[5]

Because it exhibit the most intricate electrochemical profile, the following discussion will focus on the underlying mechanism of the anodic events in **(NN^{DMP})UI_2(THF)**. Applying positive potential to **(NN^{DMP})UI_2(THF)** complexes in a THF solution of $TPABAr^F$ reveals two small events, which we attribute to a two-electron oxidation of the dissociated iodide ligands.[21, 22, 27, 28] These then are followed by two successive oxidations at 0 V and 0.8 V (A and

B in **Figure 4.7**) attributed to iron and uranium, respectively. The electrochemical behavior represented by this process depends on the switching potential. If the applied potential is switched immediately after iron is oxidized (between waves A and B in **Figure 4.7**), the event appears quasi-reversible as judged by the cathodic peak current (wave D in **Figure 4.7**). However, when the potential is swept an extra 400 mV in the same direction, a second, totally irreversible oxidation is evident (wave B in **Figure 4.7**). This in turn affects the first principal wave D as is apparent from the increase in the current generated during the reverse scan (labeled D' in **Figure 4.7**).

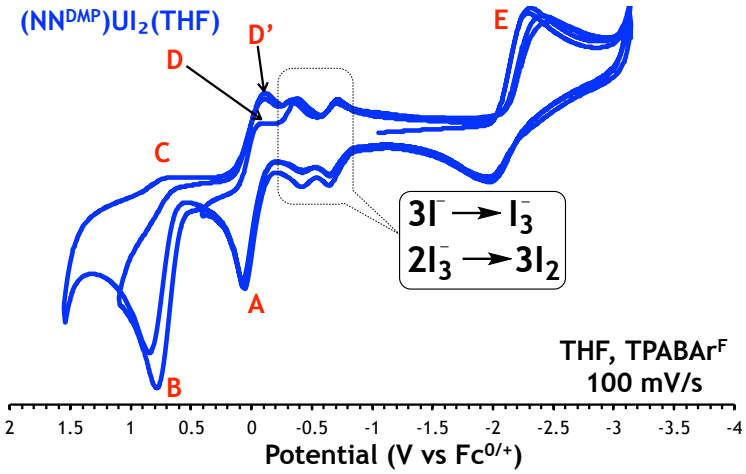

Figure 4.7. Effect of anodic switching potential on reduction of **$(NN^{DMP})UI_2(THF)$**.

We propose the following mechanism to account for our observations (**Scheme 4.3**). First, ligand-based oxidation generates a cationic [$Fe^{3+}U^{4+}$] complex (wave A in **Figure 4.7**), which is stable enough to be observed at high scan rates if the potential is switched before the second oxidation occurs. At more positive potentials, a uranium-based oxidation generates an unstable [$Fe^{3+}U^{5+}$] dication (wave B in **Figure 4.7**). The pentavalent oxidation state of uranium is stabilized by the ferrocene ligands bearing electron-donating substituents. In particular, as shown in **Figure 4.1**, this oxidation event is most reversible for NN^{TBS} and least reversible for NN^{TMS} analogues. In fact, this oxidation state is not accessible at all for the

complex with least electron-donating groups on the nitrogen substituent on ferrocene (i.e. mesityl) as deemed by the absence of a second oxidation wave in its voltammogram.

Because no current is generated when the potential is switched (wave C in **Figure 4.7**), we further postulate that the [$Fe^{3+}U^{5+}$] dication rapidly undergoes disproportionation or a secondary chemical reaction. Disproportionation is expected to generate a hexavalent uranium species and the cationic [$Fe^{3+}U^{4+}$] complex at the electrode (**Scheme 4.3**), while the secondary chemical reaction could form a product whose reduction potential coincides with that of the [$Fe^{3+}U^{4+}$] cation. Either process would account for the extra current generated on the reverse sweep at 0 V (wave D' in **Figure 4.7**)

Scheme 4.3. Postulated mechanism for oxidation of **(NN^R)UI_2(THF)**.

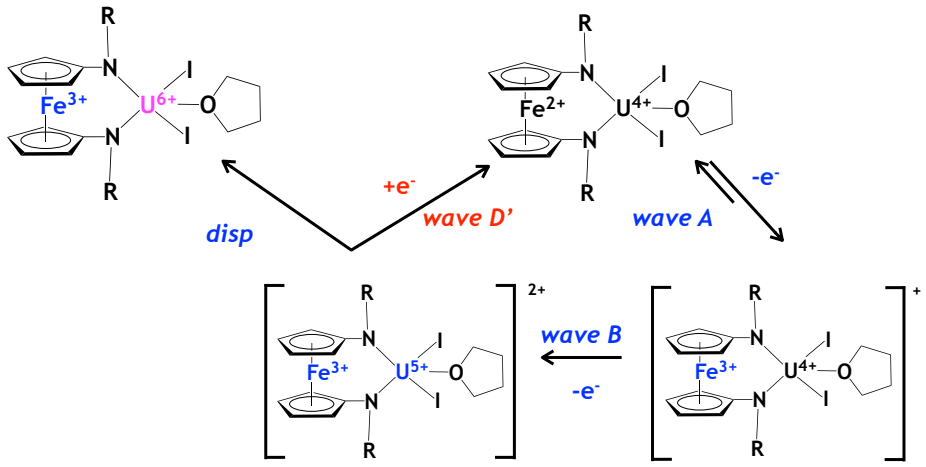

On the basis of previous studies[29-31] as well as our own, we cautiously propose that the [$Fe^{3+}U^{5+}$] dication most likely undergoes disproportionation to regenerate the [$Fe^{3+}U^{4+}$] cation and an even less stable hexavalent uranium species. The former is evident from the increased current at its formal reduction potential (wave D' in **Figure 4.7**), while effect of the latter is revealed at the principal reductive event at –2.18 V (wave E). Specifically, the reduction potential peaks at more negative values, suggesting that the rate of electron transfer from the working electrode decreases. Such a lower rate constant, in turn, is indicative of a low

concentration of U^{4+} at the electrode surface relative to when the second oxidation was not induced (i.e. potential was switched before second oxidation could take place).[25, 32, 33]

4.2.2 Uranium Bis(Aryloxide) Complexes, $(NN^R)U(OAr)_2$

Unlike its diiodide analogue, uranium bis(aryloxide) supported by one H_2NN^{DMP} ligand features two clean redox events (**Figure 4.8**). Reduction of uranium is reversible and occurs at a slightly more negative potential (-2.4 V) than that in $(NN^{DMP})UI_2(THF)$ measured in the same medium (-2.2 V). In other words, the reduction of uranium becomes more difficult when I^- is replaced by ArO^-. This is consistent with the electronic nature of iodide and aryloxide ligands.[42] Similar effects have been observed with a series of titanium complexes upon sequential substitution of aryloxide with chloride ligands.[43] Moreover, because the aryloxide ligands are less likely to dissociate and undergo side reactions, the reduction of uranium is both chemically and electrochemically reversible.

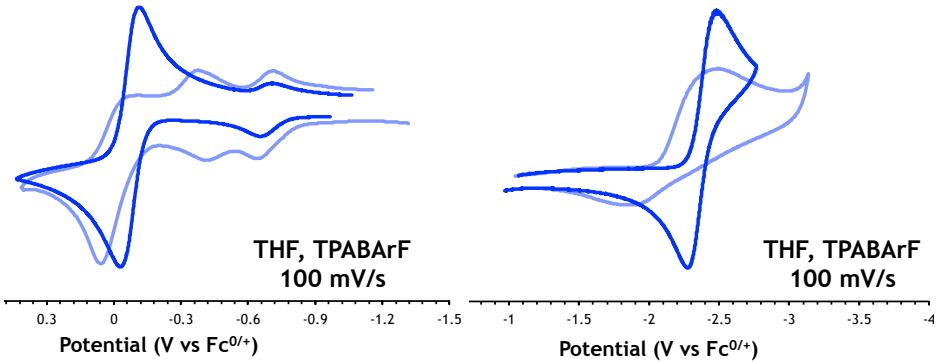

Figure 4.8. Comparison of uranium oxidation (left) and reduction (right) in $(NN^{DMP})UI_2(THF)$ and $(NN^{DMP})U(OAr)_2$.

As shown in **Figure 4.8**, $(NN^{DMP})U(OAr)_2$ exhibits a single reversible anodic event –0.07 V. On the basis of oxidation product stability, we attribute this event to oxidation of iron. Additionally, there is no change in the magnitude of the oxidation potential on going from $(NN^{DMP})UI_2(THF)$ to $(NN^{DMP})U(OAr)_2$. Accordingly, this wave cannot correspond to oxidation of uranium, which would be expected to form the pentavalent species at more positive

potentials. Moreover, addition of iodine to a THF solution of **$(NN^{DMP})U(OAr)_2$** reveals a broad band in the visible-near IR region characteristic of charge transfer from Cp ligand to Fe^{3+} (see Appendix D for details).

Relative to **H_2NN^{DMP}**, the iron center in **$(NN^{DMP})U(OAr)_2$** is harder to oxidize by approximately 700 mV. The simplest explanation for this observation again is connected to the relative distribution of electrons that the amine substituents donate. That is, the electron density that helped to stabilize the positive charge on iron in the free oxidized ligand, is now shared between two metal centers in **$(NN^{DMP})U(OAr)_2$**. Such distribution, therefore, lowers the electron density on iron, making it harder to oxidize (oxidation potential is more positive). At the same time, the electron density on uranium increases, making it harder to reduce. Indeed, the reduction potential of unsupported tetravalent uranium, **$UI_4(Et_2O)_2$**, is more than 1 V lower than that of uranium(IV) supported by diamidoferrocene ligands.

4.2.3 Uranium dibenzyl complexes, $(NN^R)U(CH_2Ph)_2$

Electrochemical measurements of uranium dibenzyl complexes supported by diamidoferrocene ligands were conducted in trifluorotoluene and diethyl ether separately with $TPABAr^F$ as the supporting electrolyte. Although tetravalent uranium alkyl complexes have been shown to activate carbon-fluorine bonds of perfluorocarbons,[34] we note that ^1H NMR spectra of all **$(NN^R)U(CH_2Ph)_2$** complexes after electrochemical experiments were conducted showed no decomposition. It is therefore safe to conclude that neutral tetravalent uranium dibenzyl complexes do not react with perfluorinated substrates.

Attempts to conduct voltammetric experiments in other solvents capable of dissolving both the supporting electrolyte and uranium dibenzyl complexes have been unsuccessful. Specifically, the former is insoluble in toluene and hydrocarbons, while the latter decomposes in coordinating solvents such as THF. Experiments conducted in diethyl ether exhibit anodic waves that could not be interpreted. The coordination ability of diethyl ether is the most

likely culprit because similar voltammetric behavior is observed upon addition of THF during the measurements in trifluorotoluene.

As shown in **Figure 4.9**, **$(NN^{TMS})U(CH_2Ph)_2$**, **$(NN^{TBS})U(CH_2Ph)_2$**, and **$(NN^{DMP})U(CH_2Ph)_2$** exhibit one reduction event between -2.7 V and -3.0 V. No current is generated on the reverse scan, suggesting that the reduction products are unstable on the measurement time scale and are consumed by chemical reactions. Increasing the scan rate reveals no change in the overall wave shapes, suggesting that the half-lives of these follow-up reactions are considerably lower than the duration of the scan.[35, 36] Furthermore, in accordance with the observations noted for uranium diiodide complexes supported by 1,1'-ferrocenediamide ligands, dibenzyl analogues require greater reduction potentials than those supported by pentamethylcyclopentadienyl ligands. In fact, uranium in **$(C_5Me_5)U(CH_2Ph)_2$** undergoes reduction at -1.95 V.[5]

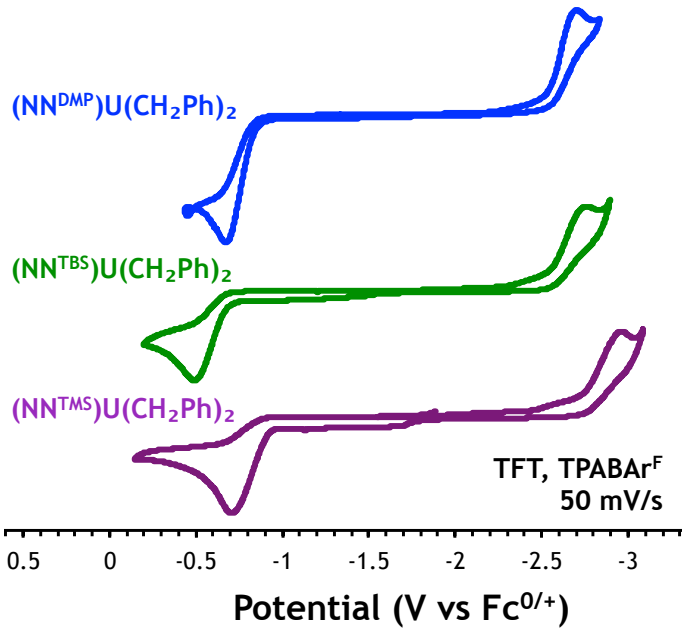

Figure 4.9. Cyclic voltammograms of **$(NN^R)U(CH_2Ph)_2$**.

The overall electrochemical profiles of **$(NN^R)U(CH_2Ph)_2$** complexes are dependent on the direction and switching of the applied potential. The following discussion focuses on the

electrochemical behavior of **(NN^{TMS})U(CH$_2$Ph)$_2$**. Moreover, we use previous studies of dialkyl complexes of group IV metal and actinides,[37-40] diarylalkanes,[41-45] as well as alkyl and aryl halides,[43, 46-51] to propose the most likely redox mechanism.

Scanning in the negative direction, uranium is reduced at approximately -2.85 V (wave A in **Figure 4.10**). Reversing the scan direction then generates two small oxidative events at -2.32 V (wave B in **Figure 4.10**) and -1.68 V (wave C in **Figure 4.10**) on the reverse sweep. As shown in **Scheme 4.4**, we propose that electron transfer from the working electrode to **(NN^{TMS})U(CH$_2$Ph)$_2$** generates a radical anion, [**(NN^{TMS})U(CH$_2$Ph)$_2$**]$^-$, which undergoes uranium-carbon bond cleavage. Either simultaneously or sequentially, elimination of a benzyl radical yields a trivalent uranium benzyl dianion, which in turn, is expected be a strong enough reductant to cleave a carbon-fluorine bond of trifluorotoluene in an overall two-electron process. That is, the first electron transfer from uranium generates a trifluorotoluene radical anion, which undergoes fragmentation to a neutral difluorotoluene radical and a fluoride anion. The latter forms a bond with the uranium center and reduces the former to an anion, which is in turn subject to protonolysis. The postulated redox mechanism is plausible because reduction of trifluorotoluene has been reported to occur at -3.0 V versus ferrocene in non-aqueous media.[52, 53] In fact, in our hands, the electrochemical window of trifluorotoluene with TPABAr^F as the supporting electrolyte was +0.50 V to –3.0 V. Moreover, such reactivity with perfluorocarbons finds precedent in low-valent metal alkyl complexes of early transition metals,[54-56] lanthanide[57] and actinides.[34, 58]

Depending on the rate of reduction, in principle, the benzyl radical can be further reduced or oxidized or undergo radical-radical coupling.[59] The benzyl radical will be further reduced if its reduction potential is more positive than that of **(NN^R)U(CH$_2$Ph)$_2$**. This can occur either at the electrode or by the anionic uranium(III) benzyl species.[60-63] The resulting

anion is both sufficiently basic to undergo protonation and generate toluene[64] and nucleophilic enough to react with the electrolyte cation.[65]

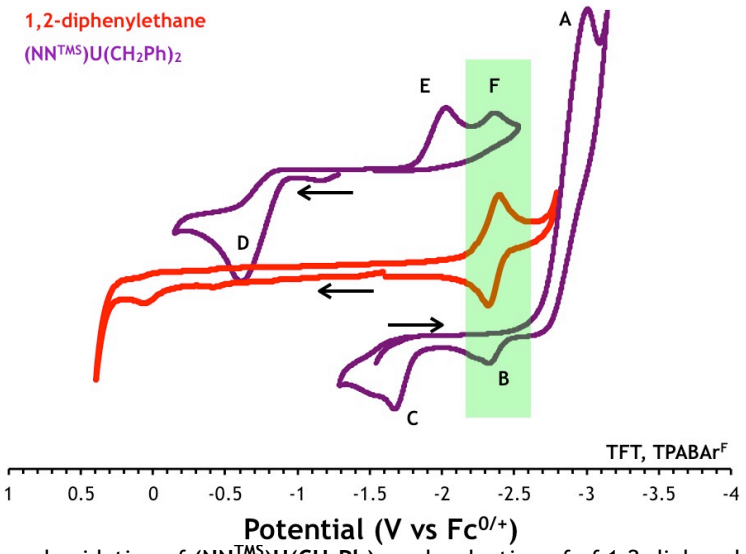

Figure 4.10. Reduction and oxidation of $(NN^{TMS})U(CH_2Ph)_2$ and reduction of of 1,2-diphenylethane.

Scheme 4.4. Proposed mechanism for reduction of $(NN^{R})U(CH_2Ph)_2$.

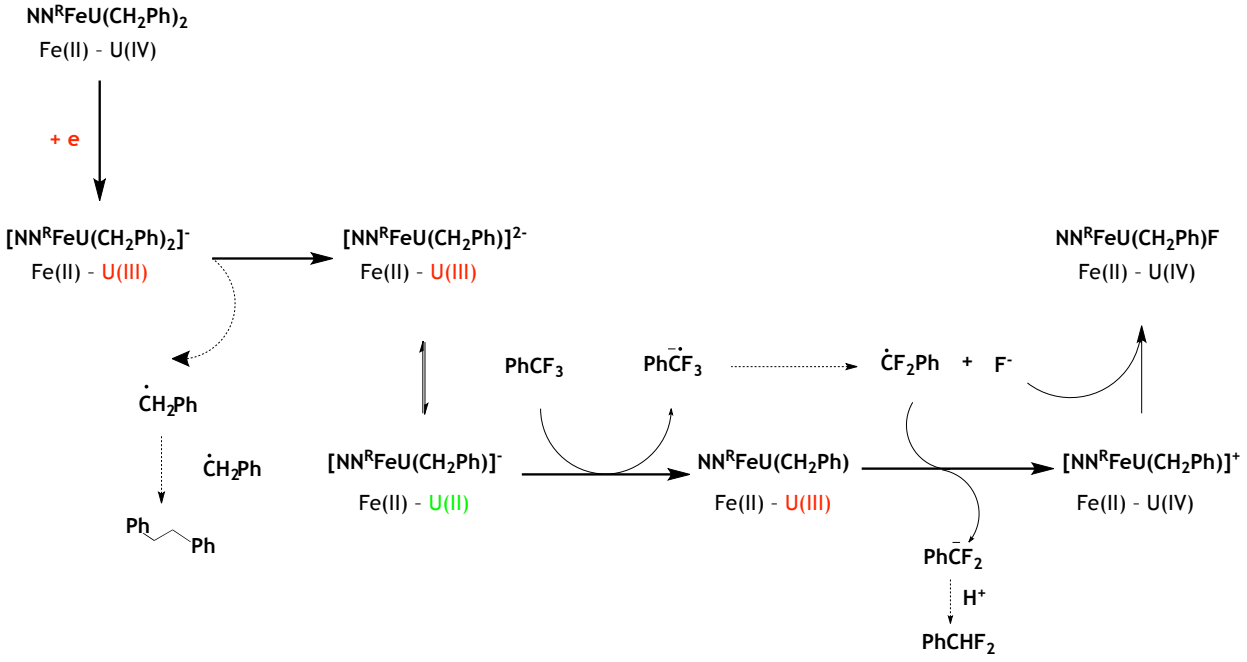

Because it is stable enough on voltammetric time scale,[43, 46, 48, 66] the benzyl radical can also dimerize to form 1,2-diphenylethane,[67] whose own redox behavior can trigger a variety of other reactions. As shown in **Figure 4.10**, comparison of the electrochemical

profile of **(NN^{TMS})U(CH$_2$Ph)$_2$** with that of 1,2-diphenylethane under the same conditions shows that the benzyl radical does indeed undergo radical-radical coupling. Consequently, this allows us to attribute the anodic event at -2.32 V to 1,2-diphenylethane (wave B in **Figure 4.10**).

Exact assignment of the anodic event observed at -1.68 V (wave C in **Figure 4.10**), however, is more difficult. It is clearly due to an electroactive species formed as a result of reduction at -2.99 V. Although this oxidation (wave C in **Figure 4.11**) is inherently irreversible, it is also affected by the positive switching potential. It can be seen from **Figure 4.11** that increasing the positive potential (to wave D in **Figure 4.11**) generates a reductive event at approximately -2.03 V (wave E in **Figure 4.11**) on the reverse scan.

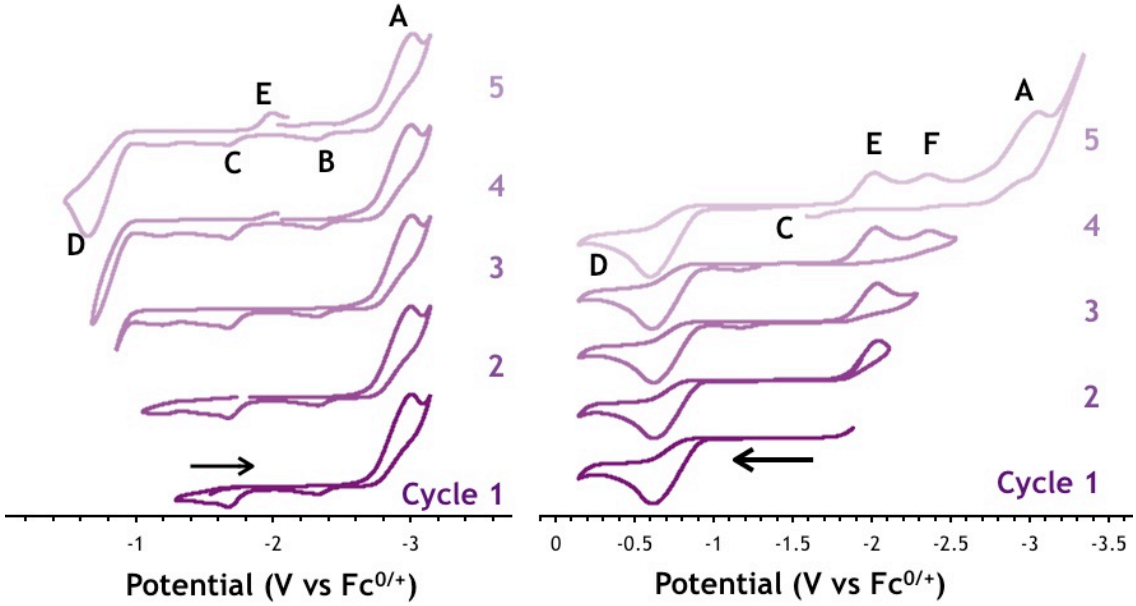

Figure 4.11. Effect of switching potential on reduction (left) and oxidation (right) of **(NN^{TMS})U(CH$_2$Ph)$_2$** in TFT with TPABAr^F as the supporting electrolyte.

The first oxidation process in **(NN^{TMS})U(CH$_2$Ph)$_2$** occurs at approximately -0.72 V (wave D in **Figure 4.11**). On the reverse scan, two reductive events at -2.03 V and -2.36 V are observed (E and F in **Figure 4.11**). The latter is attributed to reduction of 1,2-diphenylethane (bibenzyl) that generates a radical anion, which can undergo dimerization,

disproportionation, fragmentation, or protonation.[68] Bibenzyl formation is a clear indication that oxidation of uranium dialkyl complexes proceeds via a radical mechanism.

As shown in **Figure 4.12**, adding a drop of THF to the TFT solution of **$(NN^{TMS})U(CH_2Ph)_2$** and $TPABAr^F$ slightly shifts the oxidation potential to more positive values and a third oxidation event becomes apparent at approximately 0 V. Interestingly, we also observe splitting of this wave when the potential is applied at a very low scan rate (**Figure 4.12**). This is consistent with two successive, irreversible, one-electron processes (wave D in **Figure 4.11**).

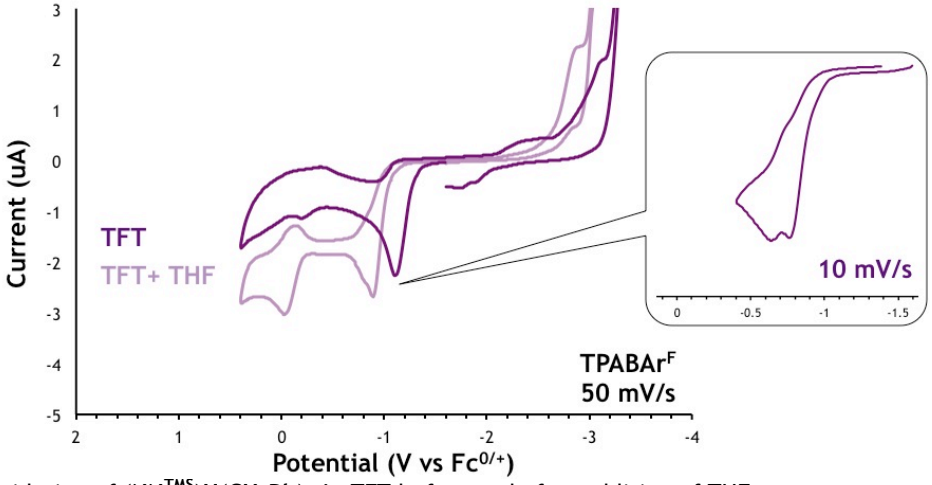

Figure 4.12. Oxidation of **$(NN^{TMS})U(CH_2Ph)_2$** in TFT before and after addition of THF.

Taken together, these results enable us to propose a mechanism involving oxidatively induced reductive elimination of both alkyl ligands. **Scheme 4.5** shows the proposed mechanism involving initial oxidation of iron, equilibration of redox states (i.e. $[Fe^{3+}U^{3+}] = [Fe^{2+}U^{4+}]$) concomitant with or followed by dissociation of a benzyl radical, and coordination of THF before the second electron is removed from a uranium-based orbital.

We propose that the splitting of the first oxidation wave at very low scan rates in presence of THF is due to oxidation of the benzyl radical immediately upon metal-carbon cleavage. The resulting benzyl cation is more reactive than the triphenylmethyl radical,[69, 70] and is expected to react with fluoro-substituted tetraarylborate electrolyte anion. Indeed, at

low scan rates and in presence of THF, the cathodic event corresponding to reduction of bibenzyl is not observed. This attests to the critical role of coordinating solvent in the oxidative pathway and fate of uranium dibenzyl complexes. Further oxidation of the resulting uranium benzyl cation at approximately 0 V generates a uranium alkyl dication, from which a second benzyl radical is ejected. Coordination of THF is stabilizing enough to allow isolation of a dicationic Fe^{2+}-U^{4+} species as a tetraphenylborate salt (**Figure 4.13**).

Scheme 4.5. Proposed mechanistic pathway for oxidation of $(NN^R)U(CH_2Ph)_2$ complexes.

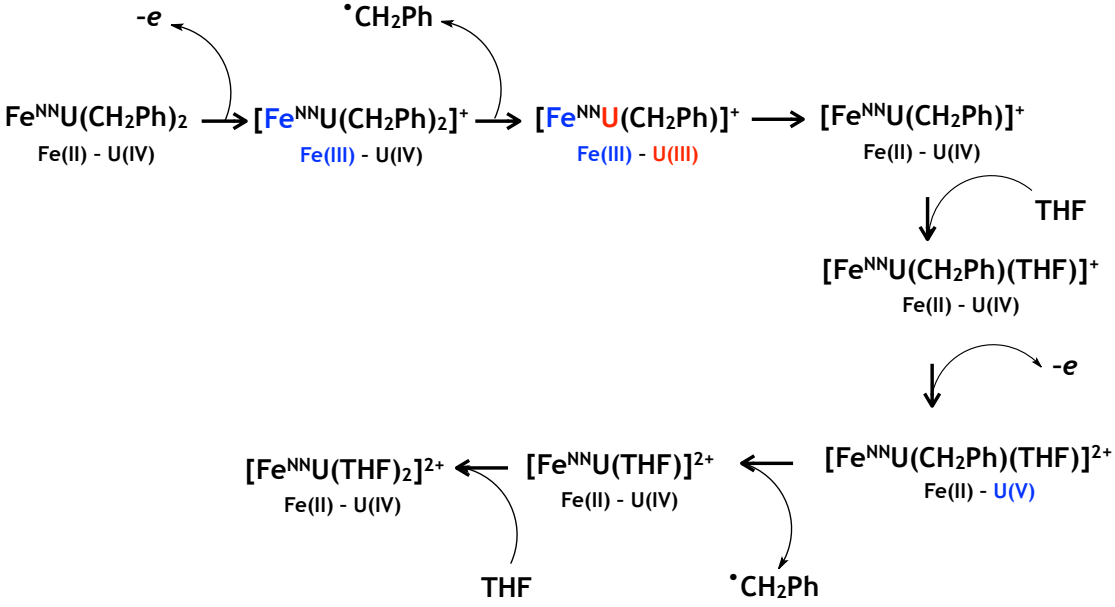

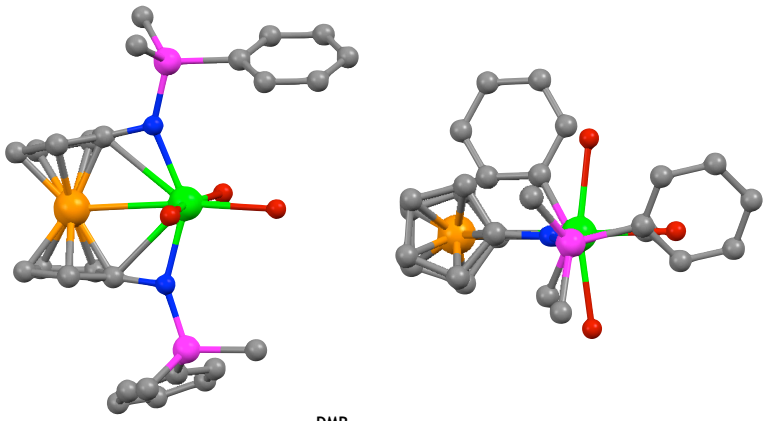

Figure 4.13. Ball-and-stick representation of $[(NN^{DMP})U(THF)_3][BPh_4]_2$ molecular structure. For clarity, hydrogen atoms and CH_2 units of THF ligands are not shown.

4.2.4 Uranium bis(amide) complexes, $(NN^{R})U(NPh_2)_2$

At a glance, the overall electrochemical profile of uranium bis(amide) complexes supported by ferrocene-based ligands appears simple (**Figure 4.14**). $(NN^{TBS})U(NPh_2)_2$ and $(NN^{DMP})U(NPh_2)_2$ undergo one oxidation and one reduction event at -0.20 and -2.40 V, respectively. The latter is assigned to reduction of uranium.

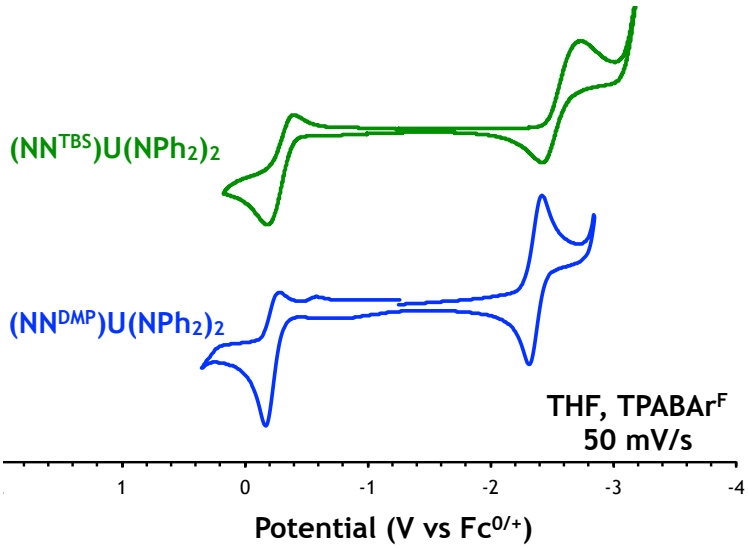

Figure 4.14. Cyclic voltammograms of $(NN^{TBS})U(NPh_2)_2$ and $(NN^{DMP})U(NPh_2)_2$.

When the rate of applied potential is varied, it quickly becomes obvious that the oxidative process is marked by something more than a simple electron transfer at the electrode. As shown in **Figure 4.15** for $(NN^{DMP})U(NPh_2)_2$, when the direction of the potential is reversed after oxidation is achieved (wave A in **Figure 4.15**), the peak potential (wave B in **Figure 4.15**) increases with scan rate. This is characteristic of an "EC" mechanism, whereby electron transfer is coupled to a chemical reaction and gain or loss of an electron activates the complex towards bond cleavage.[71] In case of $(NN^{DMP})U(NPh_2)_2$, the oxidative event appears fully reversible when the potential is scanned at 1000 mV but totally irreversible at 10 mV. In other words, with 1000 mV/s, the chemical reaction that destroys the generated cation can essential be outrun. Similar electrochemical behavior has been observed in tricyclopentadienyl uranium chloride. The authors of the study proposed that oxidation of

$(MeCp_3)UCl$ results in a cationic pentavalent uranium species, $[(MeCp)_3UCl]^+$, which undergoes disproportionation, regenerating $(MeCp_3)UCl$ with simultaneous formation of $[(MeCp)_3UCl]^{2+}$.

A crucial difference between the behavior of $(MeCp_3)UCl$ and $\mathbf{(NN^{DMP})U(NPh_2)_2}$ exists, however. In the present case, when the potential is slowly scanned over two or more cycles, a new reduction event becomes apparent at -2 V (wave C in **Figure 4.15**). Whereas simultaneous disproportionation of $[(MeCp_3)UCl]^+$ regenerates the neutral complex, the chemical reaction coupled to the oxidation of $\mathbf{(NN^{DMP})U(NPh_2)_2}$ generates a species that itself is redox active and slightly easier to reduce than the original complex. Moreover, as shown in **Figure 4.16**, reduction of the generated species is reversible.

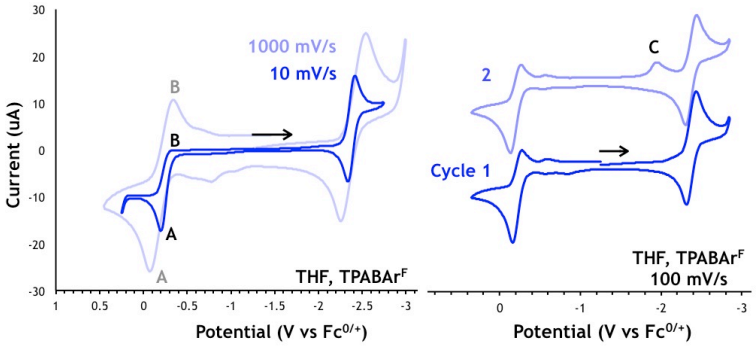

Figure 4.15. Scan rate effect on oxidation of $\mathbf{(NN^{DMP})U(NPh_2)_2}$ and cathodic evidence of coupled chemical reaction.

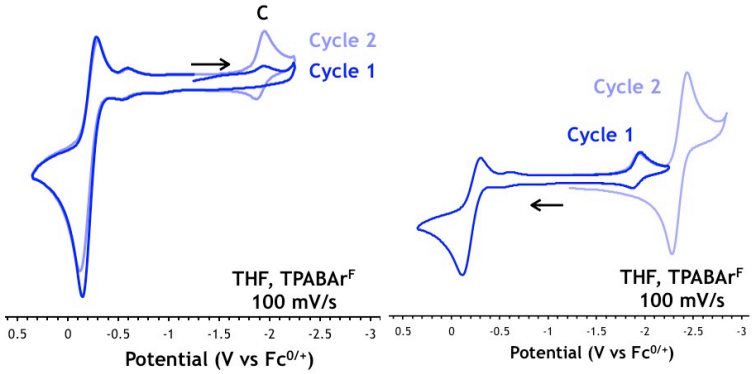

Figure 4.16. Reversible redox chemistry of species formed from decomposition of oxidation product.

Since the irreversible behavior of the main oxidation event does not appear to affect the reduction of uranium, we propose that it is iron-based. Furthermore, when the potential is scanned to more positive values, two additional irreversible oxidations are observed (D and

E in **Figure 4.17**). As shown in **Figure 4.17**, the reduction event disappears completely as a result of these oxidations. Therefore, we propose that the second and third oxidation events are uranium based ($U^{4+} \rightarrow U^{5+} \rightarrow U^{6+}$). This assignment is plausible because in the present case, uranium is coordinated to four amide ligands (**NN^{DMP}** and **NPh$_2$**), which are strong enough electron donors to allow access to its high oxidation states.

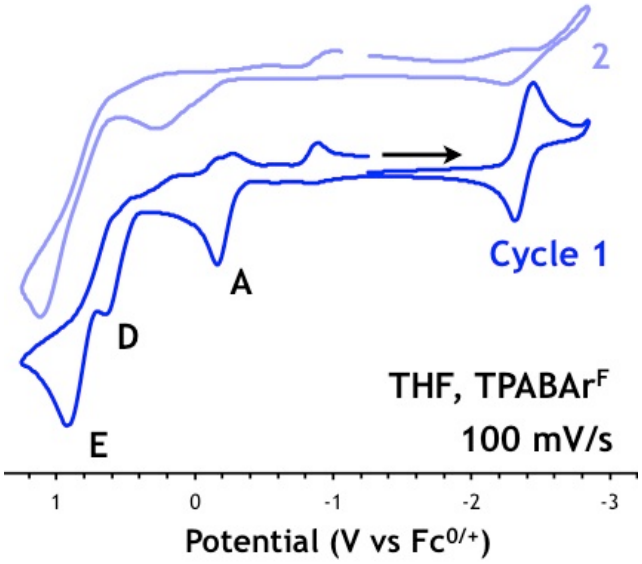

Figure 4.17. Successive one-electron oxidations of uranium in **(NN^{DMP})U(NPh$_2$)$_2$.**

*4.2.5 Uranium aryloxide iodide complexes, **(NN^R)UI(OAr)***

Cyclic voltammograms of mixed aryloxide iodide uranium complexes supported by H_2NN^{TBS} and H_2NN^{MES} ligands feature one uranium-based reductive event at approximately -2.2 V (**Figure 4.18**). Within the smallest potential range required for complete electron transfer, the reduction of uranium is electrochemically reversible. However, as shown in **Figure 4.19** for **(NN^{TBS})UI(OAr)**, applying more negative potential results in both a loss of current on the reverse sweep as well as appearance of waves corresponding to oxidation of iodide.

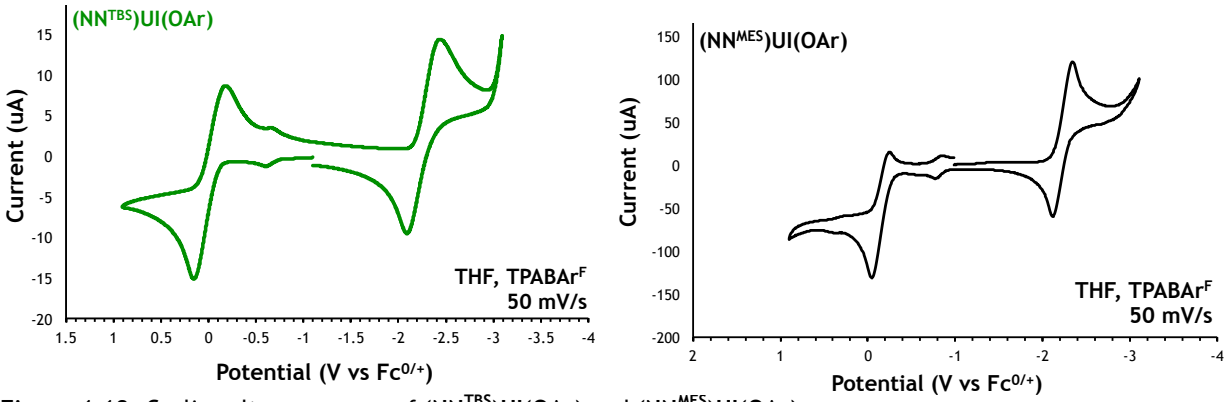

Figure 4.18. Cyclic voltammograms of **(NN^{TBS})UI(OAr)** and **(NN^{MES})UI(OAr)**.

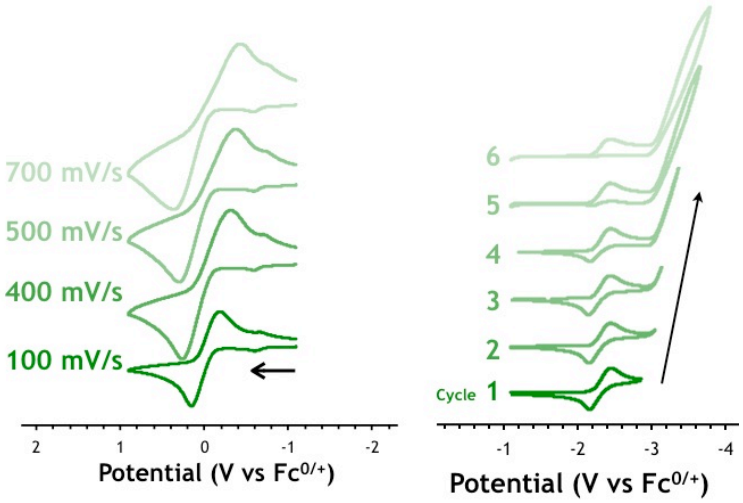

Figure 4.19. Effect of scan rate and negative switching potential on oxidation and reduction of **(NN^{TBS})UI(OAr)**, respectively.

These observations are characteristic of an electrochemical mechanism in which the electron transfer at the electrode is reversible but subsequently coupled to an irreversible chemical reaction. More specifically, addition of an electron only *activates* the uranium-iodide bond. This is in contrast to the behavior observed for **(NN^{TBS})UI$_2$(THF)**, in which the uranium-iodide bond is reversibly cleaved upon reduction. When enough potential is applied to rupture that bond, however, the subsequent chemical reaction is faster than re-oxidation at the electrode and the resulting "**(NN^{TBS})UOAr**" species instantly decomposes in THF. The proposed mechanism is shown in **Scheme 4.4**.

Scheme 4.6. Proposed mechanism for reduction of **(NN^{R})UIOAr**.

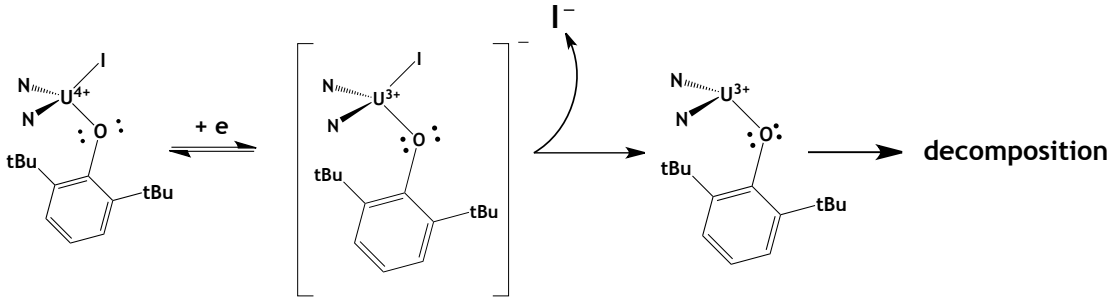

In contrast to their reduction, the oxidation of **(NN^{R})UIOAr** occurs at different potentials. Specifically, the NN^{TBS} and NN^{MES} analogues are oxidized at 0 V and –0.14 V, respectively. This process operates by a basic electron transfer mechanism, in which the reversibility of the electron transfer is greatest at slow scan rates and is dependent on the rate of diffusion to and from the electrode.[71] As shown in **Figure 4.19**, the separation of peak potentials increases with scan rate, signifying slow kinetics. At 100 mV/s, the forward and reverse electron transfers occurs almost concurrently (i.e. reversible), while at 700 mV/s, the process becomes quasi-reversible. Finally, as shown in **Figure 4.20**, applying potential beyond what is required for oxidation results in dissociation of the aryloxide anion or radical and decomposition of the generated cationic **[(NN^{TBS})UI(OAr)]$^{+}$**. Although this oxidation event is most likely iron-based, further measurements need to be conducted in order to confidently determine which metal is involved in the oxidation process.

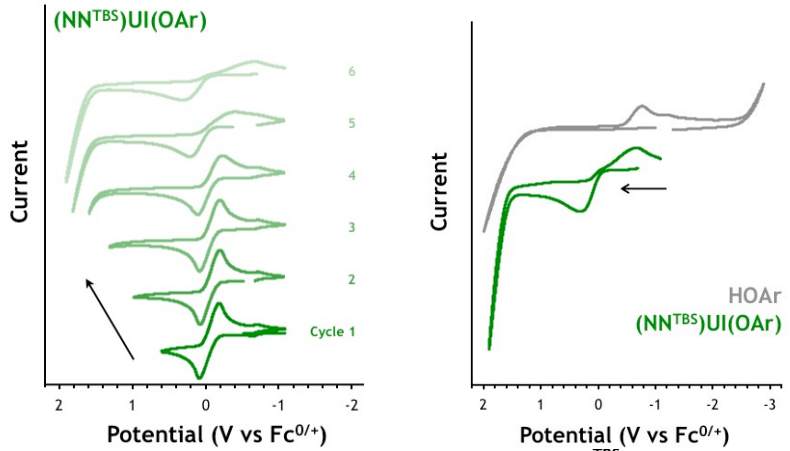

Figure 4.20. Effect of positive switching potential on oxidation in **(NN^{TBS})UI(OAr)** and its decomposition via dissociation of $^{-}$OAr.

4.3 CONCLUSIONS

In conclusion, using cyclic voltammetry, redox chemistry of various 1,1'-ferrocenediamido uranium complexes was brought to light. Specifically, uranium bis(aryloxide) derivatives show simple electrochemical behavior with reversible iron oxidation and uranium reduction events. Uranium diiodides are shown to be susceptible to reversible uranium-iodide bond cleavage upon reduction and postulated to undergo disproportionation upon oxidation. Iodide dissociation also occurs upon reduction of mixed aryloxide-iodide uranium complexes but is irreversible. Uranium dibenzyl complexes undergo irreversible oxidation and reduction events and are prone to loss of benzyl radicals. Coordinating solvent molecules stabilize the resulting cationic species. Finally, a chemical reaction is observed to accompany oxidation of iron in the electron-rich uranium bis(amide) complexes, which can also undergo two successive but irreversible one-electron uranium-based oxidations at more positive potentials.

4.4 APPENDIX D

4.4.1 Synthesis

General Considerations. All experiments were performed under a dry nitrogen atmosphere using standard Schlenk techniques or an MBraun inert-gas glove box. Solvents were purified using a two-column solid-state purification system by the method of Grubbs[72] and transferred to the glovebox without exposure to air. NMR solvents were obtained from Cambridge Isotope Laboratories, degassed, and stored over activated molecular sieves prior to use. ^{1}H and ^{13}C NMR spectra were recorded on Bruker300 or Bruker500 spectrometers at room temperature in C_6D_6 or $CDCl_3$. Chemical shifts are reported with respect to solvent residual peaks, 7.16 ppm (C_6D_6) or 7.26 ($CDCl_3$). Cyclic voltammetry measurements were conducted on a CH Instruments CHI630D potentiostat using a 2-mm platinum disk as the working electrode, 3-mm

glassy carbon disk as the counter electrode, and 0.25-mm silver wire as the pseudo–reference electrode. CHN analyses were performed on an Exeter Analytical, Inc. CE-440 Elemental Analyzer. $Me_2PhSiCl$, Et_3N, KH, 2,6-di-*tert*-butylphenol, $[Bu_4N][I]$, and nBuLi were purchased from Alfa Aesar and used as received. $[Bu_4N][PF_6]$, $[Et_3NH]Br$, and $NaBPh_4$ were purchased from Sigma Aldrich and recrystallized from THF before use. H_2NN^{TBS},[73] H_2NN^{TMS},[74] and H_2NN^{MES},[75] KCH_2Ph,[76] $LiNPh_2$,[77] $TPABAr^F$,[78] $UI_4(1,4\text{-dioxane})_2$,[79] $UI_4(Et_2O)_2$,[8] **$(NN^{TBS})UI_2(THF)$**,[79] **$(NN^{TBS})U(CH_2Ph)_2$**,[20] and **$(NN^{TMS})U(CH_2Ph)_2$**[80] were synthesized following previously published procedures.

Synthesis of potassium 2,6-di-tert-butylphenoxide (KOAr). A hexanes solution of 2,6-di-*tert*-butylphenol was filtered through alumina and stored at –35 °C for 24 h. Pale yellow-green crystals (85 mg, 0.41 mmol, 1 equiv) were dissolved in Et_2O and cooled for 15 min. Solid KCH_2Ph (53 mg, 0.41 mmol, 1 equiv) was added to the stirring solution of the phenol and the reaction mixture was allowed to stir at room temperature for 90 min. The initially bright orange gradually faded to a very light pink color. The resulting suspension was filtered through a medium-porosity frit, and the light pink solid was washed with fresh Et_2O and dried. Yield: 98 mg, 97%.

Synthesis of potassium diphenylamide ($KNPh_2$). In a 20 mL scintillation vial, solid KH (85.2 mg, 2.1 mmol, 1.2 equiv) was added to a cold diethyl ether solution of $HNPh_2$ (302.8 mg, 1.8 mmol, 1 equiv). After the white suspension was allowed to stir for 10 min, it was placed at -40 °C to allow the precipitate to settle. The solvent was decanted, after which the solid was washed with cold diethyl ether and dried under reduced pressure. Yield: 320.7 mg, 86 %.

Synthesis of $[Et_3NH][BPh_4]$. A saturated ethanol solution of $[Et_3NH]Br$ (677 mg, 3.6 mmol, 1.1 equiv) was added to an ethanol solution of $NaBPh_4$ (1.07 g, 3.3 mmol, 1 equiv). White powder precipitated immediately but the solution was allowed to stir at room temperature for 90

min. The solid was collected onto a medium-porosity frit, washed with a mixture of ethanol and water, and then thoroughly dried under reduced pressure. Yield: 1.18 g, 85 %.

Synthesis of (NN^{DMP})UI_2(THF). A slurry of $[K(OEt_2)_2]_2[NN^{DMP}]$ (95 mg, 0.013 mmol, 0.9 equiv) in THF was added to a frozen THF solution of UI_4(1,4-dioxane)$_2$ (137 mg, 0.015 mmol, 1 equiv). The reaction mixture was allowed to stir at room temperature for 1 h. It was then filtered through Celite. The crude product was dried, dissolved in toluene, filtered through Celite, and dried. Yield: 133 mg, 85 %. **(NN^{DMP})UI_2(THF)** is insoluble in hexanes, n-pentane, diethyl ether, slightly soluble in toluene, and completely soluble in THF and DCM.

Synthesis of (NN^{MES})UI_2(THF). A slurry of $[K(OEt_2)_2]_2NN^{MES}$ (420 mg, 0.610 mmol, 0.9 equiv) in THF was added to a frozen THF solution of UI_4(1,4-dioxane)$_2$ (636 mg, 0.677 mmol, 1 equiv). The reaction mixture was allowed to stir at room temperature for 2 h. The solution was filtered through a medium-porosity frit. The pale yellow solid remaining on the frit was washed with hexanes, diethyl ether, and toluene, and then dried under reduced pressure. Yield: 562 mg, 82%. **(NN^{MES})UI_2(THF)** is sparingly soluble in THF and halogenated solvents. It turns dark orange when dissolved in CH_2Cl_2 or $CDCl_3$.

Synthesis of (NN^{DMP})$U(CH_2Ph)_2$. A toluene slurry of KCH_2Ph (42.7 mg, 0.33 mmol, 2.1 equiv) was added to a cold toluene solution of **(NN^{DMP})UI_2(THF)** (163.9 mg, 0.16 mmol, 1 equiv). After 75 min of stirring at room temperature, the solution was filtered through Celite and toluene was removed under reduced pressure. The product was extracted into hexanes. Yield: 128.6 mg, 89%. **(NN^{DMP})$U(CH_2Ph)_2$** is soluble in all common organic solvents. Its stability in THF and halogenated solvents was untested.

Synthesis of [(NN^{DMP})$U(THF)_3$][BPh_4]$_2$. Solid $[Et_3NH][BPh_4]$ (52.8 mg, 0.13 mmol, 1 equiv) was added to a toluene solution of **(NN^{DMP})$U(CH_2Ph)_2$** (117.9 mg, 0.13 mmol, 1 equiv). The

reaction mixture was stirred at room temperature for 2 h, filtered through Celite, and dried under reduced pressure. The crude solid was washed with diethyl ether and the product extracted into THF. Crystals formed from a dilute solution at room temperature after several hours. Yield: trace.

Synthesis of $(NN^{DMP})U(OAr)_2$. A THF solution of KOAr (73 mg, 0.3 mmol, 1.5 equiv) was added to a THF solution of **$(NN^{DMP})UI_2(THF)$** (207.9 mg, 0.2 mmol, 1 equiv). The clear dark orange solution became cloudy while stirring at room temperature. After 1 h, the reaction mixture was filtered through Celite, the crude solid washed with hexanes, and extracted into diethyl ether. Yield: 180.4 mg, 51%. Dark red crystals formed from Et_2O at -40 ºC.

Synthesis of $(NN^{TMS})U(OAr)_2$. A THF solution of KOAr (60 mg, 0.24 mmol, 1.5 equiv) was added to a cold THF solution of **$(NN^{TMS})UI_2(THF)$** (146.6 mg, 0.16 mmol, 1 equiv). While stirring at room temperature, the reaction mixture became increasingly cloudy. It was filtered through Celite after 3 h, and then dried. The product was extracted into hexanes and filtered through Celite twice. Yield: 128.8 mg, 79%.

Synthesis of $(NN^{TBS})UIOAr$. **$(NN^{TBS})UI_2(THF)$** (165 mg, 0.16 mmol, 1 equiv) was dissolved in THF and solid KOAr (45 mg, 0.19 mmol, 1.5 equiv) was added. The solution became cloudy after 15 minutes of stirring at room temperature. The mixture was filtered through Celite after an additional 45 minutes and dried under reduced pressure. The product was extracted into hexanes, filtered through Celite, and dried. Yield = 155 mg, 94 0%. Dark red rectangular crystals formed at -40 ºC after 1 h. Upon addition of one equivalent of KCH_2Ph, formation of **$(NN^{TBS})U(OAr)(CH_2Ph)$**[81] was detected by ^1H NMR.

Synthesis of $(NN^{TBS})U(NPh_2)_2$. At room temperature, a THF solution of $LiNPh_2$ (14.2 mg, 0.07 mmol, 2 equiv) was slowly added to a stirring THF solution of **$(NN^{TBS})UI_2(THF)$** (37.3 mg, 0.03

mmol, 1 equiv). The reaction mixture was allowed to stir at room temperature. After 30 min, the solvent was removed under reduced pressure to yield red-brown oil. The product was extracted into hexanes, filtered, and dried. Finally, it was washed with cold n-pentane, and dried. Yield: 33.2 mg, 98 %. **$(NN^{TBS})U(NPh_2)_2$ is** soluble in hexanes and n-pentane, but soluble in diethyl ether, toluene, and THF.

Synthesis of $(NN^{DMP})U(NPh_2)_2$. At room temperature, a THF solution of $KNPh_2$ (56 mg, 0.27 mmol, 2.1 equiv) was added to a stirring THF solution of **$(NN^{DMP})UI_2(THF)$** (134.6 mg, 0.13 mmol, 1 equiv). After several seconds, white solid precipitated. After stirring for 15 min, the reaction mixture was filtered through Celite and dried under reduced pressure. The crude solid was washed with hexanes and the product extracted into diethyl ether. The dark yellow solution was concentrated and store at -40 °C. Dark block crystals formed after 12 h. Yield = 74.4 mg, 54%. **$(NN^{DMP})U(NPh_2)_2$** is insoluble in hexanes and n-pentane, but soluble in diethyl ether, toluene, and THF. Neither its solubility nor stability in halogenated solvents was determined.

4.4.2 Elemental analysis

$(NN^{DMP})U(CH_2Ph)_2$
$C_{40}H_{44}FeN_2Si_2U$, 903 g/mol
Calculated: 53.21 %C, 4.91 %H, 3.10 %N
Found: 52.90 %C, 4.83 %H, 3.16 %N

$(NN^{DMP})U(OAr)_2$
$C_{54}H_{72}FeN_2O_2Si_2U$, 1131 g/mol
Calculated: 57.34 %C, 6.42 %H, 2.48 %N
Found: 57.30 %C, 6.29 %H, 2.63 %N

$(NN^{TMS})U(OAr)_2$
$C_{44}H_{68}FeN_2O_2Si_2U$, 1007 g/mol
Calculated: 52.88 %C, 6.40 %H, 4.68 %N
Found: 52.48 %C, 6.81 %H, 2.78 %N

$(NN^{TBS})UI(OAr)$
$C_{36}H_{59}N_2Si_2OIFeU$, 1013 g/mol
Calculated: 42.69 %C, 5.87 %H, 2.77 %N
Found: 43.15 %C, 5.86 %H, 2.72 %N

$(NN^{TBS})U(NPh_2)_2$
$C_{46}H_{58}FeN_4Si_2U$, 1017 g/mol
Calculated: 54.32 %C, 5.75 %H, 5.51 %N
Found: 54.89 %C, 5.72 %H, 5.46 %N

4.4.3 ^{1}H NMR spectroscopy

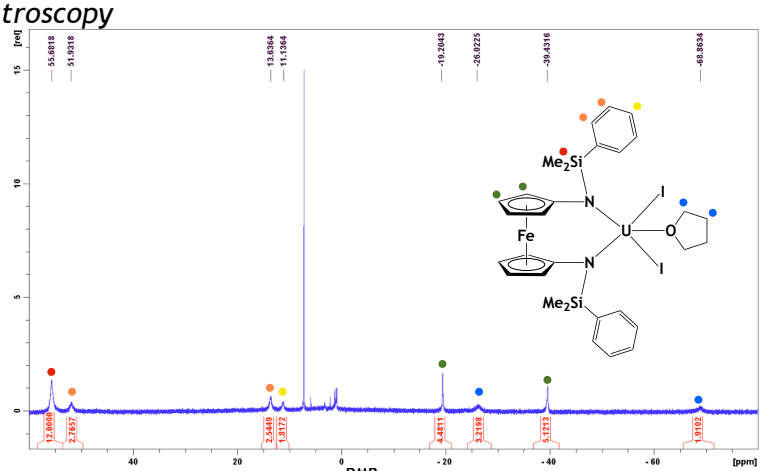

Figure D1. ^{1}H NMR spectrum (300 MHz, $CDCl_3$) of **(NN^{DMP})UI_2(THF);** δ, ppm: **55.7** (s, 12H, -Si(CH_3)$_2$), **51.9** (s, 4H, -Si(C_6H_5)), **13.6** (s, 4H, -Si(C_6H_5)), **11.1** (s, 2H, -Si(C_6H_5)), **-19.2** (s, 4H, Cp*H*), **-26.0** (s, 4H, -OC_4H_8), **-39.4** (s, 4H, Cp*H*), **-68.9** (s, 4H, -OC_4H_8).

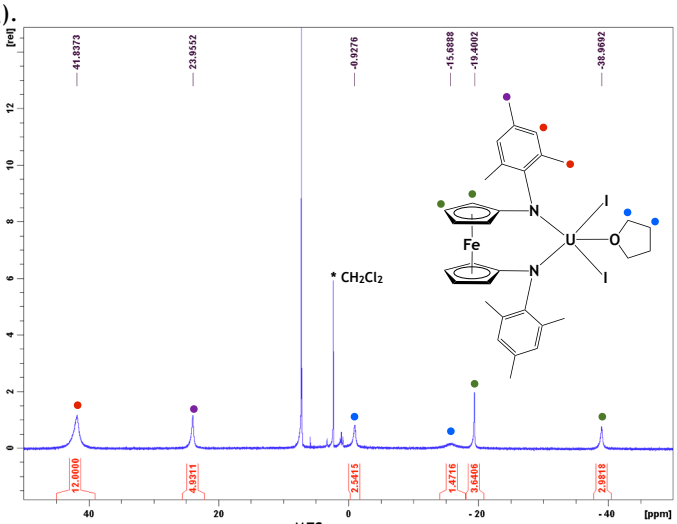

Figure D2. ^{1}H NMR spectrum (300 MHz, $CDCl_3$) of **(NN^{MES})UI_2(THF)**; δ, ppm: **42.07** (s, 4H, $Me_3C_6H_2$), **41.86** (s, 12H, ortho-(CH_3)$_3C_6H_2$), **24.07** (s, 6H, para-(CH_3)$_3C_6H_2$), **-0.6** (s, 4H, -OC_4H_8), **-6.3** (s, 4H, -OC_4H_8), **-19.14** (s, 4H, Cp*H*), **-38.57** (s, 4H, Cp*H*).

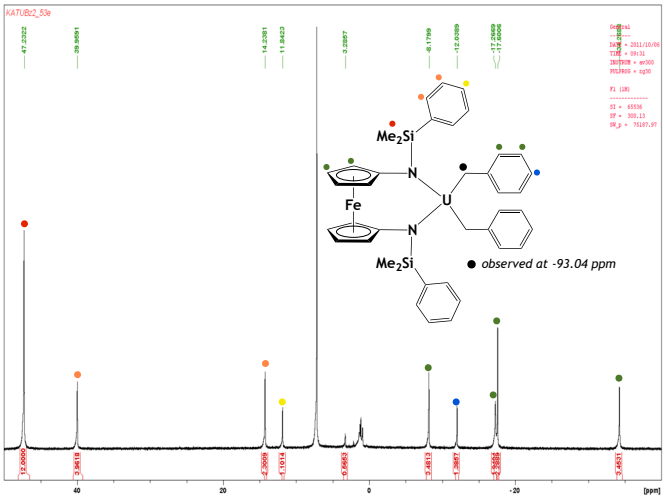

Figure D3. ^{1}H NMR spectrum (300 MHz, C_6D_6) of **(NN^{DMP})U(CH_2Ph)$_2$**; δ, ppm: **47.2** (s, 12H, -Si(CH_3)$_2$), **39.9** (s, 4H, -Si(C_6H_5)), **14.2** (s, 4H, -Si(C_6H_5)), **11.8** (s, 2H, -Si(C_6H_5)), **-8.2** (s, 4H), **-12.0** (s, 2H, -CH_2(C_6H_5)), **-17.3** (s, 4H), **-17.6** (s, 4H), **-34.3** (s, 4H).

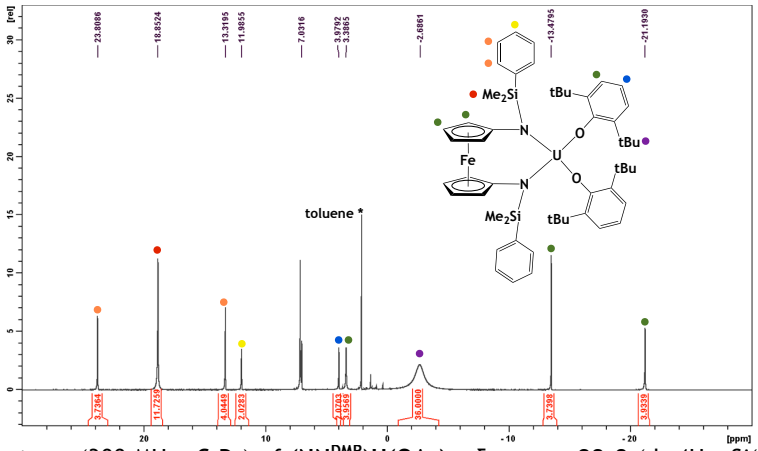

Figure D4. ^{1}H NMR spectrum (300 MHz, C_6D_6) of **(NN^{DMP})U(OAr)$_2$**; δ, ppm: **23.8** (d, 4H, -Si(C_6H_5)), **18.8** (s, 12H, -Si(CH_3)$_2$), **13.3** (t, 4H, -Si(C_6H_5)), **11.9** (t, 2H, -Si(C_6H_5)), **3.9** (t, 2H, -OPh*H*), **3.4** (s, 4H, -OPh*H*), **-2.7** (b, 36H, -OPhC(CH_3)$_3$), **-13.5** (s, 4H, Cp*H*), **-21.2** (s, 4H, Cp*H*).

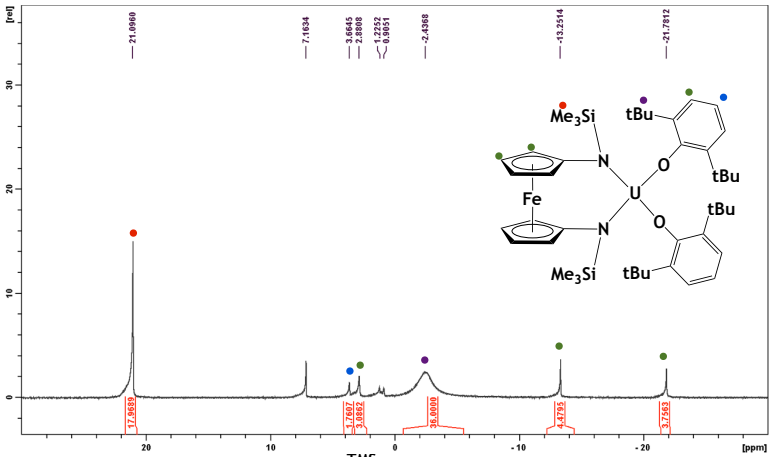

Figure D5. ^{1}H NMR spectrum (300 MHz, C_6D_6) of **(NN^{TMS})U(OAr)$_2$**; δ, ppm: **21.1** (s, 18H, -Si(CH_3)$_3$), **3.6** (s, 2H, -OPh*H*), **2.8** (s, 4H,-OPh*H*), **-2.4** (s, 36H, -OPhC(CH_3)$_3$), **-13.2** (s, 4H, Cp*H*), **-21.8** (s, 4H, Cp*H*).

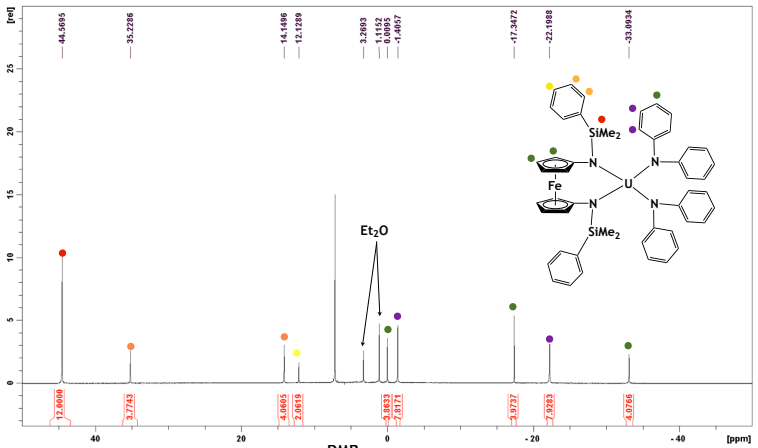

Figure D6. ^{1}H NMR spectrum (300 MHz, C_6D_6) of **(NN^{DMP})U(NPh$_2$)$_2$**; δ, ppm: **44.6** (s, 12H, -Si(CH_3)$_2$), **35.2** (s, 4H, -Si(C_6H_5)), **14.1** (s, 4H, -Si(C_6H_5)), **12.1** (s, 2H, -Si(C_6H_5)), **0.0** (s, 4H), **-1.4** (s, 8H), **-17.3** (s, 4H), **-22.2** (s, 8H), **-33.1** (s, 4H).

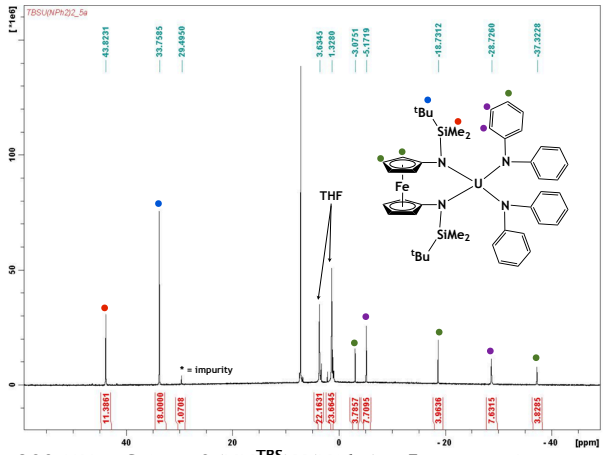

Figure D7. ^{1}H NMR spectrum (300 MHz, C_6D_6) of **(NN^{TBS})U(NPh$_2$)$_2$**; δ, ppm: **43.8** (s, 12H, -Si(C*H*$_3$)$_2$), **33.7** (s, 18H, -SiC(CH$_3$)$_3$), **-3.1** (s, 4H), **-5.2** (s, 8H), **-18.7** (s, 4H), **-28.7** (s, 8H), **-37.3** (s, 4H).

4.4.4 Cyclic voltammetry

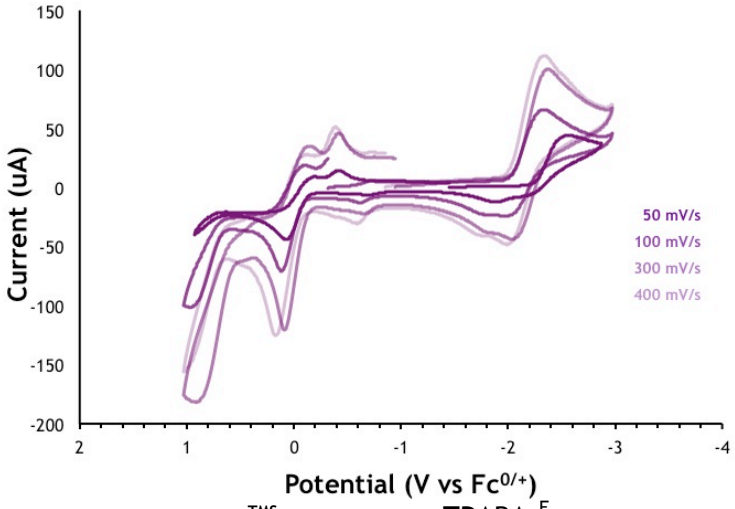

Figure D8. CV of a 2.8 mM THF solution of **(NN^{TMS})UI$_2$(THF)** with TPABAr^F as the supporting electrolyte.

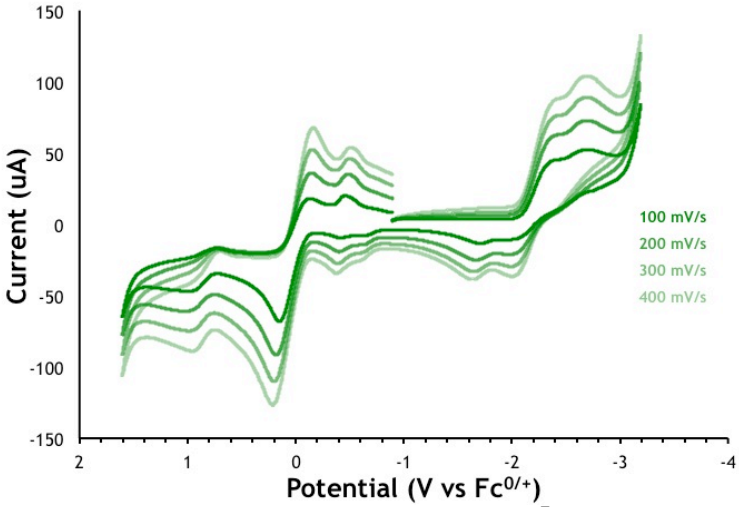

Figure D9. CV of a 3.6 mM THF solution of **(NN^{TBS})UI$_2$(THF)** with TPABAr^F as the supporting electrolyte.

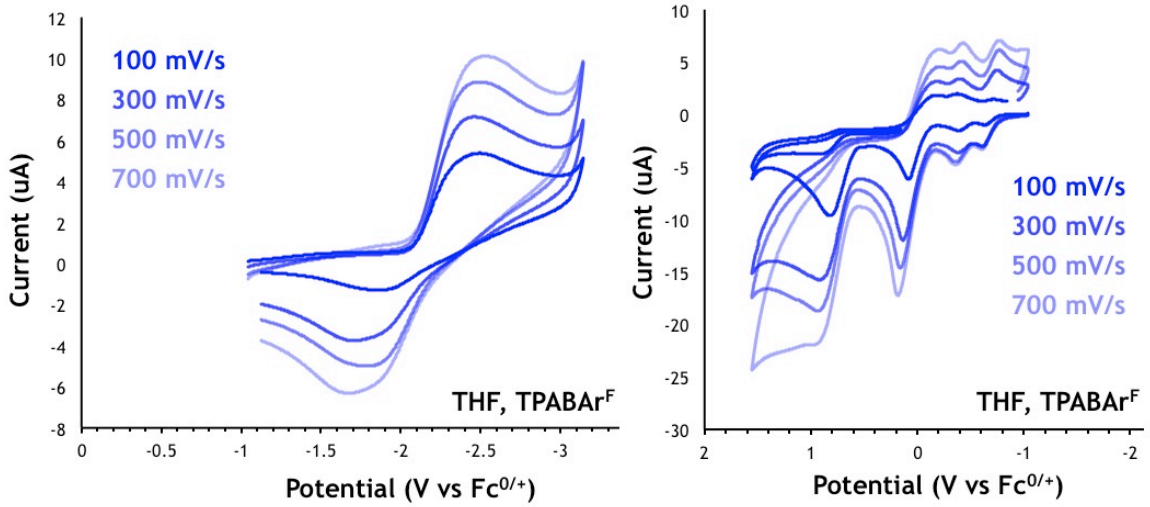

Figure D10. CV of a 1.2 mM THF solution of **(NN^{DMP})UI$_2$(THF)** with TPABAr^F as the supporting electrolyte.

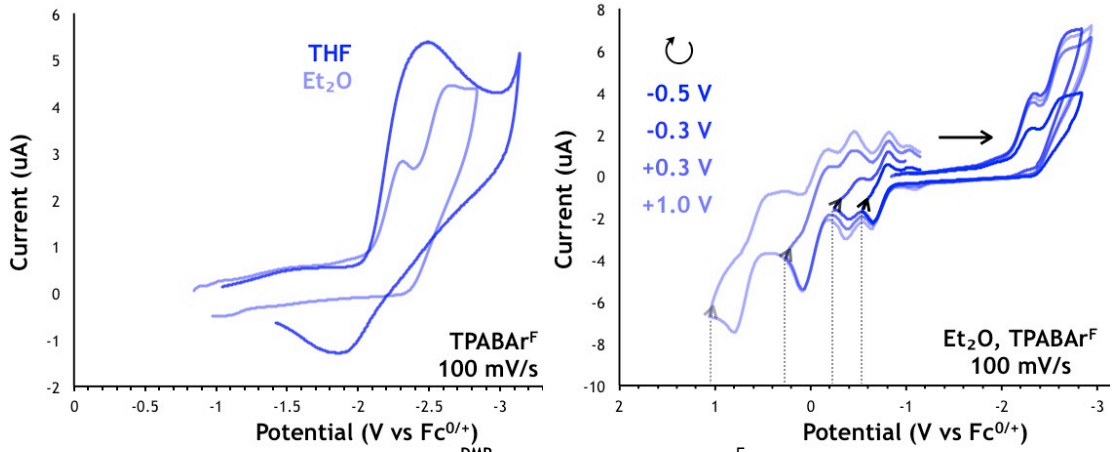

Figure D11. CV of a 1.8 mM Et_2O solution of **(NN^{DMP})UI$_2$(THF)** with TPABAr^F as the supporting electrolyte: effect of switching potential (left) and addition of THF (right).

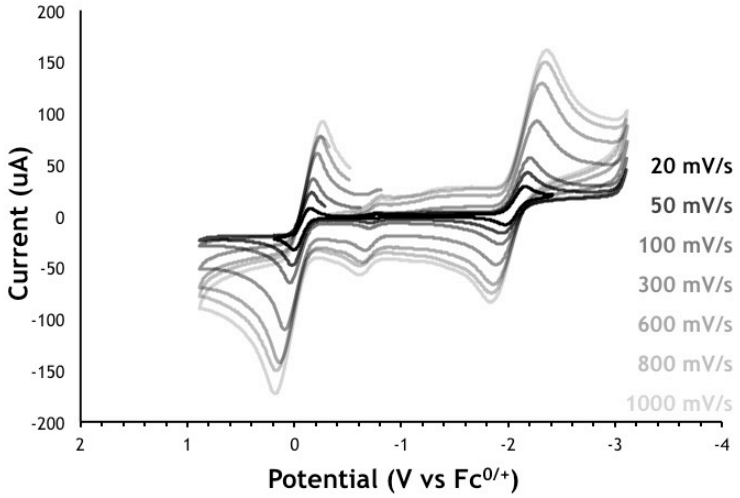

Figure D12. CV of a 2.8 mM THF solution of **(NN^{MES})UI$_2$(THF)** with TPABAr^F as the supporting electrolyte.

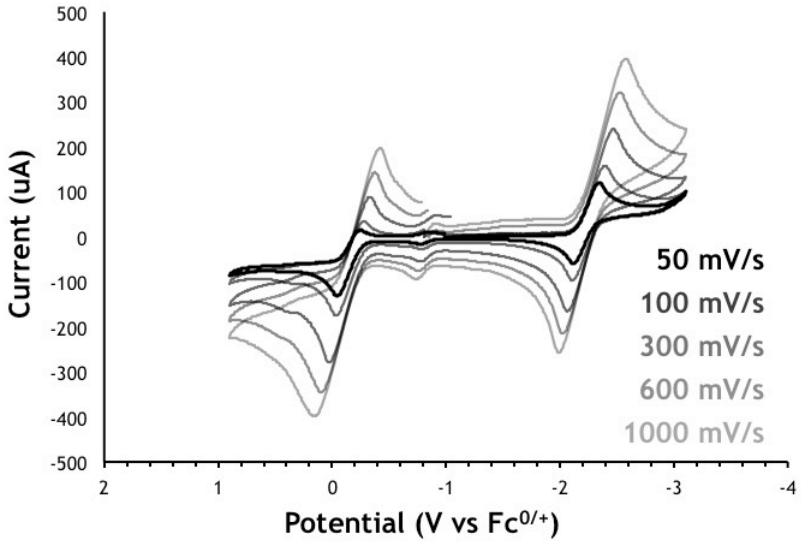

Figure D13. CV of a 6.7 mM THF solution of **(NN^{MES})UI(OAr)** with TPABAr^{F} as the supporting electrolyte.

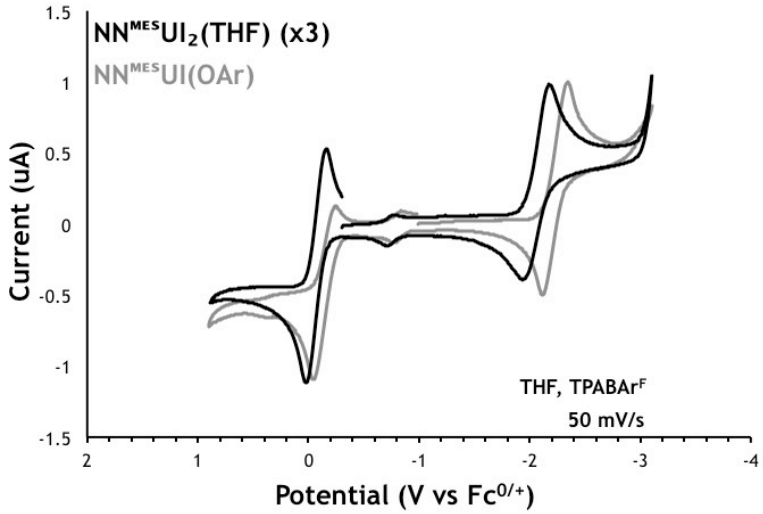

Figure D14. Comparison of **(NN^{MES})UI(OAr)** and **(NN^{MES})UI$_2$(THF)** voltammograms.

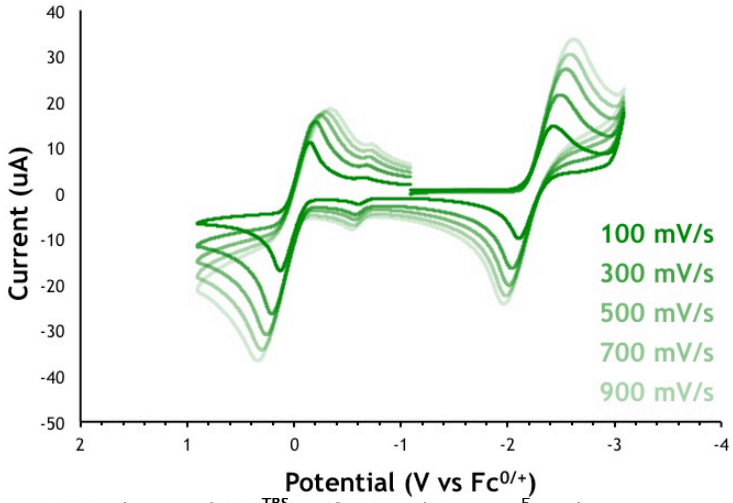

Figure D15. CV of a 3.4 mM THF solution of **(NN^{TBS})UI(OAr)** with TPABAr^{F} as the supporting electrolyte.

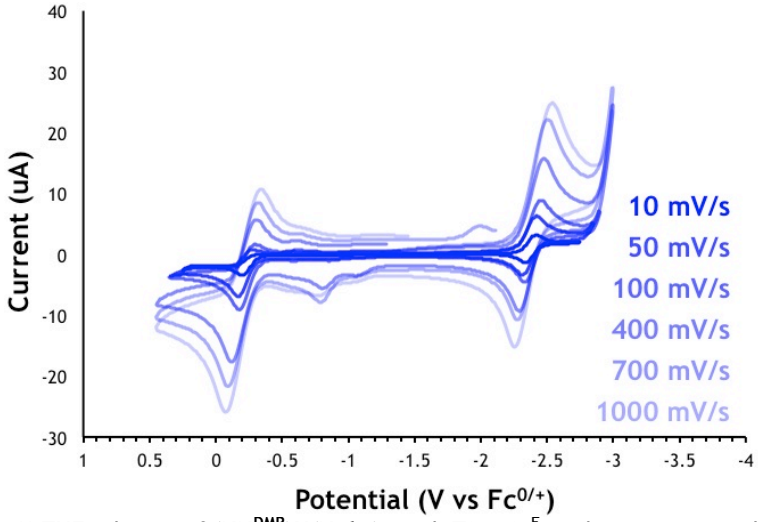

Figure D15. CV of a 2 mM THF solution of $(NN^{DMP})U(NPh_2)_2$ with $TPABAr^F$ as the supporting electrolyte.

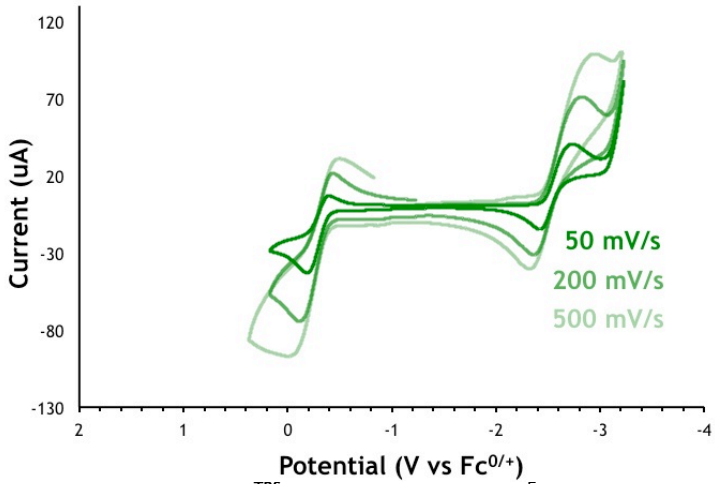

Figure D16. CV of a 3.6 mM THF solution of $(NN^{TBS})U(NPh_2)_2$ with $TPABAr^F$ as the supporting electrolyte.

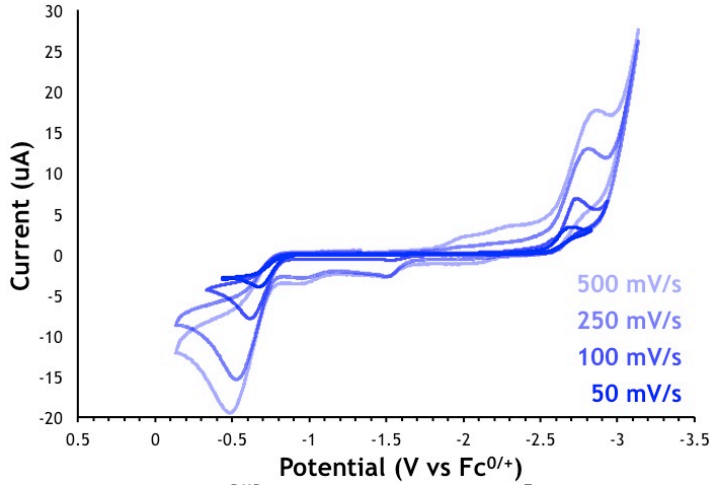

Figure D17. CV of a 4 mM TFT solution of $(NN^{DMP})U(CH_2Ph)_2$ with $TPABAr^F$ as the supporting electrolyte.

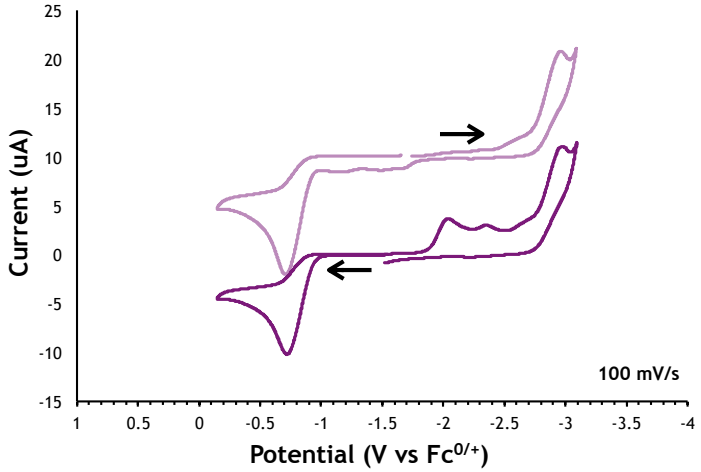

Figure D18. CV of a 5.5 mM TFT solution of $(NN^{TMS})U(CH_2Ph)_2$ with $TPABAr^F$ as the supporting electrolyte.

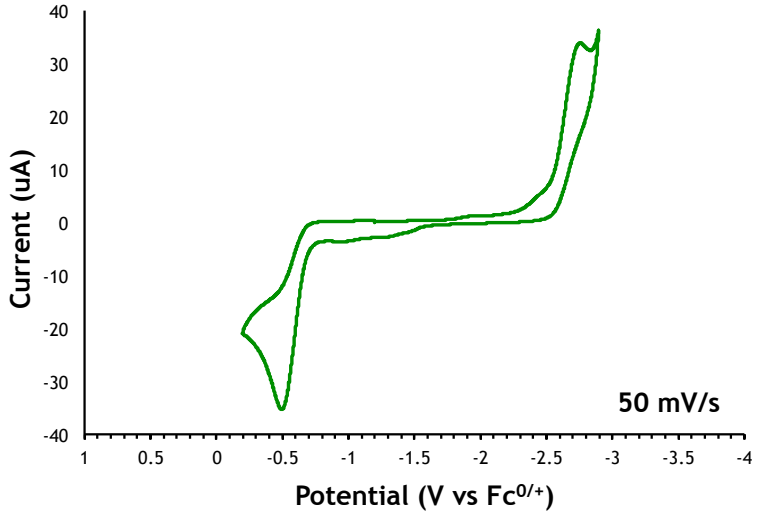

Figure D19. CV of a 1.7 mM TFT solution of $(NN^{DMP})U(CH_2Ph)_2$ with $TPABAr^F$ as the supporting electrolyte.

4.4.5 UV-Vis-NIR spectra

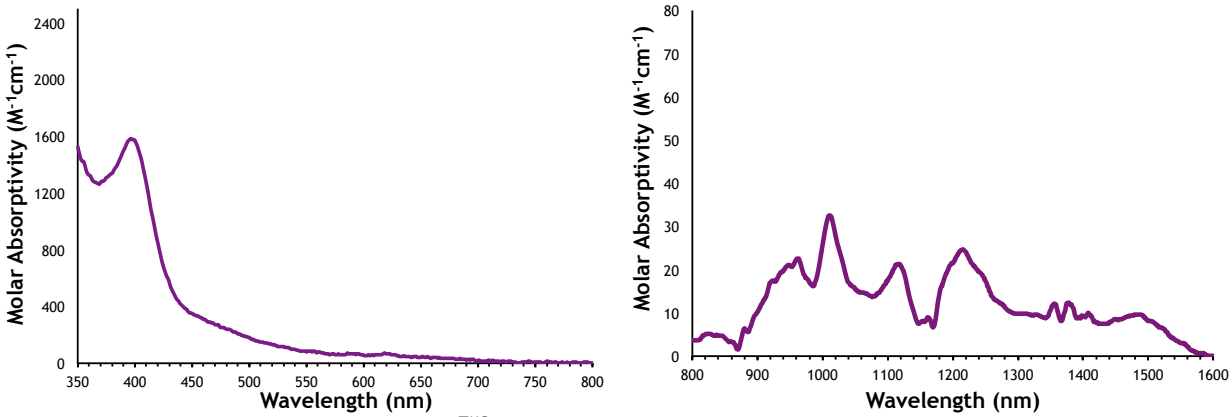

Figure D20. UV-Vis and NIR spectra of $(NN^{TMS})UI_2(THF)$ in THF (0.53 mM and 19 mM, respectively).

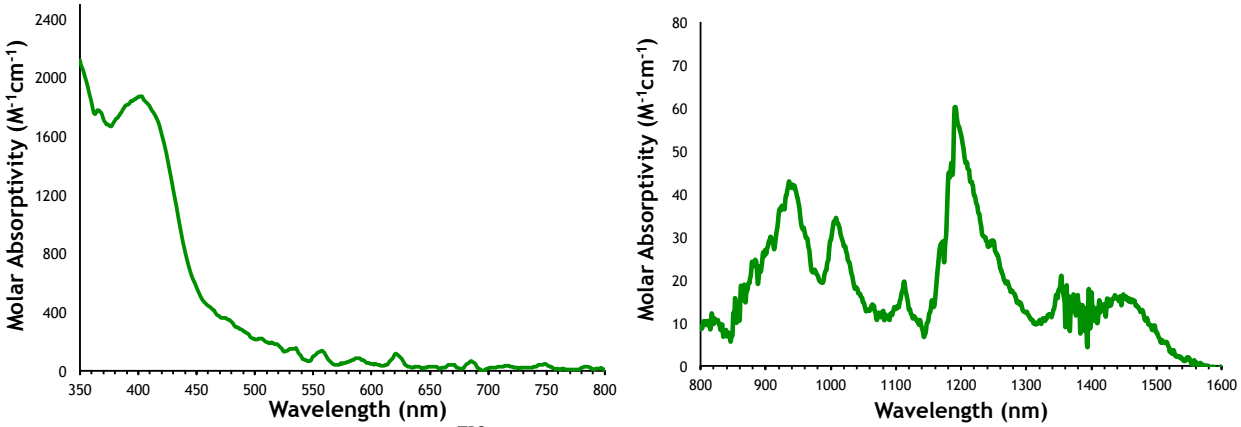

Figure D21. UV-Vis and NIR spectra of **(NN^{TBS})UI$_2$(THF)** in THF (0.38 mM and 2.6 mM, respectively).

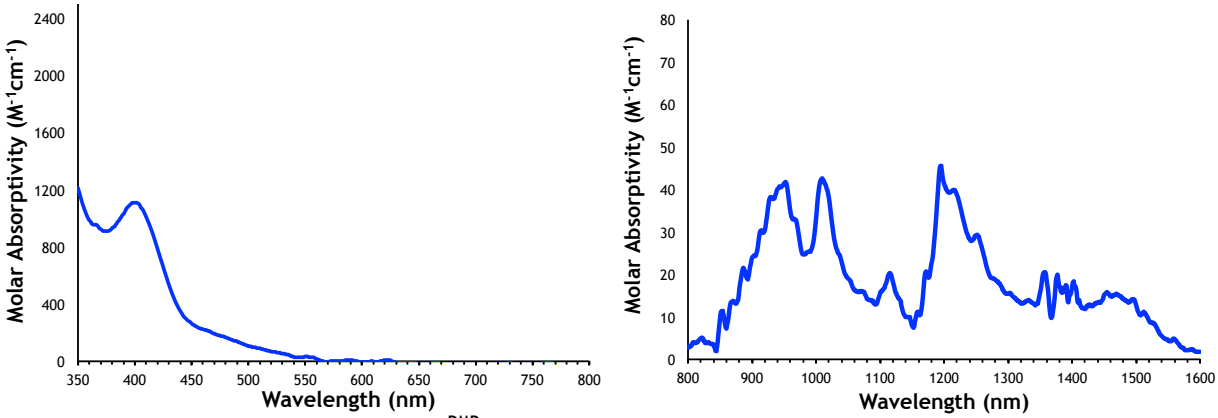

Figure D22. UV-Vis and NIR spectra of **(NN^{DMP})UI$_2$(THF)** in THF (0.67 mM and 12.2 mM, respectively).

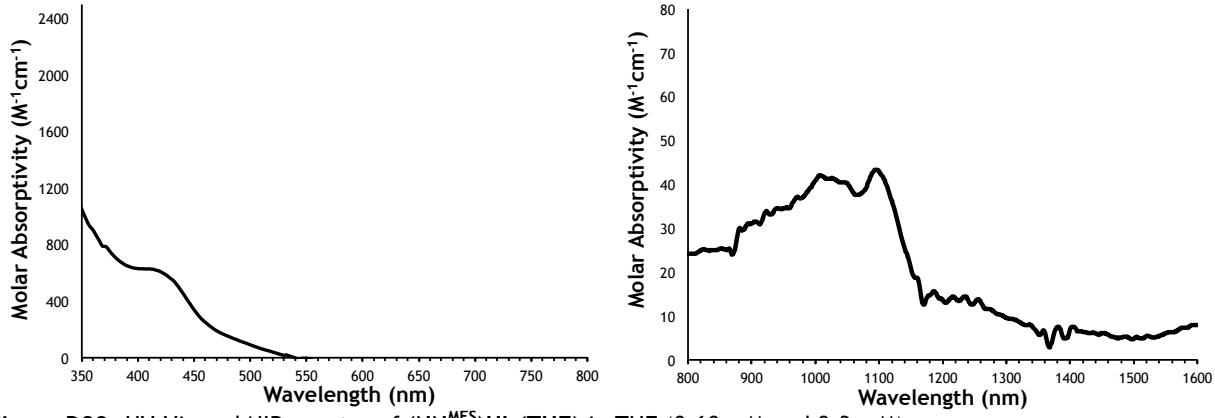

Figure D23. UV-Vis and NIR spectra of **(NN^{MES})UI$_2$(THF)** in THF (0.60 mM and 9.3 mM).

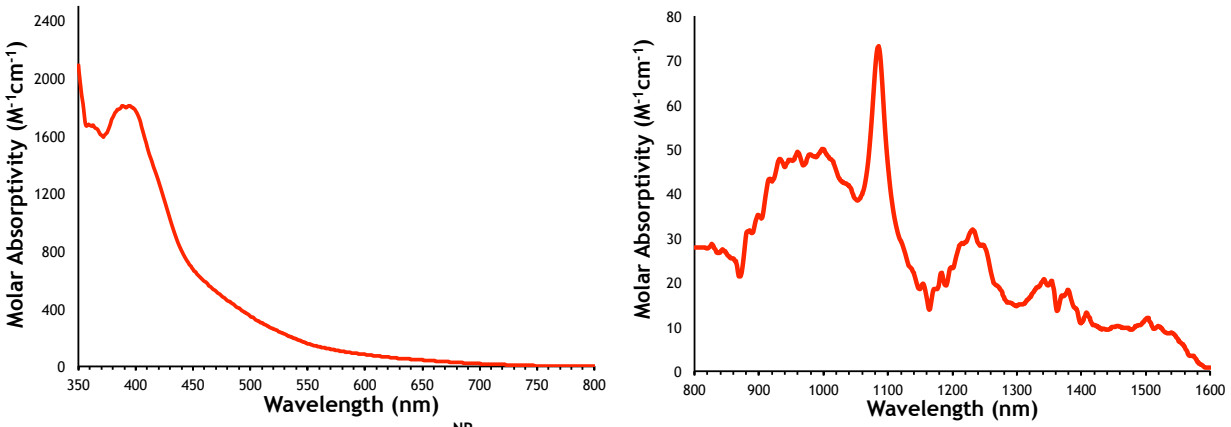

Figure D24. UV-Vis and NIR spectra of **$(NN^{NP})UI_2(THF)$** in THF (0.40 mM and 9.0 mM, respectively).

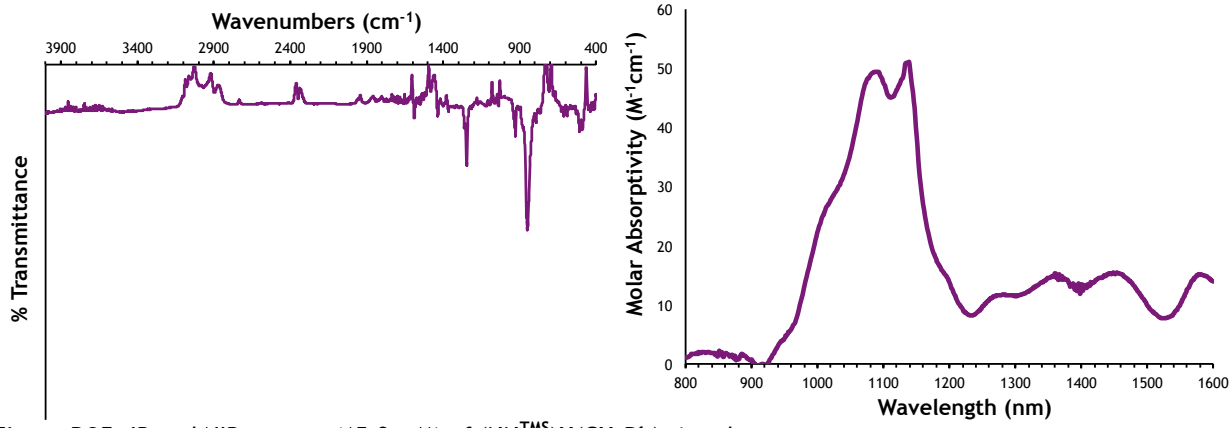

Figure D25. IR and NIR spectra (15.9 mM) of **$(NN^{TMS})U(CH_2Ph)_2$** in toluene.

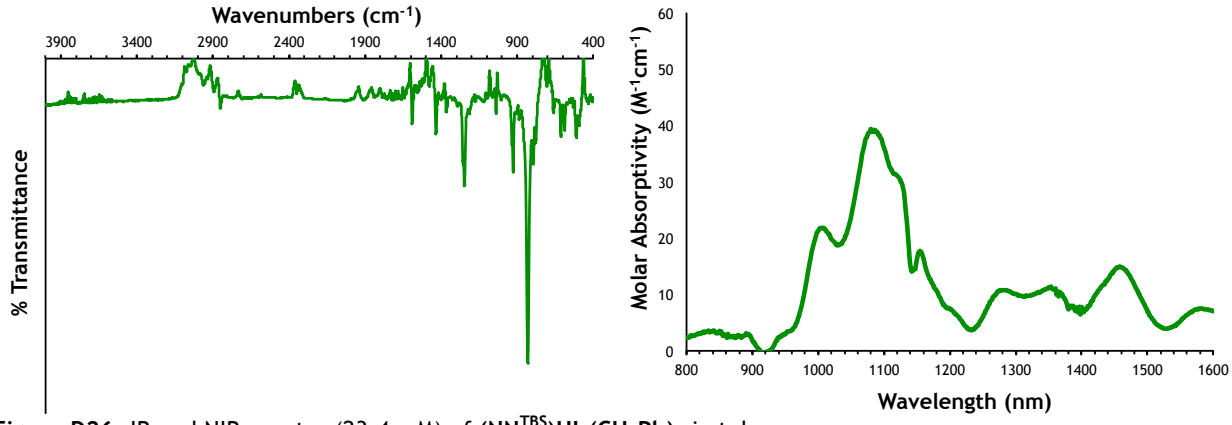

Figure D26. IR and NIR spectra (23.4 mM) of **$(NN^{TBS})UI_2(CH_2Ph)_2$** in toluene.

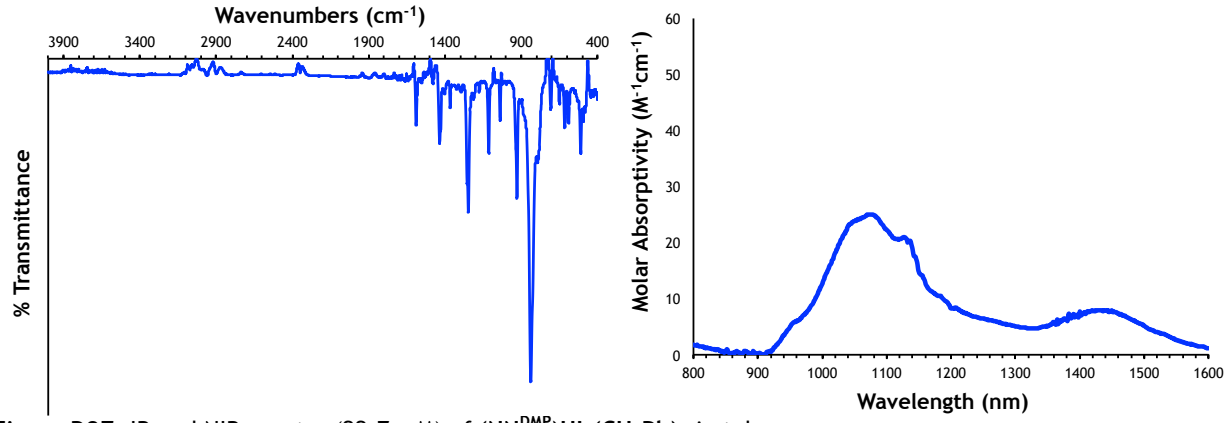

Figure D27. IR and NIR spectra (22.7 mM) of $(NN^{DMP})UI_2(CH_2Ph)_2$ in toluene.

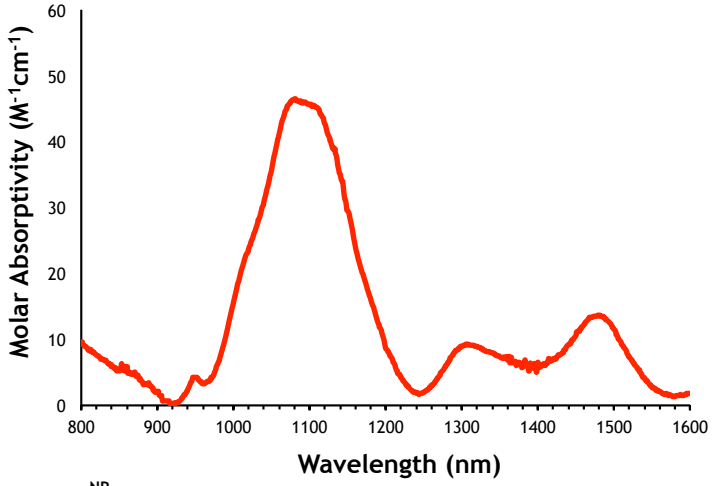

Figure D28. NIR spectrum of $(NN^{NP})UI_2(CH_2Ph)_2$ in toluene (16.5 mM).

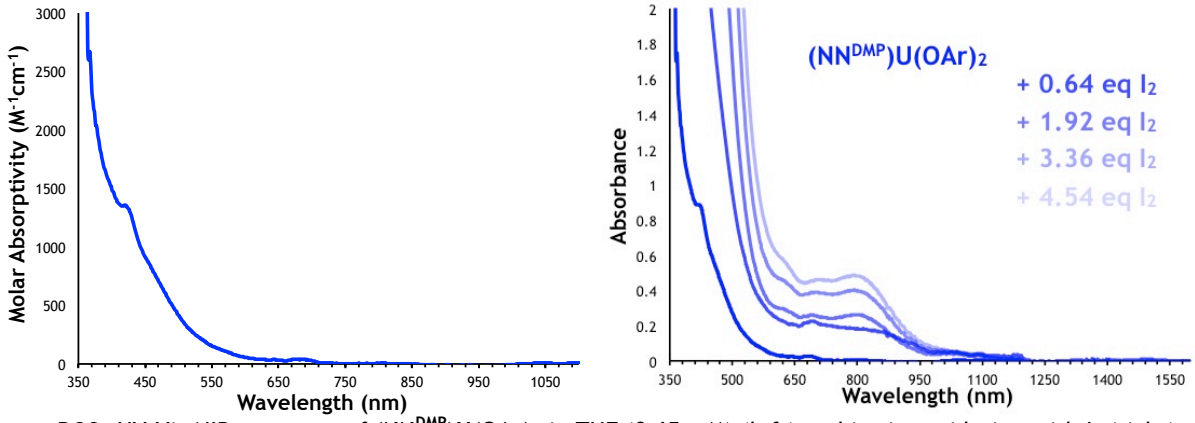

Figure D29. UV-Vis-NIR spectrum of $(NN^{DMP})U(OAr)_2$ in THF (0.65 mM) (left) and in situ oxidation with I_2 (right).

4.4.6 X-ray crystallography

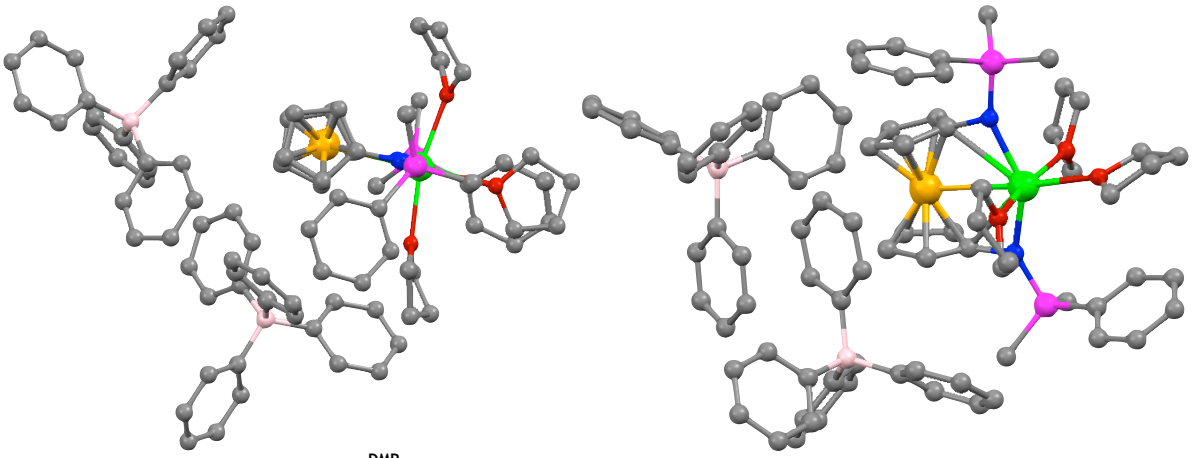

Figure D30. Crystal data for **[(NN^{DMP})U(THF)$_3$][BPh$_4$]$_2$**, formula $C_{86}H_{94}B_2FeN_2O_3Si_2U$; space group P2(1)/c; V = 8242.37 Å^3; a = 23.407(9) Å, b = 14.759(2) Å, c = 25.202(9) Å; ß = 108.80(5)°. For clarity, CH_2 units of each THF ring have been omitted in the bottom two depictions.

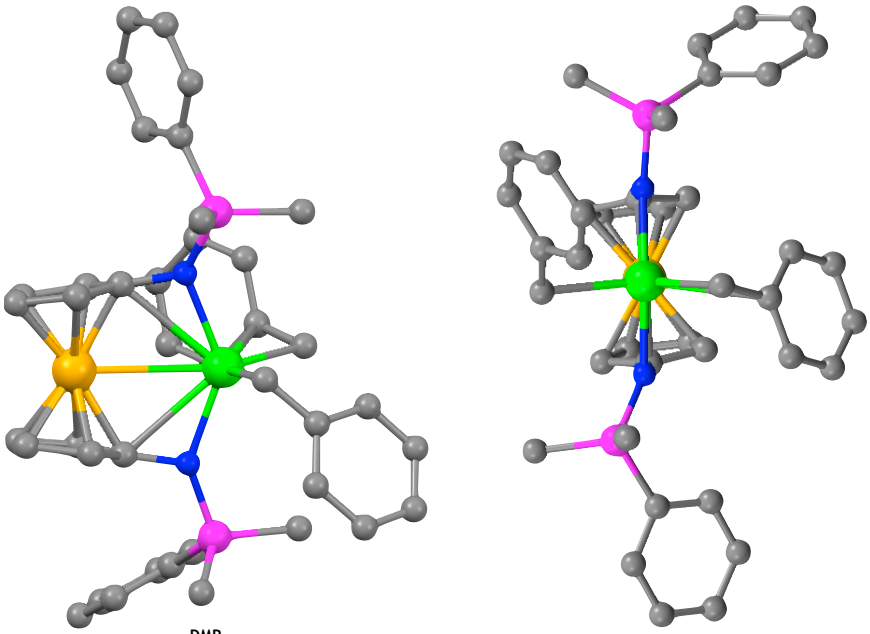

Figure D31. Crystal data for **(NN^{DMP})U(CH$_2$Ph)$_2$**, formula $C_{40}H_{44}FeN_2Si_2U$; space group *P-1*; V = 1795.08 Å^3; a = 9.881(2) Å, b = 11.904(9) Å, c = 17.141(4) Å; α = 69.95(8)°, ß = 75.04(5)°, γ = 74.61(7)°

4.4.7 Density Functional Theory

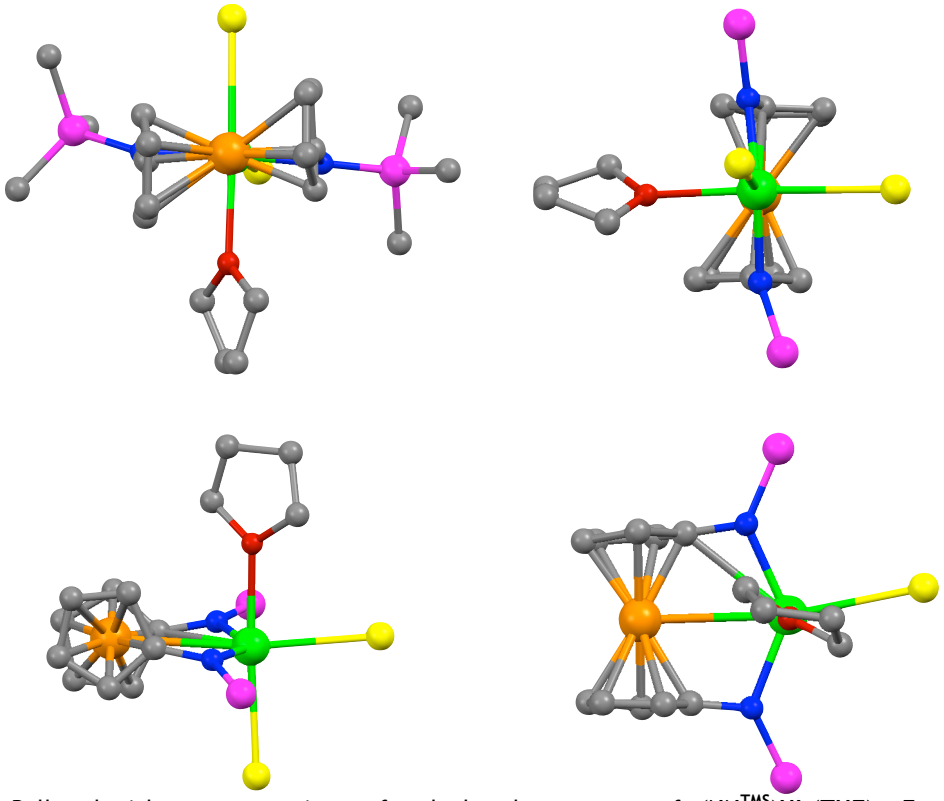

Figure D32. Ball-and-stick representations of calculated geometry of **(NN^{TMS})UI_2(THF)**. For clarity, silyl substituents were removed in the top right and bottom two figures. Hydrogen atoms are not shown. Level of theory: uB3LYP; basis sets and effective core potentials: ECP60MWB_ANO for U, ECP28MDF_VDZ for I, and 6-31G* for Fe, Si, O, N, C, and H atoms.

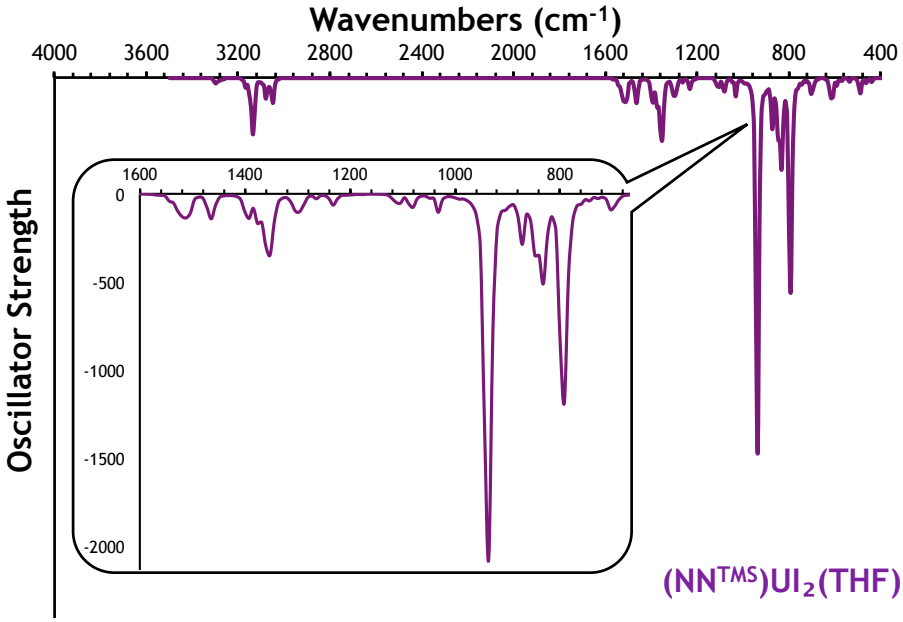

Figure D33. Calculated IR spectrum of **(NN^{TMS})UI_2(THF)** in gas phase.

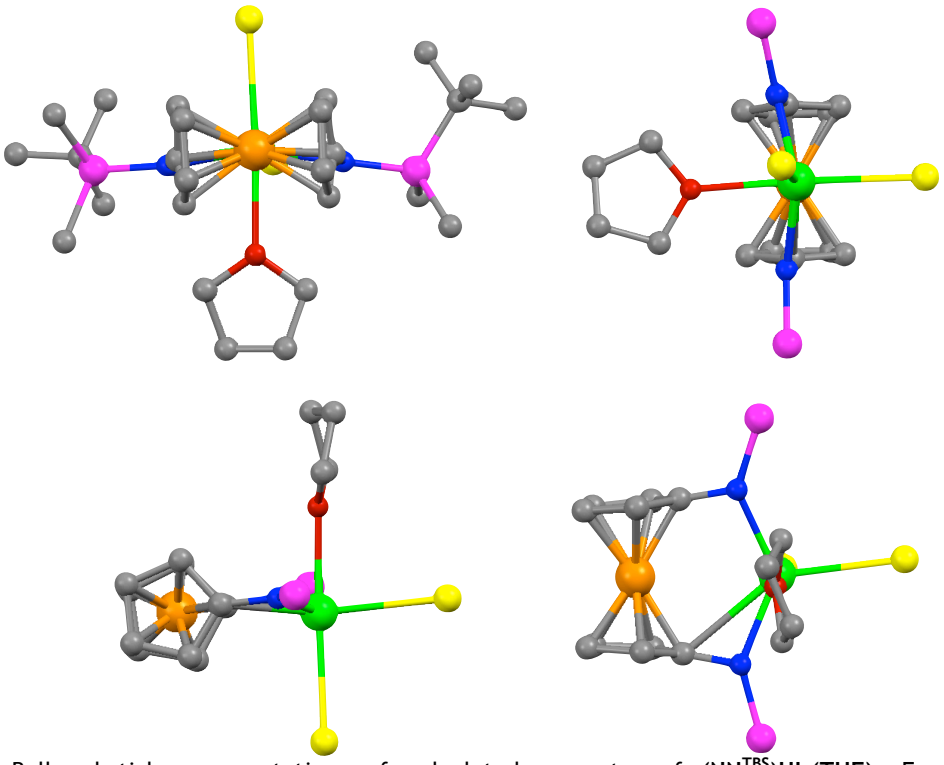

Figure D34. Ball-and-stick representations of calculated geometry of **(NN^{TBS})UI$_2$(THF)**. For clarity, silyl substituents were removed in the top right and bottom two figures. Hydrogen atoms are not shown. Level of theory: uB3LYP; basis sets and effective core potentials: ECP78MWB for U, MWB46 for I, ECP10MDF for Fe, and 6-31G for Si, O, N, C, and H atoms.

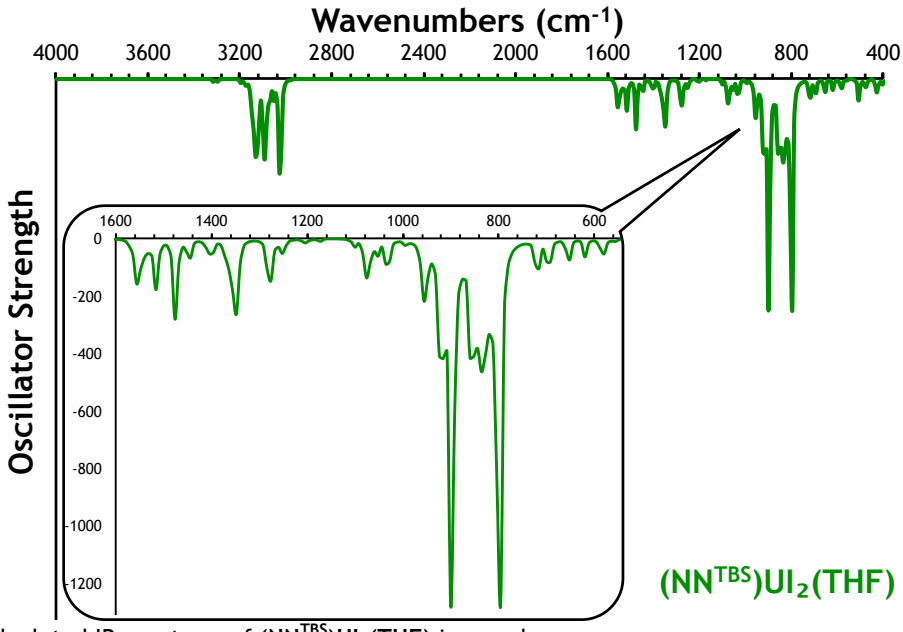

Figure D35. Calculated IR spectrum of **(NN^{TBS})UI$_2$(THF)** in gas phase.

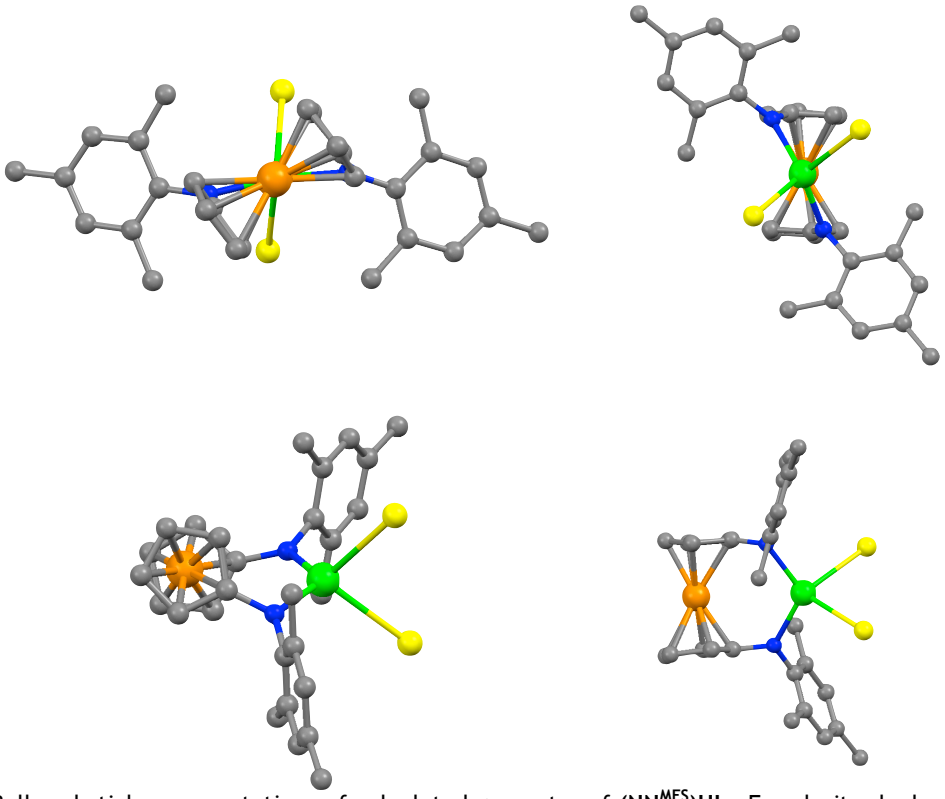

Figure D36. Ball-and-stick representations of calculated geometry of $(NN^{MES})UI_2$. For clarity, hydrogen atoms are not shown. Level of theory: uB3LYP; basis sets and effective core potentials: ECP78MWB for U, MWB46 for I, ECP10MDF for Fe, and 6-31G for Si, O, N, C, and H atoms.

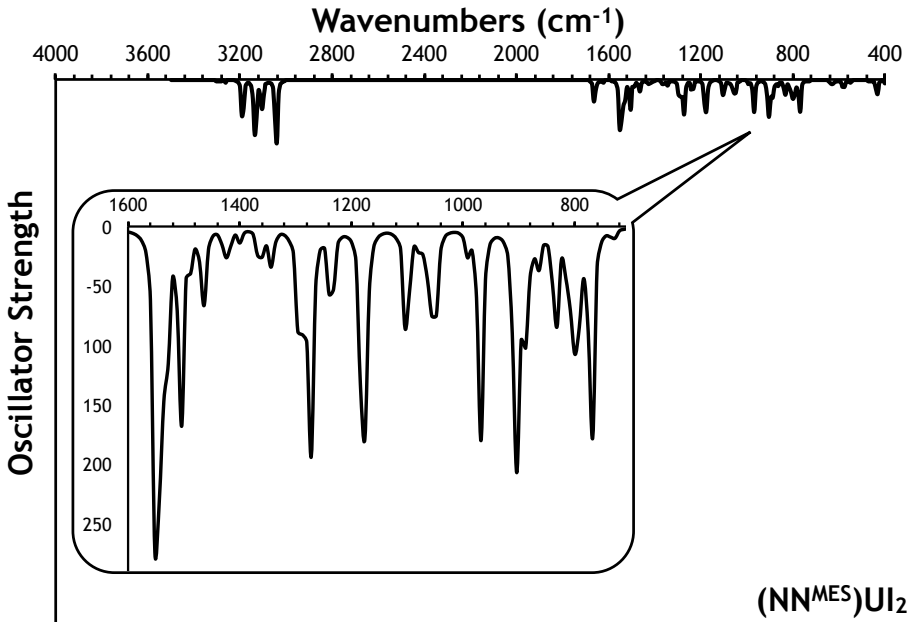

Figure D37. Calculated IR spectrum of $(NN^{MES})UI_2$ in gas phase.

Table D1. $(NN^{TMS})UI_2(THF)$			Value	Threshold	Converged?
Maximum Force			0.000015	0.00045	YES
RMS Force			0.000003	0.0003	YES
Maximum Displacement			0.001659	0.0018	YES
RMS Displacement			0.000251	0.0012	YES
Center	Atomic	Atomic	Coordinates (Angstrom)		
No.	No.	Type	X	Y	Z
1	92	0	0.23166	-0.298596	0.060216
2	53	0	-0.072319	-1.296083	-2.905529
3	53	0	2.847638	-1.956442	0.399294
4	26	0	-2.193312	1.991546	-0.131877
5	14	0	2.702789	2.435639	-0.690487
6	14	0	-2.391516	-2.848298	0.601459
7	8	0	0.498916	0.343083	2.458235
8	7	0	1.014753	1.778952	-0.406104
9	7	0	-1.791999	-1.117154	0.578064
10	6	0	-0.756583	3.57748	0.068726
11	1	0	-0.407831	3.933242	1.025192
12	6	0	-1.861596	4.076286	-0.681734
13	1	0	-2.51105	4.887029	-0.387684
14	6	0	-1.831048	3.472853	-2.003847
15	1	0	-2.542846	3.668335	-2.792348
16	6	0	-0.802497	2.538538	-2.03773
17	1	0	-0.556113	1.860033	-2.84102
18	6	0	-0.14418	2.530091	-0.725487
19	6	0	-2.962075	0.767331	1.83568
20	1	0	-2.449765	0.636502	2.776136
21	6	0	-3.941064	1.705277	1.522404
22	1	0	-4.330633	2.471193	2.177389
23	6	0	-4.321168	1.527446	0.13109
24	1	0	-5.111602	2.067716	-0.36694
25	6	0	-3.621835	0.402545	-0.388052
26	1	0	-3.743165	-0.057264	-1.356173
27	6	0	-2.676368	-0.01462	0.6334
28	6	0	3.538448	1.489186	-2.118705
29	1	0	2.926288	1.535888	-3.025219
30	1	0	3.686656	0.434774	-1.865745
31	1	0	4.518963	1.928649	-2.339134
32	6	0	2.509348	4.284955	-1.136885
33	1	0	2.030214	4.846817	-0.329045
34	1	0	1.905437	4.408922	-2.041394
35	1	0	3.498533	4.720557	-1.321176
36	6	0	3.724427	2.24526	0.915564
37	1	0	3.719798	1.207124	1.263608
38	1	0	3.334354	2.88959	1.711866
39	1	0	4.766716	2.530824	0.729521
40	6	0	-3.526428	-3.174785	-0.897597
41	1	0	-2.993488	-2.959588	-1.829427
42	1	0	-4.429087	-2.556643	-0.856934
43	1	0	-3.834201	-4.227245	-0.911716
44	6	0	-3.351908	-3.069297	2.241129
45	1	0	-4.154768	-2.329128	2.324912
46	1	0	-2.684165	-2.951381	3.101432
47	1	0	-3.800417	-4.068664	2.288712
48	6	0	-0.862471	-3.986124	0.550912
49	1	0	-0.16117	-3.783839	1.367435
50	1	0	-0.322254	-3.904708	-0.397855
51	1	0	-1.194621	-5.026716	0.651963
52	6	0	0.346218	1.71728	3.022433
53	1	0	-0.620953	2.09415	2.689875
54	1	0	1.146613	2.326402	2.595528
55	6	0	0.47491	1.537928	4.536359
56	1	0	0.875457	2.432745	5.021535
57	1	0	-0.501035	1.318012	4.985116
58	6	0	1.416302	0.318589	4.671047
59	1	0	1.328759	-0.173941	5.64355
60	1	0	2.459895	0.623714	4.536501
61	6	0	0.976558	-0.593744	3.525976
62	1	0	1.77479	-1.192482	3.086817
63	1	0	0.127837	-1.231009	3.792833

Table D2. $(NN^{TBS})UI_2(THF)$			Value	Threshold	Converged?
Maximum Force			0.000429	0.00045	YES
RMS Force			0.000065	0.0003	YES
Maximum Displacement			0.000741	0.0018	YES
RMS Displacement			0.000157	0.0012	YES
Center	Atomic	Atomic	Coordinates (Angstrom)		
No.	No.	Type	X	Y	Z
1	92	0	-0.11461	-0.31471	-0.069938
2	53	0	0.060553	-0.250035	-3.164258
3	53	0	-0.298771	-3.410029	0.075274
4	26	0	0.464595	3.0164	0.181237
5	14	0	3.646751	-0.656686	0.86367
6	14	0	-3.8815	0.763474	0.07313
7	8	0	-0.396683	-0.418665	2.438817
8	7	0	2.070538	0.207426	0.512026
9	7	0	-2.055581	0.911616	0.176206
10	6	0	2.081943	2.579401	1.464349
11	1	0	2.016095	2.331219	2.510776
12	6	0	2.240673	3.888212	0.909091
13	1	0	2.293657	4.810979	1.464493
14	6	0	2.311899	3.763317	-0.519603
15	1	0	2.422196	4.576093	-1.219415
16	6	0	2.206043	2.38011	-0.853937
17	1	0	2.236695	1.951622	-1.842332
18	6	0	2.101804	1.618496	0.380645
19	6	0	-1.336497	3.106361	1.280358
20	1	0	-1.46908	2.816408	2.309625
21	6	0	-0.995918	4.40801	0.801273
22	1	0	-0.799924	5.277071	1.408795
23	6	0	-0.951011	4.359872	-0.634081
24	1	0	-0.710903	5.185748	-1.284403
25	6	0	-1.266252	3.032444	-1.048746
26	1	0	-1.33529	2.672285	-2.062127
27	6	0	-1.548858	2.237886	0.136666
28	6	0	4.504525	0.222195	2.343835
29	1	0	3.923089	0.109559	3.266114
30	1	0	4.639542	1.2913	2.154294
31	1	0	5.492215	-0.22148	2.516463
32	6	0	3.309083	-2.473793	1.342311
33	1	0	2.831136	-3.034135	0.535468
34	1	0	2.673133	-2.560108	2.226334
35	1	0	4.266126	-2.955408	1.573303
36	6	0	-4.466278	2.011184	-1.260939
37	1	0	-4.105405	1.728996	-2.255563
38	1	0	-4.099619	3.018543	-1.041102
39	1	0	-5.560909	2.046303	-1.288255
40	6	0	-4.666169	1.319599	1.739404
41	1	0	-4.258753	2.291606	2.039344
42	1	0	-4.490489	0.604982	2.549453
43	1	0	-5.749933	1.433488	1.620225
44	6	0	0.664949	-0.835939	3.395437
45	1	0	1.564747	-0.295269	3.111801
46	1	0	0.819704	-1.913011	3.279614
47	6	0	0.087119	-0.483771	4.763252
48	1	0	0.554345	-1.058387	5.568076
49	1	0	0.225932	0.582098	4.978228
50	6	0	-1.411661	-0.817587	4.588461
51	1	0	-2.046686	-0.289996	5.305923
52	1	0	-1.575371	-1.892768	4.718822
53	6	0	-1.715271	-0.397309	3.143181
54	1	0	-2.379574	-1.084037	2.620245
55	1	0	-2.098292	0.619022	3.058035
56	6	0	-4.508564	-1.027178	-0.400568
57	6	0	-3.84558	-1.51055	-1.710527
58	6	0	-4.256427	-2.055215	0.726761
59	6	0	-6.041844	-0.922598	-0.628218
60	1	0	-4.014267	-0.810914	-2.537265
61	1	0	-2.764215	-1.644414	-1.606341
62	1	0	-4.260779	-2.484563	-2.006036
63	1	0	-4.73104	-1.751213	1.668663
64	1	0	-4.682017	-3.028742	0.443981
65	1	0	-3.188989	-2.2214	0.904294
66	1	0	-6.441504	-1.917291	-0.87105
67	1	0	-6.569981	-0.56621	0.264965
68	1	0	-6.289053	-0.256708	-1.462447
69	6	0	4.855264	-0.63357	-0.679777
70	6	0	4.098224	-1.09578	-1.945253
71	6	0	5.449669	0.777414	-0.905469
72	6	0	6.023592	-1.615822	-0.401817
73	1	0	3.684633	-2.105062	-1.826854
74	1	0	3.26822	-0.428623	-2.196986
75	1	0	4.781474	-1.119781	-2.806788
76	1	0	6.034697	1.114004	-0.040404
77	1	0	6.126127	0.760264	-1.772918
78	1	0	4.676	1.526216	-1.102155
79	1	0	6.739538	-1.579463	-1.235675
80	1	0	6.574395	-1.358338	0.51253
81	1	0	5.677136	-2.651476	-0.313355

Table D3. (NN^{MES})UI_2(THF)			Value	Threshold	Converged?
Maximum Force			0.000004	0.00045	YES
RMS Force			0.000001	0.0003	YES
Maximum Displacement			0.000901	0.0018	YES
RMS Displacement			0.000117	0.0012	YES
Center No.	Atomic No.	Atomic Type	Coordinates (Angstroms)		
			X	Y	Z
1	92	0	0.002454	-0.346697	0.074346
2	53	0	-0.120256	-2.307971	2.436739
3	53	0	0.210102	-2.642171	-1.943399
4	26	0	0.007381	3.374281	0.092381
5	7	0	-1.982301	0.707562	0.275278
6	7	0	1.85012	0.860084	-0.382502
7	6	0	-2.178722	3.26102	0.200861
8	1	0	-2.849689	3.356842	-0.638269
9	6	0	-1.708471	4.324019	1.037293
10	1	0	-1.935022	5.372917	0.925475
11	6	0	-0.864906	3.738492	2.033405
12	1	0	-0.389579	4.258374	2.850134
13	6	0	-0.979075	2.295361	1.927808
14	1	0	-0.577212	1.578229	2.629997
15	6	0	-1.818224	1.99875	0.827071
16	6	0	0.887292	2.736307	-1.808036
17	1	0	0.416904	2.140276	-2.574859
18	6	0	1.021537	4.179079	-1.826377
19	1	0	0.566419	4.836524	-2.551532
20	6	0	1.861455	4.559618	-0.76602
21	1	0	2.138459	5.568961	-0.500997
22	6	0	2.198959	3.375536	-0.017733
23	1	0	2.868903	3.335796	0.82634
24	6	0	1.698743	2.228777	-0.740068
25	6	0	3.186779	0.318658	-0.227114
26	6	0	3.910844	-0.043027	-1.392037
27	6	0	3.75864	0.157128	1.055991
28	6	0	5.18997	-0.589091	-1.243972
29	6	0	5.046405	-0.396642	1.147965
30	6	0	5.773195	-0.785028	0.017715
31	1	0	5.742496	-0.87136	-2.136073
32	1	0	5.488749	-0.520965	2.132823
33	6	0	-3.288059	0.24734	-0.135779
34	6	0	-3.621019	0.161437	-1.506894
35	6	0	-4.229367	-0.117958	0.860949
36	6	0	-4.896916	-0.309803	-1.856914
37	6	0	-5.486089	-0.581233	0.457692
38	6	0	-5.838468	-0.693979	-0.896369
39	1	0	-5.156125	-0.373679	-2.910264
40	1	0	-6.205049	-0.8667	1.220947
41	6	0	-7.193944	-1.229287	-1.299867
42	6	0	-3.893034	-0.023779	2.330811
43	6	0	-2.663923	0.560139	-2.609381
44	6	0	3.323421	0.152709	-2.769459
45	6	0	3.049385	0.560733	2.332005
46	6	0	7.142872	-1.412542	0.147928
47	1	0	-7.994378	-0.796567	-0.688689
48	1	0	-7.413767	-1.011625	-2.349764
49	1	0	-7.242603	-2.318896	-1.17209
50	1	0	-4.726337	-0.387506	2.938763
51	1	0	-3.008765	-0.6216	2.580359
52	1	0	-3.678288	1.007819	2.633996
53	1	0	-3.219533	0.907535	-3.486731
54	1	0	-1.990085	1.36348	-2.296027
55	1	0	-2.043965	-0.286588	-2.932761
56	1	0	3.146761	1.213148	-2.985459
57	1	0	3.998133	-0.241287	-3.534754
58	1	0	2.362326	-0.364438	-2.870504
59	1	0	2.328437	1.366074	2.168667
60	1	0	2.50173	-0.281195	2.774903
61	1	0	3.776582	0.899932	3.077458
62	1	0	7.084219	-2.5068	0.073625
63	1	0	7.818009	-1.070159	-0.644229
64	1	0	7.602302	-1.174159	1.112538

Table D4. (NN^{TMS})UI_2(THF)			(Hartree/Particle)
Zero-point correction=			0.506651
Thermal correction to Energy=			0.546398
Thermal correction to Enthalpy=			0.547342
Thermal correction to Gibbs Free Energy=			0.428775
Sum of electronic and zero-point Energies=			-1743.070993
Sum of electronic and thermal Energies=			-1743.031246
Sum of electronic and thermal Enthalpies=			-1743.030301
Sum of electronic and thermal Free Energies=			-1743.148868
	E (Thermal)	**CV**	**S**
	KCal/Mol	*Cal/Mol-K*	*Cal/Mol-K*
Total	342.87	139.387	249.545
Electronic	0	0	2.183
Translational	0.889	2.981	46.34
Rotational	0.889	2.981	37.638
Vibrational	341.092	133.425	163.384

Table D5. (NN^{TBS})UI_2(THF)			(Hartree/Particle)
Zero-point correction=			0.680841
Thermal correction to Energy=			0.727401
Thermal correction to Enthalpy=			0.728345
Thermal correction to Gibbs Free Energy=			0.596591
Sum of electronic and zero-point Energies=			-1978.698304
Sum of electronic and thermal Energies=			-1978.651743
Sum of electronic and thermal Enthalpies=			-1978.650799
Sum of electronic and thermal Free Energies=			-1978.782553
	E (Thermal)	**CV**	**S**
	KCal/Mol	*Cal/Mol-K*	*Cal/Mol-K*
Total	456.451	169.251	277.3
Electronic	0	0	2.183
Translational	0.889	2.981	46.6
Rotational	0.889	2.981	38.373
Vibrational	454.674	163.29	190.144

Table D6. (NN^{MES})UI_2(THF)			(Hartree/Particle)
Zero-point correction=			0.510417
Thermal correction to Energy=			0.547957
Thermal correction to Enthalpy=			0.548901
Thermal correction to Gibbs Free Energy=			0.432716
Sum of electronic and zero-point Energies=			-1391.201471
Sum of electronic and thermal Energies=			-1391.163931
Sum of electronic and thermal Enthalpies=			-1391.162986
Sum of electronic and thermal Free Energies=			-1391.279172
	E (Thermal)	**CV**	**S**
	KCal/Mol	*Cal/Mol-K*	*Cal/Mol-K*
Total	343.848	135.03	244.533
Electronic	0	0	2.183
Translational	0.889	2.981	46.404
Rotational	0.889	2.981	38.271
Vibrational	342.071	129.068	157.676

4.5 REFERENCES

1. Johnston, R. F.; Borjas, R. E.; Furilla, J. L., Investigation of the Electrochemical Properties of Substituted Titanocene Dichlorides. *Electrochim. Acta* **1995,** 40, (4), 473-477.

2. Langmaier, J.; Samec, Z.; Varga, V.; Horàček, M.; Choukroun, R.; Mach, K., Cyclic Voltammetry of Methyl- and Trimethylsilyl-Substituted Zirconocene Dichlorides. *J. Organomet. Chem.* **1999,** 584, (2), 323-328.

3. Langmaier, J.; Samec, Z.; Varga, V.; Horàček, M.; Mach, K., Substituent Effects in Cyclic Voltammetry of Titanocene Dichlorides. *J. Organomet. Chem.* **1999,** 579, (1-2), 348-355.

4. Zachmanoglou, C. E.; Docrat, A.; Bridgewater, B. M.; Parkin, G.; Brandow, C. G.; Bercaw, J. E.; Jardine, C. N.; Lyall, M.; Green, J. C.; Keister, J. B., The Electronic Influence of Ring Substituents and Ansa Bridges in Zirconocene Complexes as Probed by Infrared Spectroscopic, Electrochemical, and Computational Studies. *J. Am. Chem. Soc.* **2002,** 124, (32), 9525-9546.

5. Morris, D. E.; Da Re, R. E.; Jantunen, K. C.; Castro-Rodriguez, I.; Kiplinger, J. L., Trends in Electronic Structure and Redox Energetics for Early-Actinide Pentamethylcyclopentadienyl Complexes. *Organometallics* **2004,** 23, (22), 5142-5153.

6. Cantat, T.; Scott, B. L.; Morris, D. E.; Kiplinger, J. L., What a Difference a 5f Element Makes: Trivalent and Tetravalent Uranium Halide Complexes Supported by One and Two Bis[2-(diisopropylphosphino)-4-methylphenyl]amido (PNP) Ligands. *Inorg. Chem.* **2009,** 48, (5), 2114-2127.

7. Sonnenberger, D. C.; Gaudiello, J. G., Cyclic Voltammetric Study of Organoactinide Compounds of Uranium(IV) and Neptunium(IV). Ligand Effects on the M(IV)/M(III) Couple. *Inorg. Chem.* **1988,** 27, (15), 2747-2748.

8. Gutmann, V., Solvent Effects on the Reactivities of Organometallic Compounds. *Coord. Chem. Rev.* **1976,** 18, (2), 225-255.

9. Sullivan, M. F.; Little, W. F., Mono- and Dialkyltitanocene Dichlorides. *J. Organomet. Chem.* **1967,** 8, (2), 277-285.

10. Sipos, L.; Jeftić, L. J.; Branica, M.; Galus, Z., Electrochemical Redox Mechanism of Uranium in Acidic Perchlorate Solutions. *J. Electroanal. Chem. Interfacial Electrochem.* **1971,** 32, (1), 35-47.

11. Zanello, P.; Cospito, M., Voltammetric Determination of Uranium(IV) with a Platinized Platinum Microelectrode with Periodical Renewal of the Diffusion Layer. *J. Electroanal. Chem. Interfacial Electrochem.* **1974,** 52, (1), 133-140.

12. Mugnier, Y.; Moise, C.; Laviron, E., Electrochemical Studies of Organometallic Compounds: I. On the Reversibility of the First Reduction Stage of Titanocene Dichloride. *J. Organomet. Chem.* **1981,** 204, (1), 61-66.

13. Fakhr, A.; Mugnier, Y.; Gautheron, B.; Laviron, E., Electrochemical Studies on Organometallic Compounds: XI. Electrogeneration of the Zirconium(III) and Hafnium(III) Anions of Zirconocene and Hafnocene Dichlorides. *J. Organomet. Chem.* **1986,** 302, (1), C7-C9.

14. Renaud, S.; Dormond, A.; Roullier, L.; Mugnier, Y., Réaction de Transfert Électronique sur le Chlorure de Tris(hexaméthyldisilylamido)uranium(IV). *J. Organomet. Chem.* **1988,** 347, (1-2), 71-76.

15. Vladimir V, S., Sandwich and Bent Sandwich Complexes. Electrochemical Studies. *Coord. Chem. Rev.* **1992,** 114, (1), 1-60.

16. Larsen, J.; Skrydstrup, T.; Daasbjerg, K., Mechanistic Investigation of the Electrochemical Reduction of Cp_2TiX_2. *Organometallics* **2004,** 23, (8), 1866-1874.

17. Larsen, J.; Hjølund, G. H.; Skrydstrup, T.; Daasbjerg, K., Influence of the Halogen in Titanocene Halide Promoted Reductions. *Organometallics* **2005,** 24, (6), 1252-1262.

18. Barriere, F.; Geiger, W. E., Use of Weakly Coordinating Anions to Develop an Integrated Approach to the Tuning of E½ Values by Medium Effects. *J. Am. Chem. Soc.* **2006,** 128, (12), 3980-3989.

19. Bard, A. J.; Faulkner, L. R., *Electrochemical Methods: Fundamentals and Applications*. Wiley: 2001.

20. Monreal, M. J.; Diaconescu, P. L., A Weak Interaction between Iron and Uranium in Uranium Alkyl Complexes Supported by Ferrocene Diamide Ligands. *Organometallics* **2008,** 27, (8), 1702-1706.

21. Newson, J. D.; Riddiford, A. C., The Kinetics of the Iodine Redox Process at Platinum Electrodes. *J. Electrochem. Soc.* **1961,** 108, (7), 699-706.

22. Yaraliyev, Y. A., Oxidation of Iodide Ions by Means of Cyclic Voltammetry. *Electrochim. Acta* **1984,** 29, (9), 1213-1214.

23. Mastragostino, M.; Nadjo, L.; Saveant, J. M., Disproportionation and ECE Mechanisms: Theoretical Analysis. Relationships for Linear Sweep Voltammetry. *Electrochim. Acta* **1968,** 13, (4), 721-749.

24. Mastragostino, M.; Saveant, J. M., Disproportionation and ECE Mechanisms. II. Reduction of the Uranyl Cation in Perchloric Acid. *Electrochim. Acta* **1968,** 13, (4), 751-762.

25. Nadjo, L.; Saveant, J. M., Disproportionation and ECE Mechanisms. III. Asymmetrical Potential-Scan Method: Diagnostic Criteria and Rate-Determination Procedures and Application to the Reduction Mechanism of the Uranyl Cation in Perchloric Acid. *Electrochim. Acta* **1971,** 16, (7), 887-900.

26. Clappe, C.; Leveugle, D.; Hauchard, D.; Durand, G., Electrochemical Studies of Tricyclopentadienyl Uranium(IV) Chloride Complexes: Evidence of a Disproportionation Mechanism in Oxidation. *J. Electroanal. Chem.* **1998,** 448, (1), 95-103.

27. Popov, A. I.; Swensen, R. F., Studies on the Chemistry of Halogens and of Polyhalides. V. Spectrophotometric Study of Polyhalogen Complexes in Acetonitrile and in Ethylene Dichloride. *J. Am. Chem. Soc.* **1955,** 77, (14), 3724-3726.

28. Rogers, E. I.; Streeter, I.; Aldous, L.; Hardacre, C.; Compton, R. G., Electrode Kinetics and Mechanism of Iodine Reduction in the Room-Temperature Ionic Liquid $[C_4mim][NTf_2]$. *J. Chem. Phys. C* **2008,** 112, (29), 10976-10981.

29. Graves, C. R.; Scott, B. L.; Morris, D. E.; Kiplinger, J. L., Facile Access to Pentavalent Uranium Organometallics: One-Electron Oxidation of Uranium(IV) Imido Complexes with Copper(I) Salts. *J. Am. Chem. Soc.* **2007,** 129, (39), 11914-11915.

30. Graves, C. R.; Scott, B. L.; Morris, D. E.; Kiplinger, J. L., Tetravalent and Pentavalent Uranium Acetylide Complexes Prepared by Oxidative Functionalization with CuCCPh. *Organometallics* **2008,** 27, (14), 3335-3337.

31. Graves, C. R.; Kiplinger, J. L., Pentavalent Uranium Chemistry-Synthetic Pursuit of a Rare Oxidation State. *Chem. Commun.* **2009**, (26), 3831-3853.

32. Evans, D. H., Voltammetry: Doing Chemistry with Electrodes. *Acc. Chem. Res.* **1977,** 10, (9), 313-319.

33. Evans, D. H., Solution Electron-Transfer Reactions in Organic and Organometallic Electrochemistry. *Chem. Rev.* **1990,** 90, (5), 739-751.

34. Weydert, M.; Brennan, J. G.; Andersen, R. A.; Bergman, R. G., Reactions of a Uranium(IV) Tertiary Alkyl Bond: Facile Ligand-Assisted Reduction and Insertion of Ethylene and Carbon Monoxide. *Organometallics* **1995,** 14, (8), 3942-3951.

35. Nicholson, R. S.; Shain, I., Theory of Stationary Electrode Polarography. Single Scan and Cyclic Methods Applied to Reversible, Irreversible, and Kinetic Systems. *Anal. Chem.* **1964,** 36, (4), 706-723.

36. Nicholson, R. S., Theory and Application of Cyclic Voltammetry for Measurement of Electrode Reaction Kinetics. *Anal. Chem.* **1965,** 37, (11), 1351-1355.

37. Jordan, R. F.; Bajgur, C. S.; Willett, R.; Scott, B., Ethylene Polymerization by a Cationic Dicyclopentadienyl Zirconium(IV) Alkyl Complex. *J. Am. Chem. Soc.* **1986,** 108, (23), 7410-7411.

38. Jordan, R. F.; Dasher, W. E.; Echols, S. F., Reactive Cationic Dicyclopentadienyl Zirconium(IV) Complexes. *J. Am. Chem. Soc.* **1986,** 108, (7), 1718-1719.

39. Jordan, R. F.; LaPointe, R. E.; Bajgur, C. S.; Echols, S. F.; Willett, R., Chemistry of Cationic Zirconium(IV) Benzyl Complexes. One-Electron Oxidation of d^0 Organometallics. *J. Am. Chem. Soc.* **1987,** 109, (13), 4111-4113.

40. Borkowsky, S. L.; Baenziger, N. C.; Jordan, R. F., Generation and Reactivity of Titanocene Benzyl $Cp_2Ti(CH_2Ph)(L)^+$ Complexes. Oxidation and Protonolysis Chemistry of $Cp_2Ti(CH_2Ph)_2$. *Organometallics* **1993,** 12, (2), 486-495.

41. Williams, S. J.; Pearson, J. M.; Levy, M., Anion Radicals of a Series of [2.2]Paracyclophanes and α,ω-Diarylalkanes. II. Electron Spin Resonance Investigation. *J. Am. Chem. Soc.* **1971,** 93, (21), 5483-5489.

42. Grovenstein, E.; Bhatti, A. M.; Quest, D. E.; Sengupta, D.; VanDerveer, D., Carbanions. 23. Cleavages of 1,2-Diphenylethane and Derivatives by Cesium-Potassium-Sodium Alloy. Competitive Rates of Bond Scission. *J. Am. Chem. Soc.* **1983,** 105, (20), 6290-6299.

43. Andrieux, C. P.; Gallardo, I.; Savéant, J. M., Outer-Sphere Electron-Transfer Reduction of Alkyl Halides. A Source of Alkyl Radicals or of Carbanions? Reduction of Alkyl Radicals. *J. Am. Chem. Soc.* **1989,** 111, (5), 1620-1626.

44. Michman, M.; Oron, M., Reaction of an Electron-Rich Radical-Cation with Electrogenerated Radicals in Indirect Anodic Oxidation. *Electrochim. Acta* **1994,** 39, (18), 2781-2787.

45. Ishiguro, K.; Nakano, T.; Shibata, H.; Sawaki, Y., Redox Reaction of Benzyl Radicals with Aromatic Radical Ions Photogenerated. The Marcus Inverted Region and the Selective Formation of Carbocations or Carbanions. *J. Am. Chem. Soc.* **1996,** 118, (31), 7255-7264.

46. Andrieux, C. P.; Blocman, C.; Dumas-Bouchiat, J. M.; Savéant, J. M., Heterogeneous and Homogeneous Electron Transfers to Aromatic Halides. An Electrochemical Redox Catalysis Study in the Halobenzene and Halopyridine Series. *J. Am. Chem. Soc.* **1979,** 101, (13), 3431-3441.

47. Andrieux, C. P.; Hapiot, P.; Savéant, J. M., Fast Kinetics by Means of Direct and Indirect Electrochemical Techniques. *Chem. Rev.* **1990,** 90, (5), 723-738.

48. Andrieux, C. P.; Le Gorande, A.; Savéant, J. M., Electron Transfer and Bond Breaking. Examples of Passage from a Sequential to a Concerted Mechanism in the Electrochemical Reductive Cleavage of Arylmethyl Halides. *J. Am. Chem. Soc.* **1992,** 114, (17), 6892-6904.

49. Andrieux, C. P.; Savéant, J. M., Reactions Occurring during Mixing: Basic Reaction Schemes and Examples in Solvated Electron Reductions. *J. Chem. Phys.* **1993,** 97, (41), 10879-10888.

50. Andrieux, C. P.; Savéant, J.-M.; Tallec, A.; Tardivel, R.; Tardy, C., Concerted and Stepwise Dissociative Electron Transfers. Oxidability of the Leaving Group and Strength of the Breaking Bond as Mechanism and Reactivity Governing Factors Illustrated by the Electrochemical Reduction of α-Substituted Acetophenones. *J. Am. Chem. Soc.* **1997,** 119, (10), 2420-2429.

51. de Souza, R. F. M.; de Souza, C. A.; Areias, M. C. C.; Cachet-Vivier, C.; Laurent, M.; Barhdadi, R.; Léonel, E.; Navarro, M.; Bieber, L. W., Electrochemical Coupling Reactions of Benzyl Halides on a Powder Cathode and Cavity Cell. *Electrochim. Acta* **2010,** 56, (1), 575-579.

52. Combellas, C.; Kanoufi, F.; Thiébault, A., Reducibility of the Carbon-Fluorine Bond in the Trifluoromethyl Group. *J. Electroanal. Chem.* **1996,** 407, (1-2), 195-202.

53. Ohrenberg, C.; Geiger, W. E., Electrochemistry in Benzotrifluoride: Redox Studies in a "Noncoordinating" Solvent Capable of Bridging the Organic and Fluorous Phases. *Inorg. Chem.* **2000,** 39, (13), 2948-2950.

54. Samuel, E.; Guery, D.; Vedel, J.; Basile, F., Electrochemical Reduction Of Zirconocene Dihalides And Dialkyls Studied By Electron Spin Resonance. *Organometallics* **1985,** 4, (6), 1073-1077.

55. Kiplinger, J. L.; Richmond, T. G.; Osterberg, C. E., Activation of Carbon-Fluorine Bonds by Metal Complexes. *Chem. Rev.* **1994,** 94, (2), 373-431.

56. O'Connor, P. E.; Berg, D. J.; Barclay, T., Photolytic Zirconium Benzyl Bond Cleavage and Subsequent Aryl C-F Activation in Zirconium Complexes of Fluorinated Aryl Diamides. *Organometallics* **2002,** 21, (19), 3947-3954.

57. Klahn, M.; Rosenthal, U., An Update on Recent Stoichiometric and Catalytic C-F Bond Cleavage Reactions by Lanthanide and Group 4 Transition-Metal Complexes. *Organometallics* **2012,** 31, (4), 1235-1244.

58. Evans, W. J.; Kozimor, S. A., Expanding the Chemistry of U^{3+} Reducing Agents. *Coord. Chem. Rev.* **2006,** 250, (7-8), 911-935.

59. Koch, D. A.; Henne, B. J.; Bartak, D. E., Carbanion and Radical Intermediacy in the Electrochemical Reduction of Benzyl Halides in Acetonitrile. *J. Electrochem. Soc.* **1987,** 134, (12), 3062-3067.

60. Wipf, D. O.; Wightman, R. M., Rapid Cleavage Reactions of Haloaromatic Radical Anions Measured with Fast-Scan Cyclic Voltammetry. *J. Chem. Phys.* **1989,** 93, (10), 4286-4291.

61. Isse, A. A.; De Giusti, A.; Gennaro, A., One- Versus Two-Electron Reaction Pathways in the Electrocatalytic Reduction of Benzyl Bromide at Silver Cathodes. *Tetrahedron Lett.* **2006,** 47, (44), 7735-7739.

62. Isse, A. A.; De Giusti, A.; Gennaro, A.; Falciola, L.; Mussini, P. R., Electrochemical Reduction of Benzyl Halides at a Silver Electrode. *Electrochim. Acta* **2006,** 51, (23), 4956-4964.

63. Magdesieva, T. V.; Graczyk, M.; Vallat, A.; Nikitin, O. M.; Demyanov, P. I.; Butin, K. P.; Vorotyntsev, M. A., Electrochemically Reduced Titanocene Dichloride as a Catalyst of Reductive Dehalogenation of Organic Halides. *Electrochim. Acta* **2006,** 52, (3), 1265-1280.

64. Kochi, J. K.; Buchanan, D., The Mechanism of Toluene and Bibenzyl Formation from Benzylchromium Ion. *J. Am. Chem. Soc.* **1965,** 87, (4), 853-862.

65. Clerici, A.; Minisci, F.; Porta, O., Nucleophilic Character of Alkyl Radicals. IX: The Benzyl Radical. *Tetrahedron* **1973,** 29, (18), 2775-2779.

66. Saveant, J. M., Dynamics of Cleavage and Formation of Anion Radicals into and from Radicals and Nucleophiles. Structure-Reactivity Relationships in $S_{RN}1$ Reactions. *J. Chem. Phys.* **1994,** 98, (14), 3716-3724.

67. Brown, O. R.; Harrison, J. A., Reactions of Cathodically-Generated Radicals and Anions. *J. Electroanal. Chem. Interfacial Electrochem.* **1969,** 21, (2), 387-407.

68. Parsons, A. F., *An Introduction to Free Radical Chemistry*. Blackwell Science: 2000.

69. Jaarinen, S.; Niiranen, J.; Koskikallio, J., Relative Rates of Nucleophilic Reactions of Benzyl Carbocation Formed in Photolysis of Benzyl Chloride and Benzyl Acetate in Aqueous Solution. *Int. J. Chem. Kinet.* **1985,** 17, (9), 925-930.

70. Giacomello, P.; Angelini, G.; Sparapani, C.; Speranza, M., Aromatic Substitution by Free Benzyl Cations from the Nuclear Decay of Multi-tritiated Toluene. Competitive Benzylation of Benzene and Toluene in the Gas Phase and in Solution. *J. Phys. Org. Chem.* **1989,** 2, (6), 467-475.

71. Gosser, D. K., *Cyclic Voltammetry: Simulation and Analysis of Reaction Mechanisms*. VCH: 1993.

72. Pangborn, A. B.; Giardello, M. A.; Grubbs, R. H.; Rosen, R. K.; Timmers, F. J., Safe and Convenient Procedure for Solvent Purification. *Organometallics* **1996,** 15, (5), 1518-1520.

73. Monreal, M. J.; Carver, C. T.; Diaconescu, P. L., Redox Processes in a Uranium Bis(1,1'-diamidoferrocene) Complex. *Inorg. Chem.* **2007,** 46, (18), 7226-7228.

74. Shafir, A.; Power, M. P.; Whitener, G. D.; Arnold, J., Silylated 1,1'-Diaminoferrocene: Ti and Zr Complexes of a New Chelating Diamide Ligand. *Organometallics* **2001,** 20, (7), 1365-1369.

75. Shafir, A.; Arnold, J., Zirconium Complexes Incorporating Diaryldiamidoferrocene Ligands: Generation of Cationic Derivatives and Polymerization Activity Towards Ethylene and 1-Hexene. *Inorg. Chim. Acta* **2003,** 345, (0), 216-220.

76. Bailey, P. J.; Coxall, R. A.; Dick, C. M.; Fabre, S.; Henderson, L. C.; Herber, C.; Liddle, S. T.; Lorono-Gonzalez, D.; Parkin, A.; Parsons, S., The First Structural Characterisation of a Group 2 Metal Alkylperoxide Complex: Comments on the Cleavage of Dioxygen by Magnesium Alkyl Complexes. *Chem. Eur. J.* **2003,** 9, (19), 4820-4828.

77. Sinha, A.; Schrock, R. R.; Müller, P.; Hoveyda, A. H., Diphenylamido Precursors to Bisalkoxide Molybdenum Olefin Metathesis Catalysts. *Organometallics* **2006,** 25, (19), 4621-4626.

78. Thomson, R. K.; Scott, B. L.; Morris, D. E.; Kiplinger, J. L., Synthesis, Structure, Spectroscopy and Redox Energetics of a Series of Uranium(IV) Mixed-Ligand Metallocene Complexes. *C. R. Chim.* **2010,** 13, (6-7), 790-802.

79. Monreal, M. J.; Thomson, R. K.; Cantat, T.; Travia, N. E.; Scott, B. L.; Kiplinger, J. L., $UI_4(1,4\text{-dioxane})_2$, $[UCl_4(1,4\text{-dioxane})]_2$, and $UI_3(1,4\text{-dioxane})_{1.5}$: Stable and Versatile Starting Materials for Low- and High-Valent Uranium Chemistry. *Organometallics* **2011,** 30, (7), 2031-2038.

80. Duhović, S.; Khan, S.; Diaconescu, P. L., *In situ* Generation of Uranium Alkyl Complexes. *Chem. Commun.* **2010,** 46, (19), 3390-3392.

81. Broderick, E. M.; Gutzwiller, N. P.; Diaconescu, P. L., Inter- and Intramolecular Hydroamination with a Uranium Dialkyl Precursor. *Organometallics* **2010,** 29, (15), 3242-3251.

CHAPTER 5

Electronic Communication in Bis(1,1'-Diamidoferrocene) Uranium Complexes

TABLE OF CONTENTS

5.1 INTRODUCTION

The diverse features of mixed valence complexes have intrigued researchers seeking new materials, as well as those interested in understanding the basis of physical properties, in fields ranging from geological and environmental[1] to biological[2-4] and medicinal[5-8] chemistry. The synthesis of such compounds dates back to the preparation of Prussian blue in 1704,[9-11] which in itself holds properties used by artists and doctors alike.[12] Perhaps the most extensively studied mixed valence complex, however, is the Creutz-Taube ion.[13] This

pyrazine-bridged diruthenium pentaammine system has served as both a theoretical[14] and an experimental[15] model of the correlation between electronic structure and the extent of electron delocalization.

The resurgence of interest brought on by the discovery of the Creutz-Taube ion in the late 1960's is evident from the growing number of complexes containing both strong and weak interactions between two metal centers.[16] Today, examples of interaction between two transition metals are essentially countless.[17-37] In contrast, mixed valence complexes involving f-block elements are still relatively rare even though one of the earliest examples dates back to 1915 when the blue color of a mixed oxide of cerium and uranium was described as resulting from the "oscillating" change in oxidation state.[38] Examples of electronic communication involving lanthanides include Fe–Yb,[39] and –Nd,[40] Re–Yb[41] and –Lu,[42] Rh– and Pd–Nd,[43] Ru–Lu,[44] Ln–Y,[45] and –Ga.[46] Similar examples with actinides include U–Re,[47, 48] –Ga[49, 50] –Mn,[51] and –Fe[52] as well as Th–Ru,[53, 54] –Ni,[55-57] and –Pt.[58]

In the last five years, our group has contributed to this field by studying synergistic effects that result from the interaction of iron-based ligands with metals in various oxidation states. More specifically, we have shown that 1,1'-ferrocene diamine ligands are capable of influencing bonding and enhancing reactivity of transition metals, lanthanides, and actinides.[59-66] The study described in this chapter was borne out of our desire to control such reactivity. We have systematically analyzed the properties of several tetravalent uranium complexes supported by 1,1'-ferrocene diamine ligands (**Chart 5.1**) using electronic and vibrational spectroscopy, electrochemistry and magnetism, as well as computational methodology.

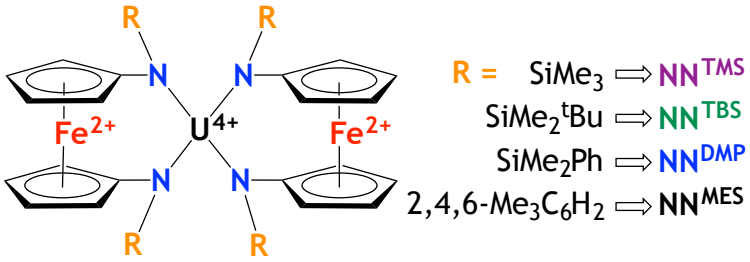

Chart 5.1. Uranium bis(1,1'-diamidoferrocene) complexes.

5.2 DISCUSSION OF RESULTS

The following discussion focuses on uranium complexes supported by two 1,1'-ferrocene diamide ligands. This section begins with a qualitative and quantitative examination of the electrochemical properties of title complexes. A discussion of chemical oxidation (**Figure 5.1**), isolation of the corresponding products, and a description of structural features are followed by a detailed analysis of spectroscopic and magnetic properties of both neutral and oxidized complexes. In order to gain a better understanding of $(NN^R)_2U$ complexes, each section draws upon the behavior of iron and uranium precursors as well as complexes bearing one 1,1'-ferrocene diamide ligand.

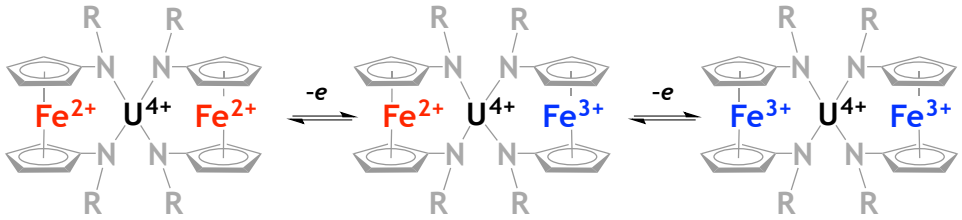

Figure 5.1. Oxidation of $(NN^R)_2U$ complexes.

5.2.1 Electrochemistry

One of the easiest methods used to investigate the existence of electronic communication between two redox-active centers is cyclic voltammetry. Before attempting to determine the presence and the extent of uranium-mediated electronic communication between two iron centers, we investigated the electrochemical properties of the

corresponding pro-ligands. Their electrochemical profiles feature one chemically reversible redox event corresponding to oxidation of Fe^{2+} to Fe^{3+}. As a result of the electron-donating nature of amine groups, 1,1'-ferrocene diamines are expected to have lower oxidation potentials than the parent ferrocene. Shafir et al. have previously reported a 600-mV decrease in the oxidation potential of iron upon functionalization of both Cp rings with NH_2.[67] We have observed that the extent of this shift quickly tapers off. That is, the difference in oxidation potential of iron is essentially negligible across the series of amino substituents on all four pro-ligands employed in our research. Nevertheless, we show that the influence each one imparts on tetravalent uranium is indeed unique.

To probe the electrochemical behavior of the corresponding **$(NN^R)_2U$** compounds, voltammetric and chronoamperometric experiments were carried out in various electrolyte media using a standard three-electrode cell. The former employed a 2-mm platinum disk as the working electrode. A 25-µm platinum disk microelectrode was used for the latter to observe the steady-state behavior and determine the number of electrons involved in each oxidation event. Due to solubility or stability factors, the scope of solvents was mostly limited to THF and dichloromethane. The former is strongly coordinating, whereas the latter is a low-donor solvent. The conducting media included both traditional electrolyte anions, such as halide, hexafluorophosphate and tetrafluoroborate salts, as well as more weakly coordinating ones, such as salts of tetrakis[3,5-bis(trifluoromethyl)phenyl]borate anions.

In principle, **$(NN^R)_2U$** complexes can undergo several redox events (**Figure 5.2**). More specifically, uranium can be reduced to U^{3+} or oxidized to U^{5+}, while each iron center can be oxidized to Fe^{3+}. If the interaction between the iron centers is strong, two redox events will be observed. Moreover, it is possible to determine the strength of this interaction by measuring the extent of potential difference. In other words, large separation between the two iron-based oxidation waves can be correlated to the thermodynamic stability of a

completely delocalized mixed valence system. It should be noted however, that factors such as ion pairing, solvation, as well as structural changes brought on by applied potential, affect the separation between the two waves. It is therefore important to survey a variety of conditions during electrochemical measurements.[68] The premise of using supporting electrolytes containing a weakly coordinating anion, for example, was to investigate the oxidative behavior of **$(NN^R)_2U$** compounds without the interference of ion pairing interactions between the corresponding cationic species and the supporting electrolyte anion, which tend to be strongest in lower-polarity solvents.[69]

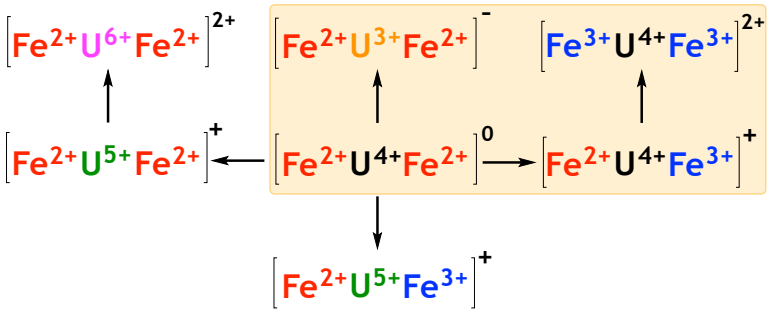

Figure 5.2. Possible redox events in **$(NN^R)_2U$** complexes; experimentally observed pathways are highlighted.

At least two redox events are observed for all **$(NN^R)_2U$** complexes. Reduction potentials vary from –2.3 V to –3.0 V in $TPABAr^F$ (**Figure 5.3**) and –2.83 V to –3.64 V in $TBAPF_6$ (**Figure 5.4**). At negative potentials, the observed event is assigned to reduction of uranium, which in a weakly coordinating medium, is quasi-reversible for **$(NN^{TBS})_2U$** and **$(NN^{MES})_2U$** but chemically irreversible for **$(NN^{TMS})_2U$** and **$(NN^{DMP})_2U$**. In contrast, the reduction process in solutions of a traditional electrolyte is chemically reversible for all species. These results suggest that in $TPABAr^F$, NN^{TMS} and NN^{DMP} ligands are not capable of stabilizing the increase in electron density on uranium. It is therefore important to emphasize the magnitude of influence that electrolytes can have on electrochemical processes. By using a smaller electrolyte anion (i.e. PF_6^- instead of BAr^{F-}) to maximize competitive ion pairing with electrolyte cation, as well as a less coordinating electrolyte cation (i.e. TBA^+ instead of TPA^+)

to minimize ion pairing with the anionic uranium complex, the reduction process becomes reversible.[70-82]

Similarly, oxidation potentials vary from –0.27 V to –0.86 V in $TPABAr^F$ and –0.56 V to –0.79 V in $TBAPF_6$. An additional one-electron oxidative event is revealed at more positive potential for **$(NN^{TBS})_2U$** and is better resolved in a THF solution of $TBAPF_6$. It is unclear whether this wave corresponds to oxidation of the second iron center or uranium itself, or whether it is merely due to oxidation of a product resulting from nucleophilic attack of the mixed-valence species.

The first anodic events are attributed to oxidation of iron. If one envisions a donor-acceptor interaction between iron and uranium, the only remarkable observation is the positive shift in potential when two H_2NN^{MES} or H_2NN^{TMS} ligands coordinate to uranium. As previously noted, relative to the parent ferrocene, the iron center becomes easier to oxidize with amino substituents on the cyclopentadienyl rings (i.e. $E_{1/2}$ becomes more negative). Moreover, the nature of substituents makes no significant difference in the oxidation potential. However, upon coordination to another –U(NN^R) moiety, the iron center in **$(NN^{MES})_2U$** and **$(NN^{TMS})_2U$** becomes slightly *harder* to oxidize relative to the corresponding pro-ligands. This effect then implies that in **$(NN^{MES})_2U$** and **$(NN^{TMS})_2U$**, uranium withdraws electron density from the iron center, which in turn signifies iron's perturbation by and an interaction with the uranium center.

Table 5.1. Oxidation of iron before and after coordination to uranium

OXIDATION *(THF/TBAPF$_6$)*	$E_{1/2}$ (V vs $Fc^{0/+}$)		ΔE (V)
	H_2NN^R	$(NN^R)_2U$	
$(NN^{TBS})_2U$	-0.69	-0.72	-0.03
$(NN^{TMS})_2U$	-0.73	-0.64	+0.09
$(NN^{DMP})_2U$	-0.70	-0.79	-0.09
$(NN^{MES})_2U$	-0.72	-0.56	+0.16

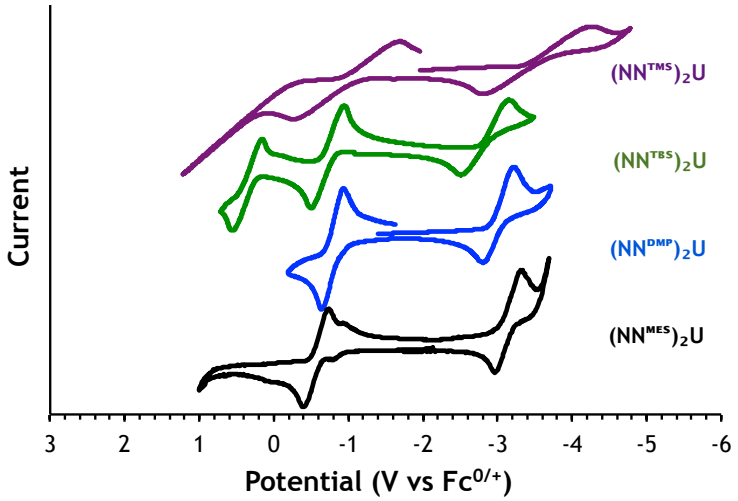

Figure 5.3. Cyclic voltammetry of $(NN^{R})_2U$ complexes in THF solutions of $TBAPF_6$ at 100 mV/s using a 2-mm platinum disk as the working electrode.

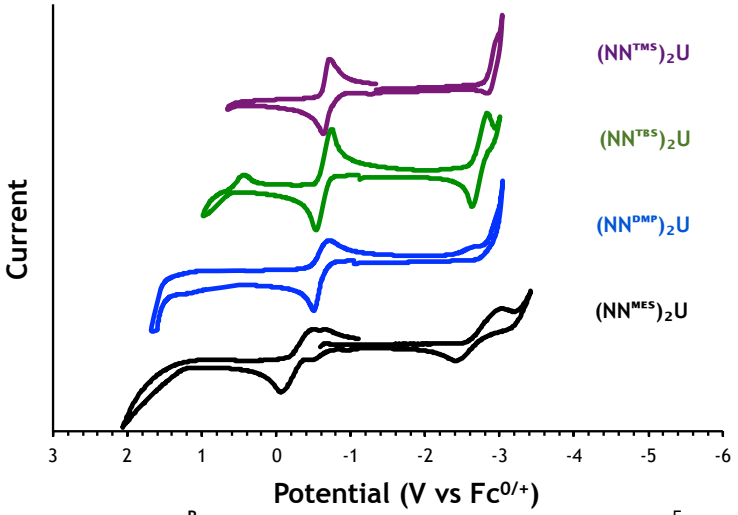

Figure 5.4. Cyclic voltammetry of $(NN^{R})_2U$ complexes in THF solutions of $TPABAr^{F}$ at 100 mV/s using a 2-mm platinum disk as the working electrode.

We initially hypothesized that the first oxidation event may be a two-electron process. So in order to induce two well-resolved one-electron processes, we used an electrolyte with a weakly coordinated anion.[70, 71, 80, 82-84] Surprisingly, the only improvement in the measurements was a decrease in uncompensated resistance (**Figure 5.4**). In order to then determine the number of electrons consumed in each oxidative event, a combination of transient and steady state methods were employed.[85-91] Chronoamperometric measurements of $(NN^{TBS})_2U$ in THF with $TBAPF_6$ and $TPABAr^{F}$ indicate that both oxidations are one-electron processes.

Measurements of $(NN^{TMS})_2U$ in THF with $TPABAr^F$ reveal that the oxidation is also a one-electron event. In the same type of medium, quantifying the electrons involved in oxidation of $(NN^{MES})_2U$ was impeded by the presence of a small oxidative wave slightly overlapping the main event. The magnitude of the potential required to induce that small wave matches the oxidation potential of free ligand. However, ^1H NMR spectrum of the cell solution after each measurement showed no corresponding shifts. Furthermore, dissociation of the ligand induced by oxidation of iron can be ruled out because the small wave is observed at more negative potentials (i.e. it occurs *before* the main event). Curiously, the current generated by the minor oxidation event is considerably smaller when the experiment was conducted in a THF solution of $TBAPF_6$, in which case a one-electron process was revealed (see Appendix E).

In contrast, analogous measurements of $(NN^{DMP})_2U$ in two different cell media (namely, THF solutions of $TBAPF_6$ and $TPABAr^F$) reveal that the sole oxidation event is actually a two-electron process. To obtain more substantial evidence, we conducted electrochemical measurements of $(NN^{DMP})_2U$ under a variety of conditions and found that using a tetraalkylammonium halide as the supporting electrolyte in a non-coordinating solvent exposes this phenomenon more clearly. Differential pulse voltammetry (DPV) measurements of $(NN^{DMP})_2U$ in a dichloromethane solution of TBABr clearly show two oxidation events (**Figure 5.5**). This is indeed a significant piece of evidence for a simultaneous transfer of two electrons and is consistent with crystallographic results (vide infra).

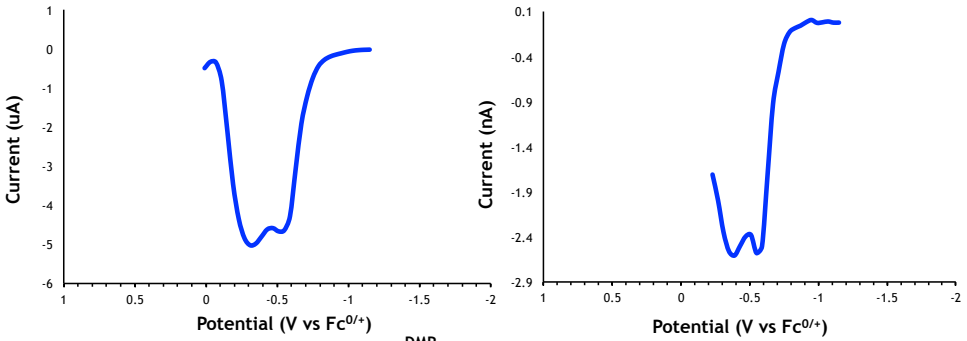

Figure 5.5. Differential pulse voltammetry of $(NN^{DMP})_2U$ in DCM solution of TBABr at 100 mV/s using a 2-mm (left) platinum disk and a 25-μm (right) as the working electrodes.

5.2.2 Chemical Oxidation of $(NN^R)_2U$ Complexes and Decomposition of Oxidized Products

Our attempts to grow single crystals of the oxidation products led us to the observation that only **$[(NN^{TBS})_2U][I_3]$** is stable (**Figure 5.6**). For example, allowing the reaction mixture to stir for 15 min, collecting the resulting powder by filtration onto a medium-porosity frit, then merely washing with it copious amounts of a hydrocarbon solvent resulted in analytically pure triiodide salts. Elemental analysis confirmed the formation of **$[(NN^{TBS})_2U][I_3]$**, **$[(NN^{MES})_2U][I_3]$**, $[(NN^{TMS})_2U][I_3]$, and $[(NN^{DMP})_2U][I_3I]$. However, subsequently dissolving the powder in THF or dichloromethane decomposes the products. For example, the color of **$[(NN^{MES})_2U][I_3]$** changes from black to orange after several minutes in solution. This decomposition is faster in THF than DCM and unsurprisingly, it is accelerated at higher temperature. The color alone is characteristic of the neutral species and this is supported by ^{1}H NMR spectroscopy. Compiled spectra in **Figure 5.9** show that the neutral species is regenerated.

Unlike **$[(NN^{MES})_2U][I_3]$**, singly oxidized **$(NN^{TMS})_2U$** and doubly oxidized **$(NN^{DMP})_2U$** are relatively stable in DCM, but decompose in THF at room temperature after several minutes. However, their decomposition does not lead to regeneration of the neutral compounds. ^{1}H NMR spectra of the decomposition products clearly show formation of new species (**Figures 5.7-5.9**). Crystallographic evidence reveals decomposition of **$[(NN^{TMS})_2U][I_3]$** to the analogous tetraiodoferrate salt, **$[(NN^{TMS})_2U][FeI_4]$** and **$[(NN^{DMP})_2U][I_3I]$** to $[(NN^{DMP})_2U][I_3I_5]$.

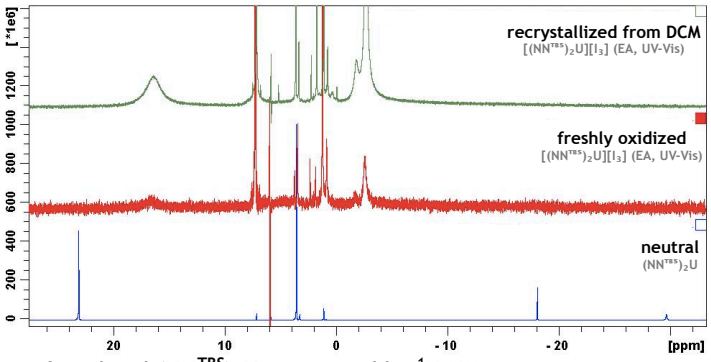

Figure 5.6. Decomposition of oxidized $(NN^{TBS})_2U$ monitored by ^1H NMR.

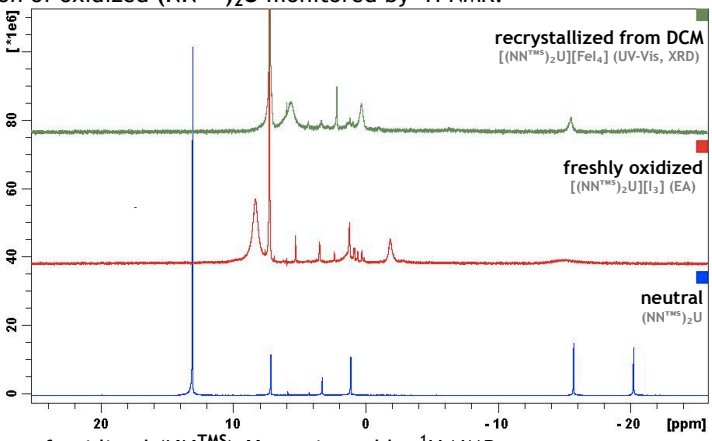

Figure 5.7. Decomposition of oxidized $(NN^{TMS})_2U$ monitored by ^1H NMR.

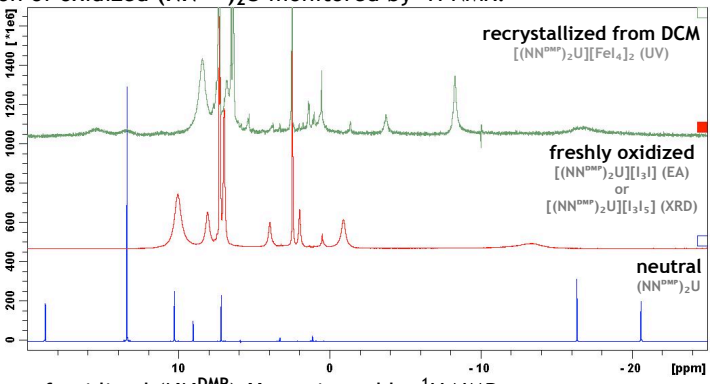

Figure 5.8. Decomposition of oxidized $(NN^{DMP})_2U$ monitored by ^1H NMR.

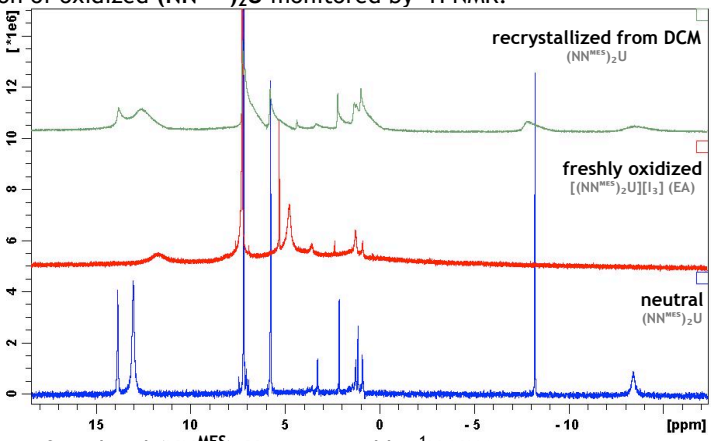

Figure 5.9. Decomposition of oxidized $(NN^{MES})_2U$ monitored by ^1H NMR.

5.2.3 Structural Features

Direct examination of the structural features of neutral, monooxidized, and dioxidized complexes can offer insight into the potential interaction between iron and uranium centers. Many coordination modes of substituted ferrocene derivatives have been revealed.[92-95] The types of deformation in disubstituted ferrocene ligands that can influence the interaction between iron and uranium include twists and tilts of Cp rings relative to one other, as well as displacement of the substituents from the plane defined by each Cp ring.[96] For example, it has been suggested that greater torsion angles between the Cp rings (**Figure 5.10**) may enforce weak metal-metal interactions in closed-bridging complexes supported by 1,1'-bis(diphenyphosphino)ferrocene ligands.[96] Likewise, theoretical treatments of interannular-bridged metallocenes have suggested that tilting of the Cp rings may change the energy of non-bonding orbitals on the iron center, redistribute the electron density around it, and by influencing the extent of back-donation, bring about an increase in its Lewis basicity.[97-100] Moreover, others have proposed that ring-tilting in mixed-valence biferrocenium systems leads to greater electron-transfer rates.[101-104]

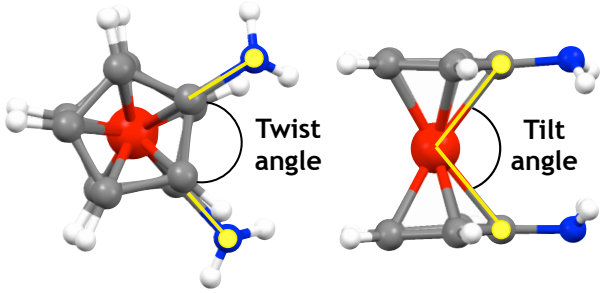

Figure 5.10. Twisting (defined by the NC-CN dihedral angle) and tilting (defined by C-Fe-C angle).

For neutral **$(NN^{R})_2U$** complexes (**Figure 5.11**), it can be seen that as the torsion angle (twist) between Cp rings increases, the distance between iron and uranium decreases (**Figure 5.12**). For example, **$(NN^{MES})_2U$** contains two structurally distinct ferrocene moieties. The ligand whose Cp rings are twisted by only 2.1° relative to each other features an iron-uranium

distance of 3.5 Å. In the ligand with rings twisted by 8.0°, the iron-uranium distance is 3.4 Å. This effect is also evident across the ligand series. For example, average torsion angles of 22.7° and 37.2° in $(NN^{TMS})_2U$ and $(NN^{TBS})_2U$ correlate with average iron-uranium distances of 3.3 Å and 3.2 Å, respectively. Like $(NN^{MES})_2U$, the torsion of Cp rings in $(NN^{DMP})_2U$ is very small. Moreover, the rings in both ferrocene backbones are perfectly eclipsed. As a result, the distance between iron and uranium is long.

Similarly, greater tilting of the Cp rings leads to a shorter iron-uranium distance (**Figure 5.12**). For example, the average iron-uranium distances of 3.5 Å and 3.5 Å in $(NN^{MES})_2U$ and $(NN^{DMP})_2U$ accompany slight increase in tilt angles of 115.6° and 117.0°, respectively while shorter iron-uranium distances in $(NN^{TBS})_2U$ and $(NN^{TMS})_2U$ accompany greater tilt angles of 120.8° and 121.9°, respectively.

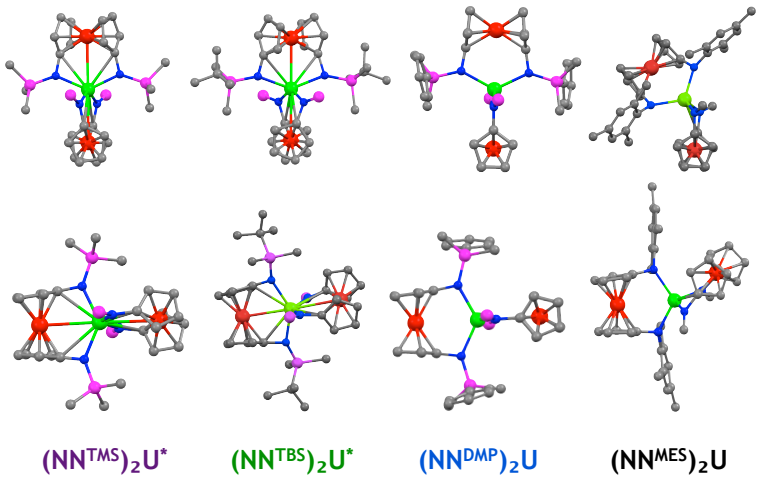

Figure 5.11. Ball-and-stick representation of molecular structures of $(NN^R)_2U$ complexes. For clarity, hydrogen atoms and two silyl substituents were removed. $(NN^{TMS})_2U$ and $(NN^{TBS})_2U$ were from reference [64].

Table 5.2. Relevant structural parameters of $(NN^R)_2U$ complexes.

	$(NN^{TMS})_2U$	$(NN^{TBS})_2U$	$(NN^{DMP})_2U$	$(NN^{MES})_2U$
Tilt (°)	120.8	121.9	117.0	115.6
Twist (°)	22.7	37.2	1.4	5.1
Fe-U-Fe (°)	178.3	177.1	178.5	135.2
Fe-U (Å)	3.33	3.21	3.51	3.47
Fe-Fe (Å)	6.65	6.42	7.02	6.41

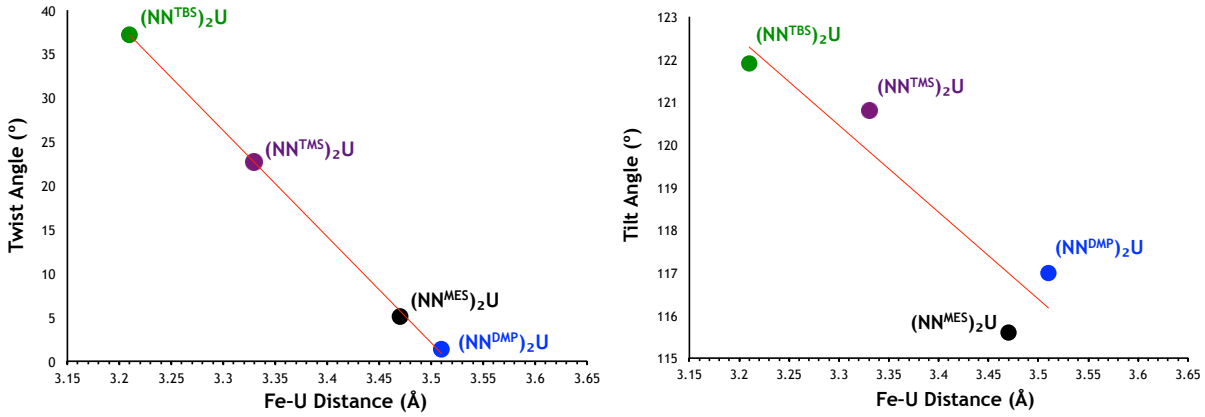

Figure 5.12. Correlation of iron-uranium distance with ring twisting and tilting.

In order to accommodate further decrease of this distance upon oxidation, both angular distortions expand even more. For example, when **$(NN^{TBS})_2U$** is oxidized, the Cp rings twist and tilt relative to each other even more, and in turn, push the iron center closer to uranium. That is, the average iron-uranium distance in **$(NN^{TBS})_2U$** decreases by 0.26 Å upon oxidation. These structural parameters are consistent with previous studies of geometrical distortions in multinuclear iron complexes,[105-109] and support the existence of a weak direct interaction between iron and uranium. More importantly, no significant difference in iron-uranium distance is observed between ferrocene and ferrocenium moieties in **$[(NN^{TBS})_2U][BPh_4]$** (**Figure 5.13**), further supporting its valence-delocalized nature.

As shown in **Figure 5.14**, oxidized **$(NN^{TMS})_2U$** bears an iron halide counteranion, whose metal-ligand bond lengths are consistent with a high-spin Fe^{3+} center (**Table 5.3**).[110] This is also consistent with the chronoamperometric data described previously and serves as evidence that the oxidation of **$(NN^{TMS})_2U$** is a one-electron event. Within the cation, the metal-metal distances are slightly longer, while both angular distortions are greater than those in **$[(NN^{TBS})_2U][BPh_4]$**. These structural parameters are consistent with spectral data, which show that mixed-valence **$[(NN^{TMS})_2U][FeI_4]$** exhibits weaker electronic communication between the ferrocene and ferrocenium moieties (*vide infra*).

Interestingly, while both iron-uranium distances, as well as the corresponding tilt angles, in the doubly oxidized **[(NN^{DMP})$_2$U][I$_3$I$_5$]** (**Figure 5.15**) are essentially identical, considerable difference is observed in the torsion angles. Specifically, both Fe^{3+} centers are 2.95 Å away from uranium, but the twisting in each pair of Cp rings differs by 7.1°.

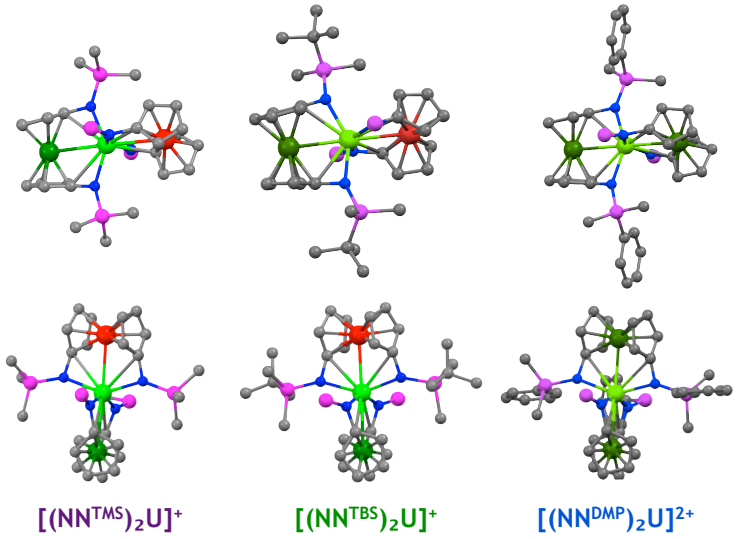

Figure 5.13. Ball-and-stick representation of molecular structure of oxidized **(NN^R)$_2$U** complexes. For clarity, anions, hydrogen atoms, and two silyl substituents were removed. **[(NN^{TBS})$_2$U]$^+$** was taken from reference [64].

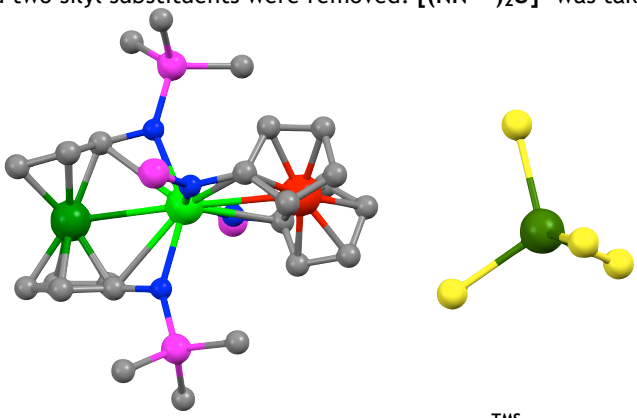

Figure 5.14. Ball-and-stick representation of molecular structure of **[(NN^{TMS})$_2$U][FeI$_4$]**. For clarity, hydrogen atoms and two silyl substituents were removed.

Table 5.3. Metal-ligand bond lengths in **[FeI$_4$]$^-$** and **[FeI$_4$]$^{2-}$**. *From reference [110].

	Fe-I (Å)*	Coordination
FeI$_2$	288.0(0)	Octahedral
Rb$_2$FeI$_4$	263.3(6)	Tetrahedral
(Et$_4$N)$_2$FeI$_4$	263.3(8)	Tetrahedral
Fe(THF)$_6$(FeI$_3$THF)$_2$	260.0(4)	Distorted Tetrahedral
Et$_4$NFeI$_4$ (I)	253.1(3)	Tetrahedral
Et$_4$NFeI$_4$ (II)	254.0(3)	Tetrahedral
[(NN^{TMS})$_2$U][FeI$_4$]	***254.3(5)***	***Tetrahedral***

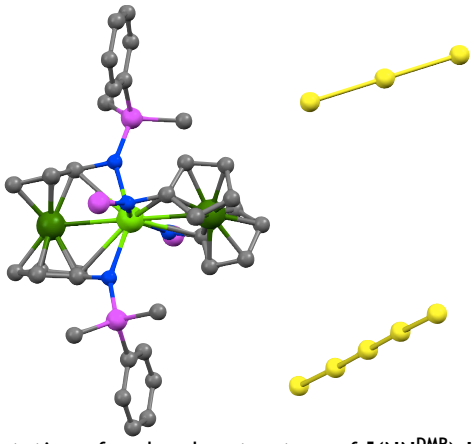

Figure 5.15. Ball-and-stick representation of molecular structure of **[(NN^{DMP})$_2$U][I$_3$I$_5$]**. For clarity, hydrogen atoms and two silyl substituents were removed.

Table 5.4. Relevant structural parameters of oxidized **(NN^{R})$_2$U** complexes.

	[(NN^{TMS})^{2}U]$^+$		[(NN^{TBS})$_2$U]$^+$		[(NN^{DMP})$_2$U]$^{2+}$	
Tilt (°)	124.7		126.6		126.9	
Twist (°)	29.4	27.4	39.4	41.7	31.4	38.5
Fe-U-Fe (°)	177.8		178.6		179.1	
Fe-U (Å)	3.04		2.95		2.95	
Fe-Fe (Å)	6.07		5.89		5.90	

5.2.4 Vibrational Spectroscopy

In order to gain further insight into the electronic structures, we analyzed the infrared spectra of both the neutral and oxidized complexes. For sake of comparison, the spectra were compared with those of uranium supported by a single ferrocene-based ligand. Finally, we relied on DFT calculations of the pro-ligands described in Chapter 1 to facilitate the interpretation of the fundamental vibrational modes. Previous studies on ferrocene and ferrocenium derivatives have found that energy of the perpendicular C-H bending on both Cp rings is most sensitive to the oxidation state of iron. For instance, the band corresponding to this vibrational mode shifts to *higher* energy upon oxidation of ferrocene.[111] Therefore, we studied the IR spectra of each complex before and after oxidation.

The most obvious difference between IR spectra of 1,1'-ferrocene diamines and those of uranium complexes is the disappearance of a strong band at approximately 1500 cm^{-1},

which corresponds to the ring C-N stretching (**Figure 5.16**). The vibrational spectrum of **$(NN^{MES})_2U$** is drastically different from the other three **$(NN^{R})_2U$** complexes. It displays more peaks, which are broader and less intense than those observed in other neutral **$(NN^{R})_2U$** complexes. These results are expected considering the symmetry differences of the two types of compounds. Due to the complexity and poor resolution of the IR spectra, no further discussion will be devoted to the vibrational modes of the mesityl analogues.

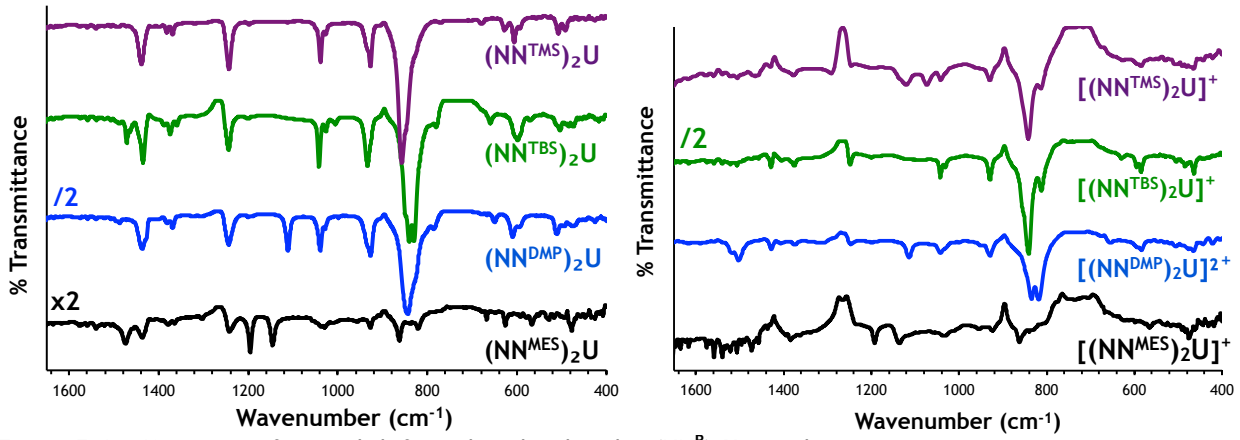

Figure 5.16. IR spectra of neutral (left) and oxidized (right) **$(NN^{R})_2U$** complexes.

Neutral **$(NN^{TBS})_2U$** and **$(NN^{TMS})_2U$** are virtually identical. The only apparent difference is in the strong band located at approximately 800cm^{-1}. In **$(NN^{TBS})_2U$**, this band appears to be split while in **$(NN^{TMS})_2U$**, it is merely shifted to a slightly higher frequency. The IR spectrum of **$(NN^{DMP})_2U$** resembles that of **$(NN^{TMS})_2U$**, with an additional band at 1034 cm^{-1}, which likely corresponds to the C-C stretch of the phenyl rings. It is unlikely that the strong band at 800 cm^{-1} arises from the aforementioned perpendicular C-H bending. To facilitate the assignment of this band, we performed geometry optimization and frequency calculation of **$(NN^{TBS})UI_2(THF)$** and compared the resulting IR spectrum to that measured experimentally. Although slightly, but systematically shifted, the former is in good agreement with experimental results (**Figure 5.17**). According to our calculations, the perpendicular C-H bending in **$(NN^{TBS})UI_2(THF)$** gives rise to a weak band at approximately 840 cm^{-1}. In our hands,

the same vibration in the parent ferrocene is observed at 820 cm^{-1}. This shift to higher energy upon coordination to a UI_2 moiety is expected and is consistent with our cyclic voltammetry data, which show that the oxidation potential of iron in **$(NN^{TBS})UI_2(THF)$** is comparable to that in ferrocene (i.e. electron density on the iron center is similar). As described in the previous section, however, the oxidation potential of iron in **$(NN^{R})_2U$** complexes is comparable to that in the related pro-ligands. Accordingly, if the perpendicular C-H bending is indeed diagnostic of the oxidation state of iron, it is expected to give rise to bands of similar energy before and after two ferrocene diamide ligands coordinate to uranium (i.e. 700-800 cm^{-1}).

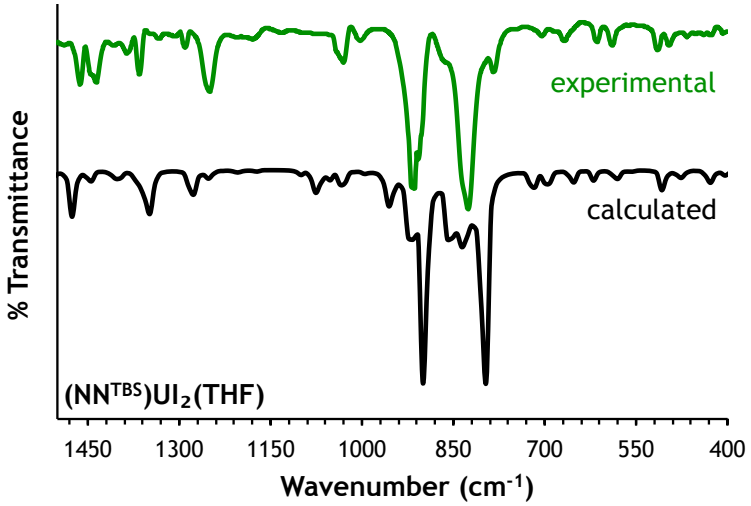

Figure 5.17. Experimental (THF) and calculated (gas phase) IR spectra of **$(NN^{TBS})UI_2(THF)$**.

Figure 5.18 shows the IR spectra of freshly oxidized complexes supported by bis(silyl)diamidoferrocene ligands. All three spectra are broader than their neutral counterparts. The band at approximately 800 cm^{-1} is nearly identical in **$[(NN^{TMS})_2U]^+$** and **$[(NN^{TBS})_2U]^+$** with a shoulder revealed at lower energy. Doubly oxidized **$(NN^{DMP})_2U$** complex, on the other hand, shows two poorly resolved bands. That no shift in energy of this band occurs upon oxidation is further evidence against its assignment as perpendicular C-H bending. Nonetheless, this spectral feature does appear to be dependent on the extent of iron oxidation (**Figure 5.19**). It would not be unreasonable to imagine then that the intense band in oxidized **$(NN^{TMS})_2U$** and **$(NN^{TBS})_2U$** complexes corresponds to various stretching and bending

modes involving methyl C-H bonds on the amino substituents of the ferrocenium moiety (Fe^{3+}), while the shoulder at lower energy corresponds to that of the ferrocene ligand (Fe^{2+}). Accordingly, the symmetric splitting of the band observed in the doubly oxidized **$(NN^{DMP})_2U$** species is likely due to vibrational modes involving methyl C-H bonds of two ferrocenium ligands. These observations are consistent with the electronic absorption findings and give further validity to the two-electron oxidation hypothesis.

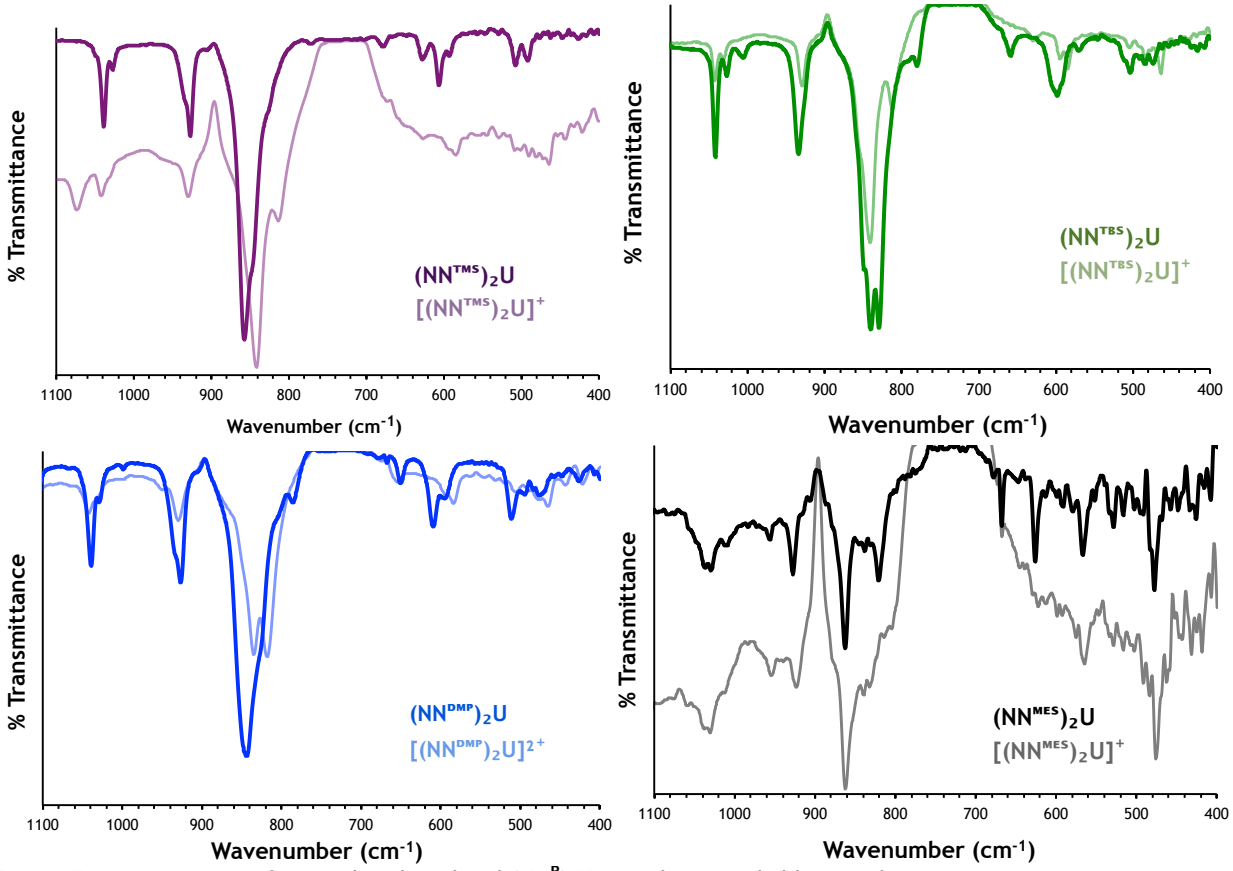

Figure 5.18. IR spectra of neutral and oxidized **$(NN^R)_2U$** complexes in dichloromethane.

5.2.5 Electronic Absorption Spectroscopy

Electronic absorption spectroscopy has been used extensively to study both homo- and hetero- polynuclear systems in which two or more metal centers have different oxidation states.[112-118] Absorption bands observed in spectra of organoactinide complexes originate from three types of electronic transitions. Intraconfigurational f → f transitions are Leporte

forbidden and are manifested as weak bands in the near–IR region.[119-122] Spectral features arising from these transitions are expected to remain roughly constant upon changing the ligand environment around the uranium center. In contrast, interconfigurational f → d transitions are allowed and thus give rise to intense absorption bands at high energy.[123] Spectra of organoactinide systems also feature absorption bands originating from charge transfer between the metal center and its ligands. Like f → d transitions, charge transfer bands are observed at high energy but are typically more intense.[124-127] Moreover, the energy of charge transfer bands is affected by both the nature of the ligand and the oxidation state of the metal, as well as the distance between them.[123] In principle, absorption bands of the uranium systems presented herein may also originate from electronic transitions based on one or both iron centers as well as their interaction with either amino substituents or uranium. In order to deduce their origin, we compared both positions and intensities of these bands to those of corresponding pro-ligands, Et_2O and THF adducts of uranium tetraiodide and triiodide, respectively, as well as uranium diiodide, dibenzyl, and bis(aryloxide) complexes supported by a single diamidoferrocene ligand. In addition to facilitating our understanding of uranium–mediated electronic communication between iron centers, absorption spectra of oxidized compounds were crucial to the characterization of complexes that failed to appropriately crystallize. Moreover, low temperature measurements of dichloromethane solutions of oxidized species aided in confirming the results of elemental analysis.

5.2.5.1 UV-Vis spectroscopy

The absorption spectrum of ferrocene contains two broad bands in the UV–Vis region. The band centered at 324 nm corresponds to a combination of a forbidden electronic transition involving some 3d character and intramolecular charge transfer, while the band centered at 439 nm (ε = 96 $M^{-1}cm^{-1}$) corresponds to a relatively pure d → d transition

(forbidden $e_{2g} \rightarrow a_{1g}$ transition).[128-131] Additionally, the ligand-to-metal charge transfer band of ferrocene is centered at 200 nm.[132, 133]

Similarly, absorption spectra of the pro-ligands (**Figure 5.20**) show one band centered between 447 nm and 452 nm (ε = 180–450 $M^{-1}cm^{-1}$). The negligible shift to longer wavelengths is expected because the origin of this transition involves orbitals of pure metal character and thus should be relatively insensitive to substitution on the Cp rings.[130, 134] The intensity of these formally forbidden transitions, however, is greater than that observed for the parent ferrocene. Finally, as a result of the electron-donating ability of diamido substituents, charge transfer from substituted cyclopentadienyl ligands to Fe^{2+} likely gives rise to absorption bands at wavelengths shorter than the solvent cutoff.

When the pro-ligands are oxidized with iodine, two intense bands at 380 nm (ε = 3000-5000 $M^{-1}cm^{-1}$) and 450 nm (ε = 3600–6200 $M^{-1}cm^{-1}$) as well as a broad band at approximately 849 nm (ε = 854 $M^{-1}cm^{-1}$) are observed. The high energy bands are assigned to spin-allowed d→d transitions, while the broad band at lower energy is assigned to a ligand → metal charge transfer transition characteristic of Fe^{3+} complexes.[132] In the parent ferrocenium cation, this band is observed at 617 nm, and has been reported to shift upon substitution of the Cp rings.[135] In the present case, the observed red shift can be explained on the basis of electron-donating ability of amino substituents and is in agreement with the electrochemical results described in the previous section. It is also important to note that no significant difference in transition energy is observed between the four ligands. This, too, is consistent with cyclic voltammetry data, which reveal a negligible change in oxidation potential across the ligand series.

Electronic transitions in the THF adduct of uranium triiodide give rise to a more complex spectrum, with bands at 340 nm (ε = 1057 $M^{-1}cm^{-1}$), 493 nm (ε = 1557 $M^{-1}cm^{-1}$), 501 nm (ε = 1654 $M^{-1}cm^{-1}$), and 578–644 nm (ε = 951–1239 $M^{-1}cm^{-1}$), which have previously been

assigned as Leporte-allowed f → d transitions within the uranium core.[136, 137] In contrast, absorption spectra of the dioxane and diethyl ether adducts of uranium tetraiodide, **UI_4(1,4-dioxane)$_2$**[138] and **$UI_4(Et_2O)_2$**,[139] possess several features between 310 nm and 400 nm (ε = 2140-6670 $M^{-1}cm^{-1}$) that correspond to metal-based transitions, as well as a weaker band at 498 nm (ε = 1130 $M^{-1}cm^{-1}$), which has been previously attributed to iodide → uranium charge transfer.[139-142]

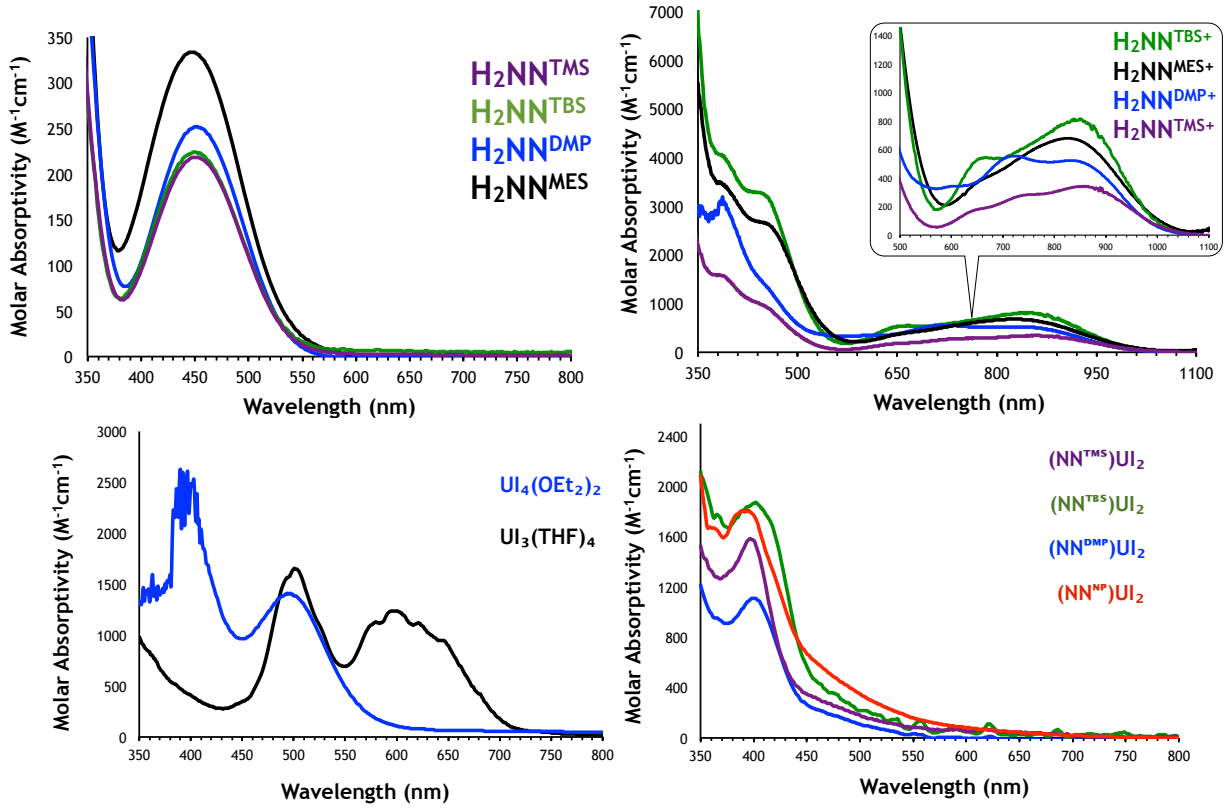

Figure 5.19. UV-Vis spectra of neutral (top left) and oxidized (top right) **H_2NN^R** in DCM, U^{4+} and U^{3+} precursors (bottom left) in diethyl ether and THF, respectively (bottom left), and **$(NN^R)UI_2$(THF)** complexes in THF (bottom right).

A solvent-insensitive absorption band at approximately 400 nm is observed when two iodides are replaced with a single dianionic 1,1'-ferrocene diamide ligand in the **$(NN^R)UI_2$(THF)** series. The extinction coefficient values (1140-1870 $M^{-1}cm^{-1}$) preclude d → d transitions within the iron center as its origin. Moreover, charge transfer between both metals

and diamidoferrocene ligands can be ruled out because the energy of the transition is nearly constant across the ligand series (**Figure 5.20**).

Based on previously reported electronic absorption spectra of tetravalent uranium complexes,[117, 118, 137, 143-147] it is likely that this band arises from either 5f → 6d transitions within the uranium core or iodide→uranium charge transfer. Although the former are typically weaker than the latter, accurate assignment of spectral features is difficult because both transitions require high energy and give rise to broad bands of vibronic nature.[124, 125, 148]

Because charge transfer is mainly a function of a given ligand, accepting it as the origin of the band at 400 nm demands an explanation for the energy increase observed on changing the ligand field from I^- to $[NN^R]^{2-}$ (assuming the 496 nm band in $\mathbf{UI_4(Et_2O)_2}$ was correctly assigned and is indeed due to iodide → uranium charge transfer). As already mentioned, two additional factors influence the energy of charge transfer: oxidation state of the metal center and its distance from the ligand in question. The former can be used to explain the energy shift from 496 nm in $\mathbf{UI_4(Et_2O)_2}$ to 400 nm in $\mathbf{(NN^R)UI_2(THF)}$. If charge transfer is viewed as an internal redox event[149] in which the uranium center is reduced by iodide, then the observed increase in energy of the transition is rationalized on the basis of uranium's relative electron affinity.[124] According to our cyclic voltammetry measurements, uranium is more electron rich in $\mathbf{(NN^R)UI_2}$ complexes than in $\mathbf{UI_4(Et_2O)_2}$. That is, its reduction potential is greater by approximately 1 V, and in turn, its electron affinity is lower. Consequently, in $\mathbf{(NN^R)UI_2}$, more energy is required to excite an electron into one of uranium-based orbitals.

Evidence against charge transfer assignment, on the other hand, is two-fold. First, energy of the bands corresponding to charge transfer is known to shift with solvent polarity.[150] In this case, however, the band's energy is insensitive to the solvent used in data acquisition. The second argument against charge transfer assignment stems from the distance

between uranium and iodide ligands. If, indeed, the band at 400 nm arises from ligand-to-metal charge transfer, then it follows that the distance between uranium and iodide ligands should be shorter in $(NN^R)UI_2$ than that in $UI_4(Et_2O)_2$. The expected decrease in bond length is based on the notion that removing an electron from an iodide ligand requires more energy when it is closer to, and thus, more covalently bound to uranium.[124] However, crystallographic evidence shows that this, in fact, is not the case. The average uranium-iodide distance in $UI_4(Et_2O)_2$ and $(NN^{TMS})UI_2$, for example, is 2.96 Å and 3.35 Å, respectively. Accordingly, iodide–uranium charge transfer band is then expected to shift to *lower* energy. To this end, we are inclined to attribute the band at 400 nm to 5f → 6d transitions within the uranium core.

As shown in **Figure 5.21**, absorption spectra of all neutral $(NN^R)_2U$ complexes feature one broad, solvent-independent absorption band in the UV–Vis region with an extinction coefficient characteristic of tetravalent uranium complexes.[137, 151-154] Neutral $(NN^{TMS})_2U$ and $(NN^{DMP})_2U$ exhibit nearly identical spectra with most intense bands at 401 nm (ε = 1276 $M^{-1}cm^{-1}$) and 405 nm (ε = 1175 $M^{-1}cm^{-1}$), respectively, while $(NN^{TBS})_2U$ gives rise to a related band at 434 nm (ε = 1810 $M^{-1}cm^{-1}$). The electronic transition in the arylamidoferrocene derivative, $(NN^{MES})_2U$, has a maximum absorption at slightly lower energy (445 nm, ε = 2299 $M^{-1}cm^{-1}$).

Both the energy and the intensity of this transition then, follow the order: $(NN^{DMP})_2U \sim (NN^{TMS})_2U > (NN^{TBS})_2U > (NN^{MES})_2U$. The energy values are similar to those of d → d transitions in pro-ligands, but the intensity of these bands is too high to be of similar origin. Moreover, because the band position is different for each ligand, f → d transitions within the uranium core can also be ruled out. Finally, attributing these bands to Cp → Fe charge transfer is not merited considering that the corresponding transition in ferrocene itself is observed at 200 nm. According to the first oxidation potential values obtained with cyclic voltammetry, iron in all four $(NN^R)_2U$ complexes is more electron-rich than that in ferrocene. Accordingly,

charge transfer from Cp ligands to Fe is expected to require greater energy and thus give rise to absorption bands at wavelengths shorter than 200 nm.

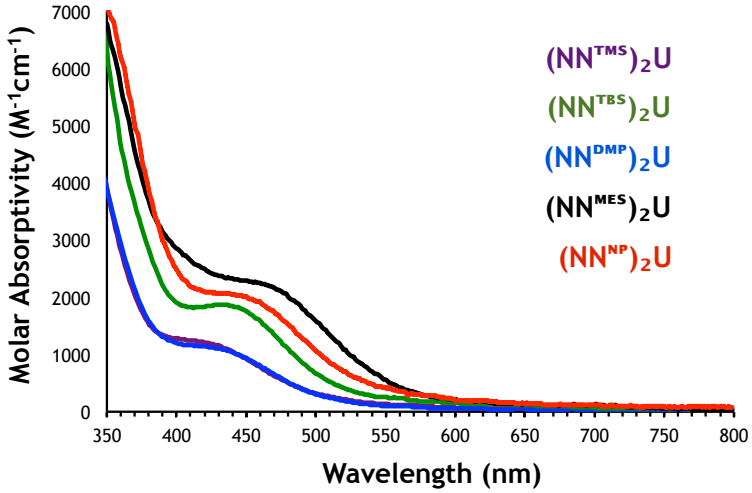

Figure 5.20. UV-Vis spectra of neutral $(NN^{R})_2U$ complexes in DCM.

To this end, it is more likely that the bands in the UV region are due to charge transfer from the Cp amido ligands to the uranium center. To illustrate, the observed trend (i.e. $(NN^{DMP})_2U$ ~ $(NN^{TMS})_2U$ > $(NN^{TBS})_2U$ > $(NN^{MES})_2U$) implies that more energy is required to excite an electron from a ligand to a uranium-based orbital in $(NN^{TMS})_2U$ than $(NN^{MES})_2U$. This, in turn, suggests that the electron affinity of uranium follows the reverse order. Specifically, uranium has a lower electron affinity in $(NN^{TMS})_2U$ than $(NN^{MES})_2U$. This is indeed consistent with our cyclic voltammetry studies, which reveal that the reduction potential of uranium follows a trend similar to the energy of the absorption bands.

Oxidation of $(NN^{R})_2U$ complexes occurs instantaneously with a mild oxidant. Addition of iodine (1.5 and 4.0 equivalents) changes the color of $(NN^{R})_2U$ solutions from yellow or orange to black. The color of 1,1'-ferrocenium diamines, on the other hand, varies from teal in H_2NN^{TMS+} to bright green in H_2NN^{DMP+}. As shown in **Figure 5.21**, two very intense bands at 295 nm and 363 nm appear upon addition of iodine. Undoubtedly, both bands are due to the triiodide counter anion and have previously been assigned to splitting of σ → σ* transitions by

the spin-orbit coupling.[155, 156] The presence of these characteristic bands suggests that oxidation products contain at least one triiodide anion.[157]

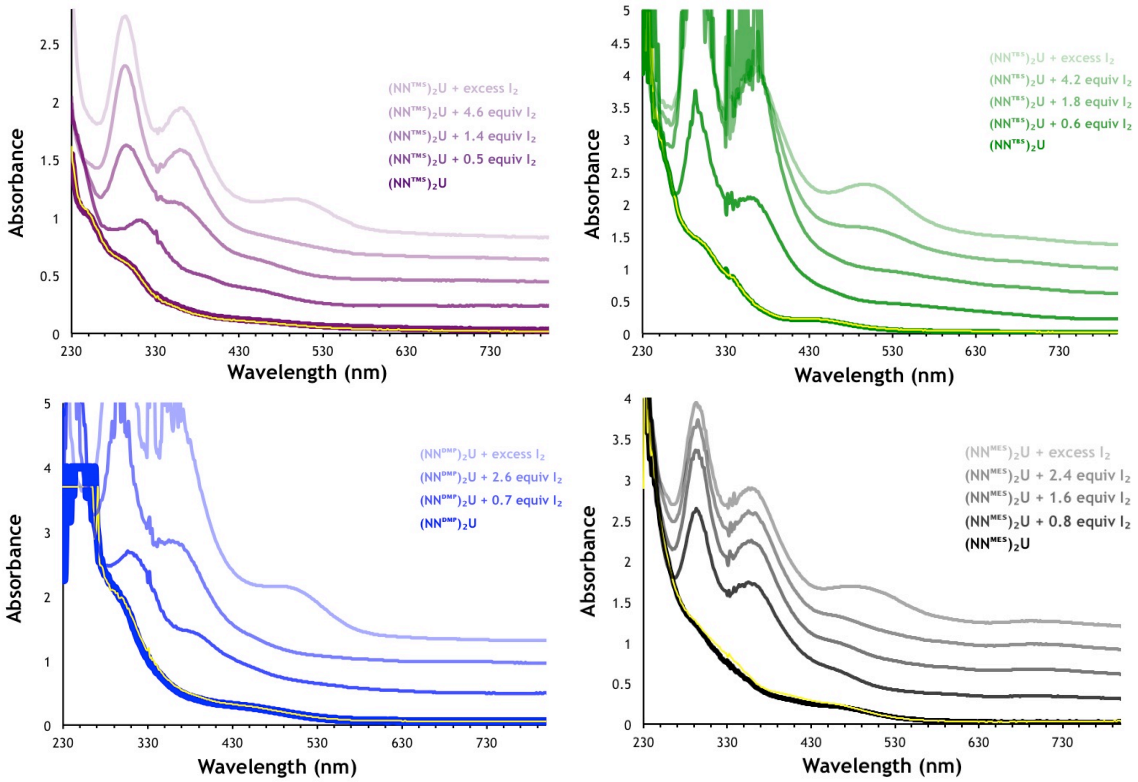

Figure 5.21. UV-Vis spectra of neutral $(NN^R)_2U$ complexes upon addition of I_2 in DCM; yellow trace represents neutral compound after exposure to air but before addition of oxidant.

Oxidation of $(NN^R)_2U$ complexes is reproducible on a large scale. As shown in **Figure 5.22**, absorption spectra of the isolated black powders show identical band energies observed during *in situ* measurements, allowing the calculation of their extinction coefficients. Specifically, absorption bands at 295 nm and 363 nm have molar absorptivity values of approximately 51000 and 32000 $M^{-1}cm^{-1}$, respectively. Elemental analysis of each precipitate confirms the formation of triiodide salts and is consistent with chronoamperometric data. For the NN^{DMP} analogue however, elemental analysis, in combination with electrochemical results described previously, supports formation and isolation of a $[I_3I]^{2-}$ salt. This explains the appearance of absorption bands characteristic of $[I_3]^-$. We note that the electronic transitions of I^- are not observed because they occur at higher energies (195 nm and 226 nm),[158] which

are outside of the solvent window used (i.e. wavelength cutoff of dichloromethane is 230 nm). Upon further addition of the oxidant, a band at 500 nm that corresponds to I_2 becomes apparent.

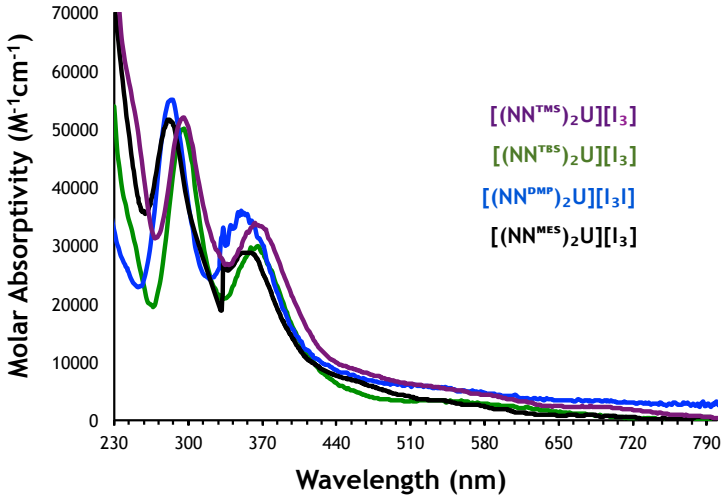

Figure 5.22. UV-Vis spectra of isolated **[(NN^{R})$_2$U][I$_x$]** compounds in dichloromethane.

All complexes undergo exchange with $[BPh_4]^-$ or $[BArF]^-$, which give rise to different electronic structures. As shown in **Figure 5.23**, for **[(NN^{TMS})$_2$U][BPh$_4$]** and **[(NN^{TBS})$_2$U][BPh$_4$]**, two bands appear at 322 nm (ε = 5500 $M^{-1}cm^{-1}$ and 10660 $M^{-1}cm^{-1}$, respectively) and 390 nm (ε = 3514 $M^{-1}cm^{-1}$ and 6500 $M^{-1}cm^{-1}$, respectively). Even though they are common to both species, it is unlikely that any of these bands correspond to the anion because the electronic transitions occurring within tetraphenylborate give rise to bands at higher energies.[159, 160] Moreover, both bands are observed in both $[I_3I_5]^{2-}$ salt of **(NN^{DMP})$_2$U** (**Figure 5.24**). Both are also evident in the spectrum of **[(NN^{MES})$_2$U][BPh$_4$]**, but they are broader and more poorly resolved.

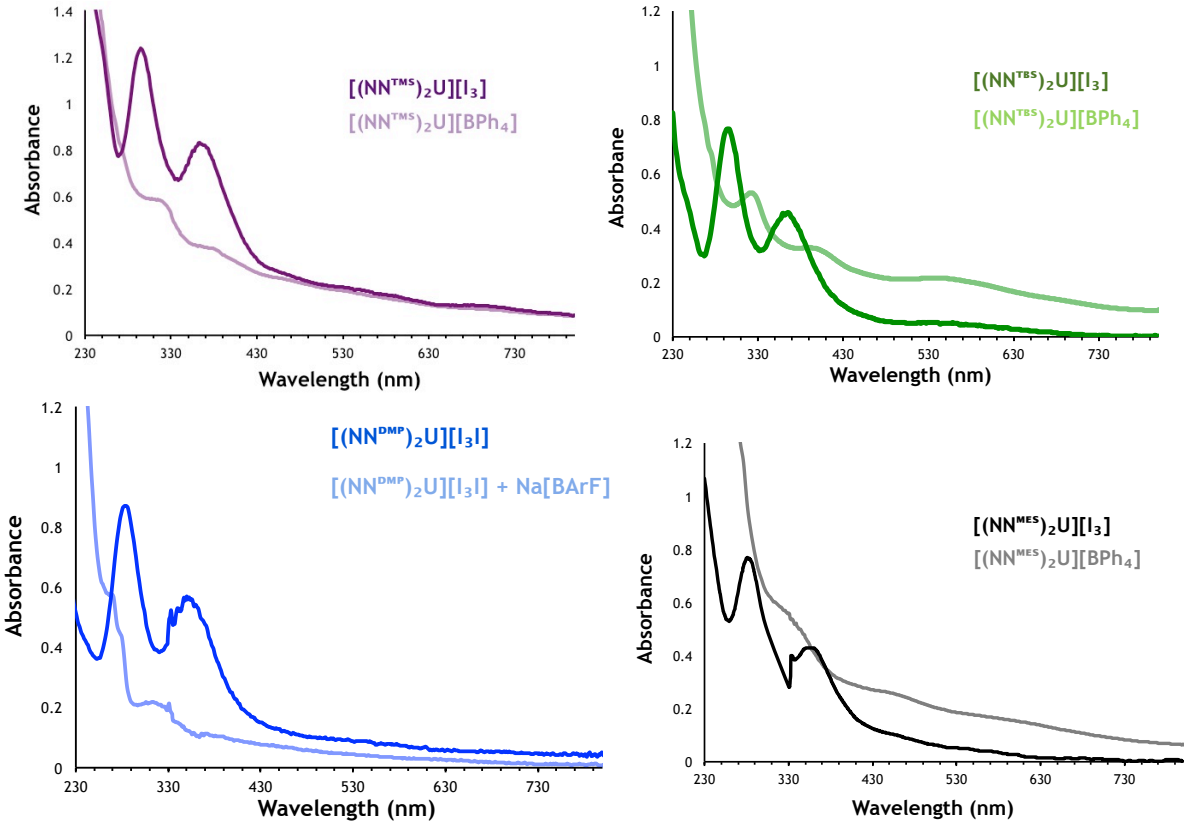

Figure 5.23. UV-Vis spectra of oxidized **[(NN^{R})$_2$U]** complexes in DCM.

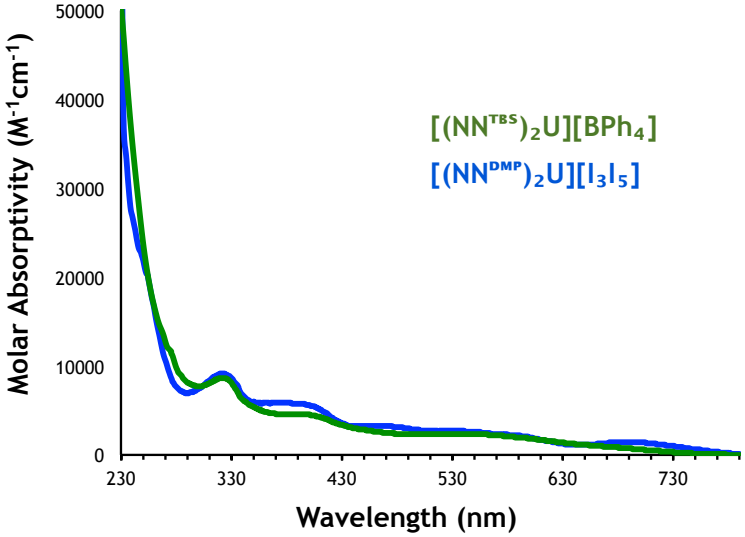

Figure 5.24. UV-Vis spectra of **[(NN^{TBS})$_2$U][BPh$_4$]** and **[(NN^{DMP})$_2$U][I$_3$I$_5$]** in DCM.

5.2.5.2 Near IR spectroscopy

We compared the near IR spectra of neutral **(NN^{R})$_2$U** complexes to those of mono(diamidoferrocene) uranium diiodide and dibenzyl complexes (**Figure 5.25**), which are

characterized by absorption bands of low intensity (ε = 20-80 $M^{-1}cm^{-1}$). Near IR spectra of **$(NN^R)UI_2(THF)$** complexes reveal several sharp bands. Specifically, the spectra of complexes bearing silylamido groups on the ferrocene ligands are nearly identical and feature four bands at approximately 950 nm, 1020 nm, 1110 nm, and 1230 nm. Near IR spectra of **$(NN^R)U(CH_2Ph)_2$**, on the other hand, show a broad band centered at approximately 1080 nm.

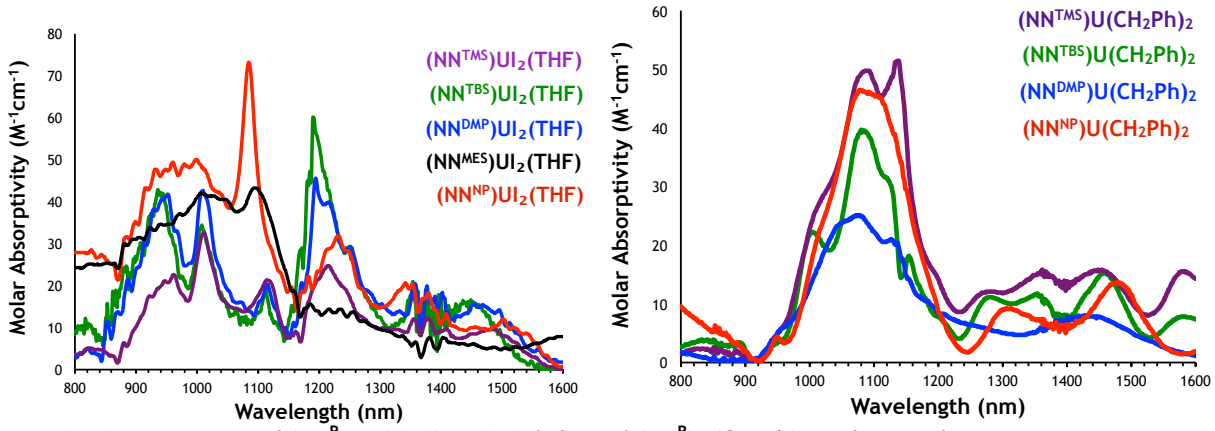

Figure 5.25. NIR spectra of **$(NN^R)UI_2(THF)$** in THF (left) and **$(NN^R)U(CH_2Ph)_2$** (right) in toluene.

For neutral **$(NN^R)_2U$** complexes (**Figure 5.26**), the absorption bands in the near IR region are not consistent across the series. Due to ligand field effects on electronic transitions within the uranium core, the observed difference in the spectra is taken as evidence of covalent interactions between 1,1'-ferrocene diamide ligands and uranium.[161] As expected, the bands are weaker than those observed in the UV-Vis region. The molar absorptivity of the most prominent bands in this region is nevertheless greater than typically observed for f → f transitions.[152, 162-164]

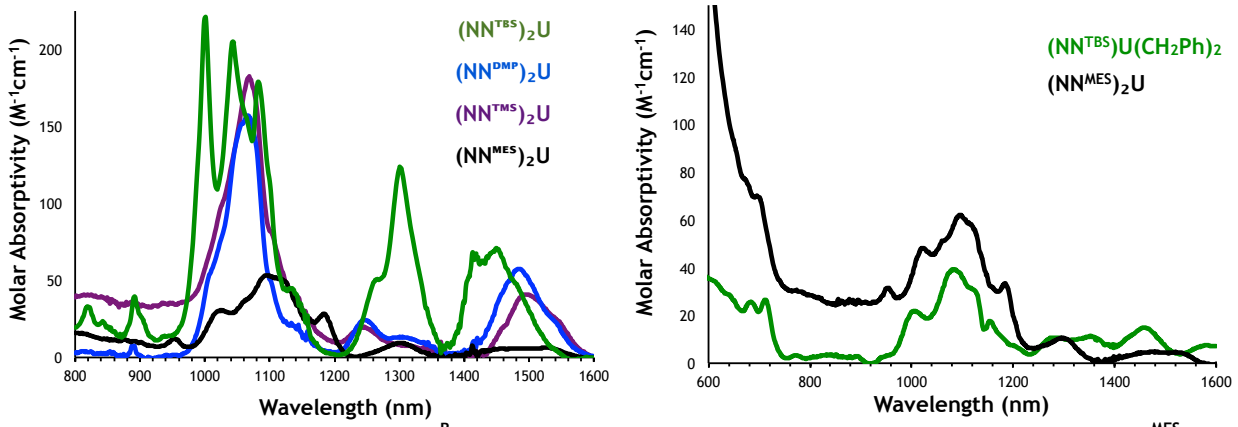

Figure 5.26. NIR spectra of neutral $(NN^{R})_2U$ complexes in dichloromethane (left) and comparison of $(NN^{MES})_2U$ in dichloromethane and $(NN^{TBS})U(CH_2Ph)_2$ in toluene (right).

Nearly identical features are observed for $(NN^{TMS})_2U$ and $(NN^{DMP})_2U$, suggesting that these complexes have similar electronic structures. Interestingly, the most intense band in $(NN^{MES})_2U$ is much weaker than those observed in analogous complexes with ligands bearing silylamino substituents. The overall spectrum of $(NN^{MES})_2U$ then likely arises from pure electronic transitions within the uranium core. In fact, the apparently uncanny resemblance to the near IR profile of $(NN^{TBS})U(CH_2Ph)_2$ (**Figure 5.26**) supports this assignment.

Finally, the spectrum of $(NN^{TBS})_2U$ contains a greater number of bands, which are more narrow and intense (ε = 210 $M^{-1}cm^{-1}$) than those found in other $(NN^{R})_2U$ complexes. Previous studies have suggested that unusually large intensities are a direct result of an intensity-stealing mechanism, whereby coupling of forbidden f→f and allowed charge transfer transitions or electronic states of similar energy increases the intensity of the former.[164-168] Therefore, the large intensity of these bands likely reflects greater ligand-field splitting of f→f orbitals and thus a stronger metal-ligand interaction. Nonetheless, no conclusion regarding the extent of iron-uranium interaction in neutral $(NN^{R})_2U$ complexes can be made from the observed near IR spectra.

Upon oxidation (**Figure 5.27**), near IR spectra of the $(NN^{R})_2U$ complexes change drastically and feature a broad band between 600 and 1600 nm with a molar absorptivity (ε =

750–2000 $M^{-1}cm^{-1}$) characteristic of intervalence charge transfer transitions.[113, 169] However, on closer inspection, it becomes clear that these spectra are indeed multifaceted.

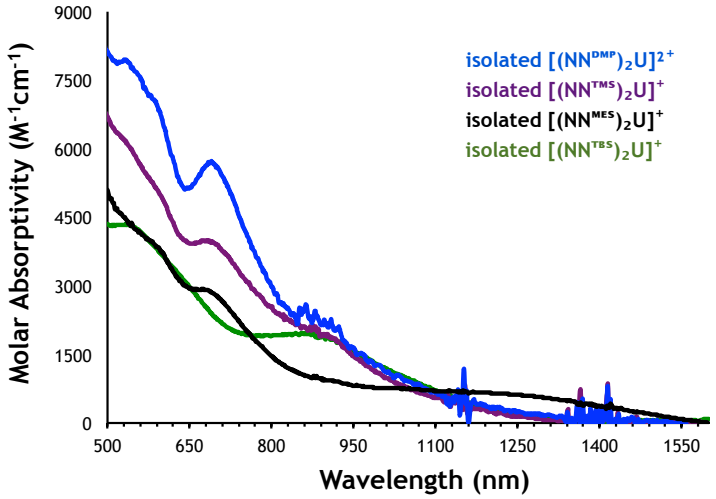

Figure 5.27. Isolated oxidized **$(NN^{R})_2U$** complexes in dichloromethane. For **$[(NN^{TMS})_2U]^+$**, **$[(NN^{DMP})_2U]^+$**, and **$[(NN^{MES})_2U]^+$**, molar absorptivity was calculated assuming tetraiodoferrate counteranions.

When iodine is added to a dilute DCM solution of **$(NN^{TMS})_2U$**, a broad, multifaceted band appears in the visible and near IR regions (**Figure 5.28**). This product can be isolated as a black powder and is shown by elemental analysis to be **$[(NN^{TMS})_2U][I_3]$**. Upon closer inspection, it becomes obvious that the band centered at 850 nm corresponds to a charge transfer transition from trimethylsilylamido-substituted Cp ligands to Fe^{3+} (compare red and purple traces in **Figure 5.28**). The broad, unresolved band between 950 and 1200 nm, then, can be attributed to inter-valence charge transfer between Fe^{2+} and Fe^{3+}. The same type of electronic structure is observed in the spectrum of an isolated **$(NN^{TBS})_2La$** complex (**Figure 5.29**), whose crystal structure reveals two distinct Fe–U distances (3.45 and 3.76 Å).[1]

A gradual transformation of the visible and near IR regions occurs with time and upon further addition of iodine. Our attempts to obtain structural information from X-ray diffraction analysis were met with a surprising result. Recrystallization from a mixture of dichloromethane and pentane at -40 °C yielded a tetraiodoferrate salt of the mixed-valence

[1] Work by Kevin Miller.

$(NN^{TMS})_2U$ complex, whose visible/near IR spectrum features a poorly resolved band (686 nm, ε = 4003 $M^{-1}cm^{-1}$) characteristic of spin-forbidden transitions within tetraiodoferrate.[170] As shown in **Figure 5.28**, this band is also observed after decomposition of the oxidized proligand, H_2NN^{TMS+}.

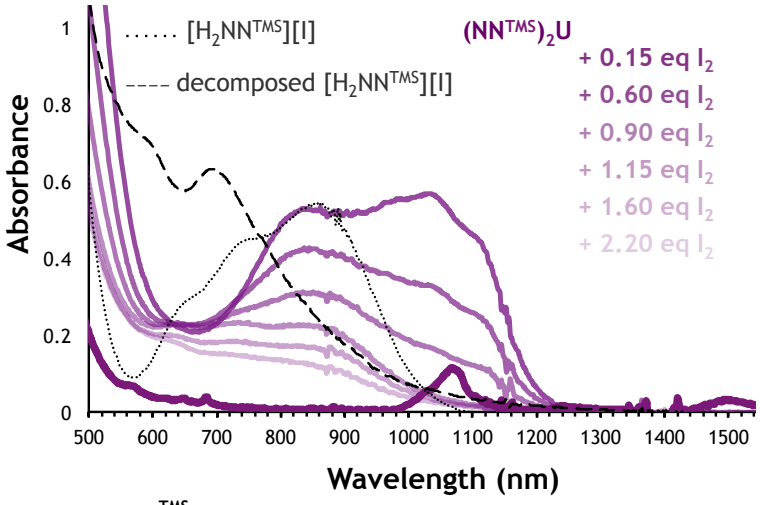

Figure 5.28. In situ oxidation of $(NN^{TMS})_2U$ monitored by visible-near IR spectroscopy compared with oxidized free ligand.

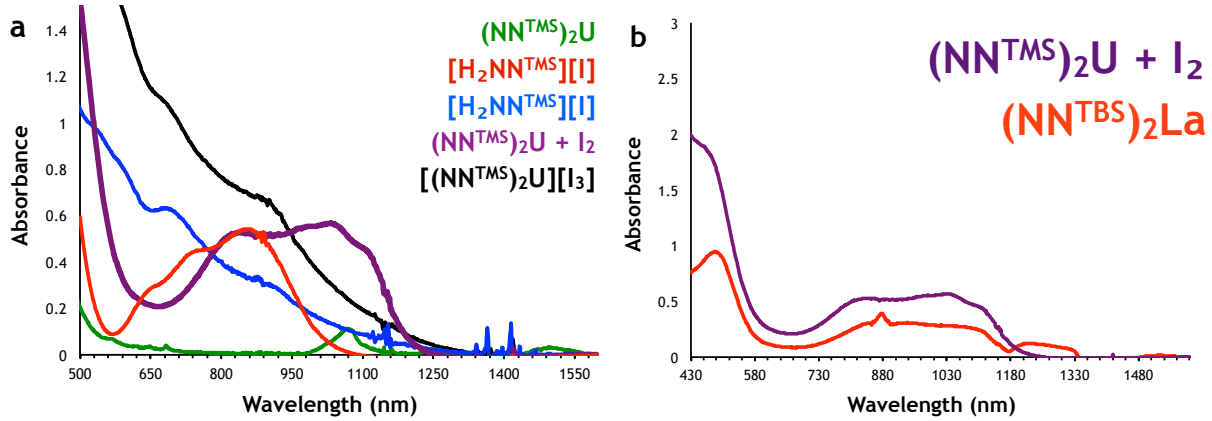

Figure 5.29. Comparison of visible-near IR spectra of $[(NN^{TMS})_2U]^+$ with (a) oxidized free ligand and neutral $(NN^{TMS})_2U$ and (b) mixed-valence $(NN^{TBS})_2La$.

Spectral deconvolution (**Figure 5.30**) of the isolated oxidized complex, **$[(NN^{TMS})_2U][FeI_4]$**, shows an intense band centered at 487 nm (ε = 5670 $M^{-1}cm^{-1}$), as well as two weaker bands at 712 nm (ε = 1775 $M^{-1}cm^{-1}$) and 880 nm (ε = 923 $M^{-1}cm^{-1}$). A broad inter-valence charge transfer band is centered at 944 nm (ε = 890 $M^{-1}cm^{-1}$). The extent of this

charge transfer can be approximated by the interaction parameter, α^2, as previously established by Marcus[171, 172] and Hush.[173, 174] More specifically, α^2 is directly proportional to the intensity and half-width of the intervalence charge transfer band, but inversely proportional to its energy as well as the distance between the two iron centers (see Appendix E for details). Accordingly, using the value of the extinction coefficient obtained by spectral deconvolution, the interaction parameter is calculated to be 0.15, which implies weak electronic interaction between Fe^{2+} and Fe^{3+}.

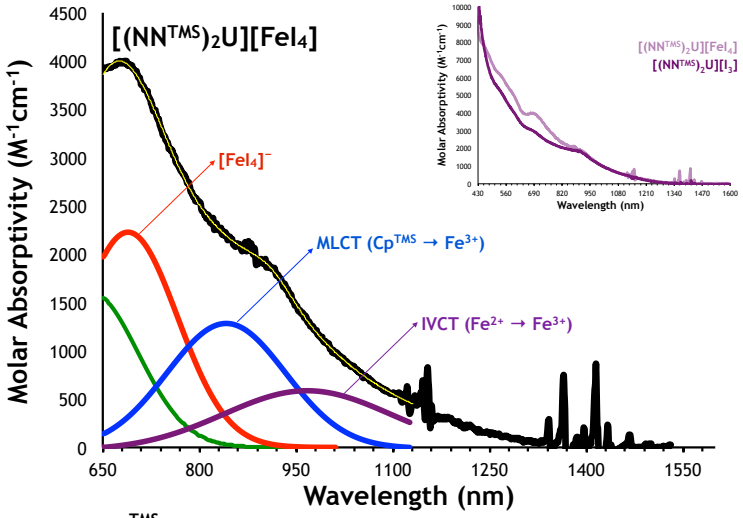

Figure 5.30. Deconvolution of **[(NN^{TMS})$_2$U][FeI$_4$]**; yellow trace represents the best fit.

For the analogous **(NN^{TBS})$_2$U** derivative, formation of **[(NN^{TBS})$_2$U][I$_3$]** is again evident in the visible/near IR region. The spectrum obtained in situ immediately upon addition of one equivalent of iodine (**Figure 5.31**) is nearly identical to that of the isolated, analytically pure triiodide salt. For both **[(NN^{TBS})$_2$U][I$_3$]** and **[(NN^{TBS})$_2$U][BPh$_4$]**, a near IR band is centered at the same wavelength as that observed in the oxidized form of the corresponding 1,1'-ferrocenium diamine. In addition to an intense band at 523 nm (ε = 4570 $M^{-1}cm^{-1}$), deconvolution of the visible and near IR regions into Gaussian shaped bands (**Figure 5.32**) revealed two overlapping bands are centered at 855 nm (ε = 1200 $M^{-1}cm^{-1}$) and 978 nm (ε = 1100 $M^{-1}cm^{-1}$). The former is assigned to ligand-to-metal charge transfer within the

ferrocenium moiety, while the latter corresponds to inter-valence charge transfer between Fe^{2+} and Fe^{3+}. The mixing coefficient, α, was calculated to be 0.156, which implies that there is a weak interaction between the ferrocene and ferrocenium moieties in $[(NN^{TBS})_2U]^+$ (Class II).[175]

Both $[(NN^{TBS})_2U]^+$ and $[(NN^{TMS})_2U]^+$ mixed-valence complexes can then be classified as valence detrapped. However, the communication between ferrocene and ferrocenium moieties is weak. **Figure 5.33** shows the extent of communication in $(NN^{TBS})_2U$ and $(NN^{TMS})_2U$ relative to that in Prussian blue, biferrocene picrate, and the Creutz-Taube ion.

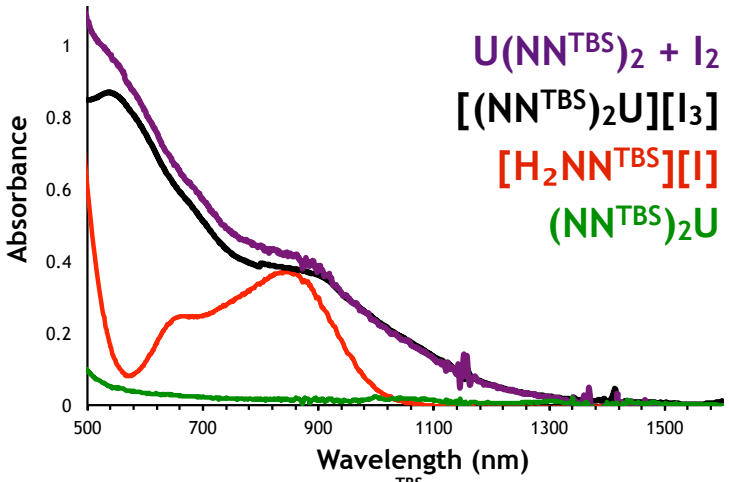

Figure 5.31. Visible and near IR spectra of neutral $(NN^{TBS})_2U$ (green), isolated $[H_2NN^{TBS}][I]$ (red), $(NN^{TBS})_2U$ oxidized in situ (x2, purple) and isolated $[(NN^{TBS})_2U][I_3]$ (black).

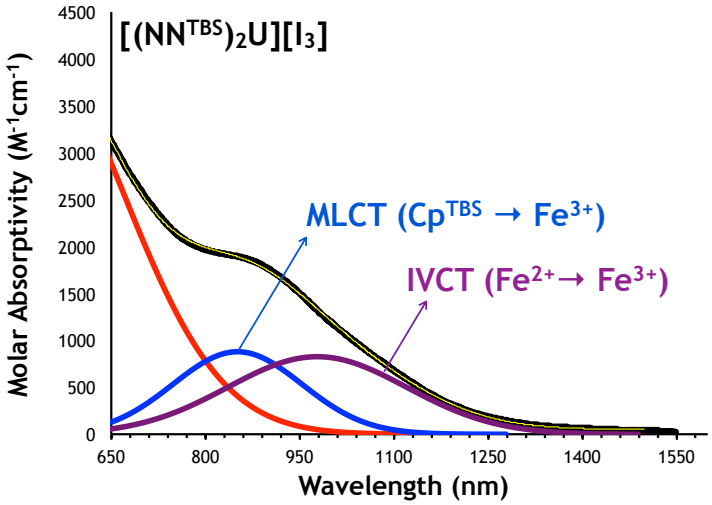

Figure 5.32. Deconvolution of $[(NN^{TBS})_2U][I_3]$; yellow trace represents the best fit.

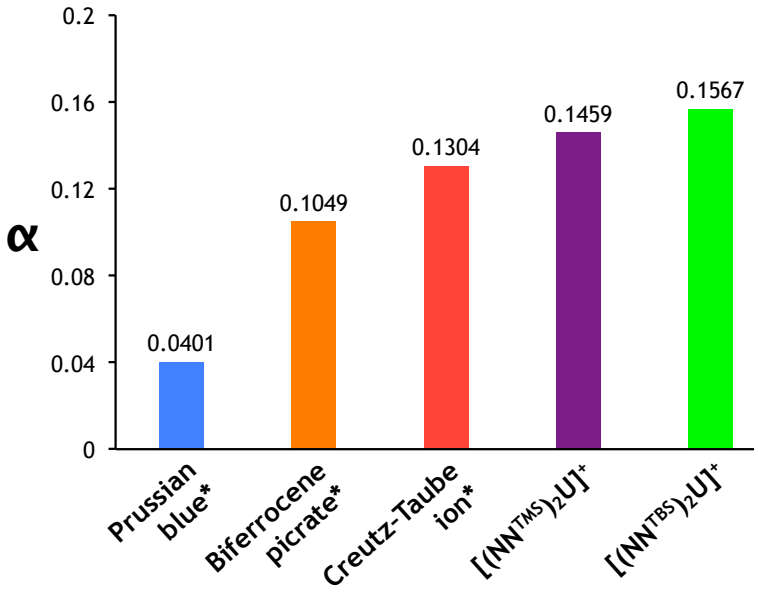

Figure 5.33. Comparison of mixing parameters for various mixed valence complexes; [a]From reference [176].

Analogous oxidation of $(NN^{MES})_2U$ also resulted in formation of an analytically pure triiodide salt, $[(NN^{MES})_2U][I_3]$, which decomposes readily in THF and DCM. As shown in **Figure 5.34**, its visible/near IR spectrum shows an intense band at approximately 690 nm (ε = 2600 $M^{-1}cm^{-1}$) and a much broader one between 1000 and 1600 nm (ε = 660 $M^{-1}cm^{-1}$). The energy, as well as the intensity of the latter, is nearly identical to the band observed when the oxidized H_2NN^{TMS} proligand and its uranium congener decompose in solution. Therefore, the band at 695 nm[177, 178] likely corresponds to electronic transitions within $[FeI_4]^-$ which along with other large anions, is known to stabilize ferrocenium cations.[179-184] The numerous tetrahaloferrate salts of ferrocenium derivatives that have been reported previously further support this assumption.[184] The band at lower energy is assigned to inter-valence charge transfer. Its weak intensity is likely a result of longer metal-metal distances and smaller Fe-U-Fe angles compared to the NN^{TBS} analogue,[185-188] which implies that the electron transfer in $(NN^{MES})_2U$ is less efficient than in $(NN^{TBS})_2U$.[189] Moreover, its width (a convolution of many individual bands) can be attributed to the lower symmetry of the system. Finally, a best curve fit (**Figure 5.35**) is produced with a third peak at 822 nm (ε = 650 $M^{-1}cm^{-1}$), which corresponds to

ligand-to-metal charge transfer within the ferrocenium moiety. Calculation of the mixing parameter is not feasible because the distance between Fe^{2+} and Fe^{3+} is unknown.

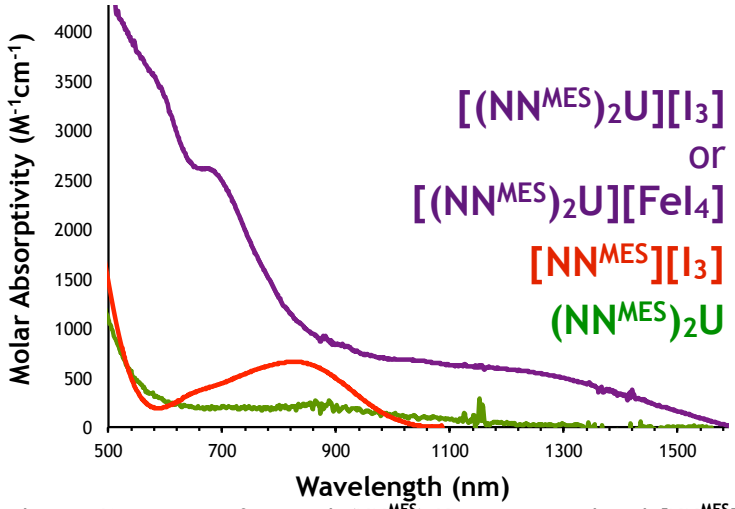

Figure 5.34. Visible and near IR spectra of neutral $(NN^{MES})_2U$ (green), isolated $[NN^{MES}][I_3]$ (red), and isolated $[(NN^{TBS})_2U][I_3]$ (purple); the band at 690 nm may correspond to $[FeI_4]^-$.

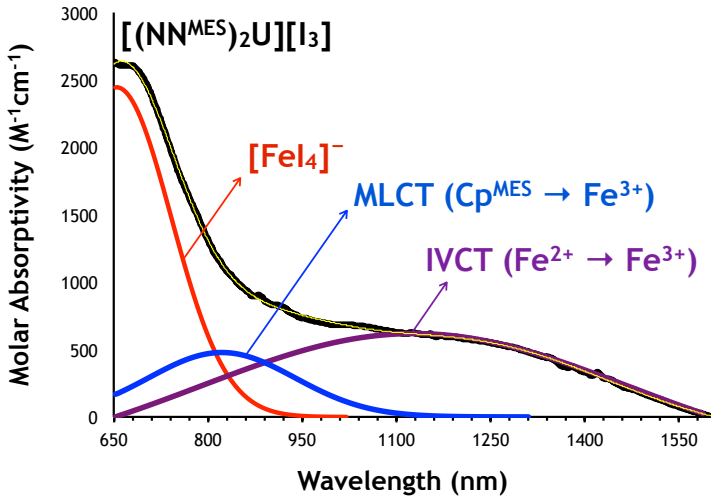

Figure 5.35. Deconvolution of $[(NN^{MES})_2U][I_3]$.

Finally, when one equivalent of iodine is added to a dilute DCM solution of $(NN^{DMP})_2U$, a broad band between 790 and 880 nm becomes apparent (**Figure 5.36**). The band centered at approximately 870 nm arises from charge transfer between Cp ligands and Fe^{3+}. It is also observed in oxidation of H_2NN^{DMP} and $(NN^{DMP})U(OAr)_2$. Because calculation of extinction

coefficients would produce imprecise values, it is not clear whether this band corresponds to oxidation of one or both iron centers.

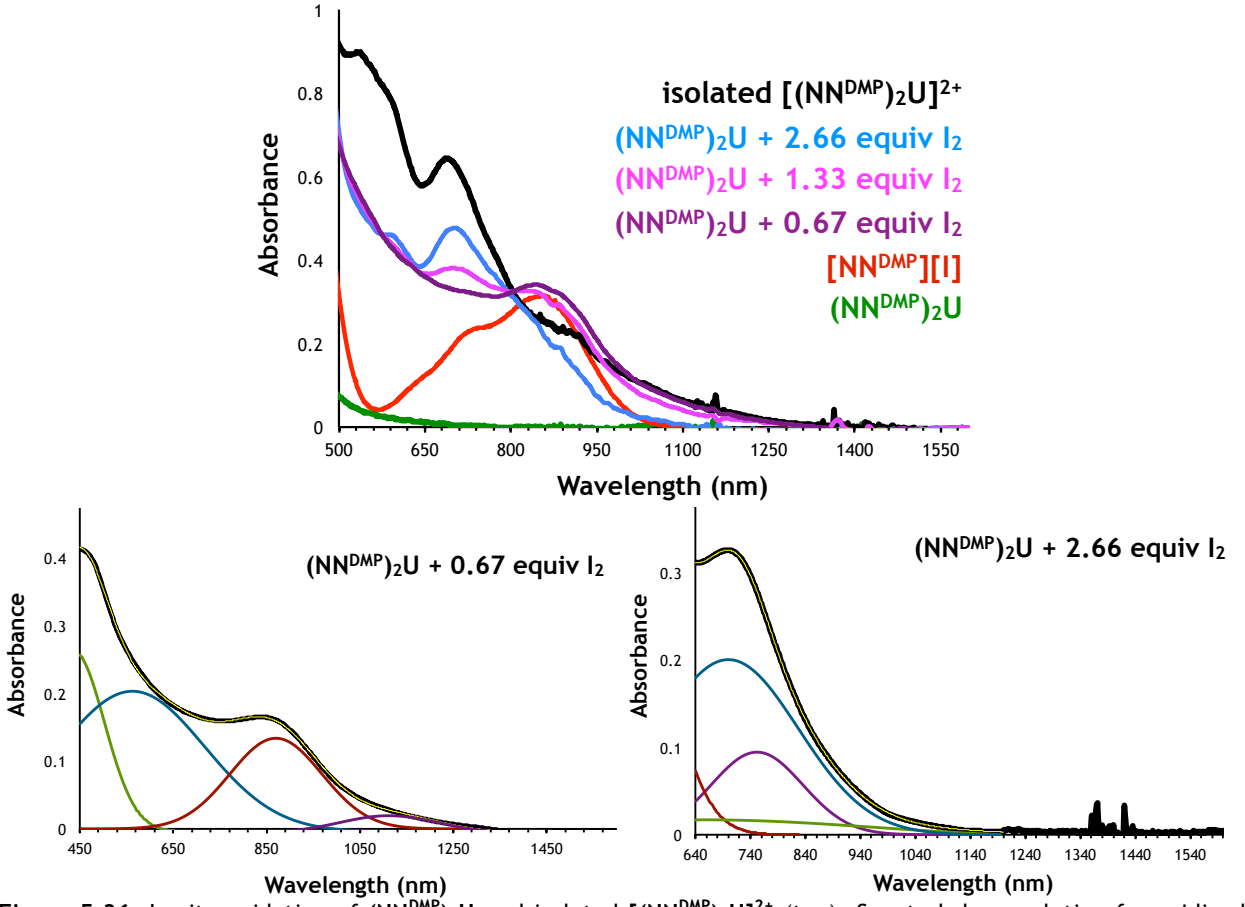

Figure 5.36. In situ oxidation of $(NN^{DMP})_2U$ and isolated $[(NN^{DMP})_2U]^{2+}$ (top); Spectral deconvolution for oxidized $(NN^{DMP})_2U$ species formed on addition of 0.67 (bottom left) and 2.66 (bottom right) equivalents of I_2.

As shown in **Figure 5.36**, a best fit of the initial spectral curve reveals three bands in the visible and near IR regions. A weak but broad band between 900 and 1300 nm is also exposed and may be due to intervalence charge transfer between Fe^{2+} and Fe^{3+} in the postulated singly oxidized species. Upon further addition of the iodine, the oxidation product decomposes and a band centered at 695 nm emerges (**Figure 5.36**). It is likely that this band is due to the tetraiodoferrate anion.

Our attempts to obtain a UV-Vis-NIR spectrum of $[(NN^{DMP})_2U][I_3I]$ or $[(NN^{DMP})_2U][I_3I_5]$ were met with little success. Instead, the spectrum of isolated species revealed a shoulder at

approximately 850 nm that is attributed to electronic transitions within the ferrocenium moieties. The presence of an intense band at 700 nm shows that the doubly oxidized **$(NN^{DMP})_2U$** does indeed decompose in solution and is consistent with the ^1H NMR study described previously. This band is also observed in the spectrum of singly oxidized **$(NN^{TMS})_2U$** and **$(NN^{MES})_2U$** analogues, prompting us to assign the product of this decomposition as **$[(NN^{DMP})_2U][FeI_4]_2$**.

Finally, **Figure 5.37** shows the spectral deconvolution of isolated doubly oxidized **$(NN^{DMP})_2U$**. Best fit of the spectrum was found with two intense absorption bands centered at approximately 694 nm (ε = 4313 $M^{-1}cm^{-1}$) and 754 nm (ε = 2387 $M^{-1}cm^{-1}$), as well as a broad band at 826 nm (ε = 2377 $M^{-1}cm^{-1}$). Consistent with oxidation of both iron centers, no intervalence charge transfer band is observed.

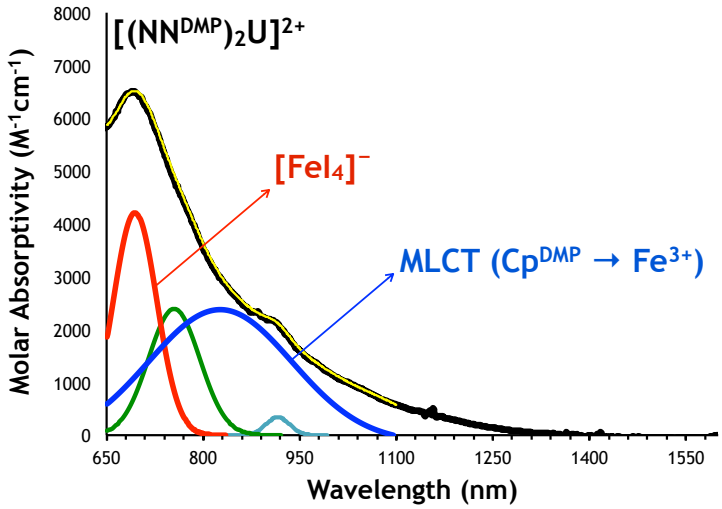

Figure 5.37. Best Gaussian fit of isolated doubly oxidized **$(NN^{DMP})_2U$**.

5.2.6 Magnetism

In order to obtain more evidence that supports the existence of interaction between two iron centers through uranium, magnetic behavior of neutral and oxidized $(NN^R)_2U$ complexes was investigated as a function of applied magnetic field and temperature. For the sake of comparison, the following discussion will refer to the magnetic properties of both iron

and uranium precursors, as well as a uranium diiodide supported by one 1,1'-ferrocene diamide ligand. Magnetic behavior of oxidized 1,1'-ferrocene diamines was described in Chapter 1, while that of uranium species is presented here.

In general, because of repulsion and spin-orbit coupling between unpaired electrons, the magnetic behavior of uranium and other heavy elements is best described using the total angular momentum.[190] In contrast, magnetic properties of iron and other light elements can be approximated by only considering the spin component.[191]

For neutral **$(NN^R)_2U$** complexes, no contribution from 1,1'-ferrocene diamide ligands is expected. This is based on the assumption that both iron centers are low spin and thus, have no unpaired electrons. This assumption is valid because, to the best of our knowledge, no ligand has been shown to impose a weak field around Fe^{2+} in ferrocene derivatives.[192] Therefore, the sole contribution defining the magnetic properties is expected to be from the tetravalent uranium center. This contribution will vary depending on the extent of ligand field splitting. For example, ground state of a free U^{4+} ion with $5f^2$ configuration is $^3H_4$, whose degeneracy is removed by a low symmetry ligand field and thus split into nine ligand field levels.[193] Assuming that these unpaired electrons are not magnetically coupled, the magnetic moment, μ_{eff}, of neutral **$(NN^R)_2U$** complexes is expected to be close to that of the free U^{4+} ion. Theoretically, this value (3.58 μB) is derived from total angular momentum[194] (Equation 5.1),

$$\mu_{eff} = g_J\sqrt{J(J+1)} \quad (5.1)$$

where J=L+S, and g_J is the Landé splitting factor, which denotes the energy difference between the split atomic orbitals created by an external magnetic field.[195] For the $5f^2$ ground state, the total angular momentum, J=4, will split into nine singlets when the crystal field symmetry is lower than tetragonal.[190] It is important to note that the above equation holds

better for lanthanides, but not actinides, which exhibit greater crystal-field splitting of the ground state than what is predicted by the Boltzmann distribution.[190]

In addition to the uranium component, the magnetic properties of oxidized $(NN^R)_2U$ complexes will be defined by contributions from one or two Fe^{3+} centers as well. The magnitude of this particular component will depend on the spin state of Fe^{3+}, as well as potential interactions between the spins within the molecule. Theoretically, the magnetic moment of low-spin Fe^{3+} is 1.73 μB, while that of high-spin Fe^{3+} is 5.92 μB.[196] Assuming that all unpaired electrons are non-interacting, the possible magnetic moment of singly oxidized $(NN^R)_2U$ complexes (with Fe^{2+}, U^{4+}, and Fe^{3+} ions) will have a lower limit of 4.56 μB, when both Fe^{2+} and Fe^{3+} centers are low-spin. The upper limit, on the other hand, is obtained if both Fe^{2+} and Fe^{3+} centers are high spin, in which case the magnetic moment would be 14.40 μB. Neither of these values takes into account any contributions from the counter anion. Similarly, for doubly oxidized **$(NN^R)_2U$** complexes, the magnetic moment is expected to be even higher due to the presence of two Fe^{3+} centers. The lower and upper limits for the magnetic moment are expected to be 6.29 μB and 15.42 μB, respectively. It is important to note that direct assignment of oxidation states based on these values is invalid because no spin interactions are taken into account.

For magnetically isolated spins, magnetization is expected to reach saturation when the applied magnetic field is much greater than thermal energy, kT.[197] Moreover, increase in magnetization is much faster for ferromagnetic than paramagnetic systems.[197] At 298 K, magnetization field dependence of neutral **$(NN^{TBS})_2U$**, and **$(NN^{MES})_2U$** complexes is nearly linear (**Figure 5.38**). Parallel alignment of the spins with the field is not possible up to 9000 Oe. Such field dependence is a result of either large zero-field splitting,[198] competing magnetic interactions,[199] or strong magnetocrystalline anisotropy.[200] The latter prevents spins within the sample from completely aligning with the external field, in which case

magnetization would become saturated and reach a constant value. This behavior is expected for lanthanide and actinide systems because of large spin-orbit coupling and stems from the energy difference that accompanies various orientations of electron density.[201] Similar responses have also been observed in single crystal magnetization studies of metallocenium salts of nickel bisdichalcogenate anions, in which the magnetic field was applied perpendicular to intermolecular chains formed by alternating anion and cation moieties exhibiting antiferromagnetic interactions.[202-204]

Magnetization field dependence of **$(NN^{TMS})_2U$**, on the other hand, deviates slightly from linearity at low field and a slight hysteresis is apparent at 298 K. Saturation is not possible even at 9000 Oe. Such behavior is characteristic of *ferrimagnetic* ordering.[205] When a low magnetic field is applied to **$(NN^{DMP})_2U$** at 298 K, magnetization quickly increases and a parallel alignment with the field is achieved at approximately 1500 Oe. Such a response to an external field is characteristic of *ferrimagnetic* interactions.[197] However, application of a greater magnetic field (~1500–3500 Oe) causes a slight shift in the direction of the moment, which again changes above 4000 Oe. Similar behavior has been observed with charge transfer salts based on decamethylferrocenium salts,[206] and is characteristic of metamagnetic materials.[200] Furthermore, as shown in **Figure 5.38**, **$(NN^{DMP})_2U$** exhibits hysteresis, which suggests that it is weakly ferromagnetic at room temperature and low magnetic field. Like that of the other three derivatives, magnetization field dependence in **$(NN^{DMP})_2U$** changes drastically when temperature decreases. As shown in **Figure 5.38**, saturation is no longer achieved at low magnetic fields.

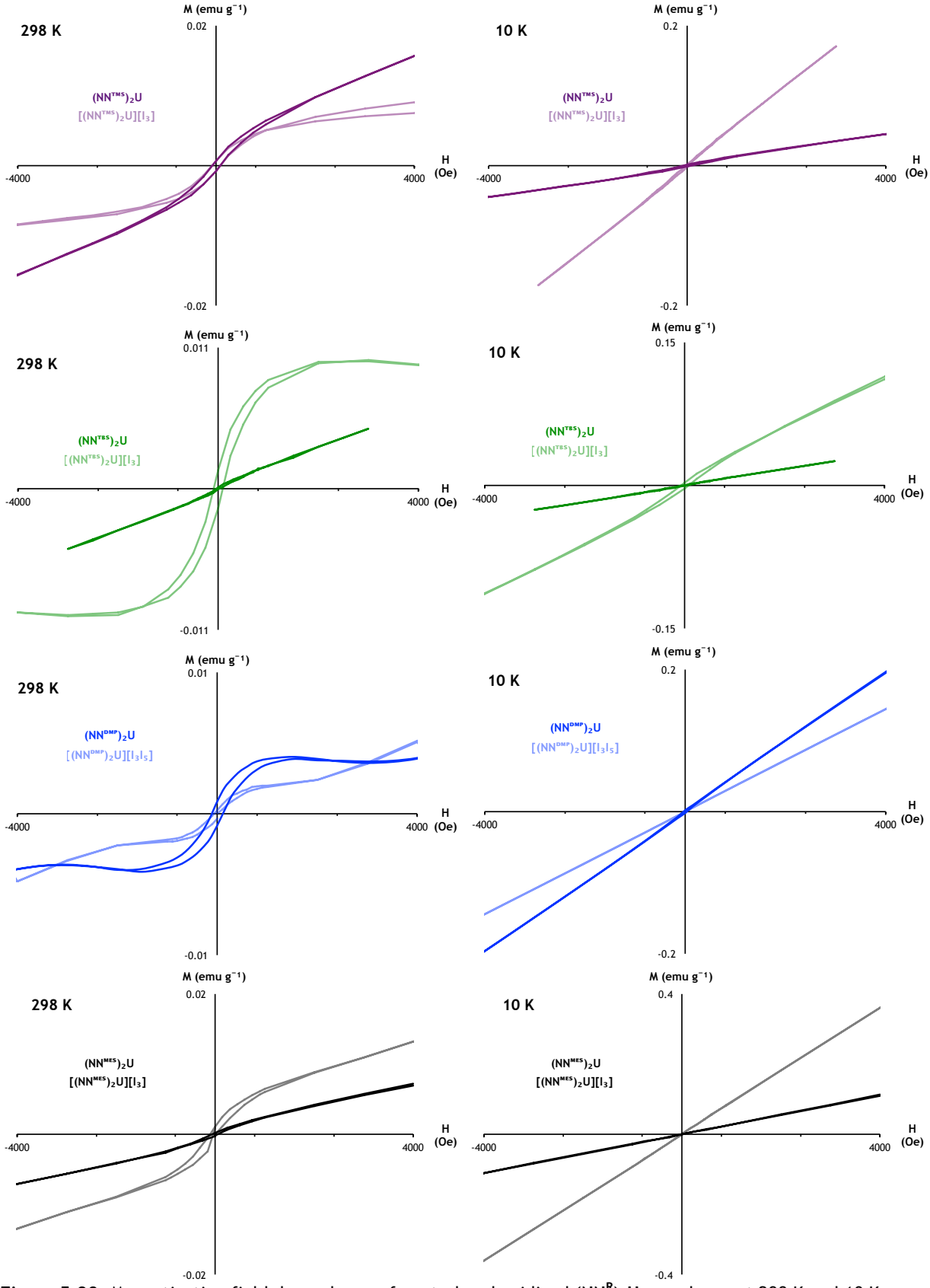

Figure 5.38. Magnetization field dependence of neutral and oxidized $(NN^{R})_2U$ complexes at 298 K and 10 K.

At 298 K, singly oxidized **[(NN^{TMS})$_2$U][I$_3$]** exhibits smaller anisotropy than the neutral congeners (**Figure 5.38**). At low magnetic fields, the magnetization of **[(NN^{TMS})$_2$U][I$_3$]** parallels that of **(NN^{TMS})$_2$U**. However, above 1500 Oe, its magnetization begins to saturate. **[(NN^{MES})$_2$U][I$_3$]** shows similar behavior but fails to reach saturation even at 9000 Oe. In contrast, magnetization of **[(NN^{TBS})$_2$U][I$_3$]** increases rapidly when small external fields are applied and saturation is reached at 2000 Oe. At this point, the magnetization reaches a maximum of 0.01 emu/g. This is considerably different from the magnetization of neutral species, which exhibits perfectly linear dependence on the applied magnetic field. The narrow hysteresis observed at room temperature is characteristic of *ferrimagnetic* ordering. Finally, the doubly oxidized **[(NN^{DMP})$_2$U][I$_3$I$_5$]** complex exhibits metamagnetic behavior. At low fields, magnetization increases rapidly, tapers off around 1500 Oe then begins to increase more rapidly above 3500 Oe. At low temperature, both singly and doubly oxidized complexes show a highly linear dependence on magnetic field, characteristic of antiferromagnetic ordering.

Temperature dependence of magnetic susceptibility of neutral **(NN^{R})$_2$U** was measured at various magnetic fields from 5 K to 298 K. Assuming that the iron center in both ferrocene diamide ligands is low-spin, only the unpaired electrons on uranium should contribute to the magnetic behavior of neutral **(NN^{R})$_2$U** complexes. At high temperature, thermal energy is greater than any magnetic interactions, so as expected, plots of reciprocal susceptibility as a function of temperature (**Figure 5.39**) reveal that between 150 K and 298 K, all four **(NN^{R})$_2$U** complexes follow the Curie-Weiss law, represented by

$$\chi = \frac{C}{T - \theta} \qquad (5.2)$$

where *X* defines molar susceptibility, T is temperature, *C* is the Curie constant in units of emu K mol^{-1} and θ is the Weiss constant in units of K. The latter is proportional to the strength of magnetic interactions and can be obtained from the linear extrapolation of the reciprocal susceptibility data at high temperature.[207] The Weiss constant has a nonzero value when no interaction between unpaired spins exists. Furthermore, positive values of θ signify ferromagnetic interactions, while negative θ values are characteristic of antiferromagnetic coupling.

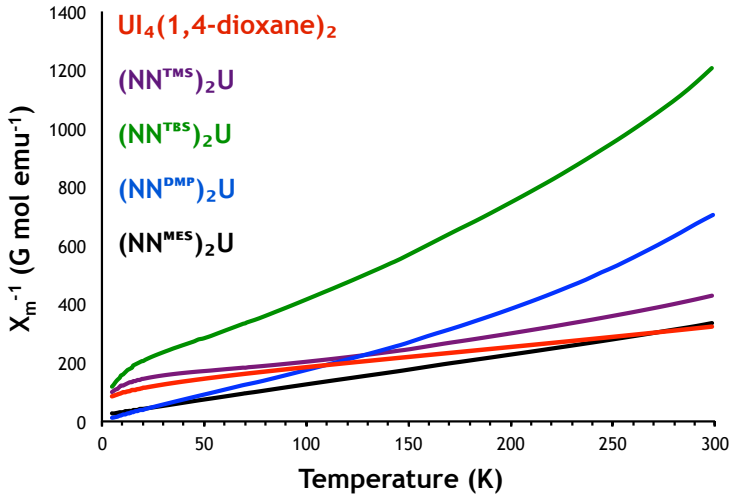

Figure 5.39. $X_m^{-1}(T)$ of **UI_4(1,4-dioxane)$_2$** and neutral **$(NN^R)_2U$** complexes.

Like its uranium precursor, **$(NN^{TMS})_2U$** exhibits strong antiferromagnetic coupling, which decreases with applied magnetic field (θ = -46.7 K at 1500 G and -37.5 K at 5000 G). Interactions in **$(NN^{MES})_2U$** are antiferromagnetic at low field (θ = -15 K) but ferromagnetic when its susceptibility is measured at a high field (θ = +19.2 K). Similarly, **$(NN^{TBS})_2U$** exhibits ferromagnetic interactions that increase with applied magnetic field (θ = +8.9 K at 1500 G and +36.7 K at 5000 G). Finally, **$(NN^{DMP})_2U$** shows strong ferromagnetic coupling (θ = +78.7 K), which is consistent with the observed magnetization hysteresis loop. The origin of such coupling may be interactions between neighboring uranium centers. For example, as shown in **Figure 5.40**, individual molecules of **$(NN^{TBS})_2U$**, **$(NN^{DMP})_2U$**, and **$(NN^{MES})_2U$** form similar crystal-

packing arrangements (at 100 K), whereby inter-chain ferromagnetic coupling may be envisioned to take place.

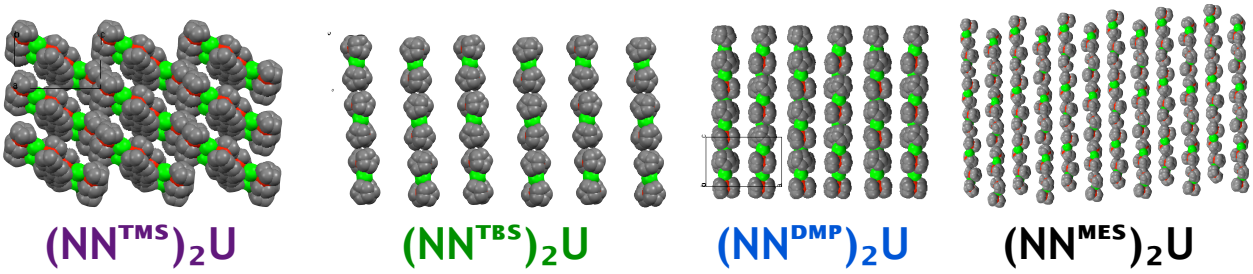

Figure 5.40. Crystal packing (3x3 unit cell) of neutral $(NN^R)_2U$ complexes viewed along the b axis.

Below 150 K, all neutral $(NN^R)_2U$ complexes deviate from the Curie-Weiss law. Antiferromagnetic interactions dominate at low temperature in both $(NN^{DMP})_2U$ and $(NN^{MES})_2U$. $(NN^{TMS})_2U$ and $(NN^{TBS})_2U$, on the other hand, exhibit more complex behavior that is likely due to a phase transition.[208]

As shown in **Figure 5.41**, molar susceptibility temperature product, X_mT, of the tetravalent uranium precursor, $UI_4(1,4\text{-dioxane})_2$, is 0.92 emu K mol^{-1} (2.68 μ_B). This is less than the predicted high temperature value of 1.60 emu K mol^{-1} (3.58 μ_B) for a $^3H_4$ uranium ion.[193] In other words, not all nine (2J+1) ligand-field states/sublevels are populated, suggesting that the energy difference between them is actually greater than the thermal energy required to populate the upper sublevels at 298 K. Much lower values of X_mT have previously been reported for tetravalent uranium complexes.[119, 193] Also shown in **Figure 5.41** is the X_mT plot for a uranium diiodide complex supported by one 1,1'-ferrocene diamide ligand. Its susceptibility temperature product (1.11 emu K mol^{-1}) is slightly higher than that observed for the uranium tetraiodide dioxane adduct. This suggests that more ligand-field states are populated and thus involved in the contribution to its magnetic properties.[193]

As shown in **Figure 5.42**, replacing both iodide ligands with 1,1'-ferrocene diamide ligands does not uniformly affect the observed magnetic contribution of uranium. For

example, below 298 K, both **(NN^{TMS})$_2$U** and **(NN^{MES})$_2$U** behave similarly to their precursor. Both possess smaller high-temperature magnetic moments (0.69 emu K mol^{-1} or 2.32 μ_B and 0.56 emu K mol^{-1} or 2.09 μ_B, respectively). The magnetic moment of the latter, however, appears to be field-dependent, yielding a greater value when a lower magnetic field (1500 G) is applied.

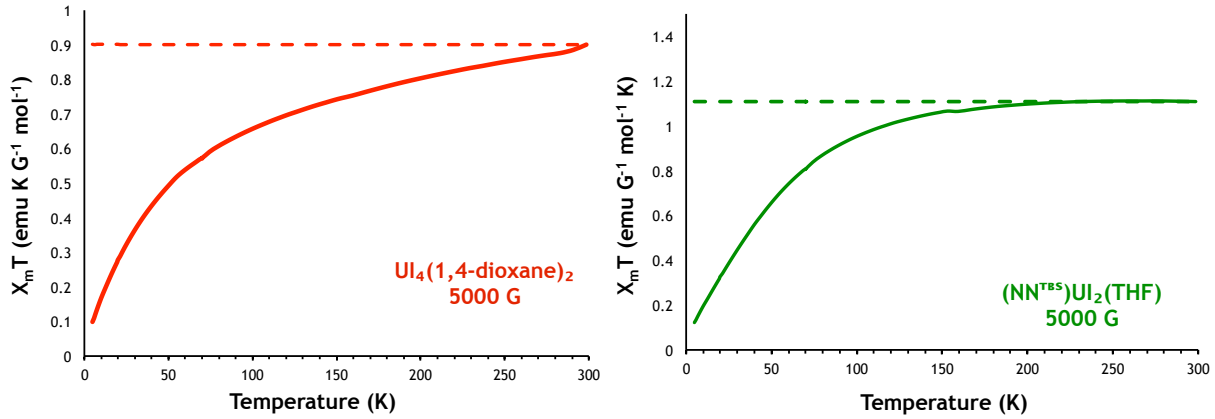

Figure 5.41. X_mT of uranium tetraiodide precursor and mono(1,1'-ferrocene diamido) uranium diiodide complex at 5000 G.

High-temperature X_mT, and thus the magnetic moment, of **(NN^{TBS})$_2$U** is even lower, suggesting that the ligand field splitting of the uranium ion is greater than that in **UI$_4$(1,4-dioxane)$_2$** and that fewer states are populated at 298 K. A previous report from our group has established the existence of a donor-acceptor interaction between iron and uranium centers through direct orbital overlap,[64] so it is possible that the low magnetic moment observed for **(NN^{TBS})$_2$U** originates from antiparallel coupling between the 5f electrons on uranium and those donated by the iron centers. As the temperature is lowered, X_mT increases gradually and reaches a maximum at 144 K (0.38 emu K mol^{-1} or 1.74 μ_B). Such behavior is characteristic of weak ferromagnetic coupling,[209-211] as was deduced from the reciprocal susceptibility plot. Further decrease in temperature results in a relatively steep decrease in X_mT, suggesting that antiferromagnetic interactions become dominant below 144 K.

Similar, but more pronounced, behavior is observed for **(NN^{DMP})$_2$U**. The representative X_mT plot in **Figure 5.42** provides a clear indication that ferrimagnetic interactions dominate above 92 K, at which point the magnetic moment reaches a maximum of 0.57 emu K mol^{-1} (2.14 μ_B). This is consistent with our interpretation of magnetization field dependence data. Moreover, below 92 K, the magnetic moment decreases more rapidly to reach a minimum of 0.42 emu K mol^{-1} (1.84 μ_B). Astonishingly, this value is identical to that measured at high temperature **(NN^{DMP})$_2$U**, which is significantly lower than predicted for a complex containing a tetravalent uranium center. Further study is needed to determine the origin of such unique temperature dependence in **(NN^{DMP})$_2$U**.

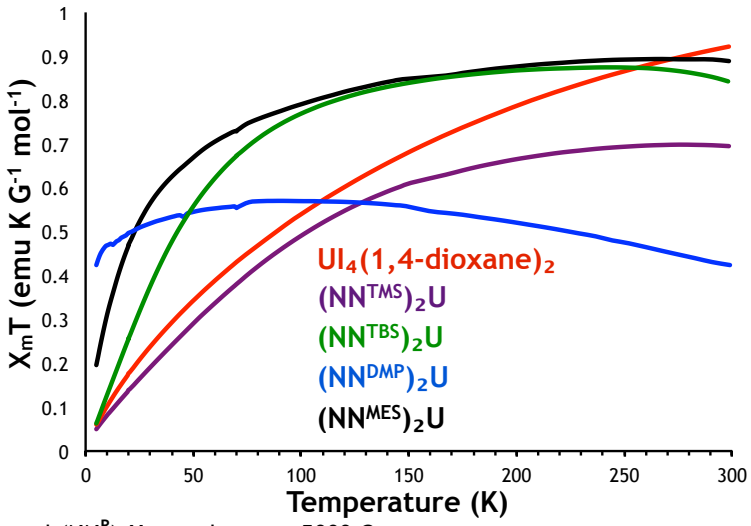

Figure 5.42. X_mT of neutral **(NN^R)$_2$U** complexes at 5000 G.

Table 5.5. Weiss (**θ**) and Curie (**C**) constants and magnetic moments (**μ**) of neutral **(NN^R)$_2$U** complexes.

	H	θ	C	μ
	(Oe)	*(K)*	*(emu K mol^{-1})*	*(μ_B)*
(NN^{TMS})$_2$U	1500	-46.70	0.82	2.57
	5000	-37.56	0.78	2.50
(NN^{TBS})$_2$U	1500	+8.94	0.25	1.43
	5000	+36.67	0.30	1.55
(NN^{DMP})$_2$U	3000	+78.70	0.33	1.62
(NN^{MES})$_2$U	1500	-15.17	0.94	2.76
	5000	+19.22	0.52	2.05

Temperature dependence of magnetic susceptibility of oxidized **$(NN^{R})_2U$** was also measured from 5 K to 298 K at various magnetic fields (**Figure 5.43**). In addition to two unpaired electrons on uranium, the magnetic behavior of oxidized complexes should also have a contribution from Fe^{3+} (one or two unpaired electrons if one or both iron centers are oxidized, respectively).

As shown in **Figure 5.43**, when 500 G is applied to **$[(NN^{TMS})_2U][I_3]$**, the Curie-Weiss law is obeyed, with the Weiss constant of -143.3 K signifying a presence of strong antiferromagnetic interactions. Expectedly, application of greater magnetic fields results in weaker magnetic ordering of the spins as indicated by the increasing Weiss constant (at 1500 G, θ = -102.9 K). In fact, when 5000 G is applied, the inverse molar susceptibility plot shows weak ferromagnetic coupling (at 5000 G, θ = +11.3 K). Similar behavior is observed for both **$[(NN^{MES})_2U][I_3]$** and **$[(NN^{TBS})_2U][I_3]$**, albeit the antiferromagnetic interactions in the latter are somewhat stronger (**Table 5.6**).

Clearly then, the value of the magnetic moment depends on the applied magnetic field. For non-interacting spins, this value is expected to consist of contributions from both U^{4+} and Fe^{3+} centers. At 298 K and 1500 G, the magnetic moment of **$[(NN^{TMS})_2U][I_3]$** is 4.68 μ_B. Assuming the contribution of the former is the same as that in the neutral analog (μ = 2.57 μ_B at 298 K in 1500 G), the contribution of Fe^{3+} then is 2.11 μ_B. Similarly, at 298 K and 1500 G, the magnetic moment of **$[(NN^{TBS})_2U][I_3]$** is 3.48 μ_B. Again assuming that the contribution of U^{4+} is the same as that in the neutral species (μ = 1.43 μ_B at 298 K in 1500 G), the contribution from Fe^{3+} of 2.05 μ_B is extracted. The same treatment of the **NN^{MES}** analogue reveals the contributing moment from the ferrocenium ligand to be 1.95 μ_B. All three contributions are very close to the predicted spin-only value for a trivalent iron center with one unpaired electron (1.73 μ_B).

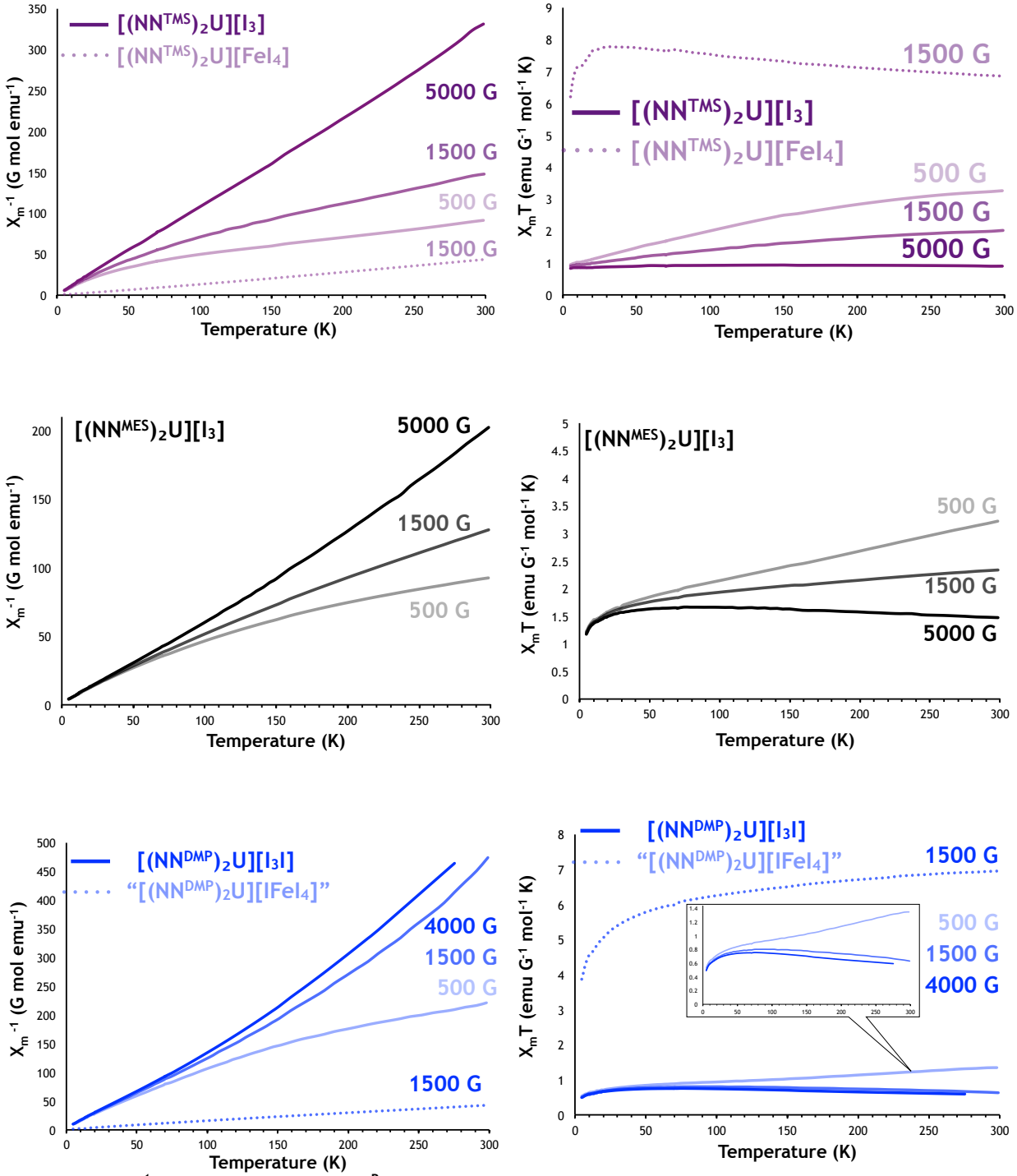

Figure 5.43. X_m^{-1} and X_mT of oxidized $(NN^R)_2U$ complexes at various magnetic fields.

Table 5.6. Weiss (**θ**) and Curie (**C**) constants and magnetic moments (**μ**) of oxidized **$(NN^R)_2U$** complexes. *From Reference 64.

	H	θ	C	μ
	(G or Oe)	*(K)*	*(emu K mol^{-1})*	*(u_B)*
$[(NN^{TMS})_2U][I_3]$	500	-143.35	4.86	**6.26**
	1500	-102.92	2.71	**4.68**
	5000	+11.28	0.87	**2.65**
$[(NN^{TMS})_2U][FeI_4]$	1500	+18.42	6.46	**7.22**
$[(NN^{TBS})_2U][I_3]$	1500	-203.94	1.50	**3.48**
	5000	-115.12	1.19	**3.10**
$[(NN^{TBS})_2U][BPh_4]$*	5000	+47.78	0.78	**2.50**
$[(NN^{DMP})_2U][I_3I]$	500	-174.91	2.77	**4.73**
	1500	+53.52	0.70	**2.37**
	4000	+46.01	0.65	**2.28**
"$[(NN^{DMP})_2U][FeI_4]$"	1500	-23.14	7.50	**7.78**
$[(NN^{MES})_2U][I_3]$	500	-177.05	5.08	**6.40**
	1500	-53.39	2.74	**4.70**
	5000	+22.97	1.39	**3.35**

Magnetic susceptibility measurements of the singly oxidized **$[(NN^{TMS})_2U][FeI_4]$** complex reveal a magnetic moment of 7.22 μ_B at 298 K and 1500 G. This is significantly higher than what is measured for the triiodide salt in the same conditions (4.68 μ_B) and reflecting the presence of another magnetic center. It has been shown previously that the Fe^{3+} in tetraiodoferrate anion has a high spin $^6S_{5/2}$ configuration,[212] so the predicted spin-only value of its magnetic moment is 5.92 μ_B. Applying the same subtraction method as described above, this value is much higher than the remainder pertaining to the combination of contributions from ferrocenium and ferrate Fe^{3+} centers. That is, after subtracting 2.57 μ_B due to U^{4+} in the neutral species, a magnetic moment of 4.65 μ_B remains even before a low-spin ferrocenium iron is taken into account. This deviation is presumably either a consequence of strong antiferromagnetic coupling involving $[FeI_4]^-$ that expectedly decreases the overall magnetic moment (from 2.57+1.73+5.92=10.22 μ_B) or the anion's Fe^{3+} is of low-spin itself, in which case its contribution to the overall magnetic moment would be 1.73 μ_B. Indeed, if the latter was

true, the predicted magnetic moment of **[(NN^{TMS})$_2$U][FeI$_4$]** would be 6.03 μ_B (2.57+1.73+1.73 μ_B), which is close to the experimentally determined value of 7.22 μ_B.

Magnetic susceptibility of the doubly oxidized **[(NN^{DMP})$_2$U][I$_3$I]** before and after decomposition was also measured. The composition of both samples was determined by elemental analysis. Before decomposition, elemental analysis confirmed the purity of **[(NN^{DMP})$_2$U][I$_3$I]**, which exhibits strong antiferromagnetic coupling (θ = -174.9 K) when a low magnetic field is applied (**Figure 5.43**). Increasing the external magnetic field to 1500 G, however, reveals significant ferromagnetic coupling (θ = +53.5 K), which does not change drastically upon further increase of the field. For example, at 4000 G, the Weiss constant decreases to only +46.0 K. This is consistent with the magnetization field dependence data. Moreover, the observed magnetic moment varies from 4.15 μ_B at 298 K and 500 G to 2.01 μ_B at 298 K and 4000 G. Both values are significantly lower than expected for U^{4+} and two low-spin Fe^{3+} centers (5.08-7.04 μ_B; lower limit is derived from using the magnetic moment of 1.62 μ_B in neutral species, while the upper limit is obtained by using the theoretical value of 3.58 μ_B for uranium).

Magnetization field dependence **[(NN^{DMP})$_2$U][I$_3$I]** after decomposition at 298 K is nearly linear. Unlike behavior of both neutral and freshly oxidized parent compounds, high magnetocrystalline anisotropy is evident and the magnetization does not saturate. The field dependence of the magnetic moment at 298 K is asymptotic. For example, room-temperature magnetic moment is 9.20 μ_B at 250 G and 6.43 μ_B at 9000 G. Both values are much higher than that observed before decomposition, which suggests formation of new magnetic centers. Furthermore, as determined from temperature-dependence measurements (**Figure 5.43**), antiferromagnetic coupling (θ = -23.4 K) is predominant. The corresponding magnetic moment (7.78 μ_B at 298 K and 1500 G) is consistent with that calculated from magnetization field dependence (7.41 at 298 K and 1500 G). It is likely that the decomposition of the doubly

oxidized **[(NN^{DMP})$_2$U][I$_3$I]** involves formation of iodo- or chloro ferrate salts[184, 213-217] and that the measured magnetic susceptibility is that of a mixture of complexes.

5.3 CONCLUSIONS

Using nuclear magnetic resonance, electrochemistry, optical and vibrational spectroscopy, as well as crystallography and magnetometry, the present Chapter describes our investigation of four uranium bis(1,1'-diamidoferrocene) complexes. Altogether, these data show the following:

(1) Ligands bearing a bulky *tert*-butyl group on the silylamido substituents impose greater torsion and tilt angles at the ferrocene backbone, creating shorter distances between uranium and iron centers, and in turn, enhancing their interaction. In addition to a single one-electron reduction of uranium, electrochemical data reveal two one-electron anodic processes, the first of which we attribute to oxidation of one iron center. Indeed, chemical oxidation of **(NN^{TBS})$_2$U** generates a tetravalent uranium center supported by both ferrocene and ferrocenium diamide ligands. This cationic complex can be isolated as a triiodide and tetraphenylborate salt, and is shown by ^{1}H NMR data to be stable in solution at room temperature indefinitely. Electronic absorption spectra of these mono-oxidized complexes show an intense band ascribed to charge transfer between Fe^{2+} and Fe^{3+} moieties. The two ligands are structurally indistinguishable, corroborating the valence delocalized nature of **[(NN^{TBS})$_2$U]$^+$**.

(2) Although they strictly enforce a staggered conformation of the Cp rings in the free ligand, mesitylamido substituents create considerably less torsion strain when the ligands coordinate to uranium, resulting in greater iron-uranium distances. In the neutral **(NN^{MES})$_2$U** complex, the iron centers are structurally distinct. More remarkably, even though the distance between them is smaller than that in the neutral **(NN^{TBS})$_2$U** complex, the intensity

and position of the intervalence charge transfer band observed upon oxidation indicate that $[(NN^{MES})_2U]^+$ is valence trapped. This is attributed to the non-linear path of travel (as defined by the Fe-U-Fe angle), which provides support for the notion that the uranium center is directly involved in mediation of electron transfer between ferrocene and ferrocenium ligands.

(3) The anomaly in this study is the uranium complex supported by two ferrocene diamide ligands bearing dimethylphenylsilyl substituents. As confirmed by voltammetric and amperometric methods, $(NN^{DMP})_2U$ undergoes a two-electron oxidation, whose product does not exhibit an intervalence charge transfer band in the near IR. Because the electronic factors of the proligand are nearly identical to those of H_2NN^{TMS}, H_2NN^{TBS}, and H_2NN^{MES}, it is likely that the observed behavior of the neutral uranium complex is simply a determined by its structure, which is revealed to contain unusually high symmetry.

5.4 APPENDIX E

5.4.1 Synthesis

General Considerations. All experiments were performed under a dry nitrogen atmosphere using standard Schlenk techniques or an MBraun inert-gas glove box. Solvents were purified using a two-column solid-state purification system by the method of Grubbs[218] and transferred to the glove box without exposure to air. NMR solvents were obtained from Cambridge Isotope Laboratories, degassed, and stored over activated molecular sieves prior to use. ^1H and ^{13}C NMR spectra were recorded on Bruker300 or Bruker500 spectrometers (supported by the NSF grant CHE-9974928) at room temperature in C_6D_6 or $CDCl_3$. Chemical shifts are reported with respect to solvent residual peaks, 7.16 ppm (C_6D_6) or 7.26 ($CDCl_3$). Cyclic voltammetry measurements were conducted on a CH Instruments CHI630D potentiostat using a 2-mm platinum disk as the working electrode, a 3-mm glassy carbon disk as the counter electrode,

and a 25-μm silver wire as the pseudo–reference electrode. UV–Vis spectra were recorded on a Varian Carey 5000 spectrophotometer from 230 to 1600 nm using matched 1-cm quartz cells; all spectra were obtained using a solvent reference blank in a cuvette with an air–free Teflon adapter. IR spectra were recorded on a JASCO FTIR420 spectrophotometer from 4000 to 400 cm^{-1} using a sealed liquid cell from International Crystals Laboratory with a 1-mm path length and KBr windows. CHN analyses were performed on an Exeter Analytical, Inc. CE-440 Elemental Analyzer. Magnetic susceptibility measurements were conducted on a Quantum Design MPMS XL superconducting quantum interference device (SQUID) magnetometer. Spectra deconvolution was performed using the computer program IgorPro.

Dimethylphenylsilyl chloride, triethylamine, and n-butyllithium were purchased from Alfa Aesar and used as received. Iodine (I_2) was also purchased from Alfa Aesar and purified by sublimation before use. Tetrabutylammonium hexafluorophosphate ($TBAPF_6$) and tetrabutylammonium bromide (TBABr) were purchased from Sigma Aldrich and recrystallized from THF before use. Tetraisopropylammonium tetrakis[3,5-bis(trifluoromethyl)phenyl]borate ($TPABAr^F$) was prepared following the procedure reported by Thomson, et al.,[219] and recrystallized from diethyl ether and THF before use. Potassium benzyl (KBz) was synthesized following a previously published procedure.[220] Shafir, et al. reported the synthesis of 1,1'-ferrocene diamine (H_2NN^H),[67] H_2NN^{TMS} ligand,[221] and H_2NN^{MES} ligand,[222] while Siemling, et al. reported the synthesis of H_2NN^{NP} ligand.[223] H_2NN^{TBS} ligand[65], $(NN^{TBS})UI_2(THF)$,[64] $(NN^{TBS})U(CH_2Ph)_2$,[65] and $(NN^{TMS})U(CH_2Ph)_2$, as well as neutral and oxidized $(NN^{TBS})_2U$[64] complexes were previously prepared in our group. Monreal, et al. reported the synthesis of $UI_4(1,4\text{-dioxane})_2$,[138] which greatly facilitated this study because all uranium complexes presently discussed can be prepared in high yield and in a relatively short period of time starting with this precursor.

Synthesis of $[K_2(OEt_2)_2]NN^{DMP}$. Solid KCH_2Ph (169 mg, 1.3 mmol) was added to a thawing 10-mL diethyl ether solution of H_2NN^{DMP} (298 mg, 0.62 mmol). The reaction mixture was stirred at room temperature for 4 h. The resulting brick red precipitate was collected on a medium-porosity frit, washed with pentane, and dried under reduced pressure. Yield: 331 mg, 96 %.

Synthesis of $[K_2(OEt_2)_2]NN^{MES}$. Solid KCH_2Ph (358 mg, 2.75 mmol) was added to a thawing 30-mL diethyl ether solution of H_2NN^{MES} (592 mg, 1.31 mmol). The reaction mixture was stirred at room temperature for 2 h. The resulting dark red precipitate was collected on a medium-porosity frit, washed with hexanes, and dried under reduced pressure. Yield: 773 mg, 87 %.

Synthesis of $(NN^{DMP})_2U$. A cold THF solution of $[K_2(OEt_2)_2]NN^{DMP}$ (510 mg, 0.72 mmol) was slowly added to a thawing THF solution of $UI_4(dioxane)_2$ (378 mg, 0.41 mmol). After stirring at room temperature for 3 h, the reaction mixture was filtered through Celite and dried under reduced pressure. The crude product was dissolved in toluene, again filtered through Celite, and dried under reduced pressure. This process was repeated two more times. The final filtrate was concentrated and placed at -40 ºC. Dark red-brown crystals formed after several days. Yield: 279 mg, 57 %. $(NN^{DMP})_2U$ is insoluble in hexanes and diethyl ether, sparingly soluble in toluene and benzene, and soluble in tetrahydrofuran, dichloromethane, and chloroform.

Synthesis of $(NN^{MES})_2U$. A cold THF solution of $[K_2(OEt_2)_2]NN^{MES}$ (1.20 mg, 1.92 mmol) was slowly added to a thawing THF solution of $UI_4(dioxane)_2$ (935 mg, 1.01 mmol). After stirring at room temperature for 3 h, the reaction mixture was filtered through Celite and dried under reduced pressure. The crude product was dissolved in toluene, again filtered through Celite, and dried. Pentane was added to the resulting dark orange film and the mixture was stirred at room temperature until powder formed. The orange powder was then collected on a medium-porosity frit and washed with diethyl ether. It was then dissolved in toluene and

placed at -40 ºC. Dark orange crystals formed after 24 h. Yield: 621 mg, 62 %. **$(NN^{MES})_2U$** is insoluble in hexanes and diethyl ether, and soluble in toluene, benzene, tetrahydrofuran, dichloromethane, and chloroform.

Synthesis of $[(NN^{TMS})_2U][I_3]$ and **$[(NN^{TMS})_2U][FeI_4]$.** In a 20-mL scintillation vial, a diethyl ether solution of iodine (4.5 mL of 0.08 M, 0.37 mmol) was added dropwise to a cold diethyl ether solution of **$(NN^{TMS})_2U$** (304 mg, 0.32 mmol). Black precipitate formed immediately. After the reaction mixture was allowed to stir at room temperature for 1 h, the powder was collected onto a medium-porosity frit, washed with diethyl ether, and dried under reduced pressure. Yield: 281 mg, 66 %. **$[(NN^{TMS})_2U][I_3]$** is insoluble in hexanes, pentane, diethyl ether, toluene, benzene, and trifluorotoluene. Although soluble in tetrahydrofuran, dichloromethane, and chloroform, **$[(NN^{TMS})_2U][I_3]$** readily decomposes after 30 min even at -40 ºC. Recrystallization from dichloromethane yields black needle crystals of **$[(NN^{TMS})_2U][FeI_3]$**. Finally, **$[(NN^{TMS})_2U][I_3]$** can be reduced back to **$(NN^{TMS})_2U$** by addition of potassium graphite in tetrahydrofuran.

Synthesis of $[(NN^{TBS})_2U][I_3]$. In a 50-mL round bottom flask, a diethyl ether solution of iodine (6.3 mL of 0.08 M, 0.51 mmol) was added dropwise to a cold diethyl ether solution of **$(NN^{TBS})_2U$** (501 mg, 0.45 mmol). After the reaction mixture was allowed to stir at room temperature for 40 min, the black powder was collected onto a medium-porosity frit, washed with diethyl ether, and dried under reduced pressure. Yield: 615 mg, 92 %. **$[(NN^{TBS})_2U][I_3]$** is insoluble in hexanes, pentane, diethyl ether, toluene, benzene, and trifluorotoluene but soluble in tetrahydrofuran, dichloromethane, and chloroform. It is stable in solution at room temperature.

Synthesis of $[(NN^{DMP})_2U][I_3I]$ and **$[(NN^{DMP})_2U][I_3I_5]$.** In a 20-mL scintillation vial, a diethyl ether solution of iodine (0.81 mL of 0.05 M, 0.04 mmol) was added dropwise to a cold diethyl ether

solution of **$(NN^{DMP})_2U$** (42 mg, 0.03 mmol). Black precipitate formed immediately. After the reaction mixture was allowed to stir at room temperature for 20 min, the powder was collected onto a medium-porosity frit, washed with diethyl ether, and dried under reduced pressure. Yield: 45 mg, 75 %. **$[(NN^{DMP})_2U][I_3I]$** is insoluble in hexanes, pentane, diethyl ether, toluene, and benzene. Like **$[(NN^{TMS})_2U][I_3]$**, it is soluble in tetrahydrofuran, dichloromethane, and chloroform, but it decomposes in solution even at -40 °C. Recrystallization from concentrated dichloromethane at -40 °C yields black crystals of **$[(NN^{DMP})_2U][I_3I_5]$** after 15 min.

Synthesis of $[(NN^{MES})_2U][I_3]$. In a 50-mL round bottom flask, a diethyl ether solution of iodine (6.8 mL of 0.05 M, 0.34 mmol) was added dropwise to a cold diethyl ether solution of **$(NN^{MES})_2U$** (334 mg, 0.29 mmol). After the reaction mixture was allowed to stir at room temperature for 40 min, the black powder was collected onto a medium-porosity frit, washed with diethyl ether and toluene, and dried under reduced pressure. Yield: 384 mg, 86 %. **$[(NN^{MES})_2U][I_3]$** is insoluble in hexanes, pentane, diethyl ether, toluene, and benzene, but soluble in tetrahydrofuran, dichloromethane, and chloroform. Unlike the **NN^{DMP}** and **NN^{TMS}** analogues, **$[(NN^{MES})_2U][I_3]$** decomposes in solution to the neutral species after several hours at room temperature.

5.4.2 Elemental analysis

$(NN^{TMS})_2U$
$C_{32}H_{52}Fe_2N_4Si_4U$ (955 g/mol)
Calculated: 40.25 %C, 5.49 %H, 5.87 %N
Found: 40.80 %C, 5.58 %H, 5.53 %N

$(NN^{TBS})_2U$
$C_{44}H_{76}Fe_2N_4Si_4U$ (1123 g/mol)
Calculated: 47.05 %C, 6.82 %H, 4.99 %N
Found: 46.71 %C, 6.62 %H, 4.97 %N

$(NN^{DMP})_2U$
$C_{52}H_{60}Fe_2N_4Si_4U$ (1203 g/mol)
Calculated: 51.91 %C, 5.03 %H, 4.66 %N
Found: 51.61 %C, 5.05 %H, 4.70 %N

$(NN^{MES})_2U$
$C_{56}H_{60}Fe_2N_4U$ (1139 g/mol)
Calculated: 59.06 %C, 5.31 %H, 4.92 %N
Found: 58.52 %C, 5.45 %H, 4.80 %N

$[(NN^{TMS})_2U][I_3]$
$C_{32}H_{52}Fe_2I_3N_4Si_4U$ (1336 g/mol)
Calculated: 28.78 %C, 3.92 %H, 4.20 %N
Found: 29.11 %C, 3.51 %H, 3.88 %N

$[(NN^{TBS})_2U][I_3]$
$C_{44}H_{76}Fe_2I_3N_4Si_4U$ (1504 g/mol)
Calculated: 35.14 %C, 5.09 %H, 3.73 %N
Found: 35.35 %C, 4.90 %H, 3.35 %N

$[(NN^{DMP})_2U][I_3I]$
$C_{52}H_{60}Fe_2I_4N_4Si_4U$ (1711 g/mol)
Calculated: 36.51 %C, 3.54 %H, 3.28 %N
Found: 35.74 %C, 3.44 %H, 3.02 %N

$[(NN^{MES})_2U][I_3]$
$C_{56}H_{60}Fe_2I_3N_4U$ (1520 g/mol)
Calculated: 44.26 %C, 3.98 %H, 3.69 %N
Found: 44.55 %C, 4.06 %H, 3.22 %N

5.4.3 ^{1}H and ^{13}C NMR spectroscopy

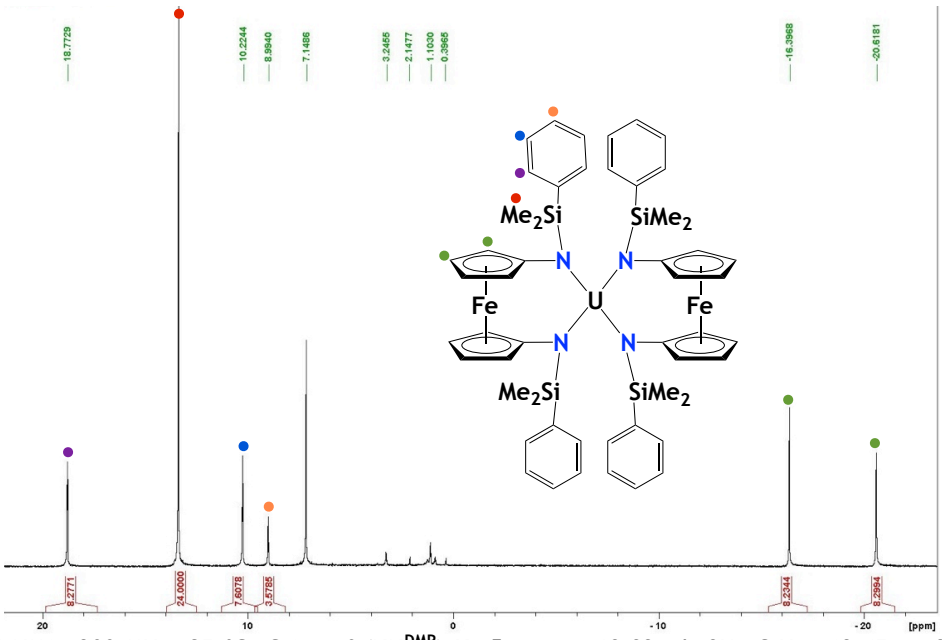

Figure E1. ^{1}H NMR (300 MHz, 25 °C, C_6D_6) of **(NN^{DMP})$_2$U**; δ (ppm): 18.83 (d, 8H, C_6H_5), 13.45 (s, 24H, Si(CH_3)$_2$), 10.28 (t, 8H, C_6H_5), 9.03 (t, 4H, C_6H_5), -16.39 (s, 8H, Cp-C*H*), -20.62 (s, 8H, Cp-C*H*).

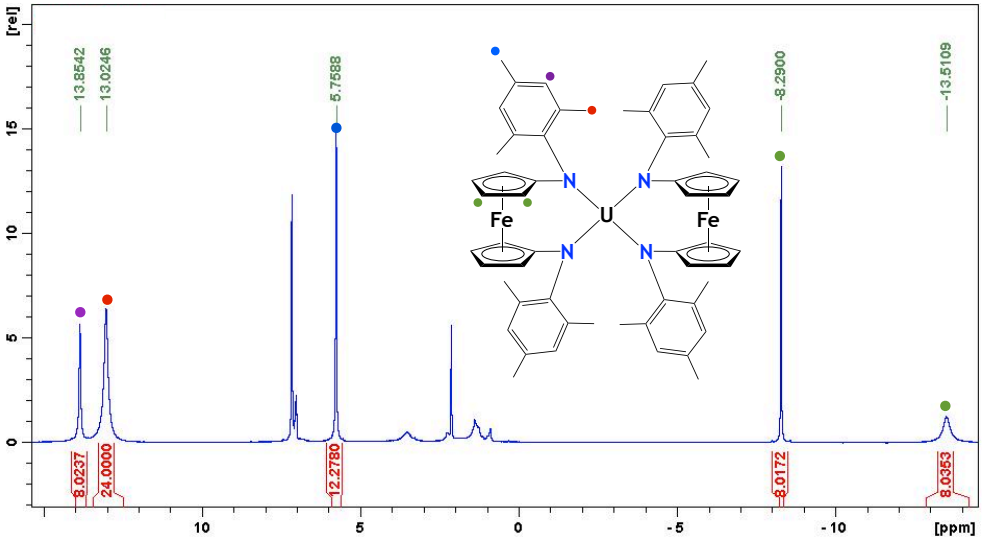

Figure E2. ^{1}H NMR (300 MHz, 25 °C, C_6D_6) of **(NN^{MES})$_2$U**; δ (ppm): 13.85 (s, 8H, C_6H_2), 13.02 (s, 24H, ortho-$CH_3C_6H_2$), 5.76 (s, 12H, para-$CH_3C_6H_2$), -8.29 (s, 8H, Cp-C*H*), -13.51 (s, 8H, Cp-C*H*).

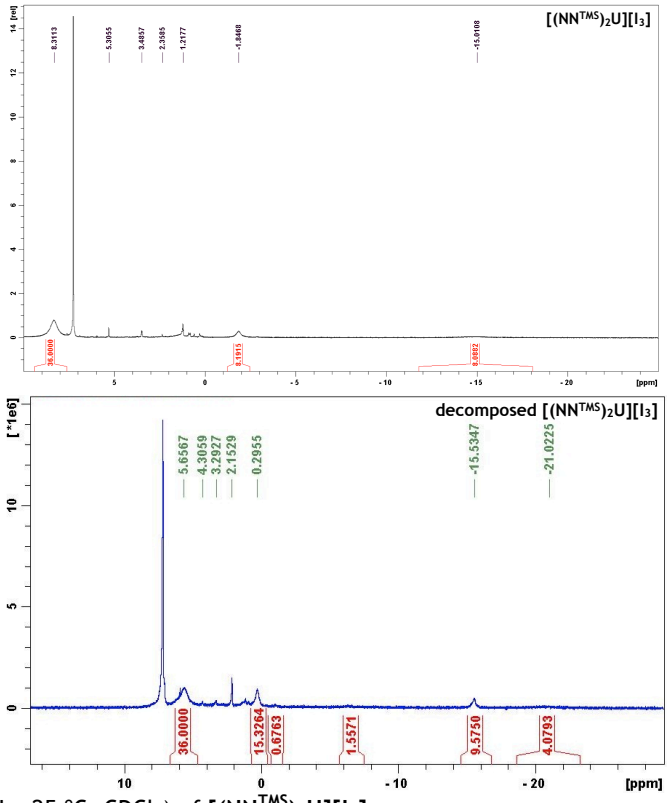

Figure E3. ^{1}H NMR (300 MHz, 25 °C, $CDCl_3$) of **$[(NN^{TMS})_2U][I_3]$**.

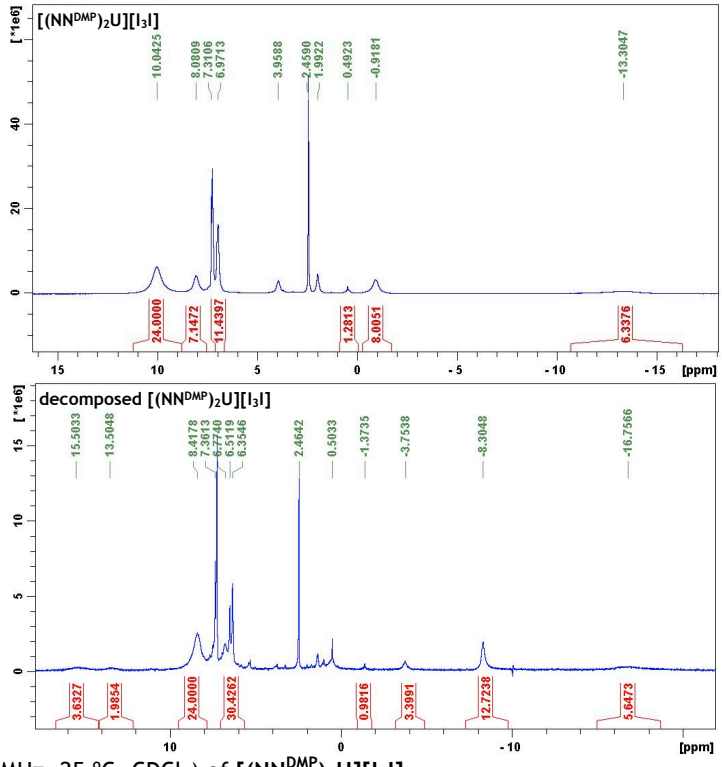

Figure E4. ^{1}H NMR (300 MHz, 25 °C, $CDCl_3$) of **$[(NN^{DMP})_2U][I_3I]$**.

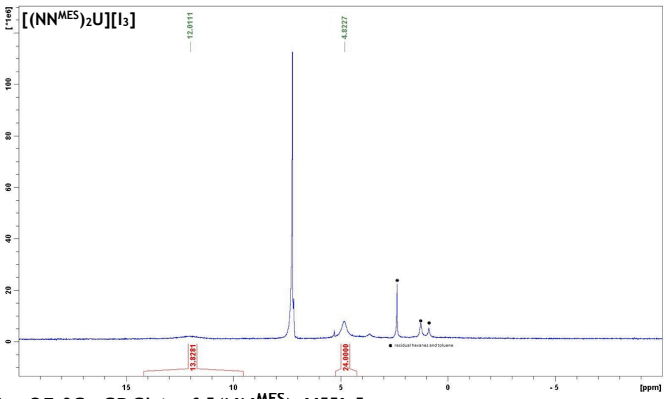

Figure E5. ^{1}H NMR (300 MHz, 25 °C, $CDCl_3$) of **[(NN^{MES})$_2$U][I$_3$]**.

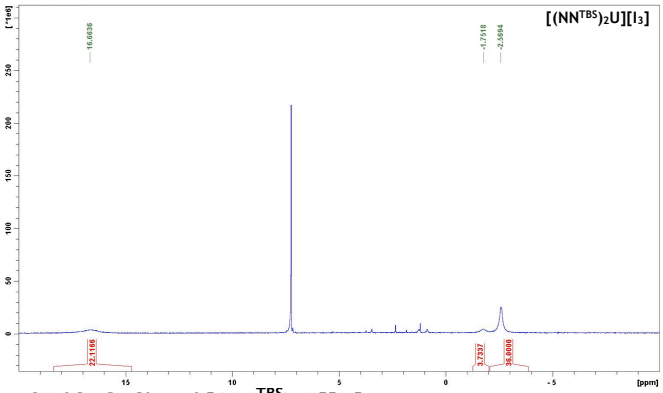

Figure E6. ^{1}H NMR (300 MHz, 25 °C, $CDCl_3$) of **[(NN^{TBS})$_2$U][I$_3$]**.

5.4.4 Crystallography

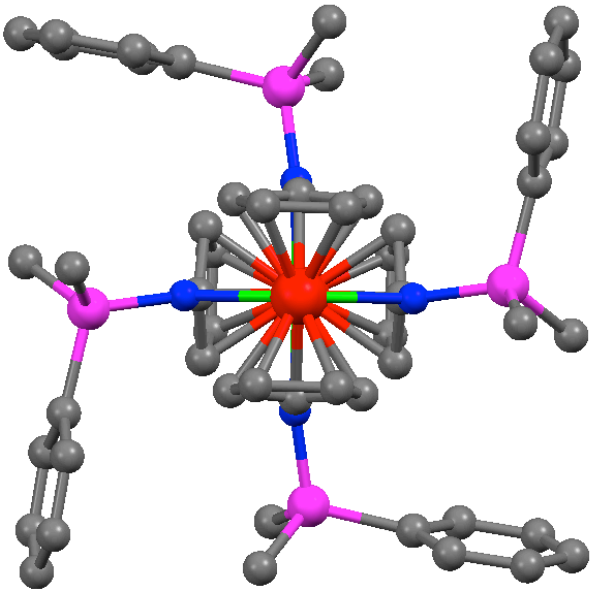

Figure E7. Crystal data for **(NN^{DMP})$_2$U**, formula $C_{52}H_{60}Fe_2N_4Si_4U$; space group P-4; V = 4907.48 Å^3; a = 19.5647(10) Å, b = 19.5647(10) Å, c = 12.8207(10) Å; β = 90.00°.

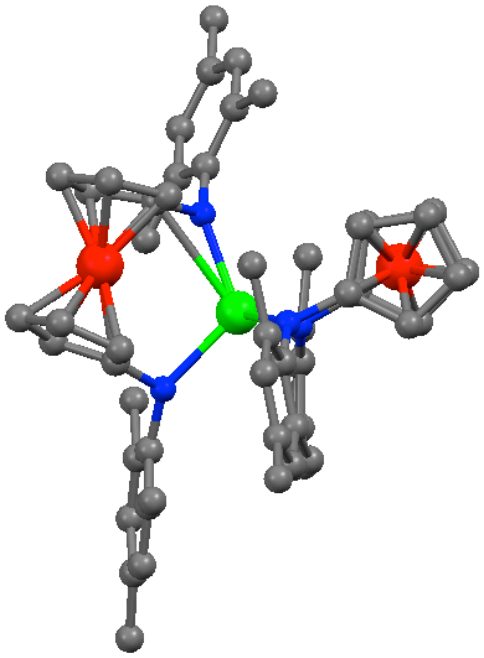

Figure E8. Crystal data for **$(NN^{MES})_2U$,** formula $C_{56}H_{60}Fe_2N_4U$; space group C2/c; V = 10716.9 $Å^3$; a = 38.797(4) Å, b = 11.7313(12) Å, c = 23.559(2)Å; ß = 91.886(1)°.

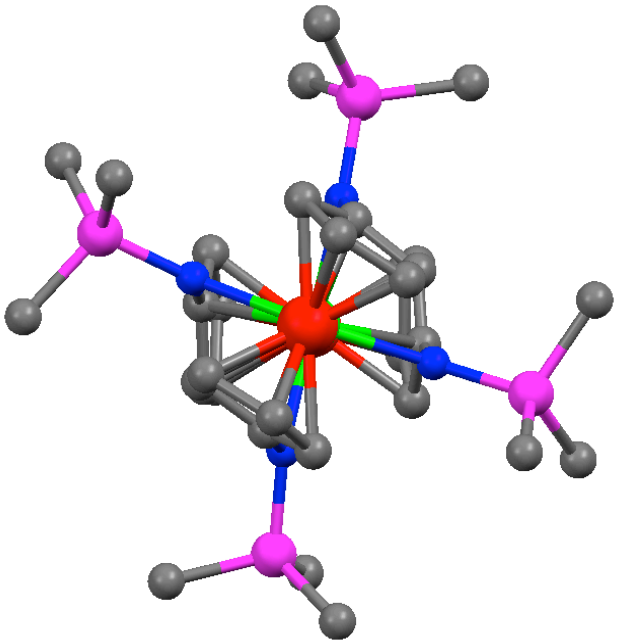

Figure E9. Crystal data for **$[(NN^{TMS})_2U][FeI_4]$**, formula $C_{32}H_{52}Fe_3I_4N_4Si_4UCH_2Cl_2$; space group $P2_1/n$; V = 5145.54 $Å^3$; a = 19.082(14) Å, b = 14.866(11) Å, c = 19.240(14) Å; ß = 109.477(7)°. $[FeI_4]^-$ anion is not included.

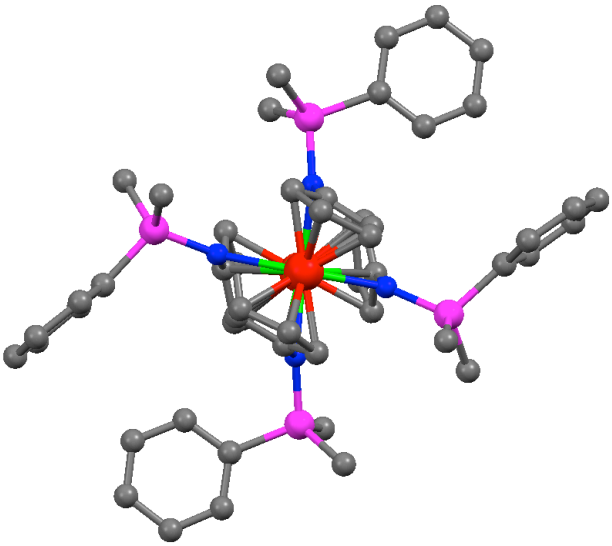

Figure E10. Crystal data for **[(NN^{DMP})$_2$U][I$_3$I$_5$],** formula $C_{52}H_{60}Fe_2N_4Si_4UI_8$; space group $P2_1/n$; V = 5604.26 Å^3; a = 13.143(2) Å, b = 23.147(4) Å, c = 19.050(3) Å; ß = 104.752(2)°. $[I_3]^-$ and $[I^5]^-$ anions are not included for clarity.

5.4.5 Cyclic voltammetry

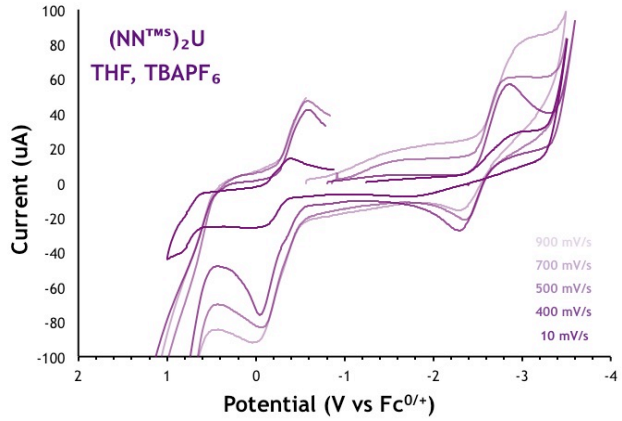

Figure E11. Cyclic voltammogram of **(NN^{TMS})$_2$U** with $TBAPF_6$ supporting electrolyte.

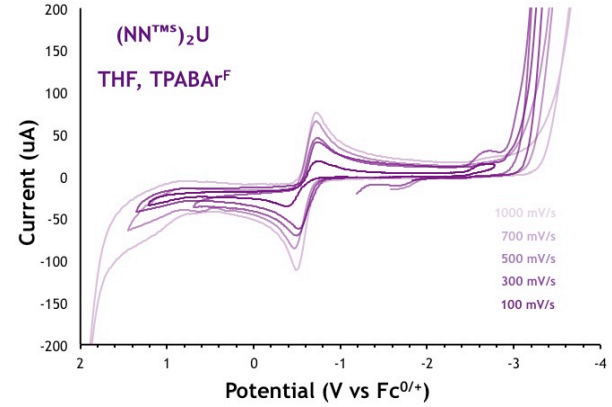

Figure E12. Cyclic voltammogram of **(NN^{TMS})$_2$U** with $TPABAr^F$ supporting electrolyte.

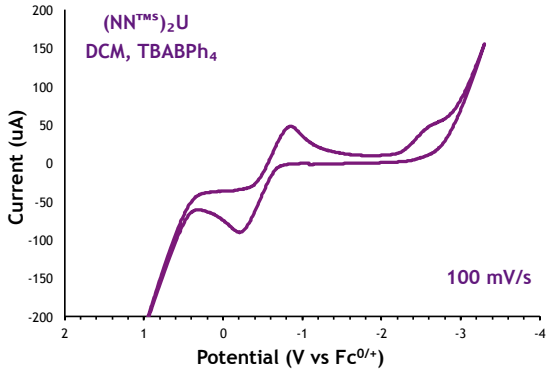

Figure E13. Cyclic voltammogram of $(NN^{TMS})_2U$ with $TBABPh_4$ supporting electrolyte.

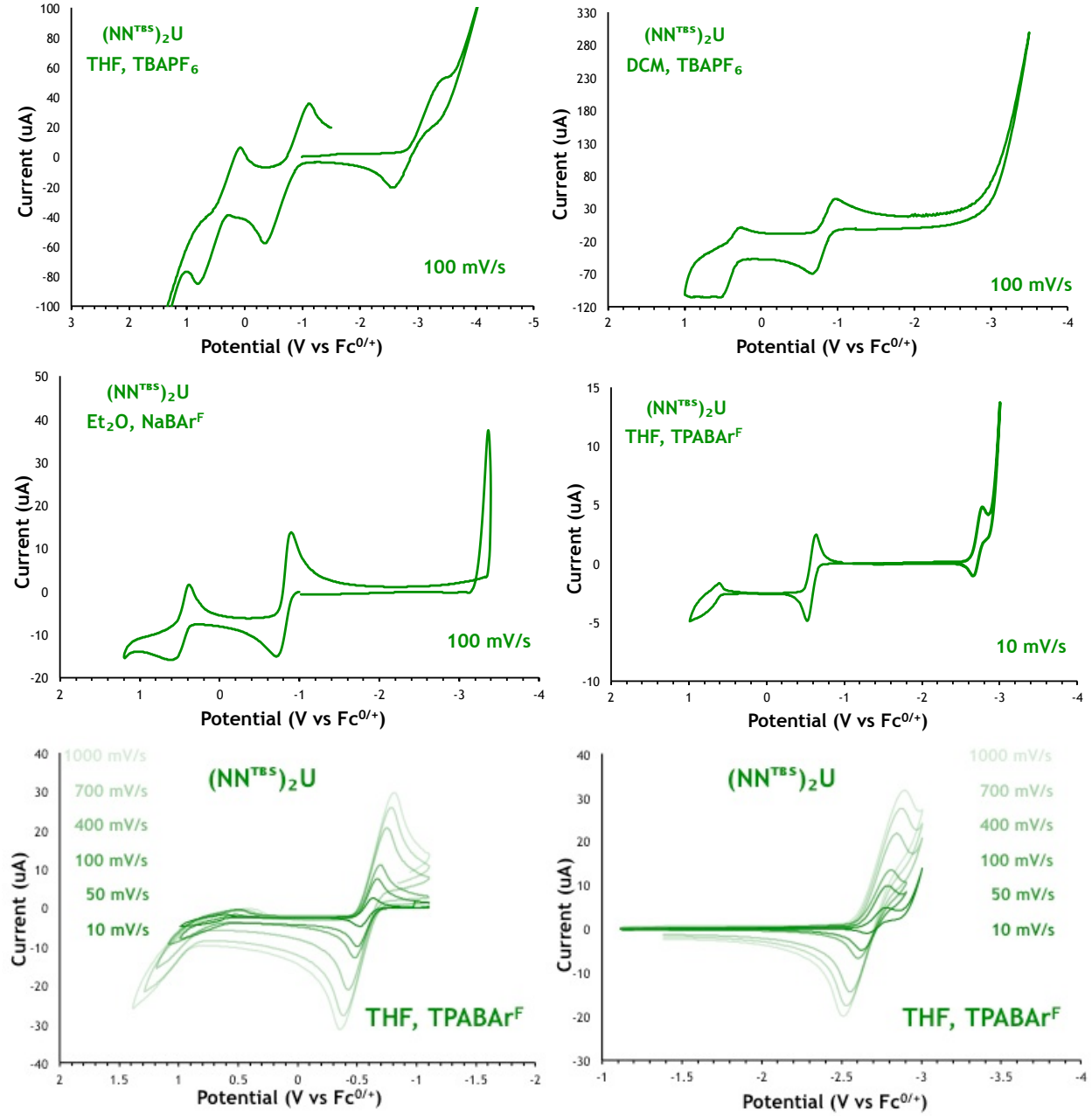

Figure E14. Cyclic voltammograms of $(NN^{TBS})_2U$.

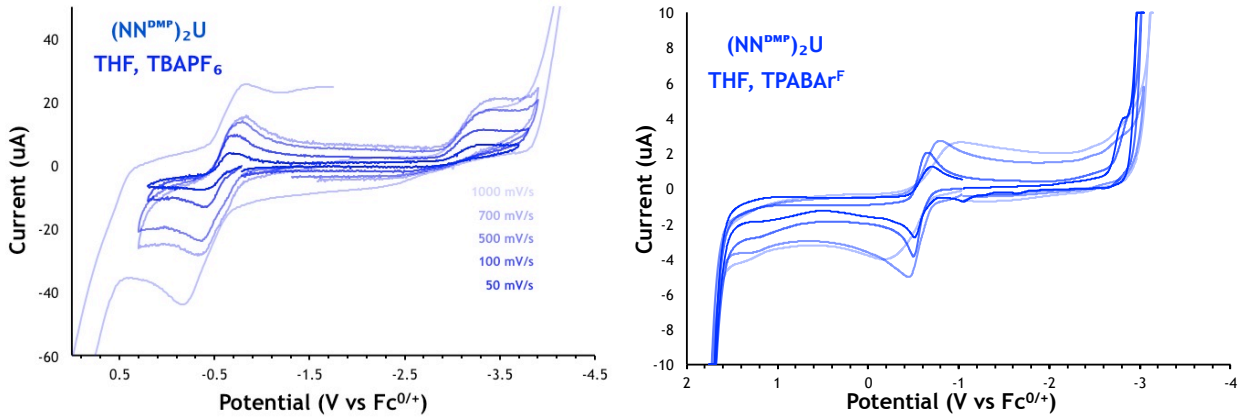

Figure E15. Cyclic voltammogram of $(NN^{DMP})_2U$.

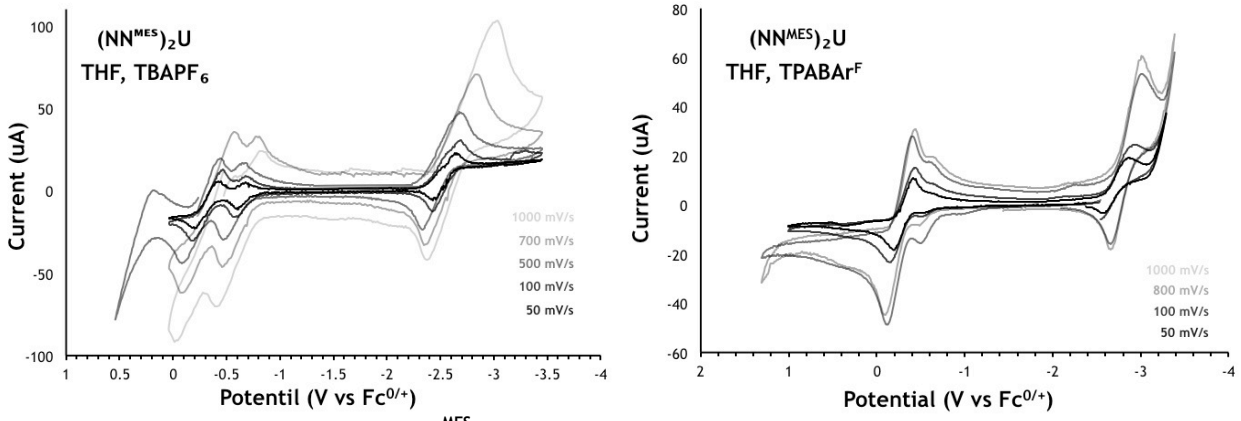

Figure E16. Cyclic voltammogram of $(NN^{MES})_2U$.

5.4.6 Differential pulse voltammetry

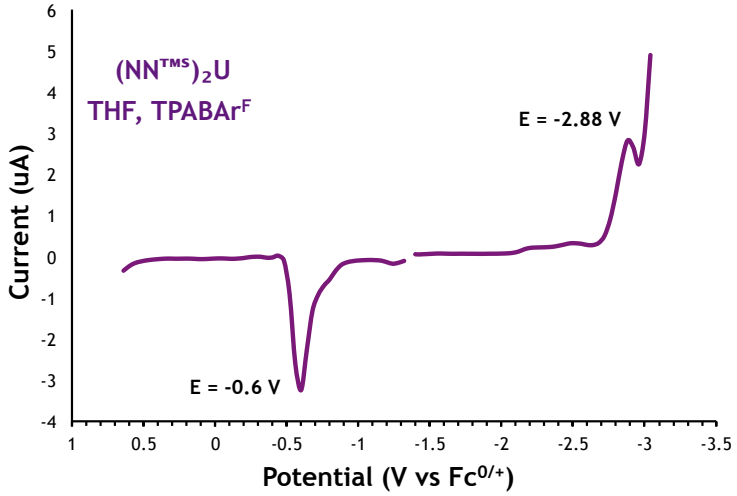

Figure E17. Differential pulse voltammogram of $(NN^{TMS})_2U$ with $TPABAr^F$ supporting electrolyte.

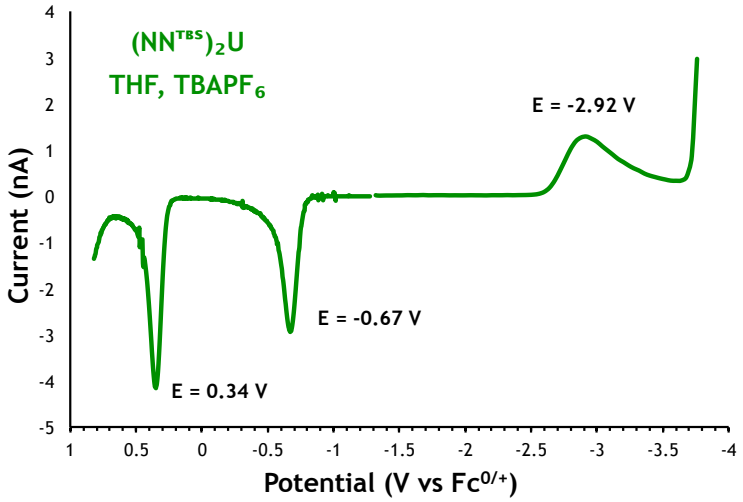

Figure E18. Differential pulse voltammogram of $(NN^{TBS})_2U$ with $TBAPF_6$ supporting electrolyte.

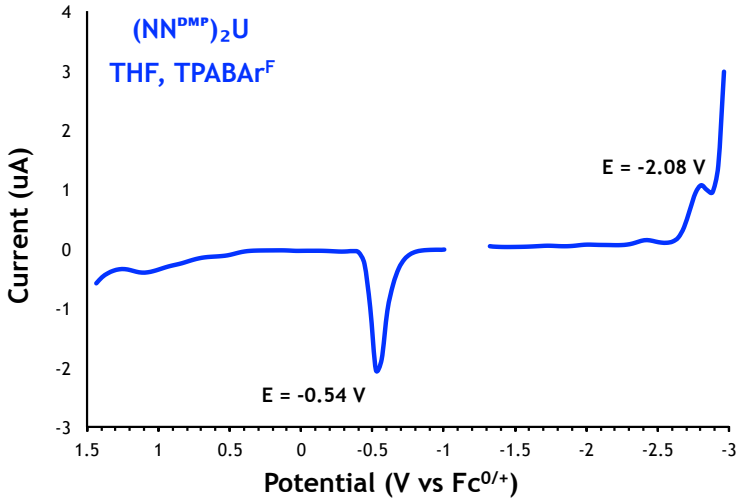

Figure E19. Differential pulse voltammogram of $(NN^{DMP})_2U$ with $TPABAr^F$ supporting electrolyte.

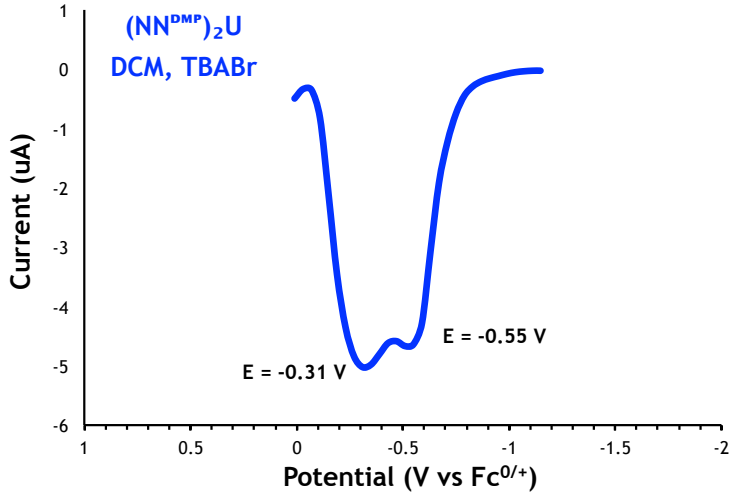

Figure E20. Differential pulse voltammogram of $(NN^{DMP})_2U$ with TBABr supporting electrolyte.

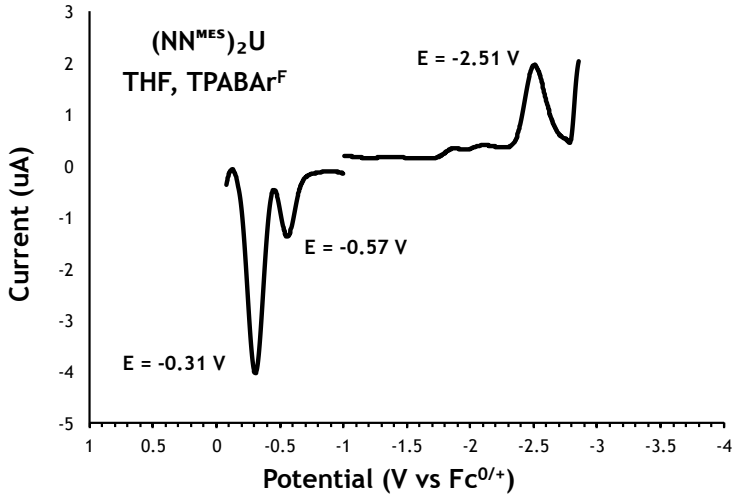

Figure E21. Differential pulse voltammogram of **$(NN^{MES})_2U$** with $TPABAr^F$ supporting electrolyte.

5.4.7 Chronoamperometry

$$i = \frac{nFAC\sqrt{D}}{\sqrt{\pi t}} = kt^{-1/2} = kv^{1/2} \qquad \mathrm{i} = \frac{\mathrm{nFAC}\sqrt{\mathrm{D}}}{\sqrt{\pi \mathrm{t}}} = \mathrm{kt}^{-1/2} = \mathrm{k}\nu^{1/2}$$

where

i = current in uA
n = number of electrons
F = Faraday constant in C mol^{-1}
A = area of electrode surface in cm^2
C = analyte concentration in mM
D = diffusion coefficient in cm^2 s^{-1}
t = time in seconds
v = scan rate in mV/s

Plotting i as a function of $v^{1/2}$ yields a straight line with slope k. Using

$$\frac{n_x}{n_{fc}} = \frac{(k_x)(i_{fc})(C_{fc})}{(k_{fc})(i_x)(C_x)}$$

where

n_x = number of electrons transferred during oxidation of $(NN^R)_2U$
n_{fc} = number of electrons transferred during oxidation of ferrocene
k_x = slope measured with a 3-mm electrode for $(NN^R)_2U$
k_{fc} = slope measured a 3-mm electrode for ferrocene
i_x = steady state current measured with a 25-um electrode for $(NN^R)_2U$
i_{fc} = steady state current measured with a 25-um electrode for ferrocene
C_x = concentration of $(NN^R)_2U$
C_{fc} = concentration of ferrocene

Table E1. Chronoamperometry in THF solutions of $TPABAr^F$.

THF, $TPABAr^F$	C	k_x	i	Trial			Electrons		
	(mM)	*(uA $s^{1/2}$)*	*nA*	1	2	3	avg	±	n
$(NN^{TMS})_2U$	1.76	4.35	-4.04	0.82	0.83	0.76	0.80	0.04	**1**
$(NN^{TBS})_2U$, **1**	0.94	3.64	-3.44	1.27	1.29	1.18	1.25	0.06	**1**
$(NN^{TBS})_2U$, **2**	0.94	4.04	-4.79	1.12	1.14	1.04	1.10	0.05	**1**
$(NN^{DMP})_2U$	2.85	11.71	-7.44	1.99	2.03	1.84	1.96	0.10	**2**

Table E2. Chronoamperometry in THF solutions of $TBAPF_6$.

THF, $TBAPF_6$	C	k_x	i	Trial			Electrons		
	(mM)	(uA $s^{1/2}$)	nA	1	2	3	avg	±	n
$(NN^{TBS})_2U$, **1**	5.17	-13.85	-14.11	0.81	0.82	0.75	0.79	0.04	**1**
$(NN^{TBS})_2U$, **2**	5.17	-16.21	-16.28	0.96	0.98	0.89	0.93	0.05	**1**
$(NN^{DMP})_2U$	0.64	3.30	-2.21	2.38	2.42	2.20	2.31	0.12	**2**
$(NN^{MES})_2U$	3.20	9.52	-7.48	1.17	1.19	1.08	1.13	0.06	**1**

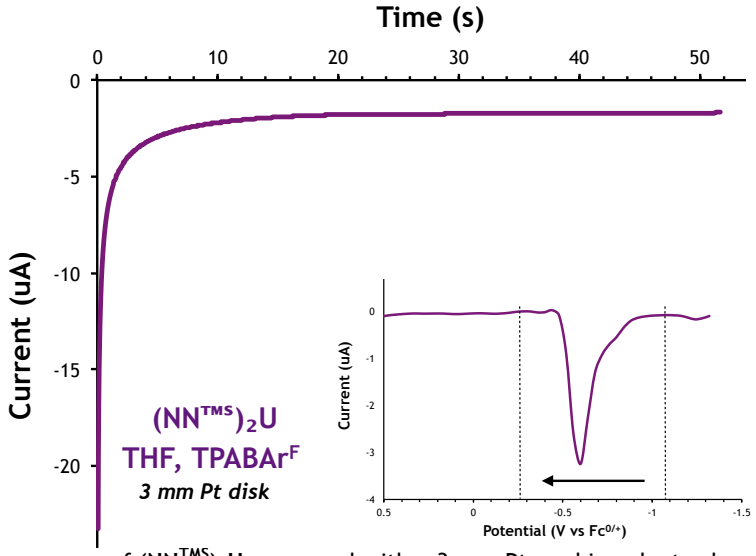

Figure E22. Chronoamperogram of $(NN^{TMS})_2U$ measured with a 3-mm Pt working electrode.

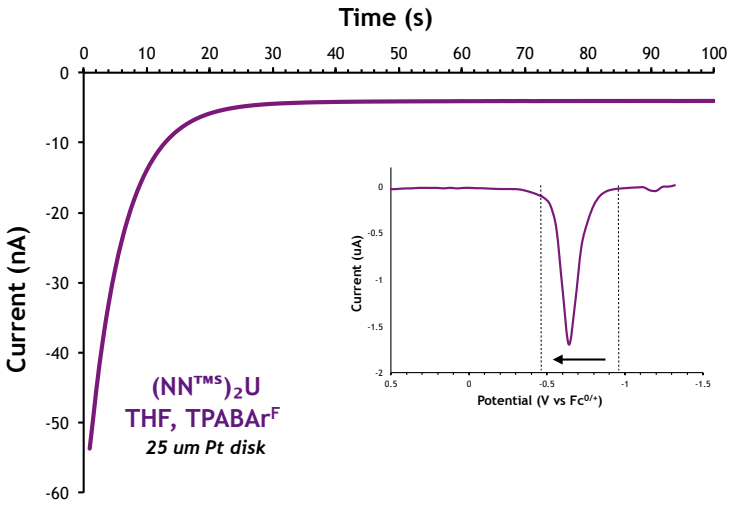

Figure E23. Chronoamperogram of $(NN^{TMS})_2U$ measured with a 25-um Pt working electrode.

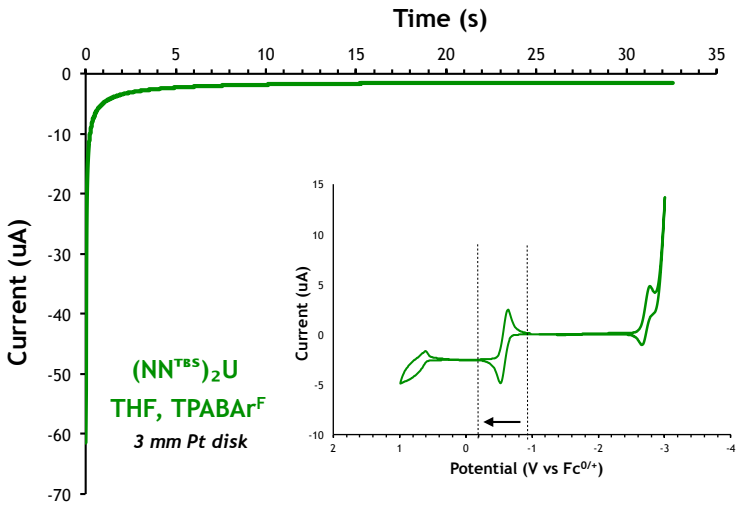

Figure E24. Chronoamperogram of $(NN^{TBS})_2U$ measured with a 3-mm Pt working electrode.

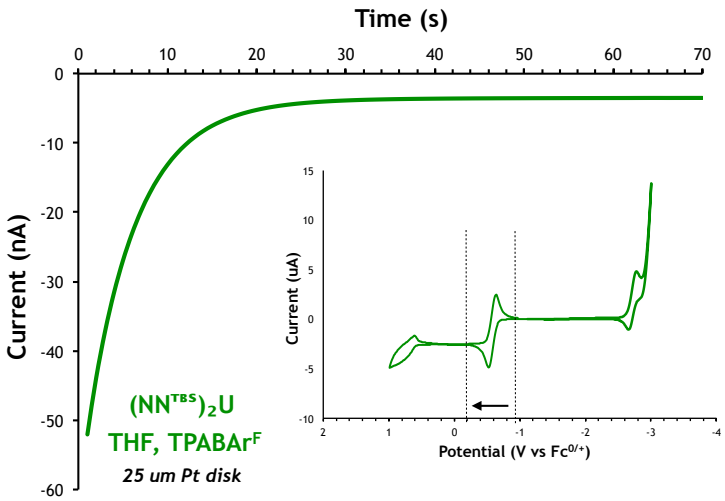

Figure E25. Chronoamperogram of $(NN^{TBS})_2U$ measured with a 25-um Pt working electrode.

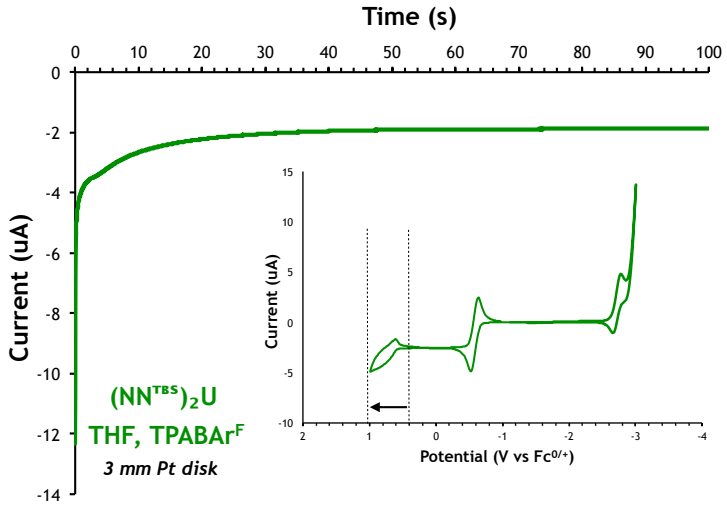

Figure E26. Chronoamperogram of $(NN^{TBS})_2U$ measured with a 3-mm Pt working electrode.

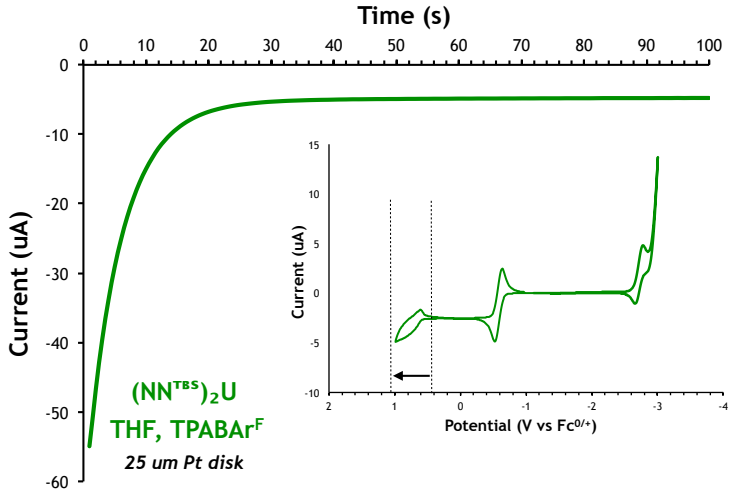

Figure E27. Chronoamperogram of $(NN^{TBS})_2U$ measured with a 25-um Pt working electrode.

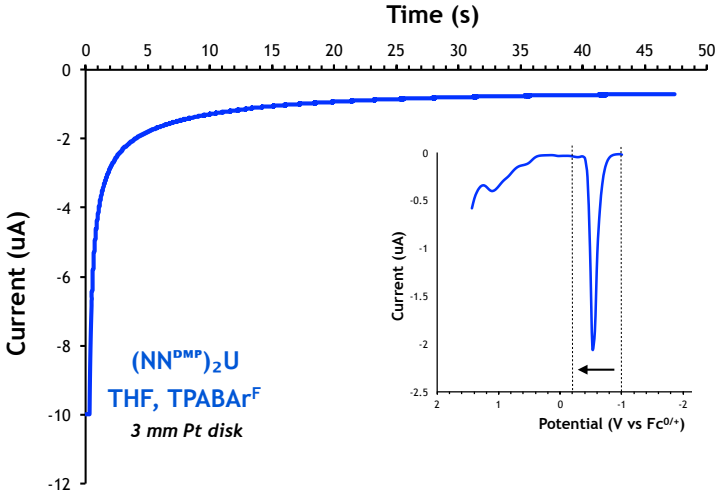

Figure E28. Chronoamperogram of $(NN^{DMP})_2U$ measured with a 3-mm Pt working electrode.

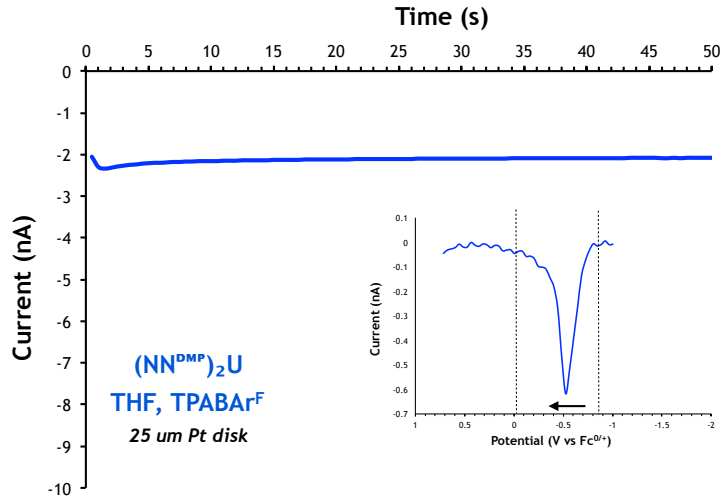

Figure E29. Chronoamperogram of **$(NN^{DMP})_2U$** measured with a 25-um Pt working electrode.

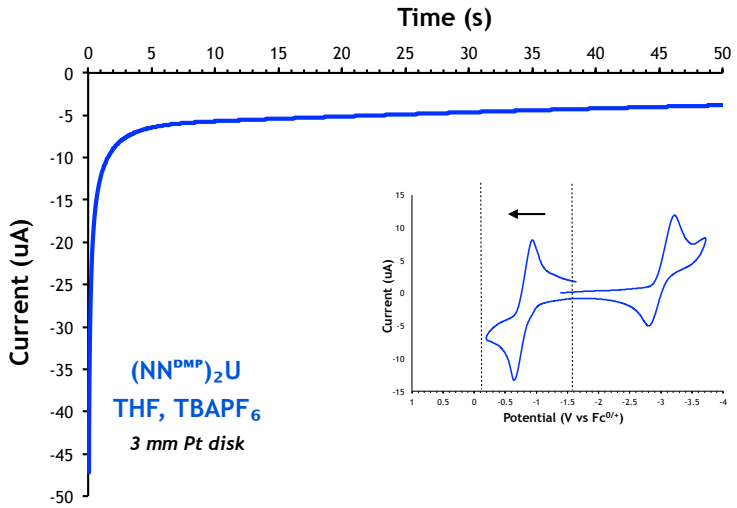

Figure E30. Chronoamperogram of **$(NN^{DMP})_2U$** measured with a 3-mm Pt working electrode.

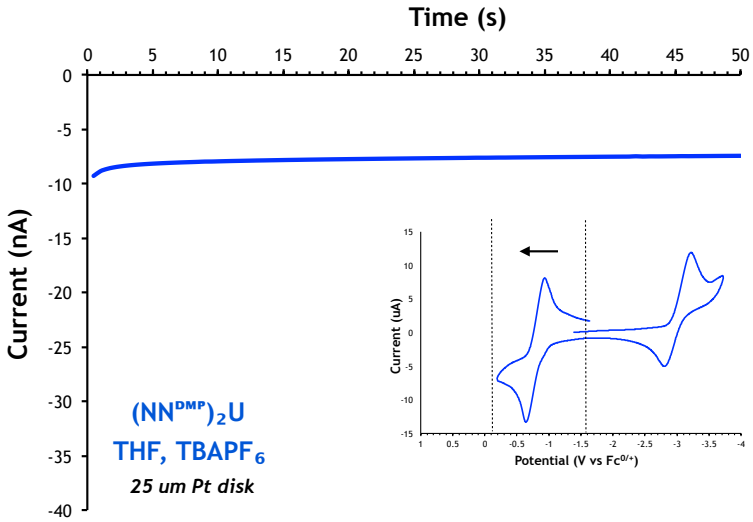

Figure E31. Chronoamperogram of **$(NN^{DMP})_2U$** measured with a 25-um Pt working electrode.

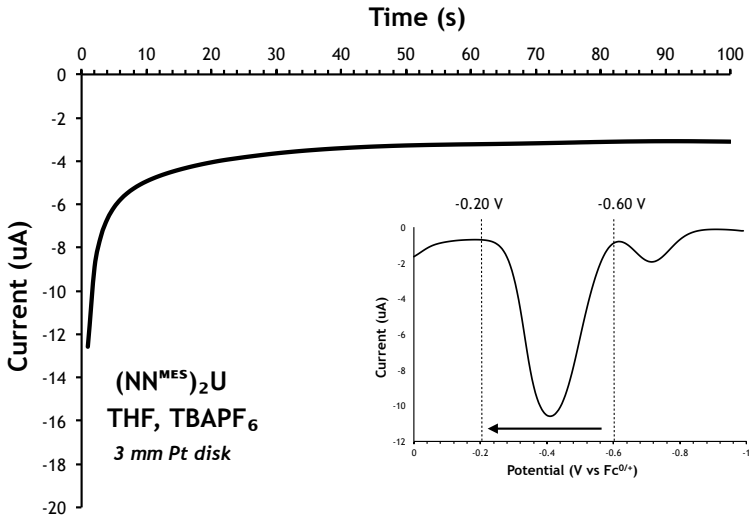

Figure E32. Chronoamperogram of **$(NN^{MES})_2U$** measured with a 3-mm Pt working electrode

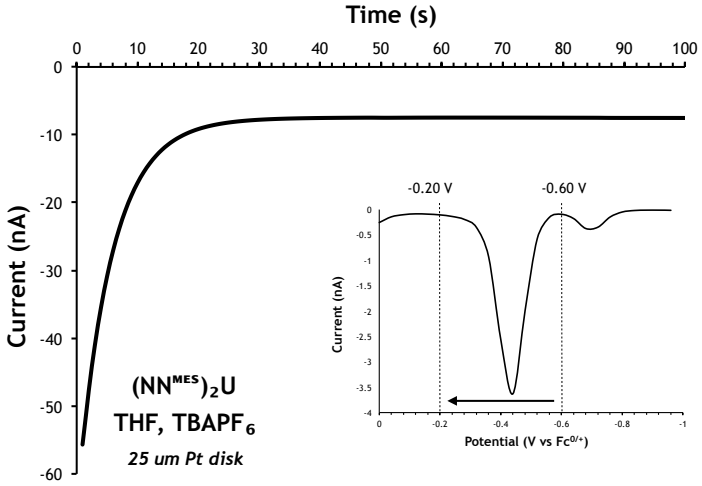

Figure E33. Chronoamperogram of **$(NN^{MES})_2U$** measured with a 25-um Pt working electrode.

5.4.8 IR spectroscopy

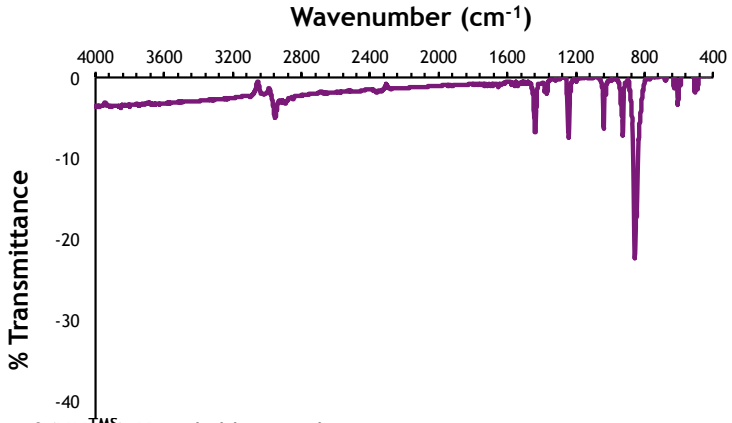

Figure E34. IR spectrum of **$(NN^{TMS})_2U$** in dichloromethane.

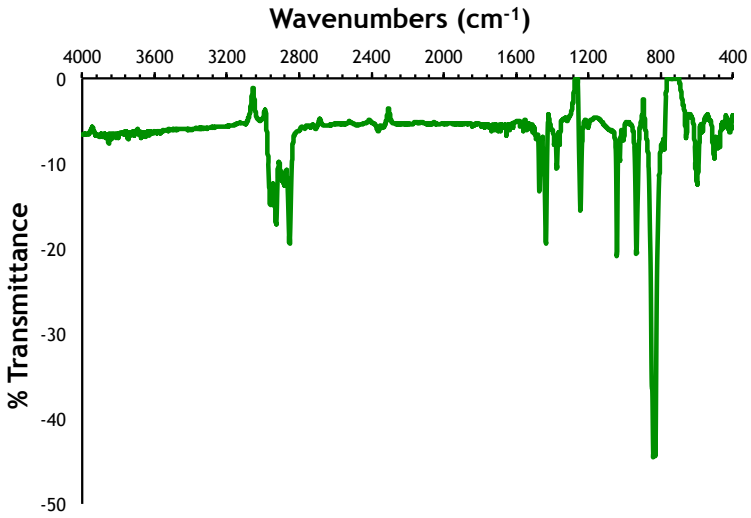

Figure E35. IR spectrum of $(NN^{TBS})_2U$ in dichloromethane.

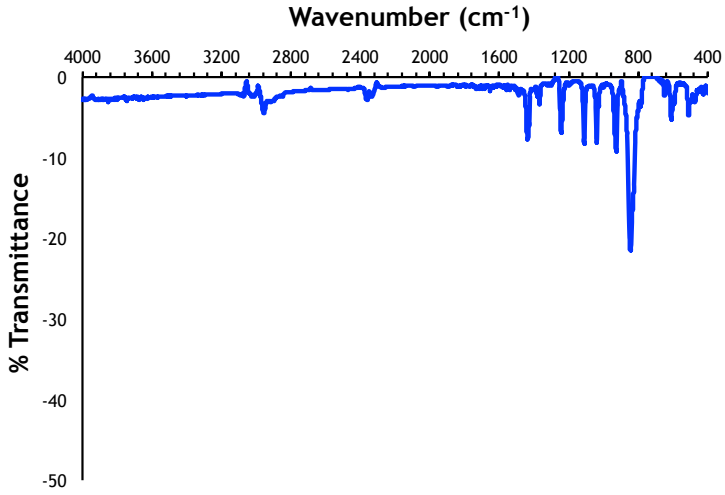

Figure E36. IR spectrum of $(NN^{DMP})_2U$ in dichloromethane.

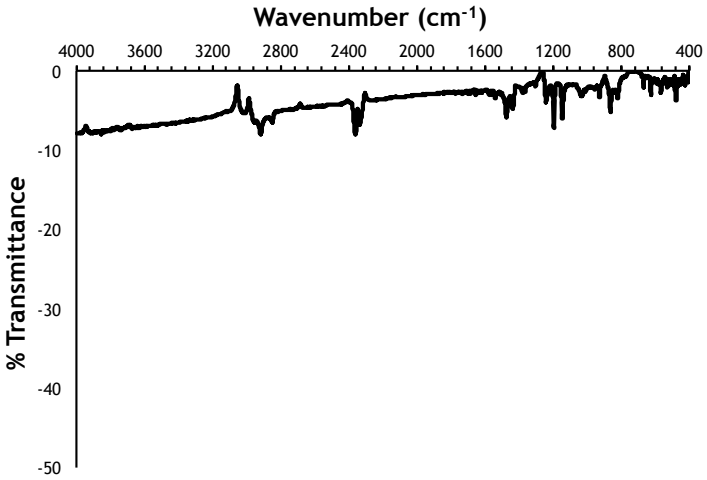

Figure E37. IR spectrum of $(NN^{MES})_2U$ in dichloromethane.

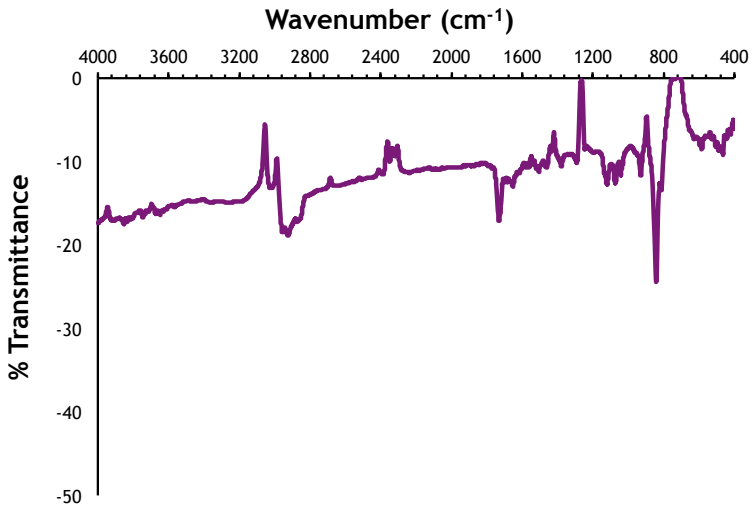

Figure E38. IR spectrum of **[(NN^{TMS})$_2$U][I$_3$]** in dichloromethane.

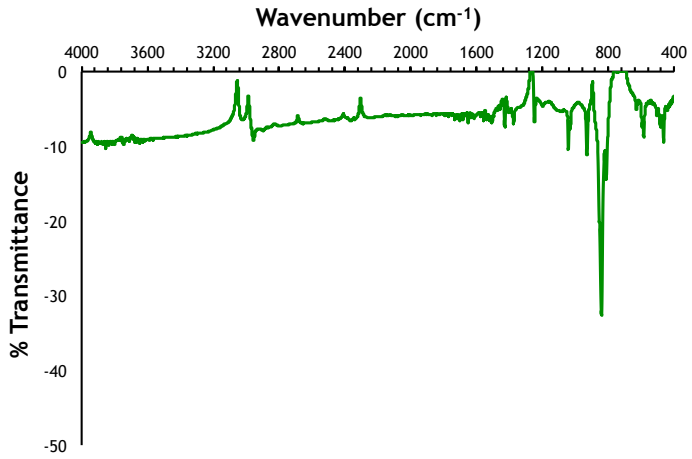

Figure E39. IR spectrum of **[(NN^{TBS})$_2$U][I$_3$]** in dichloromethane.

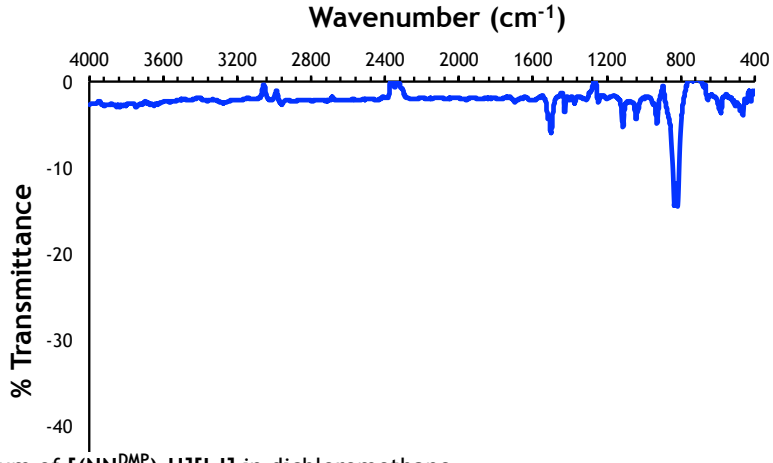

Figure E40. IR spectrum of **[(NN^{DMP})$_2$U][I$_3$I]** in dichloromethane.

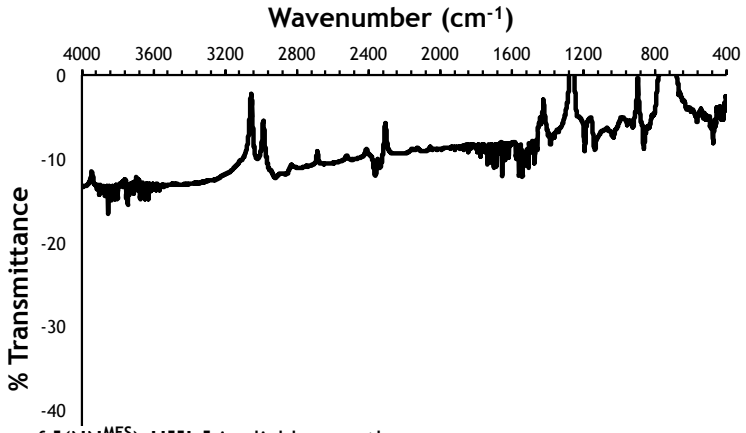

Figure E41. IR spectrum of **[(NN^{MES})$_2$U][I$_3$]** in dichloromethane.

5.4.9 UV-Vis spectroscopy

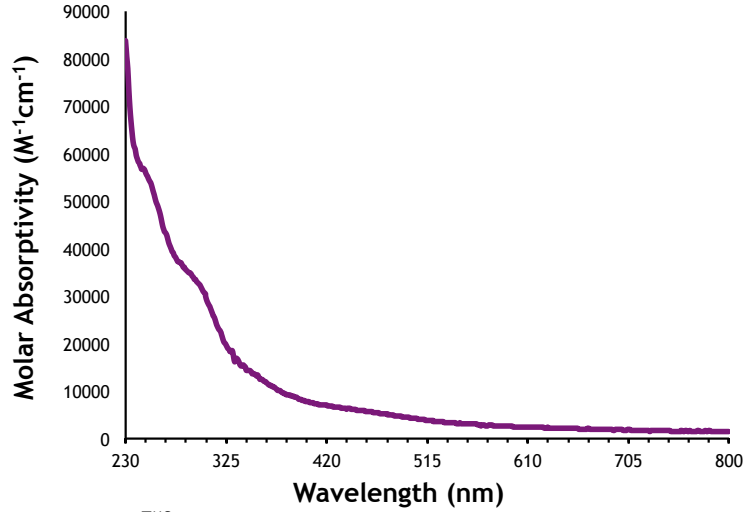

Figure E42. UV-Vis spectrum of **(NN^{TMS})$_2$U** (0.02 mM) in dichloromethane.

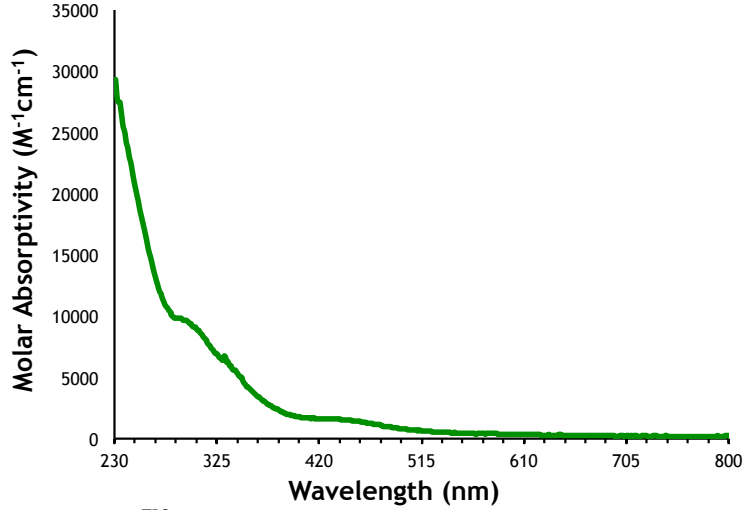

Figure E43. UV-Vis spectrum of **(NN^{TBS})$_2$U** (0.07 mM) in dichloromethane.

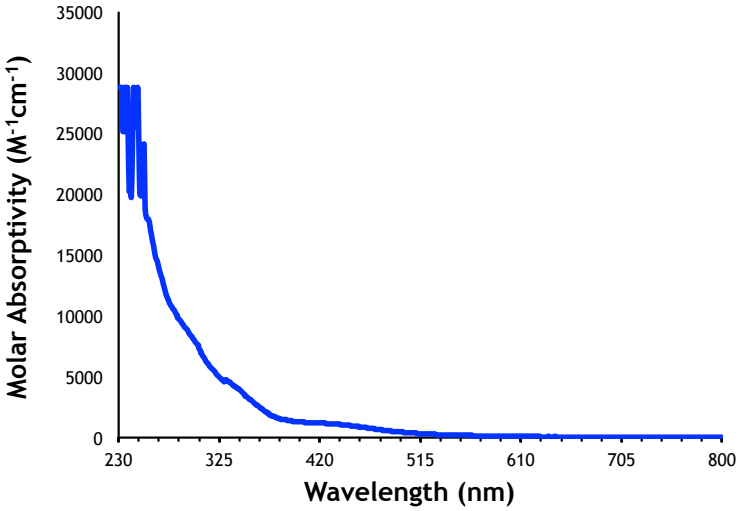

Figure E44. UV-Vis spectrum of $(NN^{DMP})_2U$ (0.17 mM) in dichloromethane.

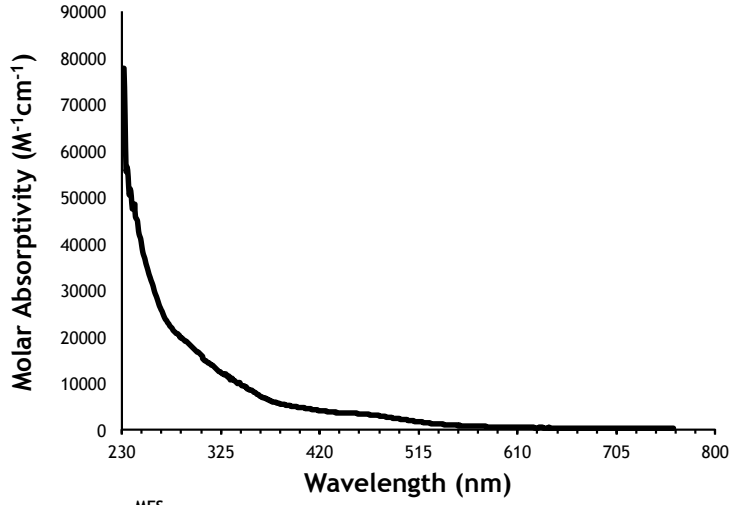

Figure E45. UV-Vis spectrum of $(NN^{MES})_2U$ (0.06 mM) in dichloromethane.

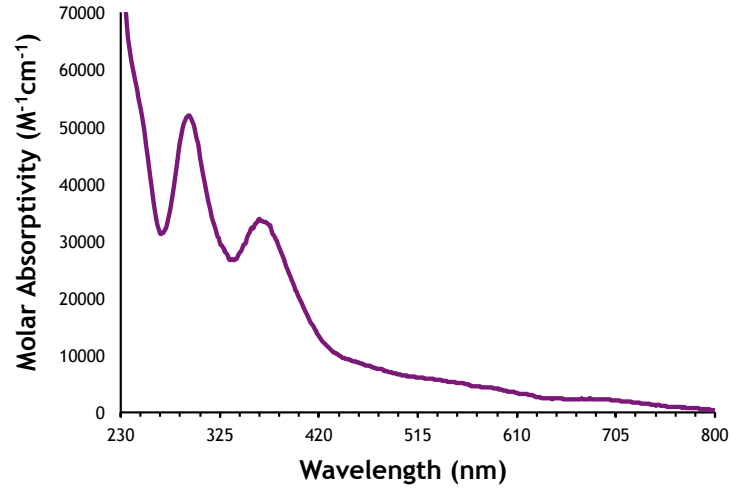

Figure E46. UV-Vis spectrum of $[(NN^{TMS})_2U][I_3]$ (0.022 mM) in dichloromethane.

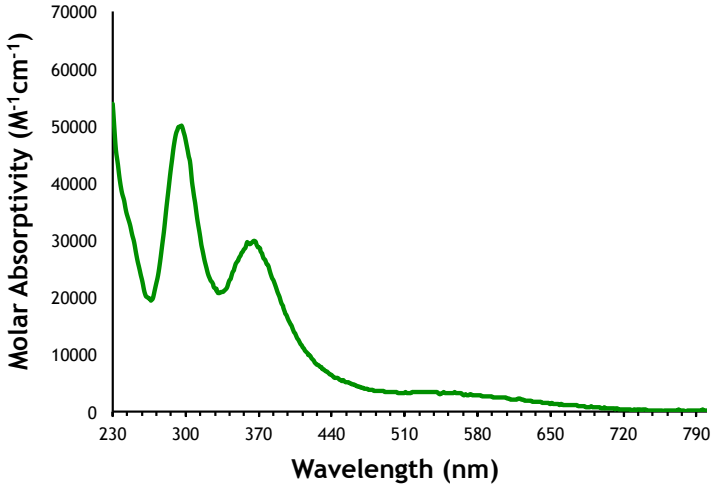

Figure E47. UV-Vis spectrum of **[(NN^{TBS})$_2$U][I$_3$]** (1.1 mM) in dichloromethane.

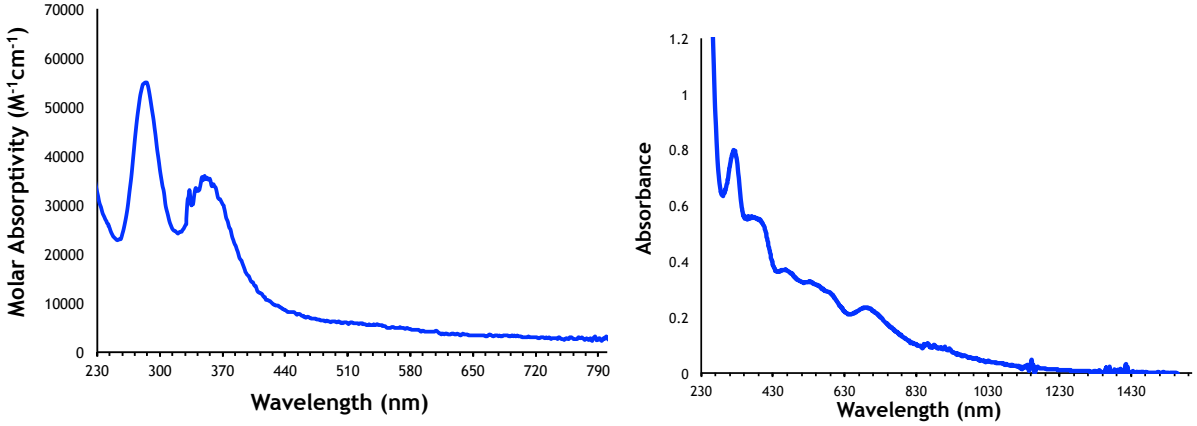

Figure E48. UV-Vis spectrum of **[(NN^{DMP})$_2$U][I$_3$I]** (0.016 mM) and decomposed [(NN^{DMP})$_2$U][I$_3$I] in dichloromethane.

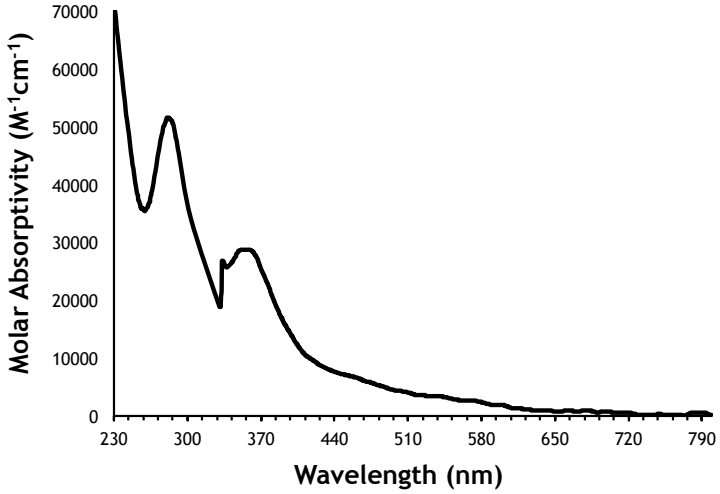

Figure E49. UV-Vis spectrum of **[(NN^{MES})$_2$U][I$_3$]** (0.015 mM) in dichloromethane.

5.4.10 NIR spectroscopy

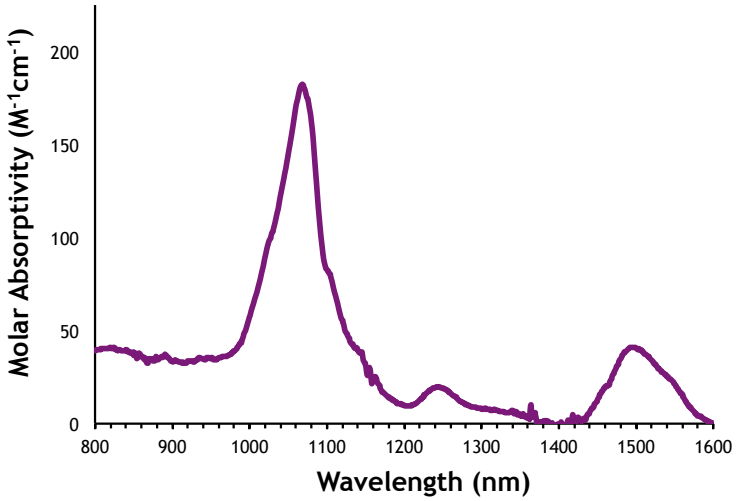

Figure E50. NIR spectrum of **(NN^{TMS})$_2$U** (5.4 mM) in dichloromethane.

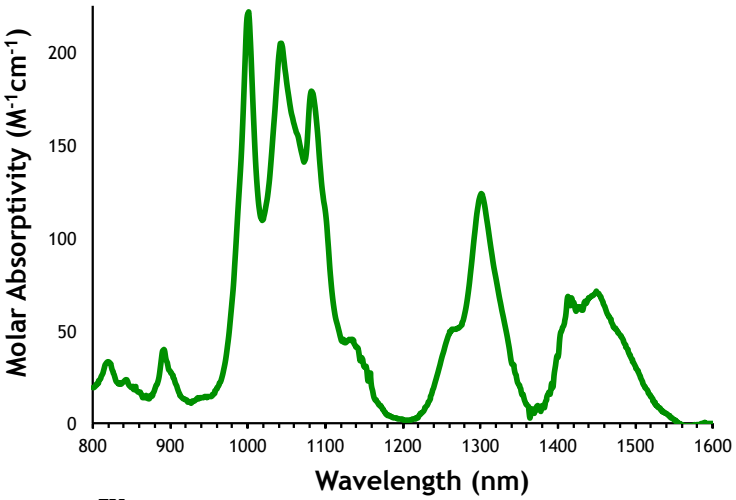

Figure E51. NIR spectrum of **(NN^{TBS})$_2$U** (4.6 mM) in dichloromethane.

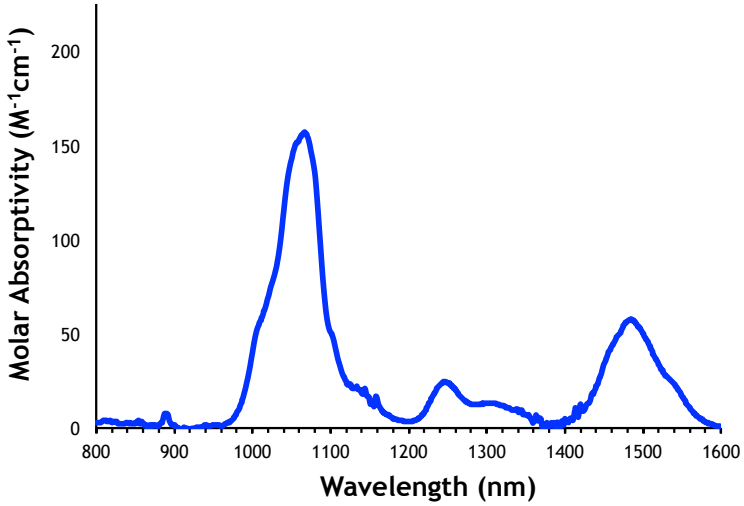

Figure E52. NIR spectrum of **(NN^{DMP})$_2$U** (6.2 mM) in dichloromethane.

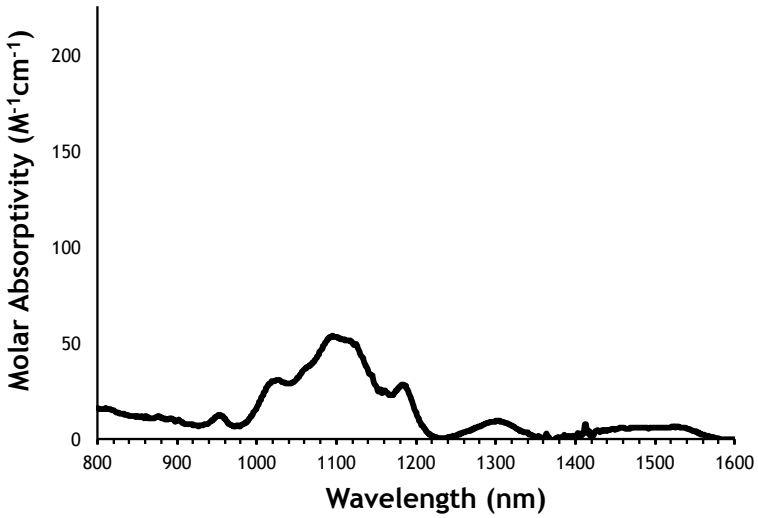

Figure E53. NIR spectrum of **$(NN^{MES})_2U$** (9.9 mM) in dichloromethane.

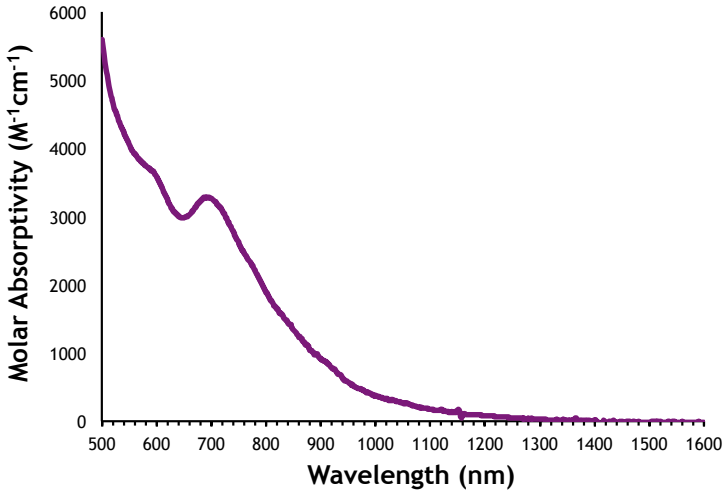

Figure E54. NIR spectrum of **$[(NN^{TMS})_2U][I_3]$** (1.9 mM) in dichloromethane.

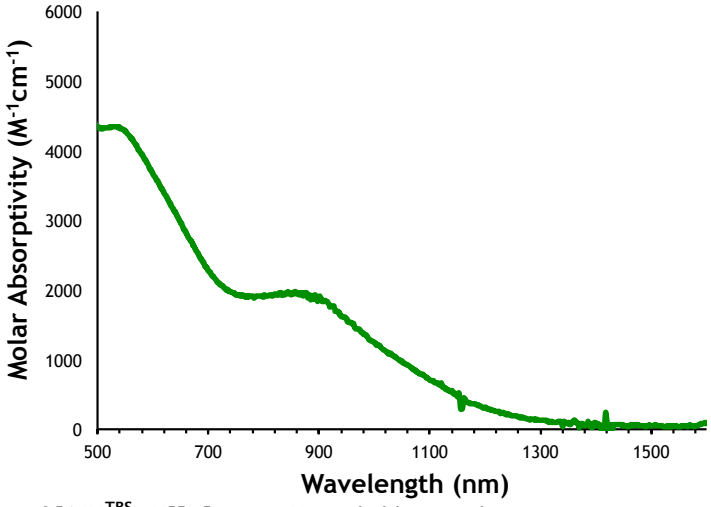

Figure E55. NIR spectrum of **$[(NN^{TBS})_2U][I_3]$** (1.1 mM) in dichloromethane.

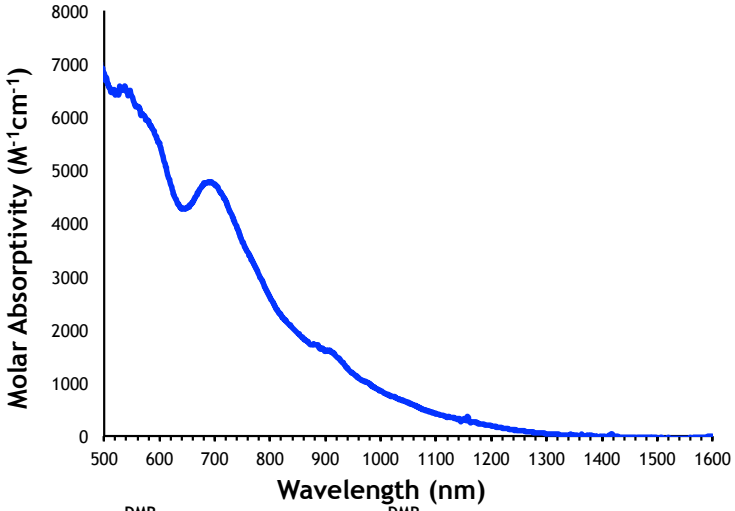

Figure E56. NIR spectrum of "$[(NN^{DMP})_2U][FeI_4]_2$" or "$[(NN^{DMP})_2U][(FeI_4)(I)]$" in dichloromethane.

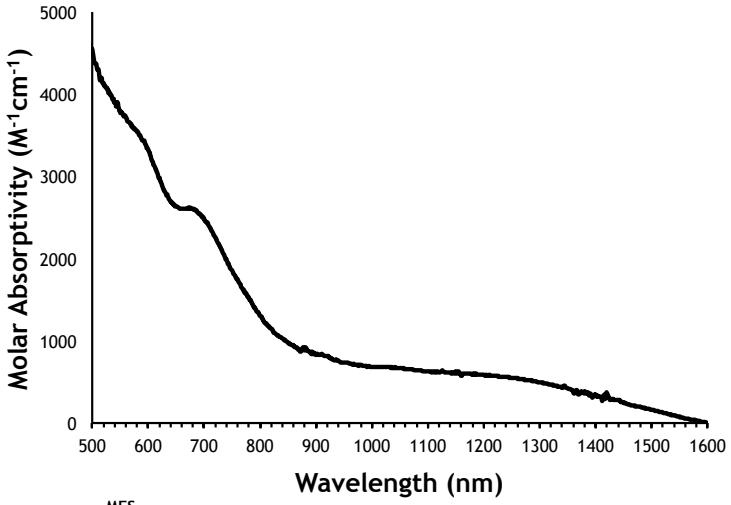

Figure E57. NIR spectrum of $[(NN^{MES})_2U][I_3]$ (3.0 mM) in dichloromethane.

5.4.11 Magnetometry

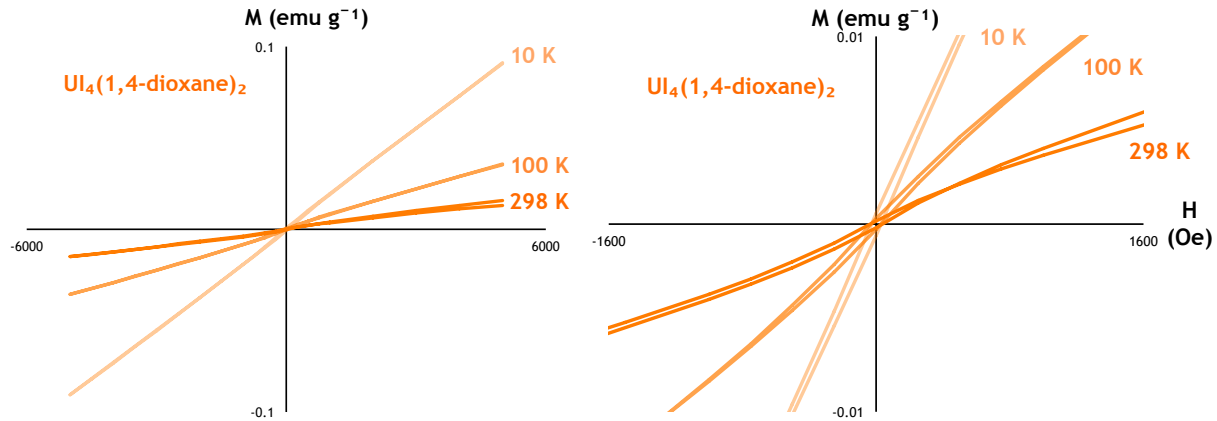

Figure E58. Magnetization field dependence of $UI_4(1,4\text{-dioxane})_2$.

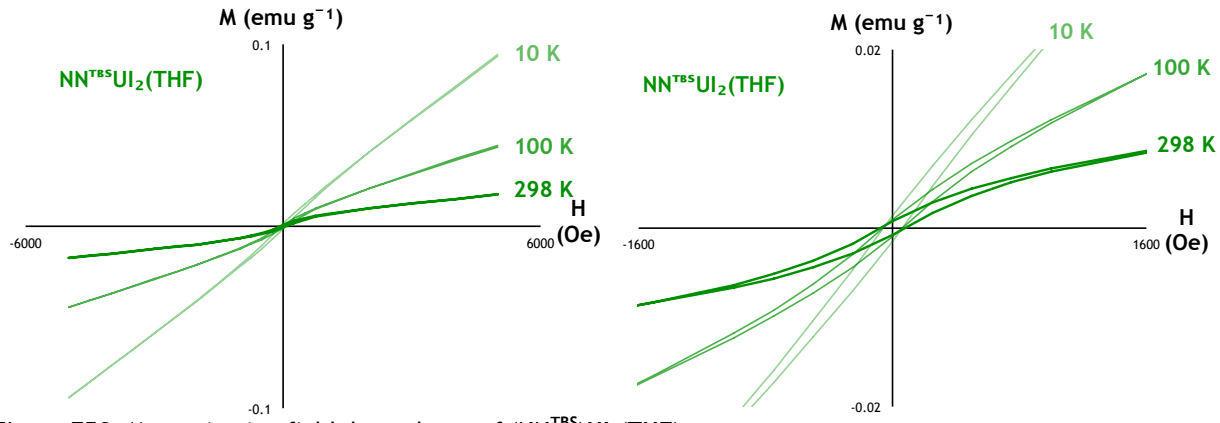

Figure E59. Magnetization field dependence of $(NN^{TBS})UI_2(THF)$.

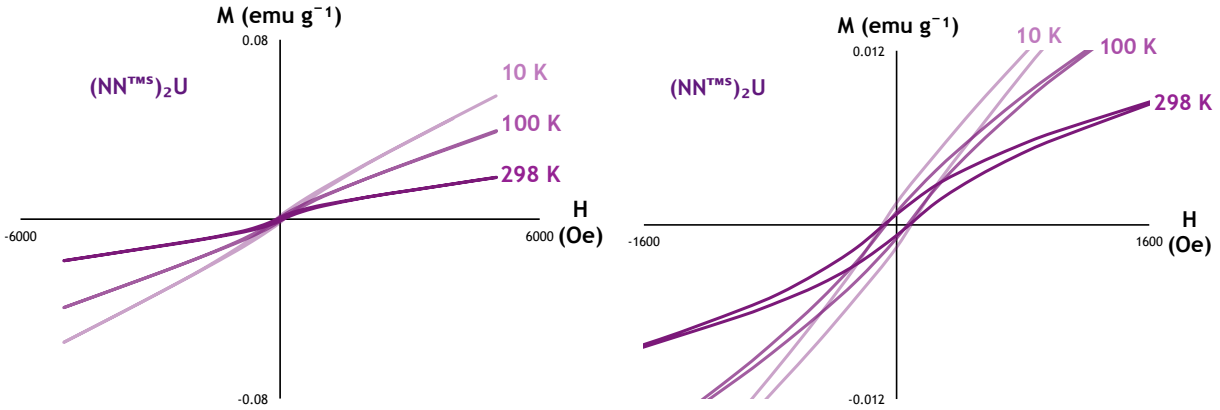

Figure E60. Magnetization field dependence of $(NN^{TMS})_2U$.

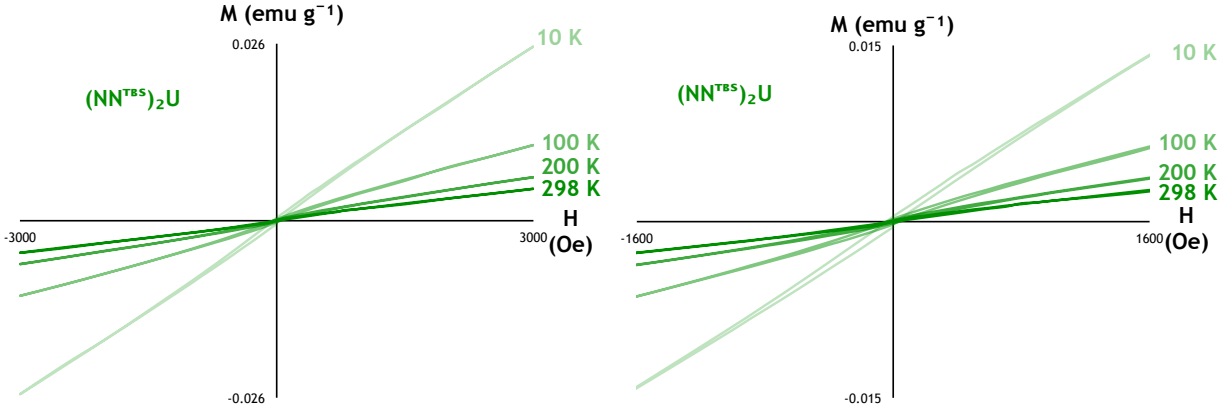

Figure E61. Magnetization field dependence of $(NN^{TBS})_2U$.

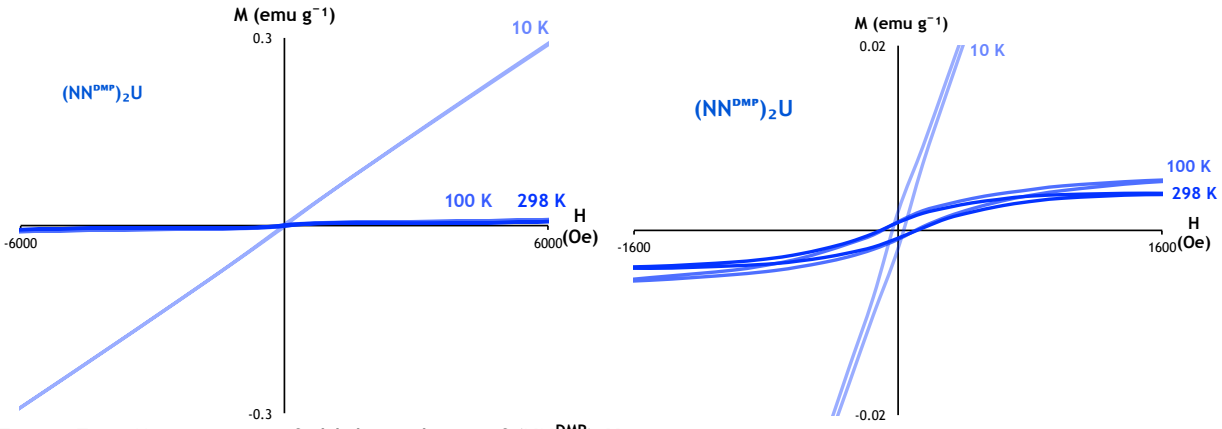

Figure E62. Magnetization field dependence of $(NN^{DMP})_2U$.

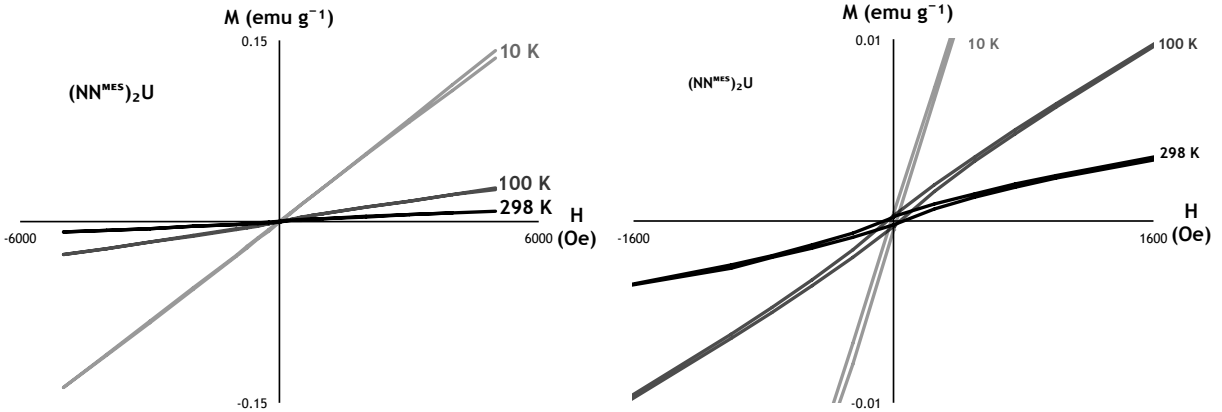

Figure E63. Magnetization field dependence of $(NN^{MES})_2U$.

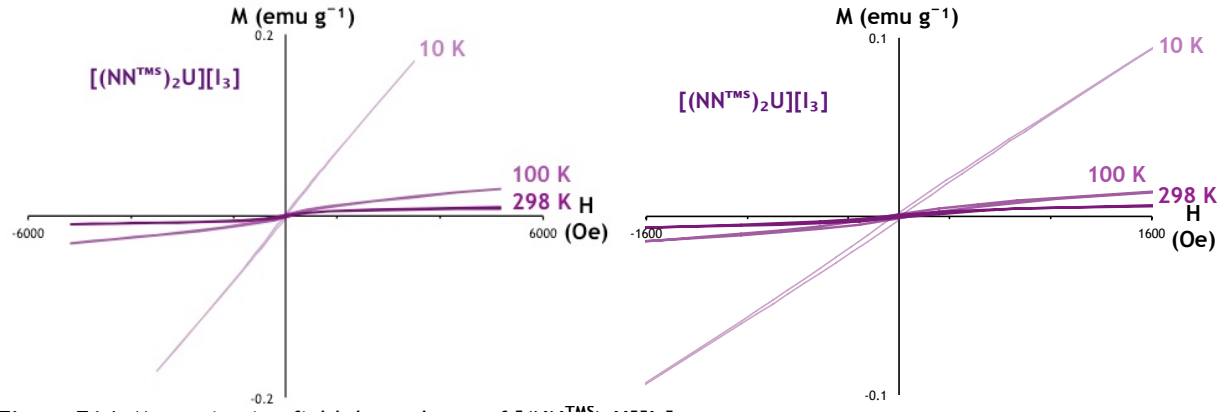

Figure E64. Magnetization field dependence of $[(NN^{TMS})_2U][I_3]$.

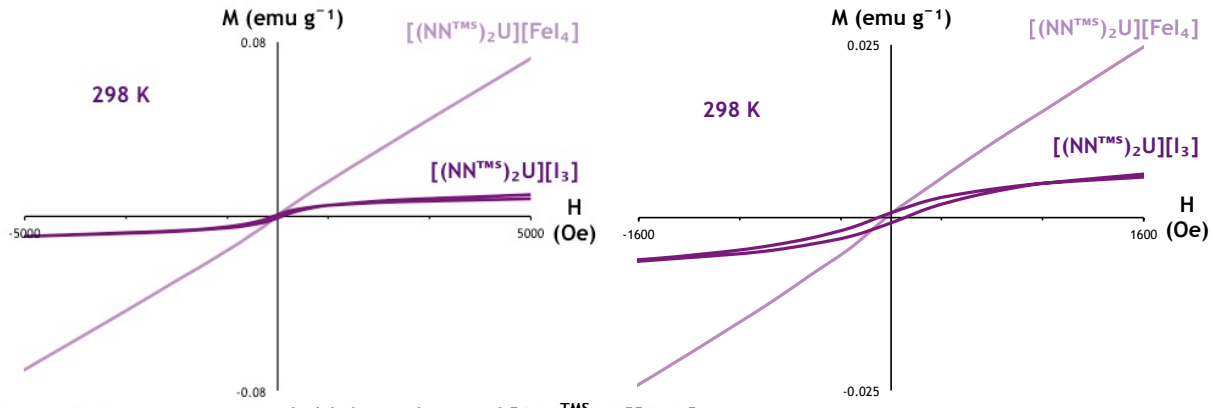

Figure E65. Magnetization field dependence of **[(NN^{TMS})$_2$U][FeI$_4$]**.

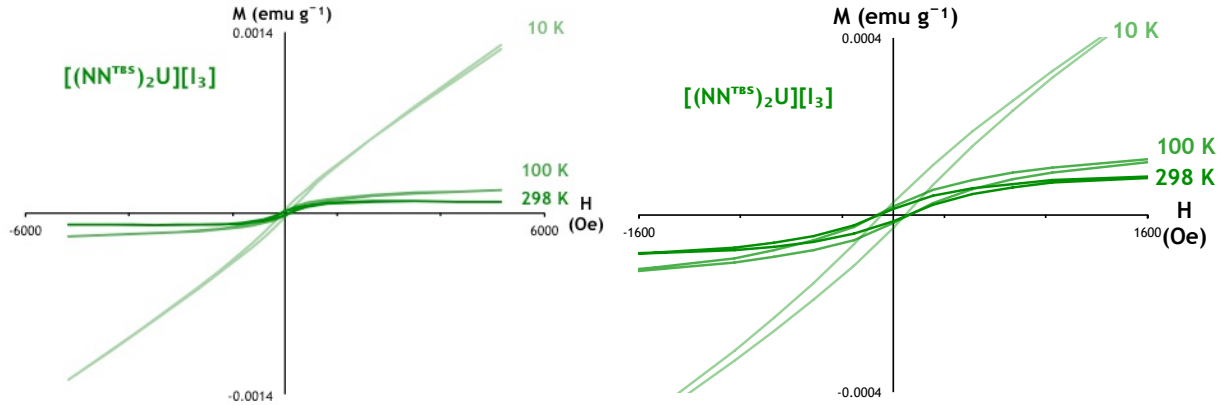

Figure E66. Magnetization field dependence of **[(NN^{TBS})$_2$U][I$_3$]**.

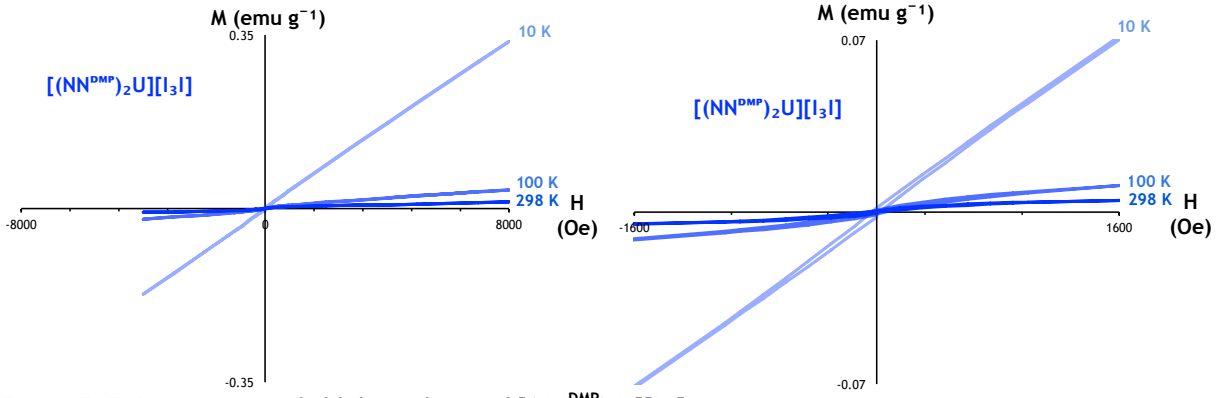

Figure E67. Magnetization field dependence of **[(NN^{DMP})$_2$U][I$_3$I]**.

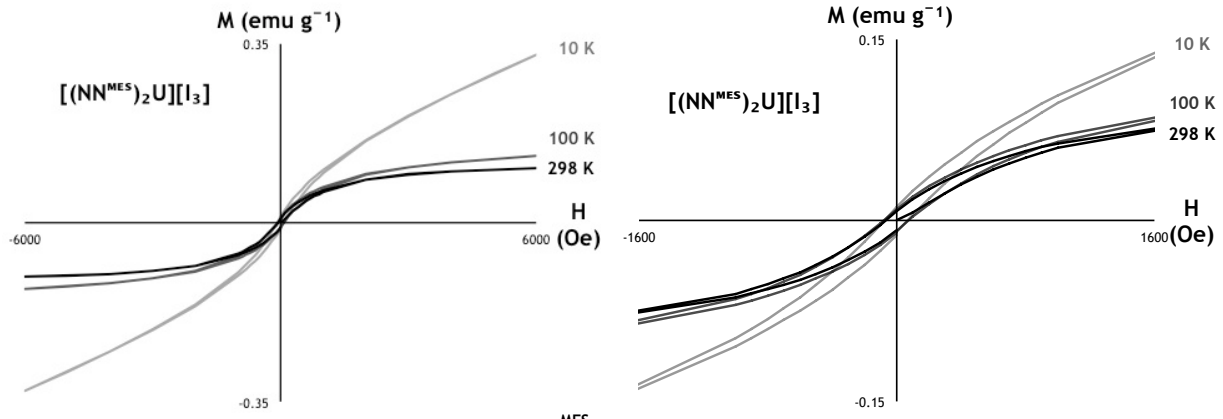

Figure E68. Magnetization field dependence of **[(NN^{MES})$_2$U][I$_3$]**.

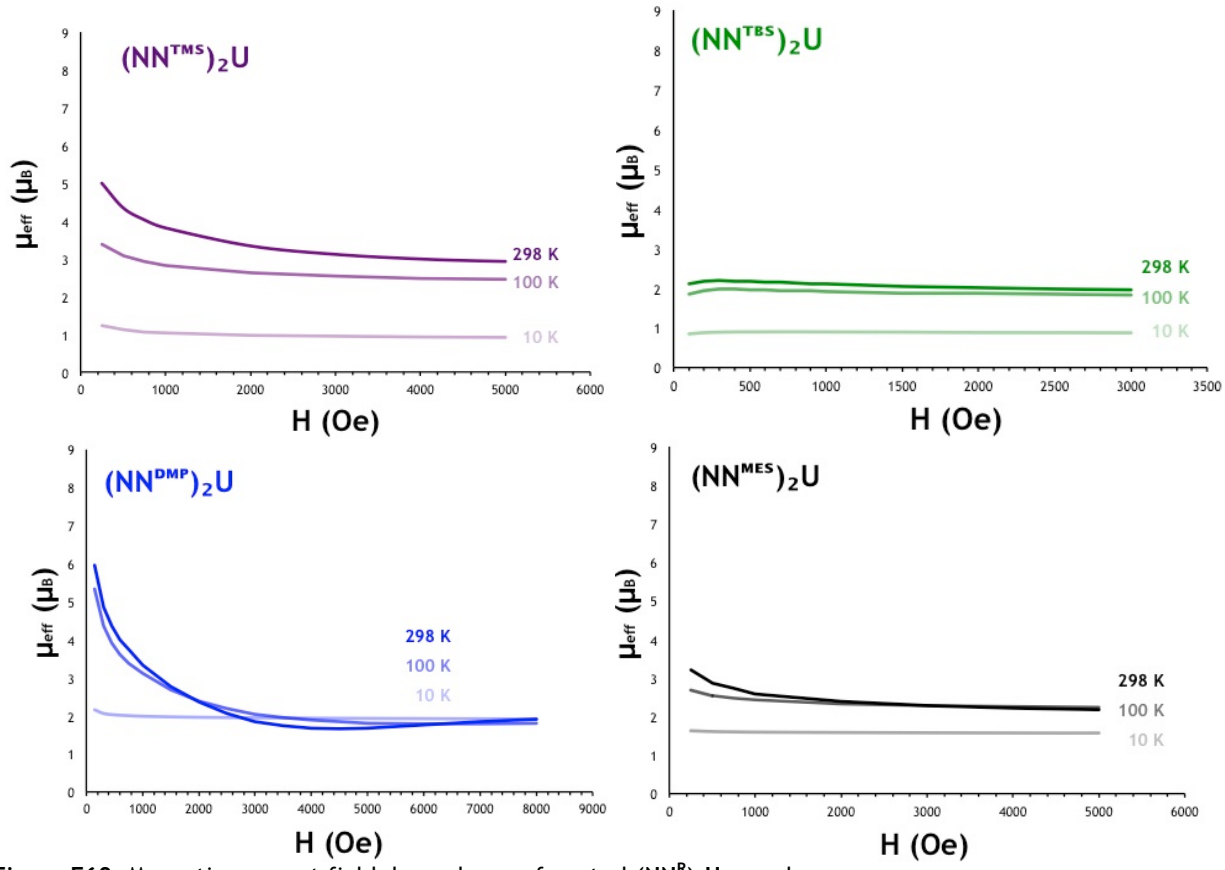

Figure E69. Magnetic moment field dependence of neutral **(NN^{R})$_2$U** complexes.

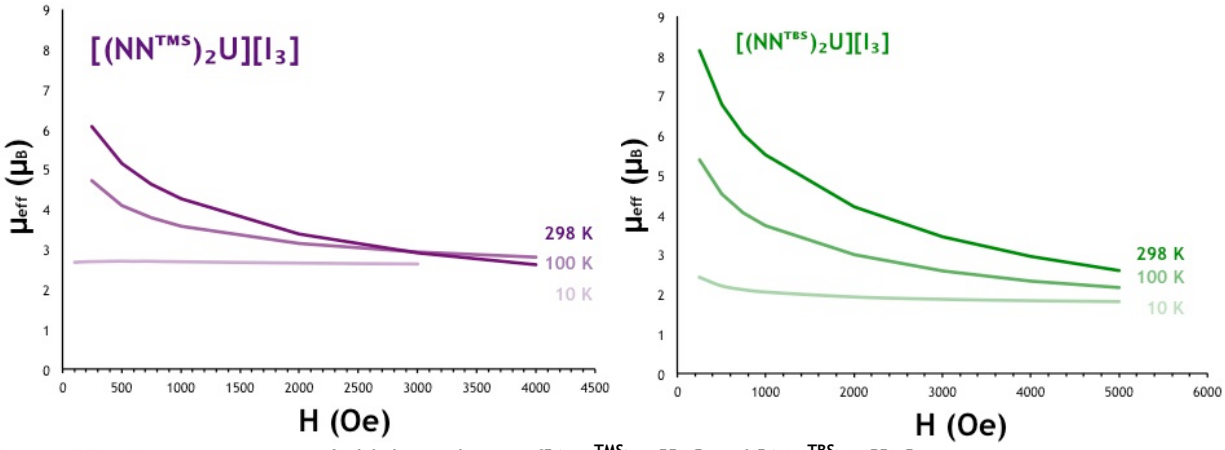

Figure E70. Magnetic moment field dependence of **$[(NN^{TMS})_2U][I_3]$** and **$[(NN^{TBS})_2U][I_3]$**.

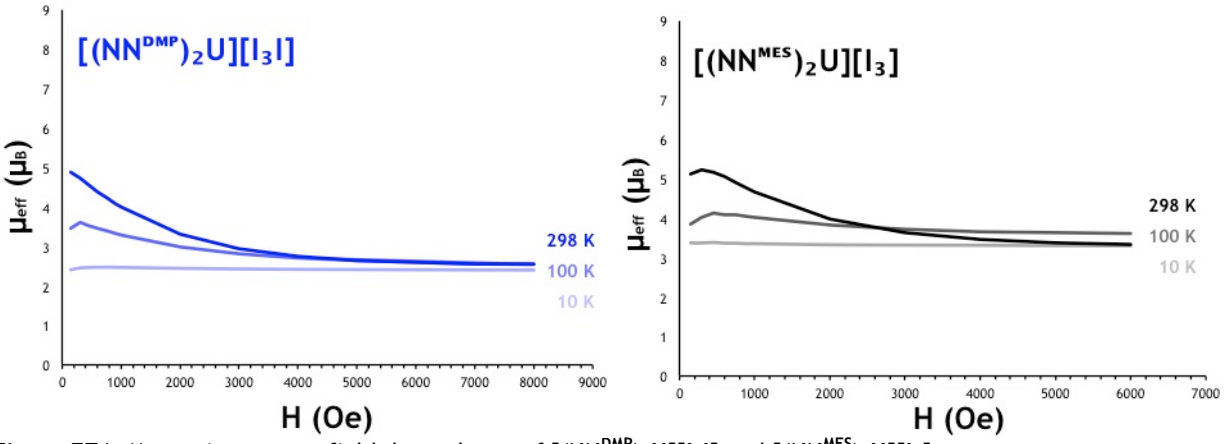

Figure E71. Magnetic moment field dependence of **$[(NN^{DMP})_2U][I_3I]$** and **$[(NN^{MES})_2U][I_3]$**.

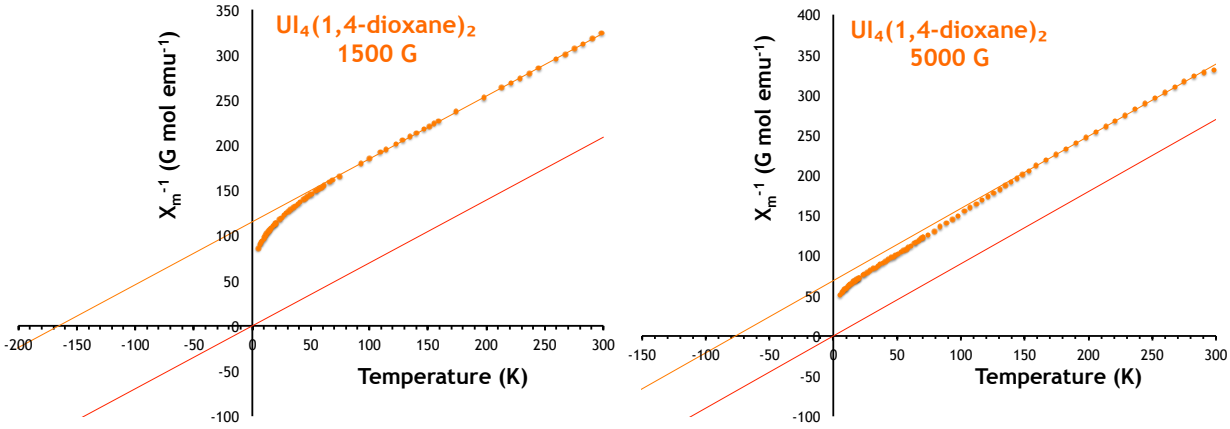

Figure E72. Inverse molar susceptibility temperature dependence of **$UI_4(1,4\text{-dioxane})_2$**.

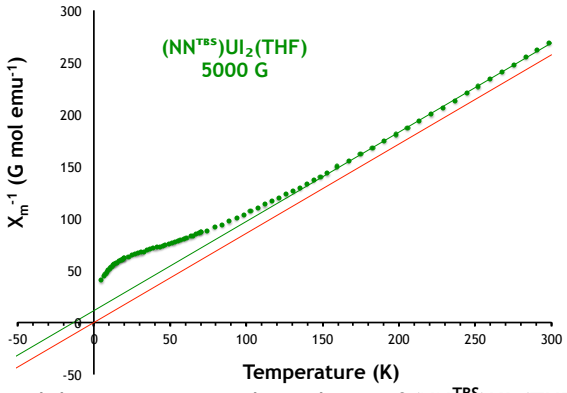

Figure E73. Inverse molar susceptibility temperature dependence of **$(NN^{TBS})UI_2(THF)$.**

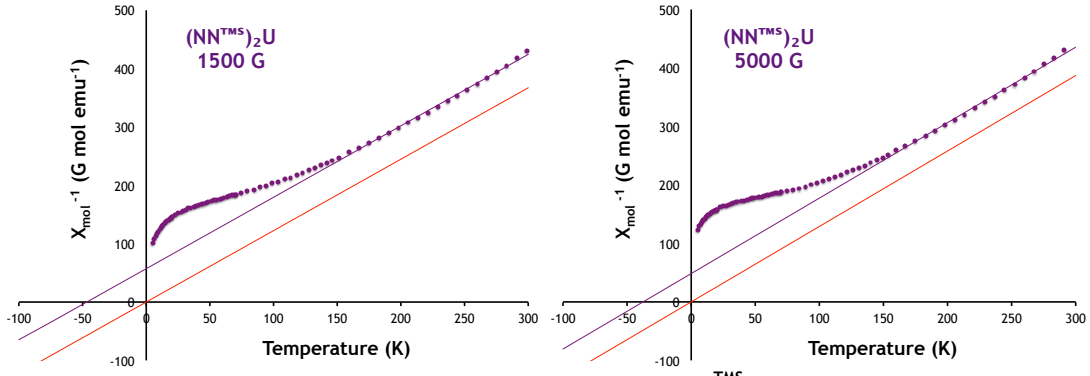

Figure E74. Inverse molar susceptibility temperature dependence of **$(NN^{TMS})_2U$.**

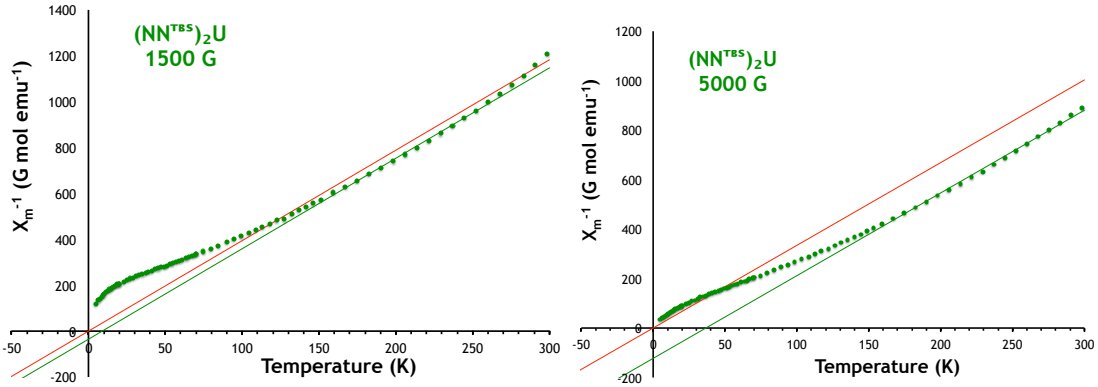

Figure E75. Inverse molar susceptibility temperature dependence of **$[(NN^{TBS})_2U][I_3]$.**

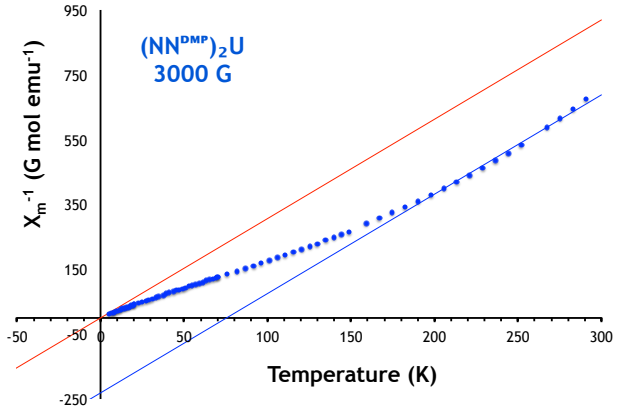

Figure E76. Inverse molar susceptibility temperature dependence of $(NN^{DMP})_2U$.

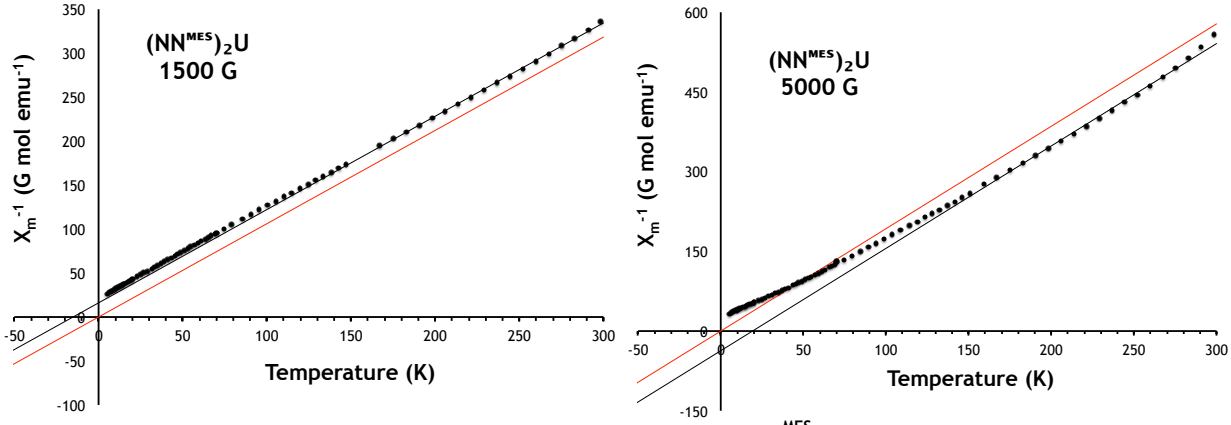

Figure E77. Inverse molar susceptibility temperature dependence of $(NN^{MES})_2U$.

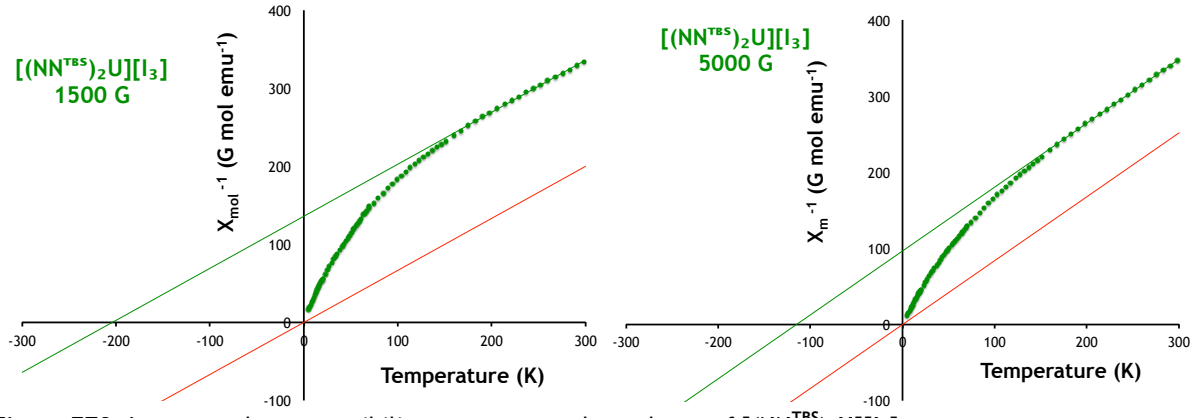

Figure E78. Inverse molar susceptibility temperature dependence of $[(NN^{TBS})_2U][I_3]$.

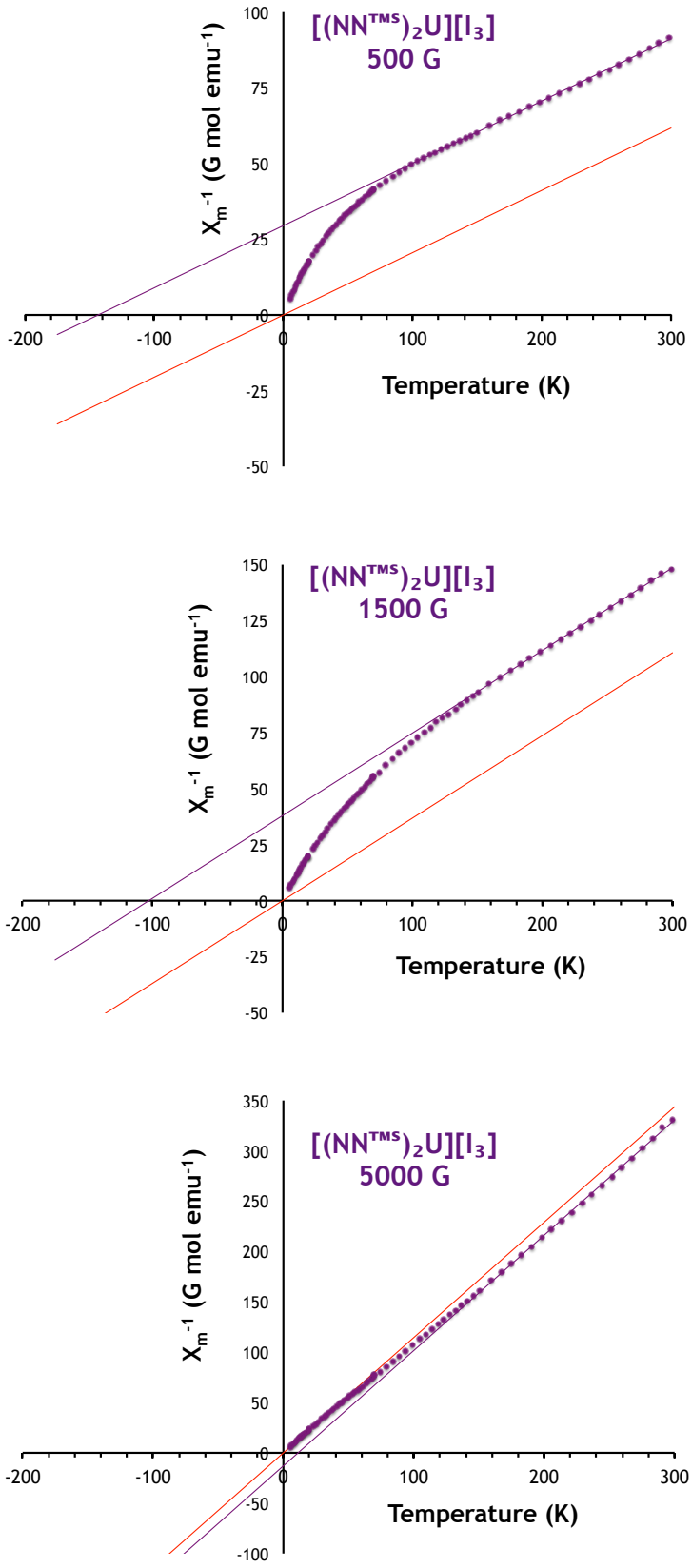

Figure E79. Inverse molar susceptibility temperature dependence of **[(NN^{TMS})$_2$U][I$_3$]**.

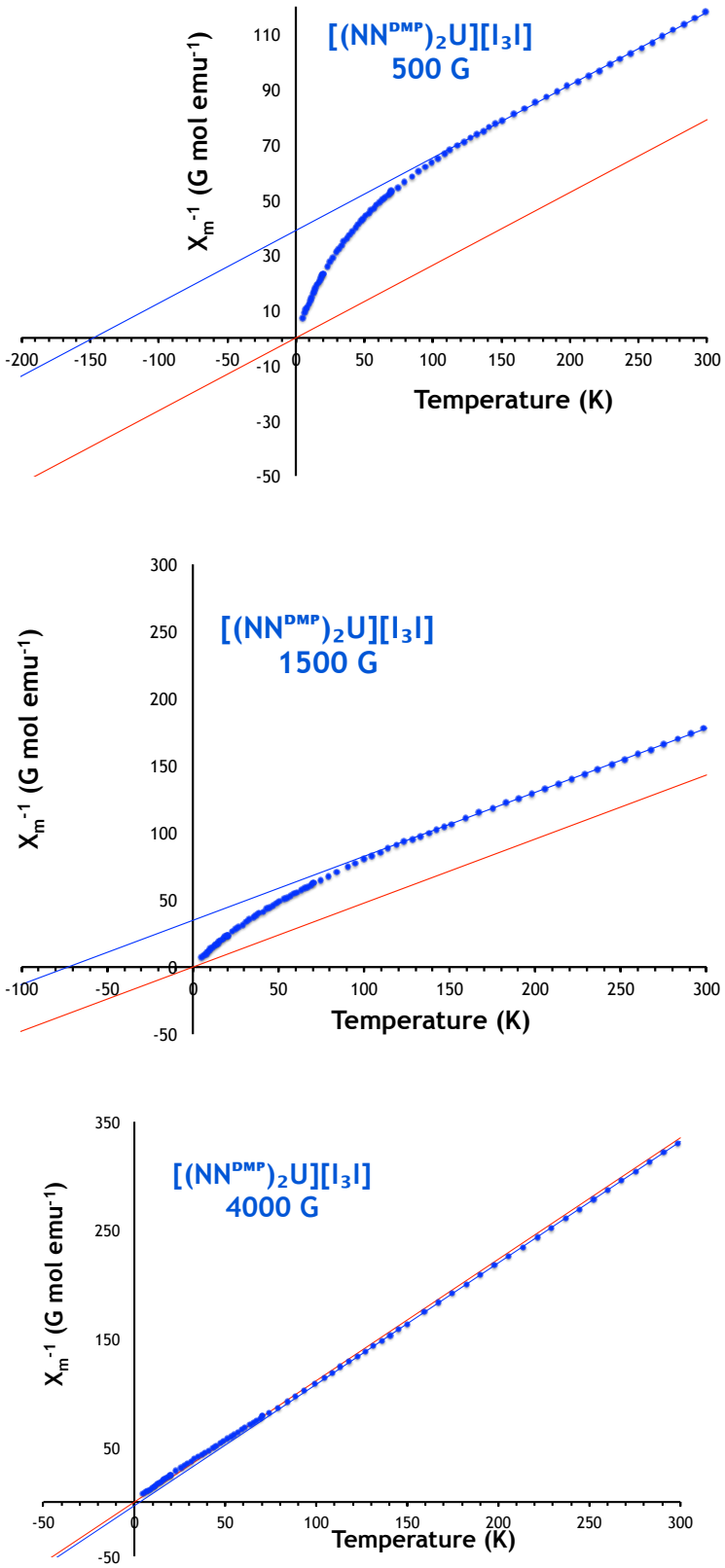

Figure E80. Inverse molar susceptibility temperature dependence of **[(NN^{DMP})$_2$U][I$_3$I].**

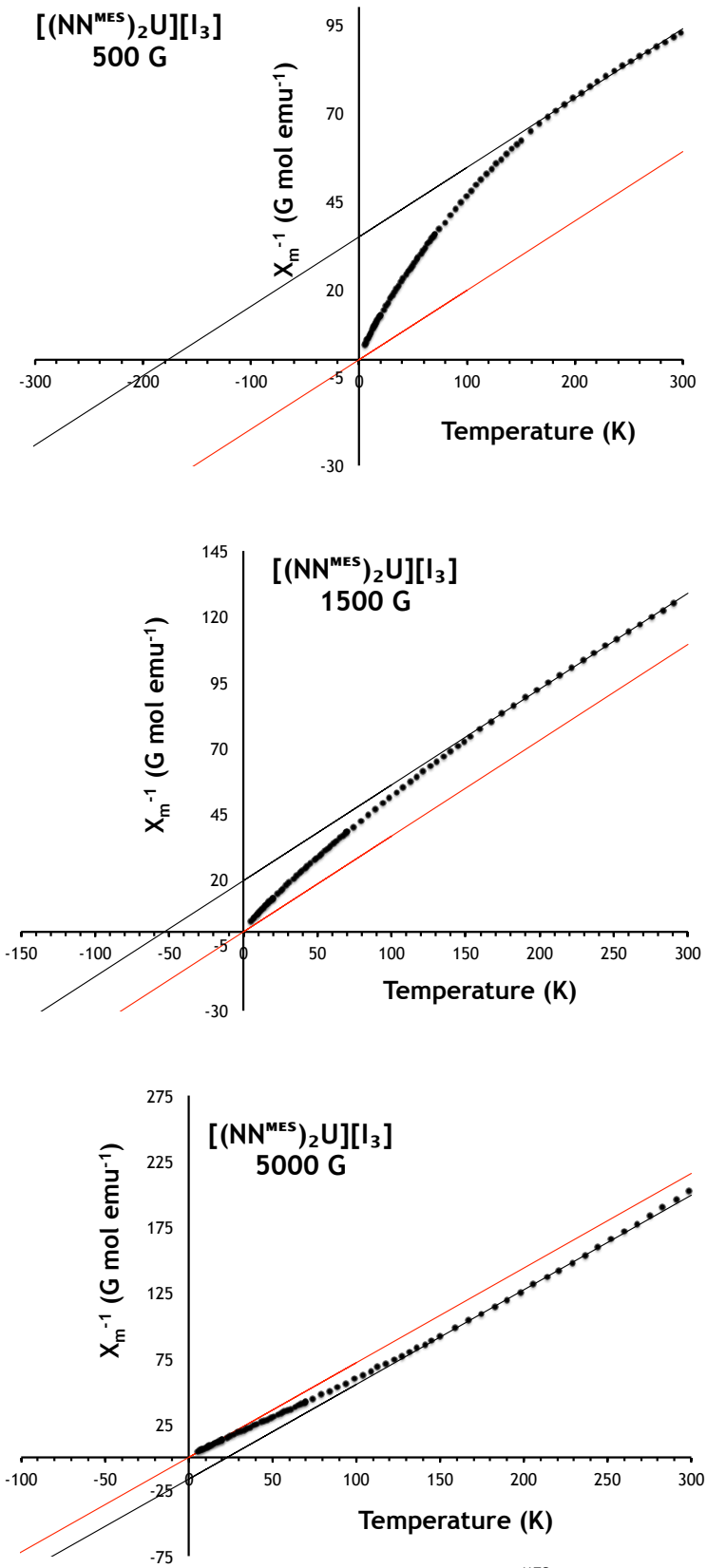

Figure E81. Inverse molar susceptibility temperature dependence of **[(NN^{MES})$_2$U][I$_3$]**.

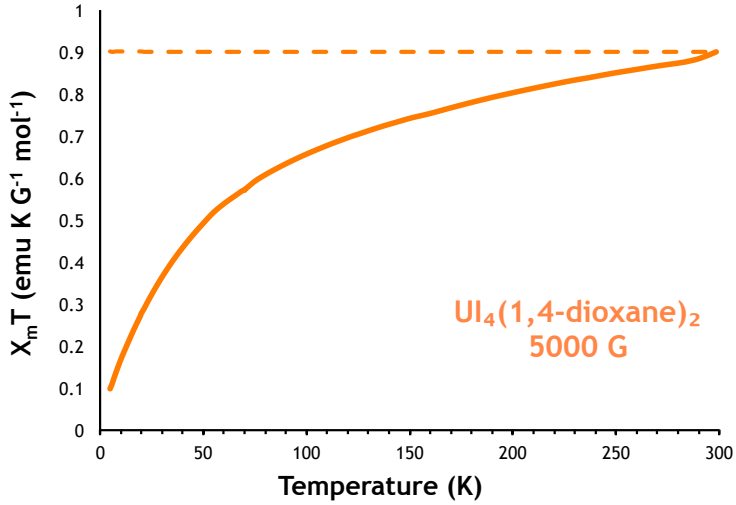

Figure E82. Molar susceptibility temperature product of $UI_4(1,4\text{-dioxane})_2$.

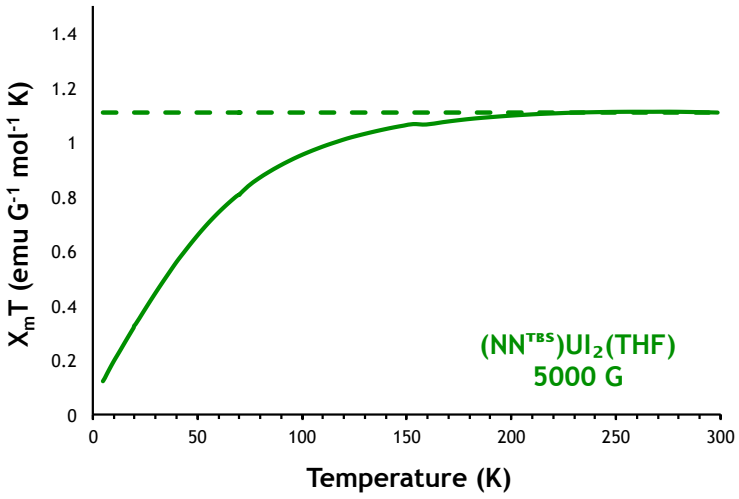

Figure E83. Molar susceptibility temperature product of $(NN^{TBS})UI_2(THF)$.

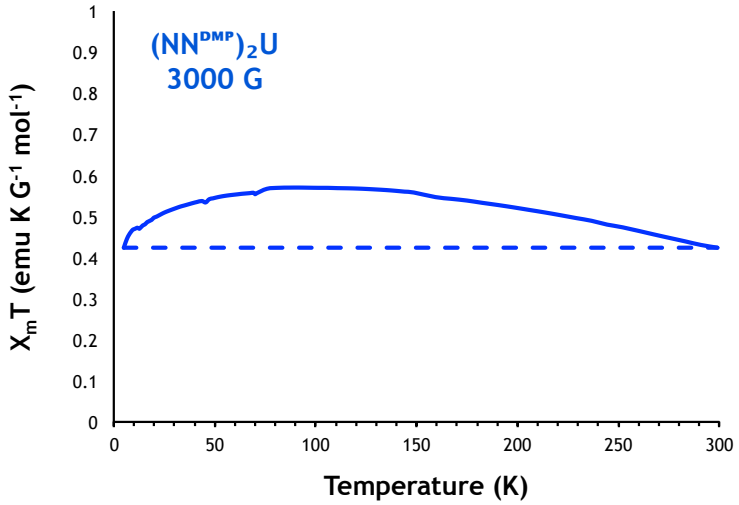

Figure E84. Molar susceptibility temperature product of $(NN^{DMP})_2U$.

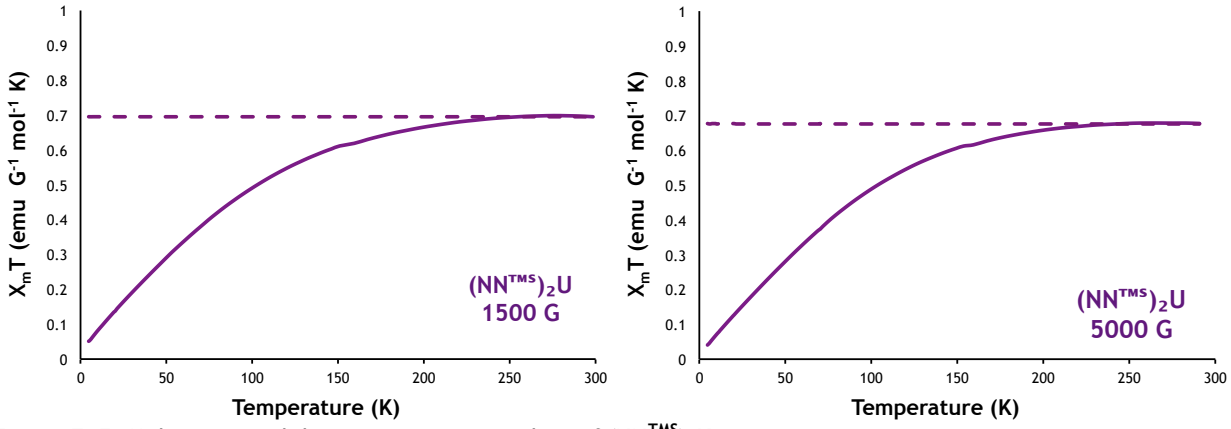

Figure E85. Molar susceptibility temperature product of $(NN^{TMS})_2U$.

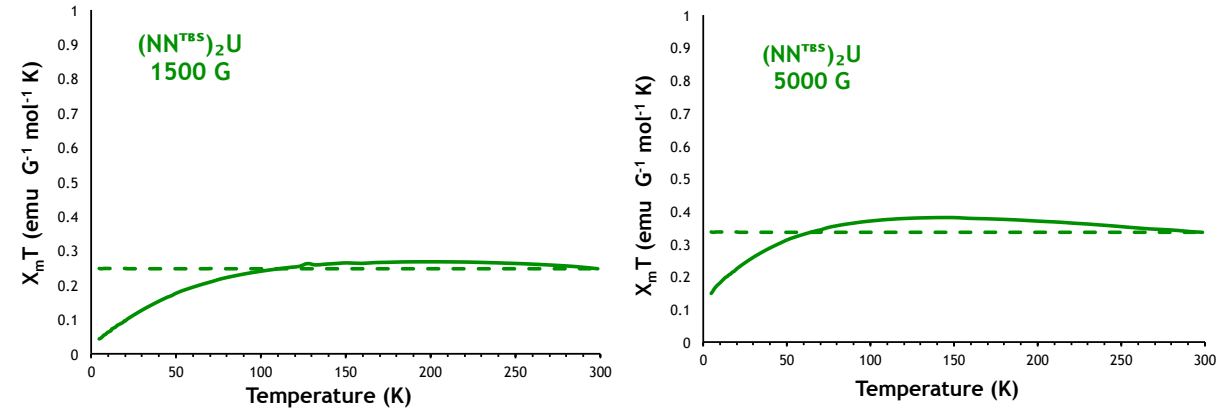

Figure E86. Molar susceptibility temperature product of $(NN^{TBS})_2U$.

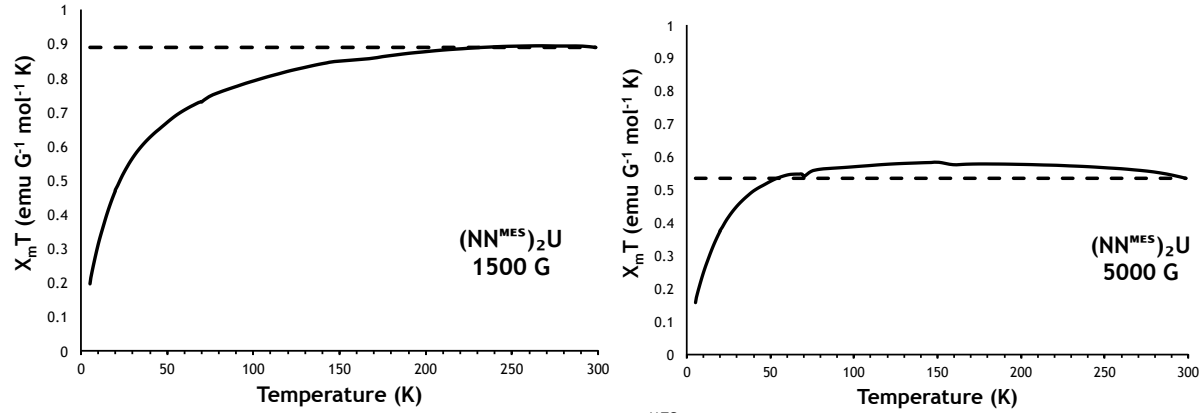

Figure E87. Molar susceptibility temperature product of $(NN^{MES})_2U$.

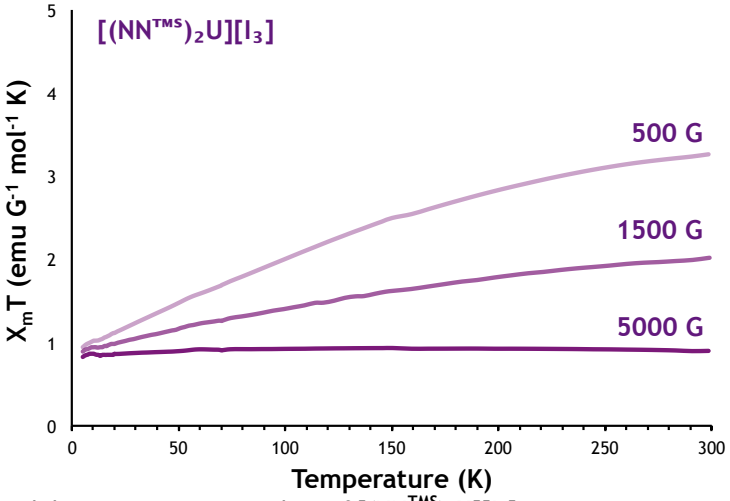

Figure E88. Molar susceptibility temperature product of **[(NN^{TMS})$_2$U][I$_3$].**

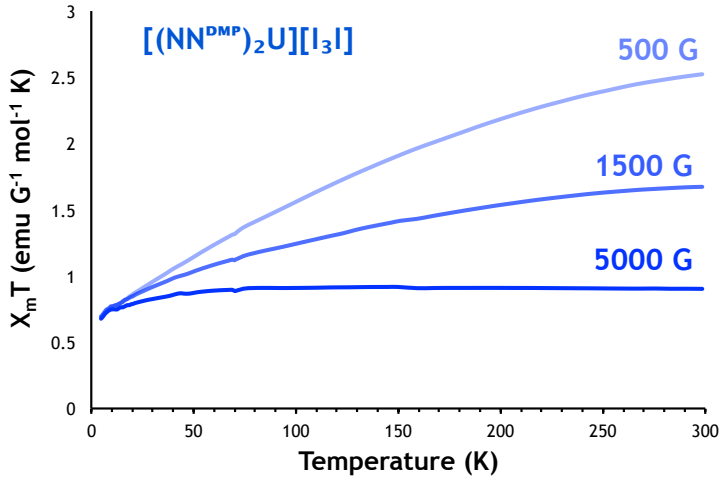

Figure E89. Molar susceptibility temperature product of **[(NN^{DMP})$_2$U][I$_3$I].**

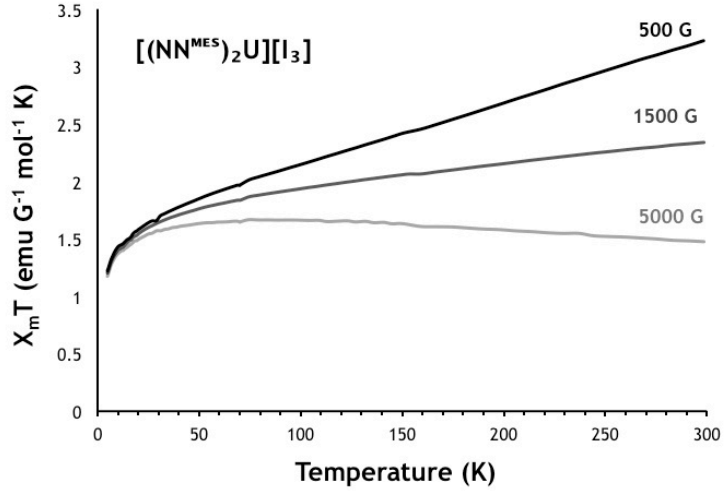

Figure E90. Molar susceptibility temperature product of **[(NN^{MES})$_2$U][I$_3$].**

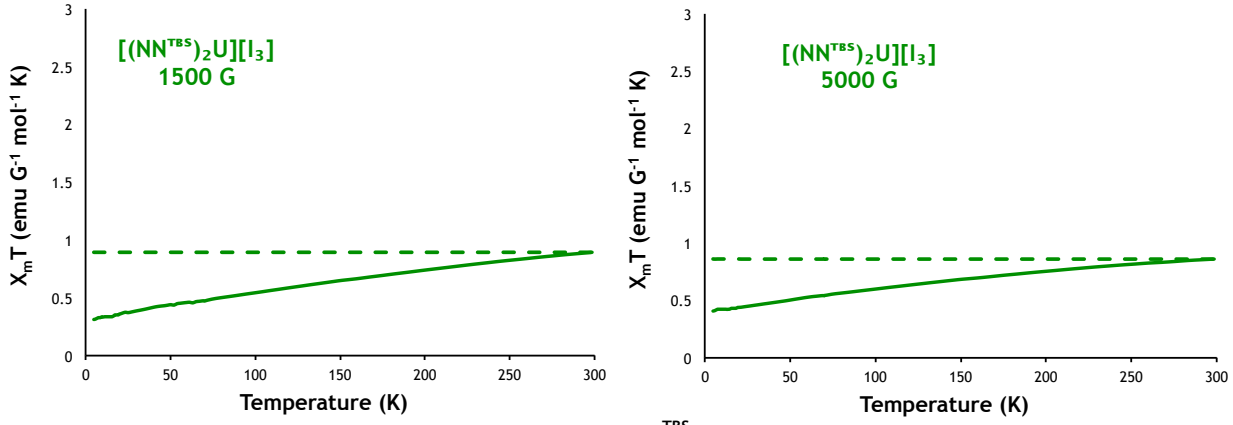

Figure E91. Molar susceptibility temperature product of $[(NN^{TBS})_2U][I_3]$.

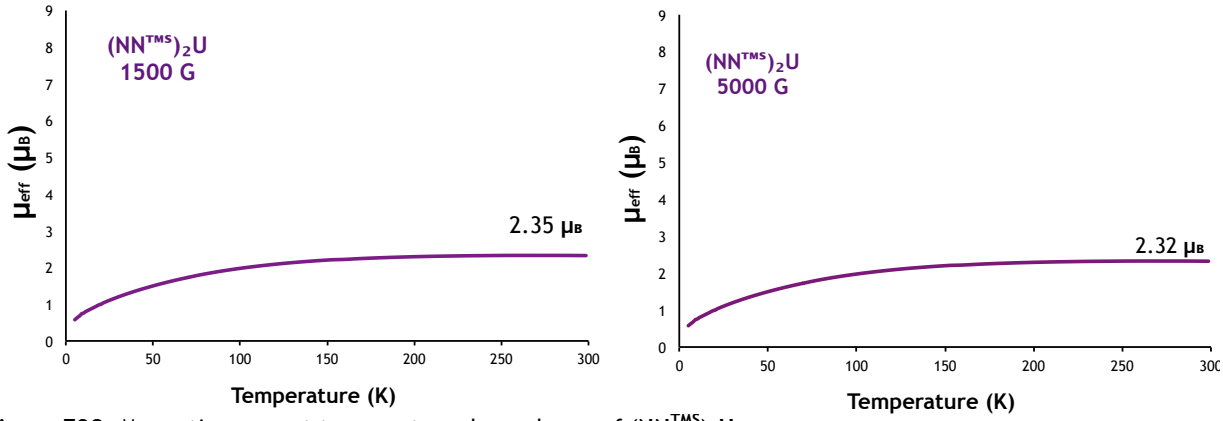

Figure E92. Magnetic moment temperature dependence of $(NN^{TMS})_2U$.

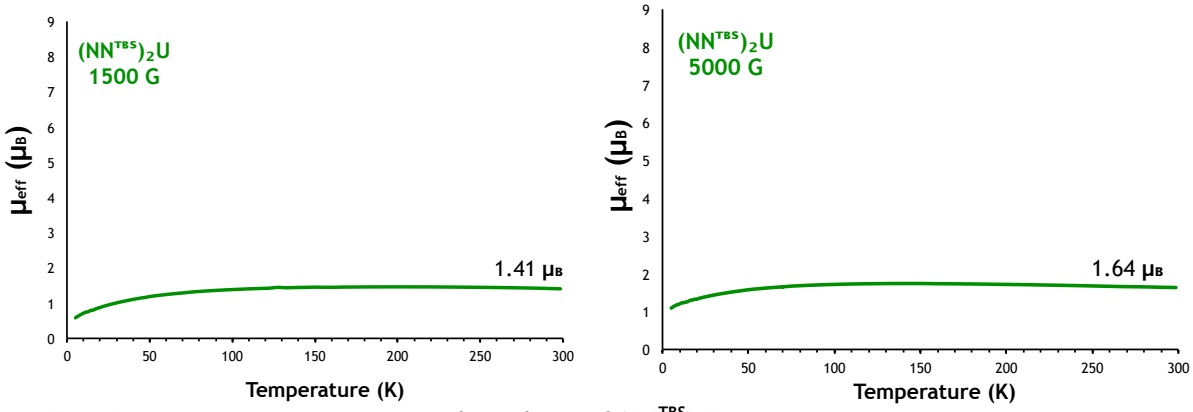

Figure E93. Magnetic moment temperature dependence of $(NN^{TBS})_2U$.

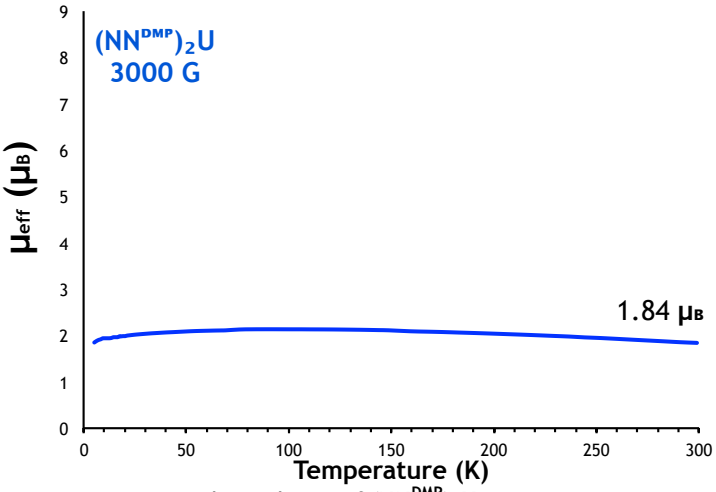

Figure E94. Magnetic moment temperature dependence of $(NN^{DMP})_2U$.

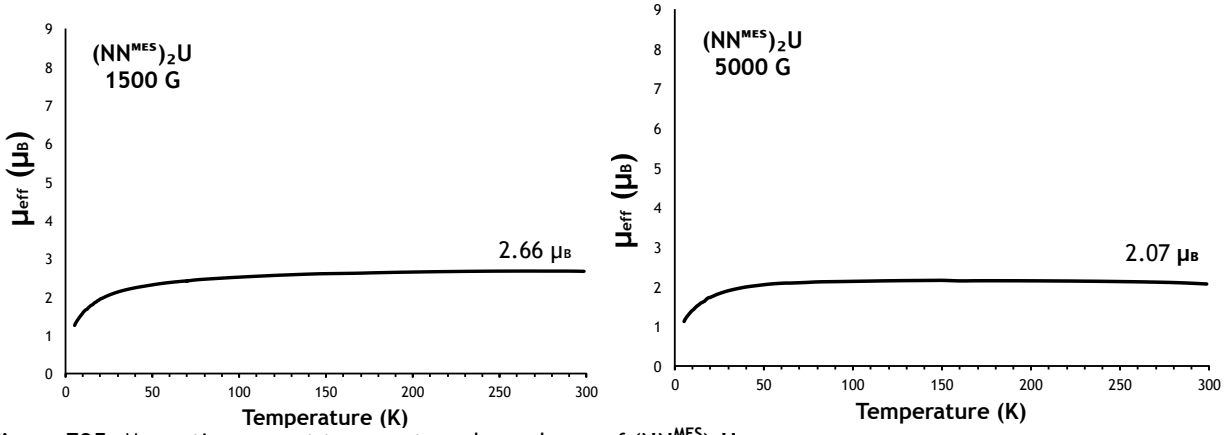

Figure E95. Magnetic moment temperature dependence of $(NN^{MES})_2U$.

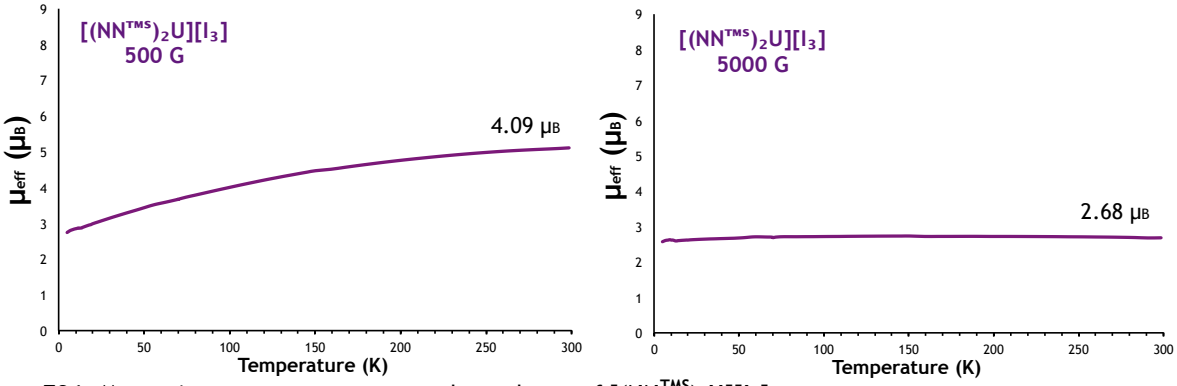

Figure E96. Magnetic moment temperature dependence of $[(NN^{TMS})_2U][I_3]$.

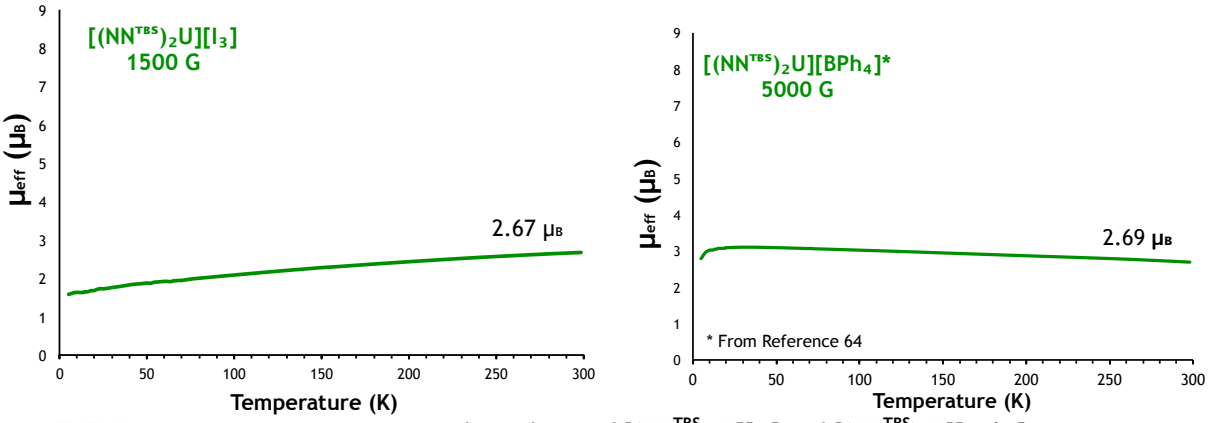

Figure E97. Magnetic moment temperature dependence of $[(NN^{TBS})_2U][I_3]$ and $[(NN^{TBS})_2U][BPh_4]$.

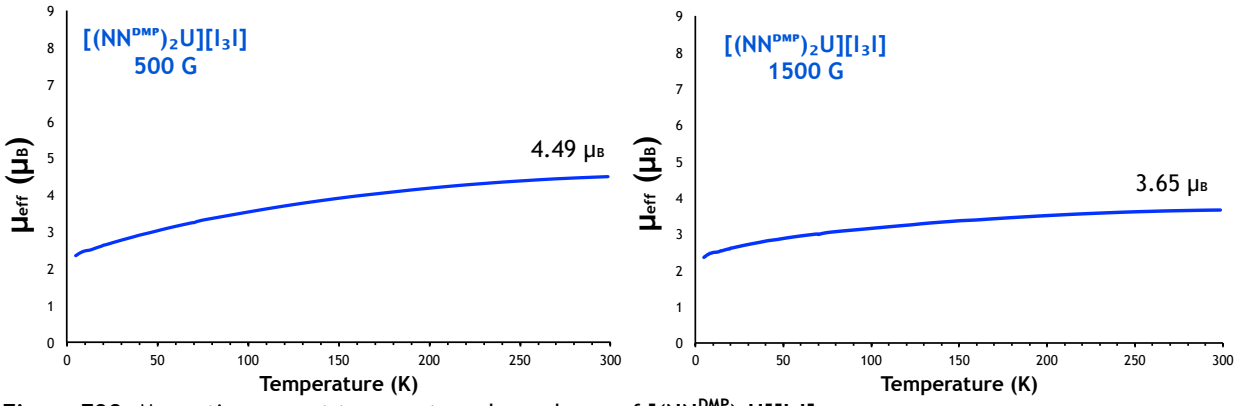

Figure E98. Magnetic moment temperature dependence of $[(NN^{DMP})_2U][I_3I]$.

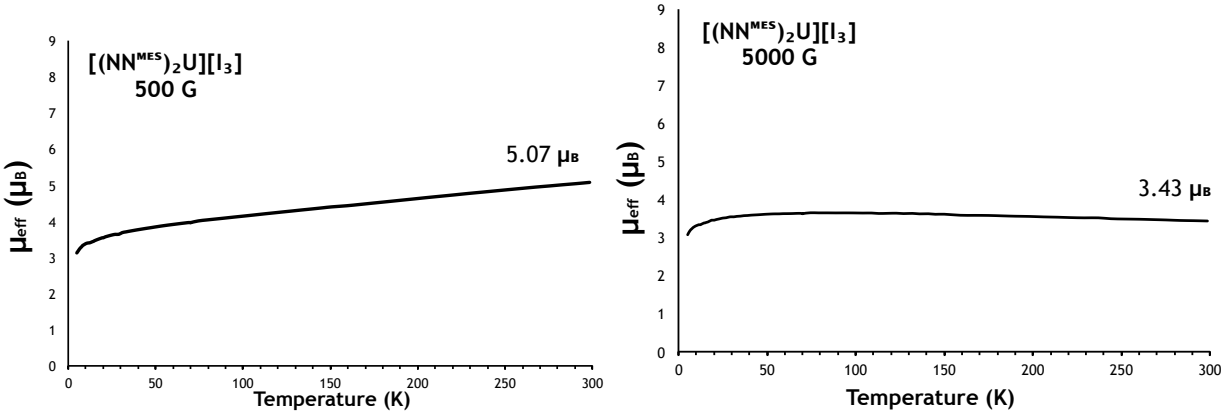

Figure E99. Magnetic moment temperature dependence of $[(NN^{MES})_2U][I_3]$.

5.5 REFERENCES

1. Rosenthal, J.; Bachman, J.; Dempsey, J. L.; Esswein, A. J.; Gray, T. G.; Hodgkiss, J. M.; Manke, D. R.; Luckett, T. D.; Pistorio, B. J.; Veige, A. S.; Nocera, D. G., Oxygen and Hydrogen Photocatalysis by Two-Electron Mixed-Valence Coordination Compounds. *Coord. Chem. Rev.* **2005,** 249, 1316-1326.

2. Borovik, A. S.; Que, L., Models for the Iron(II)Iron(III) and Iron(II)Iron(II) Forms of Iron-Oxo Proteins. *J. Am. Chem. Soc.* **1988,** 110, (7), 2345-2347.

3. van Staveren, D. R.; Metzler-Nolte, N., Bioorganometallic Chemistry of Ferrocene. *Chem. Rev.* **2004,** 104, (12), 5931-5986.

4. Hagen, H.; Marzenell, P.; Jentzsch, E.; Wenz, F.; Veldwijk, M. R.; Mokhir, A., Aminoferrocene-Based Prodrugs Activated by Reactive Oxygen Species. *J. Med. Chem.* **2011**.

5. Brown, D. B., *Mixed-Valence Compounds: Theory and Applications in Chemistry, Physics, Geology, and Biology: Proceedings of the NATO Advanced Study Institute Held at Oxford, England, September 9-21, 1979*. D. Reidel: 1980.

6. Hill, D. T.; Girard, G. R.; McCabe, F. L.; Johnson, R. K.; Stupik, P. D.; Zhang, J. H.; Reiff, W. M.; Eggleston, D. S., [μ-1,1'-Bis(diphenylphosphino)ferrocene]bis(chlorogold): Synthesis, Iron-57 and Gold-197 Mössbauer Spectroscopy, X-Ray Crystal Structure, and Antitumor Activity. *Inorg. Chem.* **1989,** 28, (18), 3529-3533.

7. Banci, L.; Bertini, I.; Briganti, F.; Luchinat, C.; Scozzafava, A.; Oliver, M. V., Proton NMR Spectra of Oxidized High-Potential Iron-Sulfur Protein (HiPIP) from Rhodocyclus Gelatinosus. A Model for Oxidized HiPIPs. *Inorg. Chem.* **1991,** 30, (24), 4517-4524.

8. Pandey, A. K.; Gupta, T.; Baranwal, B. P., Trinuclear, Oxo-Bridged, Mixed-Valence Iron Mercaptocarboxylates. *Transition Met. Chem.* **2004,** 29, (4), 370-375.

9. Woodward, J., Praeparatio Caerulei Prussiaci Ex Germania Missa ad Johannem Woodward, M. D. Prof. Med. Gresh. R. S. S. *Phil. Trans.* **1724,** 33, (381-391), 15-17.

10. Hofmann, K. A.; Resenscheck, F., Ueber die blauen Eisencyanverbindungen und die Ursache ihrer Farbe. *Justus Liebigs Annalen der Chemie* **1905,** 342, (2-3), 364-374.

11. Powell, H. M., The Beginnings of Coordination Chemistry. *Proc. Chem. Soc.* **1959**, 73-108.

12. Ware, M., Prussian Blue: Artists' Pigment and Chemists' Sponge. *J. Chem. Educ.* **2008,** 85, (5), 612.

13. Creutz, C.; Taube, H., Direct Approach to Measuring the Franck-Condon Barrier to Electron Transfer between Metal Ions. *J. Am. Chem. Soc.* **1969,** 91, (14), 3988-3989.

14. Zhang, L. T.; Ko, J.; Ondrechen, M. J., Electronic Structure of the Creutz-Taube Ion. *J. Am. Chem. Soc.* **1987,** 109, (6), 1666-1671.

15. Creutz, C.; Taube, H., Binuclear Complexes of Ruthenium Ammines. *J. Am. Chem. Soc.* **1973,** 95, (4), 1086-1094.

16. Emeleus, H. J., *Advances in Inorganic Chemistry and Radiochemistry*. Academic Press: Burlington, MA, USA, 1968; Vol. 10.

17. Watters, K. L.; Risen Jr, W. M., Spectroscopic Studies of Metal-Metal Bonded Compounds. *Inorg. Chim. Acta Rev.* **1969,** 3, (0), 129-154.

18. Sunder, S.; Bernstein, H. J., Resonance Raman Spectra of a Complex Containing the Rhenium-Iron Bond. *Inorg. Chem.* **1974,** 13, (9), 2274-2275.

19. Baker, R. T.; Calabrese, J. C.; Glassman, T. E., Unsaturated, PCy_2-Bridged Re-M Heterobimetallics (M = rhodium, iridium, palladium; Cy = cyclohexyl): Metal-Metal Bond Isomerism, Reversible Phosphorus-Hydrogen Bond Activation and Cooperative Reactivity. *Organometallics* **1988,** 7, (8), 1889-1891.

20. Van der Graaf, T.; Hofstra, R. M. J.; Schilder, P. G. M.; Rijkhoff, M.; Stufkens, D. J.; Van der Linden, J. G. M., Metal to Ligand Charge-Transfer Photochemistry of Metal-Metal-Bonded Complexes. 10. Photochemical and Electrochemical Study of the Electron-Transfer Reactions of $Mn(CO)_3$(α-diimine)(L) (L = N-, P-donor) Radicals Formed by Irradiation of $(CO)_5MnMn(CO)_3$(α-diimine) Complexes in the Presence of L. *Organometallics* **1991,** 10, (10), 3668-3679.

21. North, T. E.; Thoden, J. B.; Spencer, B.; Dahl, L. F., Experimental/Theoretical Studies of the Paramagnetic 52/53-Electron Triangular Metal $[Ni_3(\eta^5\text{-}C_5H_5)_3(\mu^3\text{-}S)_2]^n$ series (n = 1+, 0) Containing Weak Metal-Metal Bonding Interactions: Fenske-Hall MO Analysis of the Trimetal-Antibonding Frontier Orbitals Involved in the Reversible Redox-Generated Change in Nickel-Sulfur Ni_3S_2 Core Geometry. *Organometallics* **1993,** 12, (4), 1299-1313.

22. Reger, D. L.; Mason, S. S.; Rheingold, A. L.; Haggerty, B. S.; Arnold, F. P., Syntheses and Solid State Structures of $[HB(3,5\text{-}Me_2pz)_3]InFe(CO)_4$ and $[HB(3,5\text{-}Me_2pz)_3]InW(CO)_5$ (pz =

Pyrazolyl Ring). Intermetallic Complexes with Short Metal-Metal Bonds. *Organometallics* **1994,** 13, (12), 5049-5053.

23. Barlow, S.; O'Hare, D., Metal-Metal Interactions in Linked Metallocenes. *Chem. Rev.* **1997,** 97, (3), 637-670.

24. Hunstock, E.; Mealli, C.; Calhorda, M. J.; Reinhold, J., Molecular Structures of $M_2(CO)_9$ and $M_3(CO)_{12}$ (M = Fe, Ru, Os): New Theoretical Insights. *Inorg. Chem.* **1999,** 38, (22), 5053-5060.

25. Richardson, C.; Steel, P. J.; D'Alessandro, D. M.; Junk, P. C.; Keene, F. R., Mono- and Di-nuclear Complexes of the Ligands 3,4-di(2-pyridyl)-1,2,5-oxadiazole and 3,4-di(2-pyridyl)-1,2,5-thiadiazole; New Bridges Allowing Unusually Strong Metal-Metal Interactions. *J. Chem. Soc., Dalton Trans.* **2002**, (13), 2775-2785.

26. Yip, J. H. K.; Wu, J.; Wong, K.-Y.; Ho, K. P.; So-Ngan Pun, C.; Vittal, J. J., Electronic Communication Mediated by a Pt-Pt Sigma-Bond. *Organometallics* **2002,** 21, (24), 5292-5300.

27. Petrie, S.; Stranger, R., DFT and Metal-Metal Bonding: A Dys-Functional Treatment for Multiply Charged Complexes? *Inorg. Chem.* **2004,** 43, (8), 2597-2610.

28. Gauthier, N.; Argouarch, G.; Paul, F.; Toupet, L.; Ladjarafi, A.; Costuas, K.; Halet, J.-F.; Samoc, M.; Cifuentes, M. P.; Corkery, T. C.; Humphrey, M. G., Electron-Rich Iron/Ruthenium Arylalkynyl Complexes for Third-Order Nonlinear Optics: Redox-Switching between Three States. *Chem. Eur. J.* **2011,** 17, (20), 5561-5577.

29. Andrea, R. R.; De Lange, W. G. J.; Van der Graaf, T.; Rijkhoff, M.; Stufkens, D. J.; Oskam, A., Metal to Ligand Charge-Transfer Photochemistry of Metal-Metal Bonded Complexes. 5. ESR Spectra of Stable Rhenium-α-Diimine and Spin-Trapped Manganese-α-Diimine Radicals. *Organometallics* **1988,** 7, (5), 1100-1106.

30. Balch, A. L.; Guimerans, R. R.; Linehan, J.; Olmstead, M. M.; Oram, D. E., Metal-Metal Interactions in Binuclear Complexes. Structural Characterization of Isomers Resulting from Apparent Internal Oxidative Addition of a Platinum-Chlorine Bond to a Rhodium(I) Center. *Organometallics* **1985,** 4, (8), 1445-1451.

31. Cowie, M.; Dickson, R. S.; Hames, B. W., Probing Metal-Metal Bond Reactivity in a Series of Acetylene-Bridged Binuclear Complexes and the Structure of a Methylisocyanide Adduct, $[Rh_2Cl(CNMe)_2(\mu\text{-}CF_3C_2CF_3)(Ph_2PCH_2PPh_2)_2][BF_4]$. *Organometallics* **1984,** 3, (12), 1879-1890.

32. Callahan, R. W.; Brown, G. M.; Meyer, T. J., Effects of Weak Metal-Metal Interactions in Ligand-Bridged Complexes of Ruthenium. Dimeric Complexes Containing Ruthenium Ions in Different Coordination Environments. *Inorg. Chem.* **1975,** 14, (7), 1443-1453.

33. Mueller-Westerhoff, U. T.; Eilbracht, P., Bisfulvalenediiron and its Iron(II-III) Mixed Valence System. *J. Am. Chem. Soc.* **1972,** 94, (26), 9272-9274.

34. Mueller-Westerhoff, U. T.; Eilbracht, P., Bisfulvalenediiron [Fe(III)-Fe(III)]-bis-tetrafluoroborate: Evidence for Metal-Metal Interactions Through the π-ligands of a Metallocenophane. *Tetrahedron Lett.* **1973,** 14, (21), 1855-1858.

35. Shafir, A.; Arnold, J., Stabilization of a Cationic Ti Center by a Ferrocene Moiety: Remarkably Short Ti-Fe Interaction in the Diamide $\{[(\eta^5\text{-}C_5H_4NSiMe_3)_2Fe]TiCl\}_2^{2+}$. *J. Am. Chem. Soc.* **2001,** 123, (37), 9212-9213.

36. Sato, M.; Sekino, M.; Akabori, S., $Pd(BF_4)_2$ Complexes of 1,1'-Bis(alkyl- or aryl-)thio]- and 1,1'-Bis(diphenylphosphino)-ferrocenes. Bond Formation between the Fe and Pd Atoms. *J. Organomet. Chem.* **1988,** 344, (2), C31-C34.

37. Sato, M.; Shigeta, H.; Sekino, M.; Akabori, S., Synthesis, Some Reactions, and Molecular Structure of the $Pd(BF_4)_2$ Complex of 1,1'-Bis(diphenylphosphino)ferrocene. *J. Organomet. Chem.* **1993,** 458, 199-204.

38. Hofmann, K. A.; Hoschele, K., Das Magnesiumchlorid als Mineralisator. II.: Das Urancerblau und das Wesen der konstitutiven Färbung. Das Magnesiarot und das Magnesiagrün. *Berichte der deutschen chemischen Gesellschaft* **1915,** 48, (1), 20-28.

39. Deng, H.; Shore, S. G., Direct Ytterbium-Iron Interaction in an Organometallic Ladder Polymer: Synthesis and Structure of $\{[(CH_3CN)_3YbFe(CO)_4]_2{\cdot}CH_3CN\}_\infty$. *J. Am. Chem. Soc.* **1991,** 113, (22), 8538-8540.

40. Arnold, P. L.; McMaster, J.; Liddle, S. T., An Unsupported Transition Metal-Lanthanide Bond; Synthesis and Crystal Structure of an Nd-Fe Amido N-Heterocyclic Carbene Complex. *Chem. Commun.* **2009**, (7), 818-820.

41. Butovskii, M. Ä.; Tok, O. Ä.; Wagner, F. Ä.; Kempe, R., Bismetallocenes: Lanthanoid-Transition-Metal Bonds through Alkane Elimination. *Angew. Chem. Int. Ed.* **2008,** 47, (34), 6469-6472.

42. Butovskii, M. V.; Tok, O. L.; Bezugly, V.; Wagner, F. R.; Kempe, R., Molecular Lanthanoid-Transition-Metal Cluster through C–H Bond Activation by Polar Metal-Metal Bonds. *Angew. Chem. Int. Ed.* **2011,** 50, (33), 7695-7698.

43. Spannenberg, A.; Oberthur, M.; Noss, H.; Tillack, A.; Arndt, P.; Kempe, R., Metal-Metal "Communication" of Rh or Pd with Nd in Novel Heterobinuclear Complexes. *Angew. Chem. Int. Ed.* **1998,** 37, (15), 2079-2082.

44. Beletskaya, I. P.; Voskoboynikov, A. Z.; Chuklanova, E. B.; Kirillova, N. I.; Shestakova, A. K.; Parshina, I. N.; Gusev, A. I.; Magomedov, G. K. I., Bimetallic Lanthanide Complexes with Lanthanide-Transition Metal Bonds. Molecular Structure of $(C_4H_8O)(C_5H_5)_2LuRu(CO)_2(C_5H_5)$. The Use of ^{139}La NMR Spectroscopy. *J. Am. Chem. Soc.* **1993,** 115, (8), 3156-3166.

45. Gamer, M. T.; Dehnen, S.; Roesky, P. W., Synthesis and Structure of Yttrium and Lanthanide Bis(phosphinimino)methanides. *Organometallics* **2001,** 20, (20), 4230-4236.

46. Wiecko, M.; Roesky, P. W., Gallium(I)-Lanthanide(II) Donor-Acceptor Bonds. *Organometallics* **2007,** 26, (19), 4846-4848.

47. Gardner, B. M.; McMaster, J.; Lewis, W.; Liddle, S. T., Synthesis and structure of $[\{N(CH_2CH_2NSiMe_3)_3\}URe(\eta^5\text{-}C_5H_5)_2]$: A Heterobimetallic Complex with an Unsupported Uranium-Rhenium Bond. *Chem. Commun.* **2009**, (20), 2851-2853.

48. Gardner, B. M.; McMaster, J.; Moro, F.; Lewis, W.; Blake, A. J.; Liddle, S. T., An Unsupported Uranium-Rhenium Complex Prepared by Alkane Elimination. *Chem. Eur. J.* **2011,** 17, (25), 6909-6912.

49. Liddle, S. T.; McMaster, J.; Mills, D. P.; Blake, A. J.; Jones, C.; Woodul, W. D., σ and π Donation in an Unsupported Uranium-Gallium Bond. *Angew. Chem. Int. Ed.* **2009,** 48, (6), 1077-1080.

50. Liddle, S. T.; Mills, D. P., Metal-Metal Bonds in f-element Chemistry. *Dalton Trans.* **2009**, (29), 5592-5605.

51. Bennett, R. L.; Bruce, M. I.; Stone, F. G. A., Tetrakis(pentacarbonylmanganese)uranium. *J. Organomet. Chem.* **1971,** 26, (3), 355-356.

52. Sternal, R. S.; Marks, T. J., Actinide-to-Transition Metal Bonds. Synthesis, Characterization, and Properties of Metal-Metal Bonded Systems Having the Tris(Cyclopentadienyl)Actinide Fragment. *Organometallics* **1987,** 6, (12), 2621-2623.

53. Sternal, R. S.; Brock, C. P.; Marks, T. J., Metal-Metal Bonds Involving Actinides. Synthesis and Characterization of a Complex Having an Unsupported Actinide to Transition Metal Bond. *J. Am. Chem. Soc.* **1985,** 107, (26), 8270-8272.

54. Sternal, R. S.; Sabat, M.; Marks, T. J., Metal-Metal Bonds Involving Actinides. Functionalization of Activated Carbon-Hydrogen Bonds and Unusual Oligomerization Chemistry Mediated by a Thorium-Ruthenium Complex. *J. Am. Chem. Soc.* **1987,** 109, (25), 7920-7921.

55. Ritchey, J. M.; Zozulin, A. J.; Wrobleski, D. A.; Ryan, R. R.; Wasserman, H. J.; Moody, D. C.; Paine, R. T., An Organothorium-Nickel Phosphido Complex with a Short Thorium-Nickel Distance. The Structure of $Th(\eta^5\text{-}C_5Me_5)_2(\mu\text{-}PPh_2)_2Ni(CO)_2$. *J. Am. Chem. Soc.* **1985,** 107, (2), 501-503.

56. Ortiz, J. V., Molecular Orbital Calculations on the Thorium-Nickel Interaction in $Th(\eta^5\text{-}C_5H_5)_2(\mu\text{-}PH_2)_2Ni(CO)_2$. *J. Am. Chem. Soc.* **1986,** 108, (3), 550-551.

57. Makhyoun, M. A.; El-Issa, B. D.; Salsa, B. A., A Molecular Orbital Study of the Bonding between Th and Ni in a Novel Compound. *J. Molec. Struct.: Theochem* **1987,** 153, (3-4), 241-248.

58. Hay, P. J.; Ryan, R. R.; Salazar, K. V.; Wrobleski, D. A.; Sattelberger, A. P., Synthesis and X-Ray Structure of $(C_5Me_5)_2Th(\mu\text{-}PPh_2)_2Pt(PMe_3)$: A Complex with a Thorium-Platinum bond. *J. Am. Chem. Soc.* **1986,** 108, (2), 313-315.

59. Broderick, E. M.; Guo, N.; Vogel, C. S.; Xu, C.; Sutter, J.; Miller, J. T.; Meyer, K.; Mehrkhodavandi, P.; Diaconescu, P. L., Redox Control of a Ring-Opening Polymerization Catalyst. *J. Am. Chem. Soc.* **2011,** 133, (24), 9278-9281.

60. Carver, C. T.; Benitez, D.; Miller, K. L.; Williams, B. N.; Tkatchouk, E.; Goddard, W. A.; Diaconescu, P. L., Reactions of Group III Biheterocyclic Complexes. *J. Am. Chem. Soc.* **2009,** 131, (29), 10269-10278.

61. Carver, C. T.; Monreal, M. J.; Diaconescu, P. L., Scandium Alkyl Complexes Supported by a Ferrocene Diamide Ligand. *Organometallics* **2008,** 27, (3), 363-370.

62. Diaconescu, P. L., d-Metal Complexes Supported By Ferrocene-Based Chelating Ligands. *Comments Inorg. Chem.* **2010,** 31, (5-6), 196-241.

63. Huang, W.; Khan, S. I.; Diaconescu, P. L., Scandium Arene Inverted-Sandwich Complexes Supported by a Ferrocene Diamide Ligand. *J. Am. Chem. Soc.* **2011,** 133, (27), 10410-10413.

64. Monreal, M. J.; Carver, C. T.; Diaconescu, P. L., Redox Processes in a Uranium Bis(1,1'-diamidoferrocene) Complex. *Inorg. Chem.* **2007,** 46, (18), 7226-7228.

65. Monreal, M. J.; Diaconescu, P. L., A Weak Interaction between Iron and Uranium in Uranium Alkyl Complexes Supported by Ferrocene Diamide Ligands. *Organometallics* **2008,** 27, (8), 1702-1706.

66. Williams, B. N.; Huang, W.; Miller, K. L.; Diaconescu, P. L., Group 3 Metal Complexes of Radical-Anionic 2,2'-Bipyridyl Ligands. *Inorg. Chem.* **2010,** 49, (24), 11493-11498.

67. Shafir, A.; Power, M. P.; Whitener, G. D.; Arnold, J., Synthesis, Structure, and Properties of 1,1'-Diamino- and 1,1'-Diazidoferrocene. *Organometallics* **2000,** 19, (19), 3978-3982.

68. Aguirre-Etcheverry, P.; O'Hare, D., Electronic Communication through Unsaturated Hydrocarbon Bridges in Homobimetallic Organometallic Complexes. *Chem. Rev.* **2010,** 110, (8), 4839-4864.

69. Bard, A. J.; Faulkner, L. R., *Electrochemical Methods: Fundamentals and Applications*. Wiley: 2001.

70. Barriere, F.; Camire, N.; Geiger, W. E.; Mueller-Westerhoff, U. T.; Sanders, R., Use of Medium Effects to Tune the E½ Values of Bimetallic and Oligometallic Compounds. *J. Am. Chem. Soc.* **2002,** 124, (25), 7262-7263.

71. Barriere, F.; Geiger, W. E., Use of Weakly Coordinating Anions to Develop an Integrated Approach to the Tuning of E½ Values by Medium Effects. *J. Am. Chem. Soc.* **2006,** 128, (12), 3980-3989.

72. Brownie, J. H.; Baird, M. C.; Laws, D. R.; Geiger, W. E., One-Electron Oxidations of the Methyldiphenylphosphonium Cyclopentadienylide Complexes $M(\eta^5\text{-}C_5H_4PMePh_2)(CO)_3$ (M = Cr, Mo, W): Formation and Dimerization of the 17-Electron, Metal-Centered Radicals $[M(\eta^5\text{-}C_5H_4PMePh_2)(CO)_3]^+$. *Organometallics* **2007,** 26, (24), 5890-5901.

73. Chong, D.; Laws, D. R.; Nafady, A.; Costa, P. J.; Rheingold, A. L.; Calhorda, M. J.; Geiger, W. E., $[Re(\eta^5\text{-}C_5H_5)(CO)_3]^+$ Family of 17-Electron Compounds: Monomer/Dimer Equilibria and Other Reactions. *J. Am. Chem. Soc.* **2008,** 130, (8), 2692-2703.

74. Chong, D.; Nafady, A.; Costa, P. J.; Calhorda, M. J.; Geiger, W. E., Anodic Preparation of $[Re_2Cp_2(CO)_6]^{2+}$: A Dimeric Dication that Provides the Powerful One-Electron Oxidant $[ReCp(CO)_3]^+$. *J. Am. Chem. Soc.* **2005,** 127, (45), 15676-15677.

75. Geiger, W. E., Organometallic Electrochemistry: Origins, Development, and Future. *Organometallics* **2007,** 26, (24), 5738-5765.

76. Geiger, W. E.; Van Order, N.; Pierce, D. T.; Bitterwolf, T. E.; Rheingold, A. L.; Chasteen, N. D., Class II Mixed-Valent Complexes from Oxidation of Doubly Linked (Arene)Chromium Compounds. *Organometallics* **1991,** 10, (7), 2403-2411.

77. Laws, D. R.; Chong, D.; Nash, K.; Rheingold, A. L.; Geiger, W. E., Cymantrene Radical Cation Family: Spectral and Structural Characterization of the Half-Sandwich Analogues of Ferrocenium Ion. *J. Am. Chem. Soc.* **2008,** 130, (30), 9859-9870.

78. LeSuer, R. J.; Geiger, W. E., Ligand-Solvent Interactions in a Highly Reduced Metal Chelate Complex: Medium Dependence of the One-Electron Reduction of the bis(Maleonitriledithiolato)Gold Dianion. *Inorg. Chem.* **2009,** 48, (22), 10826-10836.

79. MacLachlan, M. J.; Lough, A. J.; Geiger, W. E.; Manners, I., Synthesis, Structures, and Properties of Strained Spirocyclic [1]Sila- and [1]Germaferrocenophanes and Tetraferrocenylsilane. *Organometallics* **1998,** 17, (9), 1873-1883.

80. Nafady, A.; Chin, T. T.; Geiger, W. E., Manipulating the Electrolyte Medium to Favor Either One-Electron or Two-Electron Oxidation Pathways for (Fulvalendiyl)dirhodium Complexes. *Organometallics* **2006,** 25, (7), 1654-1663.

81. Nafady, A.; Costa, P. J.; Calhorda, M. J.; Geiger, W. E., Electrochemical Oxidation of $CoCp(CO)_2$: Radical Substrate Reaction of a 17 e^-/18 e^- Pair and Production of a Unique Dimer Radical. *J. Am. Chem. Soc.* **2006,** 128, (51), 16587-16599.

82. Swarts, J. C.; Nafady, A.; Roudebush, J. H.; Trupia, S.; Geiger, W. E., One-Electron Oxidation of Ruthenocene: Reactions of the Ruthenocenium Ion in Gentle Electrolyte Media. *Inorg. Chem.* **2009,** 48, (5), 2156-2165.

83. Geiger, W. E.; Barriere, F., Organometallic Electrochemistry Based on Electrolytes Containing Weakly-Coordinating Fluoroarylborate Anions. *Acc. Chem. Res.* **2010,** 43, (7), 1030-1039.

84. LeSuer, R. J.; Buttolph, C.; Geiger, W. E., Comparison of the Conductivity Properties of the Tetrabutylammonium Salt of Tetrakis(pentafluorophenyl)borate Anion with Those of Traditional Supporting Electrolyte Anions in Nonaqueous Solvents. *Anal. Chem.* **2004,** 76, (21), 6395-6401.

85. van Asselt, R.; Elsevier, C. J.; Amatore, C.; Jutand, A., Divalent Palladium and Platinum Complexes Containing Rigid Bidentate Nitrogen Ligands and Electrochemistry of the Palladium Complexes. *Organometallics* **1997,** 16, (3), 317-328.

86. Tennyson, A. G.; Khramov, D. M.; Varnado, C. D.; Creswell, P. T.; Kamplain, J. W.; Lynch, V. M.; Bielawski, C. W., Indirectly Connected Bis(N-Heterocyclic Carbene) Bimetallic Complexes: Dependence of Metal-Metal Electronic Coupling on Linker Geometry. *Organometallics* **2009,** 28, (17), 5142-5147.

87. Han, L.-M.; Suo, Q.-L.; Luo, M.-h.; Zhu, N.; Ma, Y.-Q., Synthesis and Determination of the Electron Transfer Numbers of Alkynyl Bridged Multiferrocenyl Derivatives. *Inorg. Chem. Commun.* **2008,** 11, (8), 873-875.

88. Nishiumi, T.; Abdul, M. M.; Aoki, K., Determination of the Number of Electrons by Chronoamperometry at Small Electrodes. *Electrochem. Commun.* **2005,** 7, (12), 1213-1217.

89. Amatore, C.; Azzabi, M.; Calas, P.; Jutand, A.; Lefrou, C.; Rollin, Y., Absolute Determination of Electron Consumption in Transient or Steady State Electrochemical Techniques. *J. Electroanal. Chem. Interfacial Electrochem.* **1990,** 288, (1-2), 45-63.

90. Baranski, A. S.; Fawcett, W. R.; Gilbert, C. M., Use of Microelectrodes for the Rapid Determination of the Number of Electrons Involved in an Electrode Reaction. *Anal. Chem.* **1985,** 57, (1), 166-170.

91. Forster, R. J., Microelectrodes: New Dimensions in Electrochemistry. *Chem. Soc. Rev.* **1994,** 23, (4), 289-297.

92. Butler, I. R.; Cullen, W. R.; Kim, T. J.; Rettig, S. J.; Trotter, J., 1,1'-Bis(alkylarylphosphino)ferrocenes: Synthesis, Metal Complex Formation, and Crystal Structure of Three Metal Complexes of $Fe(\eta^5\text{-}C_5H_4PPh_2)_2$. *Organometallics* **1985,** 4, (6), 972-980.

93. Cullen, W. R.; Kim, T. J.; Einstein, F. W. B.; Jones, T., Structures of Three Hydrogenation Catalysts [(P-P)Rh(NBD)]ClO4 and Some Comparative Rate Studies. *Organometallics* **1985,** 4, (2), 346-351.

94. Bandoli, G.; Trovo, G.; Dolmella, A.; Longato, B., cis-Bis(phosphine)platinum(II) Complexes with Pyrimidyl Nucleobases. Synthesis, Characterization, and Crystal Structures of cis-(1-methylthyminato-N^3)(N,N-dimethylformamide-O)(1,1'-bis(diphenylphosphino)ferrocene)platinum(II) tetrafluoroborate-dichloromethane, [(dppf)Pt(1-MeTy(-H))(DMF)]BF4·CH2Cl2, and cis-(1-methylthyminato-N3)(1-methylcytosine-N3)(1,1'-bis(diphenylphosphino)ferrocene)platinum(II) tetrafluoroborate, [(dppf)Pt(1-MeTy(-H))(1-MeCy)]BF4. *Inorg. Chem.* **1992,** 31, (1), 45-51.

95. Watson, W. H.; Nagl, A.; Hwang, S.; Richmond, M. G., 1,1'-Bis(diphenylphosphino)ferrocene Ligand Substitution in the Benzylidyne-Capped Cluster $PhCCo_3(CO)_9$. Synthesis, X-ray Structure, and Redox Reactivity of $PhCCo_3(CO)_7$(dppf). *J. Organomet. Chem.* **1993,** 445, (1-2), 163-170.

96. Gan, K.-S.; Hor, T. S. A., 1,1'-Bis(diphenylphosphino)ferrocene: Coordination Chemistry, Organic Synthesis, and Catalysis. In *Ferrocenes: Homogeneous Catalysis, Organic Synthesis, Materials Science*, Togni, A.; Hayashi, T., Eds. VCH Publishers: New York, 1995; pp 3-96.

97. Barr, T. H.; Watts, W. E., Bridged Ferrocenes II: Conformational Properties of [*m*]ferrocenophanes. *Tetrahedron* **1968,** 24, (19), 6111-6118.

98. Barr, T. H.; Bolton, E. S.; Lentzner, H. L.; Watts, W. E., Bridged Ferrocenes IV: Steric and Conformational Effects in the Acetylation of [*m*]ferrocenophanes. *Tetrahedron* **1969,** 25, (21), 5245-5253.

99. Berces, A.; Ziegler, T.; Fan, L., Density Functional Study of the Harmonic Force Fields of Cyclopentadienyl Anion, Cyclopentadienyl Lithium, and Ferrocene. *J. Chem. Phys.* **1994,** 98, (6), 1584-1595.

100. Ballhausen, C. J.; Dahl, J. P.; Buchardt, O.; Olsen, G. E.; Pedersen, C.; Toft, J., Molecular Orbitals for the Protonated Sandwich Compounds. *Acta Chem. Scand.* **1961,** 15, 1333-1336.

101. Dong, T.-Y.; Lee, S.-H., The Effects of an Interannular Bridge on th Electronic Structure of Ferrocenium Cations. *J. Organomet. Chem.* **1995,** 487, (1-2), 77-88.

102. Chen, J.-A.; Lee, T.-S.; Dong, T.-Y.; Lee, S.-L., Effect of Twisting Mode on Electron-Transfer Rate of Mixed-Valence Biferrocenium Systems. *Chem. Phys. Lett.* **1993,** 205, (1), 80-84.

103. Dong, T. Y.; Schei, C. C.; Hwang, M. Y.; Lee, T. Y.; Yeh, S. K.; Wen, Y. S., Pronounced Effect of Substituents on the Intramolecular Electron-Transfer Rates in Mixed-Valence Biferrocenium Triiodide Complexes. *Organometallics* **1992,** 11, (2), 573-582.

104. Seyferth, D.; Withers, H. P., Phosphorus- and Arsenic-Bridged [1]Ferrocenophanes. Synthesis and Characterization. *Organometallics* **1982,** 1, (10), 1275-1282.

105. Hillman, M.; Kvick, A., Structural Consequences of Oxidation of Ferrocene Derivatives. 1. [0.0]Ferrocenophanium Picrate Hemihydroquinone. *Organometallics* **1983,** 2, (12), 1780-1785.

106. Mueller-Westerhoff, U. T., [m.m]Metallocenophanes: Synthesis, Structure, and Properties. *Angew. Chem., Int. Ed.* **1986,** 25, (8), 702-717.

107. Dahl, L. F.; Connelly, N. G., Organometallic Chalcogen Complexes. XX. Stereochemical Characterization of an Oxidized Iron-Sulfur Dimer, $[Fe(\eta_5\text{-}C_5H_5)(CO)(SCH_3)]^{2+}$. Paramagnetic Cation Effectively Containing a One-Electron Metal-Metal Bond. *J. Am. Chem. Soc.* **1970,** 92, (25), 7472-7474.

108. de Beer, J. A.; Haines, R. J.; Greatrex, R.; van Wyk, J. A., Reactions of Metal Carbonyl Derivatives. Part XV. Oxidation Studies of Some H-Cyclopentadienyl Bridging Sulphido- and Phosphino-Derivatives of Iron. *J. Chem. Soc., Dalton Trans.* **1973**, (21), 2341-2346.

109. Mason, R.; Mingos, D. M. P., Geometries of and Bonding in Bi- and Polynuclear Metal Complexes with Bridging Ligands. *J. Organomet. Chem.* **1973,** 50, (1), 53-61.

110. Pohl, S.; Saak, W., Die Kristallstrukturen von zwei Modifikationen von $(C_2H_5)_4NFeI_4$. *Z. Anorg. Allg. Chem.* **1985,** 523, (4), 25-32.

111. Kramer, J. A.; Hendrickson, D. N., Electron Transfer in Mixed-Valent Diferrocenylacetylene and [2.2]ferrocenophane-1,13-diyne. *Inorg. Chem.* **1980,** 19, (11), 3330-3337.

112. Beveridge, D.; Day, P., Charge Transfer in Mixed-Valence Solids. Part 9. Preparation, Characterization, and Optical Spectroscopy of the Mixed-Valence Mineral Voltaite [Aluminium Pentairon(II) Tri-Iron(III) Dipotassium Dodecasulphate 18-Hydrate] and its Solid Solutions with Cadmium(II). *J. Chem. Soc., Dalton Trans.* **1979**, (4), 648-653.

113. D'Alessandro, D. M.; Keene, F. R., Intervalence Charge Transfer (IVCT) in Trinuclear and Tetranuclear Complexes of Iron, Ruthenium, and Osmium. *Chem. Rev.* **2006,** 106, (6), 2270-2298.

114. Morrison, J. W. H.; Hendrickson, D. N., Intervalence Transfer in Biferricenium and Biferricenylenium Cations. *J. Chem. Phys.* **1973,** 59, (1), 380-386.

115. Hush, N. S., Intervalence-Transfer Absorption. Part 2. Theoretical Considerations and Spectroscopic Data. In *Prog. Inorg. Chem.*, John Wiley & Sons, Inc.: 2007; pp 391-444.

116. Launay, J.-P., Long-Distance Intervalence Electron Transfer. *Chem. Soc. Rev.* **2001,** 30, (6), 386-397.

117. Nugent, L. J.; Baybarz, R. D.; Burnett, J. L.; Ryan, J. L., Electron-Transfer and f→d Absorption Bands of Some Lanthanide and Actinide Complexes and the Standard (III/IV) Oxidation Potential for Each Member of the Lanthanide and Actinide Series *J. Inorg. Nucl. Chem.* **1971,** 33, (8), 2503-2530.

118. Nugent, L. J.; Baybarz, R. D.; Burnett, J. L.; Ryan, J. L., Electron-Transfer and f→d Absorption Bands of Some Lanthanide and Actinide Complexes and the Standard (II-III) Oxidation Potential for Each Member of the Lanthanide and Actinide Series. *J. Chem. Phys.* **1973,** 77, (12), 1528-1539.

119. Bagnall, K. W.; Brown, D.; Colton, R., The Magnetic and Spectral Properties of Some Uranium(IV) Complexes. *J. Chem. Soc. (Resumed)* **1964**, 2527-2530.

120. Bagnall, K. W.; Payne, G. F.; Alcock, N. W.; Flanders, D. J.; Brown, D., Actinide Structural Studies. Part 8. Some New Oxygen-Donor Complexes of Trichloro(Cyclopentadienyl)Neptunium(IV); The Crystal Structure of trichloro(η^5-cyclopentadienyl)bis(methyldiphenylphosphine oxide)neptunium(IV). *J. Chem. Soc., Dalton Trans.* **1986**, (4), 783-787.

121. Moeller, T., Periodicity and the Lanthanides and Actinides. *J. Chem. Educ.* **1970,** 47, (6), 417.

122. Denning, R. G., Electronic Structure and Bonding in Actinyl Ions and their Analogs. *J. Chem. Phys. A* **2007,** 111, (20), 4125-4143.

123. Krupa, J. C., High-Energy Optical Absorption in f-Compounds. *J. Solid State Chem.* **2005,** 178, (2), 483-488.

124. Krupa, J. C., Optical Excitations in Lanthanide and Actinide Compounds. *J. Alloys Compd.* **1995,** 225, (1-2), 1-10.

125. Gutniak, S.; Taube, M., Electronic Absorption Spectra of Uranium(IV) Chlorides in Some Organic Solvents and Fused Chlorides. *Spectrochim. Acta* **1964,** 20, (10), 1627-1632.

126. Edelstein, N. M., Comparison of the Electronic Structure of the Lanthanides and Actinides. *J. Alloys Compd.* **1995,** 223, (2), 197-203.

127. Beattie, W. H.; Maier Ii, W. B.; Holland, R. F., Spectroscopy of Solutions of Uranium(IV) Chlorides at Low Temperatures between 330 and 2500 nm. *Spectrochim. Acta A* **1984,** 40, (10), 897-906.

128. Armstrong, A. T.; Smith, F.; Elder, E.; McGlynn, S. P., Electronic Absorption Spectrum of Ferrocene. *J. Chem. Phys.* **1967,** 46, (11), 4321-4328.

129. Bigeleisen, J., Erratum: Statistical Mechanics of Isotope Effects on the Thermodynamic Properties of Condensed Systems. *J. Chem. Phys.* **1961,** 35, (6), 2246-2246.

130. Scott, D. R.; Becker, R. S., Ligand Field Absorption Bands and d-orbital Splitting in Ferrocene. *J. Organomet. Chem.* **1965,** 4, (5), 409-411.

131. Dowben, P. A.; Driscoll, D. C.; Tate, R. S.; Boag, N. M., Comparison of the Electronic Structures of Disubstituted Ferrocenes. *Organometallics* **1988,** 7, (2), 305-308.

132. Gray, H. B.; Sohn, Y. S.; Hendrickson, N., Electronic Structure of Metallocenes. *J. Am. Chem. Soc.* **1971,** 93, (15), 3603-3612.

133. Rohmer, M.-M.; Veillard, A.; Wood, M. H., Excited States and Electronic Spectrum of Ferrocene. *Chem. Phys. Lett.* **1974,** 29, (3), 466-468.

134. Weinmayr, V., The Condensation of Dicyclopentadienyliron with Aromatic Diazonium Salts. *J. Am. Chem. Soc.* **1955,** 77, (11), 3012-3014.

135. Prins, R., Visible Absorption Spectra of Substituted Ferricenium Cations. *J. Chem. Soc. D: Chem. Commun.* **1970**, (5), 280-281.

136. Avens, L. R.; Bott, S. G.; Clark, D. L.; Sattelberger, A. P.; Watkin, J. G.; Zwick, B. D., A Convenient Entry into Trivalent Actinide Chemistry: Synthesis and Characterization of $AnI_3(THF)_4$ and $An[N(SiMe_3)_2]_3$ (An = U, Np, Pu). *Inorg. Chem.* **1994,** 33, (10), 2248-2256.

137. Cohen, D.; Carnall, W. T., Absorption Spectra of Uranium(III) and Uranium(IV) in $DClO_4$ Solution. *J. Chem. Phys.* **1960,** 64, (12), 1933-1936.

138. Monreal, M. J.; Thomson, R. K.; Cantat, T.; Travia, N. E.; Scott, B. L.; Kiplinger, J. L., $UI_4(1,4\text{-dioxane})_2$, $[UCl_4(1,4\text{-dioxane})]_2$, and $UI_3(1,4\text{-dioxane})_{1.5}$: Stable and Versatile Starting Materials for Low- and High-Valent Uranium Chemistry. *Organometallics* **2011,** 30, (7), 2031-2038.

139. Schnaars, D. D.; Wu, G.; Hayton, T. W., Reactivity of UH_3 with Mild Oxidants. *Dalton Trans.* **2008**, (44), 6121-6126.

140. Van der Sluys, W. G.; Huffman, J. C.; Ehler, D. S.; Sauer, N. N., Dissolution of Uranium Metal Using Iodine and Isopropyl Alcohol. Synthesis and X-Ray Crystal Structure of Tetraiodotetrakis(Isopropoxo)Bis(Isopropanol)Diuranium. *Inorg. Chem.* **1992,** 31, (8), 1316-1318.

141. Schnaars, D. D.; Wu, G.; Hayton, T. W., Reactivity of $UI_4(OEt_2)_2$ with Phenols: Probing the Chemistry of the U-I Bond. *Dalton Trans.* **2009**, (19), 3681-3687.

142. Carmichael, C. D.; Jones, N. A.; Arnold, P. L., Low-Valent Uranium Iodides: Straightforward Solution Syntheses of UI_3 and UI_4 Etherates. *Inorg. Chem.* **2008,** 47, (19), 8577-8579.

143. Kirm, M.; Krupa, J. C.; Makhov, V. N.; Negodin, E.; Zimmerer, G.; Gesland, J. Y., 6d5f and $5f^2$ Configurations of U^{4+} Doped into $LiYF_4$ and YF_3 Crystals. *J. Lumin.* **2003,** 104, (1-2), 85-92.

144. Godbole, S. V.; Page, A. G.; Sangeeta; Sabharwal, S. C.; Gesland, J. Y.; Sastry, M. D., UV Luminescence of U^{4+} Ions in $LiYF_4$ Single Crystal: Observation of $5f^26d^1 \rightarrow 5f^2$ Transitions. *J. Lumin.* **2001,** 93, (3), 213-221.

145. Berg, J. M.; Sattelberger, A. P.; Morris, D. E.; Van der Sluys, W. G.; Fleig, P., Ion Pairing and Solvation Effects in the intra-5f2 Absorption Spectra of Dimeric Uranium(IV) Alkoxide Complexes. *Inorg. Chem.* **1993,** 32, (5), 647-653.

146. Cho, Y. H.; Kim, T.-J.; Bae, S. E.; Park, Y. J.; Ahn, H. J.; Song, K., Electronic Absorption Spectra of U(III) Ion in a LiCl–KCl Eutectic Melt at 450 °C. *Microchem. J.* **2010,** 96, (2), 344-347.

147. Krupa, J. C., Spectroscopic Properties of Tetravalent Actinide Ions in Solids. *Inorg. Chim. Acta* **1987,** 139, (1-2), 223-241.

148. Poturaj-Gutniak, S.; Taube, M., Some Remarks about 5f-6d and Charge Transfer Transitions in Uranium(IV) and Plutonium(IV) Complexes. *J. Inorg. Nucl. Chem.* **1968,** 30, (4), 1005-1012.

149. Huheey, J. E.; Keiter, E. A.; Keiter, R. L., *Inorganic Chemistry: Principles of Structure and Reactivity*. HarperCollins College Publishers: New York, NY, 1993.

150. Day, P., Electronic Spectra. In *Electronic Structure and Magnetism of Inorganic Compounds*, Day, P., Ed. The Royal Society of Chemistry: 1974; Vol. 3, pp 1-124.

151. Komyak, A.; Zazhogin, A.; Umreiko, D.; Lugovsky, A., Electronic Spectra of Uranium Tetrachloride Clusters with Electron-Donor Ligands. *J. Appl. Spectrosc.* **2009,** 76, (2), 167-173.

152. Lam, O. P.; Feng, P. L.; Heinemann, F. W.; O'Connor, J. M.; Meyer, K., Charge-Separation in Uranium Diazomethane Complexes Leading to C–H Activation and Chemical Transformation. *J. Am. Chem. Soc.* **2008,** 130, (9), 2806-2816.

153. Castro-Rodriguez, I.; Meyer, K., Small Molecule Activation at Uranium Coordination Complexes: Control of Reactivity via Molecular Architecture. *Chem. Commun.* **2006**, (13), 1353-1368.

154. Matson, E. M.; Forrest, W. P.; Fanwick, P. E.; Bart, S. C., Functionalization of Carbon Dioxide and Carbon Disulfide Using a Stable Uranium(III) Alkyl Complex. *J. Am. Chem. Soc.* **2011,** 133, (13), 4948-4954.

155. Mizuno, M.; Tanaka, J.; Harada, I., Electronic Spectra and Structures of Polyiodide Chain Complexes. *J. Chem. Phys.* **1981,** 85, (13), 1789-1794.

156. Svensson, P. H.; Kloo, L., Synthesis, Structure, and Bonding in Polyiodide and Metal Iodide-Iodine Systems. *Chem. Rev.* **2003,** 103, (5), 1649-1684.

157. Dong, T. Y.; Hsu, T. L., Electron Transfer in Mixed-Valence 1,1'-Bis(triphenylmethyl)biferrocenium Triiodide. *J. Organomet. Chem.* **1989,** 367, (3), 313-319.

158. Allsopp, C. B., The Absorption Spectra of Triiodides. *Proc. R. Soc. A* **1937,** 158, (893), 167-181.

159. Pflaum, R. T.; Howick, L. C., Spectrophotometric Determination of Potassium with Sodium Tetraphenylborate. *Anal. Chem.* **1956,** 28, (10), 1542-1544.

160. Covington, A. K.; Tait, M. J., Sodium and Potassium Tetraphenylborate Solutions in Water and 65% Dioxane-Water Mixture. II. Spectrophotometric Studies. *Electrochim. Acta* **1967,** 12, (2), 123-130.

161. Da Re, R. E.; Jantunen, K. C.; Golden, J. T.; Kiplinger, J. L.; Morris, D. E., Molecular Spectroscopy of Uranium(IV) Bis(ketimido) Complexes. Rare Observation of Resonance-

Enhanced Raman Scattering from Organoactinide Complexes and Evidence for Broken-Symmetry Excited States. *J. Am. Chem. Soc.* **2004,** 127, (2), 682-689.

162. Berg, J. M.; Clark, D. L.; Huffman, J. C.; Morris, D. E.; Sattelberger, A. P.; Streib, W. E.; Van der Sluys, W. G.; Watkin, J. G., Early Actinide Alkoxide Chemistry. Synthesis, Characterization, and Molecular Structures of Thorium(IV) and Uranium(IV) Aryloxide Complexes. *J. Am. Chem. Soc.* **1992,** 114, (27), 10811-10821.

163. Nocton, G.; Horeglad, P.; Vetere, V.; Pecaut, J.; Dubois, L.; Maldivi, P.; Edelstein, N. M.; Mazzanti, M., Synthesis, Structure, and Bonding of Stable Complexes of Pentavalent Uranyl. *J. Am. Chem. Soc.* **2009,** 132, (2), 495-508.

164. Morris, D. E.; Da Re, R. E.; Jantunen, K. C.; Castro-Rodriguez, I.; Kiplinger, J. L., Trends in Electronic Structure and Redox Energetics for Early-Actinide Pentamethylcyclopentadienyl Complexes. *Organometallics* **2004,** 23, (22), 5142-5153.

165. Graves, C. R.; Yang, P.; Kozimor, S. A.; Vaughn, A. E.; Clark, D. L.; Conradson, S. D.; Schelter, E. J.; Scott, B. L.; Thompson, J. D.; Hay, P. J.; Morris, D. E.; Kiplinger, J. L., Organometallic Uranium(V)-Imido Halide Complexes: From Synthesis to Electronic Structure and Bonding. *J. Am. Chem. Soc.* **2008,** 130, (15), 5272-5285.

166. Graves, C. R.; Scott, B. L.; Morris, D. E.; Kiplinger, J. L., Facile Access to Pentavalent Uranium Organometallics: One-Electron Oxidation of Uranium(IV) Imido Complexes with Copper(I) Salts. *J. Am. Chem. Soc.* **2007,** 129, (39), 11914-11915.

167. Schelter, E. J.; Yang, P.; Scott, B. L.; Thompson, J. D.; Martin, R. L.; Hay, P. J.; Morris, D. E.; Kiplinger, J. L., Systematic Studies of Early Actinide Complexes: Uranium(IV) Fluoroketimides. *Inorg. Chem.* **2007,** 46, (18), 7477-7488.

168. Graves, C. R.; Scott, B. L.; Morris, D. E.; Kiplinger, J. L., Tetravalent and Pentavalent Uranium Acetylide Complexes Prepared by Oxidative Functionalization with CuCCPh. *Organometallics* **2008,** 27, (14), 3335-3337.

169. Taube, H., Electronic Coupling Mechanisms in Mixed-Valence Molecules. *Ann. N.Y. Acad. Sci.* **1978,** 313, (1), 481-495.

170. Ryan, J. L., Weak or Unstable Iodo Complexes. II. Iodo Complexes of Titanium(IV), Iron(III), And Gold(III). *Inorg. Chem.* **1969,** 8, (10), 2058-2062.

171. Marcus, R. A., On the Theory of Oxidation-Reduction Reactions Involving Electron Transfer. I. *J. Chem. Phys.* **1956,** 24, (5), 966-978.

172. Marcus, R. A., On the Theory of Oxidation-Reduction Reactions Involving Electron Transfer. II. Applications to Data on the Rates of Isotopic Exchange Reactions. *J. Chem. Phys.* **1957,** 26, (4), 867-871.

173. Hush, N. S., Homogeneous and Heterogeneous Optical and Thermal Electron Transfer. *Electrochim. Acta* **1968,** 13, (5), 1005-1023.

174. Hush, N. S., Distance Dependence of Electron Transfer Rates. *Coord. Chem. Rev.* **1985,** 64, (0), 135-157.

175. Miessler, G. L.; Tarr, D. A., *Inorganic Chemistry*. Prentice Hall: 2010.

176. Cowan, D. O.; LeVanda, C.; Park, J.; Kaufman, F., Organic Solid State. VIII. Mixed-Valence Ferrocene Chemistry. *Acc. Chem. Res.* **1973,** 6, (1), 1-7.

177. Yoon, K. B.; Kochi, J. K., Ferric Iodide as a Nonexistent Compound. *Inorg. Chem.* **1990,** 29, (4), 869-874.

178. Yoon, K. B.; Kochi, J. K., Isolation and Spectral Characteristics of Ferric Iodide. *Z. Anorg. Allg. Chem.* **1988,** 561, (1), 174-184.

179. Nesmejanow, A. N.; Perewalowa, E. G.; Jurjewa, L. P., Unmittelbare Cyanierung der Ferriciniumsalze. *Chem. Ber.* **1960,** 93, (11), 2729-2735.

180. Nesmeyanov, A. N.; Perevalova, E. G.; Leoateva, L. I., Ferrocenylethylene Cationic Complex of π-Cyclopentadienyliron Dicarbonyl. *Russ. Chem. Bull.* **1977,** 26, (11), 2391-2393.

181. Nesmeyanov, A. N.; Yureva, L. P.; Materikova, R. B.; Getnarski, B. Y., Stability of Some Ferricinium Salts. *Russ. Chem. Bull.* **1965,** 14, (4), 711-713.

182. Spilners, I. J., Ferricinium Salts. *J. Organomet. Chem.* **1968,** 11, (0), 381-384.

183. Stukan, R. A.; Yureva, L. P., Investigation of Ferricinium Ferrichloride with Nuclear Gamma-Resonance Method. *Dokl. Akad. Nauk. SSSR+* **1966,** 167, (6), 1311.

184. Aharoni, S. M.; Litt, M. H., The Preparation and Some Properties of Ferricinium Trichloroferrate(II) and Ferricinium Tribromoferrate(II). *J. Organomet. Chem.* **1970,** 22, (1), 171-177.

185. Bignozzi, C. A.; Roffia, S.; Chiorboli, C.; Davila, J.; Indelli, M. T.; Scandola, F., Oligomeric Dicyanobis(Polypyridine)Ruthenium(II) Complexes. Synthesis, Spectroscopic, and Photophysical Properties. *Inorg. Chem.* **1989,** 28, (24), 4350-4358.

186. Katz, N. E.; Creutz, C.; Sutin, N., 4-Cyanopyridine-Bridged Binuclear and Trinuclear Complexes of Ruthenium and Iron. *Inorg. Chem.* **1988,** 27, (10), 1687-1694.

187. Bignozzi, C. A.; Argazzi, R.; Chiorboli, C.; Scandola, F.; Dyer, R. B.; Schoonover, J. R.; Meyer, T. J., Vibrational and Electronic Spectroscopy of Electronically Excited Polychromophoric Ruthenium(II) Complexes. *Inorg. Chem.* **1994,** 33, (8), 1652-1659.

188. Coe, B. J.; Meyer, T. J.; White, P. S., Cyano-Bridged Complexes of trans-Tetrakis(pyridine)ruthenium(II). *Inorg. Chem.* **1995,** 34, (14), 3600-3609.

189. Donoli, A.; Bisello, A.; Cardena, R.; Benetollo, F.; Ceccon, A.; Santi, S., Single Two-Electron Transfers and Successive One-Electron Transfers in Biferrocenyl-Indacene Isomers. *Organometallics* **2011,** 30, (5), 1116-1121.

190. Edelstein, N. M.; Lander, G. H., Magnetic Properties. In *The Chemistry of the Actinide and Transactinide Elements*, Morss, L. R.; Edelstein, N. M.; Fuger, J., Eds. Springer Netherlands: 2011; pp 2225-2306.

191. Fazekas, P., *Lecture Notes on Electron Correlation and Magnetism*. World Scientific: 1999.

192. Lu, S.; Strelets, V. V.; Ryan, M. F.; Pietro, W. J.; Lever, A. B. P., Electrochemical Parametrization in Sandwich Complexes of the First Row Transition Metals. *Inorg. Chem.* **1996,** 35, (4), 1013-1023.

193. Schelter, E. J.; Morris, D. E.; Scott, B. L.; Thompson, J. D.; Kiplinger, J. L., Toward Actinide Molecular Magnetic Materials: Coordination Polymers of U(IV) and the Organic Acceptors TCNQ and TCNE. *Inorg. Chem.* **2007,** 46, (14), 5528-5536.

194. Dawson, J. K., Magnetochemistry of the Heaviest Elements. Part III. The Halides of Ter- and Quadri-Valent Uranium. *J. Chem. Soc. (Resumed)* **1951**, 429-431.

195. Menzel, D. H., *Fundamental Formulas of Physics*. Dover Publications: 1955.

196. Greenwood, N. N.; Earnshaw, A., Chemistry of the Elements In 2nd ed.; Elsevier: 1998.

197. Bruce, D. W.; O'Hare, D., *Inorganic Materials*. Wiley: 1997.

198. Re, N.; Gallo, E.; Floriani, C.; Miyasaka, H.; Matsumoto, N., Magnetic Properties of a One-Dimensional Ferromagnet Containing a Mn(III)-NC-Fe(III) Linkage: Synthesis and Crystal Structure of a Chainlike $[Mn(acacen)Fe(CN)_6]_n^{2n-}$ Polyanion. *Inorg. Chem.* **1996,** 35, (21), 6004-6008.

199. Smith, J. A.; Galan-Mascaros, J.-R.; Clerac, R.; Dunbar, K. R., $\{Mn(OH_2)_2[Mn(bpym)(OH_2)]_2[Fe(CN)_6]_2\}_\infty$: A Two-Dimensional Ferrimagnet with a Partial Cubane Motif. *Chem. Commun.* **2000**, (12), 1077-1078.

200. Buschow, K. H. J.; de Boer, F. R., *Physics of Magnetism and Magnetic Materials*. Kluwer Academic/Plenum Publishers: New York, 2003; p vii, 182 p.

201. Givord, D., Introduction to Magnetism and Magnetic Materials. In *Magnetism and Synchrotron Radiation*, Beaurepaire, E.; Kappler, J.; Krill, G.; Scheurer, F., Eds. Springer Berlin / Heidelberg: 2001; Vol. 565, pp 3-23.

202. Mochida, T.; Koinuma, T.; Akasaka, T.; Sato, M.; Nishio, Y.; Kajita, K.; Mori, H., Hexagonal Supramolecular Architectures from Ferrocenium Cations Incorporating $[Ni(mnt)_2]^-$ Columns: Structures and Properties of [Alkylferrocene][$Ni(mnt)_2$]$^-$ Charge-Transfer Complexes (mnt=maleonitriledithiolate). *Chem. Eur. J.* **2007,** 13, (6), 1872-1881.

203. Mochida, T.; Takazawa, K.; Matsui, H.; Takahashi, M.; Takeda, M.; Sato, M.; Nishio, Y.; Kajita, K.; Mori, H., Biferrocene-$M(mnt)_2$ Charge-Transfer Complexes (M = Ni, Co; mnt = Maleonitriledithiolate). Structure, Valence States, and Magnetic Properties. *Inorg. Chem.* **2005,** 44, (23), 8628-8641.

204. Gama, V.; Almeida, M., Metallocenium Salts of Transition Metal Bisdichalcogenate Anions; Structure and Magnetic Properties. In *Conducting and Magnetic Organometallic Molecular Materials*, Fourmigué, M.; Ouahab, L., Eds. Springer Berlin / Heidelberg: 2009; Vol. 27, pp 97-140.

205. Moureen, C. K.; Stephanie, L. M.; Daniel, P. S.; Ram, S., Evolution of Magnetic Properties in the Normal Spinel Solid Solution $Mg_xCu_xCr_2O_4$. *J. Phys.: Condens. Matter* **2012,** 24, (4), 046003.

206. Faulmann, C.; Rivière, E.; Dorbes, S.; Senocq, F.; Coronado, E.; Cassoux, P., Ferromagnetism in $[Mn(Cp^*)_2]^+$-Derived Complexes: the "Miraculous" Stacking in $[Mn(Cp^*)_2][Ni(dmit)_2]$. *Eur. J. Inorg. Chem.* **2003,** 2003, (15), 2880-2888.

207. Miller, J. S.; Epstein, A. J., Organic and Organometallic Molecular Magnetic Materials-Designer Magnets. *Angew. Chem., Int. Ed.* **1994,** 33, (4), 385-415.

208. Hobi, M.; Gramlich, V.; Burckhardt, U.; Mensing, C.; Spahr, M.; Togni, A., Paramagnetic and Semiconducting 1:1 Salts of 1,1'-Disubstituted Ferrocenes and $[Ni(mnt)_2]^-$. Synthesis, Structure, and Physical Properties. *Organometallics* **1996,** 15, (25), 5342-5346.

209. Miller, J. S.; Epstein, A. J.; Reiff, W. M., Ferromagnetic Molecular Charge-Transfer Complexes. *Chem. Rev.* **1988,** 88, (1), 201-220.

210. Miller, J. S.; Epstein, A. J.; Silver, J., Organometallic Ferromagnets [and Discussion]. *Phil. Trans. R. Soc. A* **1990,** 330, (1610), 205-215.

211. Miller, J. S.; Glatzhofer, D. T.; O'Hare, D. M.; Reiff, W. M.; Chakraborty, A.; Epstein, A. J., Ferromagnetic Behavior in Linear Charge-Transfer Complexes. Structural and Magnetic Characterization of Octamethylferrocene: $[Fe(C_5Me_4H)_2]^+[A]^-$ (A = TCNE, TCNQ). *Inorg. Chem.* **1989,** 28, (15), 2930-2939.

212. Friedt, J. M.; Petridis, D.; Sanchez, J. P.; Reschke, R.; Trautwein, A., Structural and Magnetic Properties of $N(C_2H_5)_4FeI_4$ and $N(C_4H_9)_4FeI_4$ from Combined ^{57}Fe and ^{129}I Mössbauer Spectroscopies. *Phys. Rev. B* **1979,** 19, (1), 360-364.

213. Bancroft, G. M.; Maddock, A. G.; Ong, W. K.; Prince, R. H., Spectra of Chloroferrate(III) Compounds. *J. Chem. Soc. A* **1966**, 723-725.

214. Clark, R. J. H.; Nyholm, R. S.; Taylor, F. B., The Magnetic Susceptibility of Some Tetrahedral Tetrahalogenoferrate(II) Complexes. *J. Chem. Soc. A* **1967**, 1802-1804.

215. Flandrois, S.; Boukhari, A.; Pron, A.; Zagorska, M., Magnetic Susceptibility and Structural Studies of Polyacetylene Tetrachloroferrate, $[CH(FeCl_4)_y]_x$. *Solid State Commun.* **1988,** 67, (5), 471-475.

216. Friedman, H. L., The Visible and Ultraviolet Absorption Spectrum of the Tetrachloroferrate(III) Ion in Various Media. *J. Am. Chem. Soc.* **1952,** 74, (1), 5-10.

217. Furlani, C.; Cervone, E.; Valenti, V., Electronic Structure and Spectra of Tetrahalogenoferrates(II). *J. Inorg. Nucl. Chem.* **1963,** 25, (2), 159-163.

218. Pangborn, A. B.; Giardello, M. A.; Grubbs, R. H.; Rosen, R. K.; Timmers, F. J., Safe and Convenient Procedure for Solvent Purification. *Organometallics* **1996,** 15, (5), 1518-1520.

219. Thomson, R. K.; Scott, B. L.; Morris, D. E.; Kiplinger, J. L., Synthesis, Structure, Spectroscopy and Redox Energetics of a Series of Uranium(IV) Mixed-Ligand Metallocene Complexes. *C. R. Chim.* **2010,** 13, (6-7), 790-802.

220. Bailey, P. J.; Coxall, R. A.; Dick, C. M.; Fabre, S.; Henderson, L. C.; Herber, C.; Liddle, S. T.; Lorono-Gonzalez, D.; Parkin, A.; Parsons, S., The First Structural Characterisation of a Group 2 Metal Alkylperoxide Complex: Comments on the Cleavage of Dioxygen by Magnesium Alkyl Complexes. *Chem. Eur. J.* **2003,** 9, (19), 4820-4828.

221. Shafir, A.; Power, M. P.; Whitener, G. D.; Arnold, J., Silylated 1,1'-Diaminoferrocene: Ti and Zr Complexes of a New Chelating Diamide Ligand. *Organometallics* **2001,** 20, (7), 1365-1369.

222. Shafir, A.; Arnold, J., Zirconium Complexes Incorporating Diaryldiamidoferrocene Ligands: Generation of Cationic Derivatives and Polymerization Activity Towards Ethylene and 1-Hexene. *Inorg. Chim. Acta* **2003,** 345, (0), 216-220.

223. Siemeling, U.; Farber, C.; Leibold, M.; Bruhn, C.; Mucke, P.; Winter, R. F.; Sarkar, B.; von Hopffgarten, M.; Frenking, G., Six-Membered N-Heterocyclic Carbenes with a 1,1'-Ferrocenediyl Backbone: Bulky Ligands with Strong Electron-Donor Capacity and Unusual Non-Innocent Character. *Eur. J. Inorg. Chem.* **2009,** 2009, (31), 4607-4612.